

**Y. Hayashi**

Asst. Professor.

**T. Komori**

Asst. Professor.

Faculty of Engineering,  
Kanazawa University, Kanazawa, Japan

**K. Katayama**

Professor,  
Faculty of Engineering,  
Tokyo Institute of Technology, Tokyo, Japan

# Analytical and Experimental Investigation of Self-Freezing

*The problems of the self-freezing of a wet substance were treated as a heat conduction problem with phase change in the case of multiphase substance. The solutions for this problem were derived from the analytical procedure of Neumann's solution and were compared with the experimental results obtained through the self-freezing of the bed with wet glass powder.*

## 1 Introduction

The vacuum freeze-drying is a remarkable drying operation and is developing the food industry. In this operation, a wet substance is frozen and the moisture contained in the frozen substance is evaporated by sublimation at a low temperature in a vacuum. As drying proceeds, a dried layer forms which is distinctly separated from the frozen layer by an interface. Dyer and Sunderland [1]<sup>1</sup> analyzed the process of drying as a heat conduction problem and compared with the results of Hatcher's experiments on beef [2]. Katayama and Hayashi [3] investigated the characteristics of vacuum freeze-drying and obtained the most appropriate conditions of drying about the supplied heat.

There are two kinds of processes in the practical freeze-drying operation. One of the processes is a batch operation, in which the freezing and the vacuum drying of the substance take place separately. In such a process, the substance is dried in a vacuum after freezing operation. In the other process, the wet substance is frozen of itself due to evaporation of the moisture of the substance in a vacuum, that is, the self-freezing of a wet substance occurs. In the self-freezing process, when the pressure of the air is reduced by using a vacuum pump, the water of the substance boils vigorously and sometimes serious damage of texture of the substance or large distortion of the substance occurs. Therefore this operation is usually available for drying of the substance in a liquid state, however, since the freezing and the drying of the substance take place simultaneously in the self-freezing process, the heat efficiency for this operation is very high. Then, recently, the self-freezing opera-

tion become applied to the drying of a solid substance. In this case, distortion of substance due to vigorous boiling must be prevented by some treatment, for instance, by means of forming a thin frozen layer on the surface of the substance. The self-freezing problem is treated as a heat conduction one with phase change in case of a multiphase substance. Leech and Winter [4] treated a water-ice-vapour system which is subjected to change of phase and presented numerical results.

In this report, the solutions of this problem involving freezing and sublimation were obtained by solving the heat conduction equations using the same analytical procedure as Neumann's problem, and were compared with the experimental results obtained in the self-freezing of the bed with wet glass powder.

## 2 Analysis of the Self-Freezing Process

**2.1 Description of Heat Mass Transfer Mechanism of the Self-Freezing Process.** In the self-freezing process, ice sublimates from the surface of a frozen substance in a vacuum. (In the practical vacuum freeze-drying operations, the frozen substance is kept in a vacuum in the region of 0.01–1.0 mmHg.) Sublimation of ice yields a drop in temperature of the substance and makes it frozen.

Therefore, this problem is a heat conduction problem with phase change, which involves sublimation and freezing. In other words, a substance in the self-freezing process has two transformation temperatures and is divided into three regions: the dried region, the frozen region, and the wetted region. On the other hand, the water vapor sublimated from the frozen substance moves to the gas phase through the dried region and is excluded by a condenser or an exhaust pump as shown in Fig. 1(a). In this case, the mechanism of transfer of the water vapor diffusing into the gas phase is the same as that described for the case of the vacuum freeze-drying and may be shown in Fig. 1(b) schematically. In particular, when the thickness of the dried region covering over the frozen layer is very thin, this problem is simplified to the problem of mass transfer for sublimation of ice from the free surface of the frozen substance.

<sup>1</sup> Numbers in brackets designate References at end of paper.

Contributed by the Heat Transfer Division for publication in the JOURNAL OF HEAT TRANSFER. Manuscript received by the Heat Transfer Division, January 24, 1975. Paper No. 75-HT-VV.

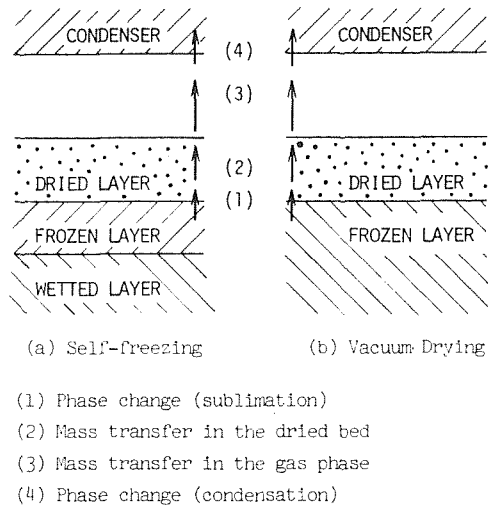


Fig. 1 Schematic model of mass transfer mechanism

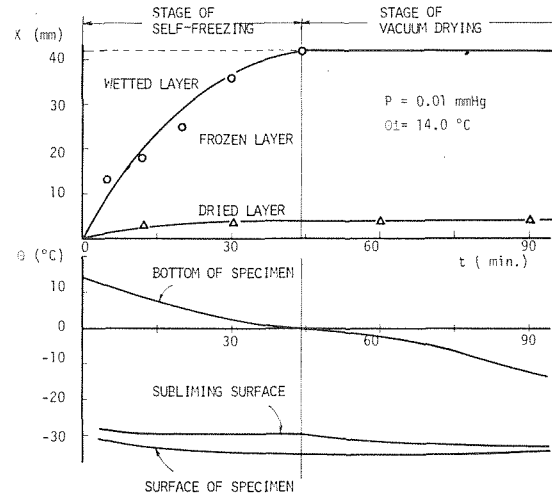


Fig. 2 Preliminary experimental results of self-freezing

Now, to explain the phenomenon of the self-freezing process with an example, some of the preliminary experimental results for a slab-shaped substance are shown in Fig. 2. As is obvious from Fig. 2, there are two moving boundaries. These moving interfaces advance to the inner part of the substance as the time proceeds. One is the surface of sublimation of ice between the dried and the frozen regions, the other is the surface of solidification between the frozen and the wetted regions. As the latent heat of sublimation of the ice is larger than that of fusion of the water, the rate of sublimation of ice is small as compared with the rate of the ice formation, so the freezing front reaches comparatively fast to the other end of the slab. After the freezing time, the substance has two regions, the dried layer and the frozen layer, and the vacuum freeze-drying process starts, furthermore, the temperature of the substance begins to fall rapidly by the dissipation of the latent heat of fusion.

According to the experimental results of the temperature distribution within the substance, at the beginning, heat is rapidly carried out of the surface of the substance, the temperature of the substance falls suddenly and shows a violent variation near the surface of the substance. Though, when the total pressure in the vacuum-chamber becomes stable and is kept at a constant state, the self-freezing process starts and the substance has three regions. In this case, the freezing point of the substance is  $0^{\circ}\text{C}$  and the freezing takes place at a constant unique temperature.

On the other hand, the temperature at the surface of sublimation may be regarded as being constant provided that the thickness of the dried region is very thin. In this work, as stated previously, since the thickness of the dried region is considerably small as compared with that of the frozen region, it has been as-

sumed that the temperature at the interface between dried and the frozen regions is approximately constant.

**2.2 Solutions.** Heat transfer problem for the self-freezing is very complicated both experimentally and theoretically. In this work, the solutions of this problem involving freezing and sublimation are obtained by solving the heat conduction equations. For simplification, the substance is assumed to be a semi-infinite slab, moreover, the following assumptions are made:

- 1 The rate of sublimation of ice is dependent on the heat flux carried to the surface of sublimation.
- 2 The temperature at the sublimation surface and the freezing temperature is constant.
- 3 The flow of the water vapor passing through the dried region is uniform.
- 4 Physical properties of the substance are independent of temperature.
- 5 The substance is a homogeneous material.
- 6 Natural convection in the wetted region and dilatation of bulk of the substance caused by phase change are neglected.
- 7 Heat flows only in one direction.

Assumptions 3, 4, 5, and 6 are available for the heat conduction problem with phase change. The second assumption has been estimated from the preliminary experimental results. In particular, the rate of sublimation of ice is dependent on transfer of the water vapor also, which vaporizes to the gas phase through the dried region. Therefore, to solve this problem, we must strictly take into account of transfer of the water vapor. However, according to the preliminary experimental results, the thickness of the dried region during the self-freezing process is very thin, so that assumption 1 will be appropriate to this case.

Thus the differential equation for the dried region is

## Nomenclature

$C_p$  = specific heat  
 $C_{pv}$  = specific heat of water vapor  
 $L_1$  = latent heat of sublimation  
 $L_2$  = latent heat of freezing  
 $n_1, n_2$  = constant represented by equation (23)  
 $t$  = time  
 $x$  = space coordinate  
 $w$  = rate of mass transfer

$\beta = k_1 C_{pv} \phi \rho_2 / \lambda_1$   
 $\delta$  = position of freezing surface  
 $\eta = x / 2\sqrt{\kappa_1 t}$   
 $\theta$  = temperature  
 $\kappa$  = thermal diffusivity  
 $\lambda$  = thermal conductivity  
 $\xi$  = position of sublimating surface  
 $\rho$  = density  
 $\phi$  = void fraction

## Subscripts

1 = refers to dried region  
 2 = refers to frozen region  
 3 = refers to wetted region  
 $a$  = refers to  $x = 0$   
 $b$  = refers to sublimating point  
 $c$  = refers to freezing point  
 $i$  = denotes the initial condition

$$\frac{\partial \theta_1}{\partial t} = \kappa_1 \frac{\partial^2 \theta_1}{\partial x^2} + \left( \frac{C_{pv}}{C_{p1}\rho_1} \right) \left( \frac{dw}{dt} \right) \frac{\partial \theta_1}{\partial x} \quad (0 < x < \xi) \quad (1)$$

where the second term of the right-hand side in equation (1) is a convective term due to mass transfer of the water vapor.

The differential equations for the frozen region and for the wetted region are

$$\frac{\partial \theta_2}{\partial t} = \kappa_2 \frac{\partial^2 \theta_2}{\partial x^2} \quad (\xi < x < \delta) \quad (2)$$

$$\frac{\partial \theta_3}{\partial t} = \kappa_3 \frac{\partial^2 \theta_3}{\partial x^2} \quad (\delta < x < \infty) \quad (3)$$

Fig. 3 show the heat balance at the sublimation surface and at the freezing front. From Fig. 3, boundary conditions at the sublimation surface and the solidification front are

$$-\lambda_1 \frac{\partial \theta_1}{\partial x} + \lambda_2 \frac{\partial \theta_2}{\partial x} = L_1 \rho_2 \phi \frac{d\xi}{dt} \quad (x = \xi) \quad (4)$$

$$-\lambda_2 \frac{\partial \theta_2}{\partial x} + \lambda_3 \frac{\partial \theta_3}{\partial x} = L_2 \rho_2 \phi \frac{d\delta}{dt} \quad (x = \delta) \quad (5)$$

$$\theta_1 = \theta_{1a} \quad (x = 0) \quad (6)$$

$$\theta_1 = \theta_2 = \theta_b \quad (x = \xi) \quad (7)$$

$$\theta_2 = \theta_3 = \theta_c \quad (x = \delta) \quad (8)$$

The initial condition is

$$\theta_3 = \theta_{3i} \quad (t = 0) \quad (9)$$

In this case, the initial condition for the dried region, both the initial condition and the boundary condition at the surface  $x = 0$  for the frozen region, and the boundary condition at  $x = 0$  for the wetted region are not useful. Then, to obtain the solution for each region, the following additional conditions are used, that is,

$$\begin{aligned} \theta_1 &= \theta_{1i} \quad (t = 0) \\ \theta_2 &= \theta_{2i} \quad (t = 0) \\ \theta_2 &= \theta_{2a} \quad (x = 0) \\ \theta_3 &= \theta_{3a} \quad (x = 0) \end{aligned} \quad (10)$$

Now, we introduce the new temperature variables defined by the following equations

$$\begin{aligned} \theta_1 - \theta_{1i} &= T_1 & \theta_{1a} - \theta_{1i} &= T_{1a} \\ \theta_2 - \theta_{2i} &= T_2 & \theta_{2a} - \theta_{2i} &= T_{2a} \\ \theta_3 - \theta_{3i} &= T_3 & \theta_{3a} - \theta_{3i} &= T_{3a} \end{aligned} \quad (11)$$

By using equations (10) and (11), the differential equations, the boundary conditions and the initial conditions for three regions are rewritten as follows

$$\frac{\partial T_1}{\partial t} = \kappa_1 \frac{\partial^2 T_1}{\partial x^2} + \left( \frac{C_{pv}}{C_{p1}\rho_1} \right) \left( \frac{dw}{dt} \right) \frac{\partial T_1}{\partial x} \quad (0 < x < \xi) \quad (12)$$

$$\frac{\partial T_2}{\partial t} = \kappa_2 \frac{\partial^2 T_2}{\partial x^2} \quad (\xi < x < \delta) \quad (13)$$

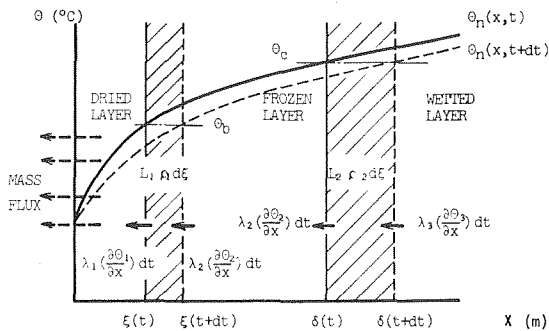


Fig. 3 Heat balances at the interfaces

$$\frac{\partial T_3}{\partial t} = \kappa_3 \frac{\partial^2 T_3}{\partial x^2} \quad (\delta < x < \infty) \quad (14)$$

$$T_1 = 0 \quad (t = 0) \quad (15)$$

$$T_1 = T_{1a} \quad (x = 0) \quad (16)$$

$$T_2 = 0 \quad (t = 0) \quad (17)$$

$$T_2 = T_{2a} \quad (x = 0) \quad (18)$$

$$T_3 = 0 \quad (t = 0) \quad (19)$$

$$T_3 = T_{3a} \quad (x = 0) \quad (20)$$

Particular solutions both for the frozen region and the wetted region are

$$\frac{T_2}{T_{2a}} = \frac{\theta_2 - \theta_{2i}}{\theta_{2a} - \theta_{2i}} = \operatorname{erfc} \left( \frac{x}{2\sqrt{\kappa_2 t}} \right) \quad (21)$$

$$\frac{T_3}{T_{3a}} = \frac{\theta_3 - \theta_{3i}}{\theta_{3a} - \theta_{3i}} = \operatorname{erfc} \left( \frac{x}{2\sqrt{\kappa_3 t}} \right) \quad (22)$$

Now, by the analytical procedure described by Neumann's problem, the relations between moving interfaces and time are supposed to be

$$\xi = n_1 \sqrt{t}, \quad \delta = n_2 \sqrt{t} \quad (23)$$

where  $n_1$  and  $n_2$  are constants which are estimated by equations (4) and (5).

On the other hand, the rate of mass transfer of the water vapor, which vaporizes from the surface of sublimation to the gas phase  $dw/dt$  may be related to the velocity of sublimation surface  $d\xi/dt$ , taking account of the void fraction of the dried region.

It follows from equation (23) that

$$\frac{dw}{dt} = \phi \rho_2 \frac{d\xi}{dt} = \frac{n_1 \rho_2 \phi}{2\sqrt{t}}$$

where  $\phi$  is the void fraction of the dried region.

From equation (23) and the foregoing equation, equation (12) may be rewritten in a form of

$$\frac{\partial T_1}{\partial t} = \kappa_1 \frac{\partial^2 T_1}{\partial x^2} + \left( \frac{n_1 \beta}{2\sqrt{t}} \right) \frac{\partial T_1}{\partial x}$$

where  $\beta = \kappa_1 C_{pv} \phi \rho_2 / \lambda_1$

To obtain the particular solution of the dried region, the dimensionless variable  $\eta = x/2\sqrt{\kappa_1 t}$  is introduced. By using the dimensionless variable, the differential equation and the boundary condition for the dried region are written as follows

$$\frac{d^2 T_1}{d\eta^2} + \left( \frac{n_1 \beta}{\sqrt{\kappa_1}} + 2\eta \right) \frac{dT_1}{d\eta} = 0 \quad (24)$$

$$T_1 = T_{1a} \quad (\eta = 0), \quad T_1 = 0 \quad (\eta = \infty) \quad (25)$$

The solution of equation (24) satisfying equation (25) is

$$\frac{T_1}{T_{1a}} = \frac{\theta_1 - \theta_{1i}}{\theta_{1a} - \theta_{1i}} = \frac{\operatorname{erfc} \frac{1}{2} \left( \frac{x}{\sqrt{\kappa_1 t}} + \frac{n_1 \beta}{\sqrt{\kappa_1}} \right)}{\operatorname{erfc} \frac{1}{2} \left( \frac{n_1 \beta}{\sqrt{\kappa_1}} \right)} \quad (26)$$

In equations (21), (22), and (26),  $\theta_{2a}, \theta_{3a}, \theta_{1i}$ , and  $\theta_{2i}$  are unknown constant terms which satisfy the differential equations (12), (13), and (14). These terms may be determined from the boundary conditions (7) and (8), and the analytical solutions for three regions can be written by the following equations.

$$\theta_1 = \frac{(\theta_{1a} - \theta_b) \operatorname{erfc} \frac{1}{2} \left( \frac{x}{\sqrt{\kappa_1 t}} + \frac{n_1 \beta}{\sqrt{\kappa_1}} \right) + \theta_b \cdot \operatorname{erfc} \frac{n_1 \beta}{2\sqrt{\kappa_1}} - \theta_a \cdot \operatorname{erfc} \frac{n_1(1 + \beta)}{2\sqrt{\kappa_1}}}{\operatorname{erfc} \frac{n_1 \beta}{2\sqrt{\kappa_1}} - \operatorname{erfc} \frac{n_1(1 + \beta)}{2\sqrt{\kappa_1}}} \quad (27)$$

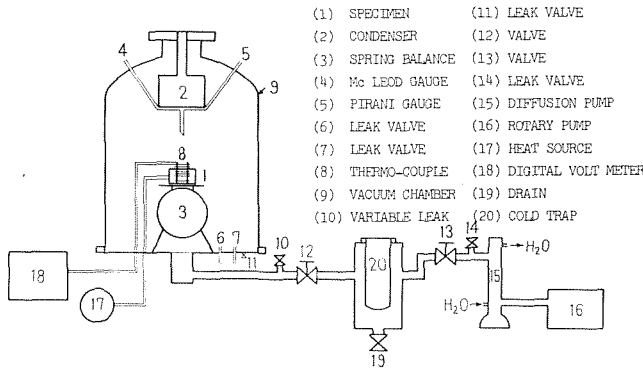


Fig. 4 Outline of the experimental installation

$$\theta_2 = \frac{\theta_b \left\{ \operatorname{erfc} \frac{n_2}{2\sqrt{\kappa_2}} - \operatorname{erfc} \frac{x}{2\sqrt{\kappa_2 t}} \right\}}{\operatorname{erfc} \frac{n_2}{2\sqrt{\kappa_2}} - \operatorname{erfc} \frac{n_1}{2\sqrt{\kappa_2}}} \quad (28)$$

$$\theta_3 = \theta_{3i} \left\{ 1 - \frac{\operatorname{erfc} \frac{x}{2\sqrt{\kappa_3 t}}}{\operatorname{erfc} \frac{n_2}{2\sqrt{\kappa_3 t}}} \right\} \quad (29)$$

By using these solutions, numerical constants  $n_1$  and  $n_2$  are determined from the boundary conditions (4) and (5).

The roots  $n_1$  and  $n_2$  may be obtained by solving the following simultaneous equations.

$$\frac{\lambda_1(\theta_{1a} - \theta_b) \exp\left(-\frac{n_1^2(1+\beta)^2}{4\kappa_1}\right)}{\left\{ \operatorname{erfc} \frac{n_1\beta}{2\sqrt{\kappa_1}} - \operatorname{erfc} \frac{n_1(1+\beta)}{2\sqrt{\kappa_1}} \right\} \sqrt{\pi\kappa_1}} + \frac{\lambda_2\theta_b \exp\left(-\frac{n_1^2}{4\kappa_2}\right)}{\left\{ \operatorname{erfc} \frac{n_2}{2\sqrt{\kappa_2}} - \operatorname{erfc} \frac{n_1}{2\sqrt{\kappa_2}} \right\} \sqrt{\pi\kappa_2}} = \frac{n_1 L_1 \beta \rho_2 \phi}{2} \quad (30)$$

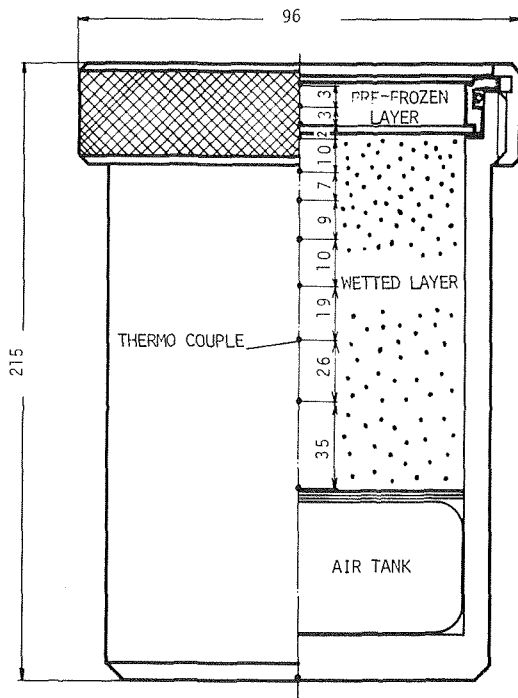


Fig. 5 Construction of a vessel for self-freezing

$$\frac{-\lambda_2\theta_b \exp\left(-\frac{n_2^2}{4\kappa_2}\right)}{\sqrt{\pi\kappa_2} \left\{ \operatorname{erfc} \frac{n_2}{2\sqrt{\kappa_2}} - \operatorname{erfc} \frac{n_1}{2\sqrt{\kappa_2}} \right\}} + \frac{\lambda_3\theta_{3i} \exp\left(\frac{n_2^2}{4\kappa_3}\right)}{\sqrt{\pi\kappa_3} \operatorname{erfc} \frac{n_2}{2\sqrt{\kappa_3}}} = \frac{n_2 L_2 \rho_2 \phi}{2} \quad (31)$$

### 3 Experiment

Fig. 4 shows the outline of the experimental installation, which is composed of the exhaust system, the measurement system, and the main system. In the exhaust system, a rotary pump, a diffusion pump, and some leak valves are involved to maintain the total pressure in the vacuum chamber at constant pressure below 4.6 mmHg. The construction of a vessel for the self-freezing of the substance is shown in Fig. 5. The vessel is composed of a main container in which the substance is charged, and an attached container. The main container is made of acrylic resin, and is covered with aluminum foil in order to isolate thermal radiation from surroundings. The attached container is a thin-walled cylinder of brass. This container is used to form an additional frozen zone which acts as a protecting layer to prevent the substance from extrusion resulted from boiling of the water. These containers are linked together by an O-ring. Both ends of the attached container were covered with a wire-netting of 200 mesh so that the dried zone does not blow off by the water vapor which vaporizes from the surface of the substance.

Throughout the experiment, total pressure in the vacuum chamber was kept constant. Measurement of the total pressure was made at the place where the partial pressure of water vapor can be neglected in comparison with the total pressure, and for this purpose MacLeod and Piranny gauges were used. In order to measure the temperature distribution in specimen, some Cu-Co thermocouples of 0.2 mm dia were inserted in the substance. The temperature at the surface of sublimation was decided from the temperature distribution by extrapolation.

From a practical point of view, food such as meat or fruit should be used as a sample for this experiment, however, the texture or the composition of the food is not necessarily uniform and there are many unclear statements in the report on the physical properties of the food. Then, we used the glass powder as a sample which had clear thermal properties and which could be regarded as being homogeneous when it was packed closely into the column.

Table 1 shows the values of physical properties of the sample in every state. Some of these results were obtained experimentally. In particular, since air and water vapor coexist within the dried region, the thermal properties of the dried bed are exactly dependent on the concentration of the water vapor and on the partial pressure of the air in it. But when the total pressure in the vacuum chamber is within the range of 0.1–1.0 mmHg where the vacuum freeze-drying starts, the air in the dried region will be forced out by flow of the water vapor. We also assumed that pores in the dried bed were filled with water vapor.

Fig. 6 shows the experimental results of thermal conductivity of

Table 1

	DRIED LAYER	FROZEN LAYER	WETTED LAYER
$\lambda$ (Kcal/mh°C)	0.10	1.42	0.49
$C_p$ (Kcal/Kg°C)	0.170	0.237	0.340
$r$ (Kg/m <sup>3</sup> )	1494	1843	1874

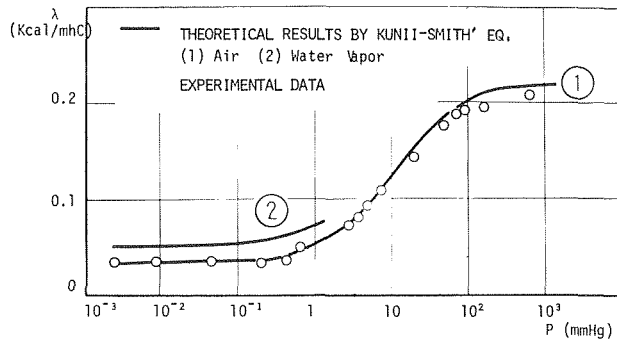


Fig. 6 Thermal conductivity of the bed of glass powder

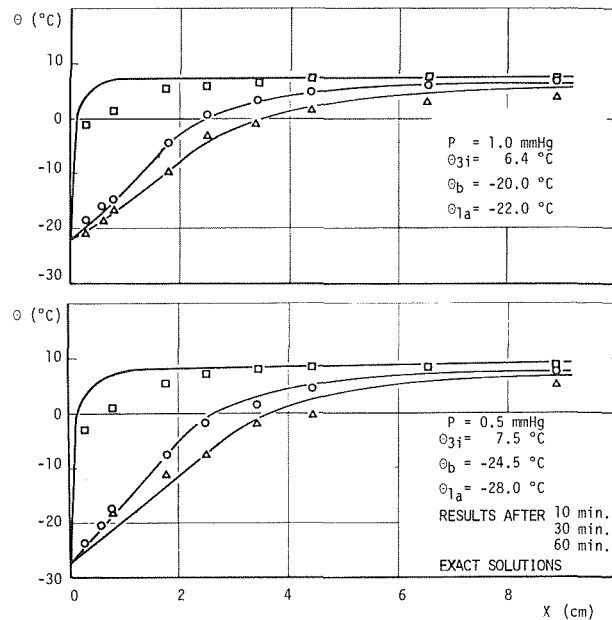


Fig. 7 Temperature distribution in the substance

a bed with glass powder whose pores are filled with air. From this figure, it is clear that the experimental results agree closely with the calculated results by Kunii-Smith's equation. Then, if pores are filled with water vapor, the thermal conductivity can be evaluated by Kunii-Smith's equation and are shown by the solid line in Fig. 6.

#### 4 Experimental Results and Discussion

Some experimental results of the distribution of temperature in the substance are shown in Fig. 7. From this figure, it is obvious that the experimental results agree almost with the calculated results, as shown by the solid line, within the expected scatter due to experimental error. However, the experimental values in the layer close to the surface of the substance are smaller than the calculated values from the analytical solutions. These deviations are due to the difference condition of the initial temperature between the theory and the experiment.

Basically the initial condition (9) for this problem is not satisfied exactly at the beginning of the experiment because of the preliminary freezing layer which is attached to the packed column. On the other hand, scatter in the observed values is caused by the unsteady total pressure in the vacuum chamber at the start of the operation. According to our observation, it takes a few minutes for the operating conditions to reach a steady state. However, for  $10 \leq$

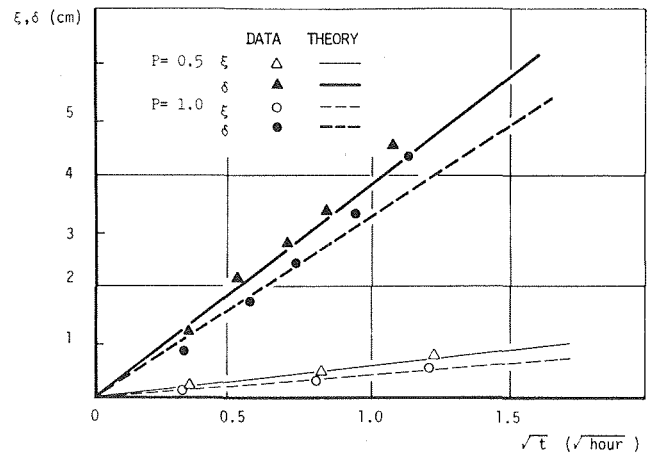


Fig. 8 Relation between moving interfaces and time

$t \leq 60$ , the experimental results of the temperature distribution within the substance agree well with the calculated results, and the analytical solutions are available for this problem.

Fig. 8 shows the relation between moving interfaces and time. The positions of interfaces  $\xi$  and  $\delta$  are plotted against  $\sqrt{t}$ . Furthermore, solid and dotted lines are calculated results by the analytical solutions. As is evident from this figure, growth of  $\delta$  is considerably larger than that of  $\xi$ , because the latent heat of sublimation is several times more than that of fusion. Therefore, it is considered that the self-freezing of the substance is of interest in its application to the practical freezing and will be especially available for freezing foods.

#### 5 Conclusion

The analytical solutions for the self-freezing of a substance in a vacuum were obtained. This problem is a transient heat conduction problem with phase change. The solutions were derived from the analytical procedure of Neumann's solution. In this report, since the dried region was very thin, the rate of sublimation was assumed to be dominated by the amount of heat conducted to the sublimation surface and the other rate determining factors were not considered.

Therefore, the generalized solutions for the self-freezing problems should be obtained by solving the differential equations with the boundary conditions appropriate for the practical cases.

The calculated results of the solutions described here were compared with the experimental results obtained in the self-freezing of the glass powder packed in a column and agreed well with the experimental results. Accordingly, when the thickness of the dried region is relatively thin compared with the other regions, the above analytical solutions will be available for the self-freezing problem of a substance, and also may be applied to the practical self-freezing, or to the vacuum freeze-drying of a substance.

#### Acknowledgments

The authors wish to acknowledge Mr. M. Kawai's assistance.

#### Reference

- 1 Dyer, D. F., and Sunderland, J. E., "The Transient Temperature Distribution During Sublimation Dehydration," *JOURNAL OF HEAT TRANSFER, TRANS. ASME, Series C*, Vol. 89, Feb. 1967, p. 109.
- 2 Hatcher, J. D., "The Use of Gamma Radiation to Measure Moisture Distribution During Drying Processes," MS thesis, Georgia Institute of Technology, Atlanta, Ga., 1964.
- 3 Katayama, K., and Hayashi, Y., "Researches on Vacuum Freeze-Drying," *Bulletin of the JSME*, Vol. 15, No. 81, 1972, p. 344.
- 4 Leech, W. J., and Winter, E. R. F., "Analytical and Experimental Investigation of One-Dimensional Heat and Mass Transfer With Multiple Phase Change," *Proceedings of the Fifth International Heat Transfer Conference*, Vol. 1, 1974, p. 230.

**W. M. Toscano<sup>1</sup>**

Research Associate, Assoc. Mem. ASME

**E. G. Cravalho**

Assoc. Professor, Mem. ASME

Cryogenic Engineering Laboratory, Department of  
Mechanical Engineering, Massachusetts Institute of  
Technology, Cambridge, Mass.

**O. M. Silveiras**

Asst. Professor, Escola Politécnica da  
Universidade de São Paulo, Caixa Postal 8174, São  
Paulo, Brazil. Assoc. Mem. ASME

**C. E. Huggins**

Assoc. Professor of Surgery, Harvard Medical  
School: Chief, Low Temperature Surgical Unit and  
Director, Blood Bank and Transfusion Service,  
Massachusetts General Hospital, Boston, Mass.

# The Thermodynamics of Intracellular Ice Nucleation in the Freezing of Erythrocytes

*A theoretical model describing the thermodynamics of intracellular ice nucleation is developed for red blood cells as a model biomaterial. Analytical expressions based on current theories of ice nucleation by both homogeneous and heterogeneous nucleation processes are coupled with a thermodynamic model for the loss of intracellular water during freezing. Numerical solutions for both modes of nucleation identify two cooling regions—high cooling rates and low cooling rates—separated by a sharp demarcation zone. The nucleation temperature for high cooling rates is approximately 20°K higher than the nucleation temperature for low cooling rates and is essentially independent of cooling rate in each region. The nucleation temperatures for heterogeneous nucleation are approximately 30°K higher than the nucleation temperatures for homogeneous nucleation in the two regions. For the case of heterogeneous nucleation, it is possible to increase the nucleation temperature by packing of catalysts via the concentration polarization effect. If the cell suspension is allowed to supercool before nucleation occurs in the extracellular medium, the sharp transition from low cooling rates to high cooling rates for heterogeneous nucleation shifts to much lower cooling rates. The dependence of the transition cooling rate on the degree of supercooling has been established for a typical freezing situation.*

## Introduction

The possibility of maintaining biomaterials in a state of suspended animation by freezing has intrigued man for centuries. Recent developments in the frozen preservation of human erythrocytes (red blood cells, RBCs) [1]<sup>2</sup> have shown that freezing biomaterials can be of significant clinical importance. Our experience with RBCs has shown that the formation of ice attendant to freezing can occur in two ways. Ice can form either outside cells only, or both inside and outside the cells. Experiments have shown that the presence of ice within a RBC suspended in a noncryoplylactic medium usually results in cell destruction. Thus, if a freezing technique is to be of any clinical value, it must avoid the formation of intracellular ice. It follows, then, that the mechanisms of intracellular ice nucleation are of major importance in the freezing of human RBCs.

There are two general mechanisms of ice nucleation; (1) homo-

geneous nucleation (commonly referred to as spontaneous crystallization) in which molecules in an existing liquid phase  $\alpha$  come together to form spontaneously a cluster of molecules in a solid phase  $\beta$ , and (2) heterogeneous nucleation in which the nucleation process is initiated by the presence of a catalyst, such as a foreign particle, container wall, or crevice.

Gibbs [2] laid the groundwork of homogeneous nucleation theory, and Volmer [3] utilized Gibbs' analysis to develop a kinetic homogeneous nucleation theory. Basically, as the temperature of a liquid phase is reduced to its freezing temperature, small particles of solid phase called embryos are constantly being formed, but because these embryos are unstable, they are quickly broken up. As the liquid phase is further supercooled, the number and size of these unstable embryos increases. When the temperature of the supercooled liquid reaches a particular value, the embryos reach a critical size and become metastable. The metastability of these special embryos, called nuclei, is characterized by the condition that the derivative of the Helmholtz free energy of formation of the embryo with respect to its radius vanishes. As a result, the nuclei (embryos with radii greater than or equal to the critical radius) will not disappear but instead will grow and form permanent clusters of solid phase. That is, the rate of embryo formation now exceeds the rate of embryo destruction. This nucleation condition marks the onset of freezing.

<sup>1</sup> Present address: Cryogenic Technology, Inc., Waltham, Mass.

<sup>2</sup> Numbers in brackets designate References at end of paper.

Contributed by the Heat Transfer Division for publication in the JOURNAL OF HEAT TRANSFER. Manuscript received by the Heat Transfer Division November 22, 1974. Paper No. 75-HT-DDD.

Becker and Doring [4] have improved Volmer's theory by taking into consideration the forward and backward reaction rates and have obtained an expression for the net nucleation rate. Turnbull and Fisher [5] have incorporated into the expression for the nucleation rate derived by Becker and Doring the contribution of the free energy of activation for motion of a liquid molecule across the embryo interface. A thorough discussion of the development of homogeneous nucleation is presented in references [6-8].

Turnbull [9] first looked at heterogeneous nucleation on a flat surface, in a conical cavity, and in a cylindrical cavity. Dufour and Defay [10] and later Fletcher [11] studied heterogeneous nucleation due to impurities or foreign particles in a liquid phase  $\alpha$ . The effect of a flat surface or a foreign particle adjacent to an embryo is to reduce the value of the Helmholtz free energy of formation of an embryo of a given radius. Consequently, in heterogeneous nucleation it is possible to form nuclei at higher temperatures than in the case of homogeneous nucleation. We would expect, then, that in most physical and biological systems, heterogeneous nucleation will more likely occur instead of homogeneous nucleation; however, it is possible that both mechanisms may occur in RBCs.

It is the purpose of this paper to present an appropriate thermodynamic model which will predict the temperature for intracellular ice formation in RBCs as a function of cooling rate. Newly developed relationships describing the kinetics of water loss from the RBCs during cooling will be coupled with a derived integral expression for the net nucleation rate. For homogeneous nucleation, this integral expression relates the nucleation temperature to the nucleation rate, the volume of intracellular water, and the number of nuclei present inside the RBC. For heterogeneous nucleation the expression relates the nucleation temperature to the nucleation rate, the total surface area of catalysts present inside the RBC, and the number of nuclei adjacent to the catalysts present inside the RBC.

A parametric study of these two mechanisms was performed in the hope that the kinetics of the nucleation process might be better understood, at least for RBCs. The results show that heterogeneous nucleation is the more likely mechanism and that depending

on the catalyst size and contact angle selected, the general trend predicted by the theory is in agreement with the trend of available experimental data. The results also show that the catalyst radius for heterogeneous nucleation that best correlates with experimental data is typical of the characteristic dimension of a hemoglobin molecule or a group of hemoglobin molecules.

## Rate of Nucleation

**Homogeneous Nucleation.** Homogeneous nucleation will be initiated in a liquid when embryos of critical radius (nuclei) are formed. If  $J$  is the net rate of formation of nuclei per unit volume in a liquid phase of volume  $V^\alpha$ , the number of nuclei formed during the time interval  $t_f - t_0$  is

$$\int_{t_0}^{t_f} J V^\alpha dt = N(r_c) V^\alpha \quad (1)$$

If the system is cooled at a constant rate

$$B = dT/dt = \text{constant}, \quad (2)$$

and equation (1) can be rewritten in the form

$$\frac{1}{B} \int_{T_0}^{T_f} J V^\alpha dT = N(r_c) V^\alpha \quad (3)$$

where  $T_f$  is the nucleation temperature at which freezing commences. The left-hand side of equation (3) represents the number of nuclei formed by collision processes, and the right-hand side represents the equilibrium number of nuclei present at the temperature and volume of the system. Homogeneous nucleation occurs when equation (3) is satisfied.

Turnbull and Fisher [5] have shown that for homogeneous nucleation the net rate of formation of embryos is given by

$$J = n_v^\alpha N_A \left[ \frac{KT}{h} \right] \frac{\Delta\Omega}{g^2 7^3} \left[ \frac{\Gamma}{9\pi} \right]^{1/2} \exp[-(\Delta f_A + \Delta F_c)/KT] \quad (4)$$

where the parameter  $\Gamma$  is proportional to the Helmholtz free energy of formation (per unit area) of the interface separating the solid

## Nomenclature

$B$  = cooling rate,  $^\circ\text{K}/\text{min}$   
 $b$  = permeability temperature coefficient,  $(^\circ\text{K})^{-1}$   
 $F$  = Helmholtz free energy, erg  
 $g$  = number of molecules contained in a nucleus, molecules/nucleus  
 $h$  = Planck's constant, erg-s  
 $h_{TP}$  = heat of reaction at constant  $T$  and  $P$ , erg/mole  
 $J$  = homogeneous nucleation rate, nuclei/ $\text{cm}^3\text{-s}$   
 $J'$  = heterogeneous nucleation rate, nuclei/ $\text{cm}^2\text{-s}$   
 $K$  = Boltzmann constant, erg/ $^\circ\text{K}$   
 $k$  = permeability of cell membrane, moles $^2/\mu^5\text{-atm-min}$   
 $M$  = molecular weight  
 $m$  = cosine of contact angle  
 $N$  = number of embryos per unit volume, embryos/ $\text{cm}^3$   
 $N_A$  = Avogadro's number, molecules/mole  
 $N_I'$  = number of impurities

$N_S$  = number of embryos  
 $n$  = number of moles  
 $P$  = absolute pressure, dynes/ $\text{cm}^2$   
 $q$  = dimensionless constant  
 $R$  = universal gas constant, erg/mole  $^\circ\text{K}$   
 $r$  = radius, cm  
 $s$  = shape factor  
 $T$  = absolute temperature,  $^\circ\text{K}$   
 $T_g$  = permeability reference temperature,  $^\circ\text{K}$   
 $t$  = time, s  
 $V$  = volume,  $\text{cm}^3$   
 $v$  = specific molar volume,  $\text{cm}^3/\text{mole}$   
 $x$  = molar fraction  
 $z$  = ratio of catalyst radius to critical radius  
 $\Gamma$  = constant in expansion of  $\Delta F$   
 $\Delta F$  = Helmholtz free energy of formation, erg  
 $\Delta f_A$  = activation energy, erg  
 $\Delta T_s$  = degree of supercooling,  $^\circ\text{K}$   
 $\eta$  = viscosity, poise

$\theta$  = contact angle, radian  
 $\Lambda$  = number of molecules of  $\alpha$  phase adjacent to nucleus per unit surface area, molecules/ $\text{cm}^2$   
 $\nu$  = osmolality, mOsm/l  
 $\sigma$  = surface tension, dyne/cm  
 $\phi$  = osmotic coefficient  
 $\Omega$  = surface area,  $\text{cm}^2$

## Subscripts

$c$  = critical embryo  
 $f$  = freezing state  
 $I$  = catalyst  
 $0$  = initial state  
RBC = red blood cell  
 $s$  = solutes  
 $\gamma$  = solvent; species; component

## Superscripts

$I$  = catalyst  
in = intracellular  
out = extracellular  
 $\alpha$  = liquid phase  
 $\beta$  = solid phase

and liquid phases, and its value will depend upon the configuration of the interface. The term  $\Omega_c$  is the surface area of the embryo exposed to the liquid phase and the term  $g$  represents the number of molecules contained within a nucleus. For a nucleus

$$\Gamma = 9(v_\gamma^\beta)^2 g^{4/3} s \sigma / KT \Omega_c^2 \quad (5)$$

where  $s$  is the shape factor and is equal to  $4\pi$  for a spherical nucleus and 20.78 for a hexagonal nucleus. The right-hand side of equation (3), the equilibrium number of nuclei present at the temperature and volume of the system, is given by [12]

$$N(r_c) V^\alpha = N_A n_\gamma^\alpha \exp(-\Delta F_c / KT_f). \quad (6)$$

Substituting equations (4), (5), and (6) into equation (3), we obtain

$$\frac{1}{B} \int_{T_0}^{T_f} (n_\gamma^\alpha)^2 \Lambda v_\gamma^\beta v_\gamma^\alpha \frac{KT}{h} (s\sigma / \pi KT)^{1/2} \times \exp[-(\Delta f_A + \Delta F_c) / KT] dT = n_\gamma^\alpha \exp(-\Delta F_c / KT_f). \quad (7)$$

The quantity  $\Delta F_c$  appearing in equation (7) is the Helmholtz free energy of formation of a nucleus and is derived in detail in [13].

$$\Delta F_c = s\sigma r_c^2 / 3 \quad (8)$$

The quantity  $\Delta f_A$  appearing in equation (7) is the activation energy for diffusion of a molecule in the liquid phase to the surface of the nucleus. It has been suggested [14] that because of certain similarities between this diffusion process and viscous flow, the activation energy may be related to the viscosity of the liquid phase.

$$\Delta f_A = KT \ln \left[ \frac{\eta_\gamma v_\gamma^\alpha}{h N_A} \right]. \quad (9)$$

**Heterogeneous Nucleation.** The process of heterogeneous nucleation is similar to homogeneous nucleation except that the nucleation occurs on the surface of impurities in the liquid phase rather than within the volume of the liquid phase itself. If  $J'$  is the net rate of formation of nuclei per unit surface area of impurity in a liquid phase of volume  $V^\alpha$  with  $N_I'$  dispersed impurities of surface area  $\Omega_I$ , the number of nuclei formed during the time interval  $t_f - t_0$  is

$$\int_{t_0}^{t_f} J' N_I' \Omega_I dt = N_S'(r_c). \quad (10)$$

Again, if the suspension is cooled at a constant rate  $B$ , equation (10) becomes

$$\frac{1}{B} \int_{T_0}^{T_f} J' N_I' \Omega_I dT = N_S'(r_c). \quad (11)$$

The left-hand side of equation (11) represents the number of nuclei formed on the impurity surface by collision processes, and the right-hand side represents the equilibrium number of nuclei present at the temperature and impurity concentration of the system. Heterogeneous nucleation occurs when equation (11) is satisfied.

Again Turnbull and Fisher [5] have shown that for heterogeneous nucleation the net rate of formation of nuclei per unit surface area of impurity is given by

$$J' = \Lambda^2 \left( \frac{KT}{h} \right) \frac{\Omega_c}{g^{2/3}} \left[ \frac{\psi}{9\pi} \right]^{1/2} \exp[-(\Delta f_A + \Delta F_c') / KT] \quad (12)$$

where the parameter  $\psi$  is proportional to the Helmholtz free energy of formation (per unit area) of the interface separating the liquid and solid phases and is given by

$$\psi = \frac{2\pi\sigma}{KT} f(m, z) [3v_\gamma^\beta / \pi h(m, z)]^{2/3} \quad (13)$$

where

$$h(m, z) = 2 + 3 \left[ \frac{1-zm}{q} \right] - \left[ \frac{1-zm}{q} \right]^3 - z^3 [2 - 3 \left[ \frac{z-m}{q} \right] + \left[ \frac{z-m}{q} \right]^3] \quad (14)$$

and as shown in [11]

$$f(m, z) = 1 + \left[ \frac{1-mz}{q} \right]^3 + z^3 [2 - 3 \left[ \frac{z-m}{q} \right] + \left[ \frac{z-m}{q} \right]^3] + 3mz^2 \left[ \frac{z-m}{q} - 1 \right] \quad (15)$$

where

$$q = (1 + z^2 - 2mz)^{1/2}. \quad (16)$$

The independent parameters  $m$  and  $z$  are the cosine of the contact angle formed between the nucleus and impurity and the ratio of the radius of the impurity to the radius of the nucleus, respectively. The right-hand side of equation (10), the equilibrium number of nuclei present at the temperature and impurity concentration of the system, is given in [12].

$$N_S'(r_c) = \Lambda N_I' \Omega_I \exp(-\Delta F_c' / KT) \quad (17)$$

The quantity  $\Delta F_c'$  appearing in equations (12) and (17) is the Helmholtz free energy of formation of a spherical embryo of critical radius in contact with a spherical impurity and is derived in detail in [13].

$$\Delta F_c' = 2\pi\sigma r_c^2 f(m, z) \quad (18)$$

Notice that for the case of  $r_I = 0$ , i.e., no catalyst is present, equation (18) reduces to equation (8) which is the result for homogeneous nucleation. The quantity  $\Delta f_A$  appearing in equation (12) has already been defined in equation (9). Substituting equations (12), (13), and (17) into equation (11), we obtain after considerable algebraic manipulation

$$\frac{1}{B} \int_{T_0}^{T_f} \Lambda^2 \frac{KT}{h} \frac{2 \left[ 1 + \left( \frac{1-zm}{q} \right) \right]}{h(m, z)} v_\gamma^\beta \left[ \frac{2\sigma f(m, z)}{KT} \right]^{1/2} N_I' \Omega_I \times \exp[-(\Delta f_A + \Delta F_c') / KT] dT = \Lambda N_I' \Omega_I \exp(-\Delta F_c' / KT_f). \quad (19)$$

For both types of nucleation the freezing temperature is determined by the value of  $T_f$  that satisfies equation (7) or equation (19) depending upon the nucleation mechanism. Because of the complex temperature dependence of the various terms appearing in the integrals on the left-hand sides of these equations, it is not possible to obtain closed form solutions. Instead, it is necessary to use a numerical method which involves selecting a value of  $T_f$  and evaluating the left-hand and right-hand sides of equations (7) or (19) independently. If the two sides are not equal, a new value of  $T_f$  is selected. The process is repeated until the two sides of the equations agree. Note that equations (7) and (19) are general in that they can be applied to open systems for which the number of molecules of the liquid phase vary with time in both the homogeneous and heterogeneous cases and the number of impurities vary with time in the heterogeneous case.

### Red Blood Cell Model

The physical dimensions and internal composition of the RBCs are given in references [15, 16]. It is assumed the cell membrane is permeable only to water and impermeable to solutes; consequently, the hemoglobin and dissociated electrolytes are not able to leave the cell during the cooling and thawing processes. The permeability of the membrane to water is assumed to be of the form [13]

$$k = 1.85 \times 10^{-15} \exp[335.174/\nu - 26.286 + b(T - T_g)] \quad (20)$$

where  $T_g = 293^\circ\text{K}$  in the present case.

The foregoing expression for the permeability of water takes into consideration not only the temperature of the system but also the osmolality of the extracellular solution. Note that the permeability decreases as the temperature decreases. During the freezing process, ice will form preferentially outside the cells due to the minute temperature gradients responsible for conduction heat

transfer from the cells to the boundaries of the suspending medium in contact with the coolant. Because of the presence of extracellular ice, a chemical potential difference will exist between extracellular and intracellular solutions. Intracellular water will begin to flow out of the cells in order to reduce this difference and maintain equilibrium. As water flows out of the cells, cell volume decreases resulting in an inward displacement of the cell membrane. Since intracellular proteins such as hemoglobin cannot penetrate healthy membranes, they accumulate along the inner surface of the membrane which produces a spatial concentration gradient of protein within the cell. In effect, the moving membrane sweeps these molecules out of the intracellular solution like so many fish caught in a net. As the temperature is reduced further, the membrane permeability to water decreases, and the presence of the randomly stacked layers of protein adjacent to the inner wall of the cell membrane further increases the resistance of the membrane to water flow. The decrease in mobility of water across the cell membrane causes the concentration of solutes within the cell to increase less rapidly than the concentration outside the cell. Since both the extracellular and intracellular media are at the same temperature, the intracellular medium becomes supercooled. As a result, conditions favorable to intracellular nucleation, either homogeneous or heterogeneous, soon develop inside the cell. Clearly, the time required for these conditions to develop will depend upon the cooling rate and the cell characteristics.

Mazur [17] first studied the volume change of RBCs due to water loss during the cooling process. A later study [13] which represents an extension of Mazur's model reveals that the osmolality of the extracellular solution as well as the degree of supercooling can significantly alter the volumetric changes of RBCs during the cooling process.

Three coupled equations describe the response of the cell to changes in temperature:

1 Rate equation:

$$\frac{dn_\gamma^{\alpha in}}{dt} = -\frac{k\Omega_{RBC}RT\phi}{B} \ln(x_\gamma^{\alpha in}/x_\gamma^{\alpha out}) \quad (21)$$

2 Mass conservation equation:

$$\frac{dn_\gamma^{\alpha in}}{dT} + \frac{dn_\gamma^{\alpha out}}{dT} + \frac{dn_\gamma^{\beta out}}{dT} = 0 \quad (22)$$

3 Equilibrium equation (external medium):

$$\frac{dn_\gamma^{\beta out}}{dT} = -\frac{dn_\gamma^{\alpha in}}{dT} - h_{TP}[n_\gamma^{\alpha out} + 2n_s^{\alpha out}]/2RT^2n_s^{\alpha out} \left[ \frac{\phi}{n_\gamma^{\alpha out}} - \frac{\frac{\partial \phi}{\partial x_s^{\alpha out}} \ln x_\gamma^{\alpha out}}{n_\gamma^{\alpha out} + 2n_s^{\alpha out}} \right] \quad (23)$$

The solutions of these equations do not predict the temperature at which intracellular ice may appear but instead show the behavior of the molar concentration of the intracellular solution as a function of the temperature of the system consisting of the cell and its suspension. To determine the intracellular freezing temperature, it is necessary to combine equations (21), (22), and (23) with either equation (7) or equation (19) depending on the nucleation mechanism.

## Results

For the case of homogeneous nucleation, we have used this technique to determine the intracellular freezing temperature in RBCs experiencing different cooling rates. These results are presented in Fig. 1. The cell volumes used in the calculations varied from  $30\mu^3$  to  $200\mu^3$  which corresponds to 99.99 percent of the Gaussian distribution of volumes of human RBCs. The nucleation temperatures only differed a degree in the volume range of  $30\mu^3$ – $200\mu^3$  at a particular cooling rate. Thus, the dependence of the homogeneous nucleation temperature on RBC volume is quite weak. Notice that

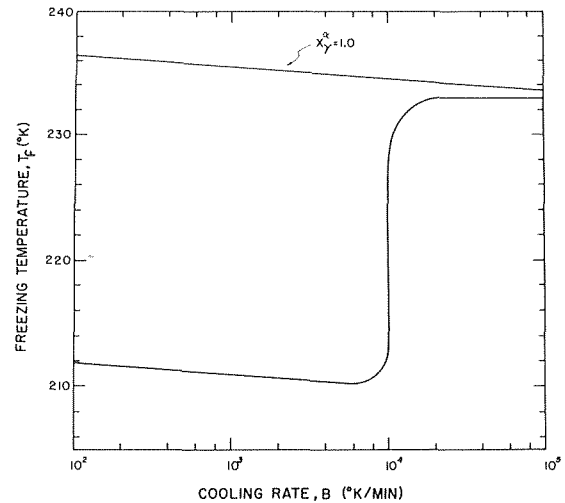


Fig. 1 Homogeneous freezing temperature of red blood cells cooled at constant rates

there exists a sharp distinction between the nucleation temperatures at cooling rates less than  $10,000^\circ\text{K}/\text{min}$  and larger than  $10,000^\circ\text{K}/\text{min}$ . The average homogeneous nucleation temperature is on the order of  $210$ – $212^\circ\text{K}$  for the lower cooling rate and on the order of  $230$ – $233^\circ\text{K}$  for the higher cooling rates. The critical radius of the nuclei corresponding to these nucleation temperatures and cooling rates is on the order of  $10\text{\AA}$ .

As a comparison, the freezing temperature for homogeneous nucleation in a RBC composed only of pure water with a volume between  $18.95\mu^3$  and  $126.30\mu^3$  (i.e., 63.15 percent of the normal RBC volume) is evaluated and is represented by the solid straight line in Fig. 1, i.e., the case for  $x_\gamma^\alpha = 1.0$ . The homogeneous freezing temperature increases as the cooling rate decreases which is evident from the form of equation (3). For cooling rates larger than  $10,000^\circ\text{K}/\text{min}$ , the two analytical curves are separated only by a small difference which is due to the initial electrolyte concentration in a RBC. However, for cooling rates smaller than  $10,000^\circ\text{K}/\text{min}$ , there is a large difference between the two analytical curves due to the formation of a solid eutectic solution at the smaller cooling rates.

The evaluation of the freezing temperature for the case of heterogeneous nucleation is a bit more involved than the homogeneous case because of the complex way in which the impurity characteristics affect the kinetics. For these calculations we have assumed the impurities on which nucleation occurs to be spheres with radii of  $32\text{\AA}$  and a number density of  $32 \times 10^7$  per cell. Both of these characteristics are typical of intracellular proteins. We also need to establish the contact angle between the embryo and impurity on which the embryos form. Since no information is available about this contact angle for typical biomaterials, we have calculated the freezing temperature,  $T_f$ , for various contact angles between  $0$  and  $\pi$  radians (or alternatively the parameter  $m$ , which is the cosine of the contact angle, was varied between  $-1.0$  and  $+1.0$ ).

The results of these calculations are presented as a function of cooling rate in Fig. 2 for a RBC with the physical dimensions noted previously and an impurity of radius  $32\text{\AA}$ . Notice that for a given value of  $m$ , the temperature for heterogeneous nucleation is a strong function of cooling rate within a narrow range of cooling rates which we have termed the demarcation zone. For cooling rates below the demarcation zone the nucleation temperature is low, but for cooling rates above the demarcation zone, the nucleation temperature is high. Notice also that as  $m$  increases from  $-1.0$  to  $+1.0$ , the range of cooling rates that influence nucleation temperatures decreases from  $9000^\circ\text{K}/\text{min}$  to  $2000^\circ\text{K}/\text{min}$ . Also for these variations of  $m$ , the nucleation temperature at any given cooling rate increases as  $m$  increases. This behavior is due to the fact that large values of  $m$  result in large values of the critical radi-

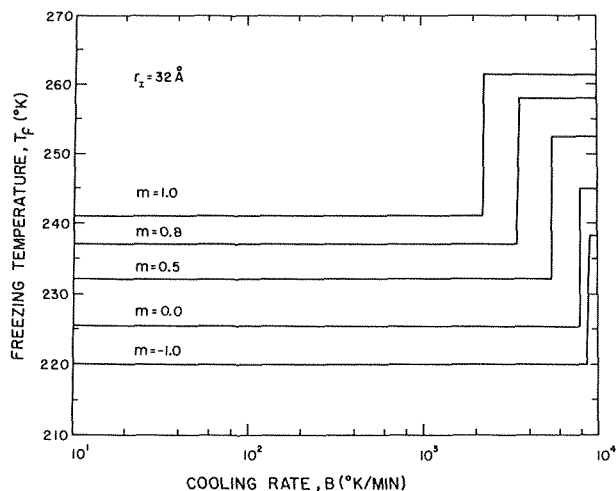


Fig. 2 Effect of contact angle on heterogeneous freezing temperatures of red blood cells cooled at constant rates

which in turn lead to high nucleation temperatures. The aforementioned demarcation zone is so narrow that we can readily quantify fast and slow cooling rates for a given value of  $m$ . The results of Fig. 2 show that the nucleation temperature for slow cooling rates ranges from 220°K to 241°K while the nucleation temperature for fast cooling rates ranges from 239°K to 262°K. These values for the heterogeneous nucleation temperature are significantly higher than the corresponding values for the homogeneous nucleation temperature. In contrast to homogeneous nucleation, the freezing temperature for heterogeneous nucleation is completely independent of RBC volume. This is to be expected since the homogeneous nucleation process depends upon the volume of the liquid phase in the cell whereas the process of heterogeneous nucleation depends on the number of nucleation sites in the cell. The number of these sites is sufficiently large in any healthy cell to saturate the cell with nucleation sites.

In the event that the impurities agglomerate, the nucleation rate will be markedly affected because the  $\Delta F_c'$  required for the formation of a nucleus will be smaller; consequently for a particular cooling rate the freezing temperature will be higher for a larger size catalyst. To determine the effect of the packing or agglomeration

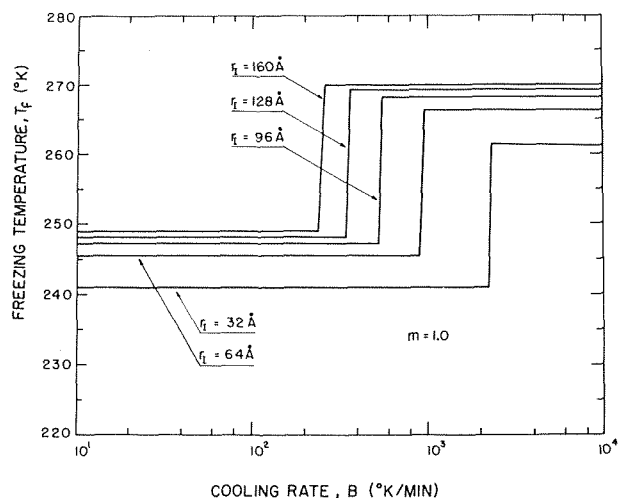


Fig. 3 Effect of catalyst radius on heterogeneous freezing temperatures of red blood cells cooled at constant rates

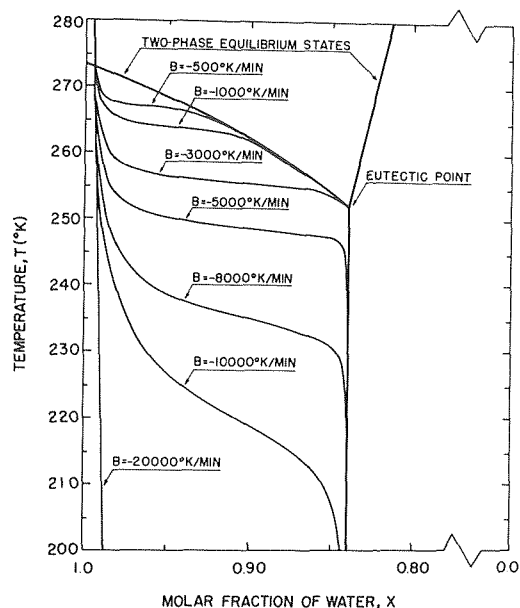


Fig. 4 Locus of states of intracellular solution of red blood cells cooled at constant rates (states of extracellular solution coincident with locus of two-phase equilibrium states)

of the impurity molecules, we varied the impurity radius in increments of 32Å from 32Å to 160Å and calculated the freezing temperature for a contact angle of zero radians (i.e.,  $m = +1.0$ ) which results in a critical radius equal to the radius of the impurity. The results of these calculations are shown in Fig. 3.

Notice that as the radius of the impurity increases from 32Å to 160Å, the cooling rate corresponding to the demarcation zone decreases from 2000°K/min to 200°K/min. The range of nucleation temperatures for low cooling rates varies from 241°K to 249°K, and the range of nucleation temperatures for high cooling rates varies from 262°K to 270°K. Fig. 3 also shows that because of the hyperbolic dependence of the critical radius on temperature, the heterogeneous nucleation temperature for a particular cooling rate increases as the impurity radius increases, but only up to a certain limit. Beyond this limit, the nucleation temperature is essentially independent of impurity size. This can be seen if one replots the analytical data in Fig. 3 for the freezing temperature versus impurity radius with cooling rate as the parameter (cf. Fig. 7).

The sharp demarcation between high and low cooling rates is of special interest because of its potential importance in clinical applications. The demarcation is due to the variation of intracellular water during freezing. Fig. 4 shows the molar fraction of intracellular water at various cooling rates for a typical RBC as obtained from simultaneous solutions of equations (21), (22), and (23). In all cases it is assumed that the external solution follows the equilibrium curve from 272.4°K, the normal freezing temperature of the solution, to the eutectic temperature 252.0°K. At the eutectic temperature, the remaining extracellular solution forms a solid solution such that the external medium consists of pure ice and the solid solution. Because of the resistance to water transport offered by the membrane, the intracellular medium is supercooled and nucleation may occur at temperatures below the eutectic temperature. In Fig. 4, notice that for cooling rates less than 3000°K/min, the cooling curves join the equilibrium curve at temperatures greater than the eutectic temperature, but for cooling rates larger than 3000°K/min, the cooling curves join the equilibrium curve below the eutectic temperature. It was shown in reference [13] that similar results can be obtained by holding the cooling rate constant and varying the membrane permeability; thus, it follows that a cell cooled at a high rate behaves as though it has a membrane with a low water permeability. That is, the heat transfer dominates over

the mass transfer so that intracellular water is trapped inside the cell and pure ice precipitates out of the intracellular solution at a supercooled temperature. At low cooling rates, the converse is true. Mass transfer dominates over heat transfer so that a considerable portion of the intracellular water leaves the cell and a solid solution forms within the cell at a subeutectic temperature.

The existence of a sharp demarcation between high and low cooling rates is in agreement with the experimental data obtained by Diller [18]. He has shown that for cooling rates larger than 850°K/min, intracellular ice is formed in 100 percent of the RBCs in the specimens, whereas for cooling rates less than 840°K/min, he was not able to detect intracellular ice by light microscopy. It is possible that the solid solution was present in these latter cases but was not detectable by his technique.

Because RBCs frequently are supercooled in clinical applications, it is worthwhile to study carefully the effect of the degree of supercooling,  $\Delta T_s$ , on the heterogeneous freezing temperature of RBCs as a function of cooling rate and catalyst radius. In Fig. 5 is presented the heterogeneous freezing temperature of RBCs for supercooling of 0°K, 5°K, 8°K, 9.8°K, and 10.1°K, respectively, for a catalyst radius of 32Å and a contact angle of 0 deg. Notice that the demarcation zone is shifted to slower cooling rates for higher degrees of supercooling. This trend is in agreement with the experimental data obtained by Diller [19]. For 0°K supercooling, the demarcation zone appeared between 840°K/min and 850°K/min, for 5°K supercooling, the demarcation zone appeared between 795°K/min and 805°K/min, and for 12°K supercooling, the demarcation zone appeared between 6°K/min and 16°K/min. In order to study the effect of impurity packing as well as supercooling, the cooling rates corresponding to the demarcation zone are presented in Fig. 6 as a function of supercooling and catalyst radius along with the experimental data of Diller [19]. Again the demarcation zone cooling rate is shifted to lower values for both a larger degree of supercooling and a larger catalyst radius.

It is also possible that the kinetics of intracellular ice nucleation may be initiated by the propagation of ice crystals from the extracellular medium through the cell membrane to the intracellular medium. Mazur [17] has proposed such a mechanism based upon a porous membrane model. When ice first appears extracellularly, the membrane acts as a barrier to the penetration of ice, but as the cell suspension is cooled further, the intracellular contents supercool. Water trapped in the membrane pores nucleates with the extracellular ice acting as a catalyst. The ice then propagates through the membrane and acts as the catalyst for the heterogeneous nucleation of ice inside the cell. The relationship between the cooling velocity, freezing temperature, and catalyst radius operative in this

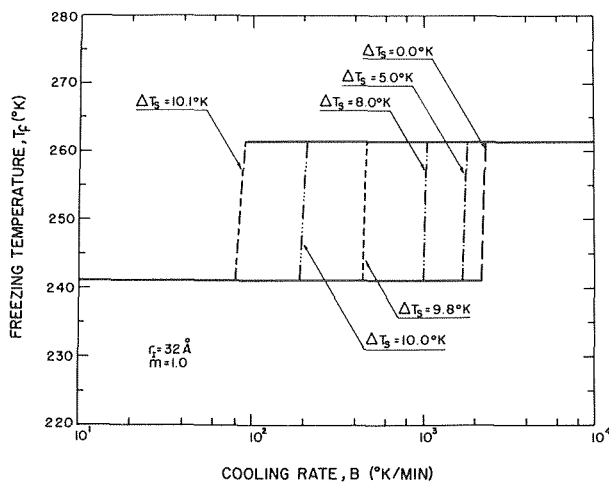


Fig. 5 Effect of supercooling on heterogeneous freezing temperatures of red blood cells cooled at constant rates

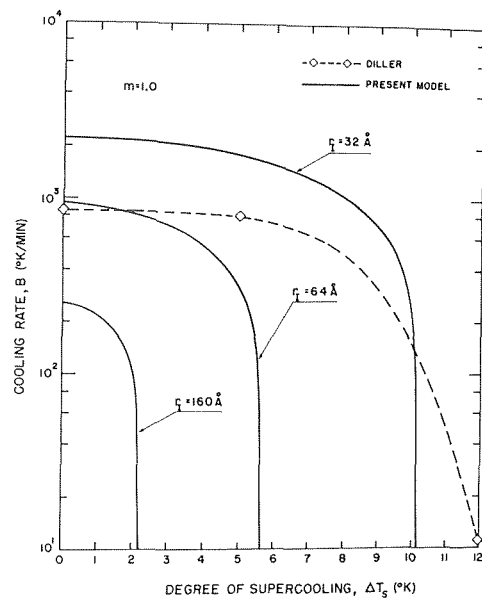


Fig. 6 Effect of catalyst radius on demarcation zone cooling rate for supercooled red blood cells

mechanism can be readily obtained from the present analysis for the RBC.

From measurements of the osmotic pressure gradient across RBC membranes [20], the number of pores in a RBC membrane can be shown to be approximately  $5.96 \times 10^4$  pores/RBC. Then with an effective catalyst radius (propagating ice crystal radius) equal to the membrane pore radius and a contact angle of 0 deg ( $m = +1.0$ ) between the ice crystal catalyst and the embryo, equation (10) can be employed with  $N_I$  the number of pores and  $\Omega_I$  the exposed surface areas of the ice crystal propagating through the pore. For a pore radius varying from 1.0Å to 32.0Å the resulting heterogeneous nucleation temperatures for the case of zero supercooling are shown in Fig. 7 together with the results of heterogeneous nucleation for  $r_I = 32\text{Å}$  previously shown in Fig. 3. The top solid line corresponds to the intracellular nucleation of pure ice whereas the bottom solid line corresponds to the nucleation of a solid solution of pure ice and eutectic solid inside the cell at subeutectic temperatures.

Note that the results for heterogeneous nucleation by ice propagation through the cell membrane are indistinguishable from the

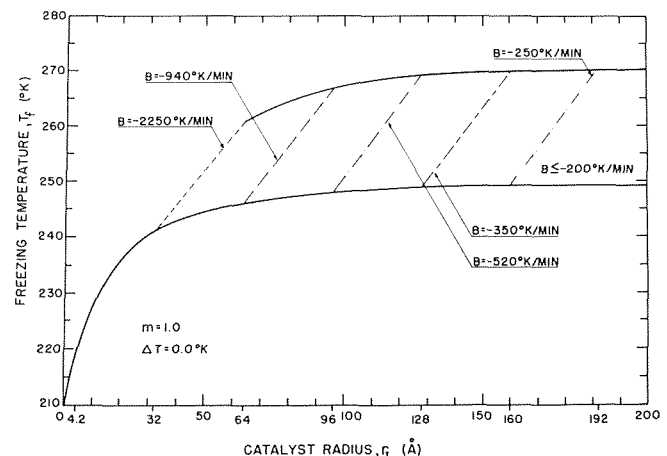


Fig. 7 Effect of catalyst radius on heterogeneous freezing temperatures of red blood cells cooled at constant rates for both heterogeneous nucleation mechanisms

results of heterogeneous nucleation on the surface of a spherical impurity because the intracellular medium in both cases is saturated with catalyst on which ice embryos can form. Thus, the freezing temperature in effect becomes a function of catalyst radius only. Note also in Fig. 7 that as the catalyst radius approaches zero, the heterogeneous freezing temperature approaches the freezing temperature for homogeneous nucleation.

### Conclusions

The results of the present study reveal that heterogeneous nucleation is a possible mechanism in RBCs. These cells contain catalyst of sufficient size and in sufficient numbers, either singly or in groups, to trigger the nucleation process. Available experimental data are not adequate to identify the nature of the catalyst, but several possibilities exist. Of course, it is also possible for the intracellular medium to nucleate even in the absence of a catalyst. However, for this homogeneous nucleation process, the freezing temperature is approximately 30°K lower than for the heterogeneous case.

Both heterogeneous and homogeneous nucleation are divided into two distinct regions—low cooling rates and high cooling rates—separated by a demarcation zone. High freezing temperatures are typical of high cooling rates and low freezing temperatures are typical of low cooling rates. For heterogeneous nucleation, the demarcation zone shifts to lower cooling rates as the size of the catalyst increases. Thus, the larger the catalyst, the higher will be the freezing temperature at a given cooling rate. All of these results of the analysis imply that intracellular freezing of human RBCs is probably due to heterogeneous nucleation triggered by some catalyst.

The analysis also shows that if the extracellular medium is allowed to supercool, the probability of finding intracellular ice in RBCs will increase since the demarcation zone shifts to lower cooling rates as the degree of supercooling increases. Furthermore, the greater the degree of supercooling, the more sensitive the RBC freezing temperature becomes to intracellular ice formation. That is, when the degree of supercooling is high, a shift in supercooling of a few tenths of a degree in temperature can shift the demarcation zone by an order of magnitude or more. The analytical results are in agreement with past experimental data and clinical experience. It follows, then, that supercooling should be minimized in clinical freezing if the lethal effects of intracellular ice are to be avoided.

### Acknowledgments

This work was supported in part by USPHS Grant 1 PO1

HL14322-03 from NHLI; and Fundacao de Amparo a Pesquisa do Estado do Sao Paulo and Escola Politecnica da Universidade de Sao Paulo, Brazil.

### References

- Huggins, C. E., "Practical Preservation of Blood by Freezing," in *Red Cell Freezing*, A technical Workshop Presented by Committee on Workshops of the American Association of Blood Banks, 1973, pp. 31-53.
- Gibbs, J. W., *Scientific Papers*, Vol. 1, Dover, New York, 1961, pp. 219-331.
- Volmer, M., "Zum Problem des Kristall wachstums," *Z. Physik, Chem.*, Vol. 102, 1922, pp. 267-275.
- Becker, R., and Doring, W., "Kinetische Behandlung der Keimbildung in Übersättigten Dämpfen," *Ann. Physik.*, Vol. 24, 1935, pp. 719-752.
- Turnbull, D., and Fisher, J. C., "Rate of Nucleation in Condensed Systems," *J. Chem. Phys.*, Vol. 17, 1949, pp. 71-73.
- Dufour, L., and Defay, R., *Thermodynamics of Clouds*, Academic Press, New York, 1963.
- Uhlmann, R., and Chalmers, B., "The Energetics of Nucleation," *Industrial and Engineering Chemistry*, Vol. 57, 1965, pp. 19-31.
- Parker, R. L., "Crystal Growth Mechanisms: Energetics, Kinetics, and Transport," *Solid State Physics*, Vol. 25, Turnbull, ed., 1970, pp. 152-301.
- Turnbull, D., "Kinetics of Heterogeneous Nucleation," *J. Chem. Phys.*, Vol. 18, 1950, pp. 198-203.
- Dufour, L., and Defay, R., "Sur la formation des germes de condensation et de solidification autour d'un noyau solide insoluble," *Tellus*, Vol. 5, 1953, pp. 293-301.
- Fletcher, N. H., "Size Effect in Heterogeneous Nucleation," *J. Chem. Phys.*, Vol. 29, 1958, pp. 572-576.
- Fisher, J. C., Hollomon, J. H., and Turnbull, D., "Nucleation," *J. Appl. Phys.*, Vol. 19, 1948, pp. 775-784.
- Silvaes, O. M., "A Thermodynamic Model of Water and Ion Transport across Cell Membranes during Freezing and Thawing: The Human Erythrocyte," PhD thesis, Massachusetts Institute of Technology, Sept. 1974.
- Glasstone, S., Laidler, K. J., and Eyring, H., *The Theory of Rate Processes*, McGraw-Hill, New York, 1941.
- Canham, P. B., and Burton, A. C., "Distribution of Size and Shape in Populations of Normal Human Red Cells," *Circulation Research*, Vol. 22, 1968, pp. 405-422.
- Wintrobe, M. M., *Clinical Hematology*, Lea and Febiger, Philadelphia, 1967, pp. 106-107.
- Mazur, P., "Physical and Chemical Bases of Injury in Single-Celled Microorganisms Subjected to Freezing and Thawing," *Cryobiology*, H. T. Meryman, ed., Academic Press, New York, 1966, pp. 213-315.
- Diller, K. R., "A Microscopic Investigation of Intracellular Ice Formation in Frozen Human Erythrocytes," ScD thesis, Massachusetts Institute of Technology, June 1972.
- Diller, K. R., "Intracellular Freezing: Effect of Extracellular Supercooling," to be published in *Cryobiology*.
- Paganelli, C. V., and Solomon, A. K., "The Rate of Exchange of Tritiated Water Across the Human Red Cell Membrane," *Journal of General Physiology*, Vol. 41, 1957, pp. 259-277.

N. Shamsundar  
E. M. Sparrow

Department of Mechanical Engineering  
University of Minnesota, Minneapolis, Minnesota

# Analysis of Multidimensional Conduction Phase Change Via the Enthalpy Model

*The basis of the enthalpy model for multidimensional phase change problems in media having a distinct phase change temperature is demonstrated, and subsequent numerical applications of the model are carried out. It is shown that the mathematical representation of the enthalpy model is equivalent to the conventional conservation equations in the solid and liquid regions and at the solid-liquid interface. The model is employed in conjunction with a fully implicit finite-difference scheme to solve for solidification in a convectively cooled square container. The implicit scheme was selected because of its ability to accommodate a wide range of the Stefan number  $Ste$ . After its accuracy had been established, the solution method was used to obtain results for the local and surface-integrated heat transfer rates, boundary temperatures, solidified fraction, and interface position, all as functions of time. The results are presented with  $SteFo$  ( $Fo =$  Fourier number) as a correlating parameter, thereby facilitating their use for all  $Ste$  values in the range investigated. At low values of the Biot number, the surface-integrated heat transfer rate was relatively constant during the entire solidification period, which is a desirable characteristic for phase change thermal energy storage.*

## Introduction

Recent interest in the storage of thermal energy from intermittent sources such as the sun as well as ongoing interest in various processes in metals casting, food technology, welding, coating, etc. has highlighted the importance of solid-liquid and solid-vapor phase change phenomena. Although numerous papers have dealt with such phase change heat conduction problems, most of them have been restricted to one-dimensional cases. The few investigations that do deal with two-dimensional problems have been primarily concerned with predicting the location of the solid-liquid interface, omitting such information as heat flux variations, freezing rates, and temperature differences. Furthermore, in the main, the results are restricted to specific problems and to a limited range of parameters. In addition, none of the solution methods appears to be general and powerful enough to be applied successfully to the wide range of practical problems encountered in the technological fields mentioned in the foregoing.

A review of the relevant literature will now be presented in order to identify the present state of knowledge about the solution of multidimensional problems. Analytical and semianalytical methods of solution are described in references [1-9].<sup>1</sup> In general, these methods are tailored to specific problems and, therefore, have a

limited range of applicability. A summary of the aforementioned references is available in the thesis [10] on which the present paper is based.

If attention is now turned to purely numerical methods, it is convenient at the outset to divide them into two groups, based on the choice of dependent variables used. In the first group, the temperature is the sole dependent variable, and energy conservation equations are written separately in the solid region and in the liquid region. This is the approach employed most often to date. Since the interface between the two regions is, in general, an unknown curve whose position and shape vary with time, any finite-difference or finite-element discretization poses a problem in handling the interface. Publications covering this method are listed as references [2, 6, 11-14] and a summarizing description of their content is given in [10].

In the second group, the enthalpy is used as a dependent variable along with the temperature. This formulation may be termed the enthalpy method and will be more fully described in the Analysis Section of this paper. In this model, the interface is eliminated from consideration in the calculations, and the problem is made equivalent to one of nonlinear heat conduction without change of phase.

In all the previous work on two-dimensional phase change that was performed using this model, the curve of enthalpy versus temperature for the phase change substance has been assumed to have a finite slope at the phase change temperature. Such a representation is valid only for materials that change phase over a range of temperatures. Meyer [15] described a purely implicit two-dimen-

<sup>1</sup> Numbers in brackets designate References at end of paper.

Contributed by the Heat Transfer Division for publication in the JOURNAL OF HEAT TRANSFER. Manuscript received by the Heat Transfer Division January 26, 1975. Paper No. 75-HT-XX.

sional finite-difference scheme for studying phase change phenomena using this model, but presented only fragmentary numerical results. Although Meyer's approach was based on a model where the phase change occurs over a range of temperatures, he was primarily concerned with substances that change phase at a single distinct temperature, as was the case in the work of Comini and co-workers [16]. Bonacina and co-workers [17] showed that even in the one-dimensional case, the magnitude of the assumed range of phase change temperatures has an appreciable effect on the results. In light of these findings, it is highly desirable to develop a method which can deal both with substances that have a discrete phase change temperature and with those that change phase over a range of temperatures.

In a study of particular interest to the present authors, owing to its solar energy application, Griggs, Pitts, and Humphries [18] employed both explicit and implicit finite-difference schemes. In their implicit formulation, the treatment of the interface is similar to that of the enthalpy method, although it was not recognized as such. All the results presented in [18] apply to the instant at the end of melting, and information such as spatial and timewise heat flux variations and melting rates is not reported.

In this paper, an easily applied implicit finite-difference scheme incorporating the enthalpy method is described and subsequently employed. At the outset, it is demonstrated that the enthalpy form of the conservation equation is equivalent to three differential equations which are the conventional energy equations, one in each of the two single phase regions and the third at the interface. The solution method is equally applicable to substances that have a discrete phase change temperature and to those that do not, is unconditionally stable, and has minimum memory requirements when used on a digital computer. The method was applied to the solution of freezing in a square domain subject to convective cooling. Results were obtained for spatially local and total heat fluxes, boundary temperatures, solidified fraction, and interface position, all as functions of time.

A detailed examination was made of various aspects of the computational scheme. The accuracy of the results presented here is believed to be high enough to suggest that they may be used as a standard of reference for other solution techniques that may be developed in the future.

## Analysis

**Verification of the Enthalpy Model.** Although the enthalpy model has been described qualitatively by Dusinberre [19] and in greater detail by Baxter [20] and by Eyres and co-workers [21] for one-dimensional problems, the authors have not seen a rigorous

demonstration of the equivalence between the enthalpy form and the conventional form of the energy conservation equations for the case of a substance with a discrete phase-change temperature. Such a demonstration will, therefore, be presented here for the general multidimensional case. In the derivation, it will be assumed that the densities of the solid and liquid phases are identical and uniform, but that the other thermophysical properties may differ between the two phases and may also depend on temperature.

Prior investigators who employed the enthalpy model based their work on a differential equation involving the terms  $\partial i/\partial t$  and  $\text{div}(k \text{ grad } T)$ , where  $i$  is the specific enthalpy. At the interface, however, both  $i$  and  $(k \text{ grad } T)$  change discontinuously, so that the aforementioned terms are indeterminate and the differential equation is not applicable at the interface. Therefore, to obtain an enthalpy-based representation of energy conservation which is valid at the interface as well as in the adjacent single phase regions, an integral relation is used.

For an arbitrary control volume  $V$  which is fixed in space, the rate of increase of its energy content with time has to be equal to the net rate at which heat is conducted into  $V$  through its surface area  $A$ , if there are no sources of energy inside  $V$  and no external work is performed. In mathematical form,

$$\frac{d}{dt} \int_V \rho u dV = \int_A k \text{ grad } T \cdot \hat{n} dA \quad (1)$$

This equation is applicable whether or not the interfacial surface passes through  $V$ . It may be noted that the pressure  $p$  is independent of time in the absence of motion. Therefore,

$$\frac{d}{dt} \int_V p dV = 0 \quad (2)$$

and, if  $\rho u$  is replaced by  $\rho i - p$ , then the following form of the energy conservation law, which will hereafter be called the enthalpy equation, emerges

$$\frac{d}{dt} \int_V \rho i dV = \int_A k \text{ grad } T \cdot \hat{n} dA \quad (3)$$

The  $i$  versus  $T$  relationship for the phase change substance is used in conjunction with equation (3).

In order to demonstrate the equivalence of this relation to the conventional forms, it will be applied first to a control volume which does not contain the interface, and then to another control volume through which the interface passes. In the first case, both  $\rho i$  and  $(k \text{ grad } T)$  are continuous throughout  $V$  and  $A$ , respectively, so that the divergence theorem may be applied to the right-hand side to get

## Nomenclature

$A$ = surface area of container	$q$ = local heat transfer rate	$\theta$ = dimensionless enthalpy variable, equation (17)
$a$ = cross-sectional area of finite-difference element	$\hat{q}$ = dimensionless local heat flux, $q/h(T_{\text{sat}} - T)$	$\lambda$ = latent heat of fusion
$Bi$ = Biot number, $hL/k_s$	$Ste$ = Stefan number, $c_s(T_{\text{sat}} - T_{\infty})/\lambda$	$\rho$ = density
$c$ = specific heat	$s$ = arc length along perimeter $P$	$\phi$ = dimensionless temperature variable, equation (17)
$F$ = solid fraction	$T$ = temperature	
$Fo$ = Fourier number $(k_s/\rho c_s L^2)t$ ; $\Delta Fo$ , dimensionless time step	$T_{\text{sat}}$ = saturation temperature	
$h$ = convective heat transfer coefficient	$T_{\infty}$ = coolant temperature	<b>Subscripts</b>
$i$ = specific enthalpy	$t$ = time	$i, j$ = spatial location
$k$ = thermal conductivity	$u$ = specific internal energy	$l$ = liquid region
$L$ = half side dimension of container wall	$v_n^*$ = local velocity of interface along its normal	$s$ = solid region
$P$ = perimeter of finite-difference element	$X, Y$ = dimensionless spatial coordinates, $x/L$ and $y/L$	$w$ = wall of container
$Q$ = surface-integrated heat transfer rate	$x, y$ = spatial coordinates	<b>Superscripts</b>
	$\delta$ = spatial step size	$m$ = time level
		$*$ = saturated state

$$\int_V \frac{\partial}{\partial t} (\rho i) dV = \int_V \text{div} (k \text{ grad } T) dV \quad (4)$$

To obtain the left-hand side of equation (4) from (3), it may be noted that the operations of volume integration and differentiation with respect to time can be performed in reversed order because  $V$  is independent of time and the integrand is continuous. In addition, when moved inside the integral,  $d/dt$  becomes  $\partial/\partial t$ . Further, since (4) can be written as

$$\int_V \left[ \frac{\partial}{\partial t} (\rho i) - \text{div} (k \text{ grad } T) \right] dV = 0 \quad (5)$$

which is true for any control volume  $V$  within a single phase region, it is necessary that

$$\frac{\partial}{\partial t} (\rho i) - \text{div} (k \text{ grad } T) = 0 \quad (6)$$

By using the relation  $di = cdT$ , the enthalpy may be eliminated to get

$$\rho c \partial T / \partial t = \text{div} (k \text{ grad } T) \quad (7)$$

This is the conventional heat conduction equation for a single phase region.

Now, we shall apply equation (3) to the control volume  $V$  which spans the interface as shown in Fig. 1. At time  $t$ , the interfacial surface  $\Sigma$  divides the control volume  $V$  into a solid portion  $V_s$  and a liquid portion  $V_l$ , and similarly divides the surface area  $A$  of  $V$  into two parts  $A_s$  and  $A_l$ . After a small increment  $\delta t$  in time, the interface occupies a new position  $\Sigma'$  and, during this time, has swept through the incremental volume  $\delta V$ , resulting in an increase in the volume of solid and a corresponding decrease in the volume of liquid. In this case,  $(k \text{ grad } T)$  and  $i$  change discontinuously across the moving surface  $\Sigma$ . Therefore, in order to derive the conservation condition at the interface, we shall split the integrals on both sides of (3) into their components for each region and study their variations in time separately. The integral on the left of (3) will be investigated first.

At time  $t$ ,

$$\begin{aligned} \int_V \rho i dV &= \int_{V_s} (\rho i)_s dV + \int_{V_l} (\rho i)_l dV = \int_{V_s} (\rho i)_s dV \\ &+ \int_{V_l - \delta V} (\rho i)_l dV + \int_{\delta V} (\rho i)_l dV \quad (8) \end{aligned}$$

and at time  $t + \delta t$ ,

$$\begin{aligned} \int_V \rho i dV &= \int_{V_s + \delta V} (\rho i)_s dV + \int_{V_l - \delta V} (\rho i)_l dV = \int_{V_s} (\rho i)_s dV \\ &+ \int_{\delta V} (\rho i)_s dV + \int_{V_l - \delta V} (\rho i)_l dV \quad (9) \end{aligned}$$

The left-hand side of (3) is obtained by subtracting (8) from (9), dividing by  $\delta t$ , and taking limits as  $\delta t$  approaches zero. Remembering that as  $\delta t \rightarrow 0$ ,  $(V_l - \delta V) \rightarrow V_l$ , we get

$$\begin{aligned} \frac{d}{dt} \int_V \rho i dV &= \frac{d}{dt} \int_{V_s} (\rho i)_s dV + \frac{d}{dt} \int_{V_l} (\rho i)_l dV \\ &+ \lim_{\delta t \rightarrow 0} \int_{\delta V} \frac{(\rho i)_{s,t+\delta t} - (\rho i)_{l,t}}{\delta t} dV \quad (10) \end{aligned}$$

Attention may now be focused on the last term on the right-hand side. This term involves an integral over the incremental volume  $\delta V$  which spans the interface. As  $\delta t \rightarrow 0$ , the ratio  $dV/\delta t$  approaches  $v_n^* d\Sigma$ , where  $v_n^*$  is the local velocity of the interfacial surface element  $d\Sigma$  normal to itself and toward the liquid region. Also, the space which is enclosed by  $\delta V$  shrinks to the surface  $\Sigma$ , so that the region of integration becomes  $\Sigma$ . Simultaneously,  $i_s$  and  $i_l$  approach their saturation values  $i_s^*$  and  $i_l^*$ . Hence,

$$\begin{aligned} \frac{d}{dt} \int_V \rho i dV &= \frac{d}{dt} \int_{V_s} (\rho i)_s dV + \frac{d}{dt} \int_{V_l} (\rho i)_l dV \\ &+ \int_{\Sigma} \rho (i_s^* - i_l^*) v_n^* d\Sigma \quad (11) \end{aligned}$$

Next, the integrals over  $V_s$  and  $V_l$  are replaced by applying the

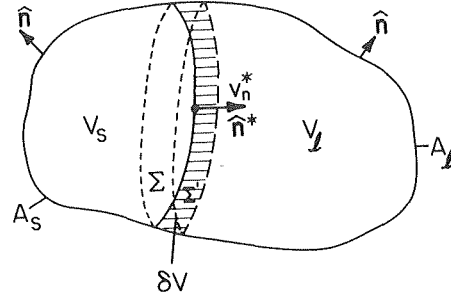


Fig. 1 Control volume for derivation of interface condition

enthalpy equation (3) to the respective single phase regions, and it is recognized that  $(i_l^* - i_s^*) = \lambda$  is the enthalpy of fusion, thereby reducing (11) to the form

$$\begin{aligned} \frac{d}{dt} \int_V \rho i dV &= \int_{A_s + \Sigma} k \text{ grad } T \cdot \hat{n} dA \\ &+ \int_{A_l + \Sigma} k \text{ grad } T \cdot \hat{n} dA - \int_{\Sigma} \rho \lambda v_n^* d\Sigma \quad (12) \end{aligned}$$

In the first term on the right-hand side,  $\hat{n}$  represents the outward normal to  $V_s$ , whereas in the second, it represents the outward normal to  $V_l$ . If we denote by  $\hat{n}^*$  the local normal to  $\Sigma$  toward the liquid region, then for the portions of the two integrals over  $\Sigma$ ,  $\hat{n} = \hat{n}^*$  and  $\hat{n} = -\hat{n}^*$  respectively. With these observations, we then split up the integrals in (12) and recombine them to get

$$\begin{aligned} \frac{d}{dt} \int_V \rho i dV &= \int_A k \text{ grad } T \cdot \hat{n} dA + \int_{\Sigma} \left[ \left( k \frac{\partial T}{\partial n^*} \right)_s - \left( k \frac{\partial T}{\partial n^*} \right)_l \right. \\ &\left. - \rho \lambda v_n^* \right] d\Sigma \quad (13) \end{aligned}$$

where the integral over  $A$  is the sum of the integrals over  $A_s$  and  $A_l$ .

Next, by subtracting from (13) the enthalpy equation (3), we find that the integral over  $\Sigma$  is equal to zero. Since  $\Sigma$  is an arbitrary part of the interface, the integrand vanishes at all points on the interface. Hence,

$$(k \partial T / \partial n^*)_s - (k \partial T / \partial n^*)_l - \rho \lambda v_n^* = 0 \quad (14)$$

This is the conventional energy conservation condition at the interface, thereby completing the derivation.

For a substance that solidifies over a range of temperatures, there is no sharp interface. The relation  $di = cdT$  also applies in the interfacial region so that the enthalpy equation (3) reduces to the heat conduction equation (7) in the solid, liquid, and interfacial regions.

#### Finite-Difference Representation of the Enthalpy Model.

The first step in obtaining a finite-difference representation is to subdivide the region of interest into a number of small elements, for example, squares for two-dimensional problems and cubes for three-dimensional problems. Then, nodal points are placed at the centers of the elements, and the values of the enthalpy and the temperature at these nodes are studied as functions of time. During the computational process, each element through which the interface passes is identified by keeping track of its total enthalpy  $I$ , where

$$I = \int_V \rho i dV \quad (15)$$

and  $V$  is the volume of the element. If  $I$  lies between the two values of the integral corresponding to  $i = i_s^*$  and  $i = i_l^*$ , then the interface passes through the element. In this case, the temperature of the element is taken to be  $T_{\text{sat}}$ .

When the  $I$  value for an element lies outside the aforementioned bounds, then the element is in a single phase region and its specific enthalpy is evaluated as

$$i = I / \rho V \quad (16)$$

The temperature of the element is calculated from the known  $i$  versus  $T$  relationship for the material.

Next, we shall describe a fully implicit difference technique. Before the implicit scheme was decided upon, numerical experiments were performed using the standard explicit method. It was found that stability limitations on the time step led to very large amounts of computer time being required for the small values of the Stefan number  $Ste$  that are encountered in the solar thermal storage applications of interest here.

The description of the finite-difference formulation will be referred to a specific problem associated with a solar energy storage unit. A long storage container with a square ( $2L \times 2L$ ) cross section contains a phase change material (PCM) that is initially in the liquid state at its saturation temperature  $T_{sat}$ . For  $t > 0$ , the container is cooled on its surface by convective heat transfer to a fluid medium having temperature  $T_\infty < T_{sat}$  and heat transfer coefficient  $h$ . Both  $T_\infty$  and  $h$  are uniform along the surface and constant with time. The wall of the container itself is assumed to have negligible thermal resistance and heat capacity. Within the knowledge of the authors, there are no existing solutions of this problem (nor of its one-dimensional form).

The ensuing transient is to be computed up to the instant when the phase change material has completely solidified. Aside from the enthalpy, the properties of the PCM are assumed to be independent of temperature.

Symmetry enables the solution to be carried out only for a representative octant of the square, as shown in the inset of Fig. 2. The symmetry lines are adiabatic and are characterized by the boundary condition  $q = 0$ . The lower boundary of the octant experiences convective cooling expressed by  $q = h(T_w - T_\infty)$ , where both  $q$  and  $T_w$  are unknown functions of time and position. Fig. 2 also contains an enlarged view of the octant showing the  $x, y$  coordinates and nomenclature pertaining to the finite-difference technique.

Before employing the finite-difference technique, it is advantageous to convert the governing equations to a dimensionless form. The dimensionless space and time coordinates are, respectively,  $X, Y$  and  $Fo$  (see Nomenclature). The parameters of the problem are the Biot number  $Bi$  and the Stefan number  $Ste$ . The Stefan number represents the importance of the heat capacity of the solid relative to the latent heat.

Inasmuch as the problem is two-dimensional, we deal with elements having cross-sectional areas  $a$  rather than volume elements  $V$  that appeared in the general three-dimensional formulation. Similarly, the three-dimensional surface area  $A$  is replaced by the arc length  $s$ . These modifications can be incorporated into the enthalpy equation (3).

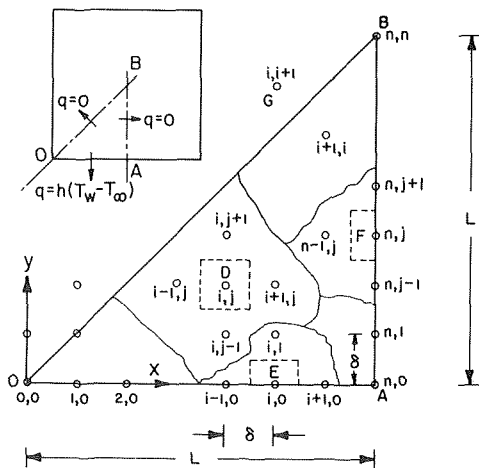


Fig. 2 Representative octant of square container and finite-difference nomenclature

According to the enthalpy model, there are two dependent variables. These are the dimensionless nodal enthalpy  $\theta$  and dimensionless nodal temperature  $\phi$  defined as follows

$$\theta = \frac{1}{\rho a} \int_a \rho \frac{(i - i_s^*)}{\lambda} da, \quad \phi = c_s(T - T_{sat})/\lambda \quad (17)$$

The  $\theta$  variable is negative within the solidified region and unity in the liquid (since the liquid is at  $T_{sat}$  and its enthalpy is  $i_s^*$ ). Also,  $\phi$  is negative in the solid and zero in the liquid. The relationship between  $\theta$  and  $\phi$  is

$$\phi = \theta \text{ for } \theta < 0, \quad \phi = 0 \text{ for } 0 \leq \theta \leq 1 \quad (18)$$

For an element through which the interface passes,  $0 \leq \theta \leq 1$  and the value of  $\theta$  is equal to the fraction of the element which is in the liquid state.

In terms of the new variables, the enthalpy equation (3) takes the form

$$(a/L^2) \partial \theta / \partial Fo = \int_P \text{grad } \phi \cdot \hat{n} ds \quad (19)$$

where  $P$  is the perimeter of the element. From the definition of  $\theta$  and the fact that the PCM is initially saturated liquid, it follows that

$$\theta = 1 \text{ at } Fo = 0 \quad (20)$$

If an element has edges lying on the boundary or on a line of symmetry, equation (19) is rewritten as

$$(a/L^2) \partial \theta / \partial Fo = \int_{P_i} \text{grad } \phi \cdot \hat{n} ds - Ste Bi \int_{P_0} \hat{q} ds \quad (21)$$

where  $P_i$  is the portion of  $P$  lying within the PCM and  $P_0$  is the portion coinciding with the boundary or line of symmetry. In equation (21),  $\hat{q}$  is the dimensionless heat flux on  $P_0$ . On the lines of symmetry,  $OB$  and  $AB$ ,  $\hat{q} = 0$ , and on the bottom boundary  $OA$ ,  $\hat{q} = (\phi + Ste)/Ste$ .

Next, equations (19)–(21) are replaced by their finite-difference counterparts. For this purpose, the sides  $OA$  and  $AB$  are divided into  $n$  equal parts each, and a lattice of squares is constructed by drawing lines parallel to the coordinate axes through the subdividing points. The nodes of the lattice, which are at intersections of these lines, are identified by pairs of indices running from  $0,0$  to  $n,n$  starting from the origin of coordinates, as shown in Fig. 2. Then, elements having the nodes at their centers are constructed, as shown by dashed lines for a few nodes in the figure.

Using subscript pairs to denote location and superscripts to denote time level, the finite-difference representation for an interior node such as  $D$  is written as

$$(\theta_{i,j}^m - \theta_{i,j}^{m-1})/\Delta Fo = (\phi_{i+1,j}^m + \phi_{i-1,j}^m + \phi_{i,j+1}^m + \phi_{i,j-1}^m - 4\phi_{i,j}^m)/(\delta/L)^2 \quad (22)$$

where  $\Delta Fo$  is a dimensionless time step and  $\delta/L$  is the dimensionless spatial step size.

At a point on the external boundary  $OA$  such as  $E$ , the difference equation is

$$(\theta_{i,0}^m - \theta_{i,0}^{m-1})/\Delta Fo = (\phi_{i+1,0}^m + \phi_{i-1,0}^m + 2\phi_{i,1}^m - 4\phi_{i,0}^m)/(\delta/L)^2 - 2 Bi (\phi_{i,0}^m + Ste)/(\delta/L) \quad (23)$$

For a typical point  $F$  on the adiabatic boundary  $AB$ , the difference equation resembles equation (23) with the  $Bi$  term deleted. Slightly different equations are written for the corners  $O$ ,  $A$ , and  $B$ . For a point such as  $G$ , the symmetry condition gives  $\theta_{i,i+1}^m = \theta_{i+1,i}^m$ .

It should be observed that in writing equations (22) and (23), derivatives with respect to time are represented by backward (implicit) differences, whereas central differences are used for the spatial derivatives that appear in the gradient operator.

The foregoing difference equations, together with the initial condition  $\theta_{i,j}^0 = 1$  (for all  $i$  and  $j$ ) and the rules in (18), form a complete set of nonlinear, simultaneous algebraic equations for the unknown temperatures and enthalpies at time level  $m$ . These

equations contain known enthalpies from time level  $m - 1$  as input.

**Solution of the Finite-Difference Equations.** A number of techniques were investigated [10] for solving the system of algebraic equations that were obtained in the preceding subsection, and the Gauss-Seidel iterative method was selected for the production runs. This method is attractive because it needs little computer memory. In addition, the iterations necessary for the solution and the iterations necessary to ascertain the applicable relationship between  $\theta$  and  $\phi$  can be carried out *simultaneously*. We shall describe the solution method for a representative equation such as (22). The other equations are treated in the same manner.

Suppose that the solution has been performed up to the time level  $m - 1$ , and it is desired to extend it to level  $m$ . To start the calculation, as a first guess, all the  $\theta^m$  values are taken equal to the corresponding  $\theta^{m-1}$  values of the previous time level. Then, proceeding in some definite order as to the way  $i$  and  $j$  are varied, the first iteration is performed as follows. Equation (22) is written in the form

$$(\delta/L)^2/\Delta Fo \theta_{i,j}^m + 4\phi_{i,j}^m = (\delta/L)^2/\Delta Fo \theta_{i,j}^{m-1} + (\phi_{i+1,j}^m + \phi_{i-1,j}^m + \phi_{i,j+1}^m + \phi_{i,j-1}^m) \quad (24)$$

As per the rules (18), if the unknown  $\theta_{i,j}^m < 0$ , the left-hand side of (24) is equal to  $((\delta/L)^2/\Delta Fo + 4)\theta_{i,j}^m$ . On the other hand, if  $0 \leq \theta_{i,j}^m \leq 1$ , the left-hand side becomes  $((\delta/L)^2/\Delta Fo)\theta_{i,j}^m$ . In either case, the coefficient of  $\theta_{i,j}^m$  is positive definite. Hence, the sign of  $\theta_{i,j}^m$  is the same as that of the right-hand side of (24), and this fact is used to determine the applicable  $\theta, \phi$  relationship as discussed in the next paragraph.

The right-hand side of (24) is evaluated by using the most recently computed values of  $\theta^m$  at the four points surrounding  $i, j$  and applying (18) to obtain the corresponding  $\phi$  values. If the right-hand side is negative, this means that  $\theta_{i,j}^m < 0$ , so that dividing the right-hand side by  $(\delta/L)^2/\Delta Fo + 4$  gives the new value of  $\theta_{i,j}^m$ . On the other hand, if the right side of (24) is positive, the new value of  $\theta_{i,j}^m$  is obtained upon dividing by  $(\delta/L)^2/\Delta Fo$  alone. After recording the change in  $\theta_{i,j}^m$  relative to the guess value, the latter is immediately replaced by the new value.

This process is then repeated for all the nodes, and the recorded changes in the  $\theta$  values relative to the first guess are examined to see if they satisfy a convergence criterion. If they do not, the whole procedure is performed a second, third, etc., time, until the criterion is satisfied. In this way, the solution is extended in time as long as required.

The dimensionless step size in time  $\Delta Fo$  may be varied as the transient progresses in order to either hasten the computations or to obtain more detailed results. Further, a substantial saving in computational effort is achieved by not solving difference equations in the liquid region, which remains at the saturation temperature.

**Stability of the Implicit Method.** Because of the nonlinear nature of the algebraic equations, the usual means of examining the question of stability are inapplicable. Application of von Neumann's method to a linearized version of the equations (i.e., with  $\phi = \theta$  everywhere) indicates unconditional stability, but the only satisfactory way of settling the question appears to be by numerical experimentation with various combinations of spatial and time-wise step sizes. During the entire course of the extensive computations that were performed, instability was never encountered, even for very large steps in time. The step sizes are, therefore, governed entirely by requirements of numerical accuracy.

**Deduction of Results.** The iterative method of the previous paragraph yields values of  $\theta$  as a function of time at all the nodal points. We shall now describe how to obtain the temperature field, surface heat flux distribution, solidified fraction, and interface location from these  $\theta$  values, at any given instant of time.

The temperatures at the nodal points are easily obtained from the  $\theta, \phi$  relationship (18) and the definition of  $\phi$  in equation (17). At those nodes where  $\theta < 0$ , the temperature is given by  $T = T_{\text{sat}} +$

$\lambda\theta/c_s$ . At the rest of nodes,  $0 \leq \theta \leq 1$  and  $T = T_{\text{sat}}$ . The temperatures  $T_w(x)$  at the nodes situated on the exposed boundary  $OA$  are then used to compute the local heat flux  $q_w(x)$  by using the relation  $q_w = h(T_w - T_\infty)$ . Then, the local flux distribution is integrated along the perimeter of the container by employing a tabular integration technique.

The fractional part of the PCM which has solidified is obtained by summing up the masses of the solid elements and the solid portions of the masses of the two-phase elements, and dividing by the total mass. In carrying out the operations, it should be noted that the solid portion of a two-phase element is equal to 1 minus the  $\theta$  value for the element.

For obtaining the solid-liquid interface, use is made of the two-phase elements. If the spatial subdivision is sufficiently fine, a close approximation of the interface may be obtained by drawing a smooth curve through these elements. If this is insufficient, greater accuracy is achieved by using the values of  $\theta$  for each of these elements and then drawing the interface by visual inspection or by a yet to be developed algorithm. A less laborious alternative is to regard the area of the liquid region, subtended between  $AB$  and a moving vertical line, as being a function of the distance between these lines, and then to obtain the ordinate of the interface by differentiation. The interface positions presented in this paper were found by such a differentiating procedure.

## Results

The calculation procedure described in the previous section was employed to obtain a complete set of results for parametric values of the Stefan number equal to 0.01, 0.05, and 0.10, and for values of the Biot number equal to 0.1, 1, and 10. These values were chosen to be consistent with the design requirements for a solar energy storage unit suitable for use in an electricity generating plant. It will suffice to mention here that  $L$  is typically of the order of 5 cm (2 in.), and  $T_{\text{sat}} - T_\infty$  is limited to around 10C ( $\sim 20^\circ\text{F}$ ). These numbers, together with the thermal properties of the various substances being considered for use as PCM's, lead to the range of Stefan numbers mentioned. Further, the pool boiling heat transfer coefficients expected in the application give rise to the previously mentioned range of Biot numbers.

**Results of Numerical Experiments.** Three operational aspects of the solution method were examined by extensive numerical experiments. The first aspect was the convergence criterion for the nonlinear algebraic equations which were solved iteratively at each time step. A convergence criterion based on the average of the absolute magnitudes of the changes of the enthalpy variable at the active nodes ( $\theta < 1$ ) was used. Convergence to three significant figures was obtained when the convergence criterion was in the range  $10^{-6}$ – $10^{-7}$ .

The effect of the time step size was the second aspect that was examined. For a given case, the time step  $\Delta Fo$  was varied as the solidification proceeded, with the steps being chosen smaller or larger to accommodate faster or slower rates of solidification. To insure that the step size  $\Delta Fo$  was not a factor in the accuracy of the results, runs were successively repeated with halved time steps. The  $\Delta Fo$  values were considered small enough when the results of two successive runs agreed to three significant digits.

The final aspect studied was the influence of the spatial step size. Experiments made with  $\delta/L = 0.2, 0.1, 0.05$ , and  $0.025$  showed definite convergence, with the results for  $0.05$  and  $0.025$  being the same to within plotting accuracy for  $Bi = 0.1$  and  $Bi = 1$ . For the final computer runs, consequently, the  $0.05$  step size was employed. For the  $Bi = 10$  case, the choice of  $\delta/L = 0.05$  was found inadequate for computing results during a brief period following the onset of solidification. The reasons for the inadequacy, and an artifice used to obtain results for this period, are described in [10]. For the rest of the transient, the  $0.05$  step size was found satisfactory.

Numerical experiments were also conducted to verify the accuracy of the fully implicit scheme itself. For this purpose, the program was altered to incorporate the Crank-Nicholson scheme, re-

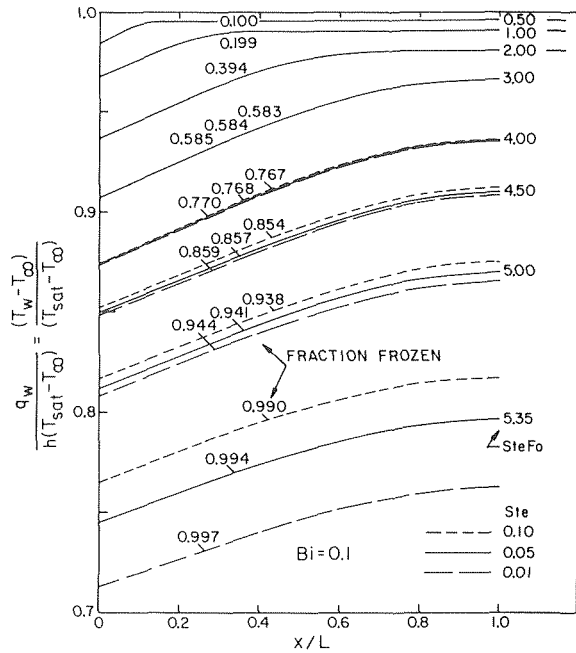


Fig. 3 Distribution of heat flux on cooled surface of phase change material,  $Bi = 0.1$

taining the Gauss-Seidel method for solving the resulting equations. In general, there was no perceptible change in the results to within three significant digits, but the computational speed suffered an appreciable degradation. For these reasons, the implicit scheme is considered superior to the Crank-Nicholson scheme for this problem.

**Heat Flux Distribution.** The distribution of heat flux on the cooled surface of the PCM is shown in Figs. 3-5. The local heat flux  $q_w$  is normalized with respect to its value  $h(T_{sat} - T_{\infty})$  at the beginning of the transient. In addition, since  $q_w = h(T_w - T_{\infty})$  at any instant of time, an alternative interpretation of the ordinate is the ratio  $(T_w - T_{\infty}) / (T_{sat} - T_{\infty})$ . Therefore, the figures also represent the surface temperature distributions.

The dimensionless time parameter for the curves is the product  $SteFo$ , values of which are shown at the right-hand end of the respective curves. The product  $SteFo$ , rather than the Fourier number  $Fo$ , is used because it correlates the results for the various values of  $Ste$ . The motivation for using this product comes from an examination of the case where  $Ste$  approaches zero. For this case, the specific heat is not involved in the solution, nor is  $Ste$  when the time variable is  $SteFo$ . For small  $Ste$ , the results of Figs. 3-5 indicate that the use of the  $SteFo$  variable accounts for most of the dependence of the results on  $Ste$ . The separate dependence on  $Ste$  gives rise to a small spread which becomes more pronounced near the termination of the solidification process. The curves associated with the different  $Ste$  values are identified by different types of lines. When they coincide, a solid line is employed.

For reference, the values of the fraction  $F$  that is frozen at the instant corresponding to each of the curves are indicated. The last triplet of curves in each figure represents the situation at an instant when solidification is nearly complete.

A characteristic common to Figs. 3-5 is the way in which the shape of the heat flux distribution evolves with time. At the start of the transient, the curve is horizontal with the ordinate equal to one for all values of  $x/L$ . As the freezing progresses, the heat flux decreases faster at the corner of the container than at the line of symmetry. This is a consequence of the higher thermal resistance of the thicker solid layer at the corner which, because of heat loss from the two adjacent faces, freezes faster. During the initial por-

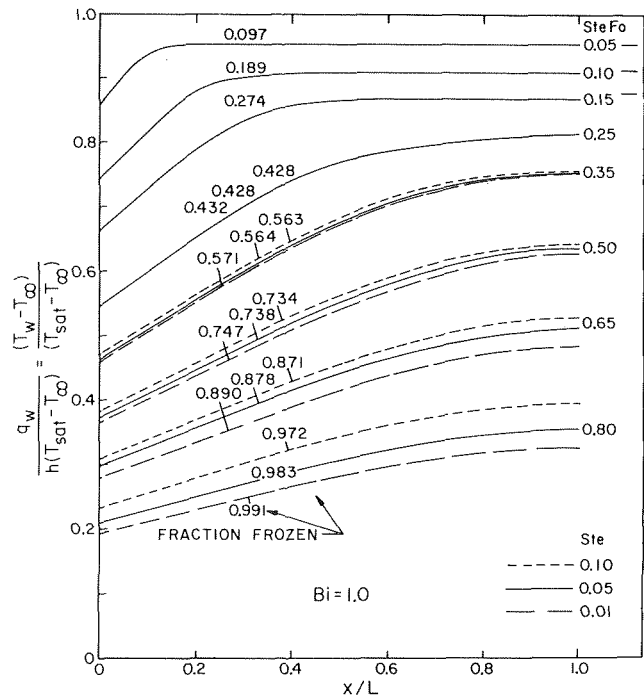


Fig. 4 Distribution of heat flux on cooled surface of phase change material,  $Bi = 1.0$

tion of the solidification, this effect is evident only in the immediate vicinity of the corner, and the heat flux is uniform away from this region. As time progresses, the corner effect propagates toward the interior of the square. The flat portions of the heat flux curves diminish in width and finally disappear, signalling fully two-dimensional heat transfer.

With respect to the effect of  $Bi$ , it may be noted that at the same level of dimensionless heat flux, the region of spatial uniformity is larger at higher  $Bi$ , with a correspondingly steeper drop-off near

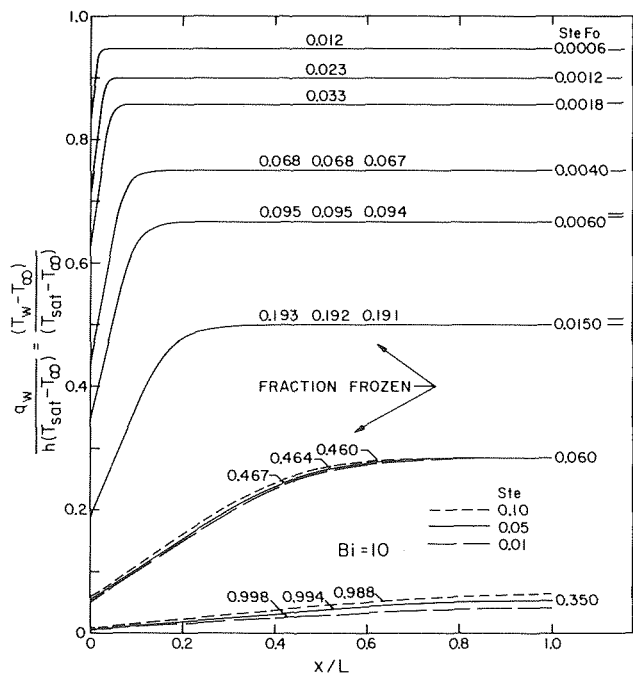


Fig. 5 Distribution of heat flux on cooled surface of phase change material,  $Bi = 10$

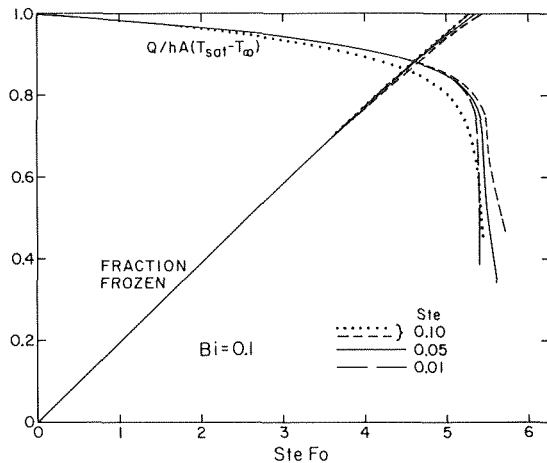


Fig. 6 Time variation of surface-integrated heat transfer rate and of frozen fraction,  $Bi = 0.1$

the corner. At comparable values of the frozen fraction, smaller values of the dimensionless heat flux are in evidence at higher  $Bi$  values.

It is interesting to compare the flat portions of the heat flux curves with the results of a one-dimensional calculation. These results are represented in Figs. 3–5 by short line segments at the right-hand margins of the respective figures. Where these values vary with  $Ste$ , as for  $Bi = 10$  and  $SteFo = 0.006$  and  $0.015$ , a pair of line segments is shown, the upper one of which is for  $Ste = 0.1$  and the lower is for  $Ste = 0.01$ . The agreement between the one-dimensional results, which were obtained by a nonfinite-difference method, and the two-dimensional numerical solution is generally very close and, hence, reassuring.

**Surface-Integrated Heat Flux and Frozen Fraction.** From the point of view of application of the results to thermal storage, the surface-integrated heat flux  $Q$  and the frozen fraction  $F$  are likely to be of more interest than the spatial distributions. The variation of  $Q$  with time is presented in dimensionless terms in Figs. 6–8. In the ordinate variable,  $A$  is the surface area of the container. The denominator of the ordinate variable is the  $Q$  value at time equal to zero. For constructing these curves, a much denser set of values of  $SteFo$  were employed than those shown in Figs. 3–5.

These curves start with an ordinate value equal to one and then show a continuous decrease with time. This decrease is markedly affected by the Biot number. For  $Bi = 0.1$ , the external convective

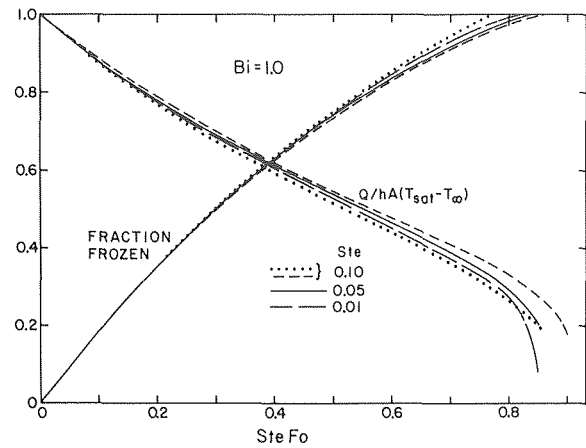


Fig. 7 Time variation of surface-integrated heat transfer rate and of frozen fraction,  $Bi = 1.0$

resistance dominates over the internal resistance of the solidified PCM. Since the external resistance does not change with time, the heat flux is essentially constant throughout the entire solidification period, dropping to about 0.8 at complete solidification. The curves exhibit almost no effect of heat capacity up to the end of solidification. Thereafter, there is no latent heat available, and  $Q$  drops off very rapidly. The heat flux is entirely fed by changes in sensible heat content, and a significant spread between the curves for different  $Ste$  develops.

Next, taking the case  $Bi = 1$ , we find that the surface-integrated heat flux decreases to a value of about 0.3 at the end of solidification. This decrease is almost linear in time and is much greater than for the  $Bi = 0.1$  case. The heat capacity influence is also slightly more significant here.

For the  $Bi = 10$  case, the heat flux behaves in a manner opposite to that for  $Bi = 0.1$ , i.e.,  $Q$  drops to a small value in a brief period at the start of the transient and slowly decreases thereafter. In this case, the internal resistance is much larger than the external resistance, and the former changes as solidification progresses. The curve for  $Ste = 0.05$  is omitted to preserve clarity.

A practical conclusion relevant to thermal storage that follows from the aforementioned results is that small values of  $Bi$  should be employed to obtain a steady rate of energy extraction. However, other design constraints such as the magnitude of the energy extraction rate and the duration of operation have to be taken into account.

Figs. 6–8 also contain curves of the frozen fraction  $F$  plotted against time, for all three Stefan numbers and for each Biot num-

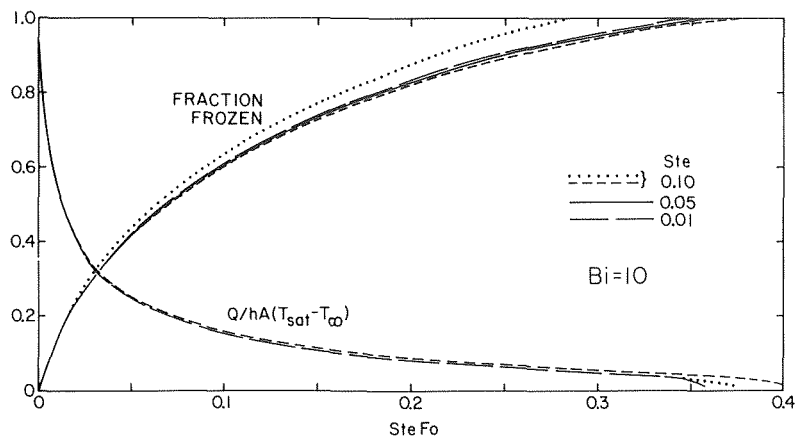


Fig. 8 Time variation of surface-integrated heat transfer rate and of frozen fraction,  $Bi = 10$

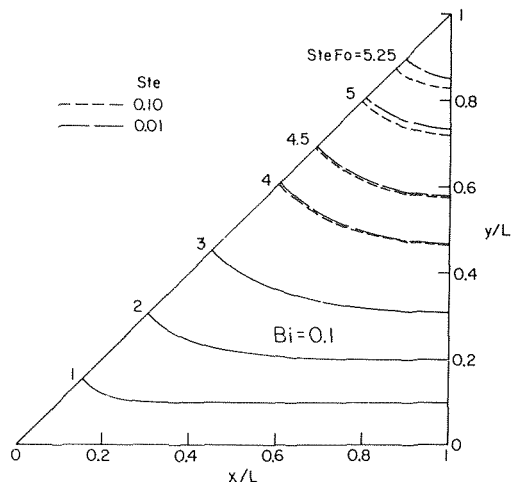


Fig. 9 Position of solid-liquid interface at various times,  $Bi = 0.1$

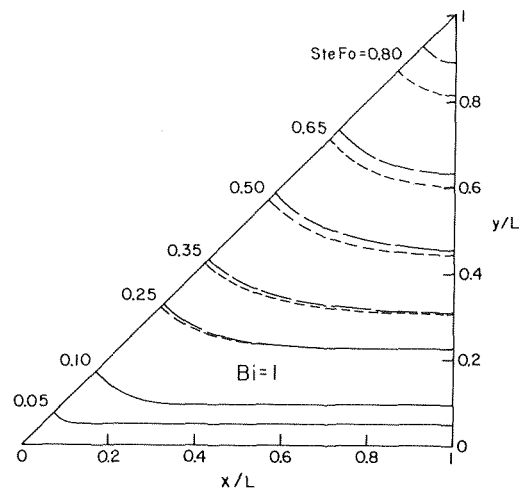


Fig. 10 Position of solid-liquid interface at various times,  $Bi = 1.0$

ber. With  $Bi = 0.1$ , the variation of  $F$  is almost linear in time, which means that the solidification rate is almost constant. As the Biot number increases, the freezing rate varies more and more with time, starting with the highest rate at the beginning and then decreasing continuously till the end. The time required for freezing to be complete is obtainable by reading from the figures the value of  $SteFo$  at  $F = 1$ .

If the heat capacity were completely negligible ( $Ste = 0$ ), then the rate of change of  $F$  with time, i.e., the freezing rate, would be exactly proportional to  $Q$ . For nonzero  $Ste$ , this proportionality may be employed to obtain an approximation to the  $Q$  versus time variation from the  $F$  values, and conversely.

The results for  $Q$  and  $F$  found in this way are plotted as dotted lines in the figures. Only results for  $Ste = 0.1$  are given since they correspond to the largest heat capacity. Inspection of the figures indicates that this procedure yields good results for  $F$  at small  $Bi$  and for  $Q$  at large  $Bi$ .

**Interface Locations.** For purposes of illustration, a set of figures has been prepared to show the position of the solid-liquid interface at various times. Each of Figs. 9-11 applies to a particular Biot number. Results are presented for  $Ste = 0.01$  and  $Ste = 0.1$ , using long and short dashed lines, respectively. Where curves for both values of  $Ste$  coincide, a solid line has been used. The values of  $SteFo$  at which interface positions are drawn are generally the same as those at which heat flux distributions are given in Figs. 2-5.

In general, for a short time following the start of solidification, the interface is straight except for a sharp curvature at the corner. As the freezing progresses, the propagation of the two-dimensionality into the growing solid region causes the interface to be more curved. In the beginning, the interface position is independent of  $Ste$ . At later times, the interface has advanced further when  $Ste$  is lower and, near the end of solidification, there is a significant effect of  $Ste$ .

### Acknowledgment

This research was performed under Grant No. GI-34871 from the National Science Foundation (RANN).

### References

- 1 Poots, G., *International Journal of Heat and Mass Transfer*, Vol. 5, 1962, pp. 339-348.
- 2 Rathjen, K. A., and Jiji, L. M., *JOURNAL OF HEAT TRANSFER*, TRANS. ASME, Series C, Vol. 93, 1971, pp. 101-109.
- 3 Budhia, H., and Kreith, F., *International Journal of Heat and Mass Transfer*, Vol. 16, 1973, pp. 195-211.
- 4 Sikarskie, D. L., and Boley, B. A., *International Journal of Solids and Structures*, Vol. 1, 1965, pp. 207-234.
- 5 Boley, B. A., and Yagoda, H. P., *Quarterly of Applied Mathematics*, Vol. 27, 1969, pp. 223-246.

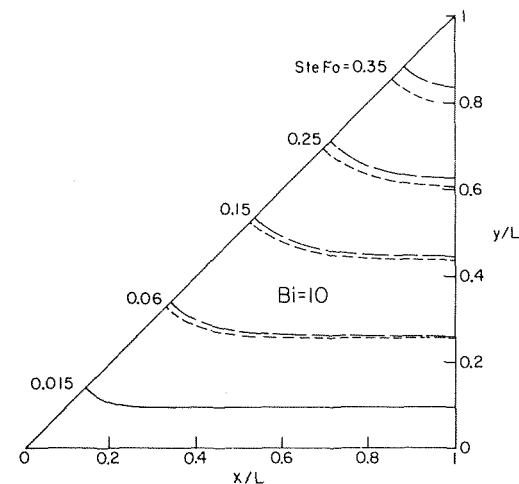


Fig. 11 Position of solid-liquid interface at various times,  $Bi = 10$

6 Spaid, F. W., et al., *International Journal of Heat and Mass Transfer*, Vol. 14, 1971, pp. 673-687.

7 Lock, G. S. H., and Nyren, R. H., *International Journal of Heat and Mass Transfer*, Vol. 14, 1971, pp. 825-834.

8 Lock, G. S. H., Freeborn, R. D. J., and Nyren, R. H., *Heat Transfer 1970, Proceedings of the Fourth International Heat Transfer Conference*, Paris, Vol. I, Paper No. Cu 2.9, 1970.

9 Siegel, R., Goldstein, M. E., and Savino, J. M., *Heat Transfer 1970, Proceedings of the Fourth International Heat Transfer Conference*, Paris, Vol. I, Paper No. Cu 2.11, 1970.

10 Shamsundar, N., PhD thesis, Department of Mechanical Engineering, University of Minnesota, 1975.

11 Allen, D. N. de G., and Severn, R. T., *Quarterly Journal of Mechanics and Applied Mathematics*, Vol. 15, 1962, pp. 53-62.

12 Springer, G. S., and Olson, D. R., ASME Paper No. 62-WA-246.

13 Lazaridis, A., *International Journal of Heat and Mass Transfer*, Vol. 13, 1970, pp. 1459-1477.

14 Bilenas, J. A., and Jiji, L. M., *Heat Transfer 1970, Proceedings of the Fourth International Heat Transfer Conference*, Paris, Vol. I, Paper No. Cu 2.1, 1970.

15 Meyer, G. H., *SIAM Journal on Numerical Analysis*, Vol. 10, 1973, pp. 522-538.

16 Comini, G., et al., *International Journal for Numerical Methods in Engineering*, Vol. 8, 1974, pp. 613-624.

17 Bonacina, C., et al., *International Journal of Heat and Mass Transfer*, Vol. 16, 1973, pp. 1825-1832.

18 Griggs, E. I., Pitts, D. R., and Humphries, W. R., ASME Paper No. 74-WA/HT-21.

19 Dusinberre, G. M., ASME Paper No. 58-HT-7.

20 Baxter, D. C., *JOURNAL OF HEAT TRANSFER*, TRANS. ASME, Series C, Vol. 84, 1962, pp. 317-326.

21 Eyres, N. R., et al., *Philosophical Transactions of The Royal Society*, Series A, Vol. 240, 1946, pp. 1-57.

H. Tanaka

Assoc. Professor,  
Department of Mechanical Engineering,  
The University of Tokyo,  
Bunkyo-ku, Tokyo, Japan

# Measurements of Drop-Size Distributions During Transient Dropwise Condensation

*Instantaneous drop-size distributions were measured during transient dropwise condensation onto an initially bare surface which forms the constituent process of the so-called steady dropwise condensation on a vertical surface. The measured distributions agreed satisfactorily with the prediction from the previous author's theory.*

## Introduction

In the so-called steady dropwise condensation on a vertical surface, the surface is cleared of condensate periodically by drops starting near the top of the surface. They sweep down the plate, exposing bare strips of the surface. On each of the newly swept regions, transient dropwise condensation takes place, until it is swept clean again. Thus, an instantaneous picture of the condensing surface (under a comparatively low heat flux) will show an array of vertical strips each of which has different time elapsed from the start of the transient condensation on it.

In recent years, considerable effort has been directed toward understanding the distribution of drops by sizes. Tanasawa and Ochiai [1]<sup>1</sup> and Graham and Griffith [2] measured drop-size distributions during the so-called steady dropwise condensation. They took a number of randomly spaced (in time), high magnification pictures of the condensing surface, and determined averaged drop-size distributions over those pictures. Glicksman and Hunt [3] performed a numerical simulation of dropwise condensation by computer, and determined a time-averaged drop-size distribution over the complete cycle of the condensation process from nucleation on an initially bare surface to formation of a drop of the departing size. Rose and Glicksman [4] presented a simplified model of the sequence of events occurring during the time interval between successive sweepings, and predicted a time-averaged drop-size distribution.

While the earlier works seem to be concerned with a time-averaged drop-size distribution, the present author considers that there is not much sense in studying the time-averaged features of the so-called steady dropwise condensation, but that the instanta-

neous features and growth of the transient dropwise condensation occurring repeatedly on newly swept regions deserves intensive studies; because, transient condensation on one newly swept region advances nearly independently of its neighboring regions, and it completely governs the instantaneous heat-transfer rate of that region. Further, the time-averaged heat-transfer rate of the region under consideration depends on the mean interval at which the region is swept by departing drops. This sweeping period is again determined by the same transient dropwise condensation occurring near the top of the surface, where the transient condensation has come up to a fairly developed stage with a number of large drops having grown near the departing size.

From this point of view, the author has recently put forward a new theory of dropwise condensation [5]. The theory is based on the following assumptions: (1) that primary droplets nucleate at discrete sites distributed at random on the condensing surface; (2) that drops are hemispherical; (3) that the governing heat-transfer resistance through a single drop is heat conduction through itself; and (4) that the temperature of the condensing surface is uniform. Basic integro-differential equations describing the transient process of dropwise condensation on a newly swept region have been derived. By solving these equations, several novel features have been predicted concerning the transient dropwise condensation on a newly swept region. Further, by introducing a model for the cycle of drop departure, a general expression for the average heat-transfer coefficient under the so-called steady dropwise condensation has been obtained.

Among others, the theory makes the following predictions with regard to the instantaneous drop-size distribution during the transient dropwise condensation.

(i) Immediately after the transient condensation starts, conspicuously large drops of an almost even size cover approximately 40 percent of the condensing surface. Those large drops obey a *universal distribution for large drop range*, and despite the passage of time the drop-size distribution at every instant is similar, only with the characteristic dimension growing with time.

<sup>1</sup> Numbers in brackets designate References at end of paper.

Contributed by the Heat Transfer Division for publication in the JOURNAL OF HEAT TRANSFER. Manuscript received by the Heat Transfer Division January 20, 1975. Paper No. 75-HT-BBB.

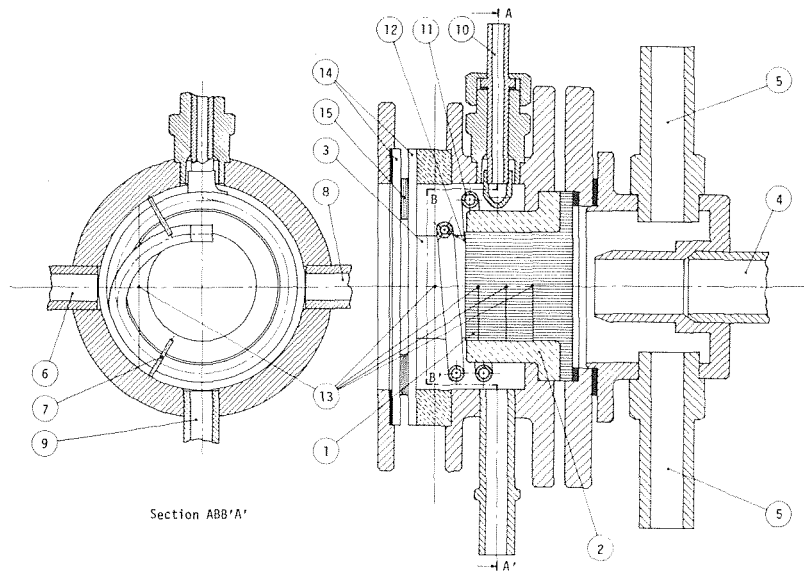


Fig. 1 Experimental apparatus: 1, condenser block; 2, Teflon insulator; 3, steam chamber; 4, coolant inlet; 5, coolant outlet; 6, steam inlet; 7, baffle; 8, steam outlet; 9, drain; 10, inlet of recirculated condensate; 11, saturated liquid tube; 12, orifice; 13, thermocouples; 14, glass window; 15, window heater

(ii) Drops smaller than the dominating ones (except the range of microscopic drops having radii smaller than the distance between the neighboring nucleation sites) form an *equilibrium region of small drops*. If probability density  $N$  of drop-size distribution is defined such that  $N(r)dr$  drops with radii in the interval  $[r, r+dr]$  exist per unit condensing area, then  $N \propto r^{-n}$  in the equilibrium region of small drops. Here, it should be noted that, if the equilibrium region of small drops be extended to zero radius (by assuming that the primary drop can nucleate everywhere and its diameter is effectively zero), then the fraction of the condensing area covered by drops would tend precisely to unity.

The assumed size of primary drops and the assumed spacing between nucleation sites determine the size distribution of microscopic, active drops, and along with the subcooling of the surface they govern the rate of the process. Further, the assumed drop-size distribution at time zero affects the early stage of the process. It should be noted, however, that, whatever we may assume for those microscopic and initial conditions, one and the same characteristic distribution mentioned previously always develops in either range of comparatively large drops.

The purpose of this work is to verify the foregoing two characteristic distributions by experiment. Then, all drops considered in this work are large as compared with the primary drops. The smallest drops counted are about  $50 \mu\text{m}$  in diameter, and are about 1000 times larger than the primary drops. In this work, a new device enables the transient dropwise condensation to take place simultaneously throughout a considerably large condensing surface.

Then, instantaneous drop-size distributions will be measured to be compared with the predictions.

### Experimental Apparatus and Procedure

The basic apparatus used in the present work is shown in Fig. 1. The test surface was a 40 mm dia, 40 mm deep, flanged, copper cylinder, and oriented so that condensation occurred on a vertical surface. In order to promote dropwise condensation, two different surface preparations were employed. In the first half of this experimental program, the surface was polished, cleaned, and promoted by the same technique before each series of runs [6]. The final polish was with grade 3000 emery paper (grain size  $5 \mu\text{m}$ ). The surface was washed with hot distilled water and absolute ethyl alcohol. Then, it was dipped in a 0.5 volume percent solution of benzyl mercaptan in benzene for 20 min. After the surface was washed several times with distilled water, it was installed in the condenser. In the second half of the experimental program, the surface was chromium-plated (after mirror finish, plated with nickel  $20 \mu\text{m}$  thick, and then coated with chromium  $0.25 \mu\text{m}$  thick). On the chromium-plated surface, perfect dropwise condensation occurred without the introduction of a promoter.

Three thermocouple holes of 1.2 mm dia were drilled radially into the test cylinder at the depths of 5, 15, and 25 mm from the condensing surface. Thermocouples used were made of copper-constantan wire of 0.2 mm dia. Outputs of those three thermocouples were read with the reference junction located in the steam flow. The surface temperature was found by linear extrapolation

### Nomenclature

$D$  = diameter of condensing surface, mm  
 $h$  = heat-transfer coefficient, kcal/m<sup>2</sup>h°C  
 $N$  = probability density of instantaneous drop-size distribution, drops/mm<sup>2</sup>/mm  
 $\bar{N}$  = probability density of time-aver-

aged drop-size distribution, drops/mm<sup>2</sup>/mm  
 $q$  = heat flux, kcal/m<sup>2</sup>h  
 $R_{\text{max}}$  = radius of departing drops, mm  
 $r$  = drop radius, mm  
 $r_{40}$  = characteristic dimension of drop-size distribution, mm

$\Delta T$  = surface-to-vapor temperature difference, °C  
 $t$  = time from start of transient condensation, s  
 $x$  = distance from top of condensing surface, mm  
 $\bar{\alpha}$  = fraction of the area covered by drops with radii larger than  $r$

from the readings of those thermocouples, and the heat flux from the temperature gradient.

Saturated steam at atmospheric pressure was generated from distilled water. To avoid the effects of noncondensibles, the steam was supplied to the condenser for at least two hours before beginning an experiment, and the steam flow was effectively concentrated on the condensing surface by baffles. The steam velocity near the surface was about 4.5 m/s. The flow of steam slightly deflected the falling condensate drops. The steam was partially condensed and the remainder passed out of the condensing chamber.

The condensing surface was cooled at the other end either by water or by air, according to the purpose of obtaining comparatively high heat flux or slowing the process down.

It was possible to observe the condensing surface through an electrically heated double-glazed window. A microscope equipped with long distance objective lenses (focal length 111 mm, numerical aperture 0.032; and f.l. 81.5 mm, n.a. 0.067) permitted high magnification observation through the glass window.

The procedure used to start the transient dropwise condensation simultaneously throughout the condensing surface was as follows. Beforehand, under the so-called steady dropwise condensation, heat flux was adjusted to a desired value. The condensate was partially recirculated to a reservoir tube installed in the steam chamber, and heated to the saturation temperature. By using a syringe, the saturated liquid in the reservoir was injected through an orifice to the top of the condenser surface where the so-called steady dropwise condensation had been taking place. For a moment, a thin liquid film flowed down the surface, sweeping it entirely bare. Then, the transient dropwise condensation took place without delay.

## Results and Comparison With the Theory

Heat-transfer coefficients under the so-called steady dropwise condensation were measured for both benzyl mercaptan promoted and chromium-plated surfaces in a range of heat flux  $q$  from  $1.8 \times 10^5$  to  $4 \times 10^5$  kcal/m<sup>2</sup>h (surface-to-vapor temperature difference  $\Delta T$  ranged from 1.1 to 2.6°C). The results are shown in Fig. 2. There now exists a considerable body of measurements of the heat transfer for steam condensing on vertical copper surfaces at atmospheric pressure. Relatively recently, however, fairly good agreement has been found between the experimental results of different investigations [1, 2, 7, 8] in which care was taken to reduce the amounts of noncondensing gases present to a minimum. And

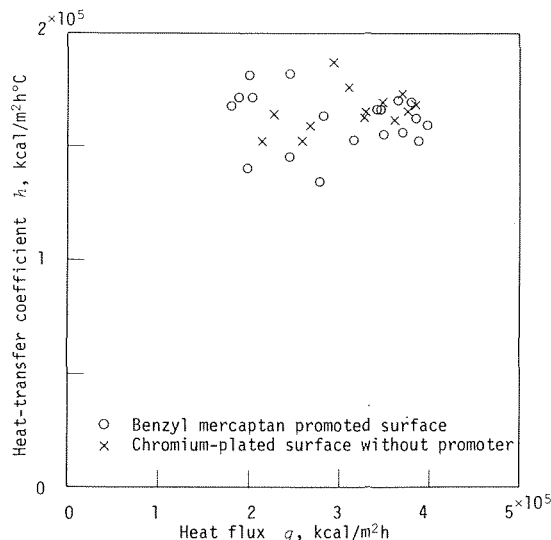


Fig. 2 Heat-transfer coefficients under the so-called steady dropwise condensation

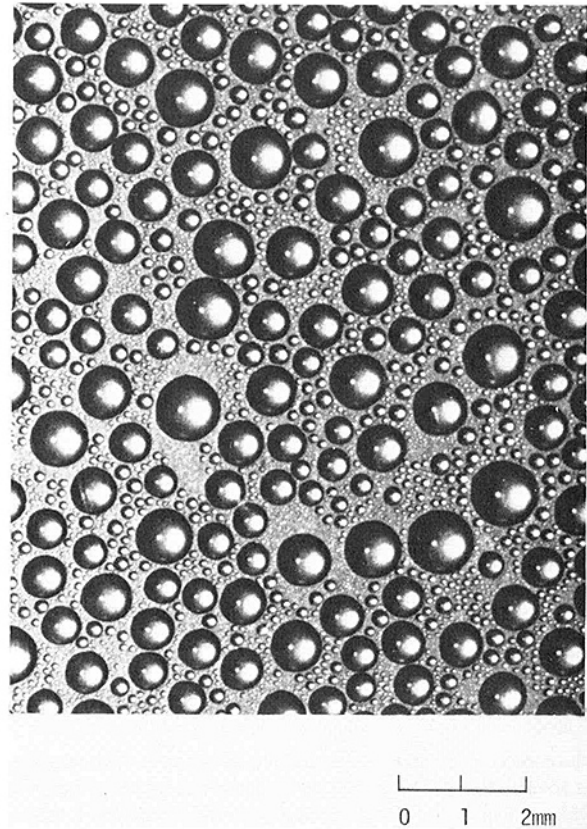


Fig. 3 Close-up photograph of condensing surface

yet, in the range of heat flux corresponding to the present measurement, the heat-transfer coefficient in those investigations ranges between  $1.5 \times 10^5$  and  $2.5 \times 10^5$  kcal/m<sup>2</sup>h°C. Although the data in Fig. 2 are somewhat scattered, they are included within the foregoing limits.

Close-up photographs of the condensing surface (the magnification on the film negatives was about 0.8 $\times$ ) were taken for the transient dropwise condensation on the benzyl mercaptan promoted surface at two different heat fluxes of  $q = 3.7 \times 10^5$  and  $2.8 \times 10^5$  kcal/m<sup>2</sup>h (corresponding  $\Delta T$ 's were about 2.3 and 1.7°C, respectively). As the first drop would roll over the surface within a couple of seconds under these heat fluxes, shots were timed at random. The photographs were enlarged approximately ten times the actual size. A photograph catching fairly grown-up drops was chosen for either heat flux. A rectangular space about 20 cm by 20 cm in size was taken on the enlarged photograph. Every drop with its center inside the rectangle and above a certain set bound in size (one-eighth of the largest drop inside the rectangle) was counted and measured. Fig. 3 shows about a quarter of the counted region of the very photograph used for  $q = 3.7 \times 10^5$  kcal/m<sup>2</sup>h. By using a computer, the counted drops (1577 and 950 in number) were arranged according to size, and reduced as shown in Table 1. The results are plotted in Fig. 4 in the form of the accumulative fraction  $\bar{\alpha}$  of the area covered by drops with radii larger than  $r$  against drop radius  $r$ , and also in Fig. 5 in the form of density  $N$  of drop-size distribution against drop radius  $r$ . Here, since the theory predicts that the drop-size distribution at every instant is similar, we define a characteristic dimension of drop-size distribution,  $r_{40}$ , such that the fraction of the area covered by drops having radii larger than  $r_{40}$  is just 40 percent. While the characteristic dimensions were 0.273 mm and 0.236 mm in the actual size for  $q = 3.7 \times 10^5$  and  $2.8 \times 10^5$  kcal/m<sup>2</sup>h, respectively, the plottings in Figs. 4 and 5 are adjusted so that  $r_{40} = 0.3$  mm. This implies that the plottings in those figures of either heat flux are for a picture magnified by a factor of  $0.3/0.273$  or  $0.3/0.236$ . Suppose, in general, that a picture

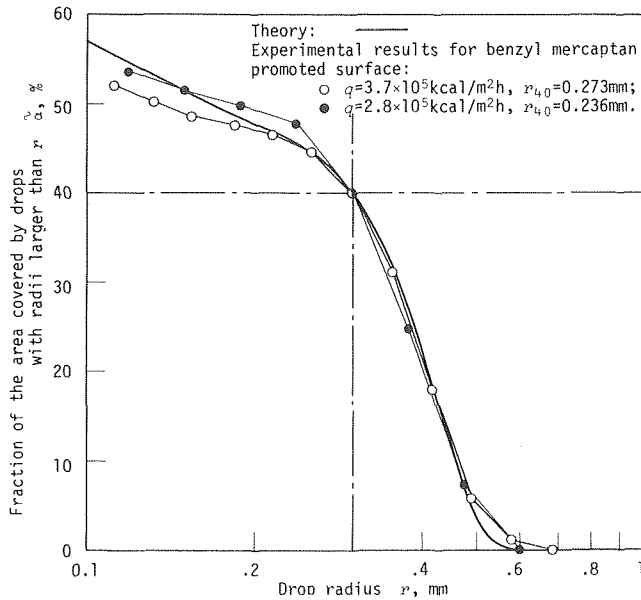


Fig. 4 Comparison between measured and theoretical drop-size distributions in large drop range under the transient dropwise condensation, plotted about accumulative coverage ratio

of the condensing surface is magnified  $m$  times the actual size, and that the fraction of the actual surface covered by drops larger than a size  $r$  is  $\tilde{\alpha}$  and the distribution density on the actual surface of drops with the size  $r$  is  $N$ . Then, it is proved easily that the fraction of the area on the magnified picture covered by drops larger than the corresponding size  $mr$  remains  $\tilde{\alpha}$ , and that the distribution density on the magnified picture of drops with the size  $mr$  becomes  $N/m^3$ . Therefore, in consequence of this transformation, the distribution curve in Fig. 4 is shifted in the horizontal direction, whereas the distribution curve in Fig. 5 is displaced parallel in the direction of  $r^{-3}$ .

The theoretical predictions from reference [5] assuming  $r_{40} = 0.3$  mm are shown by the solid lines in Figs. 4 and 5. These figures clearly demonstrate the existence of the *universal distribution for large drop range*. The universal distribution curve bears a charac-

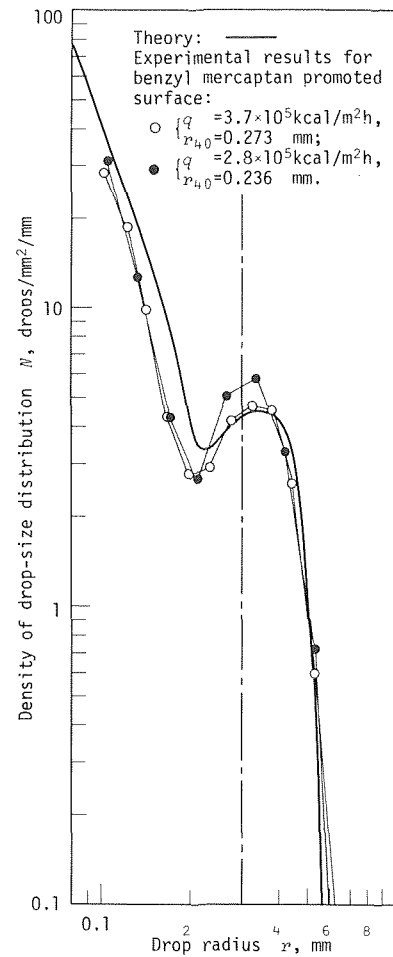


Fig. 5 Comparison between measured and theoretical drop-size distributions in large drop range under the transient dropwise condensation, plotted about distribution density

teristic hump as shown in Fig. 5. This is due to the simple fact that, when two drops coalesce, the larger one survives and the smaller one disappears. Namely, conspicuously large drops corresponding to the characteristic hump survive nearly always unless they happen to coalesce between themselves, whereas drops a little smaller than those predominant ones are apt to disappear, captured by them.

For the purpose of determining the distribution in small drop range, microphotographs (the magnification on the film negatives was about 5X, on the enlargements about 55X) were taken for the transient dropwise condensation on the chromium-plated surface at a very small heat flux of about  $1 \times 10^4$  kcal/m<sup>2</sup>h. Under this condition, the value of the heat flux, and especially that of the surface-to-vapor temperature difference, could not be determined precisely, since the readings of the various thermocouples lay in close proximity. However, the cooling rate was kept constant through the whole series of runs by adjusting carefully the conditions of the cooling system. As the first drop would slide down at about  $t = 50$  s from the start of the transient dropwise condensation under this condition, close-up photographs and then microphotographs were taken, precisely timed at  $t = 35$  s. In the first place, three close-up photographs were analyzed as before to obtain the drop-size distribution in large drop range (the numbers of counted drops were 742, 765, and 900, respectively). Fig. 6 shows the results, which are, unlike Fig. 5, plotted in real dimensions. The characteristic dimension  $r_{40}$  of drop-size distribution was found to be 0.218 mm, by taking an average of 0.221, 0.230, and 0.203 for the respective photographs. In the second place, we pro-

Table 1 Source data for  $q = 3.7 \times 10^5$  kcal/m<sup>2</sup>h

Area analyzed = 410 mm <sup>2</sup>					
Division No. $i$	Radius $r_i$ , mm	Number of drops in area covered by drops in size range: $r_{i+1} < r \leq r_i$	Fraction of area covered by drops in size range: $r_i < r$	Distribution density $N_i$ , drops/mm <sup>2</sup> /mm	Corresponding value of radius
1	0.621	5	0.000	0.130	0.572
2	0.527	26	0.012	0.794	0.485
3	0.447	95	0.057	3.42	0.411
4	0.379	143	0.178	6.07	0.349
5	0.321	125	0.310	6.25	0.296
6	0.273	96	0.396	5.66	0.251
7	0.231	56	0.444	3.89	0.213
8	0.196	45	0.464	3.69	0.181
9	0.167	60	0.475	5.80	0.153
10	0.141	115	0.486	13.1	0.130
11	0.120	184	0.501	24.7	0.110
12	0.102	238	0.519	37.7	0.0936
13	0.0862	162	0.535	—	—
14	0.0732	227	—	—	—

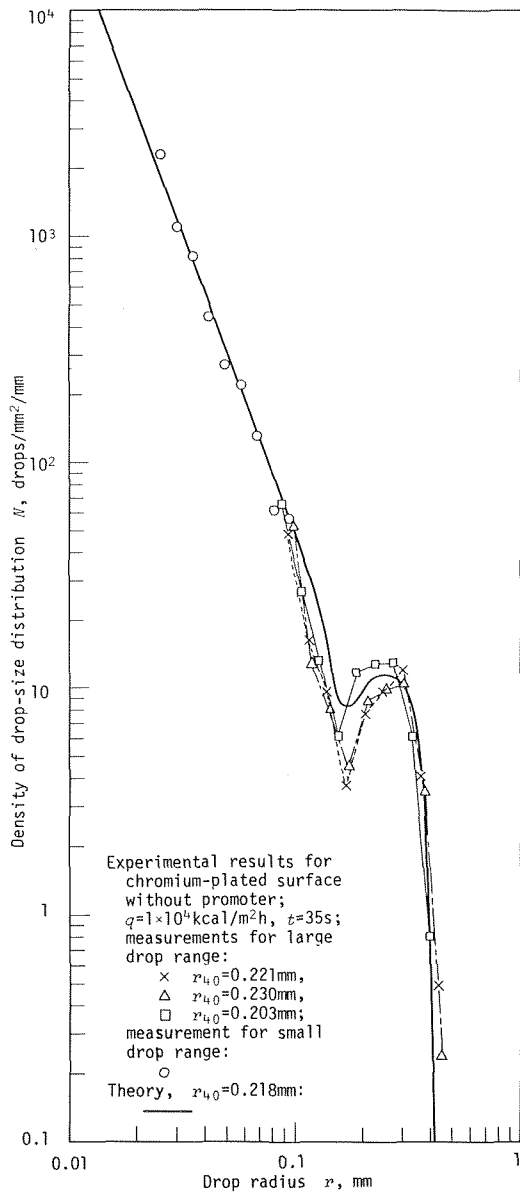


Fig. 6 Comparison between measured and theoretical drop-size distributions under the transient dropwise condensation

ceeded to analyze the microphotographs. At this time, drops inside a set rectangle whose radii were in the interval  $[r_{40}/8, r_{40}/2]$  were counted. Fig. 7 shows approximately the whole region counted of one of the microphotographs analyzed. The density of drops in the foregoing size range in the set rectangular space might well be affected by accidental overpopulation or depopulation of large drops in that space. This effect could be eliminated by the following procedure. First, we calculated the drop density with respect to the area which was left by subtracting from the rectangular space the base areas of drops with radii larger than  $r_{40}$ . Since this residual area should account for 60 percent of the condensing surface, we estimated the drop density with respect to the whole condensing surface by multiplying the density obtained previously by 0.6. Three microphotographs were analyzed and 974 drops in all were counted. The data totalized over the three photographs are given in Table 2, and are plotted in Fig. 6.

The theoretical prediction from reference [5] assuming  $r_{40} = 0.218$  mm is shown by the solid line in Fig. 6. The equilibrium region of small drops corresponds to the region  $r < 0.1$  mm, where the theoretical distribution is expressed by a straight line:

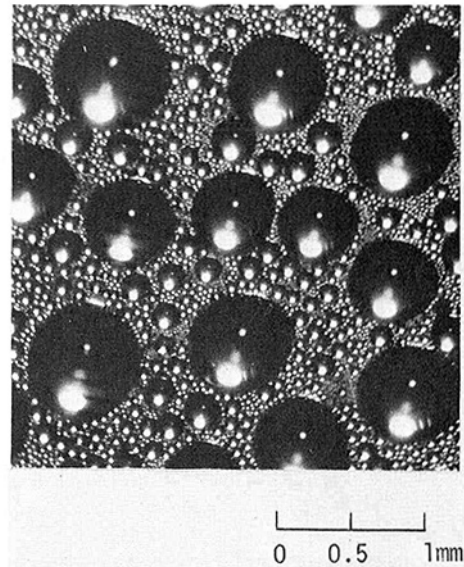


Fig. 7 Microphotograph of condensing surface

$$N \propto r^{-2.68} \quad (1)$$

The measured result in small drop range successfully falls within this region, and agrees satisfactorily with the theory. In addition, it should be noted in Fig. 6 that, as is predicted by the theory [5], the universal distribution for large drop range still develops despite the large differences in heat flux and also in surface preparation as compared with Fig. 5.

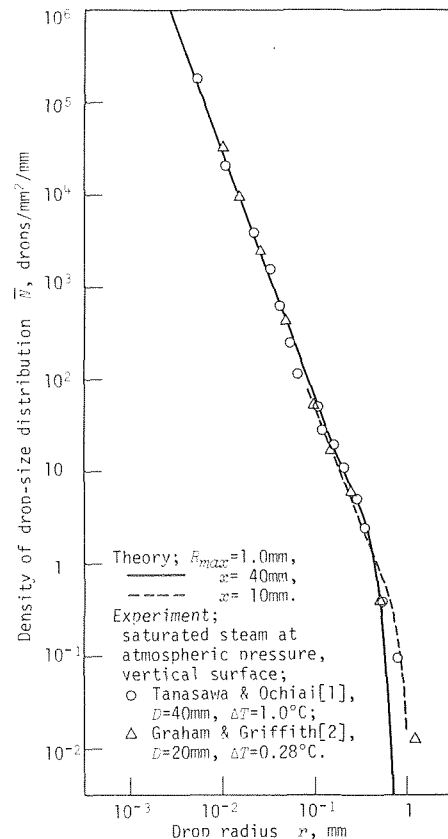


Fig. 8 Time-averaged drop-size distribution under the so-called steady dropwise condensation

**Table 2 Source data of small drop range**

Total area of the three rectangular spaces analyzed $A = 30.45 \text{ mm}^2$ ; Total area left by subtracting from $A$ the base areas of drops over $r_{20}$ $A' = 17.13 \text{ mm}^2$					
Division No. $i$	Radius $r_i, \text{mm}$	Number of drops in size range: $n_{i+1} - n_i$	Distribution density on $A'$ , drops/ $\text{mm}^2/\text{mm}$	Distribution density estimated for the whole surface $N_i, \text{drops}/\text{mm}^2/\text{mm}$	Plotted value of radius
1	0.121	5	—	—	—
2	0.102	25	94.0	56.4	0.0943
3	0.0869	23	102	61.1	0.0800
4	0.0737	42	219	132	0.0679
5	0.0625	60	369	222	0.0576
6	0.0531	62	450	270	0.0489
7	0.0450	86	736	441	0.0414
8	0.0382	135	1360	817	0.0352
9	0.0324	156	1850	1110	0.0298
10	0.0275	273	3820	2290	0.0253
11	0.0233	100	—	—	—
12	0.0198	7	—	—	—

**Discussion**

There exist two previous experimental works by Tanasawa and Ochiai [1] and Graham and Griffith [2] in measuring time-averaged drop-size distributions during the so-called steady dropwise condensation on vertical or inclined copper disks with diameter  $D = 40$  and  $20 \text{ mm}$ , respectively. The typical data from those works are reproduced in Fig. 8.

If the distribution density of drops with a radius  $r$  at time  $t$  during the transient dropwise condensation is denoted by  $N(r, t)$ , the time-averaged distribution density  $\bar{N}(r)$  of drops with the radius  $r$  is given by

$$\bar{N}(r) = \frac{1}{\tau_x} \int_0^{\tau_x} N(r, t) dt \tag{2}$$

where  $\tau_x$  signifies the mean interval at which the region under consideration is swept by departing drops, and it varies with the distance  $x$  from the top of the condensing surface. By assuming for the radius of departing drops that  $R_{\text{max}} = 1.0 \text{ mm}$  [1], the time-averaged distribution density was computed by the theory in reference [5], and the results for two different positions,  $x = 40$  and  $10 \text{ mm}$ , are included in Fig. 8. As is expected, the theoretical distribution in the small drop range:  $r < 0.1 \text{ mm}$  is represented again by equation (1), having the same inclination as the *equilibrium region of small drops* in the instantaneous distribution during the transient condensation. The characteristic hump in the instantaneous distribution curve disappears in the averaging process in equation

(2). As illustrated by the two theoretical curves in Fig. 8, the distribution density of drops near the departing size increases, according as the distance  $x$  decreases accompanied by the increase in the time interval  $\tau_x$ . In Fig. 8, the agreement between the experiments and the theory is very satisfactory.

There now exist two previous analytic works in determining time-averaged drop-size distributions during the so-called steady dropwise condensation. Glicksman and Hunt [3] have performed a numerical simulation of the condensation process by using a computer and determined a time-averaged drop-size distribution. On the other hand, Rose and Glicksman [4] have presented an approximate theory by introducing a simplified model of the sequence of events between successive sweepings, and predicted a time-averaged drop-size distribution. The result of Glicksman and Hunt and the prediction of Rose and Glicksman as well merge with the various plottings in Fig. 8, in the small drop range:  $r < 0.3 \text{ mm}$ . In fact, the theoretical distribution by Rose and Glicksman has been shown to be approximated by the following form [4].

$$\bar{N} \propto r^{-(3-1/3)} \tag{3}$$

This is in fair accord with expression (1). As for the range of drops near the departing size, however, either analysis seems to have failed in proper description of the behaviors of the dominating drops, giving a smaller decreasing rate in the distribution density in this size range than the experimental results.

**Acknowledgment**

The author wishes to acknowledge Mr. Shigeo Matsunaga and Mr. Toshio Ogawa for their assistance in this work.

**References**

- 1 Tanasawa, I., and Ochiai, J., "Experimental Study on Dropwise Condensation," *Bulletin of Japan Society of Mechanical Engineers*, Vol. 16, 1973, pp. 1184-1197.
- 2 Graham, C., and Griffith, P., "Drop Size Distributions and Heat Transfer in Dropwise Condensation," *International Journal of Heat and Mass Transfer*, Vol. 16, 1973, pp. 337-346.
- 3 Glicksman, L. R., and Hunt, A. W. Jr., "Numerical Simulation of Dropwise Condensation," *International Journal of Heat and Mass Transfer*, Vol. 15, 1972, pp. 2251-2269.
- 4 Rose, J. W., and Glicksman, L. R., "Dropwise Condensation—The Distribution of Drop Sizes," *International Journal of Heat and Mass Transfer*, Vol. 16, 1973, pp. 411-425.
- 5 Tanaka, H., "A Theoretical Study of Dropwise Condensation," *JOURNAL OF HEAT TRANSFER, TRANS. ASME, Series C*, Vol. 97, 1975, pp. 72-78.
- 6 McCormick, J. L., and Westwater, J. W., "Nucleation Sites for Dropwise Condensation," *Chemical Engineering Science*, Vol. 20, 1965, pp. 1021-1036.
- 7 Tanner, D. W., Potter, C. J., Pope, D., and West, D., "Heat Transfer in Dropwise Condensation," *International Journal of Heat and Mass Transfer*, Vol. 8, 1965, pp. 419-436.
- 8 Citakoglu, E., and Rose, J. W., "Dropwise Condensation: Some Factors Influencing the Validity of Heat-Transfer Measurements," *International Journal of Heat and Mass Transfer*, Vol. 11, 1968, pp. 523-537.

V. K. Dhir

Asst. Professor in Residence,  
Energy and Kinetics Department,  
University of California,  
Los Angeles, Calif.

# Quasi-Steady Laminar Film Condensation of Steam on Copper Spheres

An experimental study of laminar film condensation of steam on copper spheres of 1.90, 2.54, and 3.17 cm dia has been made. Experiments have been performed by submerging cold spheres in nearly stagnant water vapor at a saturation temperature of about 99°C. Values of Nusselt number based on average heat transfer coefficient are obtained for saturation to wall temperature differences of 5–65°C and for  $c_p \Delta T / h_{fg}$  in the range of 0.009–0.12. The data are compared with the steady-state predictions of Dhir and Lienhard and of Yang. Analysis has been made to show that it is valid to use steady-state solutions in quasi-steady condensation as long as the dimensionless thermal diffusion time constant is small, and the film does not move very slowly.

## Introduction

Laminar film condensation on an isothermal vertical plate and on a horizontal cylinder was first studied by Nusselt [1]<sup>1</sup> in 1916 with the assumptions that the temperature varied linearly in the film and that the inertia of the film could be neglected. Nusselt's assumption of the linear temperature profile was later corrected by Rohsenow [2]. The result of Rohsenow's analysis was to slightly increase the latent heat of vaporization used in Nusselt's earlier prediction. Subsequently, Sparrow and Gregg [3, 4] using full boundary layer solutions verified Nusselt-Rohsenow theory for the vertical plate and the horizontal cylinder.

Condensation on a stationary isothermal sphere was studied by Dhir and Lienhard [5] as a special problem of a class of axisymmetric bodies. Using an "effective gravity" that corrected both for variable gravity and for the form of the body, they obtained an expression for the film thickness at a distance  $x$  from the upper stagnation point, as<sup>2</sup>

$$\delta = \left[ \frac{4\mu k \Delta T_0 x}{(\rho_f - \rho_g) \rho_f h_{fg}' g_{\text{eff}}} \right]^{1/4} \quad (1)$$

where  $g_{\text{eff}}$  for a sphere is given as

$$g_{\text{eff}} = \frac{xg(\sin 2x/D)^{5/3}}{\int_0^x (\sin 2x/D)^{5/3} dx} \quad (2)$$

For the local Nusselt number they obtained

$$\text{Nu} = \left[ \frac{g_{\text{eff}}(\rho_f - \rho_g) \rho_f h_{fg}' x^3}{4\mu k \Delta T_0} \right]^{1/4} \quad (3)$$

and for the Nusselt number based on an average heat transfer coefficient around the sphere of diameter  $D$ ; the numerical integration resulted in

$$\text{Nu}_D = 0.785 \left[ \frac{g \rho_f (\rho_f - \rho_g) h_{fg}' D^3}{\mu k \Delta T_0} \right]^{1/4} \quad (4)$$

The foregoing expressions are restricted to low values of liquid subcooling parameter  $c_p \Delta T / h_{fg}$  and for Prandtl number, Pr, on the order of unity or greater. This is not a stringent restriction, as most of the practical condensation problems of ordinary liquids fall in this category. Yang [6] carried out full boundary layer solutions of laminar film condensation on a sphere. His result for the Nusselt number was about 2–1/2 percent higher than that given by equation (4). But, Yang's expression for the Nusselt number is based on latent heat of vaporization that does not include correction for liquid subcooling. Thus, the actual difference between the two predictions is even smaller.

Extensive experimental studies [see e.g., 7, 8, 9] of laminar film condensation on isothermal vertical plates and on vertical cylinders have been made in the past. It can be concluded from these

<sup>1</sup> Numbers in brackets designate References at end of paper.

<sup>2</sup> Symbols not explained in the text are defined in the Nomenclature section.

Contributed by the Heat Transfer Division for publication in the JOURNAL OF HEAT TRANSFER. Manuscript received by the Heat Transfer Division April 1, 1975. Paper No. 75-HT-CCC.

studies that Nusselt solutions predict heat transfer very well as long as the Reynolds number based on condensate mass flow rate is less than 50 and the film surface is free of ripples. Laminar film condensation on isothermal horizontal cylinder has also been given considerable attention in the past. Rauscher, Mills, and Denny [10] made local observation of heat flux during condensation on a horizontal tube. Their small free stream velocity data for the upper three-quarters of the film compared very well with Nusselt's predictions. More recently Mills, Tan, and Chung [11] observed that overall condensation heat transfer coefficient over a horizontal tube was about 3 percent higher than predicted by Nusselt's uniform heat flux theory. This small discrepancy was attributed to vapor drag.

In the present work, we make experimental observations of laminar film condensation of steam on copper spheres. In this study, we do not use an isothermal sphere but observe condensation on a cold sphere that is suddenly submerged in a large volume of nearly stagnant water vapor. The temperature of the center of the sphere is recorded as a function of time. Noting the rate of change of enthalpy of the sphere, the average heat flux over the sphere at a particular temperature is determined after the film is fully developed. However, before we go on to the experimental section it is appropriate to find expressions for film thickness and heat transfer coefficient for quasi-steady condensation when the sphere temperature is changing with time, but is uniform over the sphere.

### Analysis

Sparrow and Siegel [12] analyzed the problem of transient laminar film condensation on a vertical plate, the temperature of which was suddenly dropped below the saturation temperature of the surrounding stagnant vapor. Invoking Nusselt's assumption of inertia-less film with a linear temperature distribution and using the continuity, momentum, and energy equations, they obtained the governing equation for the film thickness as<sup>3</sup>

$$\left[ \frac{g\rho_f(\rho_f - \rho_g)h'_{fg}}{\mu k \Delta T_0} \right] \delta^3 \frac{\partial \delta}{\partial x} + \left[ \frac{\rho_f h'_{fg}}{k \Delta T_0} \left( 1 + \frac{c_p \Delta T_0}{2h'_{fg}} \right) \right] \delta \frac{\partial \delta}{\partial t} = 1 \quad (5)$$

<sup>3</sup> Sparrow and Siegel used  $h'_{fg} = h_{fg} + \frac{3}{8} c_p \Delta T$  but here we use a slightly higher value as suggested by Rohsenow to account for nonlinearity of the temperature profile in the film.

The boundary and initial conditions on equation (5) being that

$$\delta = 0 \text{ at } x = 0 \text{ for all } t \text{ and } \delta = 0 \text{ at } t = 0 \text{ for all } x$$

Sparrow and Siegel solved equation (5) by the method of characteristics. They found that the time required for the film to achieve steady-state condensation at any position  $x$  would be

$$t_{ss} = \left[ \frac{h'_{fg} \rho_f \mu x}{g(\rho_f - \rho_g) k \Delta T_0} \right]^{1/2} \cdot \left[ 1 + \frac{c_p \Delta T_0}{2h'_{fg}} \right] \quad (6)$$

and the film thickness  $\delta$  during the transient period would be given by

$$\delta = \delta_{ss} (t/t_{ss})^{1/2}, t \leq t_{ss} \quad (7)$$

Their steady-state value of  $\delta$  was the same as that of Nusselt, i.e.,

$$\delta_{ss} = \left[ \frac{4\mu k \Delta T_0 x}{g\rho_f(\rho_f - \rho_g)h'_{fg}} \right]^{1/4} \quad (8)$$

Now, if we include the variation of wall temperature with time, after the wall temperature has been dropped to a certain value below the saturation temperature of the vapor, the governing equation for  $\delta$  becomes.

$$\left[ \frac{\rho_f(\rho_f - \rho_g)g h'_{fg}}{\mu k \Delta T(t)} \right] \delta^3 \frac{\partial \delta}{\partial x} + \left[ \frac{\rho_f h'_{fg}}{k \Delta T(t)} \left( 1 + \frac{c_p \Delta T}{2h'_{fg}} \right) \right] \delta \frac{\partial \delta}{\partial t} = 1 + \frac{\delta^2}{2\alpha} \frac{dT_w}{dt} \frac{1}{\Delta T(t)} \quad (9)$$

Equation (9) is the same as Sparrow and Siegel's equation (5) except that the second term on the right-hand side results from variation of wall temperature with time and now  $\Delta T$  is a function of time.

In the present work, we are not interested in the transient behavior of the film but our aim is to obtain expressions for the film thickness and heat transfer coefficient after the film has achieved a quasi-steady state. Thus, without explicitly solving equation (9), we will make a few observations.

Noting that in quasi-steady state, film thickness varies as  $(\Delta T)^{1/4}$ , equation (9) can be rewritten as

$$\left[ \frac{g\rho_f(\rho_f - \rho_g)h'_{fg}}{\mu k \Delta T(t)} \right] \delta^3 \frac{\partial \delta}{\partial x}$$

### Nomenclature

Bi = Biot number, $\bar{h}R/k_c$	Pr = Prandtl number of the condensate, $\mu c_p/k$	$y$ = distance normal to the condensing surface
$c_p$ = specific heat of condensate	$q_{exp}$ = experimental value of average heat flux over the surface of the sphere	$\Gamma_c$ = mass flow rate of condensate per unit breadth
$c_{pc}$ = specific heat of condenser material	$q_{th}$ = theoretical value of average heat flux over the surface of the sphere calculated from equation (4)	$\alpha$ = thermal diffusivity of condensate, $k/\rho_f c_p$
$D$ = diameter of the sphere	$R$ = radius of curvature of an axisymmetric body	$\Delta T$ = difference between saturation temperature and sphere surface temperature
$g$ = gravitational acceleration	$R'$ = dimensionless radius of sphere, $R\sqrt{g(\rho_f - \rho_g)/\sigma}$	$\Delta T_0$ = difference between saturation temperature and constant surface temperature
$g_{eff}$ = effective gravity as defined in equation (2)	Re = Reynolds numbers, $\Gamma_c/\mu$	$\delta$ = condensate film thickness
$h$ = heat transfer coefficient	$T$ = temperature	$\delta_{qs}$ = quasi-steady state condensate film thickness
$\bar{h}$ = average heat transfer coefficient over the surface of the sphere	$T_w$ = sphere surface temperature	$\delta_{ss}$ = steady-state condensate film thickness
$h_{fg}$ = latent heat of vaporization	$t$ = time	$\mu$ = viscosity of condensate
$h'_{fg}$ = $h_{fg}$ corrected to take into account sensible heat of subcooling of the film; $h'_{fg} = h_{fg} + 0.68 c_p \Delta T$	$t_{ss}$ = time at which film achieves steady state	$\rho_c$ = density of condenser material
$k$ = thermal conductivity of condensate	$x$ = distance from the upper stagnation point or from the leading edge for a flat plate	$\rho_f, \rho_g$ = density of liquid and saturated vapor, respectively
$k_c$ = thermal conductivity of condenser material		$\sigma$ = surface tension between saturated liquid and its vapor
Nu = local Nusselt number, $hx/k$		
$Nu_D$ = average Nusselt number for the		

$$= 1 + \left\{ \left[ \frac{dT_w}{dt} \frac{1}{\Delta T(t)} \frac{\delta^2}{\alpha} \right] \left[ \frac{5}{8} + \frac{h_{fg}}{4c_p \Delta T(t)} \right] \right\} \quad (10)$$

For a sphere,  $g$  in equation (10) can be easily replaced by  $g_{eff}$  as given by equation (2). The term in curly brackets on the right-hand side results from variation of wall temperature with time and represents a ratio of dimensionless thermal diffusion time constant of the film to the sensible heat capacity of the film.<sup>4</sup> The relative magnitude of this term will depend on the size, shape, and subcooling of the condensing surface and on the thermo-physical properties of the condenser material and of the condensate.

In the present experimental work, this ratio would be maximum when steam is condensing on the smallest sphere with minimum wall subcooling. For example, when steam ( $T_{sat} = 100^\circ\text{C}$ ) is condensing on 1.90 cm dia sphere with  $\Delta T = 5^\circ\text{C}$ , the average film thickness around the sphere is  $4 \times 10^{-5}$  m and thermal diffusivity of the condensate is  $17.6 \times 10^{-8}$  m<sup>2</sup>/s. Thus, if we assume  $(dT_w/dt) \cdot (1/\Delta T)$  to be  $1 \text{ s}^{-1}$  which as we will see later is typical of the present observations and for  $c_p \Delta T/h_{fg} = 0.009$ , the ratio of the dimensionless thermal diffusion time constant and the sensible heat capacity of the film is numerically equal to 0.26. The expression for quasi-steady film thickness then becomes

$$\delta_{qs}(t) = 1.06 \left[ \frac{4\mu k \Delta T(t) x}{\rho_f(\rho_f - \rho_g) h_{fg}' g_{eff} t} \right]^{1/4} \quad (11)$$

Thus, for the smallest  $c_p \Delta T/h_{fg}$ , the quasi-steady state film will be about 6 percent thicker than a steady-state film at that temperature. However, the numerical constant in front will quickly approach unity as film becomes thicker. It may be emphasized here that actually the constant in equation (11) will vary along the path of the condensate, being minimum at the upper stagnation point and maximum at the lower stagnation point. In all of the present experiments  $c_p \Delta T/h_{fg}$  was  $> 0.009$ , thus we should expect our heat transfer data at a particular temperature to be correlated within a few percent of steady-state expressions (3) and (4).

## Experiments

A schematic diagram of the experimental setup is shown in Fig. 1. Steam at atmospheric pressure was generated in a 15.5 cm dia pyrex jar of 4 l capacity. A circular cover made out of phenolic sheet was placed on the jar. The cover had a 4.0 cm dia hole in the middle for immersion of the test spheres and it was also used as a holder for the nichrome heating wire supports and a thermometer. The maximum rated heating capacity of the nichrome heater was 3 kW. The rating of the heater was chosen so that steam in excess of the amount used in the condensation process was generated while the steam velocity in the test chamber was kept small. The velocity of the steam in the jar was always less than 0.12 m/s.

Three copper spheres of diameter 1.90, 2.54, and 3.17 cm were used in the experiments. The eccentricity of any of these spheres was less than 0.12 mm. An iron constantan thermocouple was used to note the temperature of the center of each sphere. Fig. 2 shows installation of the thermocouple and mounting of the test sphere. The output of the thermocouple was recorded on a Hewlett Packard Moseley 7035A, X-Y recorder.

Prior to making a run, steam was generated for at least half an hour to drive off any noncondensables initially present in the jar. The sphere surface was polished with a 600 grit emery paper, washed with soap and water and finally rinsed with acetone before each run. The test sphere at about room temperature was then immersed in nearly stagnant water vapor through 4.0 cm opening in the cover. Simultaneously, the X-Y recorder was started and a temperature time history was obtained on graph paper.

During the course of the experiments, it was observed that a continuous condensate film could not be achieved in the very first run on a test sphere. This was observed visually as well as by not-

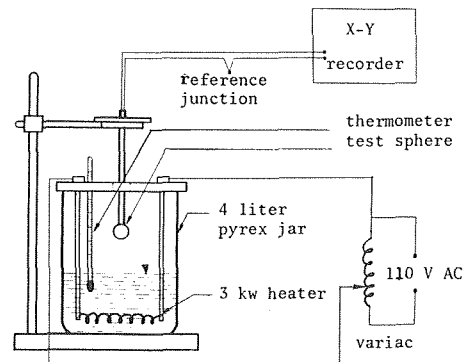


Fig. 1 Schematic diagram of the condensation experiment

ing a zigzag temperature time trace. However, a continuous film was found to occur after the hot sphere was quenched in a bath of acetone at room temperature. This procedure probably helped in obtaining a greater degree of cleanliness of the condensing surface of the sphere.

## Data Reduction

The only output of the experiments was a temperature time history of the center of the test condenser. Typical temperature time histories for 1.90 and 2.54 cm spheres are shown in Fig. 3. In Fig. 3 we also mark the range of the quasi-steady condensation. The time required to achieve quasi-steady condensation after a cold sphere is immersed in a large volume of nearly stagnant water vapor can be approximately calculated by using equation (6) in which  $g$  is replaced by  $g_{eff}$  and an average value is used for  $\Delta T$ . For all the experiments reported in this paper, the transient time was calculated to be less than half second. However, experimental evaluation of the transient time is not very easy, as this time is overlapped by a finite amount of time consumed in placing the sphere in the test chamber. The determination of the transient time was also not the purpose of this paper. Thus, we arbitrarily set the lower bound on the quasi-steady condensation, but this time was never taken to be less than half a second after the test sphere was immersed in the vapor.

The heat flux in the range of quasi-steady condensation was determined by using the lumped capacity relation

$$q = \frac{\frac{4}{3} \pi R^3 \rho_c c_{pc} \frac{dT}{dt}}{4\pi R^2} = \frac{R}{3} \rho_c c_{pc} \frac{dT}{dt} \quad (12)$$

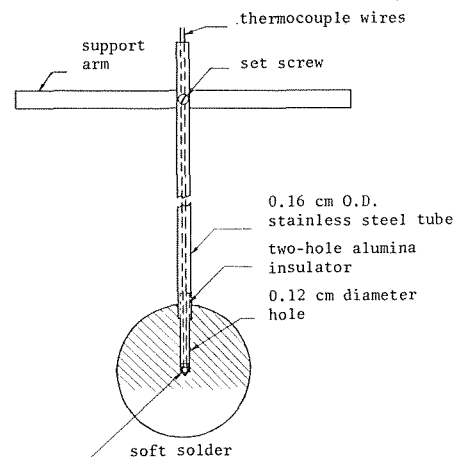


Fig. 2 Thermocouple installation and mounting of the test spheres

<sup>4</sup> Small values of  $c_p \Delta T/h_{fg}$  correspond to a sluggish film.

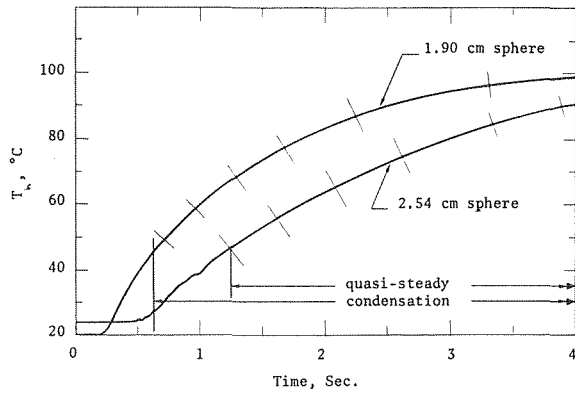


Fig. 3 Time versus center-temperature history of 1.90 and 2.54 cm dia spheres during condensation

or

$$Nu_D = \frac{\bar{h} D}{k} = \frac{D^2 \rho_c c_{pc} dT}{6k\Delta T dt} \quad (13)$$

It is valid to use the foregoing relations only when the Biot number is small. Bergles and Thompson [13] while comparing steady-state and transient pool boiling data for spheres noted that the use of lumped capacity method involved little or no error as long as Bi was less than 0.4. This restriction translates to a Nusselt number of less than 450. For Biot number greater than 0.4, the lumped capacity method should be abandoned in favor of solution of transient conduction equation for spheres. During a study of the peak pool boiling heat flux from spheres, Ded and Lienhard [14] numerically solved the transient conduction equation. Their computations showed that for  $Bi = 0.8$ , the lumped capacity method resulted in an error of about 16 percent in the peak heat flux calculations.

All the data reported in this paper are for wall subcoolings for which Nusselt number is less than about 450. Thus, the data suffer in a small way from any inaccuracies resulting from our use of lumped capacity method. The maximum error in reducing  $dT/dt$  data from the temperature-time histories was  $\pm 4$  percent. The overall maximum error in the calculation of Nusselt number from equation (13) was less than  $\pm 5$  percent.

## Results

Quasi-steady laminar film condensation data for copper spheres of 1.90, 2.54, and 3.17 cm are plotted in Figs. 4, 5, and 6 respectively. The abscissa in these figures denotes the wall subcooling whereas the ordinate denotes Nusselt number based on average heat transfer coefficient over the sphere. The data represent 5–6 ran-

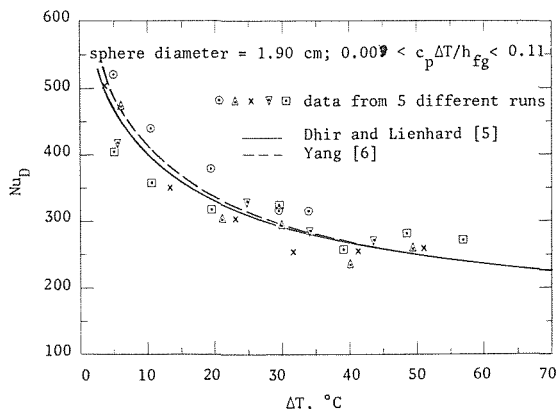


Fig. 4 Variation of Nusselt number with wall subcooling during condensation on a 1.90 cm dia sphere

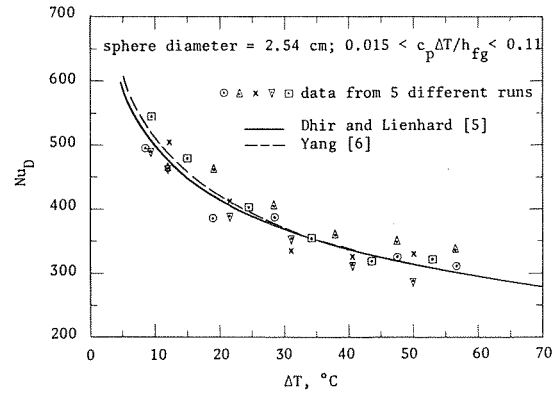


Fig. 5 Variation of Nusselt number with wall subcooling during condensation on 2.54 cm dia sphere

domly picked surface temperatures in each run. At least five runs were made for each sphere to check the reproducibility of the data. The plotted data are for wall subcoolings in the range 5–65°C and for  $c_p \Delta T / h_{fg}$  in the range 0.009–0.12. In these figures Dhir and Lienhard's equation (4) is also plotted. The dotted line represents the average Nusselt number as predicted by Yang. The physical properties used in equation (4) were obtained from reference [15] and were evaluated at

$$T = T_w + 0.3\Delta T \quad (14)$$

Slightly different values for the numerical constant in equation (14) have been suggested by various investigators. Minkowycz and Sparrow [16] suggested a value of 0.31 and Poots and Miles [17] suggested that for water it should be 0.26–0.30. However, Denny and Mills [18] used 0.33 in evaluating the condensate properties. In the present work, we have used a mean value of 0.30.

The data are free of any surface tension effects arising out of curvature of the interface, as the minimum value of  $R'$  in the present experiments was 3.75. The data are not expected to be influenced by vapor drag either. The maximum vapor velocity in the test chamber was 0.12 m/s. and this should have little or no effect [19, 20] on the average heat transfer data. The presence of condensate drop at the bottom stagnation point affects the overall heat transfer rate to a minor extent only. Numerical integration of equation (3) showed that the presence of a drop of 0.63 cm base dia at the bottom stagnation point would decrease the overall heat transfer from the smallest sphere by less than 2 percent. Visual observation showed the drop size to be smaller than 0.63 cm.

All 84 of the quasi-steady condensation data points plotted in

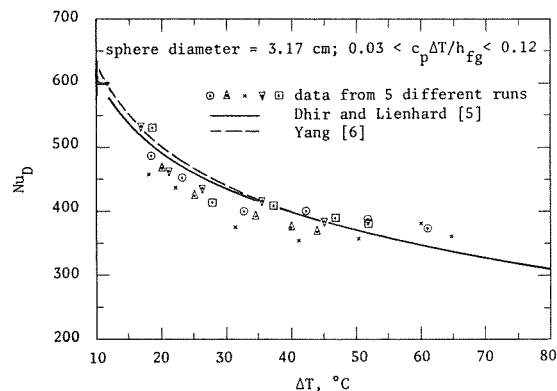


Fig. 6 Variation of Nusselt number with wall subcooling during condensation on a 3.17 cm dia sphere

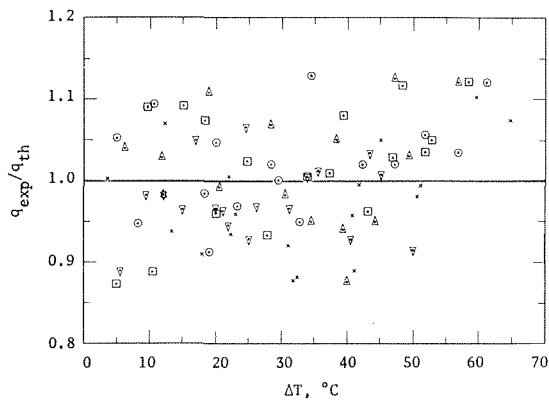


Fig. 7 Dimensionless heat flux during condensation on 1.90, 2.54, and 3.17 cm dia spheres

Figs. 4, 5, and 6 lie within  $\pm 13$  percent of equation (4) derived for steady-state condensation. Small  $\Delta T$  data for the largest sphere are generally low. This is probably due to accumulation of error in our use of the lumped capacity method to evaluate Nusselt number. In equation (13) we have used the center temperature instead of the mean temperature of the sphere. An error on this account is magnified as square of the diameter of the sphere and so is the error in reducing  $dT/dt$  data from temperature time trace. We do not suspect the data to be low because of the decreased curvature of the sphere. The radius of the sphere is still very small for any appreciable area of the upper half of the sphere to approach flat plate. The condensation mechanism is controlled by rapidly increasing gravitational component in the direction of flow; the normal component of gravity, if at all, would have a negligibly small effect near the upper stagnation point. The visual observations did not yield any additional information except that the dripping rate of the condensate decreased as the sphere temperature approached the saturation temperature of water.

It may be re-emphasized here that theoretically we should expect the quasi-steady heat transfer data to be a few percent lower than the steady-state predictions because of relatively thicker quasi-steady film. The presence of condensate drop at the bottom stagnation point also tends to decrease the average heat flux by about 1–2 percent.

Finally, in Fig. 7, the dimensionless heat flux for all the spheres is plotted as a function of wall subcooling. The data have been nondimensionalized by the heat flux calculated from equation (4). The quasi-steady data are adequately represented by the steady-state predictions.

## Conclusions

1 Analysis has been made which shows that steady-state solutions can be used to predict quasi-steady condensation heat transfer as long as the dimensionless thermal diffusion time constant for the film is small and  $c_p \Delta T / h_{fg}$  is not very small.

2 Quasi-steady laminar film condensation of steam has been

experimentally observed on three copper spheres of diameter 1.90, 2.54, and 3.17 cm.

3 The average heat transfer data for wall subcoolings of 5–65°C and for  $c_p \Delta T / h_{fg}$  of 0.009–0.12 lie within  $\pm 13$  percent of the theoretical results of Dhir and Lienhard and of Yang.

## References

- 1 Nusselt, W., "Die Oberflächenkondensation des Wasserdampfes," *Z. Ver Deutsch. Ing.*, Vol. 60, 1916, pp. 541–546, 569–575.
- 2 Rohsenow, W. M., "Heat Transfer and Temperature Distribution in Laminar Film Condensation," *TRANS. ASME*, Vol. 78, 1956, pp. 1645–1648.
- 3 Sparrow, E. M., and Gregg, J. L., "A Boundary-Layer Treatment of Laminar-Film Condensation," *JOURNAL OF HEAT TRANSFER*, *TRANS. ASME*, Series C, Vol. 81, No. 1, Feb. 1959, pp. 13–18.
- 4 Sparrow, E. M., and Gregg, J. L., "Laminar Condensation Heat Transfer on a Horizontal Cylinder," *JOURNAL OF HEAT TRANSFER*, *TRANS. ASME*, Series C, Vol. 81, No. 3, Nov. 1959, pp. 291–296.
- 5 Dhir, V. K., and Lienhard, J. H., "Laminar Film Condensation on Plane and Axis-Symmetric Bodies in Non-Uniform Gravity," *JOURNAL OF HEAT TRANSFER*, *TRANS. ASME*, Series C, Vol. 93, No. 1, Feb. 1971, pp. 97–100.
- 6 Yang, J. W., "Laminar Film Condensation on a Sphere," *JOURNAL OF HEAT TRANSFER*, *TRANS. ASME*, Series C, Vol. 95, No. 2, May 1973, pp. 174–178.
- 7 Kutateladze, S. S., *Fundamentals of Heat Transfer*, Edward Arnold, London, 1963.
- 8 Fujii, T., and Uehara, H., "Laminar Filmwise Condensation on a Vertical Surface," *International Journal of Heat and Mass Transfer*, Vol. 15, 1972, pp. 217–233.
- 9 Al-Diwany, H. K., and Rose, J. W., "Free Convection Film Condensation of Steam in the Presence of Noncondensing Gases," *International Journal of Heat and Mass Transfer*, Vol. 16, 1973, pp. 1359–1370.
- 10 Rauscher, J. W., Mills, A. F., and Denny, V. E., "Experimental Study of Film Condensation From Steam-Air Mixtures Flowing Downward Over a Horizontal Tube," *JOURNAL OF HEAT TRANSFER*, *TRANS. ASME*, Series C, Vol. 16, No. 1, Feb. 1974, pp. 83–88.
- 11 Mills, A. F., Tan, C., and Chung, D. K., "Experimental Study of Condensation From Steam-Air Mixtures Flowing Over a Horizontal Tube: Overall Condensation Rates," Paper presented at the 5th International Heat Transfer Conference, Tokyo, Sept. 3–7, 1974.
- 12 Sparrow, E. M., and Siegel, R., "Transient Film Condensation," *Journal of Applied Mechanics*, *TRANS. ASME*, Series E, Vol. 81, No. 1, Mar. 1959, pp. 120–121.
- 13 Bereghes, A. E., and Thompson, W. G. Jr., "The Relationship of Quench Data to Steady State Pool Boiling Data," *International Journal of Heat and Mass Transfer*, Vol. 13, 1970, p. 55.
- 14 Ded, J. S., and Lienhard, J. H., "The Peak Pool Boiling Heat Flux From a Sphere," *AIChE Journal*, Vol. 18, No. 2, Mar. 1972, pp. 337–342.
- 15 Reynolds, W. C., and Perkins, H. C., *Engineering Thermodynamics*, McGraw-Hill, New York, 1970.
- 16 Sparrow, E. M., and Minkowycz, W. J., "Condensation Heat Transfer in the Presence of Noncondensables, Interfacial Resistance, Superheating, Variable Properties and Diffusion," *International Journal of Heat and Mass Transfer*, Vol. 9, 1966, pp. 1125–1144.
- 17 Poots, G., and Miles, R. G., "Effects of Variable Physical Properties on Laminar Film Condensation of Saturated Steam on a Vertical Flat Plate," *International Journal of Heat and Mass Transfer*, Vol. 10, 1967, pp. 1677–1692.
- 18 Denny, V. E., and Mills, A. F., "Non-Similar Solutions for Laminar Film Condensation on a Vertical Surface," *International Journal of Heat and Mass Transfer*, Vol. 12, 1969, pp. 965–979.
- 19 Denny, V. E., and South, V., III, "Effects of Forced Flow, Noncondensables, and Variable Properties on Film Condensation of Pure and Binary Vapors at the Forward Stagnation Point of a Horizontal Cylinder," *International Journal of Heat and Mass Transfer*, Vol. 15, 1972, pp. 2133–2142.
- 20 Fujii, T., Uehara, H., and Kurata, C., "Laminar Filmwise Condensation of Flowing Vapor on a Horizontal Cylinder," *International Journal of Heat and Mass Transfer*, Vol. 15, 1972, pp. 235–246.

D. Moalem

School of Engineering,  
Dept. of Flow Mechanics & Heat Transfer,  
Tel-Aviv University, Israel

S. Sideman

Department of Chemical Engineering,  
Technion-Israel Institute of Technology,  
Haifa, Israel

# Theoretical Analysis of a Horizontal Condenser-Evaporator Elliptical Tube

*The characteristics of the various parameters affecting the films and overall heat transfer coefficients of horizontal evaporator-condenser elliptical tubes are presented for a representative range of operating conditions. Effects of the axis ratio of the tube are analyzed and compared with the equivalent circular tube. The study indicates that the ratio of the vertical to the horizontal axis of about 4 approaches the asymptotic solution for a vertical plane of constant wall temperature and the average overall transfer rate decreases at axis ratios above 4. Effects of the intermittent removal of the condensate film from the wall are presented. The effect of homogeneously distributed noncondensables is accounted for.*

## Introduction

Horizontal-tube-evaporator-condensers, where condensation takes place inside the tube bundle, while the cooling evaporating films flow over the outside of the tubes are economically more promising [1, 2, 3]<sup>1</sup> than the classical vertical arrangements suggested in various water desalination schemes.

Related theoretical studies treat evaporation [1, 4, 5] and condensation [1, 6] on inclined surfaces as independent phenomena, usually based on a constant value of the tube wall temperature. A simultaneous solution for the transfer rates of the interacting condensation and evaporation processes inside and outside a circular horizontal tube, respectively, was recently presented by Moalem and Sideman [7].

Economics stimulate a continuous quest for other means of improving the transport rate. Utilization of noncircular conduits in the horizontal-evaporator-condenser is a promising route in the search for economic and efficient desalination units. Based on past experience with other types of compact high load heat exchangers, high surface area to core volume ratio of the tubes may allow for smaller shells. Furthermore, based on the earlier study [7] of the local film thickness, evaporation and condensation rates and the local transfer coefficients around the periphery of a circular tube, it is to be anticipated that by increasing the region of maximum inclination in the conduit, a significant improvement of the overall

heat transfer coefficient will be achieved, while still maintaining the essential features of the horizontal evaporator-condenser unit. A longer path of the evaporating film may enhance rippling effects which seem to increase the transfer rate [4]. Last but not least, the envisioned elongated type conduit will allow better removal of the accumulated condensate at the bottom, and thus decrease the ratio of the ineffective to effective heat transfer area.

An elliptical cross section of the conduit is chosen here since it permits analytical representation of the momentum and energy equations and allows the study of the effect of surface to volume ratio with relative comfort. To facilitate the solution, we neglect here the effect of the wall thickness. As indicated in [7], this introduces an error of less than 5 percent in the results.

## The Theoretical Model and the Governing Equations

Consider a horizontal metal tube of an elliptical cross section. Saturated steam at  $T^*$  (corresponding to the total pressure  $p^*$ ) enters the tube at  $z = 0$  and while flowing in the  $z$ -direction condenses on the inside surface of the tube. The condensate film which is formed flows tangentially ( $x$ -direction) along the internal periphery of the tube. In the range of steam flow rates considered here,  $Re_v < 35000$ , the condensate forms a layer at the bottom of the tube so that the flow of steam and liquid is stratified. The external surface of the tube is continually wetted by saturated (sea) water at  $T_v$ , which is assumed to fall as a vertical sheet on the tube at  $x = 0$ . A liquid film is formed on the external side of the tube, flowing in  $x$ -direction along the perimeter, and draining at the bottom of the horizontal tube. As  $T^* > T_v$ , the latent heat of condensation is utilized to evaporate some of the external water film, while the pressure in the external vapor chest surrounding the tube is kept constant, corresponding to  $T_v$ .

A schematic presentation of the physical model and the coordi-

<sup>1</sup> Numbers in brackets designate References at end of paper.

Contributed by the Heat Transfer Division for publication in the JOURNAL OF HEAT TRANSFER. Manuscript received by the Heat Transfer Division February 4, 1975. Paper No. 75-HT-KKK.

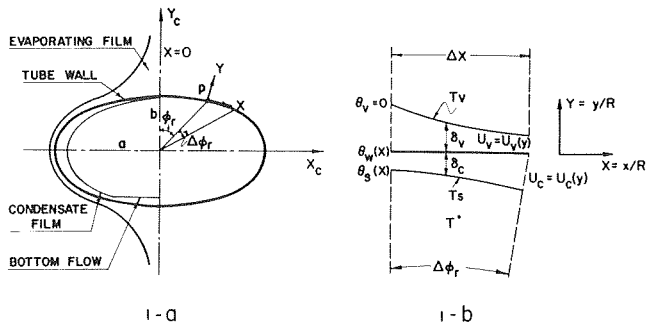


Fig. 1 Schematic presentation of the physical system and coordinates

nates used are shown in Fig. 1(a). Fig. 1(b) represents an angular cross section  $\Delta\phi_r$  at some distance  $x$  from the upper stagnation point. The thickness of the two liquid films,  $y_v$  and  $y_c$ , on the evaporation and condensation sides, respectively, is assumed to be small relative to radius vector, so that Cartesian coordinates may conveniently be used. Hence, a two-dimensional film flow is locally considered along the periphery. Note that the local angle of inclination varies with the peripheral distance  $x$  and, unlike a circular cross section, is not equal to  $\phi_r$  the slope of the radius vector.

With reference to a characteristic radius  $R$  (equal to the radius of an area equivalent circular tube) and a reference velocity  $u_r$  (to be specified in the following) we define the following dimensionless variables:

$$\begin{aligned} X &= x/R; \quad Y = y/R; \quad U = u/u_r; \quad \delta_v = y_v/R; \quad \delta_c = y_c/R \\ \theta &= (T - T_v)/(T^* - T_v) \quad \theta_s = (T_s - T_v)/(T^* - T_v) \end{aligned} \quad (1)$$

where  $(T^* - T_v) = \Delta T^*$  is the total nominal temperature driving force. Note that  $T^* = T_s$  and  $\theta_s = 1$  for pure steam, while in the presence of noncondensables  $T^* > T_s$  and  $\theta_s < 1$ . Neglecting the tangential pressure gradient, and assuming  $\lambda_s \approx \lambda_v$ , the dimensionless forms of the continuity, momentum and energy equations are:

$$\dot{M}_v = \frac{\dot{m}_v}{\rho_l u_r} = -\frac{d}{dX} \int_0^{\delta_v} U_v dY; \quad \dot{M}_c = \frac{\dot{m}_c}{\rho_l u_r} = -\frac{d}{dX} \int_0^{-\delta_c} U_c dY \quad (2)$$

$$\frac{d^2 U}{dY^2} = -C_0 \sin\phi; \quad U = U_c \text{ or } U_v; \quad C_0 = Fr \cdot Re \quad (3)$$

$$Pe \frac{d}{dX} \int_0^{\delta_v} U_v (\theta - Ja) dY = \frac{d\theta}{dY} \Big|_{Y=0} \quad (4)$$

and

$$Pe \frac{d}{dX} \int_0^{-\delta_c} U_c (\theta - \theta_s - Ja) dY = -\frac{d\theta}{dY} \Big|_{Y=0} \quad (5)$$

where  $\dot{m}$  denotes the respective mass flux due to phase change.

### The Velocity and Mass Velocity

The velocity profiles are derived by integrating the equations of momentum, assuming the classical boundary conditions of nonslip velocity on the solid surfaces and zero shear stresses on the free vapor-liquid interfaces of the two films. The neglect of the shear stress in the  $z$ -direction on the condensation side is justified for mild steam velocities inside the tube [2, 7]. The solution of equation (3) with these boundary conditions yields:

$$U_v = (2\delta_v Y - Y^2) \frac{C_0 \sin\phi}{2}; \quad U_c = (-2\delta_c Y - Y^2) \frac{C_0 \sin\phi}{2} \quad (6)$$

The dimensionless form of the mean velocities is then

### Nomenclature

$A$  = heat transfer surface  
 $a$  = semimajor axis  
 $B$  =  $x$ -dependent parameter ( $= \frac{1}{2}C_0 \sin\phi$ )  
 $b$  = semiminor axis  
 $C_{pl}$  = specific heat of liquid  
 $C_0$  = dimensionless constant ( $= Re \cdot Fr$ )  
 $D$  = inside tube diameter  
 $E$  = ratio of vertical to horizontal axis  
 $Fr$  = Froude number ( $= gR/u_r^2$ )  
 $g$  = gravitation constant  
 $h(x, z)$  = local heat transfer coefficient  
 $Ja$  = Jacob number ( $= \lambda/(T^* - T_v)C_{pl}$ )  
 $k_l$  = conductivity of liquid  
 $L$  = tube length  
 $\dot{M}$  = dimensionless mass flux  
 $\dot{m}$  = mass flux  
 $P^*$  = total pressure inside the tube  
 $Pe$  = Peclet number ( $= Pr \cdot Re$ )  
 $P_g$  = partial pressure of inerts  
 $Pr$  = Prandtl number ( $= C_{pl}\mu_l/k_l$ )  
 $P_v$  = vapor pressure in the external vapor chamber  
 $Q_s$  = volumetric steam flow rate  
 $Q_s(0)$  = inlet steam flow rate (at  $z = 0$ )  
 $R$  = radius of equivalent circular tube  
 $Re$  = Reynolds number ( $= Ru_r\rho_l/\mu_l$ );  $Re_N = 4\Gamma/\mu_l$   
 $r$  = radial coordinate  
 $S$  = vertical space between two successive tubes  
 $T^*$  = saturation temperature of steam corresponding to  $P^*$

$T_s$  = saturation temperature of steam at the condensate free surface  
 $T_v$  = saturation temperature of vapor corresponding to  $P_v$   
 $T_w$  = temperature of the tube wall  
 $\Delta T^*$  = nominal temperature difference ( $= T^* - T_v$ )  
 $\Delta T_c$  = temperature difference ( $= T_s - T_w$ )  
 $\delta T$  = local temperature difference across the (condensate or evaporating) film  
 $U$  = overall heat transfer coefficient ( $U(x, z)$ )  
 $\bar{U}^*$  = averaged overall heat transfer coefficient (based on  $\Delta T^*$ )  
 $U_c, U_v$  = dimensionless liquid velocities across the condensate and evaporating film  
 $u_c, u_v$  = dimensional liquid velocities across the condensate and evaporating film  
 $\bar{u}_c, \bar{u}_v$  =  $y$ -averaged liquid velocities across the condensate and evaporating film  
 $\bar{u}_{v,0}$  = initial (at  $x = x_D$ )  $y$ -averaged liquid velocity across the evaporating film  
 $u_r$  = reference velocity ( $= \bar{u}_{v,0}$ )  
 $\omega_c, \omega_v$  = mass flow rates across the condensate and evaporating films  
 $\omega_{c,0}, \omega_{v,0}$  = initial values of  $\omega_c, \omega_v$   
 $X$  = dimensionless tangential direction on the tube ( $= x/R$ )  
 $x_D$  = initial value for the evaporation region

$x_m$  = final values for the evaporation region  
 $Y$  = dimensionless normal coordinate ( $= y/R$ )  
 $y_c, y_v$  = condensing and evaporating film thickness  
 $y_{v,0}$  = initial film thickness ( $x = x_D$ )  
 $z$  = axial coordinate of the tube;  $z_f$  - final condensation length  
 $\Gamma_v, \Gamma_c$  = liquid mass flow rates of the evaporating film and condensate  
 $\Gamma_{v,0}$  = initial liquid mass flow rate across the evaporating film  
 $\delta_c, \delta_v$  = dimensionless film thickness ( $= y_c/R$  or  $y_v/R$ )  
 $\lambda_v, \lambda_c$  = heat of evaporation and condensation in the evaporation-condensation sides  
 $\theta$  = dimensionless temperature ( $= (T - T_v)/(T^* - T_v)$ )  
 $\theta_s$  = dimensionless temperature of the condensate free surface  
 $\theta_w$  = dimensionless temperature of the tube wall  
 $\mu_l$  = liquid viscosity  
 $\nu_l$  = kinematic viscosity ( $= \mu_l/\rho_l$ )  
 $\rho_l$  = liquid density  
 $\rho_s$  = steam density  
 $\phi$  = angle of inclination  
 $\phi_r$  = angular coordinate

$$\bar{U} = \frac{1}{3} \delta^2 C_0 \sin\phi \quad (7)$$

where  $\bar{U}$  and  $\delta$  relate to either the condensation or the evaporation side.

The dimensionless form of the local flow rates (per unit length of tube) for the two liquid films, are

$$\omega = \frac{\Gamma}{u_r \rho_l R} = \frac{1}{3} \delta^3 C_0 \sin\phi = \frac{2}{3} B \delta^3 \quad (8)$$

where  $\omega$ ,  $\delta$ , and  $\Gamma$  consistently refer to either of the liquid films with

$$\Gamma_c = \bar{u}_c \rho_l \gamma_c, \quad \Gamma_v = \bar{u}_v \rho_l \gamma_v \quad \text{and} \quad B = \frac{C_0 \sin\phi}{2}$$

Note that equation (8) is identical in form with the classical Nusselt expression for the mass flow rate. Differentiating equation (8) yields the evaporation and condensation rates:

$$\dot{M}_v = -\frac{d\omega_v}{dX} = -\frac{d}{dX} \frac{2}{3} (B \delta_v^3) = -\delta_v^2 C_0 \sin\phi \frac{d\delta_v}{dX} - \frac{1}{3} \delta_v^3 C_0 \cos\phi \quad (9)$$

$$\dot{M}_c = \frac{d\omega_c}{dX} = \frac{d}{dX} \left( \frac{2}{3} B \delta_c^3 \right) = \delta_c^2 C_0 \sin\phi \frac{d\delta_c}{dX} + \frac{1}{3} \delta_c^3 C_0 \cos\phi \quad (10)$$

### The Temperature Profiles

Linear temperature profiles are assumed for the two liquid films. Introducing the following boundary conditions:

$$\begin{aligned} Y = \delta_v \quad \theta = 0 \\ Y = 0 \quad \theta = \theta_w \end{aligned} \quad (11)$$

$$Y = -\delta_c \quad \theta = \begin{cases} 1 - \text{pure vapor} \\ \theta_s = f(z) \text{ in the presence of inerts} \end{cases}$$

yields:

$$\theta_v = \theta_w - \frac{\theta_w}{\delta_v} Y \quad (12)$$

$$\theta_c = \theta_w - \frac{\theta_s - \theta_w}{\delta_c} Y \quad (13)$$

where  $\theta_w$ , the dimensionless temperature of the tube wall, is a function of  $X$  and is related to  $\delta_v$  and  $\delta_c$  by matching the heat fluxes at the two sides of the tube wall:

$$\left. \frac{d\theta}{dY} \right|_{0^+} = \left. \frac{d\theta}{dY} \right|_{0^-} \quad (14)$$

Substituting the temperature gradient from equations (12) and (13) in equation (14) yields:

$$\theta_w = \theta_s / (1 + \delta_c / \delta_v) \quad (15)$$

### Solution of the Equations of Energy

Substituting equations (6), (12), and (13) in equations (4) and (5) and rearranging yields:

$$\frac{\theta_w}{\delta_v} = \text{Pe} \frac{d}{dX} \left[ \left( \frac{3}{8} \theta_w - \text{Ja} \right) \left( \frac{2}{3} B \delta_v^3 \right) \right] \quad (16)$$

$$\frac{\theta_s - \theta_w}{\delta_c} = \text{Pe} \frac{d}{dX} \left\{ \left[ \frac{3}{8} (\theta_s - \theta_w) + \text{Ja} \right] \left( \frac{2}{3} B \delta_c^3 \right) \right\}$$

where  $\theta_w$ ,  $B$ ,  $\delta_v$  and  $\delta_c$  are  $X$ -dependent. The differentiation of equations (16) leads to a set of first order ordinary differential equations in  $\delta_c$  and  $\delta_v$  and the solution is quite complicated and time consuming. A quick solution is obtained if, for small  $\Delta X$  steps, equations (16) are approximated by:

$$\frac{\theta_w}{\delta_v} = \text{Pe} \left( \frac{3}{8} \theta_w - \text{Ja} \right) \frac{d}{dX} \left( \frac{2}{3} B \delta_v^3 \right) \quad (17)$$

$$\frac{\theta_s - \theta_w}{\delta_c} = \text{Pe} \left[ \frac{3}{8} (\theta_s - \theta_w) + \text{Ja} \right] \frac{d}{dX} \left( \frac{2}{3} B \delta_c^3 \right) \quad (17)$$

Combining equations (9), (10), and (17) yields:

$$\omega_v^{1/3} d\omega_v = \left( \frac{C_0 \sin\phi}{3N_v^3} \right)^{1/3} dX; \quad \omega_c^{1/3} d\omega_c = \left( \frac{C_0 \sin\phi}{3N_c^3} \right)^{1/3} dX \quad (18)$$

where

$$N_v = \text{Pe} \left( \frac{3}{8} - \frac{\text{Ja}}{\theta_w} \right); \quad N_c = \text{Pe} \left( \frac{3}{8} + \frac{\text{Ja}}{\theta_s - \theta_w} \right) \quad (18a)$$

Integration of equation (18) yields

$$\omega_v = (\omega_{v,0}^{4/3} + I_v)^{3/4}; \quad \omega_c = (\omega_{c,0}^{4/3} + I_c)^{3/4} \quad (19)$$

where

$$I_c = \int_{x_0}^x 4 \left( \frac{C_0 \sin\phi}{3N_c^3} \right)^{1/3} dX; \quad I_v = \int_{x_0}^x 4 \left( \frac{C_0 \sin\phi}{3N_v^3} \right)^{1/3} dX \quad (19a)$$

$\omega_{v,0}$  and  $\omega_{c,0}$  are known (initial) values at the initial limit of the tangential integration range  $X = X_0$  of any  $\Delta X$  step. Combining with equations (9) yields:

$$\frac{\delta_c}{\delta_v} = \left[ \frac{\omega_{c,0}^{4/3} + I_c}{\omega_{v,0}^{4/3} + I_v} \right]^{1/4} \quad (20)$$

Substituting equation (20) into equation (15) we obtain:

$$\frac{\theta_w}{\theta_s} \left[ 1 + \left[ \frac{\omega_{c,0}^{4/3} + I_c}{\omega_{v,0}^{4/3} + I_v} \right]^{1/4} \right] - 1 = 0 \quad (21)$$

As  $I_c$  and  $I_v$  are a function of  $\theta_w$  and  $X$ , equation (21) is nonlinear in  $\theta_w$ . Consistent with the assumption leading to equation (17), equation (21) is also limited to small increments in the tangential coordinate, and the solution over the periphery must be step-wise executed. The apparent error introduced by this constrain is practically eliminated by the computational procedure [7, 10].

### The Tangential Evaporation—Condensation Range

It is assumed that the evaporation process starts once the developing (external) thermal boundary layer becomes identical with the thickness of the external water film. The evaporation is assumed to come to an end at the point in which the condensate film meets with the stratified condensate layer at the bottom, as it is quite reasonable to neglect the heat transferred through the condensate-layer at the bottom of the tube [1]. Equation (21) is progressively solved between these two limits.

The distance  $x_D$  downstream (from the top) where the external free surface is affected by the simultaneous condensation taking place inside the tube is given, for a circular tube, by [8]:

$$x_D = \frac{\sqrt{2}}{21.25} \frac{\nu_l \text{Re}_N}{u_g} \left( \frac{9}{128} \text{Re}_N + \frac{24.24}{\Pi} \right); \quad \text{Re}_N = \frac{4\Gamma_{v,0}}{\mu_l} \quad (22)$$

where  $\Gamma_{v,0}$  is half the mass flow rate (per unit length) of the liquid flowing on the tube,  $u_g$  is the film free-fall velocity given by  $\sqrt{2gS}$  and  $S$  is the vertical free-fall distance, usually the vertical space between two tubes. In as much as  $x_D$  is small relative to the (half) peripheral distance, it is reasonable to assume that equation (22) may be used for the elliptical shapes as well. This is substantiated by the fact that significant variation of the very small values of  $x_D$  do not noticeably affect the results. The dimensionless thermal boundary layer developing distance is related to the corresponding angle of inclination in [10].

The dimensionless film thickness,  $\delta_{v,0}$ , at  $x_D$  is obtained from equation (9) where  $\Gamma_v = \Gamma_{v,0}$  denotes the initial film mass flow rate per unit length. Choosing the  $y$ -averaged velocity at  $x = x_D$  as the reference velocity, i.e.,  $u_r = \bar{u}_{v,0}$  yields the relationship between the Reynolds number,  $\text{Re}$ , based on  $R$ , and  $\text{Re}_N$ , the Reynolds number commonly used in film-flow studies:

$$\text{Re} = \frac{\mu_r \rho_l R}{\mu_l} = \frac{\Gamma_{v,0}}{\rho_l \bar{u}_{v,0}} \frac{\rho_l R}{\mu_l} = \frac{1}{4\delta_{v,0}} \text{Re}_N \quad (23)$$

In the steam flow rate range considered here, stratification of the condensate at the bottom of the horizontal tube occurs. As shown by Chadock [9] the variation in the condensate level along the tube is relatively small and limited to a few degrees. Neglecting this variation, the length-averaged angle,  $\bar{X}_m$ , corresponding to the height of the condensate layer at the bottom of a circular tube is given by [9]:

$$\bar{X}_m = \pi - [5.06 \cdot 10^{-4} \left[ \frac{k_1^3 (\rho_1 - \rho_s) g}{\mu_1 \rho_1^3 \lambda^3} \right]^{1/4} \frac{L \Delta T_c^{3/4}}{D^{2.75}}]^{0.142} \quad (24)$$

where  $D$  and  $L$  are the diameter and length of the tube, respectively.  $\Delta T_c = T_s - T_w$  is the temperature difference between the free surface temperature of the condensate and the wall surface inside the tube.

As can easily be verified, reasonably small variations in  $\bar{X}_m$  do not noticeably affect the final results, and equation (24) is assumed to apply here too. Note that since  $\Delta T_c$  in equation (24) is not known a priori, the calculation is initiated by a reasonable guess and then corrected by an iterative procedure.

### Effect of Noncondensables

A homogeneous concentration distribution of noncondensables is assumed to occur for the intermediate steam loads range used in the water desalination unit considered here. Nevertheless, stratification of the condensate, rather than an annular regime, still prevails. The ratio of the final to initial steam flow rates in the conduit as a function of the nominal temperature driving force  $\Delta T^*$  and the inlet concentration of the inerts in the steam supplied to the system is identical with the expression derived for a circular tube [7].

### Condensation in Consecutive Sections

In order to reduce the effect of the accumulating condensate film, the condensate film is removed at arbitrary distances from the top ( $x = 0$ ), by introducing internal partitions along the periphery. The total condensation area is thus divided into a desired number of consecutive sections, and condensate buildup starts anew ( $\delta_c = 0$ ) at the beginning of each section. The average condensate film thickness is then reduced and the transfer rates should increase.

### The Heat Transfer Coefficients

The local heat transfer coefficients around the periphery at any  $z$  are obtained by:

$$h(x, z) = \frac{dq/dt}{\delta T A} = \frac{\lambda d\Gamma}{\delta T dx} = \frac{\lambda \mu}{R \delta T} \text{Re} \frac{d\omega}{dX} \quad (25)$$

where  $\delta T$  denotes the local temperature difference across the condensate ( $= T_s - T_w$ ) or the evaporating film ( $= T_w - T_v$ ).

The averaged overall heat transfer coefficient is defined by:

$$\bar{U}^* = \frac{\int_z^x U(x, z) \Delta T(x, z) dA}{A \Delta T^*} \quad (26)$$

where  $\Delta T^* = T^* - T_v$  is the nominal driving force,  $\Delta T(x, z)$  is the local temperature driving force across the two films, and  $U(x, z)$  is the local overall transfer coefficient. Clearly, equation (26) can be related to either pure or vapor containing noncondensables.

### Evaluation of Condenser-Tube Length

**For Pure Steam.**  $T_s \equiv T^*$  and  $\theta_s = 1.0$ , invariant with the axial direction of the tube, and the solution of the two-dimensional (tangential and radial) problem of heat transfer yields the condensation rate-per-unit length. This, in turn, is used to evaluate the tube length for any steam load,  $Q_s(0)$  ( $\text{cm}^3/\text{s}$ ) at the inlet by the simple relationship:

$$L = \frac{\rho_s Q_s(0)}{2 \Gamma_{c, \bar{x}_m}} \quad (27)$$

where  $\Gamma_{c, \bar{x}_m}$  is the (half-periphery accumulated) condensate film

flow rate-per-unit length at the bottom of the tube,  $x = \bar{x}_m$ .

In the presence of noncondensables, the free surface temperature of the condensate,  $T_s$ , decreases along the tube, and the two-dimensional problem must be solved progressively along the tube. The local steam flow rate along the  $z$ -axis is obtained for each  $\Delta z$  step by:

$$Q_s(z + \Delta z) = Q_s(z) - \frac{2 \Gamma_{c, \bar{x}_m}(\Delta z)}{\rho_s} \quad (28)$$

The free surface temperature of the condensate,  $\theta_s$ , is locally calculated [7, 10] utilizing the local steam flow rate given by equation (28). The length of the tube is obtained when a point is reached where  $\theta_s$  approaches zero (to within  $10^{-2}$ ).

### Results and Discussions

The analysis of the transfer characteristics of a circular horizontal condenser-evaporator tube [7] showed great variation of transfer rates around the circumference, with maximum transfer rates around  $\pi/2$ . These results prompted the search for conduits that yield high transfer rates in most of their circumference.

Whereas the study of a conduit with a finite wall thickness requires the solution of a set of nonlinear differential equations, the assumption of zero wall thickness allows for a solution of a simpler set of equations. The latter is further simplified by adopting the procedure associated with equation (17). The deviation due to this approximation, as compared with the exact solution for zero wall thickness [7] for a circular conduit, is of about 2 percent [10]. As the assumption of zero wall thickness greatly facilitates the analysis, absolute accuracy was sacrificed for expediency and less computational costs.

With reference to the definition of  $\theta_w$ , note that  $\theta_w = 1$  represents the maximum driving force possible in the absence of a film or wall resistance. As indicated by Fig. 2, when pure steam condenses inside an evaporator-condenser tube, the major part of the available temperature driving force is located in the external, evaporating film. Fig. 2 represents the dimensionless "wall" temperatures around the periphery of the conduit, for various values of  $E$ , the ratio of the vertical to the horizontal axis. The temperature drop across the evaporating film increases as the conduit

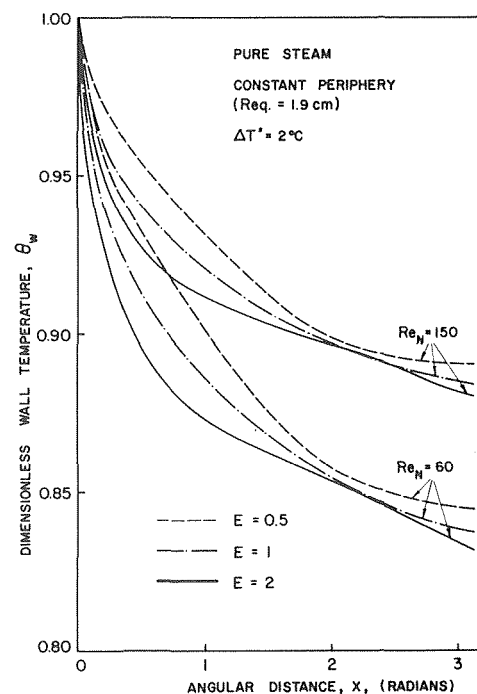


Fig. 2 Dimensionless wall temperature around the tube

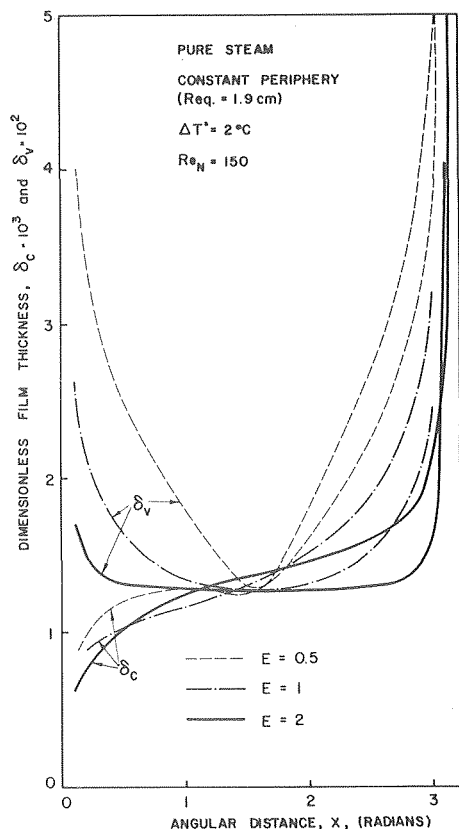


Fig. 3 Effect of axis ratio on the dimensionless thickness of the condensate and evaporating film around the conduit

changes from the prolate ( $E > 1$ ) to the oblate ( $E < 1$ ) shape. The corresponding temperature difference across the condensate film decreases as  $E$  decreases from 2 to  $\frac{1}{2}$ . Also included in Fig. 2 is the effect of the external film flow rate or the Reynolds number. Since  $T_v < T^*$ , increasing the external flow rate affects a decrease in  $T_w$  hence in  $\theta_w$ .

Fig. 3 demonstrates the variation of the dimensionless thickness of the condensate and the evaporating films along the periphery of the conduits. In general, the effect of the angle of inclination on the evaporating film thickness is much more pronounced than that of the mass flow rate change due to evaporation and the film is thinnest at  $\pi/2$ . The minimum external film thickness prevails for about 80 percent of the periphery for  $E = 2$ , as compared with approximately 30 percent for  $E = 1$  and the small, sharp, range for  $E = 0.5$ . The condensate film, on the other hand, starts to build up at the top and generally increases in thickness. It is characterized by an inflection point at about  $\pi/2$ , which indicates the opposing effects of the positive change in the mass flow rate and the negative change of the angle of inclination up to this point. Above  $\pi/2$  these two factors combine to increase the internal film thickness. However, the  $E < 1$  the condensate thickness increases sharply from the inflection point, while for  $E > 1$  the increase in the condensate film thickness is rather moderate for most of the tangential range.

The mass flux,  $\dot{m}$ , is presented in Fig. 4 for three values of  $E$ . The curves for  $E = \frac{1}{2}$  and  $E = 1$  indicate a maximum at  $\pi/2$ . The curve for  $E = 2$  yields a plateau for maximum  $\dot{m}$  for the major part of the periphery, ranging approximately between  $\pi/4$  to  $3\pi/4$ . The small differences in the  $\dot{m}_c$  and  $\dot{m}_v$  curves are due to the accumulated sensible heats in the condensate and the evaporating films. The shape of the curves, and particularly those corresponding to  $E = 2$ , are consistent with the developing thicknesses of the two films.

The local evaporation and condensation heat transfer coeffi-

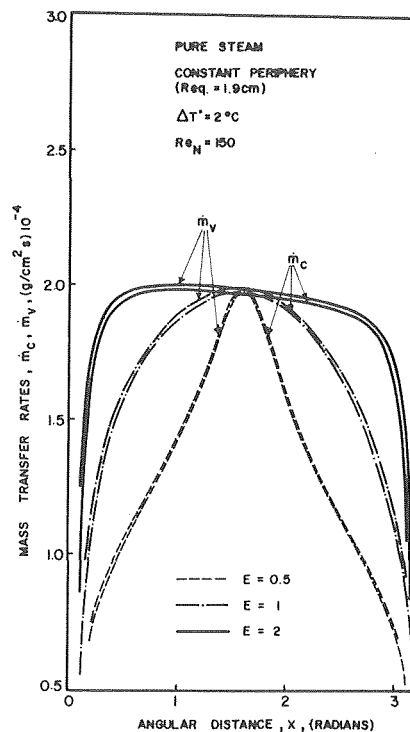


Fig. 4 Effect of axis ratio on the mass flux around the conduit

icients, calculated by equation (25), are compared in Fig. 5 for the three conduit shapes at  $Re = 150$ . Essentially similar curves were obtained for other values of the evaporating film Reynolds number. Consistent with Fig. 4, the condensation transfer decreases with the tangential axis, while the evaporation coefficient exhibits a maximum. Since  $h_v$  is an order of magnitude smaller than  $h_c$ , a conduit with  $E > 2$  is to be preferred as the maximum  $h_v$  holds for a large portion of the surface of the conduit.

The local overall heat transfer coefficients are presented in Fig. 6 for various Reynolds numbers of the evaporating film. For clarity, we compare here the prolate ( $E = 2$ ) and circular ( $E = 1$ ) conduits, and include only the curve for  $Re_N = 60$  and 150 for the  $E = \frac{1}{2}$  conduit. The controlling effect of the evaporation side coefficient is very pronounced. The decrease of the transfer coefficient with the (external) Reynolds number in this range of laminar flow is consistent with other studies (see the following). Note that the maximum transfer coefficient at a given Reynolds number in Fig. 6 is practically identical for all conduit shapes. The obvious advantage in preferring  $E > 1$  over  $E = 1$  is due to the fact that the maximum value of the local transfer coefficient prevails over a larger area. This is well demonstrated in Fig. 7, where we compare the  $x$ -averaged overall heat transfer coefficient for various conduits as a function of the external Reynolds number.

For ease of interpretation of the results, all the values of  $E$  presented so far correspond to identical transfer areas (constant periphery). Thus, Fig. 7 shows that the average overall heat transfer coefficient increase as  $E$  increases. However, as seen in Fig. 8, which is a cross plot of Fig. 7, the asymptotic value of  $\bar{U}^*$  is reached at  $E = 4$  and increasing  $E$  above this asymptotic value is not deemed advantageous. For comparison, Fig. 8 includes the overall heat transfer coefficient, calculated for a vertical flat plate by utilizing Nusselt's solution for the condensation side heat transfer coefficient, based on a constant wall temperature:

$$h_c = 1.47 \left( \frac{k^3 g}{\nu^2} \right)^{1/3} \left( \frac{4 \Gamma_{c,xm}}{\mu} \right)^{-1/3} \quad (29)$$

where  $\Gamma_{c,xm}$  is the total condensate mass flow-rate-per-unit length, at the bottom. The corresponding evaporation side heat transfer

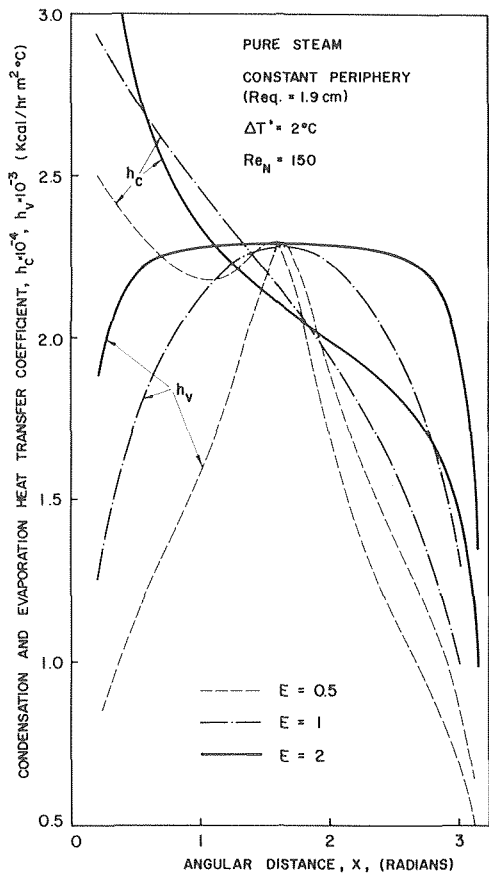


Fig. 5 Effect of axis ratio on the condensation and evaporation heat transfer coefficients around the conduit

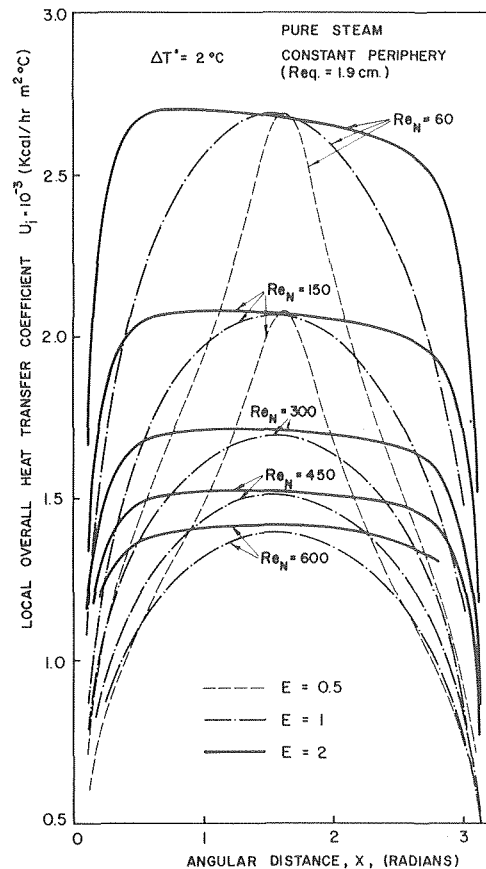


Fig. 6 Effect of axis ratio on the local overall heat transfer coefficients around the conduit

coefficient is given by [4]:

$$h_v = \left(\frac{4}{3}\right)^{1/3} \left(\frac{k^3 g}{\nu^2}\right) \left(\frac{4T_{v,0}}{\mu}\right)^{-1/3} \quad (30)$$

where, for simplicity, we neglect the relatively small mass evaporated in the process. The fact that the "asymptotic" values of the average overall transfer coefficients of this work are smaller than those of the vertical plate is not surprising, as the latter are calculated for a constant wall temperature [11]. It is interesting to note that increasing the axis ratio above 4 leads to lower  $\bar{U}^*$  values as Reynolds number increases. This is attributed to the decreasing effect of the evaporation process on the thickness of the external film as the external flow rate increases. Note that the effect of the condensate film thickness is relatively small in this case, as the vertical flow distance varies only moderately for  $E \geq 4$ . [see insert, Fig. 8].

Fig. 9 represents the dependence of the average overall heat transfer coefficient on the axis ratio of various elliptic shapes generated by keeping  $b$  constant while changing  $a$ . In this figure the periphery is not kept constant, and  $a$  increases linearly with  $E$  (see insert). The values of  $b$  were chosen to correspond to  $E = 2, 4, 8$  in Fig. 8. Consistent with Fig. 8, the overall transfer coefficient increases with increasing the axis ratio up to  $E \approx 4$ . (This increase is considered to be due to the increasing effect of the local angle of inclination, i.e., the increase of the relative portion of the transfer area which exhibits the maximum values of the local coefficients (Figs. 2 to 5).) At  $E > 4$ , the overall coefficients decrease with  $E$ . As  $E$  (or  $a$ ) increases, the effect of the accumulating condensate film is to reduce the overall transfer coefficient. This effect is more pronounced at lower external Reynolds numbers, where the films are thinner and the transfer rates are comparatively larger than at the higher Reynolds numbers. At low Reynolds numbers the over-

all heat transfer coefficient is controlled by both the condensation and the evaporation side. At the higher Reynolds numbers the evaporation side plays the dominant role, and the overall heat transfer rate is mainly affected by the decrease in the evaporating film thickness (due to evaporation). The decrease in the external film thickness is higher for larger  $b$  or larger  $a$  (constant  $E$ ). Hence, the overall transfer rate increases now (at high Reynolds number) as  $b$  increases. The interplay between these two contradicting effects, i.e., the increase in the accumulating condensate film thickness and the decrease in the evaporating film thickness, is furthermore demonstrated later in the study of condensation in consecutive sections.

Similar to the circular tube [7], the effect of the temperature driving force and the temperature level ( $T^*$ ) on the average overall transfer coefficient is quite small for the various values of  $E$ .

The increase in the overall heat transfer coefficient (relative to the transfer coefficient obtained with no internal partitions) due to equally spaced internal partitions is demonstrated in Figs. 10. Fig. 10(a) refers to a constant condensation area  $2\pi R_0$  (with  $b \rightarrow 0$ ,  $a \rightarrow \pi R_0/2 = 2.98$  cm), whereas in Fig. 10(b), the axis  $a$  ( $= 16.7$  cm) was kept constant while changing  $b$  (or  $E$ ) i.e., changing the condensation area. In both cases, a significant increase in the transfer rate is noted only at low external Reynolds numbers, reconfirming the above conclusion that the evaporating side film gains control over the overall heat transfer as the external flow rate increases. However, with the larger vertical axis tubes, (Fig. 10(b)) the condensate films are thicker and the effect of the partitions is more pronounced.

As seen from Figs. 10, the effect of intermittent removal of the condensate film decreases as  $E$ , the ratio of the vertical to horizontal axis, increases. In other words, the partitions affect a circular tube more than an elongated tube. This is explained with reference

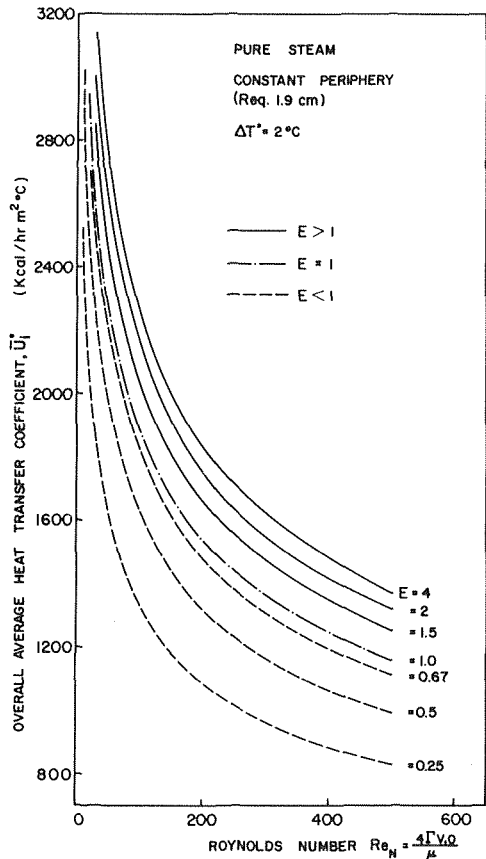


Fig. 7 Effect of the evaporating-side-film Reynolds number on the average overall heat transfer coefficients for various conduits

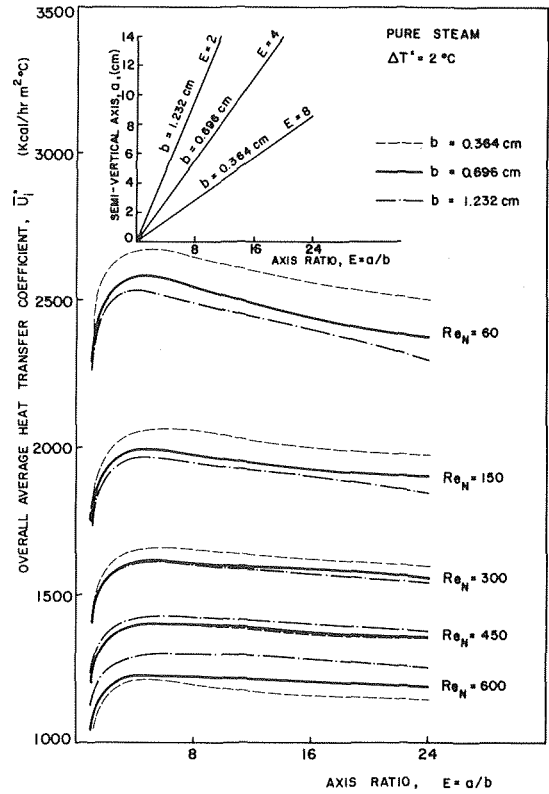


Fig. 9 Effect of axis ratio on the average overall heat transfer coefficient at various Reynolds numbers and various heat transfer area

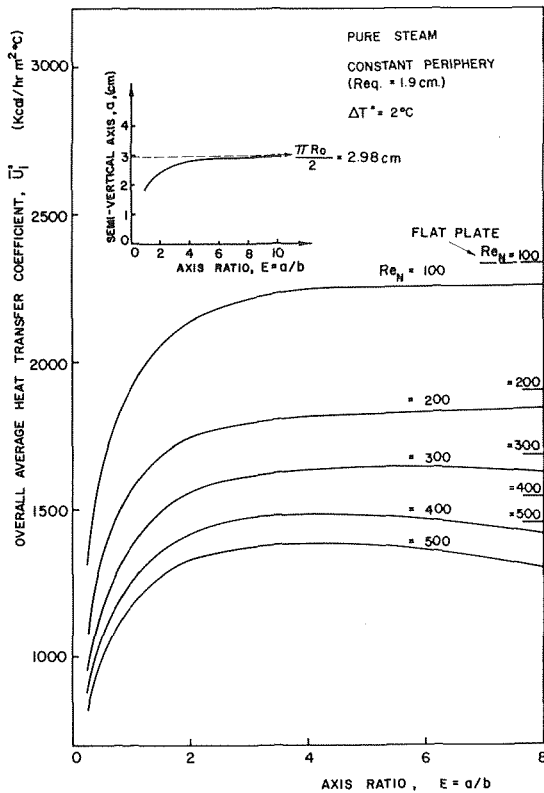


Fig. 8 Effect of axis ratio on the average overall heat transfer coefficient at various Reynolds numbers—identical heat transfer area

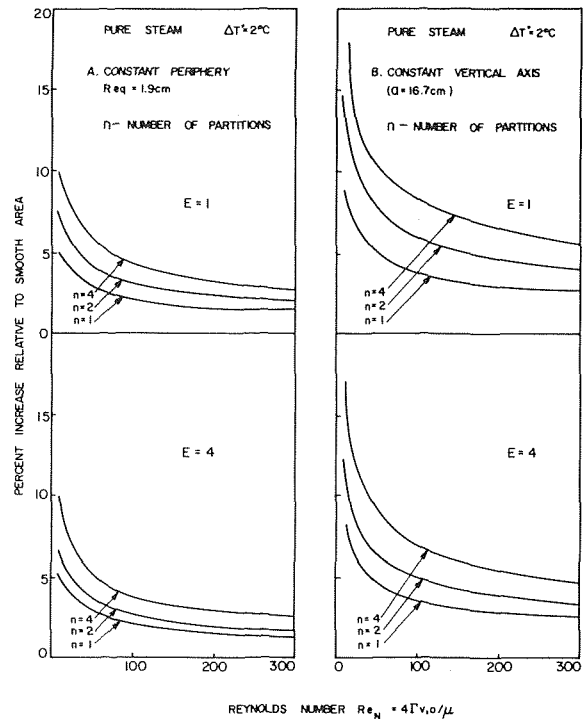


Fig. 10 The increase in the overall heat transfer coefficient due to equally spaced partitions

to Fig. 3 where it is noted that as  $E > 1$ , the increase in the condensate film thickness along the periphery is rather moderate. Thus, the location, as well as the number, of the internal partitions inside the conduit affects the enhancement of the overall transfer rates.

### Conclusions

This study indicates that the best ratio of the vertical to the horizontal axis is about 4. However, the exact ratio should be determined based on the best possible packing arrangement in the tube bundle of the industrial-scale unit. The effect of intermittent removal of the condensate film from the wall decreases with the increase of the external flow rate and the ratio of the vertical to horizontal axis of the tube.

### Acknowledgment

We acknowledge with thanks the sponsorship of the Israel Desalination Engineering, Ltd., Tel-Baruch and the financial support of the Israel National Council for Research and Development.

### References

- 1 Aqua-Chem. Inc., O.S.W. Report No. 209, Nov. 1966.
- 2 Universal Desalting Corp., O.S.W. Report No. 492, Oct. 1969.
- 3 Universal Desalting Corp., O.S.W. Report No. 740, Oct. 1971.
- 4 Chun, K. R., and Seban, R. A. TRANS. ASME Series C, Vol. 93, 1971, p. 391.
- 5 Gardner, G. C., *International Journal of Heat and Mass Transfer* Vol. 15, 1972, p. 2063.
- 6 Rohsenow, W. M., In *Handbook of Heat Transfer*, W. M. Rohsenow and J. P. Hartnett, eds., McGraw Hill New York, Section 12, 1973, pp. 12-19.
- 7 Moalem, D., and Sideman S., "Theoretical Analysis of a Horizontal Condenser-Evaporator Tube," *International Journal of Heat and Mass Transfer*, 1975.
- 8 Zfati, A., "Heat Transfer in Laminar Flow of a Liquid Film on a Horizontal Cylinder," (in Hebrew), MSc thesis, Department of Mechanical Engineering, Technion-Israel Institute of Technology, Haifa, Israel, 1971.
- 9 Chaddock, J. B., *Refrigerating Eng.*, Vol. 65, 1957, pp. 36-41, 90-94.
- 10 Moalem, D., and Sideman, S., Technion R&D Report No. 34, Mar. 1974.
- 11 Nagendra, H. R., and Tirunarayanan, M. A., *Chem. Eng. Sci.*, Vol. 25, 1970, p. 1073.

K. H. Sun

Mem. ASME

G. E. Dix

Nuclear Energy Division,  
General Electric Co.,  
San Jose, Calif.

C. L. Tien

Department of Mechanical Engineering,  
University of California,  
Berkeley, California. Fellow ASME

## Effect of Precursory Cooling on Falling-Film Rewetting

*An analytical model for falling-film wetting of a hot surface has been developed to account for the effect of cooling by droplet-vapor mixture in the region immediately ahead of the wet front. The effect of precursory cooling is characterized by a heat transfer coefficient decaying exponentially from the wet front. Based on the present model, the wet front velocity, as well as the temperature profile along a thin slab, can be calculated. It is demonstrated that the precursory cooling can increase the wet front velocity by an order of magnitude. Existing experimental data with variable flow rates at atmospheric pressure are shown to be successfully correlated by the present model.*

### Introduction

Rewetting of a very hot surface is of fundamental and practical importance to water reactor safety in the event of a postulated loss-of-coolant accident (LOCA). To evaluate the performance of the emergency core cooling systems (ECCS) during the LOCA, it is essential to obtain a better understanding of the physical mechanisms involved in rewetting by a falling water film in the case of top spray cooling and by an upflow of water in the case of bottom flooding. While the controlling mechanism for bottom flooding is not yet fully understood [1],<sup>1</sup> it is generally recognized that falling-film rewetting is conduction-controlled.

Conduction-controlled rewetting was first described by a two-region model [2, 3]. In the model, the advance of the wet front was attributed to axial conduction from an adiabatic dry region ahead of the wet front to a wet region behind the wet front. The two-region model has been extended to a three-region model, namely, an adiabatic region ahead of the wet front, a sputtering region immediately behind the wet front, and a continuous liquid film region further upstream [4]. It was shown that for the case of using water as coolant, the continuous liquid film region exerted little influence on the film wetting phenomenon as compared to the sputtering region which was bounded by the incipient boiling temperature and the temperature corresponding to the minimum heat flux in film boiling. In this case, the resultant wet front velocity of the three-region model became identical to that of the two-region model.

<sup>1</sup> Numbers in brackets designate References at end of paper.

Contributed by the Heat Transfer and presented at the Winter Annual Meeting, New York, N. Y., November 17-22, 1974, of THE AMERICAN SOCIETY OF MECHANICAL ENGINEERS. Journal manuscript received by the Heat Transfer Division April 2, 1975. Paper No. 74-WA/HT-52.

The one-dimensional axial conduction analysis based on the two-region model (or the three-region model) has proven quite successful in predicting the rewetting phenomenon of water at low mass flow rates [3, 4, 5]. Recently, it has been claimed in several investigations [6, 7, 8, 9] that a two-dimensional conduction analysis is required for predicting rewetting characteristics at high flow rates and at high pressures. However, the effect of flow rate on the physical mechanisms that govern the wetting phenomena is not entirely clear.

The present study analyzes the effect of cooling ahead of the wet front on falling-film rewetting. A previous study of this effect has been reported by Edwards and Mather [10] who considered two-dimensional rewetting with a surface heat flux variation of the exponential type. Their analysis shows certain qualitative features of the precursory cooling effect. Yet, it does not provide a clear quantitative picture because of the complexity involved in the two-dimensional analysis as well as the assumption of exponential surface heat flux variation which is mathematically convenient, but difficult to justify physically. A new one-dimensional analytical model has been developed to account for the precursory cooling effect. It is shown that precursory cooling increases the wet front velocity significantly.

### Analysis

**General Considerations.** When a liquid film progresses downward on a very hot vertical surface, the surface is first cooled to the temperature corresponding to the minimum film boiling heat flux, at which the surface begins to wet. Behind the wet front, sputtering occurs as the result of transition and nucleate boiling. Ahead of the wet front, the droplets generated in the sputtering region flow downward cooling the surrounding vapor and the dry surface. It is known that precursory cooling due to the droplet-vapor mixture

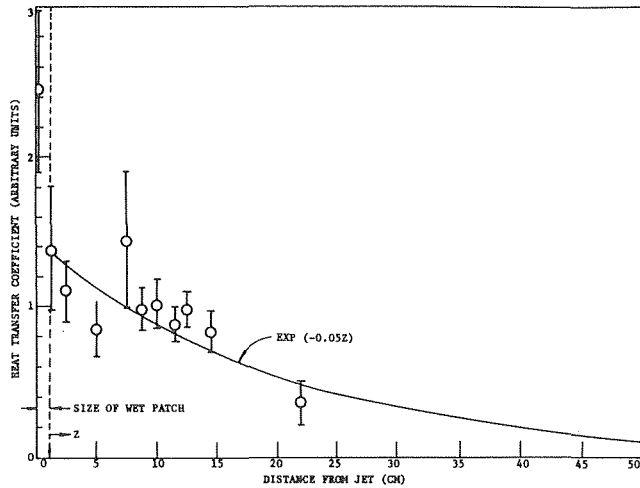


Fig. 1 The variation of heat transfer coefficient ahead of the wet front [5]

can substantially reduce the dry wall temperature ahead of the wet front.

The mechanisms for precursory cooling consist of convection and radiation from the wall to the droplet-vapor mixture. Both mechanisms can be conveniently characterized by a decaying heat transfer coefficient ahead of the wet front. Experimental evidence on precursory cooling is quite limited. Duffey and Porthouse [5] reported experiments on direct injection at spaced intervals along a central pipe into a 36-rod bundle. An axial variation of the heat transfer coefficient was observed, with peak values occurring near the injection points. In Fig. 1, curve fitting of the reported experimental data shows that the axial variation of heat transfer coefficient can be represented by an exponential decay function,  $\exp(-0.05Z)$ , for  $Z$  in centimeters.

Fig. 2 illustrates the film wetting phenomenon and the present model with consideration of precursory cooling. For the case of using water as coolant, the continuous liquid film region has virtually no influence on the wetting front velocity [4]. The wet region can be characterized by a single sputtering boiling heat transfer coefficient,  $h_b$ . The heat transfer coefficient for the precursory cooling region is generally much smaller than  $h_b$ . For convenience,

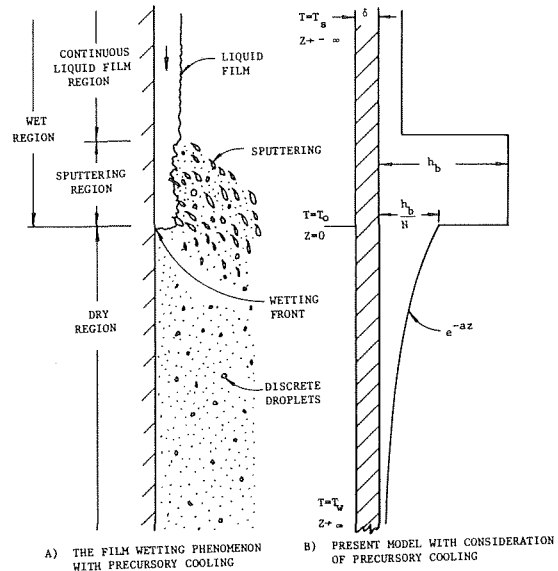


Fig. 2 The film wetting phenomenon and the present model with precursory cooling typically for water coolant

it can be characterized by a fraction of  $h_b$  at the wet front (i.e.  $h_b/N$  where  $N$  is a number followed by an exponential decay relation in the downstream direction. The magnitude of  $N$  depends on coolant flow rate. For increasing flow rate, precursory cooling is enhanced, resulting in smaller  $N$ .

**Mathematical Formulation.** It is recognized that the formulation in general is a two-dimensional conduction problem with surface boundary conditions given in Fig. 2(b). However, to avoid the complexity of numerical calculations and the loss of significance of certain physical parameters, a one-dimensional analysis is adapted to demonstrate the importance of precursory cooling on falling-film wetting. It should be noted that, strictly speaking, the one-dimensional description is accurate for thin slabs such that the Peclet number, with respect to the wet front velocity, and the Biot number, with respect to the sputtering heat transfer coefficient, are small [11]. The present analysis follows the existing approach [2, 3, 4] with particular emphasis on the effect of precursory cooling in the dry region ahead of the wet front.

For one-dimensional analysis, the slab is treated as a fin with

## Nomenclature

$a$  = exponential power, defined in equation (3),  $(\text{cm})^{-1}$   
 $B$  = Biot number with respect to the heat transfer coefficient, defined in equation (7)  
 $C_p$  = thermal capacitance,  $\text{J}/\text{kg}-^\circ\text{C}$   
 $h$  = surface heat transfer coefficient,  $\text{W}/\text{m}^2-^\circ\text{C}$   
 $h_b$  = average boiling heat transfer coefficient for the sputtering region,  $\text{W}/\text{m}^2-^\circ\text{C}$   
 $I_\nu(\ )$  = modified Bessel function of the first kind, of order  $\nu$   
 $K$  = thermal conductivity,  $\text{W}/\text{m}-^\circ\text{C}$   
 $N$  = dimensionless quantity that characterizes the magnitude of precursory cooling, defined in equation (3)

$P$  = dimensionless wet front velocity, or the Peclet number, defined in equation (6)  
 $T$  = temperature,  $^\circ\text{C}$   
 $T_0$  = wet front temperature that corresponds to the temperature at minimum film boiling heat flux,  $^\circ\text{C}$   
 $T_s$  = saturation temperature,  $^\circ\text{C}$   
 $T_w$  = initial temperature of the dry surface,  $^\circ\text{C}$   
 $u$  = wet front velocity,  $\text{m}/\text{hr}$   
 $Z$  = length coordinate,  $\text{m}$   
 $\alpha$  = dimensionless parameter defined in equation (9)  
 $\beta$  = dimensionless parameter defined in equation (15)  
 $\gamma$  = dimensionless parameter defined

in equation (14)  
 $\delta$  = wall thickness,  $\text{m}$   
 $\eta$  = dimensionless length coordinate,  $Z/\delta$   
 $\theta$  = dimensionless temperature defined in equation (5)  
 $\theta_1$  = dimensionless temperature parameter defined in equation (12)  
 $\rho$  = density,  $\text{Kg}/\text{m}^3$   
 $\psi$  = spray flow rate per unit perimeter,  $\text{gm}/\text{cm}-\text{s}$

## Subscripts

$+$  = evaluated at an infinitesimal increment of distance  
 $-$  = evaluated at an infinitesimal decrement of distance

temperature variation in the longitudinal direction only. Assuming that the wet front travels at a constant velocity, the transient problem becomes quasi-steady by setting the origin of the coordinate system (as shown in Fig. 2(b)) at the wet front. Heat balance considerations based on a differential element of the slab leads to the governing equation [2, 3, 4].

$$K\delta \frac{d^2 T}{dz^2} + \rho c_p u \delta \frac{dT}{dz} = h(T - T_s) \quad (1)$$

For the wet region behind the wet front,  $-\infty < z \leq 0$

$$h = h_b \quad (2)$$

For the dry region ahead of the wet front,  $0 \leq z < \infty$ , an exponential relation is assumed, as

$$h = \frac{h_b}{N} e^{-\alpha z} \quad (3)$$

By incorporating equations (2) and (3), equation (1) can be transformed into dimensionless forms applying to the two different regions. For the wet region,  $-\infty < z \leq 0$ ,

$$\theta''(\eta) + p\theta'(\eta) - B\theta(\eta) = 0 \quad (4)$$

where the dimensionless parameters are defined as

$$\theta(\eta) \equiv \frac{T - T_s}{T_0 - T_s}, \quad \theta'(\eta) \equiv \frac{d\theta}{d\eta}, \quad \eta \equiv \frac{z}{\delta} \quad (5)$$

The dimensionless wet front velocity (i.e., the Peclet number) is

$$p \equiv \frac{u\delta\rho c_p}{K} \quad (6)$$

and the Biot number is

$$B \equiv \frac{h_b \delta}{K} \quad (7)$$

For the dry region,  $0 \leq z < \infty$

$$\theta''(\eta) + p\theta'(\eta) - \frac{B}{N} e^{-\alpha\eta} \theta(\eta) = 0 \quad (8)$$

where

$$\alpha \equiv \alpha\delta \quad (9)$$

The boundary conditions for a long slab are: far downstream, the wall temperature is equal to its initial dry wall temperature; far upstream, the wall is cooled down to saturation temperature; and at the wet front, the wall temperature equals the wetting temperature (i.e., the temperature corresponding to the minimum heat flux in film boiling). The boundary conditions can be expressed in dimensionless form as

$$\theta(-\infty) = 0, \quad \theta(0) = 1 \quad (10)$$

for the wet region,  $-\infty < \eta \leq 0$ , and

$$\theta(0) = 1 \text{ and } \theta(\infty) = 1 + \theta_1 \quad (11)$$

where

$$\theta_1 \equiv \frac{T_w - T_0}{T_0 - T_s} \quad (12)$$

for the dry region,  $0 \leq \eta < \infty$ .

Combining equation (10) with equation (4), the solution of temperature distribution for the wet region,  $-\infty < \eta \leq 0$ , is [4]:

$$\theta(\eta) = \exp\left[-\frac{p\gamma}{2}\eta\right] \quad (13)$$

where

$$\gamma \equiv 1 - \left[1 + \frac{4B}{p^2}\right]^{1/2} \quad (14)$$

To obtain a solution for the dry region with precursory cooling, equation (8) is first transformed by the parameter defined as

$$\beta \equiv e^{-\alpha\eta} \quad (15)$$

By applying equation (15) to equation (8) and noting that

$$\theta'(\eta) = -\alpha\beta\theta'(\beta) \quad (16)$$

where

$$\theta'(\beta) \equiv \frac{d\theta}{d\beta}$$

equations (8) and (11) become

$$\theta''(\beta) + \left(1 - \frac{p}{\alpha}\right) \frac{1}{\beta} \theta'(\beta) - \frac{B}{N\alpha^2} \frac{1}{\beta} \theta(\beta) = 0 \quad (17)$$

and

$$\theta(\beta = 1) = 1 \text{ and } \theta(\beta = 0) = 1 + \theta_1 \quad (18)$$

Through simple mathematical manipulations, it can be shown that the solution for equation (17) involves the Bessel functions [12]:

$$\theta(\beta) = \beta^{\frac{p}{2\alpha}} \left\{ C_1 I_{\frac{p}{\alpha}} \left( \sqrt{\frac{4B\beta}{N\alpha^2}} \right) + C_2 I_{-\frac{p}{\alpha}} \left( \sqrt{\frac{4B\beta}{N\alpha^2}} \right) \right\} \quad (19)$$

where  $I_{p/\alpha}(\cdot)$  is the modified Bessel function of the first kind, of order  $p/\alpha$ .

Inserting the boundary conditions of equation (18) into equation (19), the constants  $C_1$  and  $C_2$  can be evaluated as

$$C_1 = \frac{1}{I_{\frac{p}{\alpha}}(2\phi)} \left\{ 1 - (1 + \theta_1) \Gamma\left(1 - \frac{p}{\alpha}\right) \phi^{\frac{p}{\alpha}} I_{-\frac{p}{\alpha}}(2\phi) \right\} \quad (20)$$

and

$$C_2 = (1 + \theta_1) \Gamma\left(1 - \frac{p}{\alpha}\right) \phi^{\frac{p}{\alpha}} \quad (21)$$

where  $\Gamma(\cdot)$  is the Gamma function and

$$\phi \equiv \sqrt{\frac{B}{N\alpha^2}} \quad (22)$$

With  $C_1$  and  $C_2$  known and the transformation given in equation (15), the temperature profile in the dry region can be obtained in terms of  $\eta$ . Thus, for  $0 \leq \eta < \infty$ ,

$$\theta(\eta) = e^{-\frac{p\eta}{2}} \left\{ C_1 I_{\frac{p}{\alpha}}(2\phi e^{-\frac{\alpha\eta}{2}}) + C_2 I_{-\frac{p}{\alpha}}(2\phi e^{-\frac{\alpha\eta}{2}}) \right\} \quad (23)$$

The condition of heat flux continuity at the origin requires

$$\theta'(0_+) = \theta'(0_-) \quad (24)$$

as given in equations (13) and (23). This results in the following implicit equation for the dimensionless wet front velocity,  $p$ ,

$$\frac{1}{2} = \frac{\alpha}{p\gamma} \left\{ C_1 \left[ \frac{p}{\alpha} I_{\frac{p}{\alpha}}(2\phi) + \phi I_{\frac{p}{\alpha}+1}(2\phi) \right] + C_2 \phi I_{-\frac{p}{\alpha}+1}(2\phi) \right\} \quad (25)$$

It is obvious from equation (25) that a trial and error method is required to solve for  $p$  based on known values of  $B$ ,  $\theta_1$ ,  $N$ , and  $\alpha$ . The Biot number  $B$  can be evaluated with the information of boiling in the sputtering region,  $\theta_1$  is known from the initial wall temperature, and  $N$  and  $\alpha$  are to be determined from the knowledge of precursory cooling.

It is of interest to examine the limiting cases of equation (25). For  $N \rightarrow \infty$ , the heat transfer coefficient ahead of the wet front is essentially zero, and the present model corresponds to the existing models without precursory cooling. Indeed, equation (25) reduces to the simple relation [3, 4]

$$\frac{1}{2} = \lim_{\phi \rightarrow 0} [\text{R.H.S. of equation (25)}] = -\frac{\theta_1}{\gamma} \quad (26)$$

Substituting  $\gamma$  from equation (14), equation (26) becomes

$$\sqrt{\frac{B}{p}} = [\theta_1(\theta_1 + 1)]^{1/2} \quad (27)$$

## Results and Discussions

In the present analysis, there exist two independent dimension-

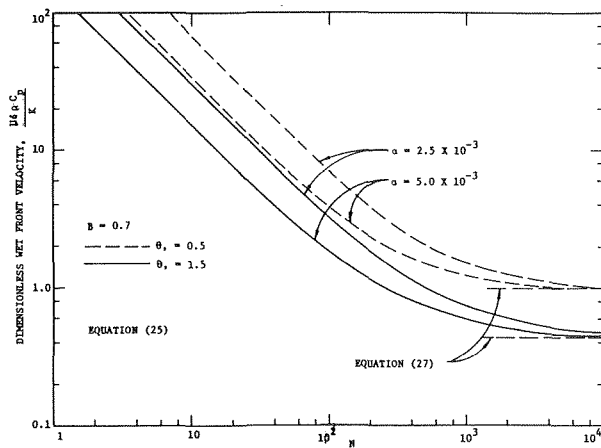


Fig. 3 The variation of dimensionless wet front velocity with  $N$  for parametric values of  $\theta_1$  and  $\alpha$

less parameters  $\theta_1$  and  $B$ , as well as two dimensionless factors  $N$  and  $\alpha$ . The latter two factors characterize the effect of precursory cooling. The parameter  $\theta_1$  characterizes the dry wall temperature far downstream with respect to the temperature at the wet front. The Biot number,  $B$ , characterizes the sputtering boiling heat transfer coefficient and the wall thickness. The factor  $N$  represents the magnitude of precursory cooling relative to the boiling heat transfer coefficient. The parameter  $\alpha$  characterizes the decay of precursory cooling along the dry region.

Fig. 3 represents the variation of dimensionless wet front velocity,  $\rho$ , with  $N$  for parametric values of  $\theta_1$  and  $\alpha$ , and a fixed Biot number. It is shown that the increase of  $\rho$  with decreasing  $\alpha$  and  $N$  for typical cases of  $\theta_1 = 0.5$  and  $1.5$  clearly demonstrates the significant effect of precursory cooling on the wet front velocity. For the limiting case of  $N \rightarrow \infty$ , which means that the magnitude of precursory cooling is insignificant, the wet front velocities approach the limiting values predicted by equation (27).

Fig. 4 depicts the temperature profiles in the vicinity of the wetting front for different values of  $N$ . It is evident that with typical values of  $\theta_1$ ,  $B$ , and  $\alpha$ , the wall temperature ahead of the wet front is lower for larger magnitudes of precursory cooling (i.e.,  $N$  smaller).

While the effect of precursory cooling on falling-film wetting is shown to be significant from the theoretical analysis, it is of interest to obtain information on the region of influence and the magni-

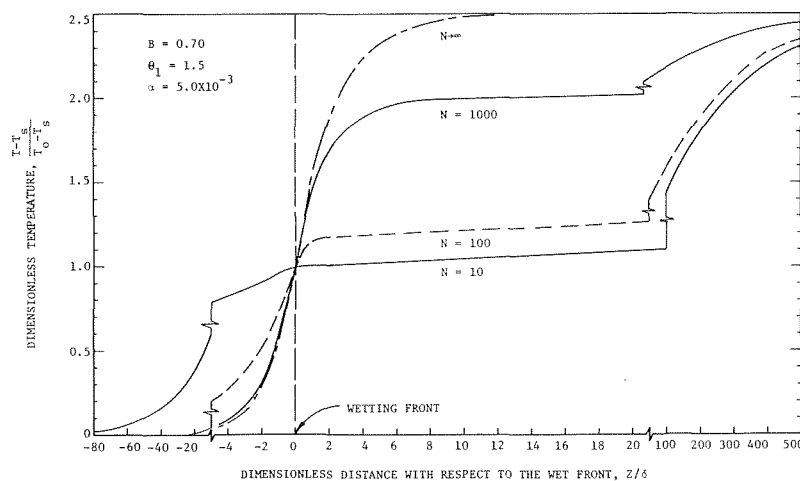


Fig. 4 Temperature profiles in the vicinity of the wetting front for different magnitude of precursory cooling

tude of precursory cooling (i.e.,  $\alpha$  and  $N$ ) from experimental results. Duffey and Porthouse [5] observed from their rod wetting experiment that droplets generated by boiling in the sputtering region were on the order of 0.05–0.1 cm dia. These droplets evaporated in the superheated steam, representing the dominant heat sink for the region of precursory cooling. Larger droplets on the order of 0.2 cm fell under gravity, and hence had relatively little effect on precursory cooling. Since surface geometry exerts little influence on droplet generation in the sputtering region, the region of precursory cooling governed by the smaller droplets (0.05–0.1 cm dia) does not vary appreciably for vertical surfaces of different curvatures. With this assumption, the exponential curve given in Fig. 1 should be generally applicable to characterize the region influenced by precursory cooling. The parameter  $N$  would be expected to be dependent on film flow rate and the geometry that confines the surface. For larger flow rates or smaller confined spaces, the number of droplets in the precursory cooling region increases, resulting in a decrease in  $N$  and stronger precursory cooling.

Comparison of the present analysis with existing data is limited to experiments with water as coolant in atmospheric steam environments. This is due to uncertainties in the wet front temperatures for higher pressures. For water at atmospheric pressure, the wet front temperature,  $T_0$ , which corresponds to the temperature at the minimum film boiling heat flux is about 260°C [4]. The heat transfer coefficient for the sputtering region,  $h_b$ , which represents the average coefficient associated with transition and nucleate boiling, is  $1.7 \times 10^4$  W/m<sup>2</sup> °C ( $3.0 \times 10^3$  Btu/ft<sup>2</sup>·hr°F) [4]. Using these values in equation (27) the low flow rate data of Yamanouchi [3] and Duffey and Porthouse [5] were correlated successfully by Sun, Dix, and Tien [4]. This indicates that, in these low flow rate tests, the effect of precursory cooling was negligible (i.e.,  $N \rightarrow \infty$ ).

Equation (27) could be used to correlate high flow rate data by adjusting the values of  $h_b$ . However, the dependence of  $h_b$  on flow rate is not clearly understood. Also, if  $h_b$  were treated as a variable parameter to correlate Duffey and Porthouse's data [5], the value of  $h_b$  could be as high as  $5 \times 10^6$  W/m<sup>2</sup> °C. This value is unreasonably high for transition and nucleate boiling at atmospheric conditions.

To compare the present model with experimental data, the values of  $T_0$ ,  $h_b$  and the exponential power,  $a$ , are kept constant, a priori with an adjustable  $N$ . Figs. 5, 6, and 7 show good agreement between the prediction and the data of Yamanouchi [3] and Duffey and Porthouse [5]. Despite the scatter of the data, which is typical in the measurement of wet front velocity, it is evident from the successful correlation that the present model is accurate in describing the effect of spray flow rate on falling-film wetting. It should be noted in Figs. 5 and 6 that Duffey and Porthouse's data

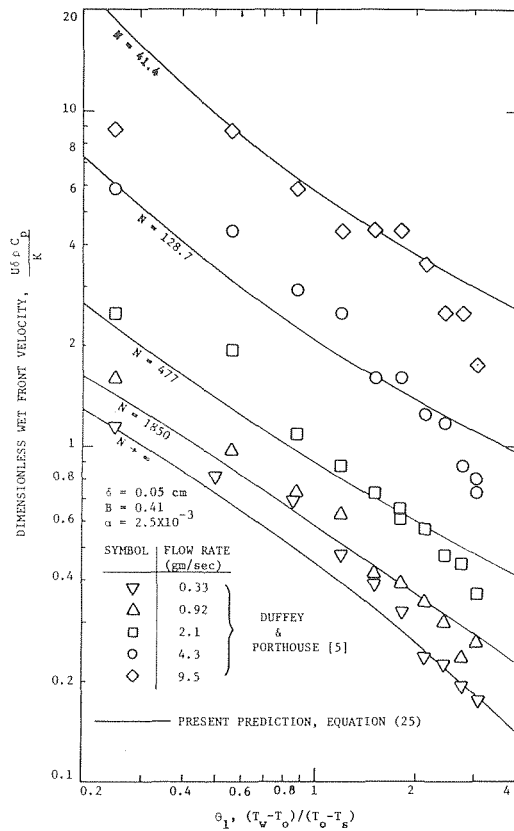


Fig. 5 Comparison of predicted wet front velocity with the experimental results of Duffey and Porthouse [5] (wall thickness 0.05 cm)

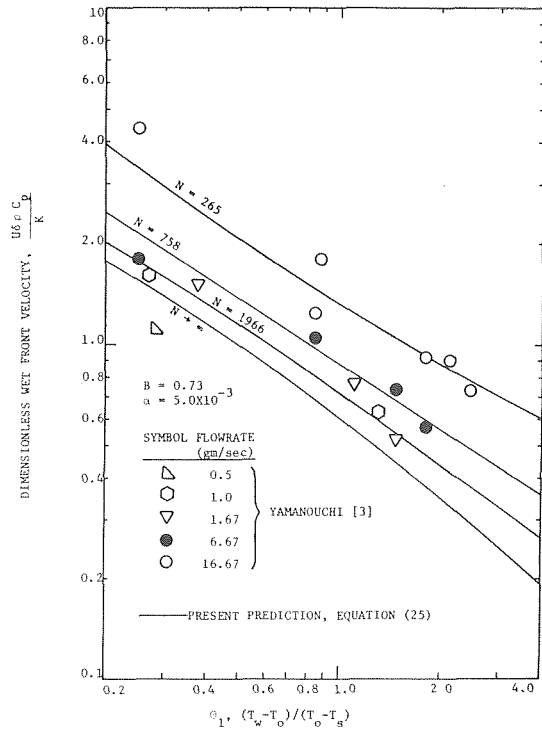


Fig. 7 Comparison of predicted wet front velocity with the experimental data of Yamanouchi [3] (wall thickness 0.10 cm)

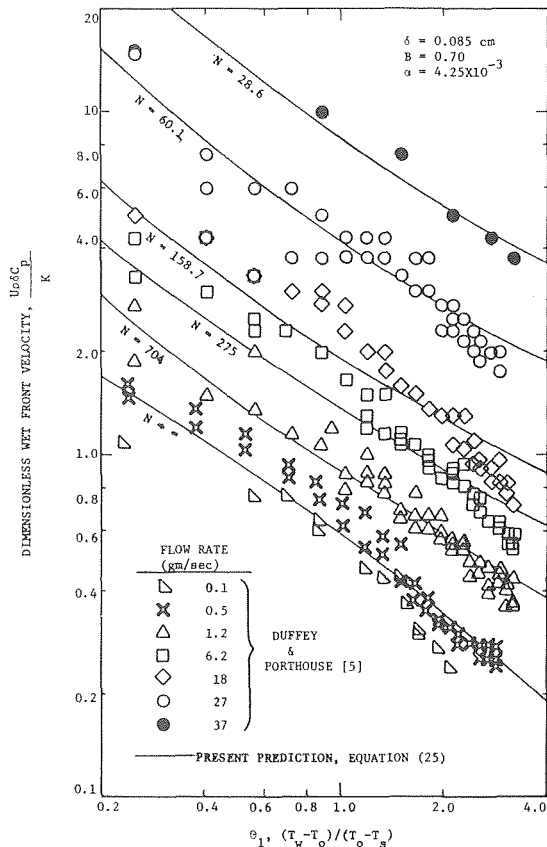


Fig. 6 Comparison of predicted wet front velocity with the experimental results of Duffey and Porthouse [5] (wall thickness 0.085 cm)

with large  $\theta_1$  appear to depart from the predictions. This could be attributed to the short test sections (10 and 18 cm), in comparison to very long surface on which the model is based. The other possible source of error is, of course, that the exponential relation,  $\exp(-0.05Z)$ , could vary with the initial dry wall temperature.

It is of interest to correlate  $N$  with flow rate for the data given in Figs. 5, 6, and 7. Since precursory cooling ahead of the wet front is

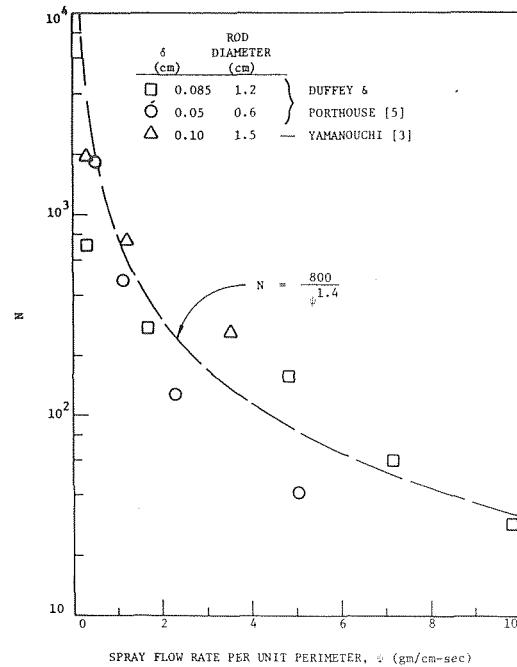


Fig. 8 The variation of  $N$  with spray flow rate per unit perimeter

due to droplets generated in the sputtering region, the variation of heat transfer coefficient with respect to the wet front for a given film flow rate should be insensitive to geometry. Indeed, it is shown in Fig. 8 that the  $N$  values for three test sections with different diameters can be correlated by the following empirical relation

$$N = 800 \psi^{-1.4} \quad (28)$$

where  $\psi$  in gm/cm-s is the spray flow rate per unit perimeter (circumference of rod). The scatter of the data at high flow rate where  $p$  is large is probably due to the effect of two-dimensional conduction. In this regard, it should be emphasized that the above empirical relation is established through comparison between experimental data and the analytical results based on the present one-dimensional model.

### Summary

1 When a liquid film progresses downward on a very hot vertical surface, sputtering occurs in the region right behind the wet front. The droplets generated by sputtering serve as a heat sink for precooling the dry surface ahead of the wet front. This phenomenon can be characterized by two regions: a wet region which consists of the sputtering region and the continuous film region, and a dry region with precursory cooling.

2 The film wetting velocity can increase substantially with precursory cooling ahead of the wet front. Precursory cooling is enhanced at higher film flow rates.

3 Assuming that the average boiling heat transfer coefficient in the sputtering region does not vary with flow rate, existing film wetting data obtained under atmospheric steam environments with variable flow rates can be successfully correlated by taking precursory cooling into account.

### References

- 1 Iloeje, O. C., Plummer, D. N., Griffith, P., and Rohsenow, W. M., "An Investigation of the Collapse and Surface Rewet in Film Boiling in Forced Vertical Flow," ASME Paper No. 73-WA/HT-20, presented at the ASME Winter Annual Meeting, Detroit, Mich., Nov. 1973.
- 2 Semeria, R., and Martinet, B., "Calefaction Spots on a Heating Wall: Temperature Distribution and Resorption," Symposium on Boiling Heat Transfer in Steam-Generating Units and Heat Exchangers, Manchester, England, Sept. 1965.
- 3 Yamanouchi, A., "Effect of Core Spray Cooling in Transient State After Loss-of-Coolant Accident," *Journal of Nuclear Science and Technology*, Vol. 5, 1968, p. 547.
- 4 Sun, K. H., Dix, G. E., and Tien, C. L., "Cooling of a Very Hot Vertical Surface by a Falling Liquid Film," JOURNAL OF HEAT TRANSFER, presented at the ASME Winter Annual Meeting, Detroit, Mich., Nov. 1973, Paper No. 73-WA/HT-22, Vol. 96, May 1974, pp. 126-131.
- 5 Duffey, R. B., and Porthouse, D. T. C., "Experiments on the Cooling of High-Temperature Surfaces by Water Jets and Drops," Report No. RD/B/N2386, Berkeley Nuclear Laboratories, England, Aug. 1972.
- 6 Thompson, T. S., "An Analysis of the Wet-Side Heat Transfer Coefficient During Rewetting of a Hot Dry Patch," *Nuclear Engineering and Design*, Vol. 25, 1972, p. 212.
- 7 Duffey, R. B., and Porthouse, D. T. C., "The Physics of Rewetting in Water Reactor Emergency Core Cooling," *Nuclear Engineering and Design*, Vol. 25, 1973.
- 8 Thompson, T. S., "On the Process of Rewetting a Hot Surface by a Falling Liquid Film," Report AEC L-4516, Chalk River Nuclear Laboratory, Chalk River, Ontario, Canada, June 1973.
- 9 Yoshioka, K., and Hasegawa, S., "A Correlation in Displacement Velocity of Liquid Film Boundary Formed on a Heated Vertical Surface in Emergency Cooling," *Journal of Nuclear Science and Technology*, Vol. 7, Aug., 1970, pp. 418-425.
- 10 Edwards, A. R., and Mather, D. J., "Some UK Studies Related to the Loss of Coolant Accident," *Topical Meeting on Water-Reactor Safety*, USAEC, Conf-730304, Mar. 26-28, 1973, pp. 720-739.
- 11 Tien, C. L., and Yao, L. S., "Two-Dimensional Conduction-Controlled Rewetting of a Vertical Surface," presented at the ASME Winter Annual Meeting, New York, N. Y., November 17-24, 1974, Paper No. 74-WA/HT-49.
- 12 Arpaci, V. S., "Conduction Heat Transfer," Addison-Wesley Publishing Co., 1966.

**A. F. Emery**

Department of Mechanical Engineering,  
University of Washington,  
Seattle, Wash.

**W. W. Dreger**

United Aircraft, Hartford, Conn.

**D. L. Wyche**

The Boeing Co., Seattle, Wash.

**A. Yang**

Department of Mechanical Engineering,  
University of Washington,  
Seattle, Wash.

# Laminar and Turbulent Free Convection Through Vertical Enclosures Filled With Non-Newtonian Fluids

*Heat transfer and fluid flow experiments were made in narrow vertical enclosures of varying aspect ratio ( $5 \leq H/W \leq 40$ ) filled with non-Newtonian fluids whose consistencies ranged from near that of water to several orders of magnitude more. Temperature and velocity profiles were obtained for thermal conditions of low convection augmentation to fully developed turbulent flow. The tests were run over periods of as much as 60 days, during which time the flow index and the consistency of the fluids changed markedly according to their thermal histories. Local hot and cold wall and average enclosure heat transfer rates and wall shear stresses were evaluated. For all the fluids, including the abnormal fluids (those which thickened with increasing temperature) the heat transfer could be correlated by*

$$\text{Nu} = C \text{Ra}^b$$

*although the constant C differed for the two classes of fluids. These correlations were valid over the entire flow regimes studied even in the presence of multiple boundary layers and secondary vortices.*

## Introduction

Although heat transfer by free convection in vertical enclosures has been studied, in the modern sense, since Mull and Reiher [1]<sup>1</sup> in 1930, the first comprehensive understanding of the phenomena was offered by Batchelor [2] in 1954. And for Newtonian fluids, the studies were effectively brought to a conclusion by the exemplary studies of Elder [3, 4].

Similar studies of non-Newtonian fluids are of very recent origin and have not reached the same degree of completion because they suffer from the lack of a unique method of characterizing the fluid properties. Furthermore, because most of the non-Newtonian fluids used to date are optically transparent, circulatory effects have been observed which have not been previously documented

for Newtonian fluids of similar consistencies because most such Newtonian fluids are opaque.

These circulatory aberrations, usually recorded as multivortex patterns and velocity and temperature inversions on single flat plates [5], have created some doubts about the accuracy of the measurements of non-Newtonian free convection effects and raised questions about the existence of similarities between Newtonian and non-Newtonian results. In addition, most non-Newtonian fluids exhibit very marked temperature and aging effects, which are not monotonic with concentration, and which hinder the reduction of the data to universal correlations.

In this paper we wish to describe some experiments conducted with several non-Newtonian power law fluids in closed vertical enclosures for which the laminar and turbulent flows were found to behave very similarly to the Newtonian fluids used by Elder. Temperature and velocity profiles are given and local and overall heat transfer correlations are derived.

These correlations are based upon the observations that the flow in the enclosures resembles two vertical boundary layers, each behaving as though it were on a single vertical flat plate. Acrivos [6] analyzed the asymptotic case of free convection with infinite Prandtl numbers and Tien [7] used an integral technique to study

<sup>1</sup> Numbers in brackets designate References at end of paper.

Contributed by Heat Transfer Division of THE AMERICAN SOCIETY OF MECHANICAL ENGINEERS and presented at the AIChE-ASME Heat Transfer Conference, San Francisco, Calif., August 11-13, 1975. Journal manuscript received at ASME Headquarters June 5, 1975. Paper No. 75-HT-59.

isothermal and constant wall flux cases. Their results for the isothermal plate can be expressed as

$$Nu_H = C(n)(Gr_H^* Pr_H^{*n})^{1/(3n+1)} = C(n) Ra^{*1/(3n+1)}$$

and for the constant wall flux by replacing  $3n + 1$  by  $3n + 2$ . The generalized Grashof and Prandtl numbers are defined by

$$Gr_H^* = \frac{g\beta(T - T_\infty)H^{(2n)/(2-n)}}{(m/\rho)^{(2/2-n)}},$$

$$Pr_H^* = \frac{C_p}{k} \left(\frac{m}{\rho}\right)^{1/(2-n)} H^{(2-2n)/(2-n)}$$

for the isothermal plate and for the constant wall flux by replacing  $T - T_\infty$  by  $qH/k$ . Further attempts to eliminate the length scale from the generalized Prandtl number have not been successful. The inclusion of a length dimension in the Prandtl number emphasizes the difficulties of trying to express non-Newtonian behavior by a Newtonian fluid correlation and suggests that such attempts will be successful only for mildly non-Newtonian fluids. The constant  $C(n)$  is a strongly increasing function of the flow index  $n$  for isothermal plates and a weakly decreasing function for constant wall flux plates.

By using the boundary layer model for the enclosure and extending the Newtonian fluid results, it is possible to derive the correlations

$$Nu_H = C(n) Ra_H^{*1/(3n+1)} \quad \text{Laminar flow}$$

and

$$Nu_H = C(n) Ra_H^{*1/(2n+1)} \quad \text{Turbulent flow}$$

for the enclosure.

**Physical Properties of the Fluids.** The fluids used were aqueous solutions of Carboxymethylcellulose (CMC) of 0.05, 0.1, and 1.0 percent and Carboxypolyethylene (Carbopol) 0.05 and 0.25 percent neutralized and 0.5 and 1.0 percent unneutralized. The solutions were made by slowly dispersing the powder in water and then allowed to stand and age. Fluid densities were measured from 50 to 120°F and found to be greater than that of water, but never by more than 0.5 percent. The thermal conductivities were those reported by Dale [8] in which the 1 percent Carbopol differed by 5 percent from pure water while all other fluids were within 2 percent.

Viscometric measurements were obtained by using a coaxial cylinder viscometer in conjunction with a temperature controlled bath. Figs. 1 and 2 illustrate the variations of the consistency and flow index with temperature for the different fluids. The properties were obtained by measurements over nearly three decades of strain rate with the lowest strain rate about one-fourth of the minimum measured in the inner portion of the boundary layers and the maximum about five times the maximum observed. For all the fluids, the shear stress was found to agree with the power law expression [9],

$$\tau = m \left| \frac{\partial u}{\partial y} \right|^{n-1} \frac{\partial u}{\partial y}$$

to within 2 percent. None of the fluids used in this series of tests were found to have a yield stress although Dale [8] had reported finding one for 0.06 percent Carbopol. The data shown in Figs. 1

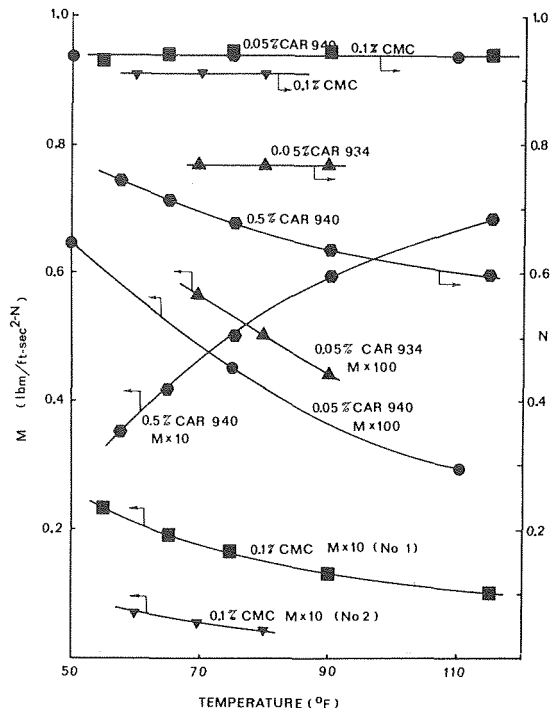


Fig. 1 Viscometric properties of low consistency test fluids

and 2 amply illustrate the fact that the viscometric properties must be measured for each fluid mixed. Although some of the fluids came from different powder batches, the 0.05 percent Carbopol data marked 1 and 2 are from the same powder batch, but mixed at different times, and are seen to have significantly different viscometric properties.

Different from the other fluids, the 1 percent Carbopol 940 was found to be slightly rheopectic at the higher rates of strain and thixotropic at the lower rates. Furthermore, the flow index  $n$  was found to increase smoothly with strain rate, although the use of two different values for low and high strain rates was found to fit the data well. The behavior of this 1 percent Carbopol 940 can be explained by the consistency of the solution, which is about three orders of magnitude greater than 1 percent Carbopol 934. The long chain polymers are very concentrated and the time needed for their alignment is not negligible as it was for the other solutions.

As each fluid was used in the free convection tests, a sample of the unused portion of the fluid was continually viscometrically tested. Fig. 3 illustrates the aging effects and although the consistency is seen to change significantly with time, the flow index is reasonably constant.

**Laminar Heat Transfer Tests.** Vertical enclosures of height to width ratios from 5 to 40 were filled with the fluids and one vertical wall was heated by a constant heat flux and the other cooled by a constant temperature to simulate typical industrial apparatus. Average wall heat fluxes ranged from 80 to 2000 Btu/hr-ft<sup>2</sup>

## Nomenclature

$b$ = slope		
$C_p$ = specific heat		
$g$ = acceleration of gravity	$Nu$ = Nusselt number	$W$ = enclosure width
$Gr$ = Grashof number	$Pr$ = Prandtl number	$x$ = distance along the vertical surface
$H$ = height of enclosure	$q$ = heat flux	$y$ = distance perpendicular to the vertical surface
$k$ = thermal conductivity	$Ra$ = Rayleigh number	$\beta$ = coefficient of thermal expansion
$m$ = consistency	$T$ = temperature	$\rho$ = density
$n$ = flow index	$u$ = velocity along the vertical surface	$\tau$ = shear stress

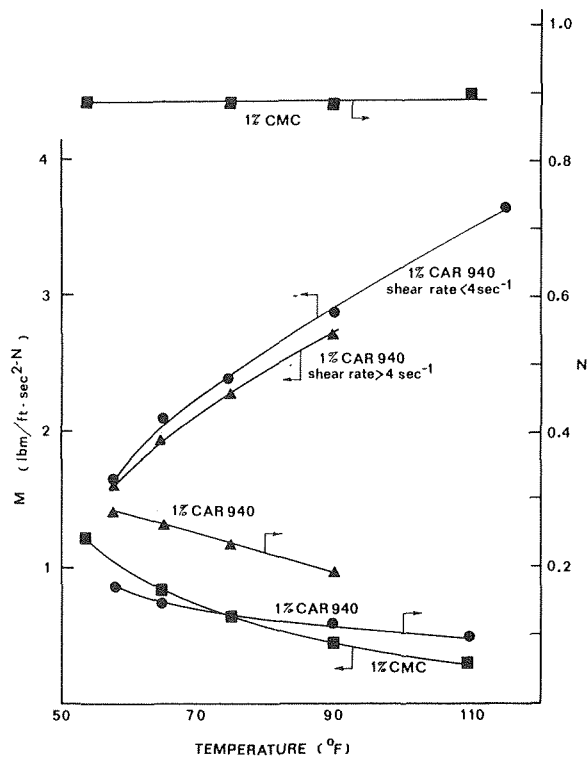


Fig. 2 Viscometric properties of high consistency test fluids

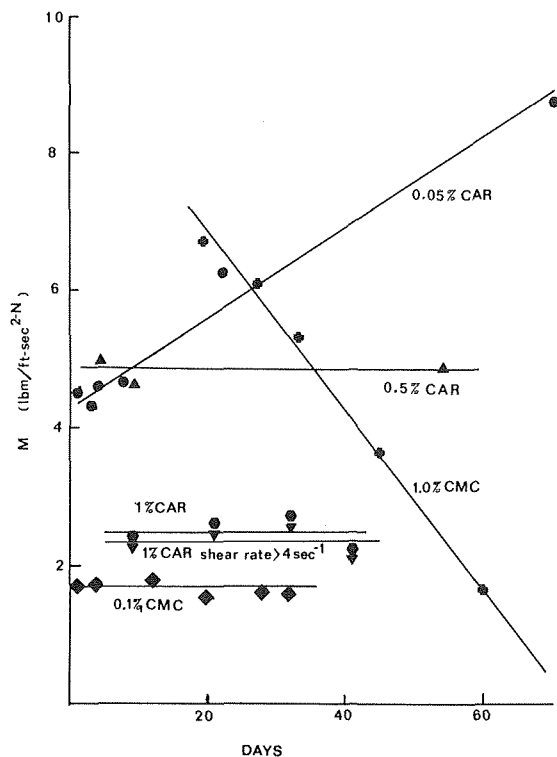


Fig. 3 Effect of aging on viscometric properties

and average temperature differences from 14 to 120°F. Full details of the apparatus are given by Emery [10]. Thermocouples were embedded in each wall and a traversing thermocouple capable of being located anywhere in the enclosure was used to measure the temperature profiles. At low circulation velocities, dye filaments were drawn, either vertically or horizontally, in the enclosure and back lighted. By taking timed multiple pictures, the local velocity profiles were obtained. Because previous studies [10, 11] had difficulties in correlating some of the overall heat transfer results, it was felt necessary to observe the effect of the history of a fluid lamina upon its viscometric properties. To do this, several drops of dye were introduced into the enclosure and their subsequent motion observed. After the dye had delineated the location of a time independent lamina in the boundary layer and another in the core, fluid samples were withdrawn from these lamina and viscometric tests were made for each different hot wall flux experiment. Even though the thermal histories of the two samples were significantly different and different aging effects were expected, no difference in viscometric properties could be detected. Further testing showed that for both normal and abnormal fluids a fluid sample withdrawn from any point in the enclosure was sufficient to characterize the viscometric properties. Apparently, the shear stress-temperature history has no effect upon the viscometric properties except in the sense that the history implies aging of the sample. Further tests were made with several unused samples of 0.05 percent Carbopol. One sample was heated to 110°F and constantly sheared at a rate equal to the minimum strain rate observed in the enclosure, another was heated but not sheared, and a third was not heated or sheared. The virgin sample's consistency increased about 1 percent, the heated and sheared sample's consistency increased by 14 percent, while the unstirred sample increased by 35 percent during a 20-hr period. The fluid in the enclosure experienced a 2 percent rise during the same time. Apparently, the straining reduces the tendency of jells to form under prolonged heating. All of the abnormal fluids showed an increase in consistency with long time heating, and all normal fluids showed a decrease.

Velocity profiles showed that the constant heat flux hot wall boundary layer differed substantially from that on the cold wall and the differences were significantly affected by the consistency of the fluids. All of the flows showed the primary and secondary flow patterns sketched schematically in Fig. 4, where the secondary flow is opposite in direction and generally equal in width to the main boundary layer. However, the maximum reverse flow velocity was rarely more than 5 percent of the maximum velocity in the boundary layer. For the 0.1 percent CMC and 0.05 percent Carbopol solutions, a tertiary flow pattern was found in the enclosure for  $H/W = 10$  at a generalized Rayleigh number of  $Ra_H^* = 8.1 \times 10^8$  and  $2.3 \times 10^9$ , respectively. Elder [3] observed similar tertiary patterns in silicone oil and medicinal paraffin at  $Ra_H^* = 2 \times 10^9$ , finding as many as eight such cells at  $Ra_w = 4.0 \times 10^9$  for  $H/W = 19$ . Possibly the number of these inner core cellular patterns is a

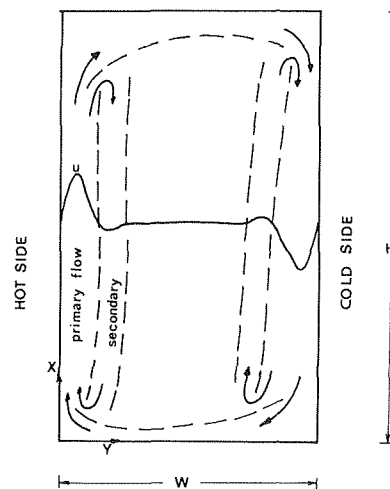


Fig. 4 Schematic of flow in the enclosure

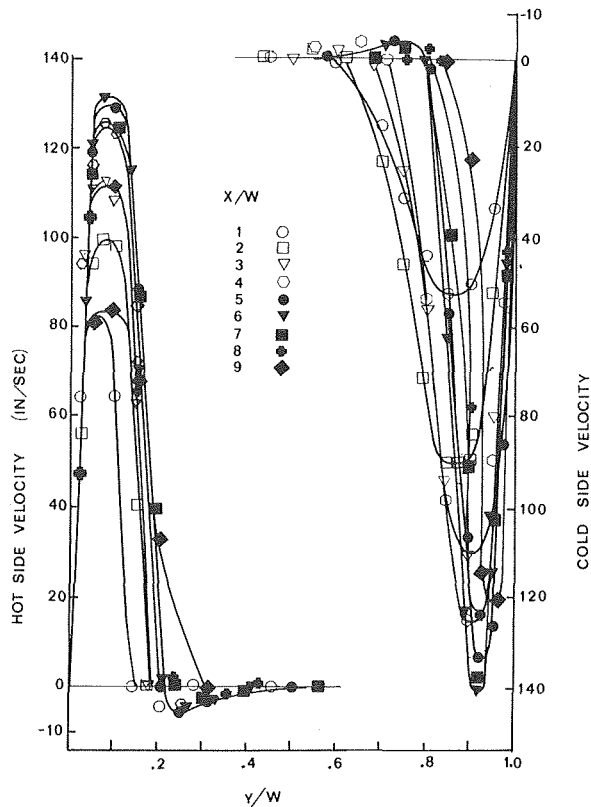


Fig. 5 Velocity profiles in 0.1 percent CMC at  $Gr_H^* = 1.09 \times 10^7$  at  $x/H = 0.5$  for  $H/W = 10.0$

function of the aspect ratio although Elder does not so state. We found none for  $H/W = 5$  and only one regardless of the value of  $Ra_H^*$  for  $H/W = 10$  and it was always located at midheight. At the next higher power setting the tertiary pattern disappeared and a series of small vortices appeared just outside of both the hot and cold boundary layers which soon led to a turbulent flow.

The velocity profiles (Fig. 5) indicated that the maximum velocities in the cold boundary layer were greater than those in the hot boundary layer at corresponding positions for the less viscous fluids, but the opposite occurred for the more viscous fluids. Since increasing consistency is generally coupled with decreasing flow

index, it is not presently known which is the cause of this effect. In all cases the wall shear stresses and the wall shear strain rates on the hot wall were found to be constant, to within 10 percent, over that portion of the hot wall which was more than two enclosure widths from the ends of the enclosure area even though the peak boundary layer velocity had a maximum near the midheight which was twice the value at  $x/W = 2$ . Although the cold boundary peak velocity behaved similarly, the wall shear stress and shear strain rate were found to decrease as the fluid moved down the wall until the cold fluid began turning to cross the enclosure. In general, the cold boundary layers behaved as though they were on a single flat plate while the hot wall boundary layers tended to be of constant thickness as indicated in Fig. 5. Some of the thinning is due to the constant wall flux on the hot wall, but most is apparently due to the reverse secondary flow. Similar effects have been noted by Wilson [5] on a single flat plate for heat fluxes sufficiently low that the hot wall was essentially isothermal.

Temperature profiles were taken and the thermal inversion noted by others [5, 8, 10, 11, 12] and clarified by Elder, was also found. As in the experiments for the Newtonian fluids, the centerline temperature gradient

$$\frac{d}{dx} \left( \frac{T - T_c}{T_H - T_c} \right)$$

was found to be a constant for the different fluids and different enclosure aspect ratios over most of the enclosure height. The net heat transfer was correlated according to the  $Nu_H = C Ra_H^{*b}$  and is shown in Fig. 6. Those fluids which thin upon heating have a higher net heat transfer performance than do fluids which thicken upon heating. Part of the explanation for the reduced heat transfer lies in this abnormal behavior. The increase in consistency with increasing temperature reduces the hot boundary layer velocity, causing a further increase in temperature, and the process continues until an equilibrium circulation is established with velocities close to those associated with Rayleigh numbers evaluated near  $T_H$ . Furthermore, for the abnormal fluids used here the temperature effect is more pronounced at lower strain rates, thus aggravating the situation. On the cold side, the opposite tendency takes place, but since the effect of temperature upon the consistency was less at high shear strain rates, the abnormal fluid effects were minimized. As a consequence, at the same vertical distance from the leading edge of the boundary layer and the same value of  $Ra_H^*$ , the abnormal hot velocities were 20 percent lower and the cold 2 percent higher than the normal fluid velocities.

Table 1 lists the values of the constants  $C$  and the slopes  $b$  for the different fluids obtained by a linear regression analysis at 95

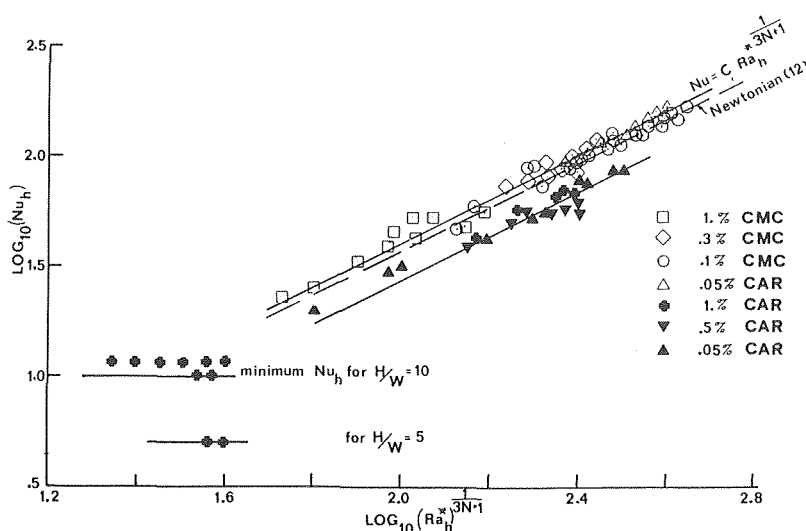


Fig. 6 Laminar heat transfer coefficients for non-Newtonian and Newtonian fluids

Table 1 Laminar heat transfer correlations

	$n$	$Pr_n^*$	$C(\text{exper-} \\ \text{imental}) \\ \text{for } b = \\ 3n + 1$	$b(\text{exper-} \\ \text{imental}) \\ 3n + 1$
Normal fluids	0.75–0.96	20.–8000.	0.396	0.955
Abnormal fluids	0.1–0.7	140.–240,000.	0.269	0.923

percent confidence. The 0.05 percent Carbopol behaved as a normal fluid in the first test, but upon mixing a new solution for the second test it behaved as an abnormal fluid as indicated in Fig. 6.

The net heat transfer for all the fluids for all enclosure aspect ratios, is well correlated by this simple expression when the flow is laminar and these correlations appear to be reasonably insensitive to the different aspect ratios, unless of course the fluid state is near that of conduction as indicated in Fig. 6.

Attempts to substantiate the effect of our hypothesis for the abnormal fluid by modifying the temperature at which the  $Ra_H^*$  was evaluated were not successful. Using the measured temperature profiles, values of  $Ra_H^*$  were computed separately for the hot and the cold boundary layers and for the entire enclosure and were found to agree to within 1 percent. The effect of the increased consistency of the hot boundary layer was compensated for by the increased temperature drop found across this layer thus giving an invariant  $Ra_H^*$ . It does not appear possible at this time to define a temperature at which a property evaluation would reconcile the normal and abnormal fluid results and we conclude that the constants  $C(n)$  are different for the two classes of fluids. Fig. 6 also

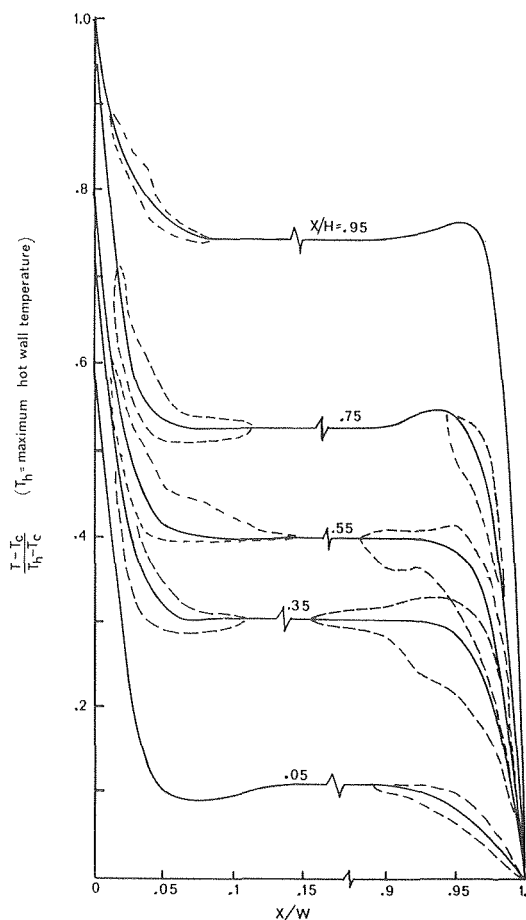


Fig. 7 Turbulent temperature profiles in 0.05 percent Carbopol for  $H/W = 10$ , at  $Ra_H^* = 1.36 \times 10^{10}$

shows the results obtained in the same cell with  $H/W = 10$  for a number of Newtonian fluids [12].

**Turbulent Heat Transfer.** Complete turbulent tests were made only for the less viscous fluids since it proved impossible to create a fully turbulent enclosure flow without inducing boiling or creating such thick gel layers that the enclosure was completely choked with the more viscous fluids. Unfortunately, this eliminated all of the abnormal fluids from our tests and in general implies that turbulent heat transfer can be achieved only with very near Newtonian fluids. Average heat fluxes were from 600 to 4300 Btu/hr-ft<sup>2</sup> and average temperature differences from 23 to 90°F.

No velocity profiles were measured for the turbulent flow, but the long chain molecules in concert with a shadowgraph system did permit the determination of the onset of turbulence and the point at which fully developed turbulence existed. Fully developed turbulence was characterized by intense interaction between the fluid near the wall and that of the interior. The wall waves which had been sinuous in form were totally destroyed by this intense action and no regular motion was detectable. For the 0.05 and 0.04 percent Carbopol ( $m = 6$  and  $2 \times 10^{-3}$ ), the onsets were at  $Ra_H^*$  of  $1.8 \times 10^9$  and  $2 \times 10^9$ , respectively. This compares reasonably well with Elder's estimate of  $1.3 \times 10^9$  for water. Since the respective Prandtl numbers were 200 and 60 as compared to 5 for water it appears that the onset of turbulence is independent of Pr and of the non-Newtonian fluid behavior.

Fig. 7 shows typical temperature profiles taken at various elevations in the enclosure. The two distinct boundary layers are readily apparent and the absence of the thermal inversion in the turbulent portion of the enclosure is easily seen. Shadowgraph observations of the core showed it to be quiescent with the only motion being that of several large particles which would rise to midchannel height at the edge of the hot boundary layer and then sink upon termination of the heating. None of the wave fronts, which were easily observed in both boundary layers, were ever seen to propagate into the core. The dashed lines indicate the extremes of the temperature fluctuations due to turbulence. The laminar sublayer remained approximately constant in width. Similarly, the fluctuations were damped out in the core and the width of the fluctuating region is seen to increase quickly as the fluid flows along the vertical walls but it soon becomes quite constant over most of the enclosure height. Even when the fluid was fully turbulent, the thermal inversions illustrated on Fig. 7 were always readily apparent at the leading edge of both boundary layers.

Attempts were made to correlate the net and local heat transfer results using the overall enclosure temperature differences and properties based upon the average enclosure temperature or upon a weighting of the hot and cold boundary layer temperatures in the form

$$Nu_H = C Ra_H^{*1/2n+1} = C Ra_H^{*b}$$

which is based upon the standard turbulent free convection Newtonian correlation of  $1/3$ , but no correlations were possible. Local heat transfer coefficients were measured and except in the end regions were found to be reasonably constant as Elder [3] and others [13] have reported for Newtonian fluids. Correlations were then made by evaluating a local generalized Rayleigh number based upon the local measured temperature difference across the boundary layer, and the properties evaluated at the local average boundary layer temperature and the results are shown in Fig. 8. Also shown is the correlation for turbulent data of Newtonian fluids taken in the same cell. Neither local nor average measurements were able to explain the increased non-Newtonian heat transfer when compared to the Newtonian data. Table 2 lists values of the constant  $C$  and the slope  $b$  for the individual boundary layers and for the combined data; similar values are reported for some Newtonian fluids and the general agreement between the Newtonian and non-Newtonian values is good. For the different wall heat fluxes, the value of  $Ra_H^*$  based upon the average enclosure properties and

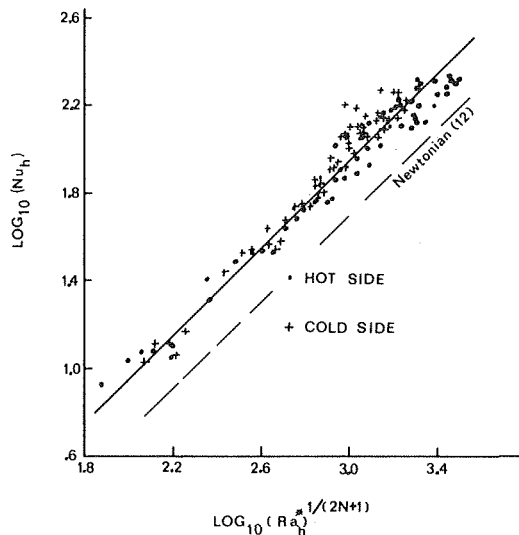


Fig. 8 Local turbulent heat transfer coefficients for 0.05 and 0.04 percent Carbopol as compared to average Newtonian data (Reference [12])

Table 2 Turbulent heat transfer correlation

	$n$	$Pr_H^*$	$C(\text{experimental})$ for $b =$ $2n + 1$	$b(\text{experimental})$ $2n + 1$
Hot boundary layer	0.9–0.95	12–23	0.083	0.935
Cold boundary layer	0.9–0.95	18–27	0.096	1.088
Combined data	0.9–0.95	13–26	0.089	0.981

the overall temperature difference was compared to the local values measured along the vertical surfaces and this average value was found to be less than 25 percent of the average surface value in turbulent flow, whereas it was equal to the average for the laminar flow. Consequently, the turbulent net heat transfer cannot be correlated by using values of  $Ra_H^*$  based upon the average enclosure properties.

Fluctuation measurements in the cold and hot boundary layers were also made to determine the power spectrum of the turbulent temperature. Although the magnitudes were considerably different from the values reported by Elder, the shape of the curve was very similar, indicating that there is no substantial difference between

the turbulent characteristics of Newtonian and non-Newtonian fluids.

## Summary

The qualitative agreement between the Newtonian and the non-Newtonian fluid evidenced by their local velocity and temperature profiles, turbulent power spectra and local and overall heat transfer reveals that for both the laminar and turbulent flow of power law fluid, available Newtonian heat transfer correlations can be used to predict the non-Newtonian fluid behavior. However, the sparsity of turbulent non-Newtonian data leaves the specification of the onset of turbulence in doubt.

## Acknowledgments

A portion of the results presented here was obtained under the sponsorship of the National Science Foundation through Grant GK-567.

## References

- Mull, W., and Reiher, H., "Der Waermeschutz von Luftschichten," *Beihefte zum Gesundheits-Ingenieur*, Reihe 1, No. 28, 1930, p. 126.
- Batchelor, G. K., "Heat Transfer by Free Convection Across a Closed Cavity Between Vertical Boundaries at Different Temperatures," *Quarterly of Applied Mathematics*, Vol. 12, 1954, pp. 209–233.
- Elder, J. W., "Laminar Free Convection in a Vertical Slot," *Journal of Fluid Mechanics*, Vol. 23, Part 1, 1965, pp. 77–98.
- Elder, J. W., "Turbulent Free Convection in a Vertical Slot," *Journal of Fluid Mechanics*, Vol. 23, Part 1, 1965, pp. 99–110.
- Wilson, J. R., "An Investigation of the Vortex Motion in the Free Convection Flow Field of Fluids About a Vertical Flat Plate," MS thesis, University of Washington, Seattle, Wash., 1973.
- Acrivios, A., "A Theoretical Analysis of Laminar Natural Convection Heat Transfer to Non-Newtonian Fluids," *AIChE Journal*, Vol. 6, 1960, pp. 585–590.
- Tien, C., "Laminar Natural Convection Heat Transfer from Vertical Plate to Power Law Fluid," *App. Sci. Res.* Vol. A-17 1967, p. 233.
- Dale, J. D., and Emery, A. F., "The Free Convection of Heat From a Vertical Plate to Several Non-Newtonian 'Pseudo-Plastic' Fluids," *JOURNAL OF HEAT TRANSFER TRANS. ASME*, Series C, Vol. 94, Feb. 1972, pp. 64–73.
- Skelland, A. H. P., *Non-Newtonian Flow and Heat Transfer*, Wiley, New York, 1967.
- Emery, A. F., Chi, H. I. T., and Dale, J. D., "Free Convection Through Vertical Plane Layers of Non-Newtonian Power Law Fluids," *JOURNAL OF HEAT TRANSFER, TRANS. ASME*, Series C, Vol. 93, May 1971, pp. 164–172.
- Dreger, W. W., "The Natural Convection of Non-Newtonian Fluids in Rectangular Vertical Enclosures," MS thesis, University of Washington, Seattle, Wash., 1971.
- MacGregor, R. K., and Emery, A. F., "Free Convection Through Vertical Plane Layers of Moderate and High Prandtl Number Fluids," *JOURNAL OF HEAT TRANSFER, TRANS. ASME*, Series C, Vol. 91, Aug. 1969, pp. 371–401.
- Jakob, M., *Heat Transfer*, Wiley, New York, Vol. I, 1949.

J. C. Dutton

Graduate Research Assistant.

J. R. Welty

Professor and Head, Mem. ASME

Department of Mechanical Engineering,  
Oregon State University,  
Corvallis, Oregon

# An Experimental Study of Low Prandtl Number Natural Convection in an Array of Uniformly Heated Vertical Cylinders

*An experimental program was conducted to study natural convection heat transfer in an array of uniformly heated vertical cylinders in mercury. The cylinders were arranged in an equilateral triangular pattern, and three bundle spacings,  $P/D = 1.5, 1.3,$  and  $1.1,$  were studied. The heat transfer results are presented as local Nusselt number—modified Grashof number correlations. The results indicate a strong dependence on cylinder spacing and the somewhat lesser effects of heat flux and circumferential position. In addition, mean radial temperature profiles were recorded for various conditions as well as the fluctuations in the fluid temperatures which were encountered. The influence of cylinder spacing and axial, radial, and circumferential position on these profiles and disturbances is discussed.*

## Introduction

The topic of natural convection in low Prandtl number fluids has received considerable attention in recent years as liquid metal-cooling is finding increasing applications. Because of its relative simplicity, the geometry which has been most widely studied is the vertical flat plate. Sparrow and Gregg [10]<sup>1</sup> extended the similarity solutions for the isothermal vertical surface to Prandtl numbers in the liquid metal range. Later, Sparrow and Guinle [11] studied the effects of transverse pressure gradient and streamwise second derivatives for the isothermal case at low Prandtl numbers. Chang, et al. [1] performed a perturbation analysis for the uniform heat flux condition and obtained results for Prandtl numbers of 0.03 and 0.1. An experimental investigation of the constant heat flux surface in mercury was carried out by Julian and Akins [5]. Their results were in agreement with the previous analytical work.

Other vertical geometries have also been studied for natural convection in the low Prandtl number range. Nagendra, et al. [7] utilized a local similarity technique to study the uniformly heated vertical cylinder. Numerical solutions for Prandtl numbers 0.01, 0.1, 0.733, and 5 were computed. Wiles and Welty [12] carried out experiments in mercury for the same situation. Their results dif-

fered significantly from the analysis of Nagendra. The vertical parallel plate channel has also been studied. Quintiere and Mueller [8] analyzed this situation for various boundary conditions by linearizing the governing equations and then integrating them with the aid of Laplace transforms. Solutions were presented for  $Pr = 0.01, 0.7,$  and  $10.$  Colwell and Welty [2] experimentally investigated the uniformly heated channel in mercury for the two cases of: (1) symmetric heating on the two walls and (2) one wall heated and the other insulated. For the low Grashof number range they obtained much higher Nusselt numbers than those predicted by the analysis of Quintiere and Mueller [8]. Their results also indicate the existence of an optimum plate spacing for which the channel is most thermally efficient.

Another geometry of practical importance, especially in relation to nuclear reactors, is the vertical rod bundle. However, very little work has been done for natural convection in this specialized geometry, and none for low Prandtl number fluids. Davis and Perona [3] analytically and experimentally investigated the development of free convection flow through a tube bundle with equilateral triangular spacing. The numerical solution implicitly assumed circumferential symmetry and results were obtained for  $Pr = 0.7.$  The experiments were carried out in air, and the heat transfer results agreed fairly well with the analysis, although the flow rate measurements did not. This configuration is also the one investigated here, with the imposed boundary condition being that of symmetric and uniform heating of the rods. Although presentation of the results of this study in the form used by Davis and Perona [3] would be convenient for purposes of comparison, it was not

<sup>1</sup> Numbers in brackets designate References at end of paper.

Contributed by the Heat Transfer Division for publication in the *Journal of Heat Transfer*. Manuscript received by the Heat Transfer Division February 10, 1975. Paper No. 75-HT-AAA.

possible since they correlated their heat transfer results with a modified Graetz number which requires knowledge of inlet velocity conditions.

### Experimental Apparatus

A view of the test section and coordinate definitions used in this investigation are shown in Fig. 1. As shown, the flow channels in the rod bundle geometry with equilateral triangular spacing are characterized by irregularly shaped symmetry units which repeat every 30 deg around the circumference of a rod. All measurements reported here were obtained in two such units adjacent to the center cylinder of the bundle (as shown in Fig. 1).

The test section consisted of seven heated cylinders with 1.365 in. (0.0347 m) mean OD and 3.825 in. (0.0972 m) heated length. A cylindrical acrylic enclosure was placed around the seven pin bundle for each spacing tested. The purpose of this enclosure was to prevent side leakage and entrainment of cool mercury from the region adjacent to the test section. Half cylinders were attached to the inside surface of the enclosure in positions corresponding to the next layer of rods in an infinite bundle. Although these acrylic half cylinders were unheated, and hence did not add to the thermal symmetry of the test section, their presence did help to maintain the flow characteristics of an infinite array. In addition, a number of rectangular slots were cut around the upper periphery of the tube to allow mercury heated in the test section to circulate freely to the ambient pool.

Data were obtained in the region adjacent to the center cylinder, which was surrounded by the six neighboring heated cylinders as shown in Fig. 1. Additional layers of heated cylinders outside those employed in this work are believed to influence conditions in the region close to the central cylinder a negligible amount, particularly with the relatively tight spacings used. Additionally, from radial temperature profiles (both those presented here and in [4]), it may be seen that radial gradients vanish at the outer edges of the units of symmetry—further suggesting that the test section adequately models an infinite array.

The heated cylinders were constructed by attaching an electrical heating unit to a core machined from acrylic rod. The heater elements consisted of a chemically etched 0.001 in. ( $2.54 \times 10^{-5}$  m) thick nichrome foil bonded on both sides to fiberglass-reinforced silicone rubber insulation. The heater units were placed on the lower section of the 10 in. (0.254 m) long cores and wrapped tightly with two-sided mylar tape to hold them to the cores. Cylindrical

steel cover plates ( $2.54 \times 10^{-4}$  m thickness), exactly the size of the heaters, were then pressed onto the tape by means of a tightening jig. The finished diameter of the heated sections closely matched that of the upper section of the acrylic cores.

The 3.825 in. (0.0972 m) heated length of the completed cylinders resulted in maximum local modified Graetz numbers on the order of  $Gr_x^* = 10^{10}$ . This spanned the laminar range which was the regime of interest. The 10 in. (0.254 m) total length placed the heated sections approximately midway between the bottom of the mercury tank and the upper free mercury surface, in order to minimize the effects of these surfaces.

The combined area of the flow slots exceeded, in all cases, the total flow area in the test section. Thus, the unheated upper portion of the test section is believed to have negligible effect on the results obtained in the lower, heated region.

Temperatures were measured by means of a specially-shaped thermocouple probe frame. A length of 0.012 in. ( $3.05 \times 10^{-4}$  m) dia support wire was stretched across the open side of the frame and a subminiature thermocouple was attached to this support wire. Near the thermocouple junction a gradual 90 deg bend was made so that the junction projected approximately 0.080 in. ( $2.03 \times 10^{-3}$  m) from the wire. The thermocouple consisted of 0.001 in. ( $2.54 \times 10^{-5}$  m) dia iron and constantan wires contained inside a 0.010 in. ( $2.54 \times 10^{-4}$  m) dia stainless steel sheath and insulated from the sheath and each other by means of a refractory material. The iron and constantan wires were brought together in a ground-heat weld bead at the probe tip. The extremely small size of the resulting junction allowed essentially point temperatures to be recorded.

The thermocouple probe was fastened to an  $x$ - $y$  positioning mechanism which, in turn, was clamped to a table which rotated about the axis of the central cylinder of the bundle. The combination of the rotating table and the traversing mechanism provided the axial, radial, and circumferential probe movements necessary to completely characterize the three-dimensional temperature field of this geometry. Surface temperatures,  $T_0$ , were measured by positioning the probe at the desired axial and circumferential positions and then moving it radially inward until it contacted the heater surface. Vernier scales on the positioning device allowed axial and radial probe locations to be determined to within  $\pm 0.001$  in. ( $\pm 2.54 \times 10^{-5}$  m); the addition of a dial gauge improved the radial positioning tolerance to  $\pm 0.0001$  in. ( $\pm 2.54 \times 10^{-6}$  m).

The mercury was contained in a  $12 \times 12 \times 16$  in. ( $0.305 \times 0.305$

### Nomenclature

$C$ = dimensionless coefficient in heat transfer correlations	$L$ = heated length	
$c_p$ = specific heat	$n$ = exponent in heat transfer correlations	
$D$ = cylinder diameter	$Nu_x$ = local Nusselt number = $\frac{hx}{k}$	from leading edge
$F'$ = dimensionless flow rate, Davis and Perona [3]	$\overline{Nu}_L$ = average Nusselt number = $\frac{\bar{h}L}{k}$	$y$ = radial coordinate measured from cylinder surface
$f(\theta)$ = circumferential correction factor in heat transfer correlations for $P/D = 1.1$	$P$ = pitch, center-to-center distance between cylinders in the bundles	$y/r_0$ = dimensionless radial coordinate
$g$ = acceleration of gravity	$P/D$ = pitch-to-diameter ratio	$\alpha$ = thermal diffusivity = $\frac{k}{\rho c_p}$
$Gr_x$ = local Graetz number	$Pr$ = Prandtl number = $\frac{c_p \mu}{k} = \frac{\nu}{\alpha}$	$\beta$ = coefficient of thermal expansion
$= \frac{g\beta x^3(T_0 - T_\infty)}{\nu^2}$	$q$ = surface heat flux	$\theta$ = circumferential angle
$Gr_x^*$ = local modified Graetz number	$r$ = radial coordinate measured from cylinder axis	$\mu$ = absolute viscosity
$= \frac{g\beta q x^4}{k\nu^2}$	$r_0$ = cylinder radius	$\nu$ = momentum diffusivity = $\frac{\mu}{\rho}$
$Gr_L^*$ = modified Graetz number based on length = $\frac{g\beta q L^4}{k\nu^2}$	$R^2$ = statistical correlation coefficient	$\rho$ = density
$h, \bar{h}$ = local and average heat transfer coefficients	$T$ = temperature	<b>Subscripts</b>
$k$ = thermal conductivity	$\frac{T - T_\infty}{T_0 - T_\infty}$ = dimensionless temperature	$\infty$ = ambient
	$x$ = axial coordinate measured	$0$ = surface
		$x$ = based on distance from leading edge
		$L$ = based on heated length

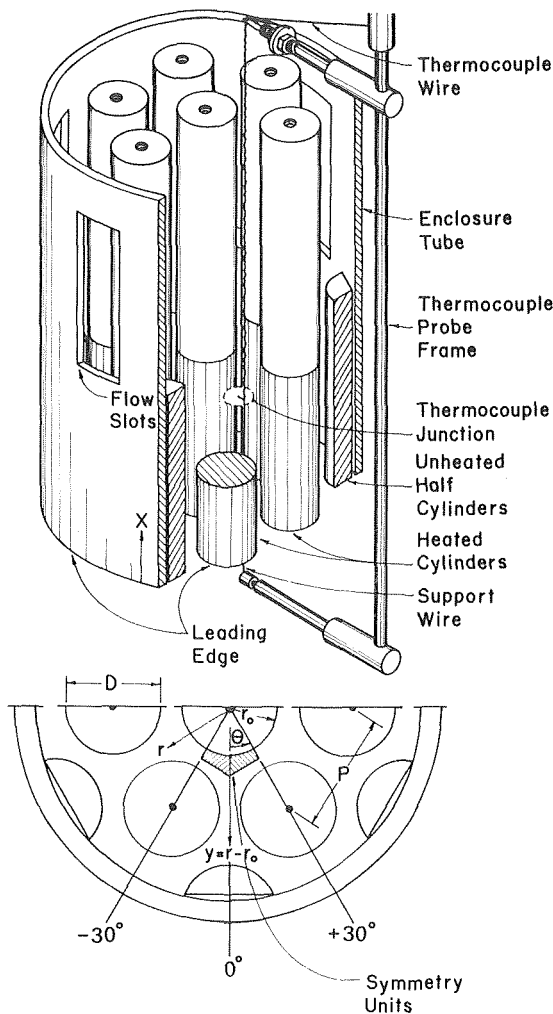


Fig. 1 Test section and coordinate axis definitions

× 0.406 m) deep stainless steel tank. This tank was surrounded by a sheet metal water bath box and outside of this was a plywood box filled with vermiculite insulation. Cooling coils were placed in the water bath to remove the heat generated in the test section. A 1 kW controller-stirrer and two auxiliary stirrers aided in maintaining the bath at a constant temperature. With this thermal control equipment, the ambient mercury temperature, which was measured approximately 2 in. (0.0508 m) below the leading edge of the test section, was typically maintained at a steady temperature to within  $\pm 0.05^\circ\text{F}$  ( $\pm 0.028^\circ\text{K}$ ).

Power was supplied to the heated cylinders with a 10.5 kW regulated d-c power supply. Since the heaters were closely matched in resistance a simple parallel wiring circuit worked well for obtaining equal heat fluxes on each of the seven heated rods. For all cases the power dissipated by the individual cylinders varied by less than  $\pm 0.8$  percent.

### Procedure

Three basic types of data were recorded: heat transfer, mean radial temperature profiles, and temperature fluctuations. For the heat transfer results, the specification of the local Nusselt and modified Grashof numbers required the measurement of: the heat flux,  $q$ , which was accomplished electrically; the axial distance from the leading edge,  $x$ ; and the surface and ambient temperatures,  $T_0$  and  $T_\infty$ . The fluid properties were evaluated at the mean film temperature,  $0.5[T_0(x) + T_\infty]$ , using the expressions suggested by Sparrow and Gregg [9] for mercury.

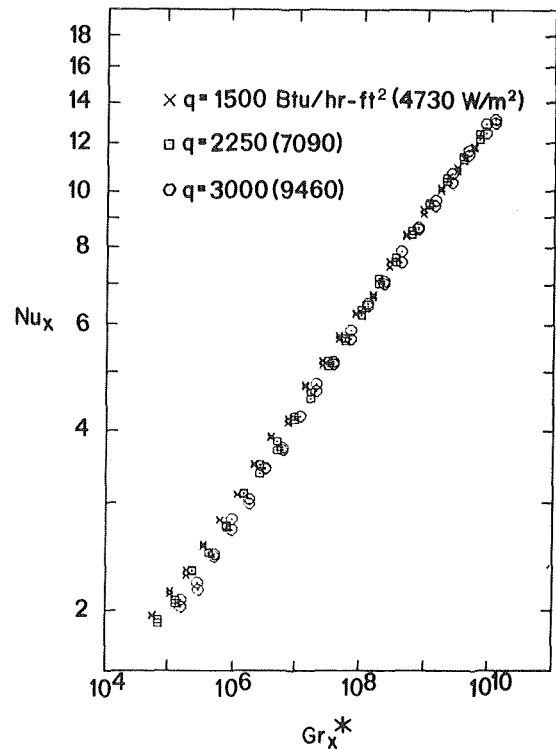


Fig. 2 Local heat transfer results for  $P/D = 1.5$ , 0 deg circumferential position

The mean radial profiles were obtained by recording the fluid temperatures at various axial and circumferential locations extending from the cylinder wall to the outer edge of the symmetry unit. The time-averaging technique involved finding the mean of the thermocouple output readings recorded at 5 s intervals for a period of 180 s. Since the fluctuations were of relatively low frequency, this method was adequate.

Recordings of the temperature disturbances were obtained with a strip chart thermocouple plotter. The disturbance plots were generally taken at six radial locations for a given profile for periods of 150 s each.

Further information concerning the equipment and procedure may be found in [4].

### Heat Transfer Results

The data were gathered for three rod bundle spacings:  $P/D = 1.5$ , 1.3, and 1.1 where  $P/D$  is the array pitch-to-diameter ratio. The lowest value tested is typical of the fuel rod spacing proposed for the liquid metal-cooled fast breeder reactors although the diameter of the fuel rods is much smaller ( $6.35 \times 10^{-3}$ – $1.27 \times 10^{-2}$  m) than the diameter of the cylinders used in this investigation.

The heat transfer results for the three arrays at the 0 deg circumferential position are presented in Figs. 2, 3, and 4. One observation of interest is that for a given array, there is a perceptible separation of the  $Nu_x - Gr_x^*$  results according to heat flux level, indicating that there is another parameter besides these two of importance for this situation. This result was not entirely unexpected as the tube bundle heat transfer results of Davis and Perona [3] for air also show a parametric dependence on a dimensionless flow rate  $F'$ , for a given  $P/D$ . The large Grashof number behavior for  $P/D = 1.1$  (Fig. 4) is that portrayed by the numerical results of Davis and Perona. For large axial distances from the leading edge, as the Nusselt number approaches its fully-developed asymptotic value, their heat transfer results are also higher for higher heat fluxes (low  $F'$ ).

Over the Grashof number range studied, the maximum devia-

tion between the correlations for the various heat fluxes used for each bundle were found to be 12 percent for  $P/D = 1.5$ , 10.4 percent for  $P/D = 1.3$ , and 9.9 percent for  $P/D = 1.1$ . Therefore the effect of heating rate is not extreme and, without losing much gen-

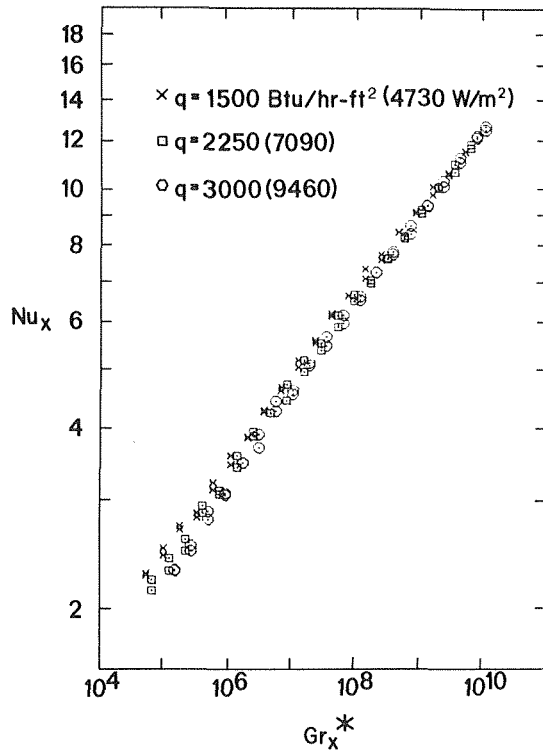


Fig. 3 Local heat transfer results for  $P/D = 1.3$ , 0 deg circumferential position

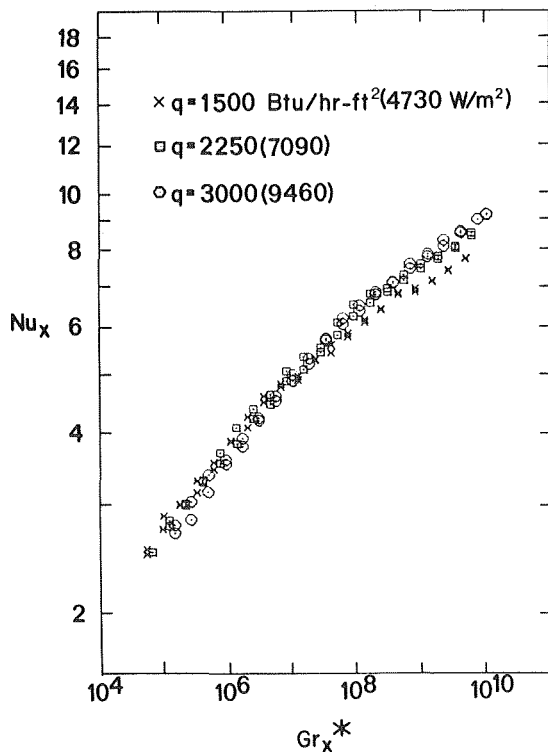


Fig. 4 Local heat transfer results for  $P/D = 1.1$ , 0 deg circumferential position

erality, heat flux-averaged correlations for the data in Figs. 2-4 may be developed. The resulting least squares equations are given in the following and are plotted in Fig. 5 along with the single cylinder ( $P/D = \infty$ ) results of Wiles and Welty [12] for their intermediate cylinder size ( $D = 0.0344$  m).

$$P/D = \infty: Nu_x = 0.217(Gr_x^*)^{0.189}, R^2 = 0.995 \quad (1)$$

$$P/D = 1.5: Nu_x = 0.305(Gr_x^*)^{0.165}, R^2 = 0.997 \quad (2)$$

$$P/D = 1.3: Nu_x = 0.439(Gr_x^*)^{0.147}, R^2 = 0.995 \quad (3)$$

$$P/D = 1.1: Nu_x = 0.898(Gr_x^*)^{0.103}, R^2 = 0.976 \quad (4)$$

The influence of the cylinder spacing is evident from Fig. 5. As the pitch is decreased from infinity, the Nusselt number *increases* in the low Grashof number range, decreases in the upper range, and in the range of  $Gr_x^*$  from about  $10^7$ – $10^8$ , it is relatively independent of the spacing. The magnitude of this effect is large. For  $Gr_x^* = 10^5$  the Nusselt number for the  $P/D = 1.1$  bundle is 54 percent higher than that for the single cylinder while at  $Gr_x^* = 10^{10}$  the cylinder Nusselt number is higher than that for  $P/D = 1.1$  by 75 percent. Of particular importance is the large change in the heat transfer results which occurs between  $P/D = 1.3$  and 1.1. Apparently, as the spacing between the rods is made very small, the characteristics of the natural convection flow are rather drastically altered. More will be said about this in relation to the temperature disturbances and mean profiles.

The intersecting nature of the results of Fig. 5 is somewhat different than the vertical parallel plate channel results reported by Colwell and Welty [2]. They found that as the channel width was reduced, the Nusselt numbers increased over essentially the entire Grashof number range investigated here. By calculating a circumferentially-averaged spacing between the cylinders for the three bundles used in this investigation, an average "aspect ratio" similar to that defined by Colwell and Welty [2] can be formed as the heated length-to-spacing ratio. The maximum deviation between

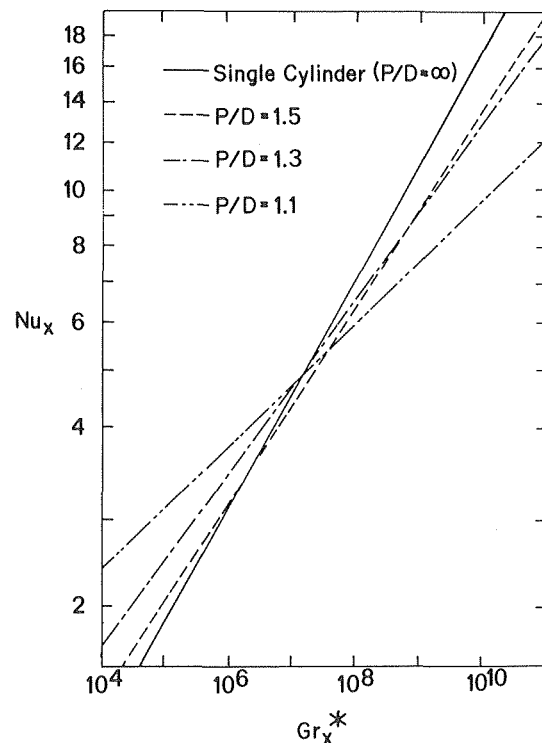


Fig. 5 Heat flux averaged correlations of experimental data for  $P/D = 1.5$ , 1.3, and 1.1 at 0 deg circumferential position; single cylinder results from [12]

the array results and the channel results for equal values of this ratio was found to be less than 14 percent. Thus for engineering purposes, it appears that the parallel plate channel results may be applied to the cylinder array situation for the corresponding average aspect ratio. However, this conclusion applies only for the comparatively large diameter cylinders used in this study, for which the effect of curvature on heat transfer is small. It should also be pointed out that the array results presented in Fig. 5 are for the 0 deg circumferential position. For cases in which the circumferential dependence is large, the agreement between the bundle results and the channel results is much poorer.

The influence of circumferential position on the heat transfer results was investigated by averaging data obtained at corresponding angular positions ( $\theta = 0, 10, 20, 30$  deg) in two adjacent symmetry units. The results show that for  $P/D = 1.5$  and  $1.3$  the circumferential effect is small while for  $P/D = 1.1$  (Fig. 6) it is quite significant. For  $P/D = 1.5$ , the average circumferential variation in the Nusselt number at a given axial location is  $\pm 2.6$  percent, and for  $P/D = 1.3$  it is  $\pm 4.1$  percent. For  $P/D = 1.1$ , on the other hand, values of the Nusselt number decrease steadily as the circumferential position is varied from 0 to 30 deg, and the average difference between the Nusselt numbers for  $\theta = 0$  deg and  $\theta = 30$  deg is over 20 percent. This trend for  $P/D = 1.1$  is the one expected. The 0 deg location is furthest from an adjacent cylinder, while the 30 deg position is the location of nearest approach. Therefore the surface temperatures for the constant flux case are expected to increase and the Nusselt numbers decrease as the circumferential angle is varied from 0 to 30 deg. What was not expected was the large change in the magnitude of the circumferential effect between  $P/D = 1.3$  and  $1.1$ .

The significance of these circumferential results is that for  $P/D = 1.5$  and  $1.3$ , the local heat transfer results given previously for the 0 deg position [equations (2) and (3)] apply equally well for all angular locations. However, because of the large circumferential dependence for  $P/D = 1.1$ , equation (4) applies well only at the 0 deg location. To account for this dependence, a correction factor was developed. This was done by noting that the local heat transfer data for the four angular positions all have approximately the same slope ( $\pm 3$  percent). Therefore, in the power law correlations,  $Nu_x = C(Gr_x^*)^n$ , the circumferential position strongly affects only the coefficient,  $C$ , while the exponent,  $n$ , is relatively independent of  $\theta$ . By finding the least squares relationship for  $C$  as a function of  $\theta$ , it was found that the results presented in Fig. 6 for  $P/D = 1.1$  are well represented by the following equation:

$$P/D = 1.1: Nu_x = 0.954 (1 - 0.408\theta) (Gr_x^*)^{0.0981} \quad (5)$$

$\theta$  in radians

Although the circumferential correction factor,

$$f(\theta) = (1 - 0.408\theta), \theta \text{ in radians}, \quad (6)$$

was obtained for a specific heat flux, it is felt that it may also be applied to the  $P/D = 1.1$  correlations for other heat fluxes; in particular to equation (4), which is the heat flux-averaged correlation.

For calculating average wall-ambient temperature differences for the constant heat flux case, rod-average heat transfer correlations are of value. For the two wider arrays,  $P/D = 1.5$  and  $1.3$ , the heat transfer results are essentially axisymmetric, and the rod-average results are obtained simply as axial averages of the local results. For  $P/D = 1.1$ , however, the circumferential dependence of the local results requires that the rod-average results be obtained by a circumferential as well as an axial integration. The results are given in the following along with the single cylinder results of Wiles and Welty [12] for comparison:

$$P/D = \infty: \overline{Nu_L} = 0.287(Gr_L^*)^{0.189} \quad (7)$$

$$P/D = 1.5: \overline{Nu_L} = 0.462(Gr_L^*)^{0.165} \quad (8)$$

$$P/D = 1.3: \overline{Nu_L} = 0.747(Gr_L^*)^{0.147} \quad (9)$$

$$P/D = 1.1: \overline{Nu_L} = 1.95 (Gr_L^*)^{0.103} \quad (10)$$

## Temperature Field Characteristics

In order to better understand this free convection rod bundle flow, the characteristics of the fluid temperature field were also studied. Mean radial profiles and temperature disturbance recordings were obtained for the three bundles at three axial locations corresponding to  $Gr_x^* = 10^6, 10^8$ , and  $10^{10}$  and at  $\theta = 0, 10, 20$ , and 30 deg.

The profiles for  $P/D = 1.1$  are shown in Fig. 7. Increasing the axial position ( $Gr_x^*$ ) clearly results in increased thermal stratification in the midchannel region which is to be expected for this developing channel flow situation. The profiles also show a significant dependence on circumferential position, and the trend is again the expected one: as the angle is increased from 0 to 30 deg, higher fluid temperatures result. The results for  $P/D = 1.5$  and  $1.3$  are similar although the axial development and circumferential dependence of the profiles for these arrays are not as pronounced. In fact the temperature profiles for  $P/D = 1.5$  are approximately axisymmetric. Hence, the results presented here for mercury indicate that the assumption of axisymmetry, as made in the numerical analysis of Davis and Perona [3] for air, is only valid for bundles with relatively wide spacing.

The disturbance recordings for the single cylinder and the three arrays at three axial locations corresponding to  $Gr_x^* = 10^6, 10^8$ , and  $10^{10}$  are shown in Fig. 8. Since the influence of angular position on the fluctuations was not appreciable, all of the recordings presented are for the 0 deg position. The radial position for the plots of Fig. 8 was  $y = 0.150$  in. ( $3.81 \times 10^{-3}$  m) which was found to be the approximate location for maximum disturbances. It was also found that the amplitude of the fluctuations decreased very little as the cylinder surface was approached from this region of maximum disturbances. This observation is in good agreement with the stability analysis of Knowles and Gebhart [6] for the zero thermal capacity, uniform flux flat plate.

The effect of cylinder spacing on the fluctuations is of interest. For the single cylinder the disturbances are of negligible amplitude and no characteristic frequency can be discerned. However, for the widest array,  $P/D = 1.5$ , relatively large amplitudes and frequen-

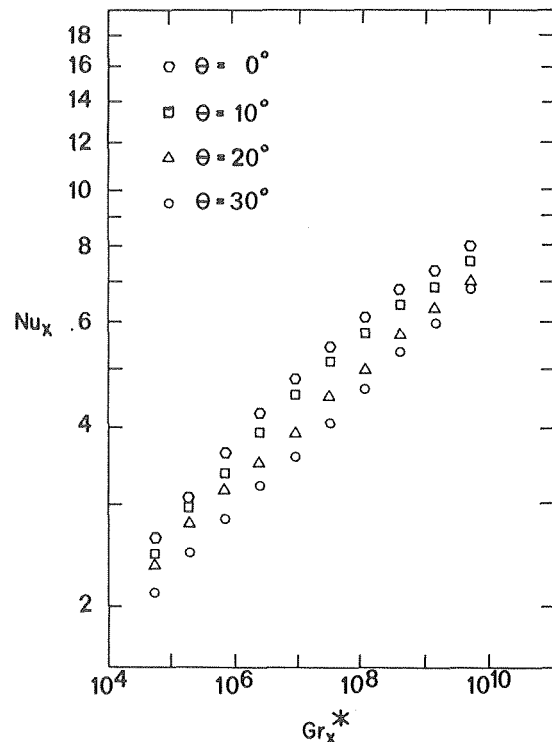


Fig. 6 Variation of heat transfer results with circumferential position for  $P/D = 1.1$ ,  $q = 1500$  Btu/hr-ft<sup>2</sup> (4730 W/m<sup>2</sup>)

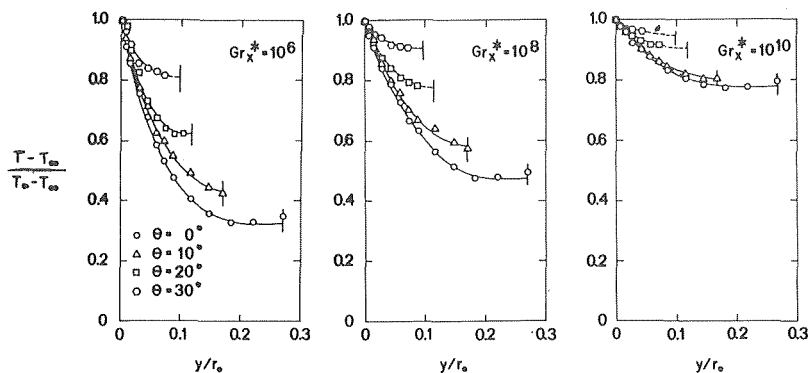


Fig. 7 Dimensionless mean radial temperature profiles for  $P/D = 1.1$ ,  $q = 3000$  Btu/hr-ft<sup>2</sup> (9460 W/m<sup>2</sup>)

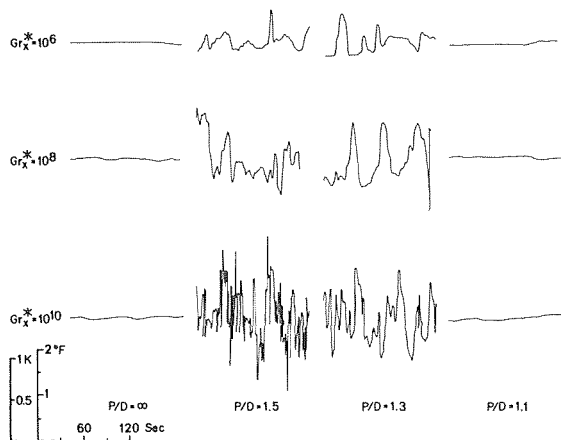


Fig. 8 Temperature disturbances for single cylinder,  $P/D = 1.5, 1.3$ , and  $1.1$  at  $Gr_x^* = 10^6, 10^8$ , and  $10^{10}$ ,  $y = 0.150$  in. ( $3.81 \times 10^{-3}$  m),  $q = 3000$  Btu/hr-ft<sup>2</sup> (9460 W/m<sup>2</sup>)

cies are encountered. As the spacing is reduced still further, the amplitudes and frequencies decrease until for  $P/D = 1.1$  they are again negligible.

The smoothness of the disturbance plots for the single cylinder indicates that the flow is laminar and stable. For the larger pitch-to-diameter ratio bundles, the characteristics of the buoyant flow would not seem to be too different from those for the single vertical surface except for the destabilizing influence caused by the merging of multiple boundary-layers. For  $P/D = 1.5$ , the regime is thought to be the unstable laminar one. As shown in Fig. 8, there is an appreciable amount of streamwise amplification, and the frequency which first appears is soon overtaken by higher frequencies. For  $P/D = 1.3$ , the situation is similar to that for  $P/D = 1.5$  except that the amplification and shift to higher frequencies are much less pronounced. It appears that the effects of the confinement of the flow, in particular the viscous interaction, hinders the amplification of frequency components which were more highly amplified for  $P/D = 1.5$ . Finally, for  $P/D = 1.1$  the disturbance plots suggest a stable, laminar flow as for the cylinder. It is felt that since the effects of the confining boundaries are so strong for this case, the flow is probably close in nature to a forced convection internal flow. Since the Reynolds number would be too small to support any instabilities, they are damped out.

## Conclusions

The results of an experimental investigation concerning the heat transfer and temperature field characteristics for free convection in a uniformly heated rod bundle have been presented. Although

all of the possible parameters (such as cylinder diameter and heated length) were not varied, the effects of several of the important variables were investigated: heat flux, cylinder spacing, and axial, radial, and circumferential positions. Also, the experiments were carried out only in mercury. However, it is known that in the low Prandtl number limit, natural convection heat transfer results are well represented by correlations involving the  $Gr_x^* \cdot Pr^2$  product which is independent of viscosity, [ $Gr_x^* \cdot Pr^2 = (g\beta q x^4 / k\alpha^2)$ ]. Thus it is expected that by recasting the correlations presented here in the inviscid form ( $Pr_{Hg} = 0.023$ ):

$$Nu_x = Nu_x(Gr_x^* \cdot Pr^2) \quad (11)$$

they will be approximately valid throughout the liquid metal range.

## Acknowledgment

The work described in this paper was supported by the Atomic Energy Commission, Contract No. AT(45-1)-2227.

## References

- 1 Chang, K., Akins, R., Burris, L., and Bankoff, S., "Free Convection of a Low Prandtl Number Fluid in Contact With a Uniformly Heated Vertical Plate," Argonne National Laboratory Report ANL-6835, 1964.
- 2 Colwell, R. G., and Welty, J. R., "An Experimental Investigation of Natural Convection With a Low Prandtl Number Fluid in a Vertical Channel With Uniform Wall Heat Flux," JOURNAL OF HEAT TRANSFER, TRANS. ASME, Series C, Vol. 96, 1974, pp. 448-454.
- 3 Davis, L. P., and Perona, J. J., "Development of Free Convection Axial Flow Through a Tube Bundle," International Journal of Heat and Mass Transfer, Vol. 16, 1973, pp. 1425-1438.
- 4 Dutton, J. C., "An Experimental Investigation of Natural Convection Heat Transfer From an Array of Uniformly Heated Vertical Cylinders to Mercury," MS thesis, Oregon State University, 1975.
- 5 Julian, D. V., and Akins, R. G., "Experimental Investigation of Natural Convection Heat Transfer to Mercury," Industrial and Engineering Chemistry-Fundamentals, Vol. 8, No. 4, 1969, pp. 641-646.
- 6 Knowles, C. P., and Gebhart, B., "The Stability of the Laminar Natural Convection Boundary Layer," Journal of Fluid Mechanics, Vol. 34, 1968, pp. 657-686.
- 7 Nagendra, H. R., Tirunarayanan, M. A., and Ramachandran, A., "Free Convection From Vertical Cylinders With Uniform Heat Flux," JOURNAL OF HEAT TRANSFER, TRANS. ASME, Series C, Vol. 92, 1970, pp. 191-194.
- 8 Quintiere, J., and Mueller, W. K., "An Analysis of Laminar Free and Forced Convection Between Finite Vertical Parallel Plates," JOURNAL OF HEAT TRANSFER, TRANS. ASME, Series C, Vol. 95, 1973, pp. 53-59.
- 9 Sparrow, E. M., and Gregg, J. L., "The Variable Fluid-Property Problem in Free Convection" TRANS. ASME, Vol. 80, 1958, pp. 879-886.
- 10 Sparrow, E. M., and Gregg, J. L., "Details of Exact Low Prandtl Number Boundary Layer Solutions for Forced and Free Convection," NASA Memo 2-27-59E, 1959.
- 11 Sparrow, E. M., and Guinle, L., "Deviations From Classical Free Convection Boundary Layer Theory at Low Prandtl Numbers," International Journal of Heat and Mass Transfer, Vol. 11, 1968, pp. 1403-1406.
- 12 Wiles, L. E., and Welty, J. R., "An Experimental Investigation of Natural Convection With Vertical Cylinders in Mercury," JOURNAL OF HEAT TRANSFER, TRANS. ASME, Series C, Vol. 96, 1974, pp. 455-458.

**M. L. Lawson**

Mechanical Engineering Department,  
Ahmadu Bello University,  
Zaria, Nigeria

**Wen-Jei Yang**

Mechanical Engineering Department,  
The University of Michigan,  
Ann Arbor, Mich.

# Thermal Stability of Binary Gas Mixtures in a Porous Medium<sup>1</sup>

*Thermal instability of a thin horizontal layer of binary gas mixture subject to an adverse temperature gradient in a porous medium is experimentally determined by applying the Schmidt-Milverson principle for detecting the onset of convective currents. The binary gas mixture consists of helium and nitrogen gases at various composition, while a packed bed of tiny steel balls constitutes the porous medium. It is disclosed that the critical Rayleigh number for pure gas is lowered by the presence of another species of different molecular weight and has a minimum value at a certain composition of the binary mixture.*

## Introduction

Since the early works of Bernard [1]<sup>2</sup> and Rayleigh [2] considerable efforts have been directed toward the investigation of the mechanisms of numerous thermal instability problems in fluid layers. Chandrasekhar [3] has summarized important knowledge pertinent to hydrodynamic and hydromagnetic instability.

In contrast with the availability of extensive literature on the effects of forces including gravity on the stability of a fluid layer, only a few works have been done on the stability of fluid-saturated porous media. By employing the modified Darcy's equations and the energy balance equation, Lapwood [4] has analyzed thermal stability of a fluid contained in a porous medium heated from below. The critical Rayleigh number for the onset of convective motion in the porous medium was found to be 39.5. Experimental studies were performed by Morrison, et al. [5], Elder [6], and Katto and Masuoka [7]. Niell [8] and Wankat and Scholwaller [9] have studied thermohaline convection in porous media and found results analogous to those of pure fluid layers. Lawson and Yang [10] have analytically investigated the stability of a layer of binary gas mixture heated from below.

The present work is to experimentally determine the onset of thermal instability in a layer of helium-nitrogen gas mixture heated from below in a packed bed of tiny steel balls. The Schmidt-Milverson principle is applied to determine the critical Rayleigh number. The composition of the binary gas mixture is varied.

## Experimental Apparatus And Procedure

An apparatus was constructed so that the Schmidt-Milverson principle for the detection of the onset of instability could be used. The following are the basic specifications for the design of the system:

- 1 Since high pressure is to be used reference [7], the system must be sufficiently rigid to ensure safety.
- 2 The porous medium must be thin enough so that thermal diffusion could attain steady state in a reasonably short time.
- 3 The temperature of the upper boundary of the medium is to be kept constant while that of the lower boundary is to be adjustable.
- 4 The temperature is to be uniform over each boundary.
- 5 The vertical wall bounding the medium is to be made from an insulating material.
- 6 There is to be no leakage of gas.

Compared with ordinary horizontal fluid layer, it is not easy to initiate convection in a porous medium. The use of thin porous medium requires high temperature difference. To keep the temperature difference  $\Delta T$  low and thereby avoid drastic changes in thermophysical properties, high pressure is utilized. This in turn requires somewhat rigid system which, with the satisfaction of the other conditions enumerated above, is depicted schematically in Figs. 1 and 2. It is designed to stand 136 atm of gas pressure, while the highest gas pressure in the present study is about 102 atm.

The porous medium consists of a layer of steel balls 0.101 cm in diameter. These are randomly packed in a space 10.16 cm in diameter, cut through a circular sheet of plexiglass 1.143 cm thick and 22.86 cm OD. It is press-fit into a brass ring to achieve high load carrying capacity. The plexiglass provided considerable insulation so that heat flow through the vertical boundary is negligible. The steel balls are retained below by a copper disk 13.21 cm in diameter and 0.635 cm in thickness. A circular sheet of asbestos, 0.0675 cm thick is sandwiched between this copper disk and a brass disk 0.159 cm thick, thus forming a heat flowmeter. The temperature of

<sup>1</sup> The work was supported by a financial aid from the H. H. Rackham School of Graduate Studies, The University of Michigan, Ann Arbor, Michigan, for which the authors wish to express their appreciation.

<sup>2</sup> Numbers in brackets designate References at end of paper.

Contributed by the Heat Transfer Division for publication in the JOURNAL OF HEAT TRANSFER. Manuscript received by the Heat Transfer Division February 20, 1974. Paper No. 75-HT-HH.

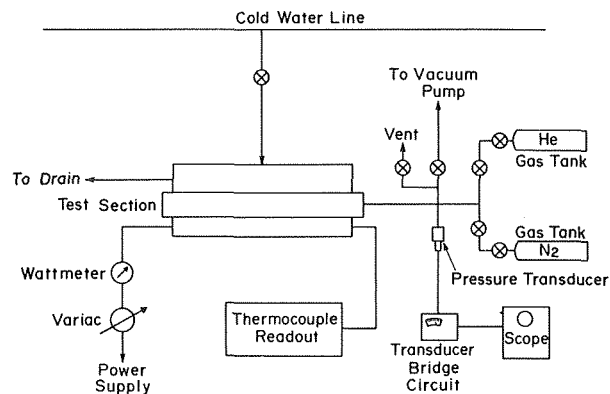


Fig. 1 Diagram of experimental apparatus

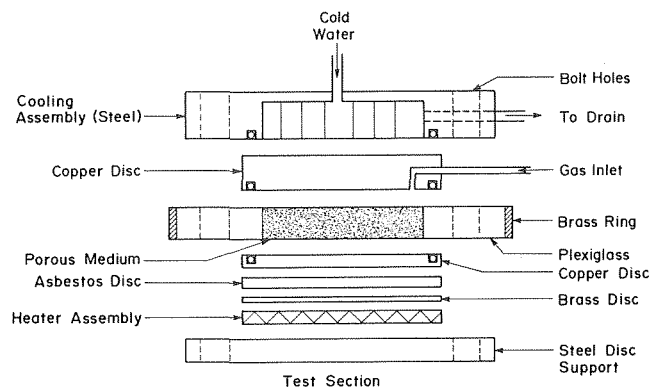


Fig. 2 Exploded view of vertical cross section of test section

the brass disk is taken by a copper-constantan thermocouple inserted at its center and the wires pass through a radial groove to the exterior. Next, below is an electric heater made from nickel-chrome wire wound into narrow straight grooves which are cut in a circular sheet of asbestos 13.21 cm in diameter and 0.3175 cm thick. It is controlled by a variac and wattmeter. On the underside is an identical guard-heater. The upper boundary of the porous medium is made of copper disk 13.21 cm in diameter and 2.54 cm thick. It is cooled by cooling water flowing in a helical vertical slot above it. Since the cooling water, being from a municipal water supply line, is at low pressure, it is necessary to make it fairly thick to prevent its distorting upward. The spiral slot is silver-soldered into a cylindrical hole cut into solid steel cylinder, 20.32 cm in outer diameter and 4.763 cm high. The spiral slot prevents water from stagnating anywhere in the cooling section. The entire system aforementioned rests on steel disk, 20.32 cm in diameter. Both the steel cylinder and disk have eight holes equally spaced through which 1.905 cm bolts are passed. They are threaded at either end with nuts and tightened to secure air-tight fit between the parts. There are six copper-constantan thermocouples used to measure temperatures of six surfaces: the upper and lower surfaces of the cooling copper disk; the upper surface of the lower copper disk; the upper and lower surfaces of the asbestos plate and the lower side of the heater. The thermocouple outputs were read on potentiometer with the accuracy of 0.01 mV. The gases used are high purity nitrogen and helium which are supplied from high-pressure cylinders and let into the porous medium via two control valves and a calibrated pressure transducer. The pressure transducer is connected to a Wheatstone-bridge arrangement and its output is read on type 205, model B oscilloscope.

Before filling the porous medium with gas, the cooling water is shut off and the entire system allowed to attain atmospheric temperature. The gas is then slowly flowed in until the desired pressure is attained. The temperatures of the boundaries of the porous

medium are then read. These are essential for accuracy estimation of the results. Power is supplied to the heater and with cooling water flowing through the cooling section, the apparatus is brought to steady-state condition. The temperature variation of the upper boundary of the porous medium is found to be less than 0.278°C during the course of obtaining each set of data. The temperature of the lower boundary is recorded with time so that when its variation becomes negligible, an extra time of one hour is allowed at which point steady state is assumed attained. The power input is progressively increased in steps of about 1 W and the variation in pressure is noted each time. A measure of the apparent thermal conductivity of the porous layer saturated with the binary gas mixture  $K_a$  is the ratio of the temperature drop across the asbestos plate  $\Delta T_a$  to that across the porous layer  $\Delta T$ . This ratio  $K_a$  is plotted against the temperature drop across the porous layer, and onset of convection is readily indicated by the sudden deflection of the curve. Subsequent operations follow the aforementioned procedure except that the porous medium is flushed with nitrogen and then pumped out about five times. This ensures that no air is left in the system before it is charged.

In computing the various dimensionless parameters, certain properties of the fluid and those of the fluid-porous medium combination have to be distinguished. The porous medium itself consists of several steel balls, 0.101 cm in diameter. These are chosen because they have almost perfect roundness and therefore enable accurate determination of the physical parameters of the medium. Near the horizontal boundaries, the porosity and permeability are locally modified by the presence of the walls. However, Katto and Masuoka [7] found that up to the  $d/h$  ratio used in the present study, the mean porosity and hence permeability are not appreciably affected by the presence of the walls. Here,  $h$  is the thickness of the porous layer and  $d$  is the diameter of the steel balls. Even higher  $d/h$  ratios do not seem to have complicated their results. The permeability of the medium  $k$  may be considered isotropic both in the theory and experiment and is evaluated from the semi-

## Nomenclature

$C_p$  = specific heat at constant pressure, J/(kg · K)  
 $d$  = diameter of filling particles (steel balls), m  
 $g$  = gravitational acceleration, m/s<sup>2</sup>  
 $h$  = vertical thickness of porous layer, m  
 $K_m$  = thermal conductivity of the porous layer saturated with binary gas mixture;  $K_a$  apparent value defined as  $\Delta T_a/\Delta T$   
 $k$  = permeability, m<sup>2</sup>

$Ra$  = Rayleigh number, defined as  $g\beta h^3 \Delta T/\nu\alpha$ ;  $R_{ac}$ , critical value defined as  $g\beta h^3 \Delta T_c/\nu\alpha$   
 $\Delta T$  = temperature difference between upper and lower bounding plates, K;  $\Delta T_c$ , critical value for the onset of thermal instability  
 $\Delta T_a$  = temperature drop across asbestos plate, K  
 $\alpha$  = special thermal diffusivity, defined as  $k_m/(\rho C_p)_f$ , m<sup>2</sup>/s

$\beta$  = cubic expansion coefficient, 1/K  
 $\epsilon$  = porosity  
 $\nu$  = kinematic viscosity, m<sup>2</sup>/s  
 $\rho$  = density, kg/m<sup>3</sup>

## Subscripts

$f$  = value of binary gas mixture  
 $m$  = value of porous medium-gas mixture combination  
 $c$  = critical value, at the onset of thermal instability

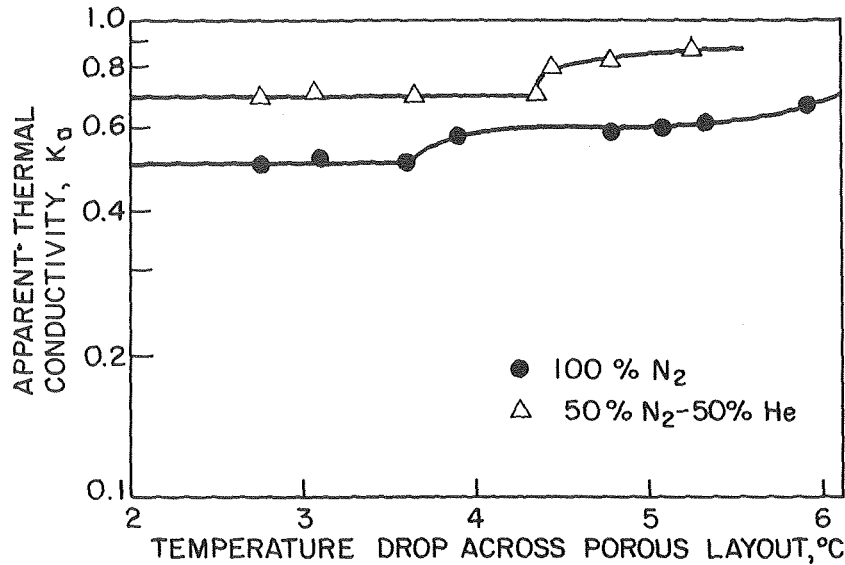


Fig. 3 Apparent thermal conductivity versus temperature drop across porous medium

empirical Kozeny equation, references [11, 12], as

$$k = \frac{\epsilon^3 d^2}{150 (1 - \epsilon)^2}$$

where  $\epsilon$  is the porosity. The special thermal diffusivity  $\alpha$  that features in the Rayleigh number is the ratio of the thermal conductivity of porous layer saturated with the binary gas mixture  $K_m$  to the thermal capacity of the gas mixture  $(\rho C_p)_f$ . As pointed out in reference [7], and also observed here, this can be up to twenty times the thermal diffusivity of the gas itself. For the mixture of helium and nitrogen, the thermal capacity is evaluated according to

$$(\rho C_p) = (\rho C_p)_{N_2} + (\rho C_p)_{He}$$

Here,  $\rho N_2$  and  $\rho He$  are the partial densities of nitrogen and helium, respectively, which with the corresponding specific heats are determined at the appropriate partial pressures and average temperature of the system. The thermal conductivity of porous medium is greatly affected by the mechanical load on it, especially when the particles have high elasticity and thermal conductivity (Luikov, et al. [13]). It increases with the load. In the experiment, the tightening of the bolts put a sealing precompression on the steel balls. As the gas is introduced and the pressure increased, the precompression is decreased reducing the thermal conductivity of the medium. This is of no consequence, however, as the thermal conductivity is necessarily measured each time the experiment is carried out. The values corresponding to the sudden deflection in slope in Fig. 3 are used in evaluating the critical Rayleigh number. The viscous effects  $\rho \nu \nabla^2 \bar{v}$  at the walls can be proved to be negligible through the combination of Darcy's law  $-\nabla^2 \bar{v} = \bar{v}$  and the no-slip condition  $\bar{v} = 0$  at the walls, where  $\bar{v}$  is the macroscopic velocity.

### Experimental Results

The relative accuracy and functioning of the apparatus were checked by conducting four runs with pure nitrogen as the gas. The lower curve in Fig. 3 shows a typical experimental result which is the plot of the measured thermal conductivity versus temperature drop across the porous layer. The average critical Rayleigh number was 39.2. This compares well with the theoretically predicted value of 39.5. Accordingly, it may be concluded that the functional accuracy of the apparatus is sufficient for this study.

The upper curve in Fig. 3 is the experimental result for a mixture of nitrogen and helium of equal proportions. The shape of the

curve is typical of all the results for mixtures of various compositions. The apparent thermal conductivity  $K_a$  remains virtually constant until some temperature difference is reached at which a further small increase in power input does not increase the temperature difference appreciably while the apparent thermal conductivity is sharply increased. Further increase in the temperature difference is accompanied by increase in the apparent thermal conductivity. The experiment was discontinued at a temperature difference short of 10°F because increasing it further is of no interest, for the point of onset of convection has been well exceeded.

The value of the temperature difference when the apparent thermal conductivity sharply rose,  $\Delta T_c$ , is used in computing the critical Rayleigh number. The experimental critical Rayleigh numbers for various compositions are plotted in Fig. 4. The uncertainty estimations for confidence limits on the mean of 95 percent are evaluated for the test data by the method of reference [14]. Experi-

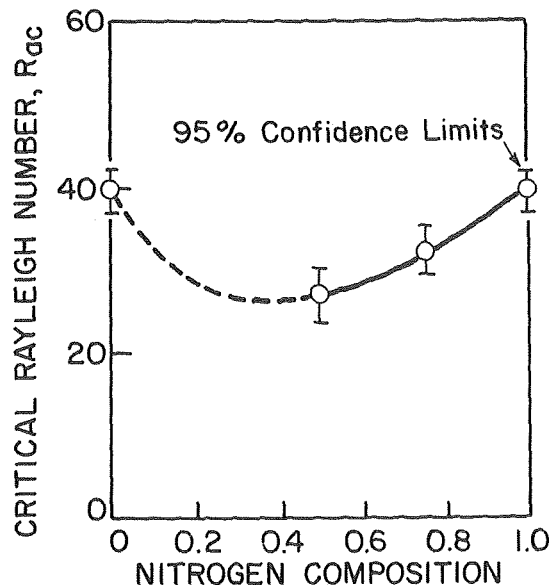


Fig. 4 Critical Rayleigh number versus nitrogen composition

ments could not be carried out for mixtures with more helium than nitrogen because calculations showed that the temperature differences required are high enough to bring the temperature of the plexiglass close to its "distortion temperature," hence the safety of the apparatus cannot be guaranteed. A line is drawn through the data points. The broken-line portion is tentative and will be confirmed by theoretical study which is presently in progress.

Fig. 4 shows that the critical Rayleigh number for the onset of thermal instability decreases from the value of 39.2 (or 39.5 by theory) due to the presence of another species of different molecular weight and has a minimum at a certain composition of the helium-nitrogen mixture.

### Conclusions

It is concluded from this study that the critical Rayleigh number for the onset of thermal instability in a horizontal layer of fluid subject to an adverse temperature gradient in a porous medium decreases in the presence of another species of different molecular weight and has a minimum at a certain composition of binary gas mixture.

### References

1 Benard, H., "Les Tourbillons cellulaires dans une nappe liquids transportant de la chaleur par convection en regime permanent," *Ann. Chim. Phys.*, Vol. 23, 1901, pp. 62-144.

- 2 Rayleigh, L., "On Convection Currents in a Horizontal Layer of Fluid, When the Higher Temperature is on the Underside," *Philosophical Magazine*, Vol. 32, 1916, pp. 529-546.
- 3 Chandrasekhar, S., *Hydrodynamic and Hydromagnetic Stability*, Oxford University Press, England, 1961.
- 4 Lapwood, E. R., "Convection of a Fluid in a Porous Medium," *Proceedings of Cambridge Philosophical Society*, Vol. 44, 1948, pp. 508-521.
- 5 Morrison, H. L., Roggers, F. T., and Horton, C. W., "Convection Currents in Porous Media, II: Observation of Conditions at Onset of Convection," *Journal of Applied Physics*, Vol. 20, 1949, pp. 1027-1029.
- 6 Elder, J. W., "Steady Free Convection in a Porous Medium Heated From Below," *Journal of Fluid Mechanics*, Vol. 27, 1967, pp. 29-48.
- 7 Katoo, Y., and Masuoka, T., "Criterion for the Onset of Convective Flow in a Fluid in a Porous Medium," *International Journal of Heat and Mass Transfer*, Vol. 10, 1967, pp. 297-309.
- 8 Nield, D. N., "Onset of Thermohaline Convection in a Porous Medium," *Water Resources Research*, Vol. 4, 1968, pp. 553-558.
- 9 Wankat, P. C., and Scholwalter, W. R., "Stability of Combined Heat and Mass Transfer in a Porous Medium," *The Physics of Fluids*, Vol. 13, 1970, pp. 2418-2420.
- 10 Lawson, M. L., and Yang, W. J., "The Stability of a Layer of Binary Gas Mixtures Heated From Below," *Journal of Fluid Mechanics*, Vol. 57, Part 1, 1973, pp. 103-110.
- 11 Bird, R. B., Stewart, W. E., and Lightfoot, E. N., *Transport Phenomena*, Wiley, New York, 1960.
- 12 Carman, P. C., *Flow of Gases Through Porous Media*, Academic Press, New York, 1956.
- 13 Luikov, A. V., Shashkov, A. G., Vasiliev, L. L., and Fraiman, Y. E., "Thermal Conductivity of Porous Systems," *International Journal of Heat and Mass Transfer*, Vol. 11, 1968, pp. 117-140.
- 14 Kline, S. J., and McClintock, F. A., "Describing Uncertainties in Single-Sample Experiments," *Mechanical Engineering*, Vol. 75, 1953, pp. 3-8.

**R. L. Reid**  
Assoc. Professor.  
Mem. ASME

**J. S. Tennant**  
Assoc. Professor.  
Mem. ASME

**K. W. Childs**  
Graduate Asst.  
Assoc. Mem. ASME

Mechanical and Aerospace  
Engineering Department,  
University of Tennessee,  
Knoxville, Tenn.

# The Modeling of a Thermosyphon Type Permafrost Protection Device

*One promising device for protection of permafrost is the concentric tube thermosyphon. In the winter, the difference in temperature between the annulus and the tube provides a buoyant driving force to move the air down the tube and up the annulus. The resultant heat transfer freezes and subcools the permafrost. The paper describes in detail the flow and heat transfer by solving the boundary layer equations for velocity and temperature considering conduction and radiation at the boundaries. The predicted thermosyphon performance is compared with experimental data. The results for heat removal rate are generally within 10-20 percent.*

## Introduction

Much of Alaskan and North Slope terrain is composed of permafrost which can reach depths of hundreds of meters [2].<sup>1</sup> In about the southern half of Alaska, the top layer of a few tenths of a meter thickness melts in the summer. The lush vegetation acts as insulation to prevent more excessive thawing. This obviously creates problems for projects such as roads, buildings, and pipelines where the top layer is destroyed during the construction process. This problem was anticipated in the design of the Trans-Alaska Pipeline [1]. Even though the pipeline will be elevated in the most unstable permafrost zones (about one half the length of the route), the destruction of the surface vegetation during construction dictated a study of the various means of permafrost protection. The device described in this paper is being considered for future pipelines and other construction activity in Alaska and Canada.

The method of attack on the problem of permafrost protection is to consider devices that will ensure complete freezing and subcooling of the permafrost in the winter. This subcooling might result in permafrost temperatures in the vicinity of pilings of 20°F (267°K) or lower instead of a normal 30 or 31°F (272 or 273°K). When summer arrives, this extra capacity for absorbing heat will tend to counteract the tendency for additional melting caused by the surface disturbance.

One class of devices for permafrost protection is a thermosyphon

type device called the air convection pile (or simply air pile). The air pile is very simple in concept and construction but quite efficient in operation. Basically, it makes use of the 18-in. (0.457 m) dia pipe used for pilings. A smaller diameter tube (approximately 10 in. (0.254 m)) is then inserted concentric with the larger pipe but about ½ ft (0.15 m) shorter. (The piling lengths may be 15-60 ft (4.57-18.3 m)). As shown in Fig. 1, a head is then placed on the device to prevent snow and rain accumulation. Various head configurations were considered. In winter, the ground is warmer than the ambient air so the air in the annulus is heated by the ground, creating an unstable situation. This air then rises up the annulus while the colder air in the tube tends to move to the bottom. A simple heat exchanger is thereby established and heat is continually removed from the ground surrounding the pile throughout the period of the year when the surface air is colder than the ground. In summer, the ground is colder than the surface air so that air in the air pile is cold and stable. The air pile then has shut itself off for the summer when no heat transfer is desired. The low cost and simplicity of construction of the air pile are advantages over other types of devices for permafrost protection (e.g., heat pipes).

Air piles have undergone limited crude field tests and gross performance tests in laboratories. The analytical results of this study were compared to experimental data collected by other investigators at Exxon Production Research Co. [3]. Their test apparatus consisted of a pit that could accommodate a 10 ft (3.05 m) long pile surrounded by a water jacket. The head and "above ground" portion of the pile were enclosed in a refrigerated box. Since the cooling of the water in the jacket was a relatively slow process, the device could be considered to be approximately in equilibrium over short time periods of data collection. The heat removal rate of the air pile for a given cold air temperature and "ground temperature" could be determined by measuring the change in temperature of the water bath. Other data collected consisted of a few axial temperatures in the tube and annulus and a rough measurement with

<sup>1</sup> Numbers in brackets designate References at end of paper.

Contributed by the Heat Transfer Division of THE AMERICAN SOCIETY OF MECHANICAL ENGINEERS, and presented at the AIAA/ASME Thermophysics and Heat Transfer Conference, Boston, Mass., July 15-17, 1974. Journal manuscript received by the Heat Transfer Division March 24, 1975. Paper No. 74-HT-46.

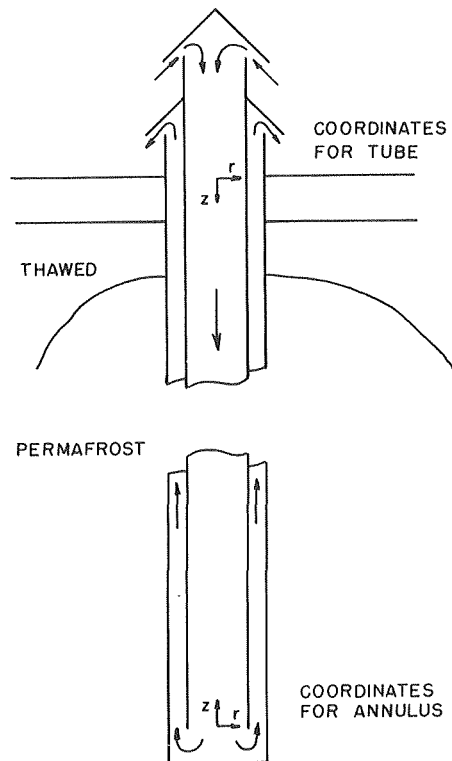


Fig. 1 Air convection pile

a velocity probe. Although detailed velocity and temperature profile traverses would have been very helpful in the analytical study, these data were not taken by Exxon.

While the air convection pile is a very simple device to construct and its principle of operation is easily understood, it is actually very complicated when examined in a fluid flow and heat transfer analysis. In the flow down the tube and up the annulus, the annulus acts as a driver for the system since the buoyancy aids the flow. However, it is not a pure natural convective situation in the annulus since the tube acts as a drag on the flow. That is, while the flow is in the category of combined forced and free convection, the case is actually one of hindered free convection. This type of convection has not been reported in the literature. The tube, on the other hand, is a case of forced and free convection with buoyancy oppos-

ing the flow since the air is "pulled" through the tube by the annulus.

### The Analytical Method

Heat transfer in the thermosyphon takes place by combined conduction thru the tube walls, radiation between the tubes, and mixed forced and free convection. Each mechanism will be discussed separately followed by a description of how they are combined to provide an overall model of the thermosyphon system.

(a) **Mixed Forced and Free Convection.** The basis of the analysis is that the flow within the pile (neglecting entrances, exits, and turns) can be adequately described by the boundary-layer equations. The basis for the choice of the boundary-layer equations to describe the flow is:

1 It is assumed that the flow is boundary layer in character i.e., large velocity and temperature gradients normal to the stream and the primary pressure gradient in the direction of flow.

2 The potential flow core between the developing boundary layers can easily be approximated by one-dimensional equations (i.e., boundary-layer equation outside the layer) since the displacement thickness of the boundary layer increases slowly streamwise.

3 The simplicity of solving only one system of equations to describe the flow.

4 The parabolic form of the boundary layer equations allows the use of a streamwise marching method of solution. This feature allows for the inversion of one relatively small matrix at each streamwise station.

The equations are:

1 *Continuity.*

$$\frac{\rho v}{r} + \frac{\partial(\rho v)}{\partial r} + \frac{\partial(\rho u)}{\partial z} = 0 \text{ where } \rho = f(T) \text{ only}$$

2 *Momentum.*

$$v \frac{\partial u}{\partial r} + u \frac{\partial u}{\partial z} = (\nu + \epsilon_t) \left( \frac{\partial^2 u}{\partial r^2} + \frac{1}{r} \frac{\partial u}{\partial r} \right) - \frac{1}{\rho} \frac{dp}{dz} \pm \frac{g(l-l_0)}{l_0}$$

3 *Energy.*

$$v \frac{\partial t}{\partial r} + u \frac{\partial t}{\partial z} = (\alpha + \bar{\epsilon}) \left( \frac{\partial^2 t}{\partial r^2} + \frac{1}{r} \frac{\partial t}{\partial r} \right)$$

Equations (1)–(3) are the boundary layer equations for axisymmetric flow of an incompressible fluid. It should be noted that the equations account for the natural convection body force due to temperature difference (i.e., buoyant force) although the remaining terms of the equations are for incompressible flow. The "g" term is for the component of the local acceleration of gravity in the axial direction. The  $\pm$  associated with this term provides for up and down flow directions. The velocity terms are taken to be time average terms when the equations are applied to turbulent flow. The properties  $\epsilon_t$  and  $\bar{\epsilon}$  are turbulent eddy properties that account

### Nomenclature

$A_{A,T,i}$  = cross-sectional areas  
 $\bar{A}_K, \bar{B}_K, \bar{C}_K$  = coefficients of nodal energy equation  
 $A_K, B_K, C_K$  = coefficients of nodal momentum equation  
 $d$  = pile diameter  
 $D$  = diameter  
 $g$  = acceleration of gravity  
 $h_B L$  = effective convection coefficient and length for the bottom of the pile  
 $K_i$  = dynamic head loss coefficient  
 $\dot{m}$  = mass flow rate  
 $M_{A,T}$  = mass of air in the annulus, tube  
 $P$  = static pressure  
 $P_{j+1} = p/\rho \Delta z$  at station  $(j+1)$

$Q_B$  = heat transfer in the pile bottom  
 $Q_c$  = calculated heat removal rate  
 $Q_{WB}$  = experimental heat removal rate  
 $Q_v$  = heat removal rate calculated from measured velocity  
 $r$  = radial location measured from center line  
 $r_i$  = inner radius of flow channel  
 $r_o$  = outer radius of flow channel  
 $t$  = temperature  
 $T_{AB}$  = temperature of the air as it leaves the tube  
 $T_{PB}$  = temperature of pile wall at the bottom

$u$  = axial component of velocity  
 $U_w$  = shear velocity at the wall  
 $U_e$  = free stream velocity (potential flow)  
 $v$  = radial component of velocity  
 $V_{AM}, V_{AC}$  = measured and calculated velocities in the annulus  
 $V_{TM}, V_{TC}$  = measured and calculated velocities in the tube  
 $y$  = distance radially from the wall  
 $z$  = axial position  
 $\nu$  = kinematic viscosity  
 $\epsilon_t$  = turbulent eddy viscosity  
 $\rho$  = density  
 $\alpha$  = thermal diffusivity  
 $\bar{\epsilon}$  = turbulent eddy diffusivity

for the Reynolds shear stress and transport gradient in turbulent flow. For laminar flow, these properties are simply taken to be zero.

The boundary conditions for the governing equations are as follows:

$$\begin{aligned} u = v = 0 @ r = r_o & \text{ (outer wall position)} \\ u = v = 0 @ r = r_i & \text{ (inner wall position)} \\ \partial u / \partial r = v = 0 @ r = 0 & \text{ (tube flow center line)} \\ t = t_o @ r = r_o & \text{ (} t_o \text{ = outer wall temperature)} \\ t = t_i @ r = r_i & \text{ (} t_i \text{ = inner wall temperature)} \\ \partial t / \partial r = 0 @ r = 0 & \text{ (tube flow center line)} \\ u = \text{constant} @ z = 0, t = \text{constant} @ z = 0 & \\ (z = 0 \text{ at the entrance to either the tube or annulus}) & \end{aligned}$$

The solution scheme generally followed that outlined by Davis [4] for laminar flows with several exceptions. Davis uses a transformation of variables to simplify the equations initially; this is impractical since the solution grid is also changed to some nonlinear function of real space which is incompatible with the grids for the solution of the entire problem. The other exceptions are the use of the annular configuration and the introduction of eddy viscosity and diffusivity properties to account for turbulent fluid behavior.

The linear system of equations resulting from the finite difference approximation follow:

#### 4 Energy Nodal Equation.

$$\bar{A}_K t_{j+1, K+1} + \bar{B}_K t_{j+1, K} + \bar{C}_K t_{j+1, K-1} = \bar{D}_K$$

#### 5 Momentum Nodal Equation.

$$A_K u_{j+1, K+1} + B_K u_{j+1, K} + C_K u_{j+1, K-1} + P_{j+1} = D_K$$

The coefficients ( $\bar{A}_K$ ,  $A_K$ ,  $\bar{B}_K$ , etc.) can be evaluated from the geometry and the previous streamwise calculations. These equations may be expressed as systems of algebraic equations in matrix form along with the boundary condition. Continuity was expressed in one-dimensional form, i.e.,

$$\sum_{K=1}^N \frac{r_K \cdot u_{j+1, K}}{T_{j+1, K}} = \frac{u_{\text{inlet}} \cdot r_o^2 - r_i^2}{T_{\text{inlet}} \cdot 2\Delta r}$$

to give the additional equations necessary to solve the momentum equation for the unknown of velocity at each radial station and the pressure for the vertical station,  $P_{j+1}$ .

The solution proceeded as follows:

- 1 A flow of uniform temperature and velocity is assumed entering the channel.
- 2 The energy equation for the next streamwise station,  $j + 1$ , was solved based on the velocities of the previous stations.
- 3 The energy and continuity equations were then solved for  $u$  and  $P$  at  $(j + 1)$  using the previously calculated temperatures and the velocity,  $v$ , from the previous station,  $j$ .
- 4 Using the new value of  $u_{j+1}$ ,  $v_{j+1}$  was calculated using the continuity equation alone.
- 5 All values of variables at  $j + 1$  were assigned to  $j$  and a new forward step was made to  $j + 1$ .
- 6 The solution proceeded stepwise in the axial direction until the calculations were complete.

The first attempts at solving the problem included an elaborate eddy viscosity model based upon a mixing length analysis for the annular portion of the flow. Later experimental evidence, specifically streamwise temperature gradients, indicated that the annular flow was entirely laminar. The existence of this laminar flow is supported by the stabilizing effect of a body force (buoyant force) in the direction of the flow. In all the results to be reported, the flow in the annulus was considered laminar.

The downflows in the tube with a buoyant force opposite to the flow direction when analyzed using the boundary-layer equations gave a flow reversal at the node adjacent to the wall. This reversal is easily explained since along the wall the fluid has very little momentum and the buoyant force is a maximum because this is also the location of highest fluid temperature. The buoyant force is sufficient to completely stop, then reverse the flow adjacent to the wall. It is supposed that the net effect of this local flow reversal is

to cause a general instability of the flow resulting in turbulence. Thus, it was assumed that the flow in the tube was turbulent. The flow reversal rendered the marching numerical technique inoperative. Thus, it was necessary to drop the gravitational term from the governing equation used in the downflow in the tube. This deviation from the real case may not be as great as it first appears since: (a) the major resistance to heat transfer in the thermosyphon is in the outer annular boundary layer, thus the importance of the tube analysis is diminished; (b) the turbulent behavior is recognized and accounted for using an eddy viscosity model; and (c) the temperature gradient in the fluid in the tube is accounted for in determining the overall driving force of the thermosyphon (see Part (d)).

The turbulent eddy viscosity model for the tube flow consisted of a boundary-layer type model in developing portions of the flow and a model for fully developed flows after the boundary layers converged at the center line. Specifically, the eddy viscosity in the developing boundary layers was described by the model due to Cebeci [5] for boundary layers in external flow. The model is a two layer model utilizing the spatially dependent law of the wall for the inner layer and an outer law of the wake model due to Clauser [6]. For the fully developed flows the model is given by Hinze [7]. The value of  $\bar{\epsilon}$  was taken to be equal to  $\epsilon_t$  since the Prandtl number for air at the temperatures involved was near one.

(b) **Other Flows (Entrances, Exits, and Turns).** The flows at entrances, exits, and at the upturn at the bottom of the thermosyphon were simply analyzed for pressure drop using loss factors for each situation which are commonly found in the literature.

(c) **Radiation Heat Transfer.** The radiation heat transfer between the vertical tube and annulus elements was determined by invoking the usual assumptions of diffuse, gray interchange with uniform radiosity over each element. The annular ring view factors necessary for this analysis had not been previously given in the literature. These were derived by integration and flux algebra and published in reference [8].

(d) **Overall Method of Solution.** Basically, the program calculates the heat transfer, temperature profiles, velocity profiles, and mass flow rate through the air convection pile. The input to the program consists of the outer pile wall temperatures, surrounding air temperature, and an initial estimate of the mass flow rate of air. (It appears to be better to assume a high, rather than low, estimate for the initial mass flow rate.) The other input data consist of property and geometry information.

The pressure drops through the head inlet are first calculated for the estimated mass flow rate. The program then makes initial estimates of the wall temperatures and calculates radiation view factors. Radiant heat fluxes are then calculated. A subroutine then performs an energy balance on the wall nodes considering conduction through and along the wall, radiant heat flows, and convective heat flows using an estimate of the air velocity immediately adjacent to the wall. This wall temperature matrix equation is then solved to provide new estimates of the wall temperatures.

The fluid flow and convective heat transfer in the tube are next considered. The solution steps down the tube with usually 50 nodes at each station. In this formulation, the pressure that is calculated at each station does not include the contribution of the buoyancy to the pressure. This effect is considered later. Upon return to the main program, an equivalent flow coefficient ( $K$  factor) is calculated for the friction losses. The pressure drop in the turn is then calculated.

The annulus convective analysis is similar to that of the tube. Also, the pressure that is obtained at each section includes the buoyancy contribution. Back in the main program, this part of the pressure is subtracted out so that an equivalent friction  $K$  factor can again be calculated.

The wall temperatures are then checked for agreement with the initial estimates and the program returns to calculate new radiant fluxes and convective heat transfer if needed.

The pressure drop through the head outlet is next determined. Then, the total friction pressure drops are compared to difference

in weight per unit area of the two air columns. If the driving force does not equal the drag, then a new estimate of the mass flow rate is obtained from:

$$\dot{m} = \left( \frac{2g(M_T/A_T - M_A/A_A)^{1/2}}{\sum \frac{K_i}{\rho_i A_i^2}} \right)$$

The program then transfers back to the point of the calculation of the radiant heat fluxes and the process is repeated until convergence is obtained. The convergence criteria was that the pressure difference due to density variations in the two columns was within 0.0001 lbf/ft<sup>2</sup> (0.0048 Pa) of the friction pressure drop through the system.

### Improvements in the Analysis

It was not known "a priori" whether the flow was laminar or turbulent in either the tube or the annulus of the thermosyphon. However, heuristic arguments can be made that in mixed forced and free convection flows a buoyant force in the fluid near the wall in the direction of the flow (as in the annulus) has a stabilizing effect on the laminar flow condition. Conversely, when the buoyant force is the opposite direction of the flow the laminar stability is degraded. Initial calculations were made assuming either laminar or turbulent flow in the tube and the annulus. A comparison with experimental data for the annulus showed a good agreement in streamwise mean temperature slope for laminar flow and a very poor agreement for turbulent flow. Thus the flow in the annulus was taken to be laminar. A similar comparison showed that the flow in the tube was turbulent.

Initial analysis did not include heat transfer from the bottom surface of the thermosyphon. The effect of this heat transfer may be seen in Figs. 7-8 as a step increase in temperature of the air as it turned upward from the tube into the annulus (at the minimum two experimental values plotted). It was discovered that these amounts of heat, although different for each set of experimental data, could be correlated by the equation

$$h_B L = \frac{Q_B}{\pi d(T_{p_B} - T_{A_B})}$$

This  $h_B L$  parameter was found to be approximately 5.15 Btu-ft/hr-ft<sup>2</sup>-°F (8.91 W-m/m<sup>2</sup>-°K) for all runs independent of pile diameter, velocity, and temperature difference. This value of  $h_B L$  was therefore introduced into the program so that the computer could then calculate the heat transfer at the bottom by the foregoing equation for all conditions that might occur.

### Comparison of Calculations with Data

Figs. 2-5 give typical velocity and temperature profiles in the annulus and tube. From the annulus velocity profiles in Fig. 2 it can be seen that the laminar boundary layers grow and accelerate near the walls by drawing fluid from the center of the stream. Eventually, in some runs, this presented a problem since if the momentum is not transferred to the center of the stream, then some center stream elements can become depleted of fluid and the program predicts negative or downward velocities. Due to the step by step method used in the analysis, this negative velocity cannot be tolerated and the program begins to generate erroneous information. This is, however, a physically possible flow configuration. Fortunately, this type of flow occurred only in a few cases and only near the end of the convergence scheme. If the convergent mass flow rate is always approached from the high side, then the convergent heat flow and outlet temperatures can be obtained by extrapolation. The program will search for the nearest mass flow rate within 5 lb/hr ( $6.3 \times 10^{-4}$  Kg/s) where no negative velocities are predicted. The program then stops executing and the residual pressure can be extrapolated to zero.

Fig. 6 shows the streamwise temperature profile for an omnidirectional head test with an 8-in. tube. The X's on this and suc-

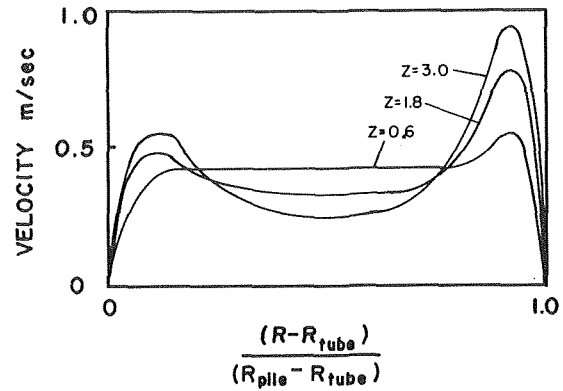


Fig. 2 Typical velocity profiles in the annulus

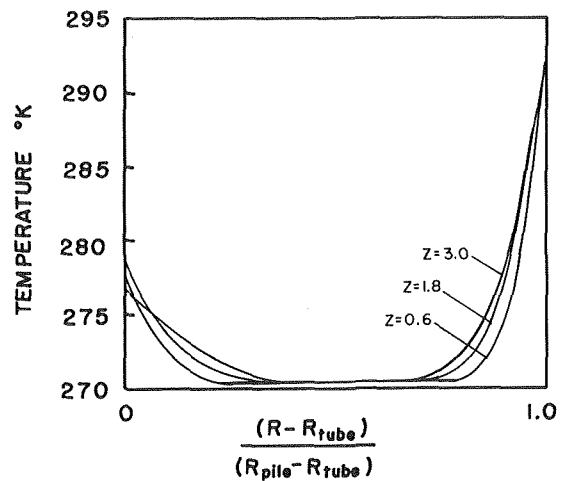


Fig. 3 Typical temperature profiles in the annulus

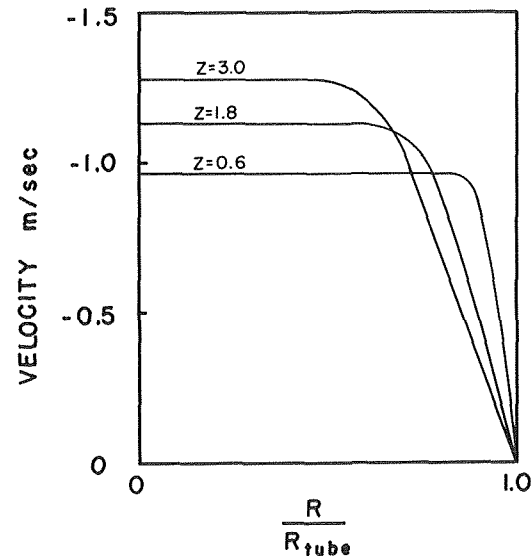


Fig. 4 Typical velocity profiles in the tube

ceeding figures indicate the actual thermocouple measurements while the solid lines represent the computer predictions of the average temperatures across the stream. None of these 8-in. tube cases converged completely although both the uncorrected and the extrapolated ( $Q_c$ ) heat removal rates are given and these are quite

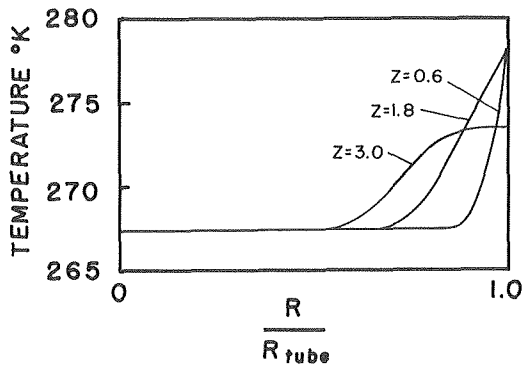


Fig. 5 Typical temperature profiles in the tube

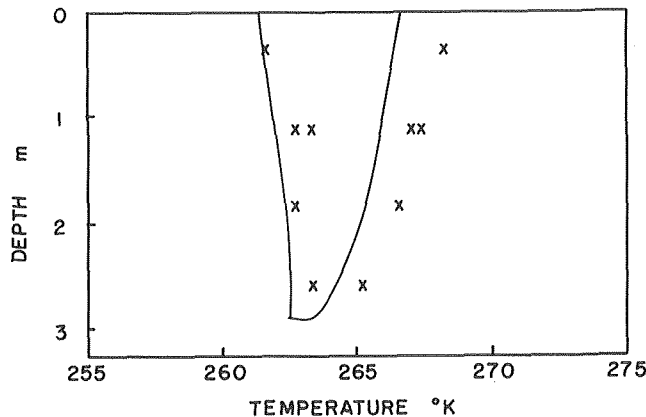


Fig. 7 Omnidirectional head test, 12 in. tube  
 $Q_{WB} = 272 \text{ W}$ ,  $Q_C = 370 \text{ W}$ ,  $V_{AC} = 0.57 \text{ m/s}$ ,  $V_{TC} = 0.64 \text{ m/s}$

close in these cases. The dotted line indicates the extrapolated exit temperature of the air. In addition to the experimental heat removal rate calculated from water bath data ( $Q_{WB}$ ), the rate calculated from the measured air velocities ( $Q_V$ ) are given. The measured and calculated tube and annulus velocities are also given ( $V_{TM}$ ,  $V_{AM}$ ,  $V_{TC}$ ,  $V_{AC}$ ). Note that in nearly all of the cases, the measured temperature profile, velocities, and heat removal rates all agree quite closely with the calculated values.

Figs. 6 and 7 give typical results for the 10 in. (0.254 m) and 12 in. (0.305 m) tubes with the omnidirectional head. All of these cases converged fully. The temperature profiles are quite close for the 10-in. tube cases although the heat removal rates are about 10 percent high. In the 12-in. (0.305 m) cases, the temperature profile is 1–2°K low and the heat removal rate is about 30 percent high. It may be that as the tube becomes larger and therefore influences more the performance, the inaccuracies in the tube flow analysis have more effect on the calculations. Recall that buoyancy was neglected in calculating the fluid flow and heat transfer in the tube.

Fig. 8 shows the results for the revised standard head. These cases did not fully converge and the extrapolation information is given. In the converged state, it appears that the temperature profile would be about 1° low and heat flow, about 10 percent high.

### Conclusions

When the omnidirectional head cases (three different tube diameters) and the revised standard head cases were analyzed, the vertical mean temperature profiles and total heat removal rates all agreed satisfactorily with experimental data. In addition predicted average velocities agreed well with experimentally determined average velocities. The agreement of all three of these dependent variables (mean velocities, mean temperatures, and heat removal rates) leads to the conclusion that the analytical model is correctly modeling the gross performance of the thermosyphon.

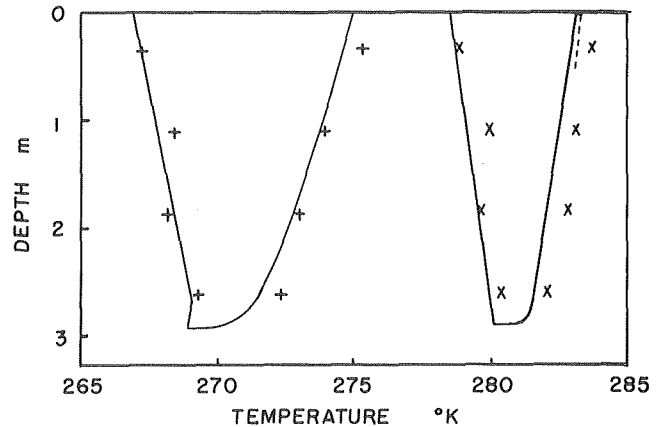


Fig. 6 Omnidirectional head test  
 8 in. tube (x)  
 $Q_{WB} = 122 \text{ W}$ ,  $Q_V = 97 \text{ W}$ ,  $V_{AM} = 0.15 \text{ m/s}$ ,  $V_{TM} = 0.50 \text{ m/s}$   
 $Q_C = 124^* \text{ W}$ ,  $V_{AC} = 0.16 \text{ m/s}$ ,  $V_{TC} = 0.60 \text{ m/s}$   
 \* Extrapolated from 127 W  
 10 in. tube (+)  
 $Q_{WB} = 407 \text{ W}$ ,  $Q_C = 442 \text{ W}$ ,  $V_{AC} = 0.36 \text{ m/s}$ ,  $V_{TC} = 0.75 \text{ m/s}$

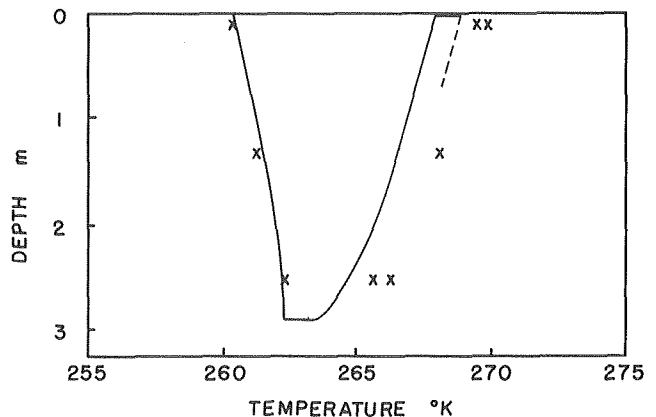


Fig. 8 Revised standard head, plastic tube  
 $Q_{WB} = 244 \text{ W}$ ,  $Q_V = 244 \text{ W}$ ,  $V_{TM} = 0.36 \text{ m/s}$   
 $Q_C = 275^* \text{ W}$ ,  $V_{TC} = 0.49 \text{ m/s}$   
 \* Extrapolated from 287 W

It should be reemphasized that detailed experimental data did not exist for comparison of local temperature and velocity profiles. In addition the analysis is deficient in two areas: the necessary neglect of the buoyant forces in the flow in the tube; and, the inability of the method to handle flow reversals in the annular section. These two deficiencies arise from the necessary use of the boundary layer relations as the governing equations.

### References

- 1 Alyeska Pipeline Service Company, *Summary-Project Description of the Trans-Alaska Pipeline System*, Aug. 1971, 64 pp.
- 2 Schindler, J. F., "Living and Working Conditions in Alaska," ASME Paper No. 73-PET-34.
- 3 Jahns, H. O., Miller, T. W., Power, L. D., Rickey, W. P., Taylor, T. P., and Wheeler, J. A., "Permafrost Protection for Pipelines," Second International Permafrost Conference, Yakutsk, USSR, July 1973.
- 4 Davis, L. P., and Perona, J. J., "Development of Free Convection Flow of a Gas in a Heated Vertical Open Tube," *International Journal of Heat and Mass Transfer*, Pergamon Press, Vol. 14, 1971, pp. 889–903.
- 5 Cebeci, T., and Smith, A. M. O., "Numerical Solution of the Turbulent Boundary-Layer Equation," Report No. DAC 33735, Douglas Aircraft Co., 1967.
- 6 Clauser, F. H., "The Turbulent Boundary-Layer," *Advances in Applied Mechanics*, H. L. Dryden and T. VonKarman, eds., Vol. IV, Academic Press, New York, 1956, p. 1.
- 7 Hinze, J. O., *Turbulence*, McGraw Hill, New York, 1959, p. 536.
- 8 Reid, R. L., and Tennant, J. S., "Annular Ring View Factors," *AIAA Journal*, Vol. 11, No. 10, 1973, pp. 1446–1448.

G. Alfano  
A. Sarnö

Istituto di Fisica Tecnica,  
Università di Napoli, Italy

# Normal and Hemispherical Thermal Emittances of Cylindrical Cavities<sup>1</sup>

*Normal and hemispherical thermal emittances of cylindrical cavities closed by a circular diaphragm have been evaluated. Diaphragms are diffuse or specular reflectors, at the cavity temperature or at a very low temperature. Results are reported and discussed.*

## Introduction

As Sparrow and Heinisch [1]<sup>2</sup> emphasized, for many applications a knowledge of the normal emittance of cavities is necessary. But up to now few numerical results were available [1-3], although many works deal with the apparent hemispherical emittance of cavities.

In this work, we evaluated the normal emittance of cylindrical cavities closed by a circular diaphragm, and we compared it with the hemispherical emittance. For the walls of the cavity, we made the following three hypotheses: (1) isothermal, (2) diffuse emitter, (3) diffuse reflector. For the internal surface of the diaphragm, we considered four cases: (i) diffuse emitter and reflector at the same temperature as the cavity walls, (ii) diffuse emitter but specular reflector at the same temperature as the cavity walls, (iii) diffuse emitter and reflector at a temperature so low as to make emission negligible, and (iv) diffuse emitter but specular reflector at a temperature so low as to make emission negligible.

The results are monochromatic values, but if the surfaces can be considered gray, they are also total values.

## Analysis

The normal thermal emittance of a cavity,  $\epsilon_n$ , can be defined as the ratio of the radiant flux arriving at the receiver from the cavity to that arriving at the receiver from a geometrically identical black-walled cavity, when the receiver,  $dA_{rec}$ , has an infinitesimal area and its normal coincides with the cavity axis (Fig. 1).

If the portion of the cavity walls which sees  $dA_{rec}$  emits and re-

flects diffusely, in terms of the wall radiosity,  $B$ , the normal thermal emittance is

$$\epsilon_n = \frac{\int_{A_s} B dA dF_{dA-dA_{rec}}}{\int_{A_s} E_b dA dF_{dA-dA_{rec}}} \quad (1)$$

with  $dA$  = infinitesimal area element of the cavity walls;

$A_s$  = portion of the cavity walls seen from  $dA_{rec}$ ;

$E_b$  = emissive power of a blackbody at the temperature of the cavity.

By the reciprocity rule of view factors, in dimensionless form for cylindrical cavities closed by circular diaphragms, equation (1) can be written

$$\epsilon_n = \frac{\int_{r=0}^{r=1} \epsilon_d(r) dF_{dA_{rec}-dA(r)} + \int_{x=x^*}^{x=L} \epsilon_d(x) dF_{dA_{rec}-dA(x)}}{\int_{r=0}^{r=1} dF_{dA_{rec}-dA(r)} + \int_{x=x^*}^{x=L} dF_{dA_{rec}-dA(x)}} \quad (2)$$

with  $\epsilon_d$  denoting the apparent thermal emittance,  $= B/\sigma T^4$ .

If the receiver does not see the cylindrical wall of the cavity, equation (2) is replaced by

$$\epsilon_n = \frac{\int_{r=0}^{r=r^*} \epsilon_d(r) dF_{dA_{rec}-dA(r)}}{\int_{r=0}^{r=r^*} dF_{dA_{rec}-dA(r)}} \quad (3)$$

In equations (2) and (3)  $x^*$  and  $r^*$  represent the coordinate value which limits the cavity surface portion seen from the receiver. By simple geometrical considerations we can write

$$x^* = H(1 - R_i)/R_i$$

and

$$r^* = R_i + LR_i/H$$

<sup>1</sup> This work was supported by the Consiglio Nazionale delle Ricerche.

<sup>2</sup> Numbers in brackets designate References at end of paper.

Contributed by the Heat Transfer Division for publication in the JOURNAL OF HEAT TRANSFER. Manuscript received by the Heat Transfer Division January 30, 1975. Paper No. 75-HT-EEEE.

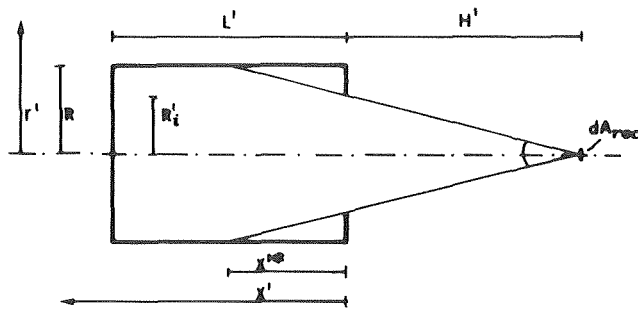


Fig. 1 Sketch illustrating nomenclature

For the view factors in equations (3) and (4), we have

$$dF_{dA_{rec}-dA(r)} = \frac{2r(L+H)^2}{[r^2 + (L+H)^2]^2} dr \quad (4)$$

$$dF_{dA_{rec}-dA(x)} = \frac{2(x+H)}{[1 + (x+H)^2]^2} dx \quad (5)$$

The hemispherical emittance of cavities, defined as the ratio of the radiant flux leaving the cavity to the radiant flux that would leave the cavity if it were a blackbody, can be evaluated by two methods. By the first one, the radiant flux leaving the cavity is evaluated as the flux crossing the opening. For cylindrical cavities it yields [1]

$$\epsilon_h = \int_0^L \epsilon_a(x) dF_{A_i-dA(x)} + \int_0^1 \epsilon_a(r) dF_{A_i-dA(r)} \quad (6)$$

with

$$dF_{A_i-dA(x)} = \left\{ + \frac{R_i^2 + x^2 + 1}{(R_i^2 + x^2 + 1)^2 - 4R_i^2} \right\}^{1/2} - 1 \left\} \frac{x}{R_i^2} dx \quad (7)$$

$$dF_{A_i-dA(r)} = \left\{ 1 - \frac{L^2 + r^2 - R_i^2}{[(L^2 + r^2 + R_i^2)^2 - 4r^2R_i^2]^{1/2}} \right\} \frac{r}{R_i^2} dr \quad (8)$$

By the second method the radiant flux leaving the cavity is evaluated, from the first law of thermodynamics, as the net rate of radiation loss from the cavity walls. For cylindrical cavities, with diffuse diaphragms at the cavity temperature, it yields [4]

$$\epsilon_h = \frac{2\epsilon}{R_i^2(1-\epsilon)} \left( \int_0^L [1 - \epsilon_a(x)] dx + \int_0^1 [1 - \epsilon_a(r)] r dr + \int_{R_i}^1 [1 - \epsilon_a(r_d)] r_d dr_d \right) \quad (9)$$

The two methods should yield the same results. In practice the first one is preferable to the second one, as the second method equation contains subtractions, which are the operation with the greatest round-off error.

From equations (2), (3), and (6) we see that the determination of  $\epsilon_n$  and  $\epsilon_h$  needs the determination of  $\epsilon_a$ . For cases (i) and (iii) it is necessary to solve the following system of integral equations [5]

$$\epsilon_a(r_d) = \frac{T_d^4}{T^4} \epsilon + (1 - \epsilon) \int_0^L \epsilon_a(x) dF_{dA(r_d)-dA(x)} + (1 - \epsilon) \int_0^1 \epsilon_a(r) dF_{dA(r_d)-dA(r)} \quad (10)$$

$$\epsilon_a(r) = \epsilon + (1 - \epsilon) \int_0^L \epsilon_a(x) dF_{dA(r)-dA(x)} + (1 - \epsilon) \int_{R_i}^1 \epsilon_a(r_d) dF_{dA(r)-dA(r_d)} \quad (11)$$

$$\epsilon_a(x_0) = \epsilon + (1 - \epsilon) \int_0^1 \epsilon_a(r) dF_{dA(x_0)-dA(r)} + (1 - \epsilon) \int_0^L \epsilon_a(x) dF_{dA(x_0)-dA(x)} + (1 - \epsilon) \int_{R_i}^1 \epsilon_a(r_d) dF_{dA(x_0)-dA(r_d)} \quad (12)$$

For cases (ii) and (iv) the integral equation system is [6]

$$\epsilon_a(r_0) = \epsilon + (1 - \epsilon) \left[ \int_0^1 \epsilon_a(r) dE_{dA(r_0)-dA(r)} + \int_0^L \epsilon_a(x) dE_{dA(r_0)-dA(x)} + \epsilon_d \frac{T_d^4}{T^4} F_{dA(r_0)-A_d} \right] \quad (13)$$

$$\epsilon_a(x_0) = \epsilon + (1 - \epsilon) \left[ \int_0^L \epsilon_a(x) dE_{dA(x_0)-dA(x)} + \int_0^1 \epsilon_a(r) dE_{dA(x_0)-dA(r)} + \epsilon_d \frac{T_d^4}{T^4} F_{dA(x_0)-A_d} \right] \quad (14)$$

with  $E$ , the exchange factor, defined as the fraction of the energy emitted diffusely by a certain surface arriving at a second surface both directly and by all possible intervening specular reflections

## Nomenclature

$A$ = surface area, $m^2$	$R_i$ = dimensionless radius of the diaphragm opening, $= R_i'/R$	dimensionless
$B$ = radiosity, $W/m^2$	$r'$ = radial coordinate, $m$	$\rho$ = reflectance, dimensionless
$E$ = exchange factor, dimensionless	$r$ = dimensionless radial coordinate, $= r'/R$	$\sigma$ = Stefan-Boltzmann constant, $W/m^2 \cdot K^4$
$E$ = emissive power, $W/m^2$	$T$ = temperature, $^\circ K$	
$F$ = view factor, dimensionless	$x'$ = axial coordinate, $m$	
$G$ = irradiation, $W/m^2$	$x$ = dimensionless axial coordinate, $= x'/R$	
$H'$ = distance of the receiver from the cavity opening, $m$	$\epsilon$ = thermal emittance, dimensionless	
$H$ = dimensionless distance of the receiver from the cavity opening, $= H'/R$	$\epsilon_a$ = apparent thermal emittance, dimensionless	
$L'$ = cavity length, $m$	$\epsilon_h$ = cavity hemispherical emittance, dimensionless	
$L$ = dimensionless cavity length, $= L'/R$	$\epsilon_n$ = cavity normal emittance, dimensionless	
$R$ = cavity radius, $m$	$\theta$ = temperature ratio, $= T_d/T$ , dimensionless	
$R_i'$ = radius of the diaphragm opening, $m$		

## Subscripts

$b$ = blackbody
$d$ = diaphragm
$i$ = diaphragm opening
$o$ = typical value
$rec$ = receiver surface
$s$ = portion of the cavity surface seen from the receiver surface

## Superscripts

$*$ = particular value
------------------------

Table 1 Normal and hemispherical thermal emittances of cylindrical cavities closed by a diffuse reflector diaphragm—comparison with results of other authors

L	ε	Cavity		ε <sub>h</sub>				ε <sub>n</sub>					
		R <sub>i</sub>	θ <sub>d</sub>	[1]	[9]	[2]	[3]	This work	[1]	[2]	[3]	This work	
2	0.50	0.50	1	—	0.952	—	—	0.953	—	—	—	0.953	
			0	—	0.884	—	—	0.884	—	—	—	0.893	
		0.75	1	—	0.891	—	—	0.892	—	—	—	0.906	
			0	—	0.854	—	—	0.853	—	—	—	0.876	
		0.70	0.50	1	0.809	0.811	—	0.808	0.810	0.858	—	0.858	0.858
				0	—	0.974	—	—	0.977	—	—	—	0.978
	0.75		1	—	0.932	—	—	0.934	—	—	—	0.941	
			0	—	0.948	—	—	0.948	—	—	—	0.956	
	0.90	0.50	1	0.904	0.905	—	0.904	0.904	0.934	—	0.933	0.933	
			0	—	0.994	0.994	—	0.994	—	0.994	—	0.994	
		0.75	1	—	0.978	—	—	0.978	—	—	—	0.981	
			0	—	0.986	—	—	0.984	—	—	—	0.988	
1		1	—	0.972	0.972	0.972	0.972	0.976	—	—	0.981		
		0	—	0.978	—	—	0.976	—	—	—	0.981		
4	0.50	0.50	1	—	0.960	—	—	0.961	—	—	—	0.985	
			0	—	0.903	—	—	0.903	—	—	—	0.965	
		0.75	1	—	0.909	—	—	0.910	—	—	—	0.969	
			0	—	0.876	—	—	0.876	—	—	—	0.958	
		0.70	0.50	1	0.833	0.833	—	0.833	0.835	0.950	—	0.950	0.949
				0	—	0.980	—	—	0.981	—	—	—	0.994
	0.75		1	—	0.942	—	—	0.943	—	—	—	0.982	
			0	—	0.956	—	—	0.955	—	—	—	0.987	
	0.90	0.50	1	0.914	0.914	—	0.914	0.915	0.978	—	0.978	0.978	
			0	—	0.996	0.996	—	0.994	—	0.998	—	0.998	
		0.75	1	—	0.980	—	—	0.981	—	—	—	0.994	
			0	—	0.991	—	—	0.987	—	—	—	0.996	
		1	1	—	0.980	—	—	0.979	—	—	—	0.994	
			0	0.974	0.974	0.974	0.975	0.974	0.994	0.995	0.994	0.994	
	8	0.50	0.50	1	—	—	—	—	0.962	—	—	—	0.997
				0	—	—	—	—	0.906	—	—	—	0.992
			0.75	1	—	—	—	—	0.912	—	—	—	0.993
				0	—	—	—	—	0.879	—	—	—	0.990
0.70			0.50	1	0.836	—	—	0.837	0.835	0.989	—	0.988	0.989
				0	—	—	—	—	0.981	—	—	—	0.998
		0.75	1	—	—	—	—	0.944	—	—	—	0.996	
			0	—	—	—	—	0.956	—	—	—	0.997	
0.90		0.50	1	0.915	—	—	0.915	0.915	0.995	—	0.995	0.995	
			0	—	—	0.996	—	0.995	—	0.999	—	0.999	
		0.75	1	—	—	—	—	0.981	—	—	—	0.998	
			0	—	—	—	—	0.987	—	—	—	0.999	
	1	1	—	—	—	—	0.979	—	—	—	0.998		
		0	0.975	—	0.975	0.975	0.974	0.999	0.998	0.998	0.998		

Table 2 Normal and hemispherical thermal emittances of cylindrical cavities closed by a specular reflector diaphragm with ε<sub>d</sub> = 0.1

Cavity				ε <sub>h</sub>	ε <sub>n</sub>	Cavity				ε <sub>h</sub>	ε <sub>n</sub>
L	ε	R <sub>i</sub>	θ <sub>d</sub>			L	ε	R <sub>i</sub>	θ <sub>d</sub>		
2	0.50	0.50	1	0.949	0.950	4	0.70	0.75	1	0.955	0.986
			0	0.935	0.939				0	0.951	0.985
		0.75	1	0.889	0.903		0.90	0.50	1	0.994	0.998
	0	0.881	0.897	0	0.993	0.998					
	0.70	0.50	1	0.977	0.977	0.75		1	1	0.987	0.996
			0	0.970	0.972		0		0.986	0.988	
0.75		1	0.947	0.955							
0.90	0.50	1	0	0.944	0.953	8	0.50	0.50	1	0.961	0.996
			1	0.994	0.994				0	0.949	0.996
		0	0.992	0.992	0.75		1	1	0.911	0.992	
	1	0.985	0.988	0		0.904		0.992			
	0	0.984	0.987	0.70		0.50	1	0.981	0.998		
	0	—	—		0		0.975	0.998			
4	0.50	0.50	1		0.959	0.985	0.75	1	1	0.956	0.997
			0	0.948	0.981	0			0.952	0.996	
		0.75	1	0.908	0.968	0.90		0.50	1	0.995	0.999
	0	0.901	0.966	0	0.993		0.999				
	0.70	0.50	1	0.981	0.994		0.75	1	1	0.987	0.999
			0	0.975	0.992	0			0.986	0.999	

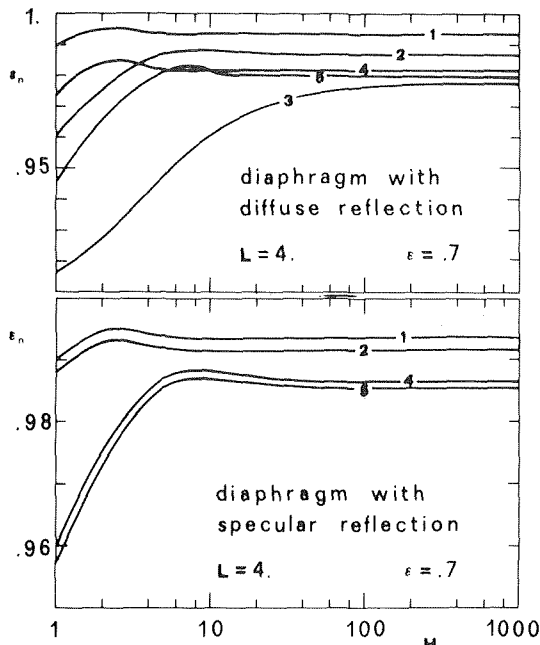


Fig. 2 Normal thermal emittance for  $L = 4$  and  $\epsilon = 0.7$ —upper portion (diaphragm with diffuse reflection); lower portion (diaphragm with specular reflection): (1)  $R_i = 0.5$ ,  $\theta_d = 1$ ; (2)  $R_i = 0.75$ ,  $\theta_d = 1$ ; (3)  $R_i = 1$ ; (4)  $R_i = 0.5$ ,  $\theta_d = 0$ ; (5)  $R_i = 0.75$ ;  $\theta_d = 0$

[7]. In equations (10), (13), and (14) the ratio  $T_d^4/T^4$  takes into account the diaphragm temperature.

### Results and Discussion

Using an electronic digital computer, we solved the integral equation systems, equations (10)–(12) and (13)–(14), by the successive approximations method. The numerical procedure used is reported in a previous work [8].

We evaluated  $\epsilon_n$  and  $\epsilon_h$  for  $L = 2, 4$ , and  $8$ ,  $\epsilon = 0.5, 0.7$ , and  $0.9$ ,  $R_i = 0.5, 0.75$ , and  $1$ . For cases (ii) and (iv), i.e., when the diaphragm is a specular reflector, we used a diaphragm emittance of  $0.1$ . The computer program allows one to obtain results rapidly for any other set of values of the parameters.

Fig. 2 shows the values of  $\epsilon_n$  obtained for  $L = 4$  and  $\epsilon = 0.70$  (for every other case we found similar curves). The normal emittance,  $\epsilon_n$ , is plotted as a function of the dimensionless distance,  $H$ , of the receiver from the cavity opening. The upper portion is relative to a

diffuse reflector diaphragm; the lower portion is relative to a specular reflector diaphragm.

From the figure it is seen that for a cavity with a diaphragm  $\epsilon_n$  increases, has a maximum and decreases tending toward an asymptotic value as  $H$  increases. The existence of a maximum depends from the  $\epsilon_a$  function [5], which has a minimum on the cylindrical surface and has the highest values at the corner near the bottom. So,  $\epsilon_n$  has the maximum value at that value of  $H$  at which the receiver sees this corner very well, without seeing the cylindrical surface portions with the lowest values of  $\epsilon_a$ .

For cavities with diaphragm the region in which  $\epsilon_n$  is practically constant begins at a value of  $H$  lower than is the case without diaphragm, generally at  $H \approx 20$ .

From Fig. 2 it is seen also that, for specular reflector diaphragms, the curves for  $\theta_d = 1$  and  $\theta_d = 0$  are parallel and nearly coincident. The reason is that for these cavities  $\epsilon_a$  is nearly independent of  $\theta_d$  (see reference [6]).

In Tables 1 and 2, we list our values of  $\epsilon_n$  and  $\epsilon_h$ . In Table 1, we list also values of  $\epsilon_n$  and  $\epsilon_h$  obtained by other authors. Our values of  $\epsilon_n$  are evaluated at  $H = 1000$ . Values of Bedford [2] and Sparrow [9] are obtained from their figures. There is evident a very close agreement between our values and those of the other authors.

The tables show that the difference ( $\epsilon_n - \epsilon_h$ ) increases with  $L$  and with  $R_i$  and, however, that in many cases, using  $\epsilon_h$  instead of  $\epsilon_n$ , a great error is made (e.g., for  $L = 8$ ,  $R_i = 1$ , and  $\epsilon = 0.50$  this error is 15 percent).

The tables show also that for  $\theta_d = 1$  the  $\epsilon_n$  values are almost independent of the diaphragm reflection characteristics.

### References

- 1 Sparrow, E. M., and Heinsch, R. P., "The Normal Emittance of Circular Cylindrical Cavities," *Appl. Opt.*, Vol. 9, 1970, pp. 2569–2572.
- 2 Bedford, R. E., and Ma, C. K., "Emissivities of Diffuse Cavities: Isothermal and Nonisothermal Cones and Cylinders," *J. Opt. Soc. Am.*, Vol. 64, 1974, pp. 339–349.
- 3 Chandos, R. J., and Chandos, R. E., "Radiometric Properties of Isothermal, Diffuse Wall Cavity Sources," *Appl. Opt.*, Vol. 13, 1974, pp. 2142–2151.
- 4 Sparrow, E. M., Albers, L. U., and Eckert, E. R. G., "Thermal Radiation Characteristics of Cylindrical Enclosures," *JOURNAL OF HEAT TRANSFER, TRANS. ASME, Series C*, Vol. 84, 1962, pp. 73–81.
- 5 Alfano, G., "Apparent Thermal Emittance of Cylindrical Enclosures With and Without Diaphragms," *International Journal of Heat and Mass Transfer*, Vol. 15, 1972, pp. 2671–2674.
- 6 Alfano, G., "Apparent Thermal Emittance of Cylindrical Enclosures with High Reflectance Diaphragms," *Proceedings of the 5th International Heat Transfer Conference*, Vol. I, Tokyo 1974, pp. 31–35.
- 7 Sparrow, E. M., and Cess, R. D., *Radiation Heat Transfer*, Brooks/Cole Publ. Co., 1966, pp. 138–149.
- 8 Alfano, G., "Emittanza Termica di Cavità Cilindriche parzialmente Chiuse da Diaframmi," *La Termotecnica*, Vol. 24, 1970, pp. 215–223.
- 9 Sparrow, E. M., Heinsch, R. P., and Shamsundar, N., "Apparent Hemispherical Emittance of Baffled Cylindrical Cavities," *JOURNAL OF HEAT TRANSFER, TRANS. ASME, Series C*, Vol. 96, 1974, pp. 112–114.

A. Dayan  
Graduate Student.

C. L. Tien  
Professor.

Department of Mechanical Engineering,  
University of California,  
Berkeley, Calif.  
Fellow, ASME

# Heat Transfer in a Gray Planar Medium With Linear Anisotropic Scattering

*Radiative transfer in an absorbing and linearly-anisotropic scattering gray medium is analyzed. The medium is confined between plane parallel, gray, diffuse walls and contains uniform heat generation. The problem is formulated in terms of coupled integral equations with the intensity-moments as the unknown variables. The set of equations is solved both numerically and in closed form. The closed-form solution consists of exact limiting solutions and approximate general solutions obtained by the kernel-substitution method. The case of combined radiation and conduction is also treated. The results reveal clearly the effects of anisotropic scattering on important characteristics such as heat flux and incident radiant energy per unit area. The approximate closed-form solutions which predict quite well these effects are very simple and convenient to use for engineering calculations.*

## Introduction

This work is concerned with the calculation of radiant heat transfer in absorbing and anisotropically scattering materials. Attention is also given to the case of combined conductive and radiative transfer with anisotropic scattering. The results of this investigation are applicable in practical engineering problems of energy transport in porous materials, powder insulations, rocket exhaust plumes, luminous flames, and clouds of particles. In particular, the simple, approximate solutions obtained in this work should be very convenient to use for engineering calculations.

Examination of the radiative transfer literature reveals that most of the previous studies have been carried out under the simplifying assumption of isotropic scattering [1, 2],<sup>1</sup> largely because of the complexity involved in anisotropic scattering. Problems involving anisotropic scattering have been addressed mainly after specifying the temperature distributions within the media, thereby, eliminating any consideration of the energy equation (see, for instance, [3, 4, 5]). For problems involving combined modes of energy transport, however, the coupling between the radiative transfer equation with anisotropic scattering and the energy equation must be considered. For the case of simultaneous conductive and radiative heat transfer with anisotropic scattering, Larkin and

Churchill [6] linearized the temperature profile and used the two-flux model to calculate efficiency of porous insulation. More recently, Bergquam and Seban [7] also used the two-flux model and showed numerically that strong forward or backward anisotropic scattering could cause a maximum variation of 20 percent in radiant heat flux. Apparently, no existing work provides a comprehensive assessment of anisotropic-scattering effects. Such information has a qualitative and quantitative importance, and is essential for justifying the use of the isotropic-scattering assumption.

The purpose of the present work is to study the effects of anisotropic scattering and to develop a simple solution for calculating radiative transfer within a linearly-anisotropic scattering planar medium. The analytical description of linear anisotropic scattering is chosen here on account of its mathematical simplicity and its ability to represent the conditions of strong forward and backward scattering [2, 5]. Specific consideration is given to a gray medium in radiative equilibrium, and a gray medium containing uniform heat generation. Each case is solved twice, once numerically and once approximately in closed form. Exact limiting solutions for the medium in radiative equilibrium are also presented. The numerical results are used to assess the accuracy of the approximate closed-form solution. The study is then extended to treat the situation of combined radiation with conduction. The approximate closed-form solution obtained indicates rather limited effects of anisotropic scattering.

## General Formulation

The physical system chosen for this investigation is a uniform plane parallel gray medium confined within gray and diffuse walls.

<sup>1</sup> Numbers in brackets designate References at end of paper.

Contributed by the Heat Transfer Division for publication in the JOURNAL OF HEAT TRANSFER. Manuscript received at ASME Headquarters February 18, 1975. Paper No. 75-HT-HHH.



$$i^+(0, \mu) = \frac{B_1}{\pi}, \quad i^-(\tau_0, \mu) = \frac{B_2}{\pi} \quad (10)$$

where  $\tau_0$  is the optical thickness of the medium. The radiosities  $B_1$  and  $B_2$  represent the radiant heat fluxes leaving the boundary surfaces toward the medium [1]. Equations (6), (9), and (10) have the following formal solution

$$i^+ = \frac{B_1}{\pi} \exp\left(-\frac{\tau}{\mu}\right) + \int_0^\tau \frac{S(t, \mu)}{\mu} \exp\left(-\frac{\tau-t}{\mu}\right) dt, \quad 1 \geq \mu \geq 0 \quad (11)$$

$$i^- = \frac{B_2}{\pi} \exp\left(\frac{\tau_0 - \tau}{\mu}\right) - \int_\tau^{\tau_0} \frac{S(t, \mu)}{\mu} \exp\left(\frac{t - \tau}{\mu}\right) dt, \quad -1 \leq \mu \leq 0$$

The intensities described by equations (11) are substituted into equations (7) and (8), and the integration is carried out to yield

$$G(\tau) = \frac{\dot{q}}{\beta} + (2B_1 - \frac{\dot{q}}{2\beta}) E_2(\tau) + (2B_2 - \frac{\dot{q}}{2\beta}) E_2(\tau_0 - \tau) + \frac{1}{2} \int_0^{\tau_0} G(t) E_1(|\tau - t|) dt + \frac{\omega_0 x}{2} \int_0^{\tau_0} q(t) E_2(|\tau - t|) \text{sign}(\tau - t) dt \quad (12)$$

and

$$q(\tau) = (2B_1 - \frac{\dot{q}}{2\beta}) E_3(\tau) - (2B_2 - \frac{\dot{q}}{2\beta}) E_3(\tau_0 - \tau) + \frac{1}{2} \int_0^{\tau_0} G(t) E_2(|\tau - t|) \text{sign}(\tau - t) dt + \frac{\omega_0 x}{2} \int_0^{\tau_0} q(t) E_3(|\tau - t|) dt \quad (13)$$

where  $E_n$  denote the exponential integrals defined by

$$E_n(t) = \int_0^1 \mu^{n-2} \exp\left(-\frac{t}{\mu}\right) d\mu, \quad n = 1, 2, 3, \dots \quad (14)$$

These integrals have the property

$$\frac{dE_n(t)}{dt} = -E_{n-1}(t) \quad (15)$$

Equations (12) and (13) are coupled integral equations for  $G(\tau)$  and  $q(\tau)$ . The solution determines the source function which is necessary and sufficient for the determination of the radiant intensity as given by equation (11). Recognizing their importance, attention will be focused on the solution of these two equations. Note also that once the  $G$ -function is found, the temperature distribution within the medium can be easily obtained by utilizing equation (3).

## Methods of Solution

**Numerical Solution.** Equations (12) and (13) have been solved numerically. The computation scheme is essentially reiterative in nature. This method is quite successful for linear problems, and is fairly inexpensive for short and moderate optical depth ( $\tau_0 \leq 3$ ). The initial values of  $G(\tau)$  and  $q(\tau)$  are those obtained from the approximate analytical solution (to be presented later). In each iteration, new values of the functions are calculated based on their previous values. The numerical results are used for assessing the accuracy of the approximate solution. The results reduce to the exact solution for isotropic scattering obtained by Heaslet and Warming [8] (including the case of uniform heat source distribution).

**Limiting Solutions for Radiative Equilibrium.** In this section, solutions for the optically thin and thick media in radiative equilibrium ( $\dot{q} = 0$ ) are developed. These solutions are later used to improve the approximate results. Treating first the optically thin limit ( $\tau_0 \rightarrow 0$ ), the exponential integrals can be expanded as

$$E_2(t) = 1 + 0(t), \quad (t \rightarrow 0) \quad (16)$$

$$E_3(t) = \frac{1}{2} - t + 0(t^2), \quad (t \rightarrow 0) \quad (16)$$

Combining equations (12), (13), and (16), and noting that the heat flux is uniform within the medium, yield a simple pair of uncoupled integral equations for which the solution is

$$G(\tau) = 2B_1 + 2B_2 + 0(\tau_0), \quad (\tau_0 \rightarrow 0) \quad (17)$$

$$q = \frac{B_1 - B_2}{1 + (1 - \frac{\omega_0 x}{4}) \tau_0} + 0(\tau_0^2), \quad (\tau_0 \rightarrow 0) \quad (18)$$

where the expansion  $(1 - \tau_0)^{-1} = 1 + \tau_0 + 0(\tau_0^2)$  has been used.

In the optically thick limit ( $\tau_0 \rightarrow \infty$ ), the radiative heat transfer is like a diffusion process, and therefore can be described by differential equations. Consider the region which is away from the boundaries, that is

$$\tau \gg 1, \quad (\tau_0 - \tau) \gg 1 \quad (19)$$

The unknown functions are expanded around  $\tau$  in a Taylor series giving

$$G(t) = G(\tau) + \frac{dG(\tau)}{d\tau} (t - \tau) + \frac{d^2G(\tau)}{d\tau^2} \frac{(t - \tau)^2}{2} + \dots, \quad (|t - \tau| \rightarrow 0) \quad (20)$$

$$q(t) = q \quad (21)$$

Combining equations (19)–(21) with (12) and (13) yields

$$G(\tau) = G(\tau) \int_0^\infty E_1(z) dz + \frac{d^2G(\tau)}{d\tau^2} \int_0^\infty z^2 E_1(z) dz \quad (22)$$

$$q = \omega_0 x q \int_0^\infty E_3(z) dz - \frac{dG(\tau)}{d\tau} \int_0^\infty z E_2(z) dz \quad (23)$$

where  $z \equiv |\tau - t|$ . Integrating equations (22) and (23) results in

$$\frac{d^2G(\tau)}{d\tau^2} = 0 \quad (24)$$

$$q = -\frac{1}{3 - \omega_0 x} \frac{dG(\tau)}{d\tau} \quad (25)$$

The solution of equations (24) and (25), which also satisfies equations (12) and (13) at the optically thick limit, is

$$G(\tau) = 4B_1 + (4B_2 - 4B_1) \frac{\tau}{\tau_0} + 0(\tau_0^{-1}), \quad (\tau_0 \rightarrow \infty) \quad (26)$$

$$q = \frac{B_1 - B_2}{(\frac{3 - \omega_0 x}{4}) \tau_0} + 0(\tau_0^{-2}), \quad (\tau_0 \rightarrow \infty) \quad (27)$$

**Approximate Solutions.** The approximate analytical solutions are derived by employing the kernel substitution method (see, for instance [1, 3]). The following exponential-integral substitution is introduced

$$E_1(t) \approx 2 \exp(-2t) \quad (28)$$

In the literature, other kernel approximations have also been suggested. Different approximations lead to better results in the optically thin or thick limits. An excellent discussion on the various possible kernel substitutions is given by Wang [3].

Equation (28) is substituted in equation (15) to obtain the approximations for  $E_2$  and  $E_3$ . Making the corresponding kernel substitutions, the governing equations (12) and (13) take the form

$$G(\tau) = \frac{\dot{q}}{\beta} + (2B_1 - \frac{\dot{q}}{2\beta}) \exp(-2\tau) + (2B_2 - \frac{\dot{q}}{2\beta}) \exp[-2(\tau_0 - \tau)] + \int_0^{\tau_0} G(t) \exp(-2|\tau - t|) dt + \frac{\omega_0 x}{2} \int_0^{\tau_0} q(t) \exp(-2|\tau - t|) \text{sign}(\tau - t) dt \quad (29)$$

$$q(\tau) = (B_1 - \frac{\dot{q}}{4\beta}) \exp(-2\tau) - (B_2 - \frac{\dot{q}}{4\beta}) \exp[-2(\tau_0 - \tau)] \quad (30)$$

$$\begin{aligned}
& + \frac{1}{2} \int_0^{\tau_0} G(t) \exp(-2|\tau - t|) \text{sign}(\tau - t) dt \\
& + \frac{\omega_0 x}{4} \int_0^{\tau_0} q(t) \exp(-2|\tau - t|) dt \quad (30)
\end{aligned}$$

Differentiating once equations (29) and (30) allows the elimination of the unknown integrals in the resulting equations. Then differentiating again the results leads to

$$\frac{d^2 G(\tau)}{d\tau^2} = \frac{\dot{q}}{\beta} (\omega_0 x - 4) \quad (31)$$

$$\frac{d^2 q(\tau)}{d\tau^2} = 0 \quad (32)$$

The solution of this pair of equations is

$$G(\tau) = C_1 + C_2 \tau + \frac{\dot{q}}{2\beta} (\omega_0 x - 4) \quad (33)$$

$$q(\tau) = A_1 + A_2 \tau \quad (34)$$

For the evaluation of the coefficients  $A_j$  and  $C_j$ , the functions  $G(\tau)$  and  $q(\tau)$  must be substituted into the integral equations (29) and (30), which contain information on the boundaries. Doing this results in two equations of the common form

$$\sum_n u_n(A_j, C_j) \psi_n(\tau) = 0 \quad (35)$$

where  $u_n(A_j, C_j)$  are coefficients dependent on  $A_j$  and  $C_j$ , and  $\psi_n(\tau)$  are functions of  $\tau$ . For equation (35) to hold, all  $u_n$ 's must vanish. This gives four algebraic equations from which all  $A_j$  and  $C_j$  are determined. Substituting the resultant coefficients into equations (33) and (34) yields

$$\begin{aligned}
G(\tau) = 2B_1 + 2B_2 + \frac{2B_1 - 2B_2}{\left(\frac{\omega_0 x}{4} - 1\right)^{-1} - \tau_0} (2\tau - \tau_0) \\
+ \frac{\dot{q}}{\beta} \tau_0 - \frac{\dot{q}}{\beta} \left(\frac{\omega_0 x}{2} - 2\right) \tau (\tau_0 - \tau) \quad (36)
\end{aligned}$$

$$q(\tau) = \frac{B_1 - B_2}{1 + \left(1 - \frac{\omega_0 x}{4}\right) \tau_0} + \frac{\dot{q}}{2\beta} (2\tau - \tau_0) \quad (37)$$

Equations (36) and (37) constitute the full approximate solution of the problem. However, it is inconvenient to have them in this form, as they do not reveal clearly the functional importance of the various parameters. The fact that the governing equations are lin-

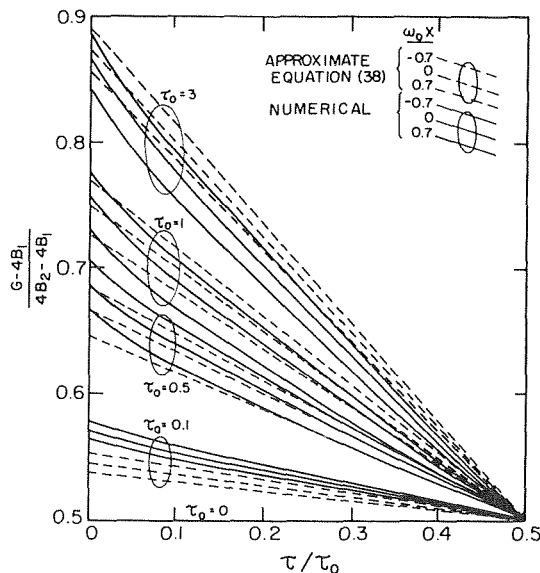


Fig. 2 Effect of anisotropic scattering on the  $G$ -function for radiative equilibrium

ear permits the use of the superposition technique. Thus, the problem is now decomposed to its elementary cases, and the results are presented in the following.

## Results and Discussion

**Radiative Equilibrium.** Attention is now directed toward a medium in radiative equilibrium. As already mentioned, this medium is free of heat sources and radiation is the predominant mode of heat transfer. The solution of this problem describes the radiant energy transport within the medium due to the incident radiosities at the boundaries.

The appropriate dimensionless parameters for this case are derived from equations (36) and (37). They are

$$\frac{G(\tau) - 4B_2}{4B_1 - 4B_2} = \frac{1}{2} + \frac{1}{1 + \left[\left(1 - \frac{\omega_0 x}{4}\right) \tau_0\right]^{-1}} \left(\frac{1}{2} - \frac{\tau}{\tau_0}\right) \quad (38)$$

$$\frac{q}{B_1 - B_2} = \frac{1}{1 + \left(1 - \frac{\omega_0 x}{4}\right) \tau_0} \quad (39)$$

The dimensionless approximate  $G$ -function as given in equation (38) is compared to its numerical result in Fig. 2. The approximation linearizes the function within the medium, and satisfies the optically thin and thick limits, equations (17) and (26). The dimensionless radiant heat flux is given in equation (39), and is compared to its numerical results in Table 1. The anisotropic-scattering effects are predicted quite accurately. The results show that strong forward scattering increases the magnitude of the heat flux. These effects are pronounced in moderate optical thickness and strong anisotropic scattering ( $|\omega_0 x| \rightarrow 1$ ). They are negligible in the optically thin and thick limits. The heat flux is uniform within the medium, due to the absence of internal heat sources.

The radiant heat flux is the most important quantity of the problem, and improvement of the approximate analytical representation is desirable. This is possible with the results of the limiting solutions given by equations (18) and (27). The heat flux as given by equation (39) satisfies the optically thin limit but does not fully satisfy the optically thick limit. By matching the two limits, the following expression is proposed

$$\frac{q}{B_1 - B_2} = \frac{1}{1 + \left(\frac{3}{4} - \frac{\omega_0 x}{4}\right) \tau_0} \quad (40)$$

Inspection of Table 1 reveals that equation (40) is more effective than equation (39) for predicting radiant heat flux.

**Uniform Heat Generation Without Solid Boundaries.** Consideration is now given to a medium free of solid boundaries and containing a uniform source of heat generation. The appropriate approximate solution of the radiative transfer problem is derived from equations (36) and (37) giving

$$\frac{G(\tau)}{\dot{q}L} = 1 + 2\left(1 - \frac{\omega_0 x}{4}\right) \tau \left(1 - \frac{\tau}{\tau_0}\right) \quad (41)$$

Table 1 Effect of anisotropic scattering on the dimensionless heat flux  $q/(B_1 - B_2)$  for radiative equilibrium

$\tau_0$	$\omega_0 x / 4 = -0.7$			$\omega_0 x / 4 = 0$			$\omega_0 x / 4 = 0.7$		
	Equ. 39	Equ. 40	Exact	Equ. 39	Equ. 40	Exact	Equ. 39	Equ. 40	Exact
0.1	0.895	0.915	0.921	0.909	0.930	0.916	0.924	0.946	0.931
0.5	0.630	0.684	0.663	0.667	0.727	0.704	0.708	0.777	0.750
1	0.460	0.515	0.505	0.500	0.571	0.553	0.548	0.635	0.611
3	0.221	0.265	0.260	0.250	0.308	0.301	0.288	0.367	0.358
10	0.078	0.098	0.091	0.091	0.118	0.109	0.108	0.148	0.148

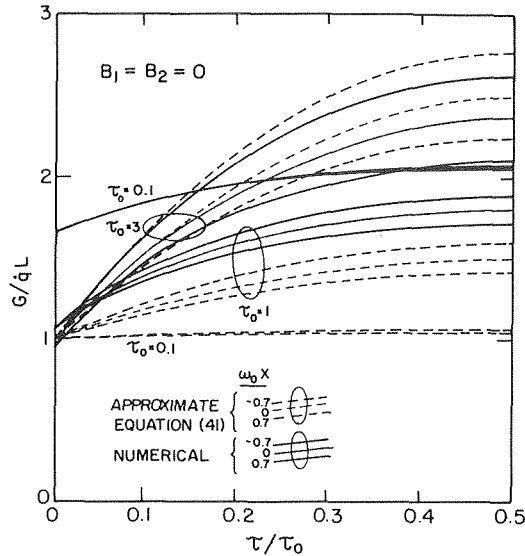


Fig. 3 Effect of anisotropic scattering on the  $G$ -function for uniform heat generation  $\dot{q}$

$$\frac{q(\tau)}{\dot{q}L} = \frac{\tau}{\tau_0} - \frac{1}{2} = \frac{y}{L} - \frac{1}{2} \quad (42)$$

where  $L$  denotes the geometrical thickness of the medium. Equation (42) describes the heat flux within the medium and can be derived from a simple energy balance on a control volume. It increases linearly from zero at the center of the layer to  $\dot{q}L/2$  at the edge of the layer. Equation (41) represents the dimensionless  $G$ -function. From the comparison with the numerical calculation given in Fig. 3, it is apparent that the approximation is satisfactory at moderate optical depths, and predicts quite accurately the anisotropic-scattering effects. At a given optical thickness, stronger backward scattering ( $\omega_0 x \rightarrow -1$ ) increases the  $G$ -function.

In general, the anisotropic scattering effects can be explained briefly as follows: radiant energy originating at a point inside the medium or at a boundary is more easily transmitted into the surroundings when a proportionately greater forward scattering exists. Therefore, the heat flux from such a point is increased, and the incident energy per unit area at this point is decreased.

**Combined Radiation and Conduction.** In many physical situations radiation and conduction are simultaneously important mechanisms of heat transfer. Here the analysis is restricted to a planar medium between black walls. According to the adopted notation,  $\dot{q}$  will represent the heat generation per unit volume due to conduction

$$\dot{q} = k \frac{d^2 T}{dy^2} \quad (43)$$

where  $k$  is the thermal conductivity and  $T$  the temperature. The governing equations for this case are equations (2), (3), and (43). The equations form a complex nonlinear set. An approximate analytical solution is derived by using the integral method. The technique consists of the two steps: first, the temperature distribution within the medium is approximated by a polynomial, and then the coefficients of the polynomial are found by satisfying the boundary conditions and the integrated governing equations. Due to conduction, no temperature jumps exist near the boundaries. Therefore, the appropriate boundary conditions are

$$T_{(\tau=0)} = T_1, \quad T_{(\tau=\tau_0)} = T_2 \quad (44)$$

It is assumed that the temperature profile within the medium can be represented reasonably well by a second-order polynomial. According to equation (43) this profile gives a uniform heat generation throughout the medium and allows the use of the radiative

heat transfer results previously obtained. This entire procedure can be interpreted physically as a search for the mean energy interchange between the two modes of heat transfer per unit volume.

Applying the boundary conditions given in equation (44) to evaluate two of the polynomial coefficients gives

$$T = T_1 + \left( \frac{T_2 - T_1}{\tau_0} - M\tau_0 \right) \tau + M\tau^2 \quad (45)$$

in which  $M$  is a constant left to be determined by satisfying the integrated energy equation. Substituting equations (43) and (45) into equation (3) (note that for black walls  $B_1 = \sigma T_1^4$  and  $B_2 = \sigma T_2^4$ ) and integrating the resultant equations from  $\tau = 0$  to  $\tau = \tau_0$  yield the following dimensionless equation

$$\frac{2\tau_0}{1 - \omega_0} \frac{\bar{M}}{N} + \frac{\tau_0}{2} (1 + \bar{T}_2^4) + \frac{2M}{N} [\tau_0^2 + (1 - \frac{\omega_0 x}{4}) \frac{\tau_0^3}{3}] = \sum_{n=0}^4 \alpha_n \bar{M}^n \quad (46)$$

where the following definitions are made

$$\bar{M} \equiv \frac{M}{T_1}, \quad \bar{T} \equiv \frac{T}{T_1} \quad (47)$$

$$N \equiv \frac{4\sigma T_1^4}{k\beta T_1}, \quad \bar{T}_{2,1} \equiv \frac{T_2 - T_1}{T_1} = \bar{T}_2 - 1$$

and

$$\begin{aligned} \alpha_0 &= \tau_0 (1 + 2\bar{T}_{2,1} + 2\bar{T}_{2,1}^2 + \bar{T}_{2,1}^3 + \frac{1}{5}\bar{T}_{2,1}^4) \\ \alpha_1 &= -\tau_0^3 \left( \frac{2}{3} + \bar{T}_{2,1} + \frac{3}{5}\bar{T}_{2,1}^2 + \frac{2}{15}\bar{T}_{2,1}^3 \right) \\ \alpha_2 &= \tau_0^5 \left( \frac{1}{5} + \frac{1}{5}\bar{T}_{2,1} + \frac{2}{35}\bar{T}_{2,1}^2 \right) \\ \alpha_3 &= -\tau_0^7 \left( \frac{1}{35} + \frac{1}{70}\bar{T}_{2,1} \right) \\ \alpha_4 &= \tau_0^9 \left( \frac{1}{630} \right) \end{aligned} \quad (48)$$

Equation (46) is a fourth-order polynomial of  $\bar{M}$ . Its four exact roots can be calculated by a closed-form expression [9]. That calculation is quite cumbersome, and instead a solution is presented which gives easily and quite accurately the correct root. The development of this solution is based on the idea that when conduction is significant, the temperature distribution within the medium cannot be too far from linear. Thus, the value of  $\bar{M}$  (which indicates the curvature of the temperature profile) is small. As a result, only the first two terms in the summation in equation (46) need to

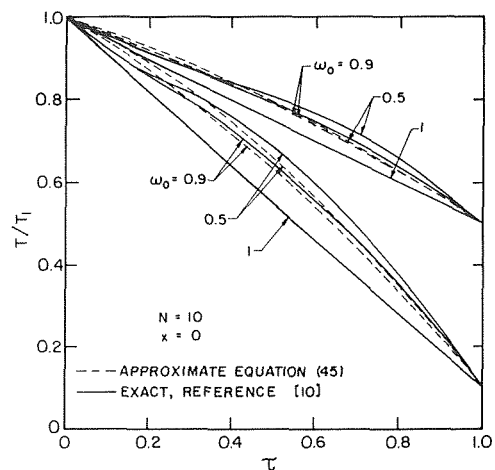


Fig. 4 Effect of albedo on the temperature distribution for combined radiation and conduction

be retained. This gives

$$\bar{M} = - \frac{1 + \bar{T}_2^4 - \frac{2\alpha_0}{\tau_0}}{(1 - \omega_0)^{-1} + \tau_0 + (1 - \frac{\omega_0^{\lambda}}{4}) \frac{\tau_0^2}{3} - \frac{\alpha_1 N}{2\tau_0}} \frac{N}{4} \quad (49)$$

The coefficient  $\bar{M}$  determines the temperature distribution within the medium as expressed in equation (45). This is the complete information needed to solve the problem. The conductive heat flux is simply  $q_c = -k(dT/dy)$  and the radiative heat flux  $q_r$  is obtained by using equations (37) and (43) thus yielding the total heat flux  $q = q_r + q_c$ .

The temperature profile of a medium in which conduction and radiation are of the same order of magnitude ( $N = 10$ ) is illustrated in Fig. 4. In the calculation process, equation (46) was solved and  $\alpha_2$ ,  $\alpha_3$ , and  $\alpha_4$  were found negligible, a fact that strengthens the validity of equation (49). The results show that linear anisotropic scattering effects on the temperature distribution are relatively small. The comparison of the isotropic scattering results with exact numerical results reported by Viskanta [10] is also shown in Fig. 4. The agreement is quite satisfactory.

In the situation where radiation is stronger than the conduction mode, the temperature profile has an inflection point [2]. In such a case a third order polynomial for the temperature profile representation must be adopted. Also, the analysis of the radiative mode must be repeated to account for a linear distribution of heat sources.

## Acknowledgment

This research was supported by the National Science Foundation in the Fire Research Program, Research Applied to National Needs (RANN), through Grant GI-43.

## References

- 1 Sparrow, E. M., and Cess, R. D., *Radiative Heat Transfer*, Brooks/Cole Publishing Co., Belmont, Calif., 1966.
- 2 Ozisik, M. N., *Radiative Transfer*, Wiley, New York, 1973.
- 3 Wang, L. S., "Anisotropic Nonconservative Scattering in a Semi-Infinite Medium," *The Astrophysical Journal*, Vol. 174, 1972, pp. 671-678.
- 4 Hsia, H. M., and Love, T. J., "Radiative Heat Transfer Between Parallel Plates Separated by a Nonisothermal Medium With Anisotropic Scattering," *JOURNAL OF HEAT TRANSFER, TRANS. ASME, Series C*, Vol. 89, 1967, pp. 197-203.
- 5 Beach, H. L., Ozisik, M. N., and Siewert, C. E., "Radiative Transfer in Linearly Anisotropic-Scattering, Conservative and Nonconservative Slabs With Reflective Boundaries," *International Journal of Heat and Mass Transfer*, Vol. 14, 1971, pp. 1551-1565.
- 6 Larkin, B. K., and Churchill, S. W., "Heat Transfer by Radiation Through Porous Insulations," *AIChE Journal*, Vol. 5, 1959, pp. 467-474.
- 7 Bergquam, J. B., and Seban, R. A., "Heat Transfer by Conduction and Radiation in Absorbing and Scattering Materials," *JOURNAL OF HEAT TRANSFER, TRANS. ASME, Series C*, Vol. 93, 1971, pp. 236-239.
- 8 Heaslet, M. A., and Warming, R. F., "Radiative Transport and Wall Temperature Slip in an Absorbing Planar Medium," *International Journal of Heat and Mass Transfer*, Vol. 8, 1965, pp. 979-994.
- 9 Abramowitz, M., and Stegun, I. A., *Handbook of Mathematical Functions*, Dover Publications, New York, 1965.
- 10 Viskanta, R., "Heat Transfer by Conduction and Radiation in Absorbing and Scattering Materials," *JOURNAL OF HEAT TRANSFER, TRANS. ASME, Series C*, Vol. 87, 1965, pp. 143-150.

T. C. Hsieh<sup>1</sup>  
A. Hashemi  
R. Greif

University of California, Berkeley,  
Department of Mechanical Engineering,  
Berkeley, Calif.

# Shock Tube Measurements of the Emission of Carbon Dioxide in the 2.7 Micron Region

*Measurements have been made of the infrared emission of carbon dioxide in the 2.7 micron region. The measurements were carried out in a free piston shock tube at temperatures of 2400 and 3500°K. Results are reported for the mean line intensity to spacing ratio and for the emissivity.*

## Introduction

In this study the infrared emission of the 2.7 micron combination bands of carbon dioxide was measured at temperatures of 2400 and 3500°K. A free piston shock tube was used to produce the high temperature gas and the spectral measurements were carried out in the end wall region behind the reflected shock wave. The particular attractiveness of the shock tube is that it produces a high temperature test gas which is uniform and stationary.

Previous measurements of the spectral absorption and emission of the 2.7 micron region of carbon dioxide were made in steady-state furnace type systems by Edwards [1],<sup>2</sup> Burch, Gryvnak and Williams [2], and Tourin [3] for temperatures up to 1500°K and in a rocket burner by Ferriso and Ludwig [4] for temperatures between 1200 and 1800°K. Theoretical calculations have been made by Malkmus [5] for temperatures up to 3000°K and these provide a comparison with the present measurements at 2400°K. To the best of our knowledge, there are no results available to compare with our measurements at 3500°K. A summary of the results available has been presented by Ludwig, et al. [13].

## Experimental System

The experimental measurements were made in a free piston shock tube. This shock tube uses a piston compression as the method for transferring energy to the driver gas behind the diaphragm. The piston is propelled by high pressure from the "driver-driver" gas which compresses the driver gas into a small volume. The driver gas pressure causes the diaphragm to rupture and the

compressed gas then expands into the expansion section driving a shock wave down the length of the tube. The piston remains essentially stationary during the time required for the shock wave to traverse the expansion section and reflect off the end wall.

The free piston shock tube, which was designed and constructed for this investigation, is shown schematically in Fig. 1. The driver section of the shock tube is a 7 ft long stainless steel tube of 5 in. ID and the piston moves within this section. The piston release mechanism is of interest and is shown in Fig. 2. When the piston is in its initial position, the high pressure driver-driver gas behind the piston acts *radially* on the rear portion of the piston. The experiment commences with the introduction of gas through a passage (cf. Fig. 2) which leads to the back face of the piston. This produces the axial force on the piston which causes the piston to move forward to the right. The piston quickly clears the release section which then allows the high pressure driver-driver gas to act over the back end of the piston and propel it down the tube. The recoil from the piston motion causes the steel tube to move in the direction opposite to that of the piston. Because of the instrumentation in the expansion section, it was decided to isolate the motion of the driver section from the expansion section. This was accomplished with a sliding joint which allowed the expansion section to remain stationary while the driver section was in motion. Additional description and figures are available (Hsieh [6]). In response to the referee's comment, we note that free piston shock tubes have been used in a variety of studies. For example, the measurements reported by Stalker [8, 9] and Greif, Bryson, and Collins [10, 11, 12] are representative of both the usefulness of free piston shock tubes and the reliability of the technique.

The driver-driver and driver regions are filled with nitrogen directly from a gas cylinder while the expansion section is filled with a mixture of helium and carbon dioxide which is taken from a mixing tank. The gases are premixed in the mixing tank for more than

<sup>1</sup> Presently at Westinghouse Nuclear Center, Pittsburgh, Pa.

<sup>2</sup> Numbers in brackets designate References at end of paper.

Contributed by the Heat Transfer Division for publication in the JOURNAL OF HEAT TRANSFER. Manuscript received by the Heat Transfer Division October 24, 1974. Paper No. 75-HT-ZZ.

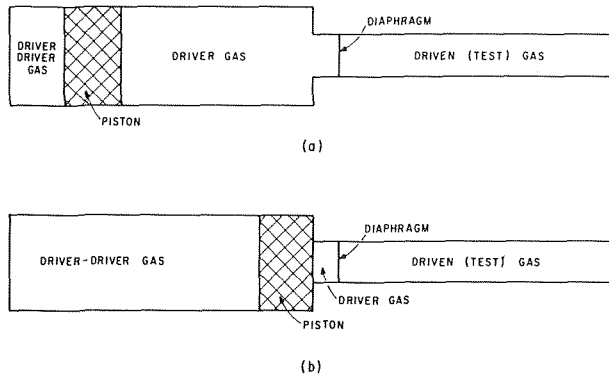


Fig. 1 Schematic drawing of free piston shock tube; (a) prior to piston compression; (b) after piston compression, but just before diaphragm rupture

twenty-four hours prior to use and, before filling, the expansion section was evacuated to a pressure of  $10^{-5}$  mm Hg. The expansion section is a 9 ft long aluminum tube of 3 in. square cross section and  $\frac{1}{8}$  in. thickness. Thin film platinum thermometers were mounted on the tube wall to detect the passage of the shock wave and thereby yield the shock speed. We note that for the high temperature runs, the driver section was filled with a mixture of nitrogen and helium so as to attain the required higher sound speed for the driver gas behind the diaphragm.

The radiation emitted from the shock heated gas is first transmitted through a  $\frac{7}{8}$  in. dia,  $\frac{1}{4}$  in. thick magnesium oxide window that is built into the shock tube near the end wall. The radiation is then directed by a plane mirror and focused by two spherical mirrors upon the entrance slit of a 5 m McPherson grating polychromator. An Optical Coating Laboratory long wavelength pass filter is mounted at the entrance slit in order to prevent extraneous radiation from the shorter wavelengths,  $\lambda/2$ ,  $\lambda/3$ , etc., from entering the grating spectrometer. The filter has a short wavelength cutoff at 2.332 microns.

The radiation passing through the entrance slit of the spectrometer is collimated and directed by a concave mirror upon a 150 lines/mm grating plate and then focused by another concave mirror onto the exit slits. Two slits, 1 mm in width and 16.5 mm apart, are used with a spectral slit width of 0.015 microns. The two monochromatic rays passing through the exit slits are directed to two Philco 1SC-363 photovoltaic infrared detectors by plane mirrors. Each detector has a sensitive area of 4 mm<sup>2</sup> and operates at liquid nitrogen temperature, i.e., approximately 77°K.

The wavelength readings of the polychromator were first calibrated using a Bausch and Lomb mercury lamp, and then checked with a prism monochromator using the absorption bands of carbon dioxide and water vapor in the atmosphere. In addition, the wavelength readings were further checked by using a helium discharge lamp and also a helium-neon gas laser (Spectra-Physics Stabilite

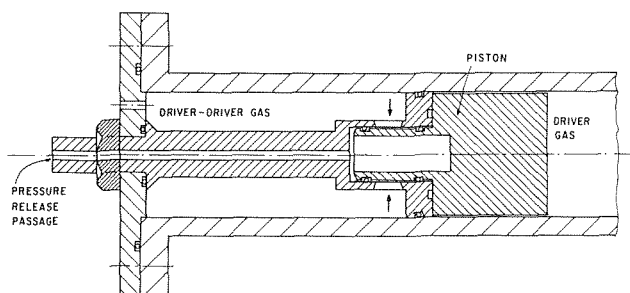


Fig. 2 Piston release mechanism

Model 125). The signals from the detectors were amplified and monitored on Tektronix 565A oscilloscopes. During absolute intensity calibration, a standard globar was used as the radiation source and the temperature was determined with a Leeds and Northrup Company optical pyrometer. The calibration was made over the wavelength range of interest, and in particular, at those wavelengths at which the shock wave heated measurements were made. The calibration source is relatively uniform with respect to wavelength variations over the band width. However, there is a significant wavelength variation for the filter, the detector and the atmospheric absorption due to the presence of carbon dioxide and water vapor. The inclusion of these effects is specified in the Analysis section.

## Analysis

The system voltage output from a spectral region  $\Delta\lambda$  due to radiative emission from the shock heated gas at a temperature  $T$  may be expressed as

$$V_{\lambda,T} = \int_{\Delta\lambda} E_{b\lambda,T} [1 - \exp(-k_{\lambda,T} X)_{\text{CO}_2}] \exp(-k_{\lambda,T_r} X)_{\text{air}} \tau_{s\lambda} d\lambda \quad (1)$$

where  $E_{b\lambda,T}$  is the black body radiance,  $k_{\lambda,T}$  is the spectral absorption coefficient of carbon dioxide,  $k_{\lambda,T_r}$  is the spectral absorption coefficient of air at room temperature,  $T_r$ ,  $X_{\text{CO}_2}$  is the pressure pathlength of the shock-heated carbon dioxide gas,  $X_{\text{air}}$  is the pressure pathlength of air along the line of sight from the shock tube window to the detector, and  $\tau_{s\lambda}$  is the spectral transmission coefficient of the optical system including mirrors, spectrometer, filter, and detector. If we consider a narrow spectral region  $\Delta\lambda$ , equation (1) may be approximated by

$$V_{\lambda,T} = E_{b\lambda,T} \tau_{s\lambda} \left\{ \int_{\Delta\lambda} \exp(-k_{\lambda,T_r} X)_{\text{air}} d\lambda - \int_{\Delta\lambda} \exp[-(k_{\lambda,T_r} X)_{\text{air}} - (k_{\lambda,T} X)_{\text{CO}_2}] d\lambda \right\} \quad (2)$$

where the black body radiance and the spectral transmission coefficient are evaluated at a given wavelength within the wavelength interval. Now, if the shock tube is replaced by a calibration source having an emissivity  $\epsilon_r$  at temperature  $T_c$ , the system voltage output over a narrow spectral region is then given by

$$V_{\lambda,T_c} = \epsilon_c E_{b\lambda,T_c} \tau_{s\lambda} \int_{\Delta\lambda} \exp(-k_{\lambda,T_r} X)_{\text{air}} d\lambda \quad (3)$$

For well overlapped lines we may introduce a mean line intensity,  $\bar{S}$ , and a mean line spacing,  $d$ , over a narrow spectral interval according to [7]

$$\int_{\Delta\lambda} \exp(-k_{\lambda} X) d\lambda = \exp(-\bar{k} X) \Delta\lambda = \exp(-\bar{S} X/d) \Delta\lambda \quad (4)$$

Thus, equations (2) and (3) may be written as

$$V_{\lambda,T} = E_{b\lambda,T} \tau_{s\lambda} \exp(-\bar{S} X/d)_{\text{air}, T_r} \Delta\lambda [1 - \exp(-\bar{S} X/d)_{\text{CO}_2, T}] \quad (5)$$

and

$$V_{\lambda,T_c} = \epsilon_c E_{b\lambda,T_c} \tau_{s\lambda} \exp(-\bar{S} X/d)_{\text{air}, T_r} \Delta\lambda \quad (6)$$

This relation may then be combined to yield the spectral emissivity,  $\epsilon_\lambda$ , according to

$$\epsilon_\lambda = 1 - \exp(-\bar{S} X/d)_{\text{CO}_2, T} = \frac{\epsilon_c E_{b\lambda,T_c} V_{\lambda,T}}{E_{b\lambda,T} V_{\lambda,T_c}} \quad (7)$$

## Discussion of Results and Conclusions

Measurements were made of the spectral emission of the 2.7 micron region of carbon dioxide at temperatures of 2400 and 3500°K. The radiation was transmitted through a magnesium oxide window that was located on the side wall (adjacent to the end wall). The amplified voltage output from the two photovoltaic infrared detectors is shown in Fig. 3. As shown on the figure, the signal from the detectors changes after passage of the "first" reflected shock wave.

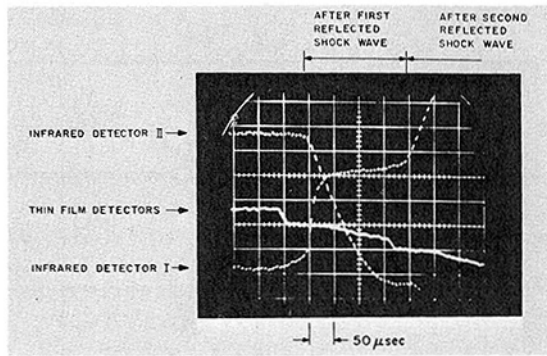


Fig. 3 Typical oscillograms 25 percent CO<sub>2</sub>, 75 percent He; end wall gas temperature 3500°K

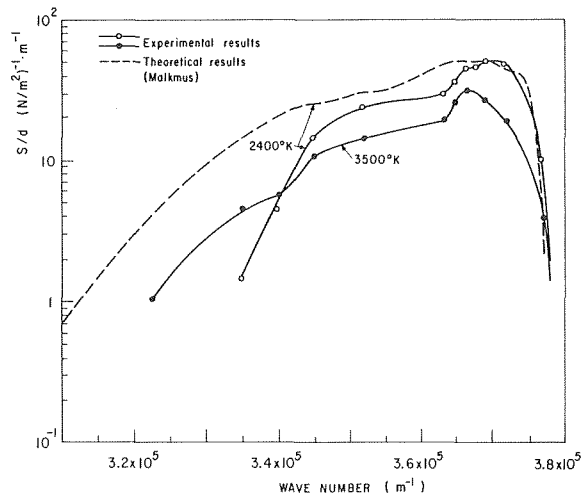


Fig. 4 Results for mean absorption coefficient

Due to the proximity of the window to the end wall, the effect of the incident shock wave cannot be distinguished from the contribution resulting from the passage of the reflected shock wave. The change in the voltage output from each detector is due to the increase in emission from the heated gas. The conditions in the end wall region behind the reflected shock wave are determined from the conservation equations of mass, momentum, and energy across the primary, and reflected shock waves based on the measured values of the initial temperature and pressure and the shock speed.

The test gas was a mixture of helium and carbon dioxide. For the low temperature runs, the partial pressures for helium and carbon dioxide were 2000 and 667 N/m<sup>2</sup> (15 and 5 mm Hg), respectively; for the high temperature runs the corresponding values were 1500 and 500 N/m<sup>2</sup> (11.25 and 3.75 mm Hg). The maximum variation in temperature behind the reflected shock wave due to the slight variations in shock speed, initial temperature, etc., was  $\pm 150^\circ\text{K}$ . However, in most cases the variation in temperature was much smaller.

The output from the thin film shock wave detectors is also shown in Fig. 3. A total of five detectors were mounted on the shock tube wall with the first being used to trigger the oscilloscope sweep. For greater accuracy, the outputs from two detectors are displayed in this figure. It should be noted that the oscilloscope sweeps for the infrared detectors were triggered after a time delay (of the order of 500  $\mu\text{s}$ ) so that the outputs displayed in Fig. 3 correspond to different times.

The experimental results were used to determine the mean spectral absorption coefficient,  $\bar{S}/d$ , which is presented in Fig. 4 along with the theoretical calculations of Malkmus [5]. For a temperature of 2400°K there is good agreement between the theoretical

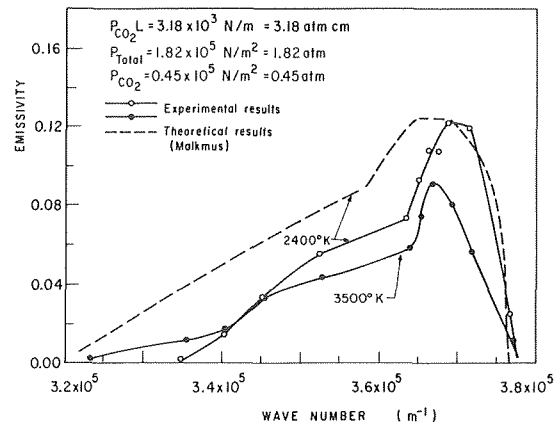


Fig. 5 Results for emissivity

calculations and the experimental data for wave numbers greater than 350,000  $\text{m}^{-1}$ . However, for the smaller wave numbers the intensity, and thus the corresponding output, is reduced which results in a less accurate determination of the mean spectral absorption coefficient. This could account for the discrepancy with Malkmus' calculations at the smaller wave numbers. At 3500°K, there are no results available to compare with our measurements. However, there is good qualitative confirmation of the results based on the calculations of Malkmus at temperatures up to 3000°K. It is also noted that several runs were repeated and the reproducibility of the results was demonstrated. For completeness, the spectral emissivity,  $\epsilon_\lambda$ , was also determined and these results are presented in Fig. 5.

#### Acknowledgment

The authors acknowledge with appreciation the support of this research by the National Science Foundation.

#### References

- Edwards, D. K., "Absorption by Infrared Bands of Carbon Dioxide Gas at Elevated Pressures and Temperatures," *J. Opt. Soc. Am.*, Vol. 50, 1960, p. 617.
- Burch, D. E., Gryvnak, D. A., and Williams, D., "Total Absorptance of Carbon Dioxide in the Infrared," *Applied Optics*, Vol. 1, 1962, pp. 759-765.
- Tourin, R. H., "Infrared Spectral Emissivities of CO<sub>2</sub> in the 2.7 Micron Region," *Infrared Physics*, Vol. 1, 1961, p. 105.
- Ferriso, C. C., and Ludwig, C. B., "Spectral Emissivities and Integrated Intensities of the 2.7- $\mu$  CO<sub>2</sub> Band Between 1200° and 1800°K," *J. Opt. Soc. Am.*, Vol. 54, 1964, p. 657.
- Malkmus, W., "Infrared Emissivity of Carbon Dioxide (2.7- $\mu$  Band)," *J. Opt. Soc. Am.*, Vol. 54, 1964, p. 751.
- Hsieh, T. C., "The Free Piston Shock Tube and Infrared Radiation Studies," PhD dissertation, University of California, Berkeley, 1972.
- Plass, G. N., "Models of Spectral Band Absorption," *J. Opt. Soc. Am.* Vol. 48, 1958, p. 690.
- Stalker, R. J., "An Investigation of Free Piston Compression of Shock Tube Drive Gas," National Research Council of Canada, MT-44, Ottawa, 1961.
- Stalker, R. J., and Horning, H. G., "Two Developments With Free Piston Drivers," *Proceedings of the Seventh International Shock Tube Symposium*, Toronto, 1969, p. 241.
- Greif, R., and Bryson, A. E., Jr., "Measurements in a Free Piston Shock Tube," *AIAA Journal*, Vol. 3, 1965, p. 183.
- Collins, D. J., Greif, R. and Bryson, A. E., Jr., "Measurements of the Thermal Conductivity of Helium in the Temperature Range 1600 to 6700 Degrees Kelvin," *International Journal of Heat and Mass Transfer*, Vol. 8, 1965, p. 1209.
- Collins, D. J., "Measurement of the Thermal Conductivity of Noble Gases in the Temperature Range 1500 to 5000 Degrees Kelvin," *JOURNAL OF HEAT TRANSFER*, TRANS. ASME, Series C, Vol. 88, 1966, p. 52.
- Ludwig, C. B., Malkmus, W., Reardon, J. E., and Thomson, J. A. L., *Handbook of Infrared Radiation From Combustion Gases*, National Aeronautics and Space Administration, NASA SP-3080, Washington, D. C., 1973.

Y. Mori  
K. Hijikata  
Y. Yamada

Department of Physical Engineering,  
Tokyo Institute of Technology,  
O-Okayama, Meguro-Ku,  
Tokyo, Japan

# Radiation Effects on Heat Transfer in the Reactor Core and Heat Exchangers of an HTGR

*A general and fundamental study of the effect of radiation between duct walls on the heat transfer performance of duct flows of nonradiating gas such as helium is made by an approximate analysis and numerical calculations. Laminar and turbulent flows in a duct simulating a coolant passage in an HTGR and flows in counterflow and parallel-flow heat exchangers in an HTGR heat transfer system are investigated. An approximate analytical solution, based on the assumption that radiation from a point of duct wall produces an effect only on the narrow region opposite the point, agrees well with numerical results. The increase of radiative heat transfer causes a decrease of temperature difference between the duct walls and improves the heat transfer performance. For heat exchangers the heat transfer effectiveness is shown to depend on three nondimensional parameters and can be improved by the increase of these parameters.*

## Introduction

The high temperature gas cooled reactor (HTGR) is considered to be the only nuclear heat source in the near future which can supply heat at such a high temperature level as 1000°C required [1]<sup>1</sup> for such processes as steel making, steam reforming, coal gasification, and others used in chemical industries. From the viewpoint of safety, metallic recuperative heat exchangers should be installed between the HTGR primary loop and heat-consuming process loops. Helium is considered as the working medium in the reactor loop and the intermediate loop, which should be used between the primary and process loops of an HTGR at a high temperature such as 1000°C. Helium itself is nonradiating in this temperature region. The heat exchanger in the high temperature region is required to provide excellent heat transfer performance. Many methods of heat transfer augmentation in forced convective flow have been reported [2], and the improvement of heat transfer performance of convective internal flow of a radiating gas has been investigated by many researchers [3, 4]. In the latter case, due to the complexity of the fundamental equations, the calculations have been made by numerical methods under conditions of

laminar flow and isothermal duct wall or constant heat flux [5, 6]. The effects of radiation on the channel flow between two black parallel plates were analyzed by Keshock and Siegel [7]. However in the HTGR heat supply system, it is not generally true that the temperature of the duct wall along the flow direction is constant, that the wall emissivity is unity, or that the flow is laminar.

The purpose of this paper is to make a general and fundamental study of the radiation effects between walls of a duct on heat transfer performance under the condition of nonradiating gas flow, a varying wall temperature distribution along the flow direction, and the wall surface emissivity below unity. Flows in a duct and heat-exchangers of counter-flow and parallel-flow type consisting of two ducts are studied by an approximate analysis and numerical calculations.

## Fundamental Equations

A flow model to introduce fundamental equations is shown in Fig. 1. The flow ducts consist of three parallel flat plates, simulating a parallel-flow heat exchanger. The emissivities of the walls of the ducts are  $\epsilon_1$ ,  $\epsilon_2$ , and  $\epsilon_3$ , respectively, and radiation is assumed to be diffusely reflected. The working fluid is a nonradiating gas, the flow field is assumed not to be affected by radiation, and the velocity and temperature of the fluid are represented by their mean values in the cross section. The heat flux  $\dot{q}_c$  between the fluid and the duct wall is assumed to be given by use of the convective heat transfer coefficient  $h_c$ , the mean temperature of fluid  $\bar{T}_m$  and the wall temperature  $\bar{T}_w$ . In front of the inlet and at the rear of the outlet of the duct, the wall temperature is to be equal to its local fluid temperature. This assumption is equivalent to the fact that

<sup>1</sup> Numbers in brackets designate References at end of paper.

Contributed by the Heat Transfer Division and presented at the Winter Annual Meeting, New York, N.Y., November 17-22, 1974, of THE AMERICAN SOCIETY OF MECHANICAL ENGINEERS. Journal manuscript received by the Heat Transfer Division June 26, 1975. Paper No. 74-WA/HT.

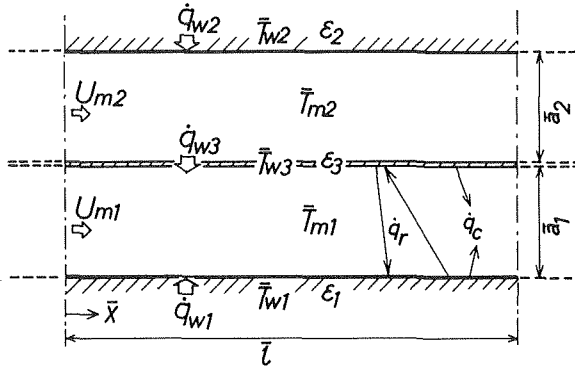


Fig. 1 Schematic model of flows

at both ends there exist reservoirs whose wall temperature are equal to those of the fluid.

$U_{m1}$  and  $U_{m2}$  represent the mean fluid velocities, and  $\bar{a}_1$  and  $\bar{a}_2$  the duct width. The coordinate  $\bar{x}$  is taken along the duct from the inlet of low temperature fluid, and  $\bar{l}$  denotes the total duct length. The subscript  $i = 1, 2$  expresses values for the cold and hot fluids and the subscript  $j = 1, 2, 3$  expresses those for the low temperature wall, high temperature wall, and intermediate wall, respectively. The subscript  $ij$  in the following discussion expresses values for the wall  $j$  in contact with the fluid  $i$ , and  $ij$  takes the values 11, 13, 22, 23. Under these conditions the heat balance for the cold ( $i = 1$ ) and hot ( $i = 2$ ) fluids is expressed as follows:

$$\rho_i C_{p_i} U_{m_i} \bar{a}_i \frac{d\bar{T}_{m_i}}{d\bar{x}_i} = h_{ij}(\bar{T}_{w_j} - \bar{T}_{m_i}) + h_{i3}(\bar{T}_{w_3} - \bar{T}_{m_i}), \quad (i = j = 1, 2) \quad (1)$$

The equation of energy balance for the low temperature ( $j = 1$ ), the high temperature ( $j = 2$ ) and the intermediate walls ( $j = 3$ ) can be obtained as follows:

$$\dot{q}_{w_j} - \dot{q}_{c_{ij}} = \dot{q}_{r_{ij}} = \dot{q}_{r, \text{out } ij} - \dot{q}_{r, \text{in } ij} \quad (2)$$

where  $\dot{q}_{w_j}$ ,  $\dot{q}_{c_{ij}}$ , and  $\dot{q}_{r_{ij}}$  express the heat flux through the wall  $j$ , the convective heat flux ( $h_{ij}(\bar{T}_{w_j} - \bar{T}_{m_i})$ ) from the wall  $j$  to the fluid  $i$  and the radiative heat flux from the wall  $j$  in contact with the fluid  $i$ , respectively;  $\dot{q}_{w_1}$  and  $\dot{q}_{w_2}$  are the externally imposed heat input (or heat loss), and  $\dot{q}_{w_3}$  is the heat flow from the high temperature side to the low temperature side through the intermediate wall.

$\dot{q}_{r, \text{out } ij}$  and  $\dot{q}_{r, \text{in } ij}$  can be expressed as follows:

$$\dot{q}_{r, \text{out } ij} = \epsilon_j \sigma \bar{T}_{w_j}^4 + (1 - \epsilon_j) \dot{q}_{r, \text{in } ij} \quad (3)$$

$$\dot{q}_{r, \text{in } ij} = \int_{-\infty}^{\infty} \frac{\dot{q}_{r, \text{out } ik}}{\bar{F}_i(\bar{l}, \bar{x})} d\bar{l} \quad (4)$$

where  $ik$  denotes the opposite wall of the wall  $j$  in contact with the fluid  $i$  and  $\bar{F}_i(\bar{l}, \bar{x}) = 2[\bar{a}_i^2 + (\bar{l} - \bar{x})^2]^{3/2} / \bar{a}_i^2$  is the inverse of the configuration factor for strips on parallel plates. The combinations of  $ij$  and  $ik$  take only four cases, ( $ij, ik$ ) = (11, 13) (13, 11) (22, 23), (23, 22). By using equations (2), (3), and (4),  $\dot{q}_{r, \text{out } ij}$  and  $\dot{q}_{r, \text{in } ij}$  can be obtained.

$$\dot{q}_{r, \text{out } ij} = \sigma \bar{T}_{w_j}^4 - \frac{1 - \epsilon_j}{\epsilon_j} \{ \dot{q}_{w_j} - h_{ij}(\bar{T}_{w_j} - \bar{T}_{m_i}) \} \quad (5)$$

$$\dot{q}_{r, \text{in } ij} = \int_{-\infty}^{\infty} \frac{\sigma \bar{T}_{w_k}^4 - \frac{1 - \epsilon_k}{\epsilon_k} \{ \dot{q}_{w_k} - h_{ik}(\bar{T}_{w_k} - \bar{T}_{m_i}) \}}{\bar{F}_i(\bar{l}, \bar{x})} d\bar{l} \quad (6)$$

The boundary conditions are given by the inlet temperatures of cold and hot fluids as,

$$\bar{T}_{m_1}(0) = \bar{T}_0;$$

$$\bar{T}_{m_2}(\bar{l}) = \bar{T}_0 + \Delta \bar{T}, \text{ (counterflow) or}$$

$$\bar{T}_{m_2}(0) = \bar{T}_0 + \Delta \bar{T}, \text{ (parallel-flow)} \quad (7)$$

Substituting equations (5) and (6) into equation (2) and nondimensionalizing them lead us to the following equations.

$$\frac{dT_{m_i}}{dx_i} = (-1)^{(i-1)(n-1)} [St_{ij}(T_{w_j} - T_{m_i}) + St_{i3}(T_{w_3} - T_{m_i})] \quad (8)$$

$$M_{ij} T_{w_j}^4 + T_{w_j} - T_{m_i} - Q_{ij} M_{ij} \int_{-\infty}^{\infty} \frac{T_{w_3}^4}{F_i} dt_i + M_{ij} \int_{-\infty}^{\infty} \frac{(1 - \epsilon_3)}{M_{i3} F_i} (T_{w_3} - T_{m_i} - Q_{i3}) dt_i \quad (9)$$

$$M_{i3} T_{w_3}^4 + T_{w_3} - T_{m_i} - Q_{i3} = M_{i3} \int_{-\infty}^{\infty} \frac{T_{w_1}^4}{F_i} dt_i + M_{i3} \int_{-\infty}^{\infty} \frac{(1 - \epsilon_j)}{M_{ij} F_i} (T_{w_j} - T_{m_i} - Q_{ij}) dt_i \quad (10)$$

$n = 0$ ; counterflow,  $n = 1$ ; parallel-flow, ( $i = j = 1, 2$ ). In these equations the following nondimensional values are introduced:

$$St_{ij} = \frac{h_{ij}}{\rho_i C_{p_i} |U_{m_i}|}, \quad M_{ij} = \frac{\epsilon_j \sigma \bar{T}_0^3}{h_{ij}}, \quad Q_{ij} = \frac{(-1)^{i+j} \dot{q}_{w_j}}{h_{ij} \bar{T}_0} \quad (11)$$

Given  $M_{ij}$ , Stanton number  $St_{ij}$ , emissivity  $\epsilon_j$  and heat input (or loss)  $Q_{11}$ ,  $Q_{22}$ , equations (8), (9), and (10) can be solved, and fluid temperature  $T_{m_i}$ , wall temperature  $T_{w_j}$  and heat flux through the intermediate wall  $Q_{i3}$  can be obtained. The parameter  $M_{ij}$  indi-

## Nomenclature

$\bar{a}$  = width of flow duct (m)

$C_p$  = specific heat at constant pressure (J/kg·°K)

$h$  = heat transfer coefficient (W/(m<sup>2</sup>·K))

$\bar{l}$  = length of flow duct (m)

$l$  = nondimensional length of flow duct =  $\bar{l}/\bar{a}$

$M$  = radiation-convection parameter =  $\epsilon \sigma \bar{T}_0^3 / h$

$N$  = radiation-conduction parameter =  $2\bar{a} \sigma \bar{T}_0^3 / \lambda$

$Nu$  = Nusselt number =  $2\bar{a}h/\lambda$

$Pr$  = Prandtl number =  $\mu/C_p \lambda$

$Q$  = nondimensional heat flux =  $\dot{q}/h\bar{T}_0$

$\dot{q}$  = heat flux (W/m<sup>2</sup>)

$Re$  = Reynolds number =  $2\bar{a}\rho|U_m|/\mu$

$St$  = Stanton number =  $Nu/Re \cdot Pr = h/\rho C_p |U_m|$

$\bar{s}, \bar{t}, \bar{x}$  = coordinate in flow direction (m)

$s, t, x$  = nondimensional coordinate in flow direction =  $\bar{s}/\bar{a}, \bar{t}/\bar{a}, \bar{x}/\bar{a}$

$\bar{T}$  = temperature (°K)

$T$  = nondimensional temperature =  $\bar{T}/\bar{T}_0$

$\Delta \bar{T}$  = temperature difference (°K)

$\Delta T$  = nondimensional temperature difference =  $\Delta \bar{T}/\bar{T}_0$

$U_m$  = mean velocity (m/s)

$\epsilon$  = emissivity of wall

$\lambda$  = thermal conductivity (W/(m·°K))

$\mu$  = viscosity (Pa·s)

$\rho$  = density (kg/m<sup>3</sup>)

$\sigma$  = Stefan Boltzmann constant (W/(m<sup>2</sup>·K<sup>4</sup>))

$\eta$  = heat transfer effectiveness of heat exchanger

## Subscripts

$c$  = convection

$i$  = fluid

$j$  = wall

$ij$  = wall  $j$  in contact with fluid  $i$

$n$  = grid point

$r$  = radiation

$r, \text{in}$  = incoming radiation

$r, \text{out}$  = outgoing radiation

$w$  = wall

0 = inlet of low temperature side

1 = low temperature wall or fluid

2 = high temperature wall or fluid

3 = intermediate wall

— = dimensional value

cates the ratio of radiative heat flux to convective heat flux, and  $Q_{ij}$  is the ratio of the heat flux through the wall to the convective flux.

In a heat exchanger where the temperature variation of the fluid is considerable and radiative heat transfer is effective, the change of physical properties of the fluid can not be neglected. When helium is the working fluid,  $\lambda$  and  $\mu$  are nearly proportional to  $T^{0.5}$  and  $Pr$  is nearly constant.  $St$  is proportional to  $T^{0.1}$  and  $M$  to  $T^{-0.1}$  for turbulent flows; therefore, the effect of temperature change on these two parameters is neglected in our analysis.

### Approximate Solution

The fundamental equations (9) and (10) are nonlinear integral equations. Since it is not easy to obtain their exact solution by an analytical method, consideration of an approximate solution is required. The integrals in equations (9) and (10) take the following form:

$$\int_{-\infty}^{\infty} \frac{g(t)}{2[1 + (x-t)^2]^{3/2}} dt \quad (12)$$

If  $g(t)$  is expanded in polynomials of  $(t-x)$  around the point  $x$ ,  $g(t)$  can be written in terms of  $g(x)$ , odd terms of  $(t-x)$  and even terms of  $(t-x)$ . In a heat exchanger, temperature and other physical properties vary monotonically along the flow direction and do not have maxima nor minima between the inlet and the outlet. Here, the coefficients of the even terms can be neglected compared with those of the odd terms of the polynomials, and the integrals of equation (12) of the odd terms vanish. Hence, only the term  $g(x)$  should be considered, and equation (12) can be approximated well by the following equation (13) at most parts of the duct except at the inlet and outlet parts.

$$\int_{-\infty}^{\infty} \frac{g(t)}{2[1 + (t-x)^2]^{3/2}} dt = g(x) \quad (13)$$

This means that the effect of radiation from a point of a wall is produced only on the narrow region opposite the point.

**One Duct and Constant Heat Flux Case.** The present analysis is first applied to the cooling of the reactor core of an HTGR by helium. Generally in this case, heat flux is added from one wall of the annular duct while the other wall is thermally insulated. By comparing the configuration factors for parallel plates to those for an annular duct as was done in the proceeding discussion, the difference that arises in assuming an annular duct as a parallel duct is found to be less than 5 percent when the ratio of the radii is 1.1 or less.

By assuming that  $Q_{11}$  and  $Q_{13}$  are constant and that  $h_{11}$  is equal to  $h_{13}$ , the fundamental equations in the low temperature can be derived by putting  $i = 1$  in equations (8), (9), and (10). The application of equation (13) to equations (9) and (10) gives us

$$T_{w3} + T_{w1} - 2T_{m1} = Q_{13} + Q_{11} \quad (14)$$

and by substituting this into equation (8)

$$T_{m1} = 1 + St_{11}(Q_{13} + Q_{11})x \quad (15)$$

can be obtained.

Equation (16) is assumed as follows;

$$T_{wj} = 1 + \tau_{wj} + \omega_{wj}x \quad (j = 1, 3),$$

$$\omega_{w1} = St_{11}(Q_{13} + Q_{11})(1 + \beta_1), \quad \omega_{w3} = St_{11}(Q_{13} + Q_{11})(1 - \beta_1) \quad (16)$$

and the approximation (17) is used.

$$\begin{aligned} \tau_{w1}^2 + \tau_{w3}^2 &\approx (\tau_{w1} + \tau_{w3})^2/2, \\ \tau_{w1} \cdot \tau_{w3} &\approx (\tau_{w1} + \tau_{w3})^2/4 \end{aligned} \quad (17)$$

Equation (17) is rigorous when  $\tau_{w1} = \tau_{w3}$ . Since in this paper the difference of  $\tau_{w1}$  and  $\tau_{w3}$  is regarded as small, equation (17) is a fairly good approximation. Equations (13), (16), and (17) lead us to obtain  $T_{w1}$  and  $T_{w3}$  from equations (9) and (10).

$$T_{w1} = 1 + [\gamma_1 Q_{13}/2 - (1 + \gamma_1/2)Q_{11}]/(1 + \gamma_1) + St(Q_{13} + Q_{11})(1 + \beta_1)x \quad (18)$$

$$T_{w3} = 1 + [(1 - \gamma_1/2)Q_{13} + \gamma_1 Q_{11}/2]/(1 + \gamma_1) + St(Q_{13} + Q_{11})(1 - \beta_1)x \quad (19)$$

where

$$\begin{aligned} \beta_1 &= 3M'J_1^2(Q_{13} - Q_{11})/(1 + M'J_1^3)^2, \quad \gamma_1 = M'J_1^3, \\ M' &= M/(2 - \epsilon), \quad J_1 = 2 + Q_{13} + Q_{11} \end{aligned} \quad (20)$$

When the cold wall is adiabatic ( $Q_{11} = 0$ ) and not heated by radiation,  $\bar{T}_{w1} = \bar{T}_{m1}$ , and the heat flux to the fluid is given only by  $h_{13}(\bar{T}_{w3} - \bar{T}_{m1})$ . On the other hand, when the cold wall is heated by radiation from the wall 3, the heat flux supplied to the fluid is increased by  $h_{11}(\bar{T}_{w1} - \bar{T}_{m1})$ . Therefore, when one defines the following heat transfer coefficient  $h_{rc}$  considering the radiation effect, the ratio of  $h_{rc}$  to the purely convective heat transfer coefficient  $h_c$  is given as

$$\frac{h_{rc}}{h_c} = \frac{h_{13}(\bar{T}_{w3} - \bar{T}_{m1}) + h_{11}(\bar{T}_{w1} - \bar{T}_{m1})}{h_{13}(\bar{T}_{w3} - \bar{T}_{m1})} \quad (21)$$

In order to discuss the effect of radiation by equation (21), as an example, heat transfer in a parallel duct simulating an annular passage in a reactor core is calculated, and the result is shown in Fig. 2.

**Counterflow Heat Exchangers.** In a counterflow heat exchanger the heat flux through the intermediate wall varies slightly in the flow direction, but is almost constant. Since  $T_{m1}$ ,  $T_{w1}$ , and  $T_{w3}$  are given by equations (15), (18), and (19),  $T_{m2}$ ,  $T_{w2}$  and  $T_{w3}$  can be shown as the functions of  $Q$  as follows if  $Q_{13} = -Q_{23} = Q = \text{Const.}$  is assumed:

$$T_{m2} = 1 + \tau_{m2} + St(Q - Q_{22})x \quad (22)$$

$$T_{w2} = 1 + \tau_{m2} - [(1 + \gamma_2/2)Q_{22} + \gamma_2 Q/2]/(1 + \gamma_2) + St(Q - Q_{22})(1 - \beta_2)x \quad (23)$$

$$T_{w3} = 1 + \tau_{m2} - [-\gamma_2 Q_{22}/2 + (1 + \gamma_2/2)Q]/(1 + \gamma_2) + St(Q - Q_{22})(1 + \beta_2)x \quad (24)$$

where

$$\begin{aligned} \beta_2 &= 3M'J_2^2(Q + Q_{22})/(1 + M'J_2^3)^2, \quad \gamma_2 = M'J_2^3, \\ \tau_{m2} &= \Delta T - St \cdot l(Q - Q_{22}), \quad J_2 = 2 + 2\tau_{m2} + Q + Q_{22} \end{aligned} \quad (25)$$

Equation (24) has to be identical with equation (19). However, under the condition that  $Q$  is constant, both equations cannot be identical at every point of the wall 3. Therefore, the values given by equation (24) and equation (19) are assumed to be equal only at  $x = l/2$ , and we then get the following equation for  $Q$  as the first approximation:

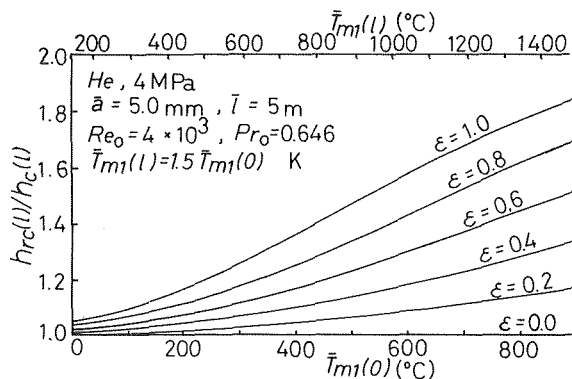


Fig. 2  $h_{rc}/h_c$  versus inlet temperature of cold fluid

$$\frac{3St \cdot l \cdot M'}{2} \left[ \sum_{i=1}^2 \frac{J_i^2}{(1 + \gamma_i)^2} \right] Q^2 - \left[ St \cdot l + \sum_{i=1}^2 \frac{1 + \gamma_i/2}{1 + \gamma_i} \right] Q + \Delta T - \sum_{i=1}^2 \left[ \frac{3St \cdot l \cdot M' J_i^2 Q_{ij}^2}{2(1 + \gamma_i)^2} - (-1)^i \left( \frac{St \cdot l}{2} + \frac{1 + \gamma_i/2}{1 + \gamma_i} \right) Q_{ij} \right] = 0, \quad (i = j) \quad (26)$$

Using the solution of equation (26), the temperature distributions of cold and hot fluids,  $T_{m1}$  and  $T_{m2}$ , are obtained, respectively, from equations (15) and (22), and  $T_{w3}$  is calculated as the average value of equations (19) and (24). Elimination of  $Q$  from equations (9) and (10) by applying equation (13) gives us

$$M'(T_{w_j}^4 - T_{w_3}^4) + T_{w_j} - T_{m_i} - Q_{ij} = 0, \quad (i = j = 1, 2) \quad (27)$$

By making use of  $T_{m1}$  and  $T_{m2}$  obtained above,  $T_{w1}$  and  $T_{w2}$  can be newly obtained from equation (27). Using  $T_{m1}$ ,  $T_{m2}$ ,  $T_{w1}$ ,  $T_{w2}$ ,  $T_{w3}$ , the final form of  $Q$  can be given as a linear function of  $x$ .

The heat transfer effectiveness of a counterflow heat exchanger is calculated from the following relation by using the approximate solution obtained in the foregoing.

$$\eta = \frac{T_{m1}(l) - T_{m1}(0)}{T_{m2}(l) - T_{m1}(0)} = \frac{St \cdot l \cdot Q}{\Delta T} \quad (28)$$

When  $St \cdot l$ ,  $M'$  and  $\Delta T$  are given,  $Q$  is calculated and  $\eta$  may be obtained. In Fig. 3, an example is shown in the case of  $Q_{11} = Q_{22} = 0$ . The effect is seen to increase with the parameter  $M'$  which indicates the radiation effect. Circles in this figure show the exact values obtained from numerical calculation described below; and the accuracy of the approximate solution is considered to be fairly good within the region of  $\Delta T \leq 1.0$ . In practical heat exchanger for high temperatures,  $\Delta T$  could hardly exceed unity.

**Parallel-Flow Heat Exchangers.** In a parallel-flow heat exchanger, the thermal condition of the intermediate wall is nearly isothermal rather than of constant heat flux. The temperature distributions of cold fluid, hot fluid, cold wall, and hot wall and the heat flux through the intermediate wall are expressed by an exponential function. Following the same procedure as that described in the foregoing for the counterflow heat exchanger, one gets,

$$T_{m1} = 1 + \frac{\Delta T(1 - e^{-bx})}{2} + St \cdot Q_{11}x \quad (29)$$

$$T_{m2} = 1 + \frac{\Delta T(1 + e^{-bx})}{2} + St \cdot Q_{22}x \quad (30)$$

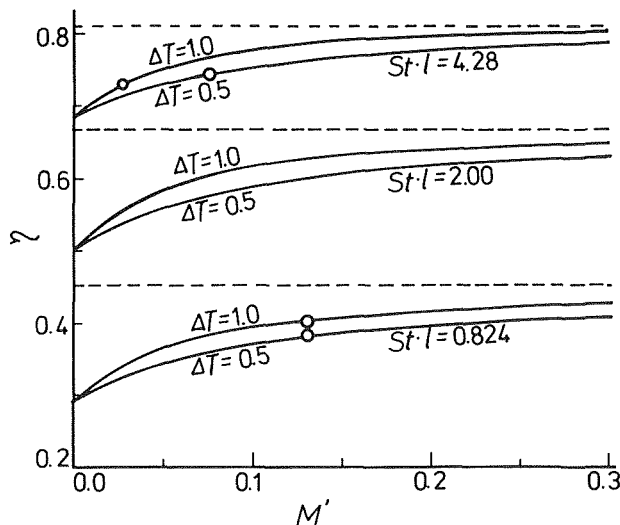


Fig. 3 Heat transfer effectiveness of counterflow heat exchangers

$$T_{w1} = 1 + Q_0 - \frac{\Delta T}{2} + (\Delta T - Q_0)(1 - e^{-bx}) + St(3Q_{11} - Q_{22})x/2 \quad (31)$$

$$T_{w2} = 1 - Q_0 + \frac{3\Delta T}{2} - (\Delta T - Q_0)(1 - e^{-bx}) + St(3Q_{22} - Q_{11})x/2 \quad (32)$$

$$T_{w3} = 1 + \frac{\Delta T}{2} + St(Q_{11} + Q_{22})x/2 \quad (33)$$

$$Q = Q_0 e^{-bx} \quad (34)$$

where

$$b = 2St \cdot Q_0 / \Delta T, \quad Q_0 = \frac{1/2 + 4M'(1 + \Delta T/2)^3}{1 + 4M'(1 + \Delta T/2)^3} \Delta T \quad (35)$$

The heat transfer effectiveness of parallel-flow heat exchanger is calculated from the following relation:

$$\eta = \frac{1}{2} [1 - \exp(-2St \cdot l \cdot Q_0 / \Delta T)] \quad (36)$$

## Numerical Calculation

In the preceding section, an approximate solution for the fundamental equation was obtained, while in this section the exact solution for equations (8), (9), and (10) is obtained by a numerical iteration method.

In a numerical calculation, the approximate solutions obtained in the preceding section are used as initial values for an iteration calculation of temperature distributions of walls and fluids. The calculation method of integral (12) by finite difference is explained in the following. For a given  $x$ , putting  $s = t - x$  the finite difference can be expressed as  $\Delta s$ , and a linear temperature distribution can be assumed in the region of  $n\Delta s \leq s \leq (n+1)\Delta s$ . The integral (12) is reduced to

$$\int_{-\infty}^{\infty} \frac{T^4(t) dt}{[1 + (t-x)^2]^{3/2}} = \sum_{n=-\infty}^{\infty} \int_{n\Delta s}^{(n+1)\Delta s} [T^4(n\Delta s) \times \{1 + \alpha_n(s - n\Delta s)\}^4 / (1 + s^2)^{3/2}] ds \quad (37)$$

where  $\alpha_n$  is the temperature gradient. Equation (37) can be written as follows by integrating its right-hand side:

$$\int_{-\infty}^{\infty} \frac{T^4(t) dt}{[1 + (t-x)^2]^{3/2}} = \sum_{n=-\infty}^{\infty} \left\{ \sum_{k=0}^4 A_{kn} B_{kn} \right\} \quad (38)$$

where  $A_{kn}$  is a coefficient of  $s$  when the numerator of equation (37) is expanded in the power series of  $s$ , and  $B_{kn}$  is a given function of  $n$  and  $s$ . In order to insure the convergence of equation (38) for large  $n$ , the calculation proceeds until  $\sum_{k=0}^4 A_{kn} B_{kn}$  is less than one hundredth of  $\sum_{k=0}^4 A_{k0} B_{k0}$ .

**Counterflow Heat Exchangers.** In a counterflow heat exchanger, the constant heat flux condition is considered to be fairly well satisfied even when radiation is significant. Therefore, Nusselt numbers reported for laminar [9] and turbulent [10] flows are used.  $T_{w1}$ ,  $T_{w2}$ ,  $T_{w3}$ ,  $T_{m1}$ , and  $T_{m2}$  are obtained by making use of the equations reduced by eliminating  $Q_{i3}$  from equations (8), (9) and (10). The heat flux through the intermediate wall  $Q$  was calculated by equation (10), and the heat transfer effectiveness was obtained from equation (28).

**Parallel-Flow Heat Exchangers.** In a parallel-flow heat exchanger, the heat transfer condition along the intermediate wall 3 is nearly isothermal rather than of constant heat flux. Therefore Nusselt numbers for the isothermal cases of laminar [11] and turbulent [12] flows were used. The procedure of numerical calculation by iteration is the same as that for the counterflow heat exchanger.

## Results and Discussions

**Constant Heat Flux Cases.** As a typical example of turbulent convective flow in a duct with constant heat flux along a wall, a numerical calculation is done, when  $Re_0 = 10^4$ ,  $Pr = 1.0$ ,  $\epsilon_1 = \epsilon_3 = 0.7$ ,

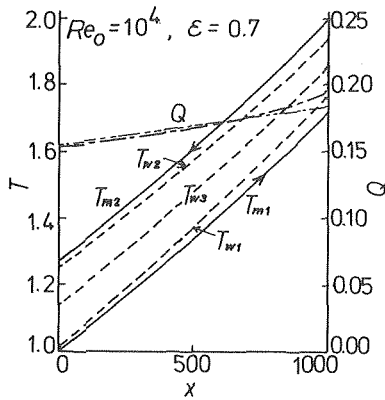


Fig. 4 Counterflow heat exchanger (turbulent flows)

$Q_{11}$  (heat input) = 0,  $Q_{13}$  (supplied heat flux) = 0.117,  $Nu_0=42.8$ ,  $T_0 = 780^\circ\text{K}$  and  $\Delta T = 0.5$ . It is shown that  $h_{rc}/h_c$  increases from 1.05 at the inlet to 1.15 at the outlet.

**Counterflow Heat Exchangers.** A representative result of numerical calculations for the counterflow heat exchanger is shown in Fig. 4. Fully developed turbulent flows are assumed in the ducts of the same width,  $St = 4.28 \times 10^{-3}$  and  $M' = 0.0252$ . The rapid increase of the temperature of the cold wall at the cold fluid exit and the rapid decrease of the temperature of the hot wall at the hot fluid inlet are due to the condition that the wall temperatures coincide with the fluid temperature at the both ends. The approximate solutions for fluid and wall temperatures obtained from equations (22), (23), (24), and (25) agree very well with those shown in Fig. 4, except in the narrow region of sharp change of wall temperatures near the both ends cited in the foregoing. The temperature difference between  $T_{m2}$  and  $T_{w2}$  and between  $T_{w1}$  and  $T_{m1}$  are due to the radiation effect. These differences become larger in the higher temperature regions. It is easily understood that for larger values of  $M'$ ,  $T_{w2}$  and  $T_{w1}$  approach  $T_{w3}$ . In Fig. 4 the heat flux through the intermediate wall  $Q$  is shown by the chain line for the numerical result and the double-dotted chain line for the approximate solution.

In Fig. 3, the values of heat transfer effectiveness obtained from the numerical calculation are shown with circles, and a good agreement is seen between numerical and analytical solutions. Therefore the effectiveness of counterflow heat exchangers is accurately calculated by equation (28). With the increase of the radiation effect, the heat delivered from the hot gas is the summation of that transferred by convection from the hot wall and the intermediate wall; therefore, the effective heat transfer surface area approaches

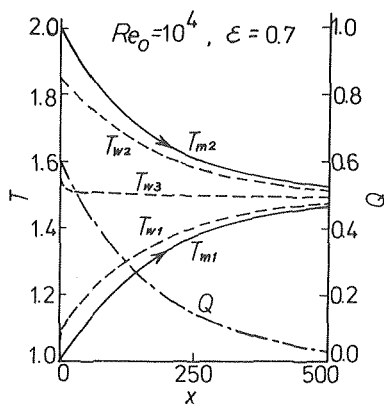


Fig. 5 Parallel-flow heat exchanger (turbulent flows)

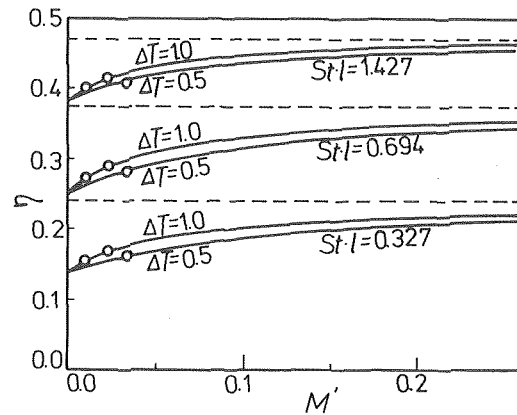


Fig. 6 Heat transfer effectiveness of parallel-flow heat exchanger

twice of that without radiation with the increase of  $M'$ . As seen from this figure, the radiation effect becomes important above  $M' = 0.01$ . When the flow is laminar and the duct is not long enough, the effect of the entrance region cannot be neglected. The heat transfer coefficient is smaller for laminar flow than for turbulent flow. Thus, the effect of radiation is more remarkable in laminar flow.

**Parallel-Flow Heat Exchangers.** The temperature distributions in a parallel-flow heat exchanger for the same  $Re_0$  and  $Pr$  as those used in Fig. 4 for the counterflow heat exchanger are shown in Fig. 5. The lines are those obtained from numerical calculation, and the temperature of the intermediate wall  $T_{w3}$  is almost constant except in the inlet region. The effect of radiation is remarkable near the inlet and brings about a rapid increase of cold wall temperature and a decrease of hot wall temperature. The approximate solution agrees very well with this numerical result. In Fig. 6, the heat transfer effectiveness of a parallel-flow heat exchanger calculated by the approximate analysis is shown by the solid line and that obtained numerically is expressed with circles. A good agreement is seen between them, and the propriety of the approximate solution is proved. The tendency for an increase of effectiveness with  $St-l$ ,  $\Delta T$  and  $M'$  is almost similar to that for counterflow.

## Conclusion

A general and fundamental study of the effect of radiation between duct walls on the heat transfer performance of nonradiating gas flow in ducts was made by an approximate analysis and numerical calculations. An investigation was first carried out on laminar and turbulent flows in a duct simulating an annular reactor coolant passage when a constant heat flux is supplied along one side wall, and, secondly, on flows in counterflow and parallel-flow heat exchangers consisting of two ducts. The results can be summarized as follows.

1 Although the temperature of the duct wall varies along the flow direction, an approximate analytical solution, based on the consideration that radiation from a point of a wall produces an effect only on the narrow region opposite the point agrees well with numerical results and is suitable for practical uses.

2 Increase of radiative heat transfer causes decrease of the temperature difference between the duct walls and improves the heat transfer performance of the duct flow and heat exchangers analyzed here. The effect of radiation is more noticeable in laminar flows than in turbulent flows.

3 For counterflow and parallel-flow heat exchangers consisting of two ducts, the heat transfer effectiveness is proved to depend on three parameters:  $St-l$ ,  $M'$  and  $\Delta T$ . The effectiveness can be improved by increase of these parameters.

## References

- Hosegood S. B., Gutmann H., Hansen U., Smith E., McIver R. F.,

Harper C., Mancini G., and Del Beccaro R., "Preliminary Outline for a 1000°C Prismatic Fuelled HTR to Supply Process Heat and Electricity," Papers of Meeting on Industrial and Technological Importance on Process Heat and Its Substitution Possibilities by Nuclear Energy, Brussels, 1973.

2 Bergles A. E., and Webb R. L., "Bibliography on Augmentation of Convective Heat and Mass Transfer," Augmentation of Convective Heat and Mass Transfer, Winter Annual Meeting of ASME, Dec. 1970.

3 Siegel R., and Howell J. R., *Thermal Radiation Heat Transfer*, McGraw-Hill, New York, 1972, pp. 627-658.

4 Hasegawa S., Echigo R., Ichimiya K., and Kamiuto K., "Augmentation on Heat Transfer by Thermal Radiation Shielding Plate Placed in a Duct," *Heat Transfer 1974*, JSME/JSChE, Tokyo, 1974, Vol. I, pp. 108-112.

5 Siegel R., and Perlmutter M., "Convective and Radiant Heat Transfer for Flow of a Transparent Gas in a Tube With a Gray Wall," *International Journal of Heat and Mass Transfer*, Vol. 5, 1962, pp. 639-660.

6 Liu S. T., and Thorson R. S., "Combined Forced Convection and Radiation Heat Transfer in Asymmetrically Heated Parallel Plate Channels," *Proceedings of the 1970 Heat Transfer and Fluid Mechanics Institute*,

Stanford University Press, Stanford, Calif., 1970, pp. 32-44.

7 Keshock E. G., and Siegel R., "Combined Radiation and Convection in an Asymmetrically Heated Parallel Plate Flow Channel," *JOURNAL OF HEAT TRANSFER*, TRANS. ASME, Series C, Vol. 86, No. 3, 1964, pp. 341-350.

8 Perlmutter M., and Siegel R., "Effect of Specularly Reflecting Gray Surface on Thermal Radiation Through a Tube and From Its Heated Wall," *JOURNAL OF HEAT TRANSFER*, TRANS. ASME, Series C, Vol. 85, No. 1, 1963, pp. 55-62.

9 Rohsenow W. M., and Hartnett J. P., *Handbook of Heat Transfer*, McGraw-Hill, New York, 1973, pp. 7-80, Table 21.

10 Rohsenow W. M., and Hartnett J. P., *Handbook of Heat Transfer*, McGraw-Hill, New York, 1973, pp. 7-101, Table 26.

11 Rohsenow W. M., and Hartnett J. P., *Handbook of Heat Transfer*, McGraw-Hill, New York, 1973, pp. 7-78, Table 19 and pp. 7-24, Fig. 9.

12 Rohsenow W. M., and Hartnett J. P., *Handbook of Heat Transfer*, McGraw-Hill, New York, 1973, pp. 7-100, Table 25 and pp. 7-32, equation (45).

# ERRATUM

Erratum: U. Magrini and E. Nannei, "On the Influence of the Thickness and Thermal Properties of Heating Walls on the Heat Transfer Coefficients in Nucleate Pool Boiling," published in the May 1975 issue of the JOURNAL OF HEAT TRANSFER, pp. 173-178.

Page 175, equation (3):  $\Delta T = 0.27 \left(\frac{g}{A}\right)^{0.25} \left\{1 + \frac{4.10^4}{\sqrt{k\rho c}} [1 - \exp(-4.5 \cdot 10^9 (kd)^3)]\right\}^{0.75}$ .

Page 176, right-hand column, paragraph 2, line 2: 0.9 mm.

Reference 23, line 3; Izv. Akad. Nauk.

Reference 25, line 1: Walls.

Reference 28, line 3: Sept. 12-15, 1973.

Fig. 1: schematic.

Figs. 3 and 4: thicknesses.

D. M. Burch  
B. A. Peavy

Department of Mechanical Engineering,  
University of Maryland,  
College Park, Md.

# Transient Temperature Distributions in Heat-Generating Transpiration- Cooled Tubes and Plates

*This paper investigates the transient temperature distribution in transpiration-cooled porous matrices, after sudden initiation of uniform internal heat generation. Analytic solutions are derived for the tube and plate geometries that include the effect of forced convection heat transfer at the gas-exit surface where the conventional heat-transfer coefficient is used to define the boundary condition.*

## 1 Introduction

A transpiration-cooled matrix with internal heat generation may be used as a compact heat exchanger or chemical reactor. In these applications, a porous matrix is made to generate internal heat by passing a constant electric current longitudinally through it. In a compact heat exchanger, a gas is very efficiently heated by forcing it to transpire through a porous heat source. In a chemical reactor, the injection of transpiration-heated catalyst gas is used to control the rate of a chemical reaction taking place between the species of a gas mixture flowing at the gas-exit surface. In the starting operation of either of these applications, the forcing function may be treated as a stepwise increase in the rate of internal heat generation, uniform with space and constant with time. For a chemical reactor, the flow of reacting gas at the gas-exit surface gives rise to significant forced convection heat transfer between the matrix surface and the bulk of the reacting gas mixture.

In many porous heat transfer matrices, heat is readily conducted perpendicular to the gas flow direction, and the internal wetted surface area and the interstitial convective heat transfer coefficient between the gas and matrix are large. These conditions cause the temperature of the gas and matrix to become substantially equal within only a few pore diameters from the gas-entry surface.<sup>1</sup> A direct consequence of this condition is that the gas and matrix temperature may be treated as being equal, affording a significant simplification in the mathematical analysis. Another consequence

of this condition is that the conventional heat-transfer coefficient definition may be used to define a convective boundary condition at the gas-exit surface of the porous matrix. Studies of transpiration-cooled matrices [1-4]<sup>2</sup> indicate that the assumption of equal fluid and matrix temperature is not unreasonable.

Green [2] derived analytic solutions for the steady-state temperature distribution in a heat-generating transpiration-cooled plate. The gas-exit surface was taken to be adiabatic. Schneider [3] used the finite-difference technique to analyze the steady-state temperature distribution in power-producing transpiration-cooled cylinders and slabs for the case of nonuniform heat generation and variable thermal properties. Later Schneider [4] extended Green's analytic solution to include the effect of forced convection heat transfer at the gas-exit surface of a porous slab generating uniformly distributed heat and presented similar solutions for porous cylinders.

Previous time-dependent heat-transfer solutions [8-11] were derived for cases involving an initial step increase in the rate of convective heat transfer at one of the bounding surfaces of a transpiration heat transfer system. In the following section analytic solutions are derived for predicting transient temperature distributions for transpiration-cooled or -heated plates in which the forcing function is a step increase in the rate of internal heat generation.

## 2 Analysis

Assumptions made in the analysis are outlined in the following:

- 1 Thermal, physical, and transport properties are constant.
- 2 Rate of internal heat generation is constant.
- 3 Heat conduction and fluid flow are one dimensional in a direction normal to the bounding surfaces.
- 4 The gas and matrix temperature are equal at any position within the matrix.

<sup>1</sup> During the review of this paper it was pointed out that within compact heat exchangers the temperature difference between the fluid and matrix may become large as the transpirant flow rate is made to increase. For such cases, the analytic solutions of the present paper will represent approximate solutions for the actual matrix startup.

Contributed by the Heat Transfer Division for publication in the JOURNAL OF HEAT TRANSFER. Manuscript received by the Heat Transfer Division October 21, 1974. Paper No. 75-HT-111.

<sup>2</sup> Numbers in brackets designate References at end of paper.

**A Tube Solution.** With the flow of transpirant radially inward, a heat balance may be performed on a cylindrical element of unit length and thickness,  $dr$ , of the porous cylinder system of Fig. 1. The sum of the net rates of heat conduction, increase in fluid energy content, and the internal heat generation is equal to the rate of energy storage in the cylindrical element, giving the partial differential equation:

$$2\pi k_m \frac{\partial}{\partial r} \left( r \frac{\partial T}{\partial r} \right) + \dot{m} C_g \frac{\partial T}{\partial r} + 2\pi r \lambda = 2\pi r \rho_m C_m \frac{\partial T}{\partial t}$$

OR

$$\frac{\partial^2 v}{\partial \eta^2} + \frac{(1 + 2\nu)}{\eta} \frac{\partial v}{\partial \eta} + 1 = \frac{\partial v}{\partial F_0} \quad (1)$$

where the dimensionless temperature excess, flow rate, radial distance, and time are given by

$$v = \frac{T - T_0}{\lambda a^2 / k_m}, \quad \nu = \frac{\dot{m} C_g}{4\pi k_m}, \quad \eta = r/a, \quad \text{and} \quad F_0 = \left( \frac{k_m}{\rho_m C_m} \right) \frac{t}{a^2}$$

Assuming a solution of the form

$$v(\eta, F_0) = \psi(\eta) + \phi(\eta, F_0)$$

the following general solution to (1) is obtained:

$$v = A_0 + B_0 \eta^{-2\nu} - \frac{\eta^2}{4(\nu + 1)} + \eta^{-\nu} \sum_{n=1}^{\infty} e^{-\beta_n^2 F_0} [A_n J_\nu(\beta_n \eta) + B_n Y_\nu(\beta_n \eta)] \quad (2)$$

where  $\beta_n$  is the separation constant, and  $J_\nu(\beta_n \eta)$  and  $Y_\nu(\beta_n \eta)$  are Bessel functions of the first and second kind, respectively, of order  $\nu$ . At the fluid-entry surface, the rise in fluid energy is equal to the rate of heat conduction from the surface, or

$$-2\pi b k_m \frac{\partial T}{\partial r} = \dot{m} C_g (T - T_0) \quad \text{at} \quad r = b \quad (3)$$

At the fluid-exit surface, the rate of heat conduction is equal to the convective heat transfer from the surface, or

$$-K_m \frac{\partial T}{\partial r} = h(T_f - T) \quad \text{at} \quad r = a \quad (4)$$

The foregoing boundary conditions may be expressed by the dimensionless relations:

$$\frac{\partial v}{\partial \eta} = -2\nu(a/b)v \quad \text{at} \quad \eta = b/a \quad (5)$$

$$\frac{\partial v}{\partial \eta} = H(v - v_f) \quad \text{at} \quad \eta = 1 \quad (6)$$

where the Biot number  $H = ha/K_m$  and the temperature excess  $v_f = (T_f - T_0)/(\lambda a^2/K_m)$ . Applying these boundary conditions to the

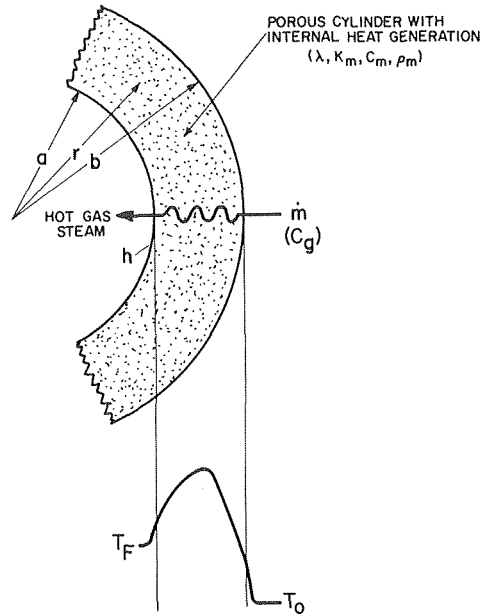


Fig. 1 Porous cylinder system

complementary function  $A_0 + B_0 \eta^{-2\nu}$  gives the initial condition

$$v = \frac{H v_f}{H + 2\nu} \eta^{-2\nu} \quad \text{for} \quad F_0 \leq 0 \quad \text{and} \quad 1 \leq \eta \leq b/a \quad (7)$$

Applying the boundary condition at the fluid-entry surface (5) leads to

$$A_0 = (b/a)^2 / 4\nu \quad (8)$$

$$A_n [H J_\nu(\beta_n) + \beta_n J_{\nu+1}(\beta_n)] + B_n [H Y_\nu(\beta_n) + \beta_n Y_{\nu+1}(\beta_n)] = 0 \quad (9)$$

From the boundary conditions at fluid-exit surface (6)

$$B_0 = \frac{H - 2}{4(H + 2\nu)(\nu + 1)} + \frac{v_f H}{H + 2\nu} - \frac{H(b/a)^2}{4\nu(H + 2\nu)} \quad (10)$$

$$B_n [2\nu Y_\nu(\beta_n b/a) - (b/a)\beta_n Y_{\nu+1}(\beta_n b/a)] + A_n [2\nu J_\nu(\beta_n b/a) - (b/a)\beta_n J_{\nu+1}(\beta_n b/a)] = 0 \quad (11)$$

Combining equation (9) and (11), the following characteristic equation is obtained:

$$Q_n R_n - S_n P_n = 0 \quad (12)$$

where

$$P_n = 2\nu Y_\nu(\beta_n b/a) - (b/a)\beta_n Y_{\nu+1}(\beta_n b/a)$$

## Nomenclature

$a$  = inside tube radius  
 $b$  = outside tube radius  
 $C$  = specific heat  
 $F_0$  = dimensionless time (Fourier modulus),  $F_0 \left( \frac{K_m}{\rho_m C_m} \right) \frac{t}{a^2}$  (tube), or  $F_0 = \left( \frac{K_m}{\rho_m C_m} \right) \frac{t}{\delta^2}$  (slab)  
 $g$  = dimensionless mass flow rate of transpirant,  $g = GC_g \delta / K_m$   
 $G$  = superficial mass flux of transpirant approaching fluid-entry surface  
 $h$  = convective heat-transfer coefficient  
 $H$  = dimensionless heat-transfer coefficient (Biot number),  $H = \frac{ha}{K_m}$  (tube), or  $H = \frac{h\delta}{K_m}$  (slab)

$K$  = thermal conductivity  
 $\dot{m}$  = transpirant mass flow rate  
 $t$  = time  
 $T$  = temperature  
 $x$  = distance from fluid-entry surface (slab)  
 $\beta_n$  = roots of characteristic equation  
 $\delta$  = slab thickness  
 $\eta$  = dimensionless radial distance,  $\eta = r/a$   
 $\lambda$  = rate of internal heat generation per unit volume  
 $\nu$  = dimensionless flow rate,  $\nu = \frac{\dot{m} C_g}{4\pi K_m}$   
 $\epsilon$  = dimensionless distance from fluid-entry surface,  $\epsilon = x/\delta$

$\rho$  = density  
 $v$  = dimensionless temperature,  $v = \frac{T - T_0}{\lambda a^2 / K_m}$  (tube), or  $v = \frac{T - T_0}{\lambda \delta^2 / K_m}$  (slab)  
 $\phi$  = time-dependent portion of solution  
 $\psi$  = steady-state portion of solution

## Subscripts

$f$  = refers to bulk fluid stream at fluid-exit surface  
 $g$  = refers to transpirant  
 $m$  = refers to matrix  
 $o$  = refers to transpirant supply condition

$$\begin{aligned}
Q_n &= 2\nu J_\nu(\beta_n b/a) - (b/a)\beta_n J_{\nu+1}(\beta_n b/a) \\
R_n &= HY_\nu(\beta_n) + \beta_n Y_{\nu+1}(\beta_n) \\
S_n &= HJ_\nu(\beta_n) + \beta_n J_{\nu+1}(\beta_n)
\end{aligned}$$

The eigen values  $\beta_n$  are the roots of the characteristic equation (12). Solving equation (11) for  $B_n$  gives

$$B_n = -A_n \frac{Q_n}{P_n} = -A_n \rho_n \quad (13)$$

where

$$\rho_n = Q_n/P_n = S_n/R_n$$

Substituting (13) into the general solution (2) and introducing the cylinder function  $C_\nu(\beta_n \eta)$ , we obtain

$$v = A_0 + B_0 \eta^{-2\nu} - \frac{\eta^2}{4(\nu+1)} + \eta^{-\nu} \sum_{n=1}^{\infty} e^{-\beta_n^2 F_0} E_n C_\nu(\beta_n \eta) \quad (14)$$

where

$$\begin{aligned}
C_\nu(\beta_n \eta) &= P_n J_\nu(\beta_n \eta) - Q_n Y_\nu(\beta_n \eta) \\
E_n &= A_n/P_n
\end{aligned}$$

Application of the initial condition (7) gives the following expression for  $E_n$ :

$$\sum_{n=1}^{\infty} E_n C_\nu(\beta_n \eta) = -A_0 \eta^\nu - B_0 \eta^{-\nu} + \frac{\eta^{\nu+2}}{4(\nu+1)} \quad (15)$$

The cylinder function has the following orthogonal property

$$\int \eta C_\nu(\beta_m \eta) C_\nu(\beta_n \eta) d\eta = 0 \quad \text{for } m \neq n \quad (16)$$

For  $m = n$  the integral becomes

$$\frac{1}{2} \eta^2 [C_\nu^2(\beta_n \eta) + C_{\nu+1}^2(\beta_n \eta) - C_\nu(\beta_n \eta) C_{\nu+1}(\beta_n \eta)] \quad (17)$$

Multiplying both sides of (15) by  $\eta C_\nu(\beta_n \eta)$ , integrating with respect to  $\eta$  over the width of the tube, and applying the orthogonal property (16), the following expression for the series coefficient  $E_n$  is obtained:

$$\begin{aligned}
E_n \int_1^{b/a} \eta C_\nu^2(\beta_n \eta) d\eta &= - \int_1^{b/a} \eta [A_0 \eta^\nu + B_0 \eta^{-\nu}] C_\nu(\beta_n \eta) d\eta \\
&\quad + \int_1^{b/a} \frac{\eta^{\nu+3}}{4(\nu+1)} C_\nu(\beta_n \eta) d\eta \quad (18)
\end{aligned}$$

The first integral on the right side of (18) is equal to

$$\frac{\eta}{\beta_n} [A_0 \eta^\nu + B_0 \eta^{-\nu}] C_{\nu+1}(\beta_n \eta) - \frac{2\nu B_0}{\beta_n^2} \eta^{-\nu} C_\nu(\beta_n \eta) \quad (19)$$

The second integral on the right side of (18) is equal to

$$\frac{1}{\beta_n^3} [(\beta_n \eta)^2 - 4\nu - 4] \eta C_{\nu+1}(\beta_n \eta) + \frac{2}{\beta_n^2} \eta^{\nu+2} C_\nu(\beta_n \eta) \quad (20)$$

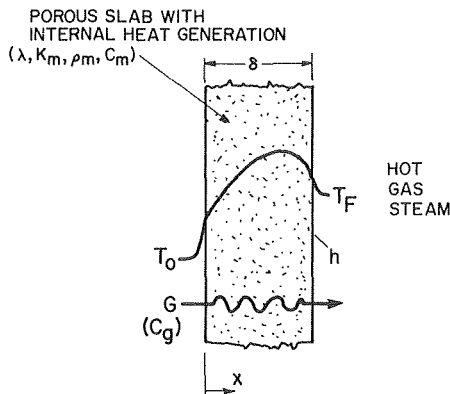


Fig. 2 Porous slab system

Using the Wronskian relation,

$$J_{\nu+1}(Z)Y_\nu(Z) - J_\nu(Z)Y_{\nu+1}(Z) = 2/\pi Z$$

the discrete values of the cylinder function are found to be

$$C_\nu(\beta_n b/a) = 2/\pi, \beta_n C_{\nu+1}(\beta_n) = 2H\rho_n/\pi$$

$$C_\nu(\beta_n) = -2\rho_n/\pi, \text{ and } \beta_n(b/a)C_{\nu+1}(\beta_n b/a) = 4\nu/\pi \quad (21)$$

Substituting the integral expressions (17), (19), and (20) into (18), and evaluating this expression at the upper limit,  $\eta = b/a$  and the lower limit,  $\eta = 1$ , and making use of the discrete values of the cylinder function (21), the series coefficient  $E_n$  is found to be

$$E_n = \frac{\pi}{\beta_n^4} \frac{H\rho_n - 2\nu(b/a)^\nu}{[(b/a)^2 - \rho_n^2 - (H\rho_n/\beta_n)^2 - 2\nu(\rho_n/\beta_n)^2 H]} \quad (22)$$

The final time-dependent solution is expressed by

$$\begin{aligned}
v &= \frac{(b/a)^2}{4\nu} + \left[ \frac{H-2}{4(H+2\nu)(\nu+1)} \right. \\
&\quad \left. + \frac{\nu H}{H+2\nu} - \frac{H(b/a)^2}{4\nu(H+2\nu)} \right] \eta^{-2\nu} - \frac{\eta^2}{4(\nu+1)} \\
&\quad + \eta^{-\nu} \sum_{n=1}^{\infty} E_n e^{-\beta_n^2 F_0} C_\nu(\beta_n \eta) \quad (23)
\end{aligned}$$

The steady-state portion of this solution is identical to Schneider's solution [4]. In the limit as the transpirant flow rate  $\nu$  approaches zero and  $\nu_f = 0$ , the foregoing time-dependent solution reduces to

$$\begin{aligned}
v &= \frac{1}{2H} [(b/a)^2 - 1] - \frac{1}{4} (\eta^2 - 1) + \frac{(b/a)^2}{2} \ln(\eta) \\
&\quad + \sum_{n=1}^{\infty} A_n e^{-\beta_n^2 F_0} [Y_1(\beta_n b/a) J_0(\beta_n \eta) - J_1(\beta_n b/a) Y_0(\beta_n \eta)] \quad (24)
\end{aligned}$$

where

$$A_n = \frac{-\pi(b/a)HJ_1(\beta_n b/a)Y_1(\beta_n b/a)}{\beta_n [\beta_n^2 (b/a)^2 Y_1^2(\beta_n b/a) - (\beta_n^2 + H^2) J_1^2(\beta_n b/a)]} \quad (25)$$

The eigen values  $\beta_n$  are the roots of the following characteristic equation:

$$\begin{aligned}
HJ_0(\beta_n)Y_1(\beta_n b/a) + \beta_n J_1(\beta_n)Y_1(\beta_n b/a) - HJ_1(\beta_n b/a)Y_0(\beta_n) \\
- \beta_n J_1(\beta_n b/a)Y_1(\beta_n) = 0 \quad (26)
\end{aligned}$$

**B Slab Solution.** Performing a heat balance on an elemental slice of the porous slab system of Fig. 2, the sum of the net rates of heat conduction, increase in fluid energy content, and internal heat generation is equal to the rate of energy storage in the elemental slice, giving the partial differential equation:

$$K_m \frac{\partial^2 T}{\partial x^2} - GC_g \frac{\partial T}{\partial x} + \lambda = \rho_m C_m \frac{\partial T}{\partial t}$$

or

$$\frac{\partial^2 v}{\partial \epsilon^2} - g \frac{\partial v}{\partial \epsilon} + 1 = \frac{\partial v}{\partial F_0} \quad (27)$$

where the dimensionless temperature excess, distance, flow rate, and time are given by

$$v = \frac{T - T_0}{\lambda \delta^2 / K_m}, \quad \epsilon = x/\delta, \quad g = \frac{GC_g \delta}{K_m}, \quad \text{and } F_0 = \frac{K_m}{\rho_m C_m} \frac{t}{\delta^2}$$

Assuming a solution of the form

$$v(\epsilon, F_0) = \psi(\epsilon) + \phi(\epsilon, F_0)$$

the general solution to (24) is found to be

$$\begin{aligned}
v &= A_0 + B_0 e^{g\epsilon} + \epsilon/g + \sum_{n=1}^{\infty} \exp\left[\frac{g}{2}\epsilon - (\beta_n^2 + \frac{g^2}{4})F_0\right] \\
&\quad \times [A_n \cos(\beta_n \epsilon) + B_n \sin(\beta_n \epsilon)] \quad (28)
\end{aligned}$$

At the fluid-entry surface, the rise in fluid energy is equal to the rate of heat conduction from the surface, or

$$GC_g(T_0 - T) = -K_m \frac{\partial T}{\partial x} \quad \text{at } x = 0 \quad (29)$$

At the fluid-exit surface, the rate of heat conduction is equal to the convection heat transfer from the surface, or

$$-K_m \frac{\partial T}{\partial x} = h(T - T_f) \text{ at } x = \delta \quad (30)$$

The foregoing boundary conditions may be expressed by the dimensionless relations

$$g v = \frac{\partial v}{\partial \epsilon} \text{ at } \epsilon = 0 \quad (31)$$

$$\frac{\partial v}{\partial \epsilon} = -H(v - v_f) \text{ at } \epsilon = 1 \quad (32)$$

where the dimensionless heat transfer coefficient and dimensionless temperature difference are defined by

$$H = \frac{h\delta}{K_m} \text{ and } v_f = \frac{T_f - T_0}{\lambda\delta^2/K_m}$$

Applying boundary conditions (31) and (32) to the complementary function,  $A_0 + B_0 e^{g\epsilon}$ , the following initial condition is obtained:

$$v = \frac{v_f H}{H + g} e^{g(\epsilon-1)} \text{ for } F_0 \leq 0 \text{ and } 0 \leq \epsilon \leq 1 \quad (33)$$

Applying boundary condition (31) leads to

$$A_0 = 1/g^2 \quad (34)$$

$$A_n = B_n \left( \frac{2\beta_n}{g} \right) \quad (35)$$

Boundary condition (32) gives

$$B_0 = e^{-g} \left[ \frac{H}{H + g} (v_f - \frac{1}{g}) - \frac{1}{g^2} \right] \quad (36)$$

and leads to the characteristic equation

$$\tan(\beta_n) = \frac{\beta_n(H + g)}{\beta_n^2 - \frac{g}{2}(H + \frac{g}{2})} \quad (37)$$

The eigen values  $\beta_n$  are the roots of the foregoing transcendental equation. Introducing (34), (35), and (36) into (28) gives

$$v = \left[ \frac{H}{H + g} (v_f - \frac{1}{g}) - \frac{1}{g^2} \right] e^{g(\epsilon-1)} + \frac{1}{g^2} + \epsilon/g + \sum_{n=1}^{\infty} A_n \exp\left[\frac{g}{2}\epsilon - (\beta_n^2 + \frac{g^2}{4})F_0\right] \left[ \cos(\beta_n\epsilon) + \left(\frac{g}{2\beta_n}\right) \sin(\beta_n\epsilon) \right] \quad (38)$$

Applying the initial condition (33), leads to the following relation:

$$\left( \frac{1}{g^2} + \frac{H}{(H + g)g} \right) e^{g(\frac{\epsilon}{2} - 1)} - \frac{1}{g^2} e^{-g\epsilon/2} - \frac{\epsilon}{g} e^{-g\epsilon/2} = \sum_{n=1}^{\infty} A_n \left[ \cos(\beta_n\epsilon) + \frac{g}{2\beta_n} \sin(\beta_n\epsilon) \right] \quad (39)$$

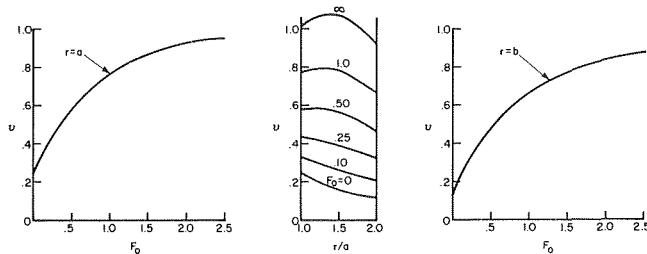


Fig. 3 Transient temperature distribution in a transpiration-cooled tube after sudden initiation of internal heat generation ( $\nu = 0.5$ ,  $H = 1$ ,  $b/a = 2$ , and  $\nu_f = 0.5$ )

The Sturm-Liouville theorem may be used to obtain the orthogonal property

$$\int_0^1 \left[ \cos(\beta_n\epsilon) + \frac{g}{2\beta_n} \sin(\beta_n\epsilon) \right] \left[ \cos(\beta_m\epsilon) + \frac{g}{2\beta_m} \sin(\beta_m\epsilon) \right] d\epsilon = 0 \text{ for } m \neq n \quad (40)$$

Multiplying equation (38) by  $(\cos(\beta_m\epsilon) + g/2\beta_m \sin(\beta_m\epsilon))$ , applying the orthogonal relation (40), evaluating the integrals, and making use of (37) gives the series coefficient

$$A_n = \frac{-2\beta_n \left[ g\beta_n + \frac{H}{H + g} (\beta_n^2 + \frac{g^2}{4}) e^{-g/2} \sin(\beta_n) \right]}{(\beta_n^2 + \frac{g^2}{4})^2 \left[ 1 + \frac{\beta_n^2 + \frac{g}{2}(H + \frac{g}{2})}{\beta_n^2(H + g)} \sin^2(\beta_n) \right]} \quad (41)$$

The final time-dependent solution is given by equation (38) with the series coefficient given by (41). The steady-state portion of the foregoing solution is identical to that of Schneider [4]. In the limit as the transpirant flow rate,  $g$  approaches zero and  $v_f = 0$ , the foregoing time-dependent solution reduces to the well-known solution of Cawslaw and Jaeger [12]:

$$v = \frac{1}{H} + \frac{1}{2} - \frac{\epsilon^2}{2} - 2H \sum_{n=1}^{\infty} \frac{\cos(\beta_n\epsilon) e^{-\beta_n^2 F_0}}{\beta_n^2 [\beta_n^2 + H^2 + H] \cos(\beta_n)} \quad (42)$$

where the eigen values  $\beta_n$  are given by the characteristic equation

$$\beta_n \tan(\beta_n) = H \quad (43)$$

### 3 Analytical Results

A sample solution for the transient temperature distribution in a transpiration-cooled tube after sudden initiation of internal heat generation is shown in Fig. 3. A radius ratio,  $b/a = 2$ , an inside Biot number,  $H = 1$ , a transpirant flow rate,  $\nu = 0.5$ , and a temperature excess,  $v_f = 0.5$ , were used for this example. In the center plot radial temperature distributions are plotted for selected Fourier numbers (elapsed times). Initially ( $F_0 = 0$ ), the tube is at its initial condition. As time progresses, the temperature distributions rise in the tube until a steady-state distribution ( $F_0 = \infty$ ) is reached. To the left of the center plot, the variation of temperature with time is plotted for the inside fluid-exit surface. To the right of the center plot, a similar plot is given for the outside fluid-entry surface. At both surfaces the temperature response appears to be exponential and approximately the same time is required for a steady-state condition to be reached. A similar set of graphs is presented in Fig. 4 for the transient temperature distribution in a transpiration-cooled slab after sudden initiation of internal heat generation.

The transpirant flow rate significantly affects the transient temperature distribution within a heat generating, transpiration-cooled or -heated matrix through its enthalpy transport action within the matrix and at the boundary layers at its bounding surfaces. Variations in the transpirant flow rate will have a strong influence on the heat transfer coefficients at the bounding surfaces. Mickley, et al. [5] has shown that the following relation may be

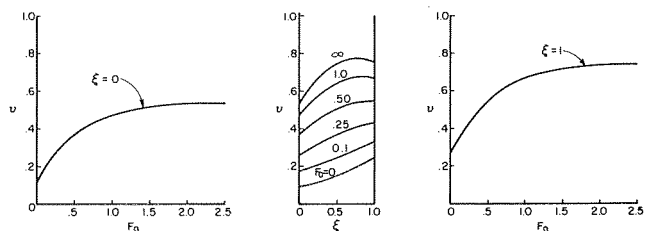


Fig. 4 Transient temperature distribution in a transpiration-cooled slab after sudden initiation of internal heat generation ( $g = 1$ ,  $H = 1$ , and  $\nu_f = 1/2$ )

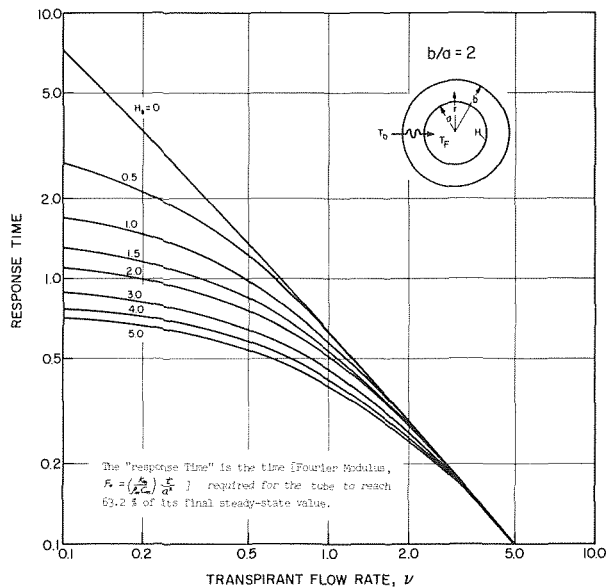


Fig. 5 Response times at gas-exit surface of a transpiration-cooled tube, after sudden initiation of internal heat generation

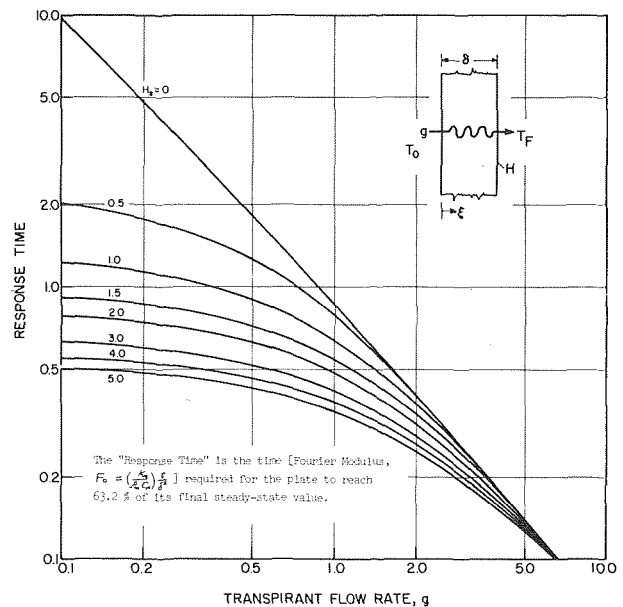


Fig. 6 Response times at gas-exit surface of a heat-generating transpiration-cooled plate, after sudden initiation of internal heat generation

used to adjust heat transfer coefficients for the blowing enthalpy transport action for flow along smooth plates:

$$H = \frac{g}{e^{g/H_*} - 1} \quad (44)$$

where  $H_*$  is the Biot number without blowing. Recent studies [6, 7] indicate that this correlation (after substituting  $2\nu$  for  $g$ ) is approximately valid for flow at the inside surface of a cylindrical annulus.

For compact transpiration heat exchangers and chemical reactor applications, the time required for fluid-exit surface to reach a steady-state condition (after sudden initiation of internal heat generation) is of particular interest. For the purposes of the present analysis, the "response time" is defined as the time (Fourier modulus) required for the temperature to reach 63.2 percent of its final steady-state value. Using the precedingly derived analytic solutions and relation (44), charts were prepared which correlate response times at the fluid-exit surface with respect to dimensionless flow rates and Biot numbers for the tube (Fig. 5) and the plate (Fig. 6) geometries. The Biot number,  $H_*$ , is the dimensionless heat transfer coefficient calculated by conventional correlations that neglect the effect of the blowing enthalpy transport action. In both charts the curve corresponding to  $H_* = 0$  represents a condition of no forced convection heat transfer at the fluid-exit surface. This condition is approached in heat-generating, transpiration heat exchangers. The other curves correspond to finite rates of forced convection heat transfer that would exist inside chemical reactors. Notice that for chemical reactors ( $H_* > 0$ ), the response time initially decreases slowly as the transpirant flow rate is increased. For large values of transpirant flow rate, the effect of this

variable becomes large. The effect of forced convection heat transfer,  $H_*$ , on the response time diminishes as the transpirant flow rates increase and vanish for large transpirant flow rates.

## References

- Weinbaum, L., and Wheeler, H. L., Jr., "Heat Transfer in Sweat Cooled Porous Metals," *Journal of Applied Physics*, Vol. 20, Jan. 1949.
- Leon Green, Jr., "Gas Cooling of a Porous Heat Source," *Journal of Applied Mechanics*, TRANS. ASME, Vol. 19, No. 2, 1952, p. 173.
- Schneider, P. J., "Numerical Method for Porous Heat Sources," *Journal of Applied Physics*, Vol. 24, No. 3, Mar. 1953.
- Schneider, P. J., "Temperature and Thermal Stresses in Transpiration-Cooled Power-Producing Plates and Tubes," *Jet Propulsion*, Vol. 27, Aug. 1957.
- Mickley, H. S., Ross, R. C., Squyers, A. L., and Steward, W. E., "Heat, Mass, and Momentum Transfer for Flow Over a Flat Plate With Blowing or Suction," NACA TN 3208, July 1954.
- Kalny R., "Measurements of the Effect of Suction on Friction and Heat Transfer at the Outer Wall of an Annular Turbulent Flow," PhD thesis, Department of Mechanical Engineering, University of Maryland, 1970.
- Aggarwal, J. K., and Hollingsworth, M. A., "Heat Transfer for Turbulent Flow With Suction in a Porous Tube," *International Journal of Heat and Mass Transfer*, Vol. 16, 1973, pp. 591-609.
- Schneider, P. J. and Brogan, J. J., "Temperature Response of a Transpiration-Cooled Plate," *Journal of the ARS*, Vol. 32, No. 1, Jan. 1962.
- Jiji, L., "Transient Response of a Transpiration-Cooled Cylindrical Surface," *AIAA Journal*, Vol. 3, No. 11, Dec. 1965.
- Burch, D. M., Peavy, B. A., and Allen, R. W., "Time-Dependent Transpiration Heat Transfer in Porous Cylinders," *JOURNAL OF HEAT TRANSFER*, TRANS. ASME, Series C, Vol. 96, May 1974.
- Burch, D. M., "Thermal Analysis for a Transpiration-Cooled Plate," Paper for Masters Degree at University of Maryland, July 1970.
- Cawslaw, H. S., and Jaeger, J. C., *Conduction of Heat in Solids*, Clarendon Press, Oxford England, 1959.

N. Hay

Senior Lecturer, Department of Mechanical Engineering, University of Nottingham, England

P. D. West

Lecturer, Department of Mechanical and Production Engineering, Derby College of Art and Technology, Derby, England

## Heat Transfer in Free Swirling Flow in a Pipe

*The local heat transfer coefficient, for air flowing through a pipe with a swirling motion, was measured at various stations downstream of the swirling air inlet. The swirling motion of the air was produced by a single tangential slot, initially at 90 deg to the pipe axis, through which the air was introduced. The dimensions of the slot and the angle of tangency were varied and the resultant flow field inside the pipe was measured and expressed in the form of local "swirl numbers." The augmentation of heat transfer was found to be a function of the swirl number and a correlation for this function is presented. At some locations, the augmentation can be as much as eight times the value for fully developed nonswirling turbulent flow.*

### Introduction

This investigation stems from the field of gas turbine blade cooling. More effective blade cooling is continually being sought, in order to be able to operate at higher turbine inlet temperatures, and hence higher efficiency. Various methods of augmenting the heat transfer coefficient on the cooling air side of the blade have been tried, as detailed by Halls [1, 2].<sup>1</sup> Some of the cooling passages in the rotating blades are small and circular. Augmentation of the heat transfer coefficient in these passages may be achieved by side entries giving the cooling air a swirling motion. The objective of this investigation was to measure the local heat transfer coefficients for air flowing through a circular pipe with a swirling motion such as might occur in a turbine blade cooling situation.

### Previous Work

In the investigations of swirling flows, the most useful development has been the concept of the swirl number which adequately defines the local flow field.

The swirl number is defined as

$$S = \frac{G_{\theta}}{G_x R}$$

which is effectively the ratio of the angular momentum to linear momentum flux of the swirling airstream. This concept was used by Leuckel [3] and Kawaguchi and Sato [4] and later by Senoo and

Nagata [5] who have used the swirl number to correlate friction coefficient measurements for swirling flow in pipes.

The heat transfer aspects of swirling flows were investigated by Gutstein, Converse, and Peterson [10] who used helical vane inserts along the heated tubular test section in which air was the working fluid. The heat transfer rates and pressure drops increased substantially as the insert pitch to tube diameter ratio decreased. Lopina and Bergles [11] have carried out tests with full length twisted tapes along the test section tube, with water as the working fluid. For a constant pumping power a comparison of swirl and straight flow indicated an improvement in heat transfer rate of at least 20 percent with swirling flow.

Narezhny and Sudarev [12] and Ivanova [13] used swirl generators at the pipe inlet only, in the form of helically twisted inserts and vane swirl generators, respectively. These produced a free swirling flow in the heated test sections and increases in the heat transfer rates which depended on inlet angle. Migay and Golubev [14] also show that free swirling flow increases the heat transfer rate, and present theoretical and experimental data which are in agreement.

In work by Blum and Oliver [15] the local heat transfer coefficients were determined for air and carbon dioxide in an electrically heated tube. An initial vortex generator, with four square slots was used to inject the gas tangentially into the tube. The heat transfer coefficients were derived from the tube wall temperatures assuming a uniform heat flux and a linear temperature rise for the fluid. The directions of the flow were explored in a separate experiment.

It is interesting to point out the similarities and differences between the experimental arrangements of Blum and Oliver [15] and the present work. In both cases air was swirled in a pipe with a swirl generator at the inlet. The method of swirl generation was different being symmetrical in the former and unsymmetrical in the latter. In the present work all heat transfer and flow field measurements are taken in the same pipe and the swirling flow is

<sup>1</sup> Numbers in brackets designate References at end of paper.

Contributed by the Heat Transfer Division for publication in the JOURNAL OF HEAT TRANSFER. Manuscript received by the Heat Transfer Division November 18, 1974. Paper No. 75-HT-YY.

cooled. The local heat transfer coefficient is measured at the wall using heat flux meters.

Blum and Oliver measured a local heat transfer coefficient at the pipe inlet which was about 10 times that for fully developed nonswirling turbulent flow and about 2.5 times the value at pipe entry without swirl.

In all cases of swirling flow the heat transfer rates are increased at the expense of increased pumping power.

In this investigation the concept of the swirl number, which has been used so far to describe the flow field only, is successfully extended to correlate the heat transfer performance of cooled swirling air flows.

### Apparatus

Fig. 1 shows the arrangement of the experimental apparatus. A full description is given by West [17]. Air is induced from the atmosphere by a centrifugal fan and delivered through a flow straightener, metering orifice, and heater to a mixing chamber. The air heated to 75°C then flows through a single rectangular cross-sectioned inlet duct of variable aspect ratio, and enters the swirl pipe test length tangentially, at an angle of 90, 60, or 30 deg to the pipe axis. This single inlet slot produces a swirling air flow down the pipe to the end open to atmosphere. A long inlet pipe is used when testing for fully developed nonswirling turbulent flow.

The swirl pipe is a clear acrylic (perspex) cylinder 50.8 mm (2 in.) ID, 15.9 mm ( $\frac{5}{8}$  in.) wall thickness and 914 mm (36 in.) long.

There are holes in the pipe at 10 axial measuring positions for locating heat flux meters, velocity probes and temperature probes.

A three-tube probe is used for traversing and determining the magnitude and direction of the velocities of the swirling air stream. This probe was designed using tube dimensions given by Bryer, Walshe, and Garner [16].

### Heat Flux Meters (HFM)

Eighteen heat flux meters (HFM) are situated in the wall of the

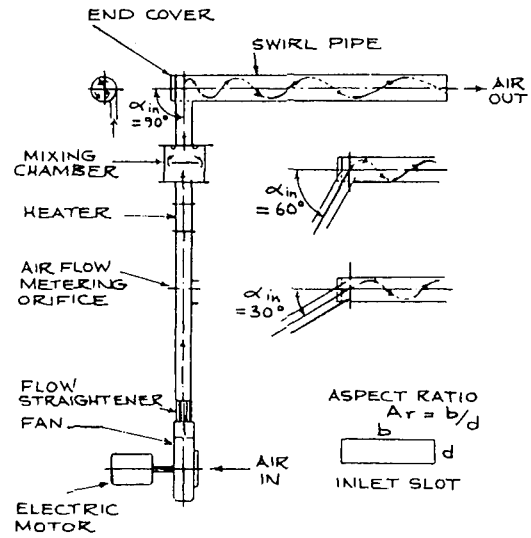


Fig. 1 Swirling flow rig

swirl pipe at various axial and angular positions from the pipe inlet to determine the local heat flux densities from the airstream. The heat flux meters are in the form of cylindrical plugs fitted into the wall of the swirl pipe. The pure iron sensing area is made flush with the inside surface of the pipe and is in contact with the airstream.

The HFM (Fig. 2) consists of a pure iron core, a cork internal insulator, and a cork sleeve insulator. Constantan wires are soldered to each end face in grooves, and to each end of the central stem of the iron core. These wires together with the pure iron core and an iron wire, provide iron-constantan thermocouple combinations for temperature measurement.

### Nomenclature

$A$  = cross-sectional area of the swirl pipe ( $m^2$ )

$D$  = nominal inside diameter of the swirl pipe

$G_x$  = local axial flux of linear momentum ( $kg\ m/s^2$ )

$$G_x = 2\pi \int_{r=0}^{r=R} \rho r u^2 dr$$

$G_\theta$  = local axial flux of angular momentum ( $kg\ m^2/s^2$ )

$$G_\theta = 2\pi \int_{r=0}^{r=R} \rho r^2 u v dr$$

$h$  = local heat transfer coefficient (fluid to wall) ( $W/m^2K$ )

$$h = \frac{\dot{q}''}{T_b - T_w}$$

$h_w$  = heat transfer coefficient for fully developed nonswirling turbulent flow in a pipe ( $W/m^2K$ )

$k$  = thermal conductivity of the airstream ( $W/mK$ )

$Nu$  = local Nusselt number,  $Nu = \frac{hD}{k}$

$Nu_x$  = local Nusselt number,  $Nu_x = \frac{hx}{k}$

$Nu_w$  = Nusselt number for fully developed nonswirling turbulent flow in the pipe  $Nu = \frac{h_w D}{k}$

$Nu/Nu_w$  = heat transfer augmentation

$Pr$  = Prandtl number

$\dot{q}''$  = local heat flux density from the air stream to the pipe wall ( $W/m^2$ )

$r$  = any radius in the swirl pipe

$R$  = inside radius of the swirl pipe

$Re$  = Reynolds number  $Re = \frac{\rho U D}{\mu}$

$Re_x$  = local Reynolds number  $Re_x = \frac{\rho U x}{\mu}$

$S$  = local swirl number  $S = \frac{G_\theta}{G_x R}$

$T_b$  = local bulk stagnation temperature of the airstream ( $^{\circ}C$ )

$T_w$  = local wall surface temperature inside the swirl pipe ( $^{\circ}C$ )

$u$  = axial component of point helical velocity of the airstream in the swirl pipe ( $m/s$ )

$U$  = mean axial velocity of the airstream ( $m/s$ )

$v$  = tangential component of point helical velocity of the airstream in the swirl pipe ( $m/s$ )

$x$  = axial distance along the swirl pipe from the inlet

$\alpha$  = local airstream angle, measured from the swirl pipe center line upstream direction (deg)

$\alpha_{in}$  = inlet duct angle (deg)

$\phi$  = "a function of"

$\mu$  = dynamic viscosity of the airstream ( $Ns/m^2$ )

$\rho$  = density of the airstream ( $kg/m^3$ )

$\theta$  = angular position in the swirl pipe (deg)

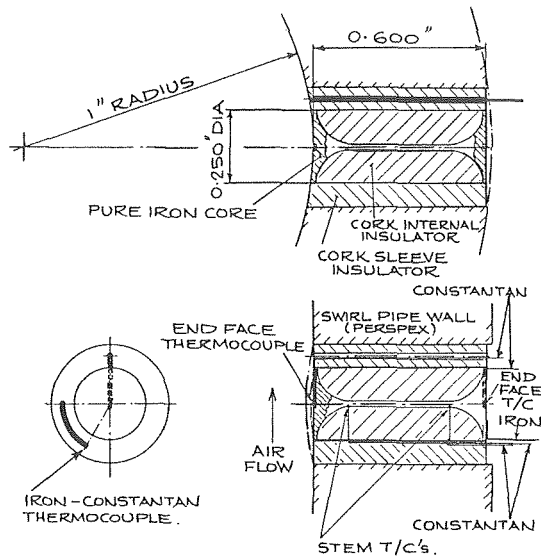


Fig. 2 Heat flux meter

The heat flux density is calculated from the temperature difference across the end faces and the thermal resistance of the HFM. This value was checked using the temperature drop along the stem and the thermal resistance of the stem, and indicated some heat leakage.

Calibration tests were carried out on the HFM, and while it was difficult to determine the accuracy exactly, it is estimated to be in the order of  $\pm 5$  percent.

The iron sensing surface of the HFM is at a lower temperature than the surrounding wall inside surface. This causes a local distortion and step in the temperature boundary layer of the air flow, and produces a local heat transfer coefficient which is higher than for the immediate surrounding surface. The magnitude of this increase was estimated from thermocouples mounted in the HFM cork end face adjacent to the sensing surface and found to be about 40 percent. Additionally, the heat transfer coefficients measured by the HFM for fully developed nonswirling turbulent flow were found to be about 40 percent higher than the values given by the correlation

$$Nu = 0.023Re^{0.8}Pr^{0.3}$$

This thermal entry effect on the HFM together with any heat leakage effects can be compensated for to a large extent by looking at the augmentation of heat transfer given by the ratio of Nusselt numbers,  $Nu/Nu_{\infty}$  where both  $Nu$  and  $Nu_{\infty}$  are obtained in the same pipe, over the same range of Reynolds number using the same heat flux meter, except that for  $Nu_{\infty}$  the flow is not swirling. This approach has been adopted here for presenting the majority of the heat transfer results.

## Tests and Discussion of Results

Table 1 presents a summary of the tests carried out with the main flow parameters. The results will be discussed first from the flow field aspect and then the heat transfer aspect will be covered.

**Swirling Flow Field.** Detailed probing of the flow field for various geometries and flow rates were made. Typical distribution of air stream angle, axial velocity component, and tangential velocity component are shown in Fig. 3. These nondimensional profiles are similar for the range of Reynolds numbers. The velocity profile shapes are similar to those obtained by Senoo and Nagata [5], Kreith and Sonju [6], Johnson [7], Bruum [8], and Linderstrom-Lang [9] in swirling and vortex flows with symmetrical swirl generation at the pipe inlet. An unsymmetrical swirling flow is produced

in this work, which tends to become more symmetrical as the swirl gradually decays down the pipe. The main mass flow rate of air down the pipe is concentrated in the outer regions, and there is some recirculation or reverse flow of about 3 percent in the central region within a core of  $r/R = 0.4$ . The center of the swirling flow is offset from the pipe center line (this is caused by the single tangential entry) and is helical about the pipe center line. The unsymmetrical swirling flow may be visualized as a helical band or ribbon of air with regions of recirculation in between as indicated in Fig. 3. An inlet swirl generator with symmetrical vanes would have produced a more symmetrical swirling flow, but the practical case of turbine blade cooling, from which the project arose, would most probably have the simpler single tangential entry.

The results from tests with a smaller aspect ratio of 2.0 and a smaller inlet area, show that higher tangential velocities at inlet are created, and continue for the whole length of the swirl pipe. The airstream angles and axial velocity components vary in a similar way to Fig. 3, but with some distortion due to the higher turbulence level.

Fig. 4 shows how the swirl number varies with the axial distance parameter  $x/D$  in the swirl pipe, for the tests with the 90 deg inlet duct and aspect ratio of 3.76. There is a scatter of points due to the unsymmetrical nature of the swirling flow and they show that the swirl number is not a simple function of  $x/D$  and  $Re$ . The most consistent results are for a low Reynolds number with a lower turbulence level, and a mean curve can be drawn for a natural decay having the simple equation  $S = 1.72 \exp(-0.04 x/D)$ .

For an aspect ratio of 2.0 and various inlet duct angles (30, 60 and 90 deg) the scatter of points is much greater as shown in Fig. 5, indicating the swirling ribbon of air flowing down the pipe with less swirl in the airstream outside the main ribbon. This ribbon effect is exhibited at low  $x/D$  and is more pronounced at the lower inlet duct angle of 30 deg. The 90 deg inlet may produce a tighter flow helix and a more rapid convergence to a symmetrical swirl. The degree of asymmetry of the swirl depends on the inlet duct angle but in all cases the flow fuses toward uniformity after  $x/D \approx 5$ .

**Augmentation of Heat Transfer.** In all cases the swirling flow gives higher values of local heat transfer coefficients than for fully developed nonswirling turbulent flow. Also the local heat transfer coefficient increases with increasing Reynolds number. Fig. 6 shows a plot of heat transfer augmentation,  $(Nu/Nu_{\infty})$ , against the axial distance parameter ( $x/D$ ). The test results with the 90 deg inlet and aspect ratio 3.76 show hardly any variation with  $Re$ . The local heat transfer coefficients are about eight times higher at the pipe inlet and reduce with axial distance down the pipe to about three times higher than for fully developed nonswirling turbulent flow at the pipe outlet ( $x/D = 17.5$ ). It will be noted that with parallel flow there is a thermal entry region in a pipe for several diameters from the inlet where the local heat transfer coefficients are higher than for fully developed values. With swirling flow the thermal entry length is much shorter and the two effects of pipe thermal entry and swirling flow, are merged to give the high values of local heat transfer coefficients.

The effect of reducing the aspect ratio to 2.0, with the 90 deg inlet duct, is to increase the local heat transfer coefficients, which is to be expected owing to the higher values of tangential velocities.

If the aspect ratio is constant at 2.0, it can be seen that the local heat transfer coefficients increase with increasing inlet duct angle from 0 to 90 deg. This is to be expected also due to the increasing tangential velocities and extended helical flow path of the air.

A plot of the heat transfer augmentation  $(Nu/Nu_{\infty})$  against swirl number ( $S$ ) for a large number of tests as shown in Fig. 7 yielded the following correlation

$$\frac{Nu}{Nu_{\infty}} = (S + 1)^{1.75} \quad (1)$$

In this correlation the condition that  $Nu/Nu_{\infty} \rightarrow 1$  as  $S \rightarrow 0$  is satisfied. Generally with the low Reynolds number the experimental

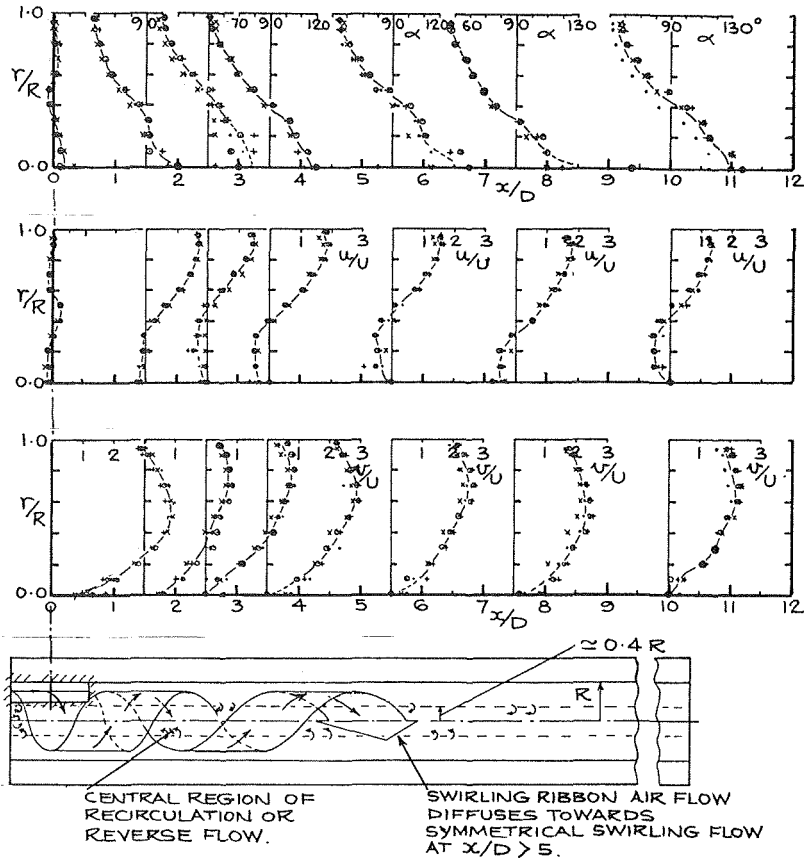


Fig. 3 Air stream angle, axial and tangential velocity distributions in free swirling flow; 90 deg inlet duct, aspect ratio of 3.76

results are consistent. The swirling flow is more symmetrical and the scatter of points is about  $\pm 15$  percent. However, with the higher Reynolds numbers the swirling flow is unsymmetrical and this together with the higher level of turbulence, reduces the accuracy of measurements; hence the scatter of points is greater, but the majority of the readings are still within  $\pm 40$  percent.

### Comparison With Other Work

Data from the paper by Blum and Oliver [15] have been reprocessed and shown in Fig. 6 for comparison. Their results for swirling flow appear to be about 25 percent higher than the results presented in this paper. This may be due to a higher degree of swirl

produced in their apparatus, where the air enters the swirl tube through four slots at 90 deg to the tube axis. Also the results presented in this paper are for air which is being cooled while the air was being heated in Blum and Oliver's experiment.

The lower line in Fig. 6 gives Blum and Oliver results for non-swirling turbulent flow showing the thermal entry effect in the inlet region of a pipe. The authors results for swirling flow are higher than this line, as would be expected.

Narezhnyy and Sudarev [12] gave a correlation for the heating of swirling flow in the form

$$Nu_x = c Re_x^{0.8}$$

where

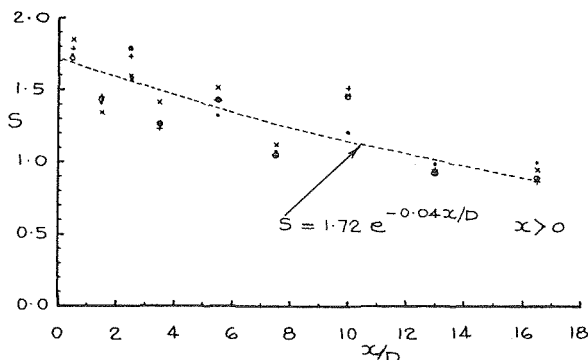


Fig. 4 Local swirl number variation in the swirl pipe with 90 deg inlet duct of aspect ratio 3.76

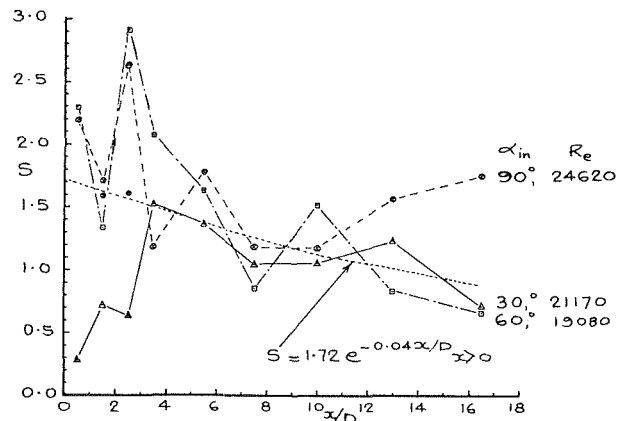


Fig. 5 Local swirl number variation in the swirl pipe with 30, 60, and 90 deg inlet ducts of aspect ratio 2.0

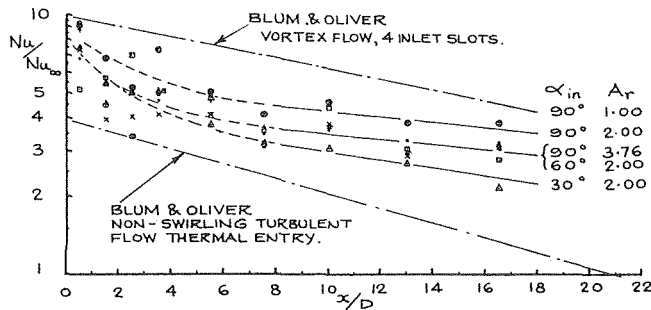


Fig. 6 Local heat transfer augmentation in the swirl pipe for air in free swirling flow

$$Nu_x = \frac{hx}{k}$$

$Re_x = \rho Ux/\mu$  and  $c$  is a function of the inlet angle  $\alpha_{in}$  and the ratio  $(l/D)$  of the total length of pipe. The Nusselt numbers and Reynolds numbers are expressed in terms of the distance along the tube because the flow is continually developing. Fig. 8 shows a plot of  $Nu_x$  against  $Re_x$  for the full range of the present swirling flow tests. There is a scatter of points and the effects of different flows, aspect ratios, and inlet angles are not obvious. However, a mean straight line can be drawn through the points and a lower line to allow for thermal entry effects on the heat flux meter previously estimated to be 40 percent gives the correlation

$$Nu_x = 0.119 Re_x^{0.8} \quad (2)$$

Fig. 8 also shows the highest of the Narazhnyy and Sudarev results for a swirl generator inlet angle of 75 deg. Their line lies below and parallel to this correlation. The slopes correspond to an index of 0.8 in both cases but the Nusselt number is 20 percent lower than the present result in contrast with Blum and Oliver's results which were 25 percent higher.

### Conclusions

The local swirl number ( $S$ ) appears to adequately define the flow locally and is therefore considered a suitable parameter in swirling flow heat transfer data correlation. For a single tangential air entry the following correlation applies for  $x/D > 0$ :

$$\frac{Nu}{Nu_\infty} = (S + 1)^{1.75}$$

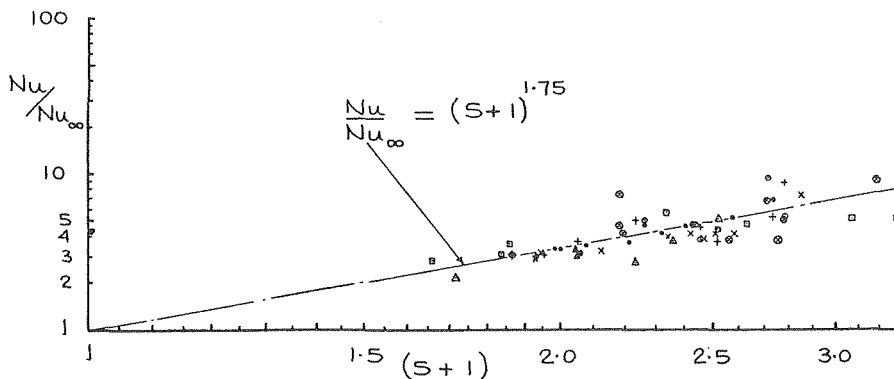


Fig. 7 Local heat transfer augmentation ( $Nu/Nu_\infty$ ) correlation with local swirl number ( $S$ ) for air in free swirling flow in a pipe

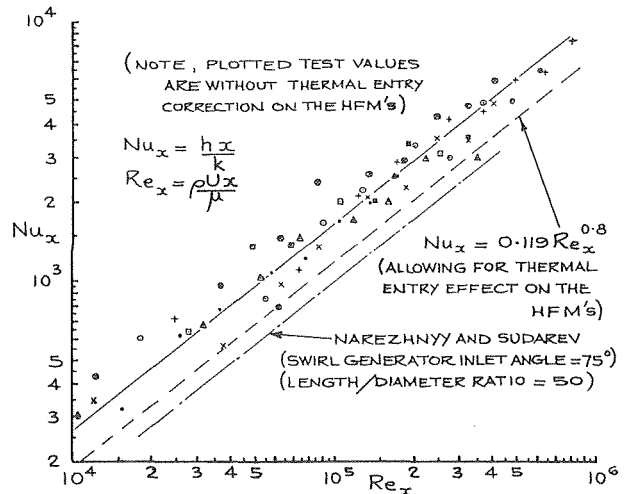


Fig. 8 Local Nusselt number ( $Nu_x$ ) correlation with local Reynolds number ( $Re_x$ ) for air in free swirling flow in a pipe

to  $\pm 40$  percent for the full range of inlet duct angles, aspect ratios, and Reynolds numbers, and to  $\pm 15$  percent for a 90 deg inlet duct and low Reynolds number ( $Re \sim 10000$ ).

The values of  $Nu_\infty$  should be obtained from a relevant correlation for fully developed nonswirling turbulent flow. For example, for cooling of a fluid the Dittus-Boelter equation would be used

$$Nu_\infty = 0.023 Re^{0.8} Pr^{0.3}$$

An expression for the local swirl number in terms of pipe and flow parameters is more complex. With a single tangential inlet duct to the swirl pipe, a correlation for the swirl number may be of the form

$$S = \phi \left\{ \frac{x}{D}, \theta, \alpha_{in}, Re \right\}$$

For low Reynolds numbers ( $Re \sim 10000$ ) and an inlet duct angle of  $\alpha_{in} = 90$  deg and when the swirling flow is reasonably symmetrical and decaying naturally,

$$S \approx \phi \left\{ \frac{x}{D} \right\}$$

The present tests gave for this condition

$$S = 1.72 \exp(-0.04 x/D)$$

Table 1 Summary of test program with the main flow parameters

Test No.	Inlet duct angle $\alpha_{in}$ (deg)	Inlet duct aspect ratio $A_r = \frac{b}{d}$	Air mass flow rate $\dot{m}$ (g/s)	Reynolds number $Re = \frac{\rho UD}{\mu}$	Mean axial velocity $U(m/s) = \frac{\dot{m}}{\rho A}$	Maximum inlet velocity m/s	Fig. symbols
Nonswirling turbulent flow							
73	0	—	15.4	18640	7.67	—	
71	0	—	19.8	24040	9.85	—	
72	0	—	25.2	30670	12.56	—	
Swirling flow							
29-38	90	3.76	8.5	10500	4.15	16.4	●
14-28	90	3.76	20.0	24600	9.8	38.3	×
39-48	90	3.76	30.0	36700	14.46	56.5	⊙
49-58	90	3.76	40.1	49000	19.3	72.1	+
59-70	90	2.0	20.1	24620	9.75	64.9	⊗
74-83	30	2.0	17.1	21170	8.45	50.1	△
84-93	60	2.0	15.5	19080	7.6	49.1	□

The values of local heat transfer coefficients and correlations compare well with work of other authors and fall between those of Blum and Oliver [15] and Narazhnyy and Sudarev [12].

References

- Halls, G. A., "Air Cooling of Turbine Blades and Vanes," *Aircraft Engineering*, Vol. 39, Aug. 1967, pp. 4-14.
- Halls, G. A., "Nozzle Guide Vane Cooling. The State of the Art," *Paper No. 25, AGARD Conference on High Temperature Turbines*, Florence 1970, A GARD CP-73-71, Neuilly-Sur-Seine, 1971.
- Leuckel, W., "The Aerodynamics of Swirling Flows," *Rev. Gen. Thermique*, Vol. 7, Dec. 1968, pp. 1367-1383.
- Kawaguchi, O., and Sato, G. T., "Experimental Investigation of Premixed Swirling Jet Flames," *Bulletin of the JSME*, Vol. 14, No. 69, 1971, pp. 248-256.
- Senoo, Y., and Nagato, T., "Swirl Flow in Long Pipes With Different Roughness," *Bulletin of the JSME*, Vol. 15, No. 90, Dec. 1972, pp. 1514-1521.
- Kreith, F., and Sonju, O. K., "The Decay of a Turbulent Swirl in a Pipe," *Journal of Fluid Mechanics*, Vol. 22, Part 2, 1965, pp. 257-271.
- Johnson, B. V., "Exploratory Flow and Containment Experiments in a Directed Wall-Jet Vortex Tube With Radial Outflow and Moderate Superimposed Axial Flows," *NASA Contractor Report*, C.R.-992, 1968.
- Bruun, H. H., "Experimental Investigation of the Energy Separation in Vortex Tubes," *The Journal of Mechanical Engineering Science*, Vol. 11,

No. 6, 1969, pp. 576-582.

- Linderstrom-Lang, C. U., "The Three Dimensional Distributions of Tangential Velocity and Total-Temperature in Vortex Tubes," *Journal of Fluid Mechanics*, Vol. 45, Part 1, 1971, pp. 161-187.
- Gutstein, M. U., Converse, G. L., and Peterson, J. R., "Augmentation of Single-Phase Heat Transfer in Tubes by Use of Helical Van Inserts," *Paper No. F.C.4.7, 4th International Heat Transfer Conference*, Paris 1970.
- Lopina, R. F., and Bergles, A. E., "Heat Transfer and Pressure Drop in Tape-Generated Swirl Flow of Single-Phase Water," *JOURNAL OF HEAT TRANSFER*, TRANS. ASME, Series C, Vol. 91, No. 3, 1969, pp. 434-441.
- Narezhnyy, E. G., and Sudarev, A. V., "Local Heat Transfer in Air Flowing in Tubes With a Turbulence Promotor at the Inlet," *Heat Transfer—Soviet Research*, Vol. 3, No. 2, Mar.-Apr. 1971, pp. 62-66.
- Ivanova, A. V., "Increasing the Rate of Heat Transfer in a Round Air-Cooled Tube," *Proceedings 2nd All-Soviet Union Conference on Heat and Mass Transfer*, Vol. 1, 1967, pp. 243-250.
- Migay, V. K., and Golubev, L. K., "Friction and Heat Transfer in Turbulent Swirl Flow With a Variable Swirl Generator in a Pipe," *Heat Transfer—Soviet Research*, Vol. 2, No. 3, May 1970, pp. 68-73.
- Blum, H. A., and Oliver, L. R., "Heat Transfer in a Decaying Vortex System," *ASME Paper No. 66-WA/HT-62*, 1967.
- Bryer, D. W., Walshe, D. E., and Garner, H. C., "Pressure Probes Selected for Three-Dimensional Flow Measurement," *Aeronautical Research Council, Reports and Memoranda R & M No. 3037*, 1958.
- West, P. D., "Heat Transfer in Free Swirling Flow in a Pipe," *M. Phil., Thesis*, University of Nottingham, 1973.

N. V. Suryanarayana

Assoc. Professor,  
Michigan Technological University,  
Houghton, Mich.  
Mem. ASME

# Transient Response of Straight Fins

The transient response of a fin of constant area of cross section and perimeter, with its end insulated, is analyzed using Laplace transforms. Solutions are developed for small and large values of times when the base is subjected to a step change in temperature or heat flux. Fins with base subjected to sinusoidal temperature or heat flux are also analyzed. Typical results are represented in graphical form.

The performance of fins under steady-state conditions has been studied in considerable detail but the transient response of such surfaces to changes in either base temperature or base heat flux has not received much attention. The results of only one study by Chapman [1]<sup>1</sup> appear in the literature. Chapman determined the transient response of an annular fin to a step change in the base temperature. The solution obtained by the separation of variables is given in the form of a series.

There are situations where straight fins of constant area of cross section and perimeter may be subjected to a variety of unsteady conditions at the base. Two such possibilities are the base temperature or base heat flux being some known arbitrary function of time. Using Laplace transforms, solutions are developed for a step change in base temperature or heat flux and for the case of the base temperature or heat flux being a sinusoidal function of time with unit amplitude. These solutions, when combined suitably, will yield the transient response to an arbitrary time dependent base temperature or heat flux by expressing these as a Fourier series. Laplace transform technique is preferred to that of separation of variables for two reasons. Solutions to the conduction equation obtained by the use of either technique, quite often tend to be slow in convergence for small values of time. However, with Laplace transforms, rapidly convergent approximate solutions, valid for small values of time, can be more easily obtained. Secondly, it is simpler to develop solutions to the conduction equation with sinusoidal boundary conditions (with respect to time).

The model of the fin analyzed is shown in Fig. 1. A fin of constant area of cross section and perimeter is perfectly insulated at the end ( $X = 0$ ). When the end is not insulated, Harper and Brown [2] have shown, that under certain circumstances, an equivalent

fin with end insulated can be obtained by suitably increasing its length. It is assumed that one-dimensional analysis is valid. One-dimensional analysis has been shown to be valid under steady-state conditions for small Biot modulus by Irey [3] and Levitsky [4], Lau and Tan [5], and Crank and Parker [6]. Initially, the fin is in equilibrium with the surrounding fluid. The base of the fin ( $X = L$ ) may be subjected to a time dependent temperature or heat flux. The convective heat transfer coefficient, the temperature  $T_\infty$  of the surrounding fluid, and properties of the material of the fin are all assumed to be constant.

(i) **Step Change in Base Temperature.** The differential equation for the temperature of the fin is

$$\frac{\partial^2 T}{\partial X^2} - \tilde{m}^2(T - T_\infty) - \frac{1}{\alpha} \frac{\partial T}{\partial \tau} = 0 \quad (1)$$

where  $\tilde{m}^2 = hP/KA$ . The boundary and initial conditions are

$$\begin{aligned} \tilde{\tau} &= 0 & T &= T_\infty \\ \tilde{X} &= 0 & \frac{\partial T}{\partial X} &= 0 \\ \tilde{X} &= L & T &= T_0 \end{aligned} \quad (2)$$

In terms of the nondimensional variables,

$$\begin{aligned} \frac{\partial^2 \theta}{\partial X^2} - m^2 \theta - \frac{\partial \theta}{\partial \tau} &= 0 \\ \tau &= 0 & \theta &= 0 \end{aligned} \quad (3)$$

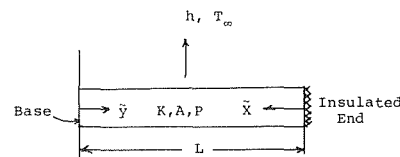


Fig. 1 Model of fin

<sup>1</sup> Numbers in brackets designate References at end of paper.

Contributed by the Heat Transfer Division for publication in the JOURNAL OF HEAT TRANSFER. Manuscript received by the Heat Transfer Division March 10, 1975. Paper No. 75-HT-GGG.

$$\begin{aligned} X = 0 \quad \frac{\partial \theta}{\partial X} &= 0 \\ X = 1 \quad \theta &= 1 \end{aligned} \quad (4)$$

Taking the Laplace transform with respect to time, the transformed equation and associated boundary conditions are

$$\frac{d^2 \bar{\theta}}{dX^2} - (m^2 + s)\bar{\theta} = 0 \quad (5)$$

$$X = 0 \quad \frac{d\bar{\theta}}{dX} = 0 \quad (6)$$

$$X = 1 \quad \bar{\theta} = \frac{1}{s}$$

The solution in the transformed plane is given by

$$\bar{\theta} = \frac{1}{s} \frac{\cosh(\sqrt{m^2 + s}X)}{\cosh(\sqrt{m^2 + s})} \quad (7)$$

The inverse transform is then obtained from

$$\begin{aligned} \theta &= \frac{1}{2\pi i} \int_{\gamma-i\infty}^{\gamma+i\infty} \frac{e^{\tau z} \cosh(\sqrt{m^2 + z}X)}{z \cosh(\sqrt{m^2 + z})} dz = \frac{\cosh mX}{\cosh m} \\ &+ \sum_{n=1}^{\infty} \frac{(-1)^n (2n-1)\pi e^{-[(2n-1)^2 \frac{\pi^2}{4} + m^2]\tau} \cos\{(2n-1)\frac{\pi}{2}X\}}{(2n-1)^2 \frac{\pi^2}{4} + m^2} \end{aligned} \quad (8)$$

The convergence of this series is rather slow for small values of  $m^2\tau$  and it is desirable to find a more rapidly convergent solution for small values of time, i.e., for large values of  $s$  in the transformed plane. From equation (7) we have

$$\begin{aligned} \bar{\theta} &= \frac{1}{s} \frac{\cosh(\sqrt{m^2 + s}X)}{\cosh(\sqrt{m^2 + s})} \\ &= \frac{1}{s} \frac{e^{-(1-X)\sqrt{m^2+s}} + e^{-(1+X)\sqrt{m^2+s}}}{1 + e^{-2\sqrt{m^2+s}}} \end{aligned} \quad (9)$$

For large values of  $s$ ,

$$(1 + e^{-2\sqrt{m^2+s}})^{-1} \approx 1 - e^{-2\sqrt{m^2+s}} \quad (10)$$

Substituting equation (10) into (9),

$$\bar{\theta} = \frac{1}{s} [e^{-(1-X)\sqrt{m^2+s}} + e^{-(1+X)\sqrt{m^2+s}} - e^{-(3-X)\sqrt{m^2+s}} - e^{-(3+X)\sqrt{m^2+s}}] \quad (11)$$

The inverse transform of a term of the type  $e^{-f(X)\sqrt{m^2+s}/s}$  is given by

$$\mathcal{L}^{-1}\left[\frac{e^{-f(X)\sqrt{m^2+s}}}{s}\right] = \int_0^\tau e^{-m^2 t} \mathcal{L}^{-1}[e^{-f(X)\sqrt{s}}] dt \quad (12)$$

In general, the value of  $m$  in engineering practice rarely exceeds 5 and hence small values of  $\tau$  also imply small values of  $m^2\tau$ . For values of  $m^2\tau = 0.01$ ,  $e^{-m^2 t}$  in equation (12) varies from 1.0 ( $\tau = 0$ ) to 0.99 ( $m^2\tau = 0.01$ ), a variation of 1 percent. Hence, the term  $e^{-m^2 t}$  in the integral of equation (12) can be replaced by its integrated mean value defined by

$$e^{-m^2 t}|_{\text{mean}} = \frac{1}{\tau} \int_0^\tau e^{-m^2 t} dt = \frac{1 - e^{-m^2 \tau}}{m^2 \tau} \quad (13)$$

We then have, for  $m^2\tau \leq 0.01$ ,

$$\begin{aligned} \mathcal{L}^{-1}\left[\frac{e^{-f(X)\sqrt{m^2+s}}}{s}\right] &= \frac{1 - e^{-m^2 \tau}}{m^2 \tau} \int_0^\tau \mathcal{L}^{-1}[e^{-f(X)\sqrt{s}}] dt \\ &= \frac{1 - e^{-m^2 \tau}}{m^2 \tau} \mathcal{L}^{-1}\left[\frac{e^{-f(X)\sqrt{s}}}{s}\right] \end{aligned} \quad (14)$$

The inverse transform in equation (14) is readily obtained using a table of transforms [7] and the temperature valid for small values of time is given by

$$\begin{aligned} \theta &= \frac{1 - e^{-m^2 \tau}}{m^2 \tau} \left[ \operatorname{erfc}\left(\frac{1-X}{2\sqrt{\tau}}\right) + \operatorname{erfc}\left(\frac{1+X}{2\sqrt{\tau}}\right) \right. \\ &\quad \left. - \operatorname{erfc}\left(\frac{3-X}{2\sqrt{\tau}}\right) - \operatorname{erfc}\left(\frac{3+X}{2\sqrt{\tau}}\right) \right] \end{aligned} \quad (15)$$

The nondimensional heat flux at the base of the fin ( $X = 1$ ) is given by

$$q_0'' = \frac{\tilde{q}_0'' L}{K\theta_0} = \frac{\partial \theta}{\partial X} \Big|_{X=1} \quad (16)$$

Using equation (15) for small values of time and equation (8) for large values of time, the heat flux at the base is then given by, for large values of time

$$q_0''(X=1) = \frac{m \sinh m}{\cosh m} + \sum \frac{(2n-1)^2 \frac{\pi^2}{2} e^{-[(2n-1)^2 \frac{\pi^2}{4} + m^2]\tau}}{[(2n-1)^2 \frac{\pi^2}{4} + m^2]} \quad (17)$$

and for small values of time,

$$q_0''(X=1) = \frac{1 - e^{-m^2 \tau}}{\sqrt{\pi m^2 \tau^{3/2}}} \left[ 1 - 2e^{-\frac{1}{\tau}} + e^{-\frac{4}{\tau}} \right] \quad (18)$$

The temperature distribution  $\theta(X, \tau)$  obtained by using ten terms in the series of equation (8), and equation (15) are shown plotted in Fig. 2 for different values of  $m$  and  $\tau$ . A comparison of the values obtained from these two equations shows that equation (15) for  $\tau \leq 0.01$  and equation (8) (with ten terms) for  $\tau \geq 0.01$  would be appropriate for the range of values of  $m$  considered here,  $m = 0.01$  to  $m = 10$ . From an examination of equation (8) it can be seen that the value of the temperature reaches within 1 percent of its steady-state value when

## Nomenclature

$A$  = area of cross section of fin  
 $C$  = specific heat of fin  
 $h$  = convective heat transfer coefficient  
 $K$  = thermal conductivity of material of fin  
 $L$  = length of fin  
 $\tilde{m} = \frac{hP^{1/2}}{KA}$   
 $m = \tilde{m}L$   
 $P$  = perimeter of fin  
 $p$  = dimensionless temperature amplitude equations (26) and (35)

$\tilde{q}_0''$  = heat flux at base of fin  
 $q_0''$  = dimensionless heat flux  $\frac{\tilde{q}_0'' L}{K\theta_0}$  at base of fin  
 $T$  = temperature of fin  
 $T_0$  = temperature at base of fin  
 $T_\infty$  = temperature of fluid surrounding fin  
 $\tilde{X}$  = distance from insulated end  
 $X$  = dimensionless distance  $\tilde{X}/L$   
 $Y$  = dimensionless distance from base  $(1 - \tilde{X}/L)$   
 $\alpha$  = thermal diffusivity ( $K/\rho C$ )

$\eta$  = dimensionless temperature  $\frac{(T - T_\infty)}{(q_0'' L/K)}$   
 $\theta$  = dimensionless temperature  $\frac{T - T_0}{T_0 - T}$   
 $\rho$  = density of material of fin  
 $\tilde{\tau}$  = time  
 $\tau$  = dimensionless time  $\frac{\alpha \tau}{L^2}$   
 $\tilde{\omega}$  = period of oscillation  
 $\omega$  = dimensionless period of oscillation  $(\frac{\tilde{\omega} L^2}{\alpha})$

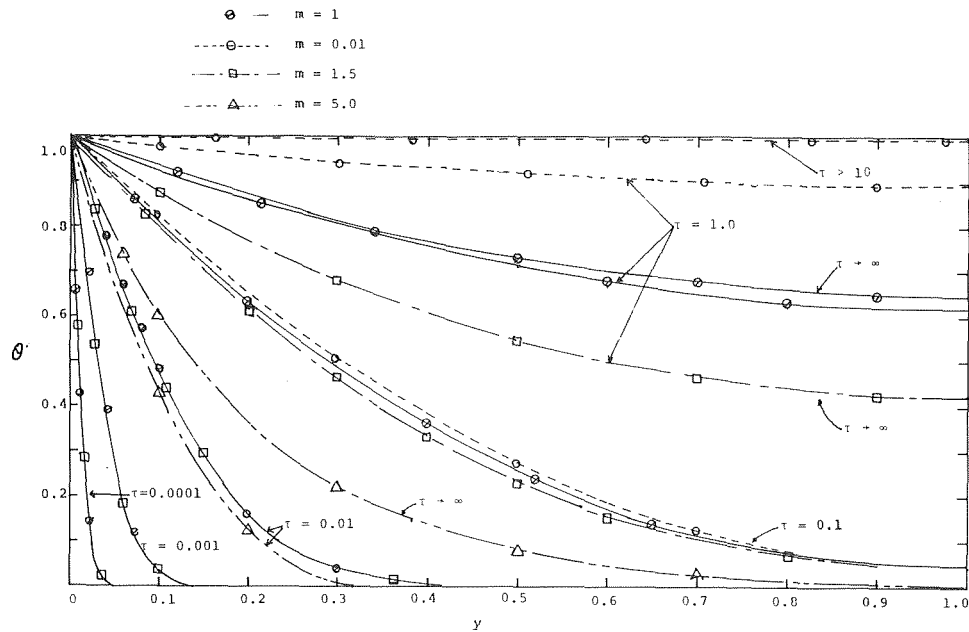


Fig. 2 Transient fin temperature

$$\frac{\pi e^{-\left(m^2 + \frac{\pi^2}{4}\right)\tau} \cosh m}{m^2 + \pi^2/4} < 0.01$$

or

$$\tau > \frac{1}{m^2 + \pi^2/4} \ln \left( \frac{100\pi \cosh m}{m^2 + \pi^2/4} \right) \quad (19)$$

Minimum values of  $\tau$  obtained from equation (19) for different values of  $m$  are given in the following:

$m$	0.01	0.1	1.0	2.0	5.0	10
$\tau_{\min}$	1.96	1.95	1.42	0.805	0.245	0.101

For short fins (corresponding to small values of  $m$ ), the dimensional time to reach "steady state" should increase with increase in length of fins. The values given in the foregoing confirm this. When  $m$  is increased from 0.01 to 0.1, the nondimensional time remains approximately constant, indicating that the dimensional

time ( $\tau = \frac{\alpha \bar{\tau}}{L^2}$ ) increases substantially. However, with values of  $m$

beyond 2, the fin rapidly approaches the infinite fin. In this case, the dimensional time to attain steady state should be relatively insensitive to increases in length (or  $m$ ) i.e., the nondimensional time should decrease. This is also confirmed by the values given in the foregoing for  $m > 2$ .

Values of base heat flux for different values of  $m$  and  $\tau$  are shown in Table 1.

From an inspection of the values given in Table 1, two interesting features can be noted. The value of the base heat flux  $q_0''$ , is relatively insensitive to changes the value of  $m$  for small values of  $\tau$ . An inspection of equation (18) leads to the same conclusion. The value of the terms in parenthesis in the equation is close to 1.0 for small values of  $\tau$  and

$$q_0'' \approx \frac{1 - e^{-m^2\tau}}{\sqrt{\pi} m^2 \tau^{3/2}} \approx \frac{1 - (1 - m^2\tau)}{\sqrt{\pi} m^2 \tau^{3/2}} = \frac{1}{\sqrt{\pi} \tau} \quad (20)$$

In dimensional form equation (20) becomes

$$\tilde{q}_0'' = \frac{\sqrt{K\rho C}(T_0 - T_\infty)}{\sqrt{\pi} \bar{\tau}}$$

indicating that, initially, the base heat flux is essentially independent of the convective heat transfer coefficient. This can be explained as follows. Physically, for a given configuration (with  $h$  as the only variable), different values of  $m$  indicate different heat transfer coefficients. But initially, all the energy transfer at the base goes to increase the internal energy of the fin, and hence, the convective heat transfer coefficient has little effect on the base heat flux. The second feature is the lack of symmetry in the minima for the base heat flux for  $\tau = 0.01 - 0.1$ . At these values of  $\tau$ ,  $q_0''$  reaches a minimum at  $m = 2-5$ . This can be explained as follows. Considering the length of the fin as the only variable, the behavior of a fin is essentially that of an infinite fin for values of  $m$  greater than, say, 3. In such cases the dimensional time ( $\bar{\tau}$ ) to reach steady state and the steady-state base heat flux ( $\tilde{q}_0''$ ) should both

Table 1 Base heat flux for different values of  $m$  and  $\tau$

$m$	0.0001	0.001	0.01	0.1	1.0	10.0	100.0
0.01	56.32	17.8	11.28	3.57	0.339	$0.999 \cdot 10^{-4}$	$0.999 \cdot 10^{-4}$
0.1	56.32	17.8	11.27	3.56	0.344	$0.997 \cdot 10^{-2}$	$0.997 \cdot 10^{-2}$
0.6	56.4	17.8	11.0	3.37	0.5288	0.3222	0.3222
0.8	56.4	17.8	10.82	3.263	0.6733	0.5312	0.5312
1.0	56.4	17.8	10.6	3.157	0.8504	0.7616	0.7616
1.5	56.4	17.8	10.18	2.984	1.376	1.3577	1.3577
2.0	56.4	17.8	9.8	2.979	1.9304	1.928	1.928
5.0	56.3	17.6	8.99	5.0398	4.9995	4.9995	4.9995
10.0	56.15	16.98	11.01	10.00	10.00	10.00	10.00

be insensitive to increases in  $m$ . Consequently the corresponding dimensionless time  $\left(\frac{\alpha\tau}{L^2}\right)$  should decrease with an increase in  $m$

and the base heat flux  $\left(\frac{q_0''L}{K\theta_0}\right)$  should be directly proportional to  $m$ . Thus, doubling the value of  $m$  from 5 to 10, reduces the dimensionless time taken to reach steady state from approximately 1.0 to around 0.1 and almost doubles the base heat flux from 4.995 to 10.00.

(ii) **Transient Response to a Sinusoidal Base Temperature With Unit Amplitude.** The differential equation and the boundary and initial conditions are the same as equations (3) and (4) except that the last boundary condition in equation (4) is to be replaced by,  $X = 1, \theta = \sin\omega\tau$ . In the transformed plane this boundary

condition becomes  $X = 1, \bar{\theta} = \frac{\omega}{s^2 + \omega^2}$  and the solution to  $\bar{\theta}$  is given by

$$\bar{\theta} = \frac{\omega}{s^2 + \omega^2} \frac{\cosh(\sqrt{m^2 + s}X)}{\cosh(\sqrt{m^2 + s})} \quad (21)$$

$$\begin{aligned} \theta &= \frac{1}{2\pi i} \int_{\gamma-i\infty}^{\gamma+i\infty} \frac{\omega e^{s\tau} \cosh(\sqrt{m^2 + z}X)}{(z^2 + \omega^2) \cosh(\sqrt{m^2 + z})} dz \\ &= \text{Res}(i\omega) + \text{Res}(-i\omega) + \sum_{n=1}^{\infty} \text{Res}(z_{on}) \Big|_{(\cosh \sqrt{m^2+z_{on}}=0)} \quad (22) \end{aligned}$$

Defining  $r = \sqrt{m^2 + \omega^2}$ ,  $\beta = \frac{1}{2} \tan^{-1} \frac{\omega}{m^2}$ ,  $a = \sqrt{r} \cos \beta$ ,

$$\begin{aligned} b &= \sqrt{r} \sin \beta, \text{ with some algebraic manipulations it can be shown that} \\ \text{Res}(i\omega) + \text{Res}(-i\omega) &= \frac{1}{2i} \left[ \frac{e^{i\omega\tau} \cosh(\sqrt{m^2 + i\omega}X)}{\cosh(\sqrt{m^2 + i\omega})} - \frac{e^{-i\omega\tau} \cosh(\sqrt{m^2 - i\omega}X)}{\cosh(\sqrt{m^2 - i\omega})} \right] = \frac{F_1}{F_2} \quad (23) \end{aligned}$$

where

$$\begin{aligned} F_1 &= \sin \omega\tau (\cosh aX \cos bX \cosh a \cos b + \\ &\quad + \sinh aX \sin bX \sinh a \sin b) - \\ &\quad - \cos \omega t (\cosh aX \cos bX \sinh a \sin b - \\ &\quad - \sinh aX \sin bX \cosh a \cos b) \end{aligned}$$

and

$$F_2 = \cosh^2 a \cos^2 b + \sinh^2 a \sin^2 b$$

Equation (23) can be reset as

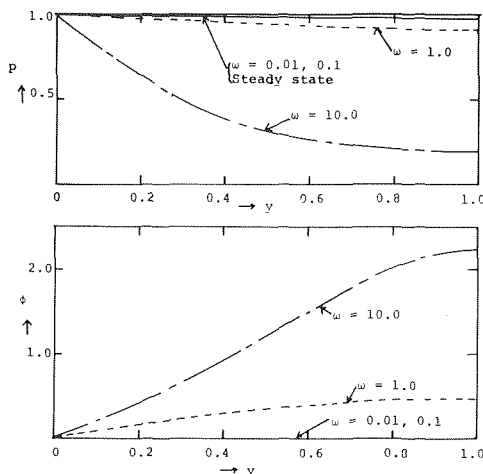


Fig. 3 Amplitude ( $q$ ) and phase angle ( $\phi$ )  $m = 0.1$

$$\frac{F_1}{F_2} = p \sin(\omega t - \phi) \quad (24)$$

where the phase angle  $\phi$  is given by

$$\phi = \tan^{-1} \left( \frac{\cosh aX \cos bX \sinh a \sin b - \sinh aX \sin bX \cosh a \cos b}{\cosh aX \cos bX \cosh a \cos b + \sinh aX \sin bX \sinh a \sin b} \right) \quad (25)$$

and the amplitude  $p$  by

$$p = \frac{\sqrt{Nr^2 + Dr^2}}{F_2} \quad (26)$$

Here  $Nr$  and  $Dr$  represent the numerator and denominator in equation (25).

The zeros of  $\cosh \sqrt{m^2 + z}$  are given by

$$z_{on} = -(2n-1)^2 \frac{\pi^2}{4} + m^2$$

and

$$\begin{aligned} &\sum \text{Res}(z_{on}) \\ &= \sum_{n=1}^{\infty} \frac{(-1)^{n+1} (2n-1) \frac{\pi}{2} e^{-[(2n-1)^2 \frac{\pi^2}{4} + m^2] \tau} \cos(2n-1) \frac{\pi}{2} X}{[(2n-1)^2 \frac{\pi^2}{4} + m^2]^2 + \omega^2} \quad (27) \end{aligned}$$

The temperature response is then given by the sum of equations (24) and (27). Equation (27) represents the initial transient response immediately after the base is subjected to the sinusoidal temperature and equation (24) represents the steady periodic response to the oscillating base temperature. The inverse transform of equation (21), valid for small values of  $\tau$  (large values of  $s$ ) can be developed following a procedure similar to the one adopted in arriving at equation (15) but an examination of equation (27) shows that the series is fairly rapidly convergent and can be used even for small values of time by taking a reasonable number of terms (say ten). The initial temperature response for small values of time can be easily evaluated from equations (24) and (27) but it is more interesting to examine the steady periodic response given by equation (24). Figs. 3, 4, and 5 are plots of temperature amplitude and phase angle for a few discrete values of  $m$  and  $\omega$ . From these figures it can be seen that for  $\omega < 1.0$ , the amplitude of tem-

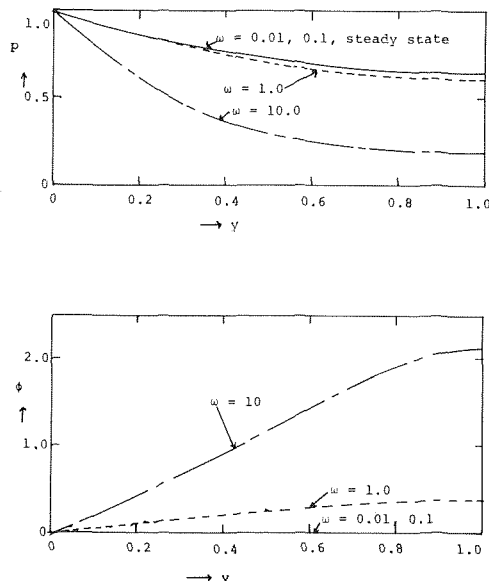


Fig. 4 Amplitude ( $p$ ) and phase angle  $\phi$ ,  $m = 1.0$

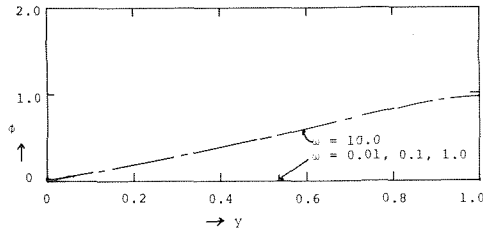
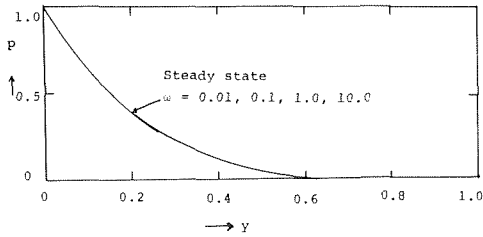


Fig. 5 Amplitude ( $\rho$ ) and phase angle  $\phi$ ,  $m = 5.0$

perature oscillation at any point on the fin is approximately the same as the steady-state temperature at the same point with a unit base temperature. However, for  $\omega > 1.0$ , considerable damping takes place (except for high values of  $m$ ). As can be expected, the phase angle increases with an increase in  $\omega$  and up to a distance of about 0.8 from the base, the phase angle increases almost linearly with distance from the base. The phase angle is also dependent on  $m$ ; for the same  $\omega$ , the phase angle decreases with an increase in  $m$ .

While developing the Fourier series for a time dependent base temperature, equation (26) can be used to determine a value of  $\omega$  beyond which the effect of oscillating base temperature becomes insignificant. The number of terms to be retained in the Fourier series can then be fixed.

(iii) **Step Change in Base Heat Flux.** The differential equation and boundary and initial conditions are the same as equations (3) and (4) with  $\theta$  now replaced by the nondimensional temperature  $\eta$ , and the last boundary condition by  $X = 1, \frac{d\eta}{dx} = 1$ .

The solution in the transformed plane is given by

$$\bar{\eta} = \frac{\cosh \sqrt{m^2 + s} X}{s \sqrt{m^2 + s} \sinh \sqrt{m^2 + s}} \quad (28)$$

By employing the inversion theorem, we obtain

$$\eta = \frac{\cosh mX}{m \sinh m} - \frac{e^{-m^2\tau}}{m^2} + \sum_{n=1}^{\infty} \frac{2(-1)^{n+1} e^{-(n^2\pi^2 + m^2)\tau} \cos n\pi X}{n^2\pi^2 + m^2} \quad (29)$$

For  $\tau \ll 1$  and  $m^2\tau \ll 1$ , a more rapidly converging solution for small values of  $\tau$  (large values of  $s$ ) can be obtained by the same procedure as adopted for finding the response for small time for a step change in base temperature. The resulting solution is

$$\eta = \frac{1 - e^{-m^2\tau}}{m^2\tau} \left\{ 2 \left( \frac{\tau}{\pi} \right)^{1/2} \left[ e^{-(1-X)^2/4\tau} + e^{-(1+X)^2/4\tau} + e^{-(3-X)^2/4\tau} + e^{-(3+X)^2/4\tau} \right] - (1-X) \operatorname{erfc} \left( \frac{1-X}{2\sqrt{\tau}} \right) - (1+X) \operatorname{erfc} \left( \frac{1+X}{2\sqrt{\tau}} \right) - (3-X) \operatorname{erfc} \left( \frac{3-X}{2\sqrt{\tau}} \right) - (3+X) \operatorname{erfc} \left( \frac{3+X}{2\sqrt{\tau}} \right) \right\} \quad (30)$$

The temperature profiles obtained for a few representative values of  $m$  for different values of  $\tau$  are shown in Figs. 6 and 7.

From an examination of equation (29) it is easily shown that the temperature within the fin reaches a value within 1 percent of the steady-state value when  $\tau$  reaches a minimum value  $\tau_{\min}$  given by

$$\tau_{\min} = \frac{1}{m^2} \ln \left( \frac{100 \sinh m}{m} \right) \quad (31)$$

A few values  $\tau_{\min}$  obtained from equation (37) are given in the following.

$m$	0.01	0.1	1.0	2.0	5.0
$\tau_{\min}$	46052	460.7	4.76	1.3	0.292

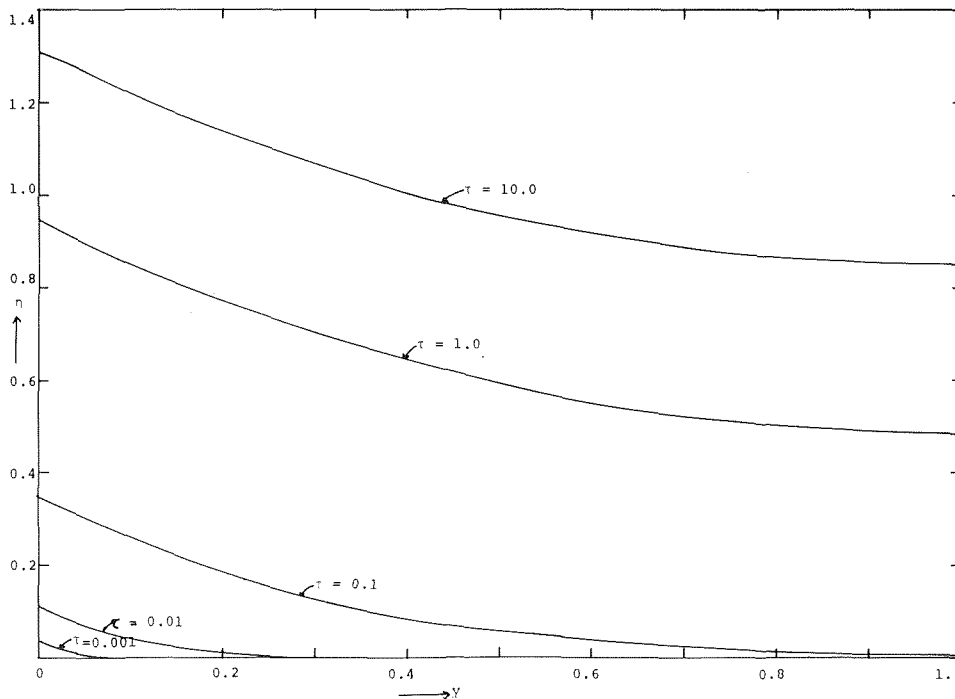
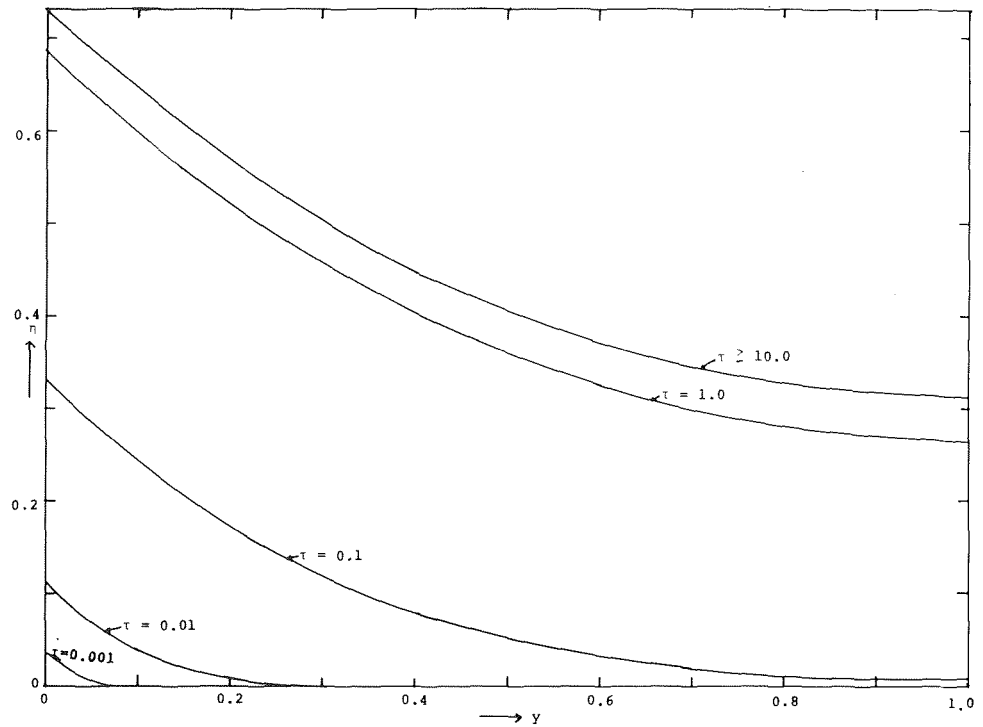


Fig. 6 Temperature ( $\eta$ )  $m = 1.0$

Fig. 7 Temperature ( $\eta$ )  $m = 1.5$



A comparison of the values of  $\tau_{\min}$  obtained in the foregoing, with those obtained from equation (19) for a step change in temperature, shows that it takes a much longer time to reach steady-state conditions when the base is subjected to a step change in heat flux than when it is subjected to step change in temperature, particularly at low values of  $m$  (short fins). The reason for this is quite simple. A step change in base temperature is initially accompanied by very high values of base heat flux; the base heat flux gradually decreases with time finally reaching the steady-state value. In the case of the step change in heat flux, the base heat flux remains constant at its steady-state value. Hence with a step change in base temperature, steady-state conditions are achieved relatively quicker than with a step change in base heat flux.

(iv) **Periodic Heat Flux at Base.** The set of equations to be solved in this case are the same as those of case (iii) except that the boundary condition at  $X = 1$  is to be changed to  $X = 1, \frac{\partial \eta}{\partial X} = \sin \omega \tau$ . The solution in the transformed plane is given by

$$\bar{\eta} = \frac{\omega \cosh(\sqrt{m^2 + s}X)}{(s^2 + \omega^2)\sqrt{m^2 + s} \sinh(\sqrt{m^2 + s})} \quad (32)$$

$$\eta = \frac{1}{2\pi i} \int_{\gamma-i\infty}^{\gamma+i\infty} \frac{\omega e^{s\tau} \cosh(\sqrt{m^2 + z}X)}{(z^2 + \omega^2)\sqrt{m^2 + z} \sinh(\sqrt{m^2 + z})} dz$$

$$= \text{Res}(i\omega) + \text{Res}(-i\omega) + \text{Res}(-m^2) + \sum_{n=1}^{\infty} \text{Res}(z_{0n}) \Big|_{\sinh \sqrt{m^2 + z_{0n}} = 0} \quad (33)$$

$$\text{Res}(i\omega) + \text{Res}(-i\omega) = \frac{e^{i\omega\tau} \omega \cosh(\sqrt{m^2 + i\omega}X)}{2i\omega\sqrt{m^2 + i\omega} \sinh(\sqrt{m^2 + i\omega})} - \frac{e^{-i\omega\tau} \omega \cosh(\sqrt{m^2 - i\omega}X)}{2i\omega\sqrt{m^2 - i\omega} \sinh(\sqrt{m^2 - i\omega})} \quad (34)$$

Letting

$$r = \sqrt{m^4 + \omega^2}, \quad \beta = \frac{1}{2} \tan^{-1}\left(\frac{\omega}{m^2}\right)$$

$a = \sqrt{r} \cos \beta, \quad b = \sqrt{r} \sin \beta$ , it can then be shown that

$$\text{Res}(i\omega) + \text{Res}(-i\omega) = \frac{\sqrt{u^2 + v^2} \sin(\omega t - \phi)}{\sqrt{m^4 + \omega^2} (\sinh^2 a \cos^2 b + \cosh^2 a \sin^2 b)} = p \sin(\omega t - \phi) \quad (35)$$

In equation (35)  $u$  and  $v$  represent

$$u = \cosh aX \cos bX (a \sinh a \cos b - b \cosh a \sin b) + \downarrow$$

$$+ \sinh aX \sin bX (a \cosh a \sin b + b \sinh a \cos b),$$

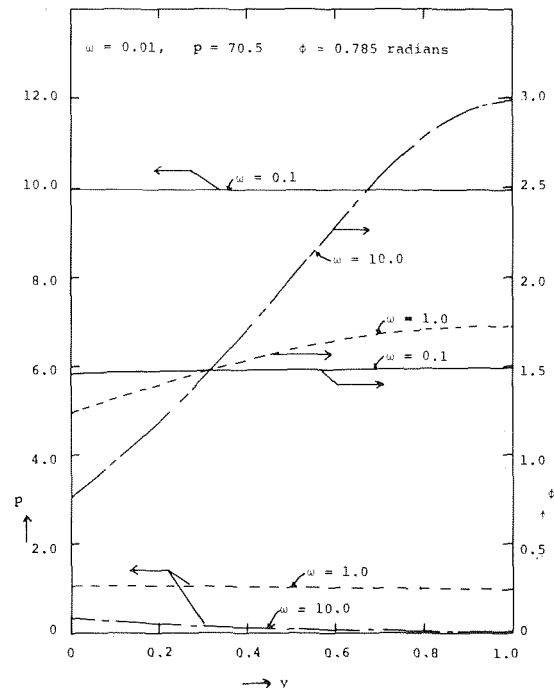


Fig. 8 Amplitude ( $p$ ) and phase angle  $\phi$ ,  $m = 0.1$

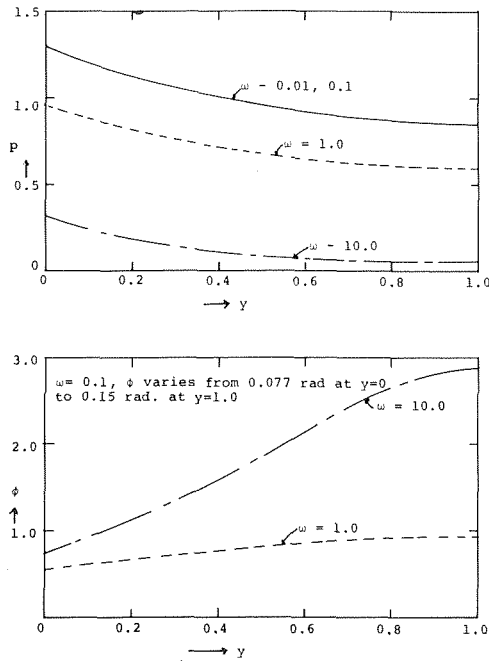


Fig. 9 Amplitude ( $\rho$ ) and phase angle  $\phi$ ,  $m = 1.0$

$v = \cosh aX \cos bX (a \cosh a \sin b + b \sinh a \cos b) - \downarrow$   
 $-\sinh aX \sin bX (a \sinh a \cos b - b \cosh a \sin b)$   
 and

$$\phi = \tan^{-1} \left( \frac{v'}{u} \right)$$

$$\text{Res}(-m^2) + \sum_{n=1}^{\infty} \text{Res}(z_{on}) \Big|_{\sinh \sqrt{m^2 + z_{on}^2} = 0}$$

$$= \frac{\omega e^{-m^2 \tau}}{m^4 + \omega^2} + \sum_{n=1}^{\infty} \frac{2(-1)^{n+1} \omega e^{-(n^2 \pi^2 + m^2) \tau} \cos n\pi X}{(n^2 \pi^2 + m^2)^2 + \omega^2} \quad (36)$$

The complete solution is then given by the sum of equations (35) and (36). Here equation (35) represents the steady periodic response to the oscillating base flux and equation (36) the initial transient response. Values of the amplitude  $p$ , of the steady periodic response and the phase angles for representative values of  $m$  and different values of  $\omega$  are plotted in Figs. 8-10.

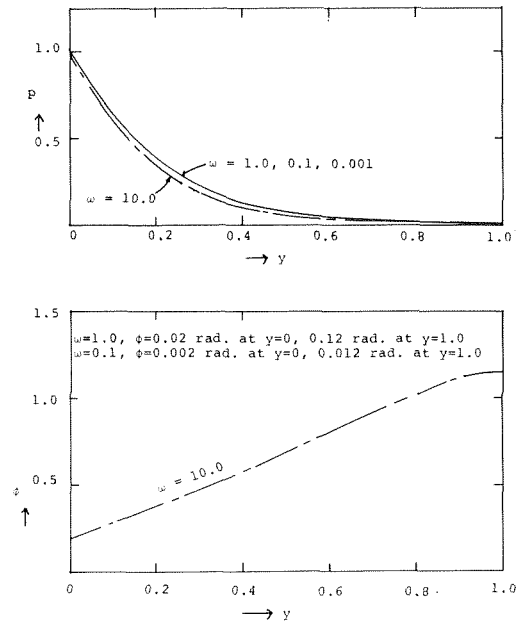


Fig. 10 Amplitude ( $\rho$ ) and phase angle  $\phi$ ,  $m = 5.0$

## References

- 1 Chapman, A. J., "Transient Heat Conduction in Annular Fins of Uniform Thickness," *Chemical Engineering Symposium Series*, Vol. 55, No. 29, 1959, pp. 195-201.
- 2 Harper, W. B., and Brown, D. R., "Mathematical Equations for Heat Conduction in the Fins of Air Cooled Engines," NACA Report No. 158, 1922, pp. 679-708.
- 3 Irey, R. K., "Errors in the One-Dimensional Fin Solution," *JOURNAL OF HEAT TRANSFER*, TRANS. ASME, Series C, Vol. 90, 1968, pp. 175-176.
- 4 Levitsky, Myron, "The Criterion for Validity of the Fin Approximation," *International Journal of Heat and Mass Transfer*, Vol. 10, 1972, pp. 1960-1963.
- 5 Lau, Wah, and Tan, C. W., "Errors in One-Dimensional Heat Transfer Analysis in Straight and Annular Fins," *JOURNAL OF HEAT TRANSFER*, TRANS. ASME, Series C, Vol. 95, 1973, pp. 549-551.
- 6 Crank, J., and Parker, I. B., "Approximate Methods for Two Dimensional Problems in Heat Flow," *Quart. Journal Mech. and Applied Math.*, Vol. 19, Part 2, 1966, pp. 167-181.
- 7 Arpacı, V. S., *Conduction Heat Transfer*, Addison-Wesley, 1966.

J. C. Chato  
Professor.

S. Y. Chern  
Research Assistant.

Department of Mechanical and Industrial  
Engineering,  
University of Illinois at Urbana-Champaign,  
Urbana, Ill.

# The Effects of Nonuniform Cooling on the Heat Transfer From an Insulated Electric Cable

*Due to the geometric configurations of convectively cooled underground electric power cable systems, nonuniform cooling of the individual cables can occur. A numerical analysis has been performed on the effects of nonuniform surface cooling on the temperature distribution inside the insulation of a single cable. The results show that with the typical geometries considered, the coolant temperature would have to be lowered significantly in order to maintain a given amount of heat dissipation per unit length in comparison to uniform cooling. It is useful, therefore, to promote uniform cooling around the circumference of each cable by changing the fluid flow pattern and by the use of metal sheathing around the circumference. To evaluate this latter effect, a dimensionless parameter representing the relative magnitudes of heat conduction in the sheathing and in the insulation is proposed.*

## Introduction

The current carrying capacity of underground electric power cables is limited primarily by the highest temperature tolerated by the insulation wrapped around the cables. The most common material used for such insulation is oil-impregnated paper with a temperature limit of about 85°C and a usual maximum operating temperature of 75°C. Because of this limitation, cooling of underground electric cables can significantly increase their current carrying capacities. There have been numerous investigations of the heat transfer and pressure drop in power cable systems cooled at or slightly below ambient temperatures, and a representative, but by no means exhaustive, sample of publications is listed in references [1-9].<sup>1</sup> In all of these investigations, however, only mean heat transfer coefficients were determined and relatively little attention was paid to local variations in heat transfer rates and temperatures.

A typical cable configuration is shown in Fig. 1. Three cables for the three phases are located inside a pipe which is filled with a dielectric oil under pressure. The configuration shown is one of the worst cases with the three cables packed closely together in a triangular pattern. There are three distinct areas left open for oil circulation. The main flow occurs in the largest free-flow area surrounding the three cables. However, the two triangular areas be-

tween the cables are almost independent channels with considerably greater resistance to flow than in the main channel. It is quite possible that in these narrow passages the coolant temperature is higher and the heat transfer coefficient is lower than in the main channel. Thus the cables are not cooled uniformly.

The purpose of this study was to investigate the effects of nonuniform, steady, convective cooling on the heat transfer from underground electric power cables.

## Analysis

Fig. 1(b) shows a typical cross section of a single cable. Since the conductor is made of copper, which has high thermal conductivity, it can be assumed that around its periphery the temperature is constant at the maximum operating temperature of  $t_{in} = 75^\circ\text{C}$ . The insulation can be assumed to be isotropic with a constant thermal conductivity of  $k_i = 1/550 \text{ W/cm}^\circ\text{C}$ . Dielectric losses within the insulation are assumed to be inversely proportional to the square of the local radius. The sheathing is a very thin single or multiple layer of metal. Typical patterns for the nonuniformities are shown in Fig. 1(a). For cable A on top, approximately  $1/6$  of the outer surface is exposed to a potentially warmer environment and lower heat transfer rates. For the lower cables, B and C, approximately  $1/2$  of the outer surfaces are in such adverse environments. Under all circumstances each cable develops the same amount of heat, which has to be transmitted at the surface regardless of the distribution of either temperature or heat flux. For calculation purposes the total heat generation rate was taken as 87.26 W/m. Two types of boundary conditions at the outer surface were investigated as shown in Fig. 2: two levels of uniform temperatures and two levels of uniform heat fluxes.

<sup>1</sup> Numbers in brackets designate References at end of paper.

Contributed by the Heat Transfer Division and presented at the Winter Annual Meeting, Detroit, Mich., November 1974, of the American Society of Mechanical Engineers. Journal Manuscript received by the Heat Transfer Division March 17, 1975. Paper No. 74-WA/HT-25.

To achieve the needed flexibility, a standard numerical method was employed using a relatively coarse grid as shown schematically in Fig. 3. The size of the grid was chosen to give results within 3 percent of known analytical solutions. This was found to be with angular increments of 15 deg and 15 divisions in the radial direction within the insulation. Because of symmetry only a half-circle was needed.

The working equation for a typical point  $(r, \theta)$  in the grid can be shown to be

$$\left(\frac{1}{\Delta r^2} + \frac{1}{2r\Delta r}\right)t(r + \Delta r, \theta) + \left(\frac{1}{\Delta r^2} - \frac{1}{2r\Delta r}\right)t(r - \Delta r, \theta) + \frac{t(r, \theta + \Delta\theta)}{r^2\Delta\theta^2} + \frac{t(r, \theta - \Delta\theta)}{r^2\Delta\theta^2} - 2\left(\frac{1}{\Delta r^2} + \frac{1}{r^2\Delta\theta^2}\right)t(r, \theta) = -\frac{Q_d}{k_i} \quad (1)$$

where

$$Q_d = c/r^2$$

Since at the inside interface,  $r_1$ , a constant temperature is assumed, no grid points are needed on it. There are as many equations as grid points. These can be solved simultaneously by any convenient way, such as the Gauss elimination method applied to the coefficient matrix.

For the fixed temperature case, Fig. 2(a), the cooler surface temperature,  $t_1$ , was taken as that corresponding to the completely symmetrical case, i.e., when  $t_1 = t_2$ . The hotter surface temperature,  $t_2$ , was chosen in increments up to a maximum, equal to the temperature of the copper conductor,  $t_{in}$ . For this case the grid points along the outer surface have fixed temperatures and need no calculations.

For the uniform heat flux case, Fig. 2(b), the lower heat flux,  $q_{II}$ , was also chosen in increments down to zero. For all values the total heat dissipated from the cable was kept the same. Thus, when  $q_{II}$  was lowered, the magnitude of  $q_I$  had to be increased by an appropriate amount.

For this case the heat balance equation for a typical grid point at the outer surface had to be modified to account for a given heat flux as well as the presence of metal sheathing.

$$k_i\left(\frac{1}{\Delta r} - \frac{1}{2r_2}\right)t(r_2 - \Delta r, \theta) + \left(\frac{k_i\Delta r}{2} + \Sigma k_m b\right)\frac{1}{r_2^2\Delta\theta^2}t(r_2, \theta + \Delta\theta) + \left(\frac{k_i\Delta r}{2} + \Sigma k_m b\right)\frac{1}{r_2^2\Delta\theta^2}t(r_2, \theta - \Delta\theta) - \left(\frac{k_i}{\Delta r} - \frac{k_i}{2r_2} + \frac{k_i\Delta r}{r_2^2\Delta\theta^2} + 2\frac{\Sigma k_m b}{r_2^2\Delta\theta^2}\right)t(r_2, \theta) = q - Q_d\left(1 - \frac{\Delta r}{4r_2}\right)\frac{\Delta r}{2} \quad (2)$$

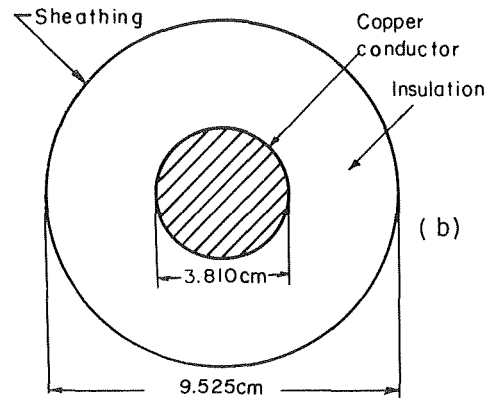
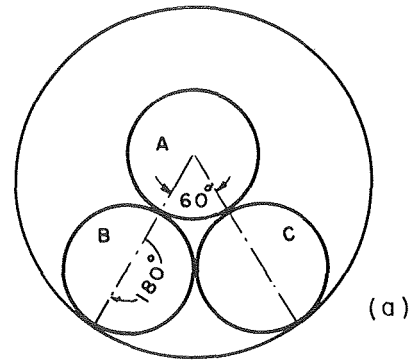


Fig. 1 Typical cross sections of: (a) the complete underground cable system; and (b) a single cable with typical dimensions

where  $\Sigma k_m b$  indicates the possibility of more than one very thin layer of metal [ $b \ll (r_2 - r_1)$ ].

For the grid points on the lines of symmetry the adiabatic boundary condition can be satisfied in equations (1) and (2) by

$$t(r, \theta + \Delta\theta) = t(r, \theta - \Delta\theta) \quad (3)$$

## Discussion

Because of the relative coarseness of the grid system, the two representative subtended angles for the hot sides were chosen as  $\theta_0 = 75$  and  $165$  deg, which made the calculations somewhat simpler. The following parameters were used for the calculations:

## Nomenclature

$b$ = thickness of sheathing, cm	$\bar{Q}$ = total heat dissipation per unit length, W/m or W/cm	sheathing, °C
$c$ = constant for dielectric losses, W/cm	$\bar{Q}_0$ = required total heat dissipation rate per unit length, W/m or W/cm	$t_0$ = uniform outer surface temperature, °C
$k_i$ = thermal conductivity of insulation, W/cm °C	$r$ = radial distance, cm	$t_1$ = temperature on "cool" surface, °C
$k_m$ = thermal conductivity of metal sheathing, W/cm °C	$r_1$ = radius of copper conductor, cm	$t_2$ = temperature on "hot" surface, °C
$q$ = heat flux, W/cm <sup>2</sup>	$r_2$ = outer radius of cable, cm	$\Delta t_0 = t_{in} - t_0$ when $t_1 = t_2 = t_0$ , °C
$Q_d = c/r^2$ , heat generated in unit volume due to dielectric losses, W/cm <sup>3</sup>	$t$ = temperature, °C	$W_c$ = conductor losses, W/m or W/cm
$Q_i$ = heat conducted radially in the insulation, W	$t_{in}$ = uniform temperature of copper conductor at $r_1$ , °C	$W_d$ = dielectric losses, W/m or W/cm
$Q_m$ = heat conducted circumferentially in sheathing, W	$t_m$ = outer surface temperature with metal sheathing, °C	$\Delta$ = increment
	$t_{wm}$ = outer surface temperature without sheathing, °C	$\theta$ = angle from axis of symmetry on hot side
		$\phi$ = dimensionless parameter defined by equation (4)

Thermal conductivity of insulation,  $k_i = 1/550 \text{ W/cm}^\circ\text{C}$   
 Thermal conductivity of copper sheathing,  $k_m = 3.81 \text{ W/cm}^\circ\text{C}$   
 Thermal conductivity of aluminum sheathing,  $k_m = 2.04 \text{ W/cm}^\circ\text{C}$   
 Typical thicknesses for sheathing,  $b = 0.00635, 0.00889, 0.01524 \text{ cm}$   
 Radius ratios,  $r_1/r_2 = 0.2, 0.4$  (standard value used in all figures except Fig. 9),  $0.6$

The outer radius was kept constant at  $r_2 = 4.76 \text{ cm}$  (Fig. 1) and the temperature at the inner radius was  $t_{in} = 75^\circ\text{C}$  for all cases.

Fig. 4 shows the effect of increasing the temperature levels within the subtended angles at the outer surface of the standard geometry chosen for this study (Fig. 1(b)). No sheathing was considered at the outer surface for these cases and all losses were assumed to occur in the conductor ( $W_d = 0$ ). Although the condition of two constant temperature levels with an abrupt change between them is somewhat unrealistic, the orders of magnitude of the results shown in Fig. 4 would not change significantly if a smoother temperature profile were assumed. The curves show that the total heat

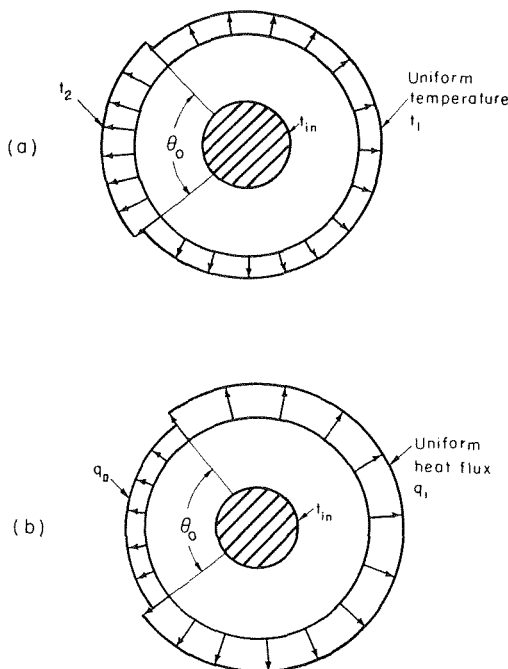


Fig. 2 Typical boundary conditions assumed at the outer surface of a cable

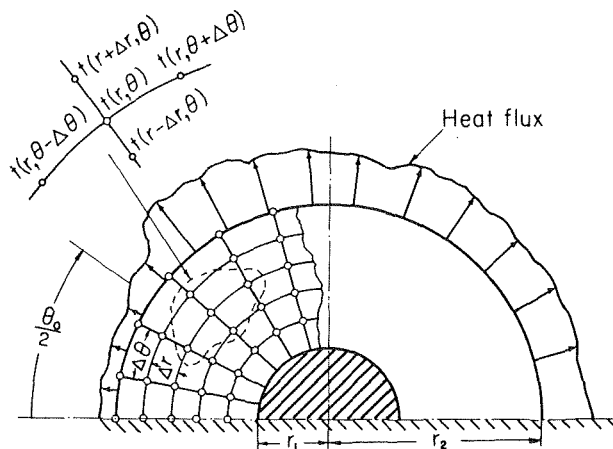


Fig. 3 Schematic layout of the grid used for the numerical calculations

dissipation rate decreases linearly as the temperature is increased along the hot surface. At the limit when the temperature on the hot surface reaches that of the copper conductor, the heat dissipation is reduced by 24 and 47 percent for subtended angles of  $\theta_0 = 75$  and  $165 \text{ deg}$ , respectively.

Perhaps more significant are the results obtained when the heat fluxes are specified along the outer surface of the standard geometry, again without sheathing and without dielectric losses. Figs. 5 and 6 show the changes in the temperature profile along this surface as the relative magnitude of the heat flux along the hot side is reduced. For all these cases the overall heat transfer was kept constant as stated before. Perhaps the most significant effect is the required reductions of the temperature along the cool side from the uniform value of  $t_0 = 6.4^\circ\text{C}$ , particularly at  $\theta = 180 \text{ deg}$ . These amount to a maximum change of  $17.2^\circ\text{C}$  ( $\theta_0 = 75 \text{ deg}$ ) and  $52.5^\circ\text{C}$  ( $\theta_0 = 165 \text{ deg}$ ) for the most extreme case of zero heat flux on the hot side. These magnitudes are quite considerable, amounting to maximum of 25 percent ( $\theta_0 = 75 \text{ deg}$ ) and 77 percent ( $\theta_0 = 165 \text{ deg}$ ) of the temperature difference between inside and outside,  $\Delta t_0 = 68.6^\circ\text{C}$ , for the completely uniform heat flux case. It is, therefore, prudent to enhance heat transfer in the restricted flow areas by whatever means are available. One approach is to increase the flow in these areas by utilizing skid wires as flow diverters, or by opening up these areas by spacers, or by twisting the cables in a helical form. Such essentially fluid mechanical methods are investigated separately. For our purposes these can be interpreted as reductions of the external nonuniformities between the hot and cool sides. Another method, however, is quite relevant in this study, namely, the addition of high conductivity sheathing wrapped around the periphery of each cable.

Fig. 7 shows the reduction in the nonuniformities for various typical sheathing configurations. Even though the thicknesses are small, the effects are quite significant.

Although the effects for any particular configuration can be calculated by the computer programs developed, it is very useful to determine governing dimensionless parameters whose magnitude can give clear indication of the thermal effect of the sheathing considered. We may assume that the effects of the sheathing can be correlated in terms of its heat transfer in the circumferential direction as compared to the heat conducted in the radial direction within the insulation. In each case the heat transfer is proportional to the thermal conductivity and the cross-sectional area, and is inversely proportional to the mean length of the heat flow path.

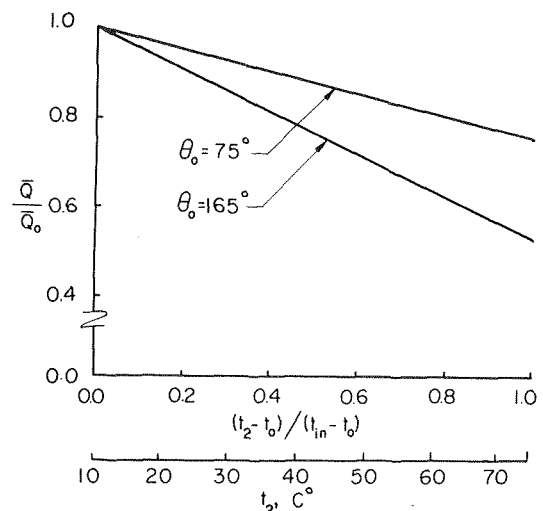


Fig. 4 Effect of increasing temperature,  $t_2$ , within subtended angle  $\theta_0$  on overall heat lost,  $\bar{Q}_0$ , from "standard" cable without sheathing and without dielectric losses— $\bar{Q}_0$  is heat transferred with  $t_2 = t_1 = t_0$

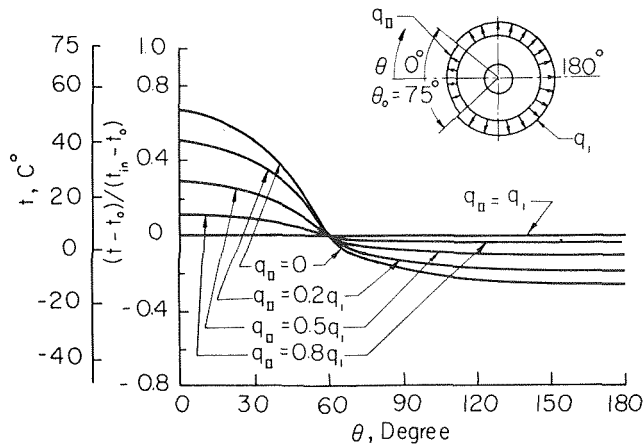


Fig. 5 Effect of decreasing heat flux,  $q_n$ , within a subtended angle of 75 deg on temperature,  $t$ , along outer surface—standard cable without sheathing and without dielectric losses

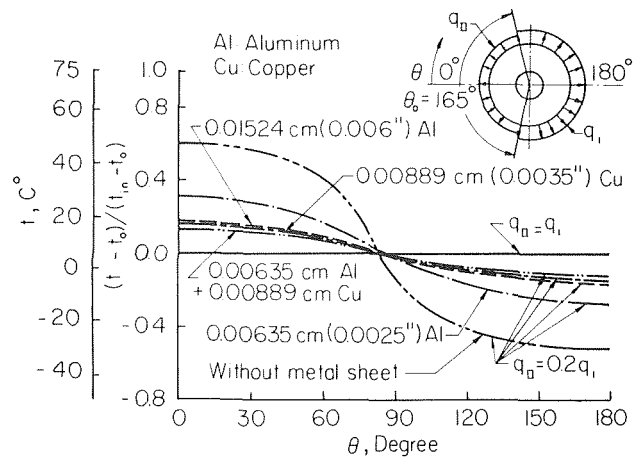


Fig. 7 Effect of conductive sheathing in reducing nonuniformities of temperature distribution with  $\theta_0 = 165$  deg—standard cable without dielectric losses

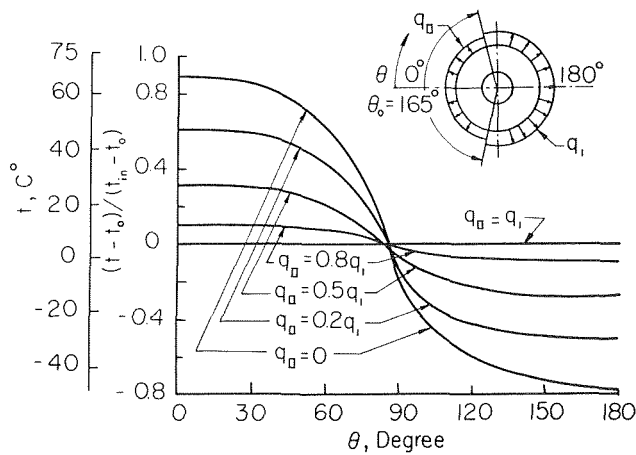


Fig. 6 Effect of decreasing heat flux,  $q_n$ , within a subtended angle of 165 deg on temperature,  $t$ , along outer surface—standard cable without sheathing and without dielectric losses

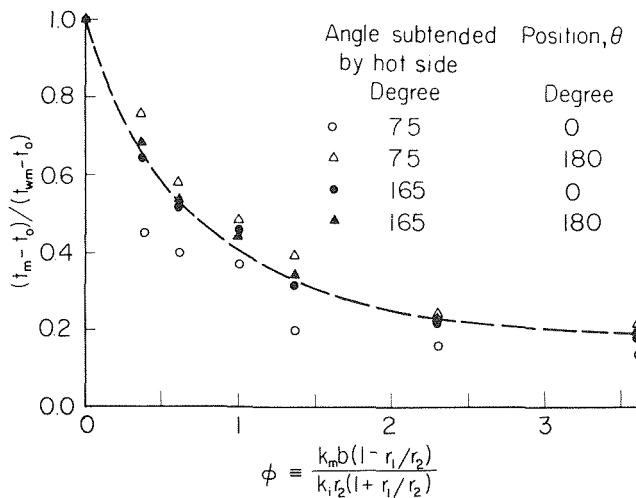


Fig. 8 Dimensionless correlation of effect of conductive sheathing around cable insulation—curve represents fractional reduction of temperature deviation from uniformly cooled case without dielectric losses

Thus, for the heat conducted circumferentially in the sheathing

$$Q_m \propto \frac{k_m b}{r_2}$$

where  $k_m b$  is to be interpreted as  $\Sigma k_m b$  if more than one layer is used.

For the heat conducted radially in the insulation

$$Q_i \propto k_i \left( \frac{r_2 + r_1}{r_2 - r_1} \right)$$

Dividing the two expressions creates a dimensionless parameter which may serve as an index for the influence of sheathing

$$\phi = \frac{k_m b (r_2 - r_1)}{k_i r_2 (r_2 + r_1)} = \frac{k_m b (1 - r_1/r_2)}{k_i r_2 (1 + r_1/r_2)} \quad (4)$$

This parameter is similar to the "wall parameter" used by Morcos and Bergles [10] to correlate the effects of circumferential conduction in the pipe wall on the convective heat transfer inside the pipe.

Fig. 8 is a correlation showing the fractional decrease of the temperature deviation from the uniform case as a function of  $\phi$ . Although there is a considerable spread among the data points, the trend is unmistakable. It should be pointed out that part of the spread among points may be due to the relatively coarse grid used. This effect is particularly significant for the smaller subtended

angle  $\theta_0 = 75$  deg at  $\theta = 0$ . From the approximate curve drawn on the graph we may conclude that the nonuniformities may be ignored within the cable if  $\phi > \sim 4$ . It should be emphasized, however, that the coolant temperature still has to be lowered by an appropriate amount since the total heat has to be dissipated over a smaller, effective surface with a higher heat flux.

Basic heat transfer considerations suggest that the lowest surface temperatures are needed when all losses occur in the conductor at the center. If part of the losses are in the surrounding insulation as dielectric losses, the outer surface temperatures can increase since the total heat has to travel a shorter average distance to the surface. Fig. 9 shows that, indeed, as the relative magnitude of the dielectric losses is increased, the surface temperature profiles shift upward with virtually no change in shape.

## Conclusions and Recommendations

It has been shown by means of a numerical analysis that nonuniform cooling produced by secondary channels between cables can strongly affect the heat transfer from liquid-cooled electric power cables. The most significant result is the need for lowering the coolant temperature in order to maintain a required heat dissipation rate. Even though a change of, say, 6°C is only about 9 percent

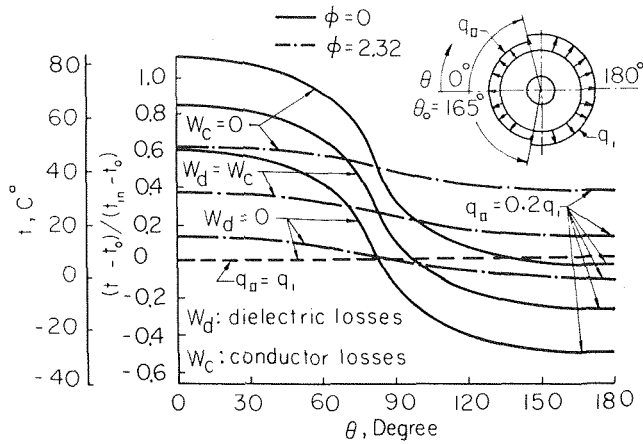


Fig. 9 Effect of relative magnitudes of conductor and dielectric losses

of the temperature difference between the copper conductor and the uniformly cooled outer surface,  $\Delta t_o$ , its effect on the refrigeration requirements for the coolant can be quite significant.

Two principal methods can be recommended to reduce such effects:

- 1 Enhance as uniform flow pattern as possible around the cables by such means as twisting the cables in a helical pattern, or by the use of spacers, or by utilizing the skid wires wound around the individual cables to separate cables as well as to direct the flow into the narrower channels. Just laying three cables next to each other, flat on the bottom of the outer pipe should produce somewhat better heat transfer behavior than the triangular pattern shown in Fig. 1 because less surface is exposed to restricted channels.

- 2 Use thick sheathing, preferably made out of copper, compatible with other design (e.g., needed flexibility) and economic con-

siderations. Making the skid wires out of a high thermal conductivity material will also help to some extent. To estimate this effect a dimensionless parameter,  $\phi$ , has been developed. When its value exceeds  $\sim 4$ , the nonuniformities within the cable may be ignored. The coolant temperature, however, still has to be lowered because the effective heat transfer area is reduced with a corresponding increase in the heat flux required.

### Acknowledgments

This work was supported in part by Contract No. 14-01-0001-1568 (RP78-21) from the Electric Power Research Institute and the U.S. Energy Research and Development Administration.

### References

- 1 Buller, F. H., "Artificial Cooling of Power Cable," *AIEE Transactions on Power Apparatus and Systems*, Vol. 71, 1952, pp. 634-641.
- 2 Neher, J. H., "The Calculation of Temperature Rise and Load Capability of Cable Systems," *AIEE Transactions on Power Apparatus and Systems*, Vol. 76, 1957, pp. 752-772.
- 3 Burrell, R. W., "Application of Oil-Cooling in High-Pressure Oil-Filled Pipe-Cable Circuits," *IEEE Transactions on Power Apparatus and Systems*, Vol. 84, 1965, pp. 795-806.
- 4 Flamand, C. A., "Forced Cooling of High-Voltage Feeders," *IEEE Transactions on Power Apparatus and Systems*, Vol. 85, 1966, pp. 980-986.
- 5 Zanona, A., and Williams, J. L., Jr., "Forced-Cooling Model Tests," *IEEE Transactions on Power Apparatus and Systems*, Vol. 89, 1970, pp. 491-503.
- 6 Williams, J. L., Jr., Zanona, A., and Nease, R. J., "Forced-Cooling Tests on a 138 kV Pipe Cable Circuit," *IEEE Transactions on Power Apparatus and Systems*, Vol. 90, 1971, pp. 1246-1255.
- 7 Notaro, J., and Webster, D. J., "Thermal Analysis of Forced Cooled Cables," *IEEE Transactions on Power Apparatus and Systems*, Vol. 90, 1971, pp. 1225-1231.
- 8 Slutz, R. A., Glicksman, L. R., and Rohsenow, W. M., "Cooling of Underground Transmission Lines," Report No. DSR-80610-83, Heat Transfer Laboratory, Department of Mechanical Engineering, M.I.T., Cambridge, Mass., 1973.
- 9 IEEE Underground Transmission Conferences, 1972-1974.
- 10 Morcos, S. M., and Bergles, A. E., "Combined Forced and Free Laminar Convection in Horizontal Tubes," HTL-1, ISU-ERI-Ames 74008, 1974, Engineering Research Institute, Iowa State University, Ames, Iowa.

P. W. Dietz

J. R. Melcher

Department of Electrical Engineering,  
Massachusetts Institute of Technology,  
Cambridge, Mass.

# Field Controlled Charge and Heat Transfer Involving Macroscopic Charged Particles in Liquids

*When an electric field is applied to a system of electrically conducting particles in an insulating liquid, the rates of charge and heat transfer are augmented. Charged during collisions in the field, the particles execute field-induced excursions between the electrodes interrupted by collisions with other particles. Thus a combination of particle migration and particle-induced fluid convection results in the increase in heat transfer. Experimental values for the Nusselt number are obtained for heat transfer across the parallel electrode configuration. The model developed using these results consists of a well-mixed central region with thermal boundary layers about one particle diameter thick near each electrode.*

## 1 Introduction

When metallic particles are introduced into an electrically insulating liquid between parallel electrodes (see Fig. 1), the rate of heat transfer through the fluid-particle medium can be rapidly controlled by varying the potential difference and hence the electric field strength. The particles, inductively charged during collisions in the presence of the electric field, experience accelerations due to the coulomb force. The motion of the particles through the fluid results in mixing. Thus, the heat transfer is augmented (over pure thermal conduction) by a combination of particle migration and fluid convection. Since the particles' motions are driven by the electric field, the rate of heat transfer can be controlled by simply varying the voltage.

To understand the particle dynamics, consider a single particle held against the lower electrode by gravity. When a voltage is applied to the electrodes, the particle acquires a charge proportional to the electric field and hence experiences a force proportional to the square of the electric field. As the voltage is increased, the electrical force on the particle increases until it is equal to the gravitational force. For larger values of the voltage, the particle will "bounce" back and forth between the plates, exchanging charge and hence reversing the electrical force on each impact [1, 2, 3].<sup>1</sup> As more particles are introduced, collisions occur between oppos-

itely streaming particles, leading to charge exchange within the volume and random particle motions perpendicular to the field. In a sense, the mean free path is then less than the distance between electrodes, and the ordered kinetic energy acquired by the particles from the field goes into a random form analogous to thermal energy at the molecular level. Most important to the transfer of heat and mass in the liquid is the mixing associated with the particle motions.

Min and Chao [4] have investigated the augmentation of heat transfer in a gas-solid suspension with an imposed electric field. Their study relates to the present work in that heat transfer is improved through the coupling between the charged particles and the electric field. However, Min and Chao used small (less than  $300\mu$ ), nonconducting particles which were charged by frictional electrification. Also, since they worked in air, the rate of heat transfer from the wall to the fluid was dominated by particle migration (See Dietz [5] for a more complete bibliography of electromechanical augmentation of heat transfer.)

Although particle dynamics are studied in an effort to understand the process of heat (or mass) transfer in a multiple particle system, the results have applications in other areas as well. The study of the single particle dynamics extends the basic understanding of conduction by macroscopic particles in insulating liquids [3, 6, 7]. Further, the work on multiple particle dynamics has applications to electrofluidized beds—that is, fluidized beds stressed by an electric field. Electrofluidized beds are presently being investigated (Zahedi and Melcher [8, 9]) with applications in mind to air pollution control.

## 2 Single Particle Theory and Experiments

In the case of a single conducting sphere of radius  $R$  in an insu-

<sup>1</sup> Numbers in brackets designate References at end of paper.

Contributed by the Heat Transfer Division for publication in the JOURNAL OF HEAT TRANSFER. Manuscript received by the Heat Transfer Division November 15, 1974. Paper No. 75-HT-WW.

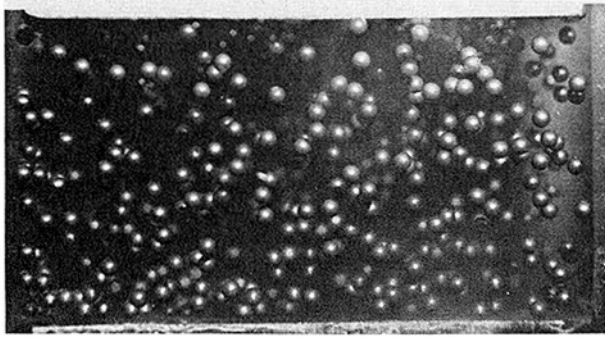


**Fig. 1** Single strobe picture of conducting particles in motion between parallel electrodes (the voltage across the plates is 28kV; the distance between the plates is 2.7 cm; there are 500 particles in the system)

lating liquid, the problem of determining the electric field distribution can be decoupled from the fluid mechanics. Using energy arguments [10] and bispherical coordinates [11, 12], an expression has been obtained for the electric field around a sphere between parallel electrodes [5] as a function of the distance between the sphere and the lower electrode ( $\xi$ ). Following the method given by Schneider [13], the charge acquired by a sphere contacting an electrode (the "Maxwell charge" [14]) can be shown to be

$$Q_M = -4\pi\epsilon R^2 \left(\frac{V}{l}\right) \frac{\pi^2}{6} \quad (1)$$

Similarly, the force on the sphere can be determined by numerically integrating the field solution over the particle surface (the force on a particle carrying the Maxwell charge is shown in Fig. 2).

As the sphere approaches the opposite electrode, a small arc occurs. Given the breakdown strength of the liquid, it is possible to use the computed electric field to calculate the position at which breakdown will occur [5].

(a) **Mechanical Dynamics.** Using the results obtained for the electrical force on a sphere between parallel electrodes, the particle velocity can now be computed. Writing Newton's second law for the sphere, we have

$$\frac{4}{3}\pi\rho_p R^3 \frac{d^2\xi}{dt^2} = f^e + f^D - \frac{4}{3}\pi R^3(\rho_p - \rho_l)g \quad (2)$$

The assumption is made that the conventional steady-state drag

curve for a sphere [16] applies to the acceleration of the sphere. Newton's second law is numerically integrated using two approximations. First, the drag curve is approximated by

$$C_D = \begin{cases} 24 \text{Re}^{-1} & \text{Re} < 1 \\ 24 \text{Re}^{-0.6} & 1 < \text{Re} < 800 \\ 0.44 & \text{Re} > 800 \end{cases} \quad (3)$$

And second, the electrical force is approximated by the average force

$$f = Q_M E \quad (4)$$

As can be seen from Fig. 2, this approximation is accurate except within a few radii of either electrode.

From these results, the particle transit times ( $\tau_1$  and  $\tau_2$ ; with and against gravity, respectively) can be calculated (see Fig. 2; the solid lines represent theory). Impacts with the electrodes are modeled as being completely inelastic. Thus, after each collision, the particle must reaccelerate from rest. (In a more inviscid fluid this assumption might be violated.) Also, using the Maxwell charge, the theoretical time-average current is

$$\langle i \rangle = \frac{2Q_M}{\tau_1 + \tau_2} \quad (5)$$

(see Fig. 4; the solid lines represent theory).

(b) **Experimental System and Results.** The experimental apparatus consists of an aluminum sphere in transformer oil between parallel electrodes. The square electrodes are housed in a plexiglas structure. Because of the strong temperature dependence of the viscosity of transformer oil [17], the system temperature is maintained within 1°C of 23.5°C. At this temperature the viscosity is 0.016 kg/m-s.

An oscilloscope is placed in series with the system. Each time the particle impacts an electrode, a pulse of current is detected on the oscilloscope. By measuring the time elapsed between successive pulses, the particle transit times can be determined (see Fig. 3).

Then, with a 6.8 microfarad capacitor in parallel with the oscilloscope, the time-average current is measured (see Fig. 4).

The experimental values for the time-average current and particle transit times as functions of the electric field show excellent agreement with theory.

## Nomenclature

$A$ = electrode area	$Q_M$ = Maxwell charge on sphere	and center of sphere
$B$ = particle mobility (inertialess model $V_{st} = BE$ )	$Q_S$ = net space charge	$\beta$ = length characterizing viscous dissipation in a particle wake
$c$ = heat capacity	$Q_T$ = total heat transferred	$\delta$ = thermal boundary layer thickness
$C_D$ = drag coefficient ( $f^D / (\frac{1}{2}\rho V_{st} \pi R^2)$ )	$Q_C$ = heat transfer due to conduction in absence of convection ( $k_l A T_l / l$ )	$\epsilon$ = dielectric constant
$E$ = electric field intensity	$Q_D$ = heat transfer due to particle transport	$\eta$ = viscosity
$f^e$ = electrical force	$Q_l$ = heat transfer due to liquid convection	$\rho$ = mass density
$f^D$ = particle drag force	$R$ = particle radius	$\sigma$ = electrical conductivity
$g$ = gravity	$\text{Re}$ = Reynolds number ( $(2R) V_{st} \rho_l / \eta$ )	$\tau_1, \tau_2$ = particle transit times (between electrodes)
$h$ = sphere surface coefficient of heat transfer	$T_1$ = top electrode temperature	$\tau$ = charge relaxation time
$i$ = current	$T_0$ = lower electrode surface temperature	$\tau_w$ = time characterizing particle's collision with an electrode
$k$ = thermal conductivity	$T_l$ = temperature across fluid ( $T_1 - T_0$ )	$\tau_s^*$ = sphere to fluid thermal relaxation time
$l$ = electrode spacing	$V$ = top electrode potential (referenced to bottom electrode)	$\omega$ = collision frequency with electrode
$N$ = number of particles in system	$V_{st}$ = particle terminal velocity	
$n$ = number density of particles in system	$V_{fm}$ = mean square fluid velocity	
$\text{Nu}$ = Nusselt number ( $Q_T / Q_C$ )	$\xi$ = distance between lower electrode	
$\text{Pe}$ = Peclet number ( $V_{fm} \rho_l c_l / k_l$ )		
$\text{Pr}$ = Prandtl number ( $c_l \eta / k_l$ )		

## Subscripts

$l$  = fluid  
 $p$  = particle  
 $in$  = inconel

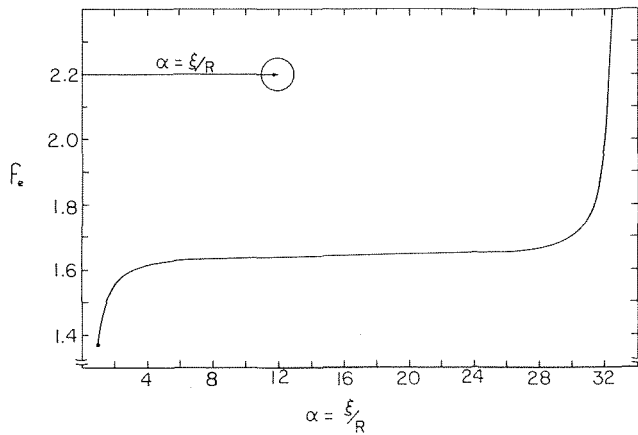


Fig. 2 Normalized electrical force  $f_e$  on the sphere as a function of position (normalized to particle radius) for  $l/R = 34$  ( $f_e = f_o(4\pi\epsilon R^2 E^2)$ )

Also, by examining pictures of the oscilloscope trace of the current transient which occurs when the particle impacts an electrode, further experimental verification for the theory can be obtained. It is possible to determine from the pictures the total charge transferred during the arc as well as the distance between the particle and the plate at which breakdown occurs [5]. These values are compared with those obtained theoretically and reasonable agreement is obtained.

### 3 Multiple Particle Motions and Charge Transfer

As particles are added to the system, multiple particle effects that are not represented in the single sphere model begin to become important. These are evident in the results summarized by Fig. 5, where experimental values for the time average current and for the number of collisions per second with both electrodes are shown as functions of the number of particles in the system. The current and frequency are normalized to the values of these quantities predicted by the single particle model at the same field strength. Thus, field strength is an implicit parameter and all of the measurements can be summarized on a single graph.

If all of the particles behaved as independent single spheres, then the frequency and time-average current would be  $N$  times that for the single sphere. This would place all of the data points on the solid line of Fig. 5. Actually, the measurements drop below the solid line. Presumably, the fact that the frequency results are even lower at the high end of the curve than the time-average current results is due to the inability of the counter to separate overlapping pulses. An examination of the current waveform confirms that above  $N \sim 100$  it becomes difficult to identify individual pulses. However, the disparity between the observations and the solid curve clearly reflects particle interactions.

These interactions can be attributed to three physical mechanisms. First, a difference in average transit times for positively and negatively charged particles can lead to a net space charge. This space charge can contribute to the electric field and hence alter the particle motions. Second, the presence of the moving particles alters the flow pattern and affects the drag on the spheres. And finally, the particles can collide.

A perturbation analysis for the magnitude of the space charge shows that once all of the particles are in motion the effect of the space charge is relatively minor. Typically, the variation in the electric field (from  $E_0 = V/l$ ) is less than ten percent. In addition, the electric field is high near the upper electrode and low near the lower electrode. Thus the effects of the perturbed electric field on the mean particle dynamics tend to average out. However, it should be noted that if there is an excess of particles resting on the lower electrode, then space charge effects can make an essential contribution [18].

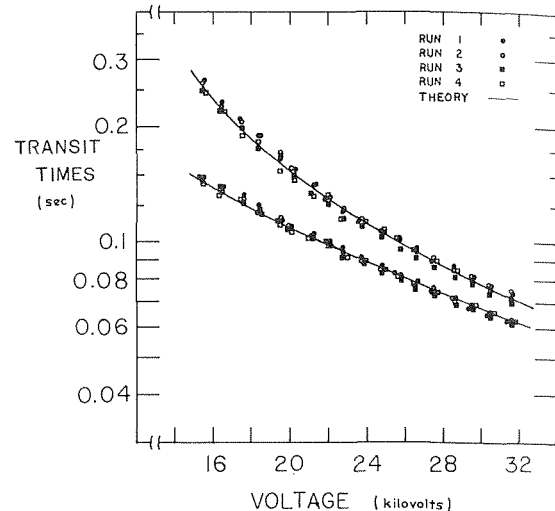


Fig. 3 Comparison between theoretical (solid lines) and experimental values of particle transit times (lower curve for  $\tau_1$  and upper for  $\tau_2$ ) as a function of applied voltage for a 2.7 cm electrode spacing

An order of magnitude calculation for the root-mean-square fluid velocity ( $V_{fm}$ ) can be performed by equating the electrical power delivered to the system to the fluid dissipation (the power dissipated in the arcs is small [5])

$$Nf^2 V_{st} = \eta \frac{V_{fm}^2}{\beta^2} Al \quad (6)$$

where  $\beta$  is a length characterizing the region over which the dissipation occurs. Here, it is reasonable to take  $\beta \sim R$ . For a 500 particle system

$$\frac{V_{fm}}{V_{st}} \sim 0.5 \quad (7)$$

Thus, since the fluid velocities are not small, particle-particle, particle-wake, and particle-wall hydrodynamic interactions must be recognized [19–21] as possible contributions to the drag and hence the transfer processes. However, for a low volume fraction of solids (0–4 percent) and particle Reynolds numbers between 10 and 100, the single sphere drag is a reasonable approximation [20, 22, 23].

From the data, mutual effects become important when the num-

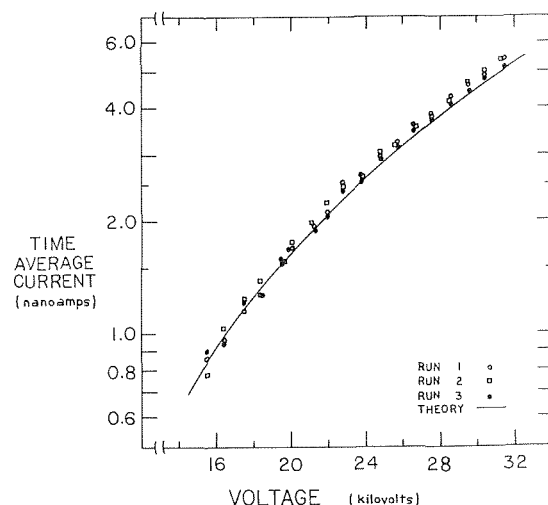


Fig. 4 Comparison between theoretical (solid lines) and experimental values of the time-average current as a function of applied voltage (for a 2.7 cm electrode spacing)

ber of particles exceeds 200–300. Since it takes approximately 1100 particles to cover the entire lower electrode one sphere deep, this suggests that collisions between particles moving in opposite directions accounts for much of the mutual effect apparent in Fig. 5. This is especially plausible if it is recognized that the collision cross section is augmented by the electrical force of attraction.

The effects of collision are evident from a multiple exposure photograph showing the particle trajectories. Five exposures are shown in Fig. 6. A typical single-particle trajectory would extend one third of the way across the gap under the same conditions so that it is evident that a large fraction of the particles are diverted or slowed by interactions. Because of glancing collisions, some particles can be seen to “float,” with little movement. Such collisions are possible because when particles collide with each other in the ambient field, they can in general exchange charge. For a head-on collision, the charge exchange is complete. Each particle completely reverses its charge. If, however, the collision is a glancing one, then the charge on the particles is somewhat less. Thus, a grazing collision can result in a particle whose charge is such that the electrical force balances gravity and it appears to float in the volume.

If the single sphere model for the particle dynamics is assumed to be accurate between collisions and the particles lose all of their inertia during the collisions, then it can be shown that under the particular conditions studied, head-on collisions have little effect on the average particle transit times or the charge transport [5]. Thus, the collisional charge transfer effects are dominated by the extent to which collisions are off-center.

#### 4 Heat Transfer

(a) **Experimental System and Results.** The heat transfer apparatus shown in Fig. 7 consists of the same metal electrodes and plexiglas housing as used for the charge transfer experiments. Copper-Constantan thermocouples (0.039 mV/°C) are embedded in the upper (aluminum) electrode to within 3 mm of the electrode's lower surface. A Bronwill Constant Temperature Circulator (Model 22 Jr.) maintains a bath of transformer oil to within 1°C above the upper electrode. A bath of ice water is stirred below the inconel electrode. Again, the particles are  $1.59 \times 10^{-3}$  m dia aluminum spheres and the liquid is transformer oil.

Thermal data are taken as a function of voltage at two electrode spacings and for several values of the number of particles in the

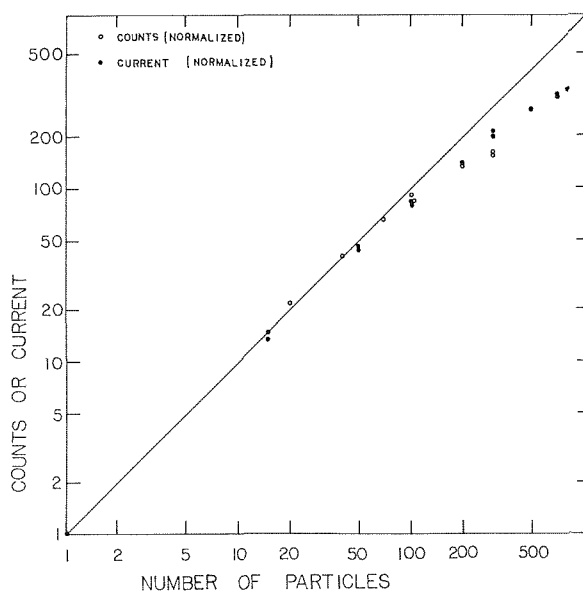


Fig. 5 Counts and time-average current normalized to the single particle theory as a function of the number of particles in the system—the solid line represents  $N$ -times the single particle value (Note: all field strengths are represented on these curves)

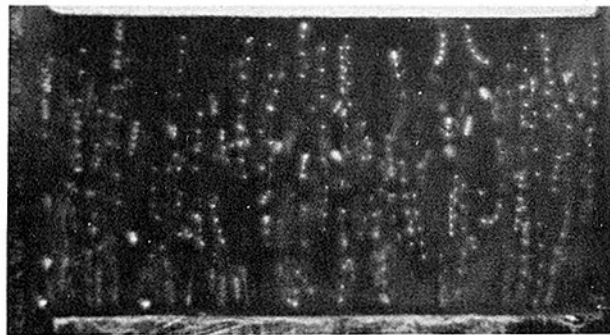


Fig. 6 Five-flash strobe picture of the particles in motion—a single particle trajectory would extend about  $\frac{1}{3}$  of the distance between the plates under these conditions (electrode spacing is 2.7 cm; voltage is 28kV; 125 flashes/s)

system. The data points are taken 30–40 min apart to allow the system to achieve a steady state. Thus, the temperature profile through the inconel electrode is linear (checked by the center thermocouple) and the Nusselt number can be calculated based on the thermal conductivities of inconel and transformer oil.

Typical experimental values for the Nusselt number are plotted in Fig. 8 as a function of the applied voltage. In Fig. 9, the Nusselt number at a constant voltage is plotted against the number of particles in the system.

With care taken to be certain that thermal equilibrium is established, measurements show a small but nevertheless discernible hysteretic dependence on electric field. The Nusselt number is consistently slightly higher when the electric field is being increased than when it is being decreased. This is reflected in the data of Fig. 8.

(b) **Mechanisms of Heat Transfer.** Since the effect of applying an electric field to the particle-fluid system is large (a factor of 10), pure thermal conduction can be eliminated as the primary mechanism of heat transfer. Similarly, the small effect caused by applying an electric field to the zero particle system, means that thermally induced property gradients and the associated electrohydrodynamic instability do not play an important

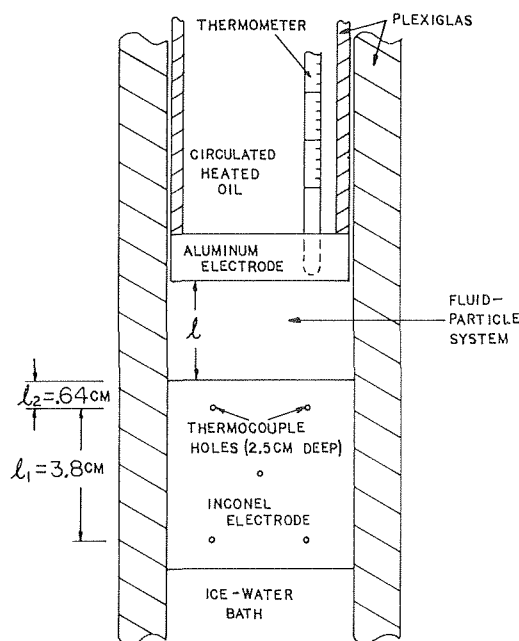


Fig. 7 Schematic diagram of the experimental configuration for thermal measurements

role either. Thus, either the particles carry the heat from electrode to electrode, or the particles mix the fluid and fluid convection is responsible for the augmentation in heat transfer.

An order of magnitude calculation of the Peclet number (the ratio of heat transfer by fluid transport to that by conduction) based on the root-mean-square velocity derived in section 3 gives  $Pe \sim 10^4$ . For  $Pe \gg 1$ , the central region between the electrodes is thermally, thoroughly mixed. Thus, particle induced mixing acts like conventional turbulence to make the temperature profile essentially uniform across most of the gap, and most of the temperature drop is across thin boundary layers near each electrode. This result is consistent with temperature profiles in conventional fluid-beds [24, 25].

If the regions near the electrodes are modeled as boundary layers of relatively motionless fluid, then an equivalent boundary layer thickness can be calculated from

$$\delta = \frac{k_f A T_1}{2Q_T} \quad (8)$$

This thermal boundary layer thickness has been calculated for several values of the electrode spacing and particle density [5]. Typically, the boundary layer thickness decreases with increasing field strength from just under one particle diameter (as soon as all the particles are in motion) to about one radius (just below the breakdown field intensity.)

The boundary layer model is consistent with the shape of the Nusselt number curves. In Fig. 8, as soon as all the particles are in motion, most of the thermal augmentation has taken place. The central region is well-mixed as soon as all the particles are in motion and the temperature drop is across the boundary layers. Any additional increase in the electric field increases the heat transfer rate relatively little, because the thickness of the boundary layer is reduced only as the rate of particle impacts and the velocity of the particles on impact increases. Similarly, Fig. 9 shows a rapid increase in heat transfer as particles are first introduced (the central region becomes mixed) and then a slower increase (the number of impacts with the boundary increases).

The boundary layer model must be amended somewhat to recognize the contribution to heat transferred by the particles themselves. Using the Nusselt number for heat transfer from an isothermal sphere [26] gives a characteristic thermal relaxation time for the sphere

$$\tau_s^* = \frac{\rho c_p R}{3h} \quad (9)$$

which, when evaluated for  $Re = 25$ , gives a relaxation time of about 0.1 s. Thus, the relaxation time is of the order of a particle transit time. The sphere spends most of the time in the constant temperature, well-stirred central region. The short time it spends in the boundary layer is not sufficient (compared to the relaxation time) to transfer a significant quantity of heat. However, since there are many particles in the system, the sum of all the contributions can be significant. To evaluate this contribution, consider that the total amount of heat transferred by the particles is proportional to the number of spheres striking the electrode per second ( $\omega$ ), the ratio of a time characterizing the particles' residence in the boundary layer ( $\tau_\omega$ ) to the particles' thermal relaxation time ( $\tau_s^*$ ) and the maximum amount of heat that could be accepted (based on the time-average mean temperature difference between the sphere and the liquid). Thus

$$Q_P \sim \omega \left(\frac{1}{8} T_1\right) (\rho_p c_p \frac{4}{3} \pi R^3) (1 - \exp(\tau_\omega / \tau_s^*)) \quad (10)$$

Since  $\tau_\omega / \tau_s^* \ll 1$  and  $\omega \sim N / (\tau_1 + \tau_2)$ ,

$$Q_P \sim \frac{N}{(\tau_1 + \tau_2)} \left(\frac{1}{8} T_1\right) (\rho_p c_p \frac{4}{3} \pi R^3) \left(\frac{T_\omega}{\tau_s^*}\right) \quad (11)$$

Using typical values for the variables in equation (11) gives  $Q_P = 0.6$  W. From the experimental data, the actual rate of heat transfer can be calculated (for the same values) to be 3 W. Thus, although

the calculation for  $Q_P$  is only approximate, it does indicate that the particles transfer a significant fraction of the energy from the electrodes. Also, since the particle relaxation time (based on terminal velocity) is approximately equal to the transit time, all the particles will relax to the bulk temperature before colliding with the opposite electrode. Thus, the heat transfer model consisting of a sphere at the bulk temperature impacting the thermal boundary layer near each electrode is consistent.

## 5 Concluding Remarks

Because the theoretical model developed for the electromechanical dynamics of a single conducting sphere in an insulating liquid accurately predicts the single particle charge transfer (see Fig. 4), it has been possible to use the charge transfer in an  $N$ -particle system to study collective effects. The difference between  $N$  times the single-particle current and the  $N$ -particle current is caused by particle-particle interactions. These are found to come into play for  $N \sim 100$  and become important for  $N > 300$ . Thus, mutual effects come into play for a volume density ( $n$ ) of  $1.4 \times 10^6$  particles/m<sup>3</sup> and become important for a volume density of about  $4.3 \times 10^6$  particles/m<sup>3</sup> and an average interparticle spacing of 8 particle radii. This finding supports the view [27] that these interactions become important in systems of bicharged particles when (neglecting inertia) the particle's residence time is equal to a time constant defined by

$$\tau_R \equiv \frac{\epsilon_1}{BQ_p n} \quad (12)$$

where

$$B = \frac{V_{st}}{E}$$

Using this criterion, it follows that electrically-induced interactions between particles can be expected if

$$n \gtrsim [(1.64)(4\pi)(lR^2)]^{-1} \quad (13)$$

Typically, for these experiments, this number is  $2.8 \times 10^6$  particles/m<sup>3</sup> which agrees well with the observed interaction particle densities of between 1.4 and  $4.3 \times 10^6$  particles/m<sup>3</sup>.

The results developed here for charge transport can be extended [5] to other fluid-particle systems as long as the following criteria are satisfied:

1 The charge relaxation time of the fluid  $\epsilon_l / \sigma_l$  is long compared to a particle transit time  $\tau_T$  and the particle transit time is long compared to the charge relaxation time  $\epsilon_p / \sigma_p$  of the particle.

2 The particles are large enough so that surface forces do not cause sticking after particle-particle and particle-wall collisions (in air,  $R \gtrsim 100\mu$  [18]; in vacuum,  $R \gtrsim 1\mu$  [28]).

3 The particle number density is low enough that all of the particles are in motion and the system is not space-charge limited.

An order of magnitude increase in the Nusselt number is obtained by applying an electric field to the transformer oil—aluminum sphere system. This increase is achieved with little expenditure of electrical power. (Typically, the ratio of electrical power in watts to the augmented heat transfer in watts is less than  $10^{-4}$ .) Consistent with the experimental results is a heat transfer model in which the volume transfer is dominated by particle-induced fluid mixing. Due to the turbulent nature of this central region, the temperature profile there is relatively constant. Heat is transferred across the boundary layers by a combination of conduction, fluid convection and particle transport. Thus, the boundary layers are somewhat thicker than calculated in Section 4 where  $\delta$  is based on thermal conduction alone.

## Acknowledgment

Pictures were taken by T. W. Johnson. The first author was supported during the period of this research by an N.S.F. Fellowship.

This work forms a portion of the Master's thesis "Heat, Charge, and Energy Transfer in a Zero-Flow Electrofluidized Bed" submit-

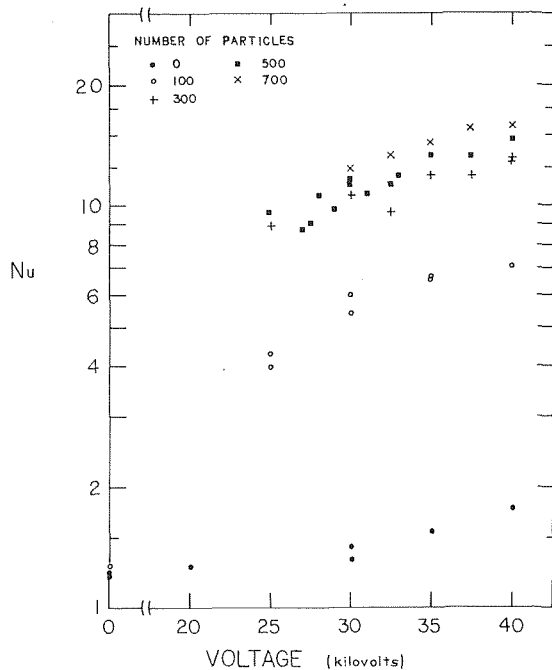


Fig. 8 Nusselt number as a function of voltage for various numbers of particles (electrode spacing is 2.7 cm)

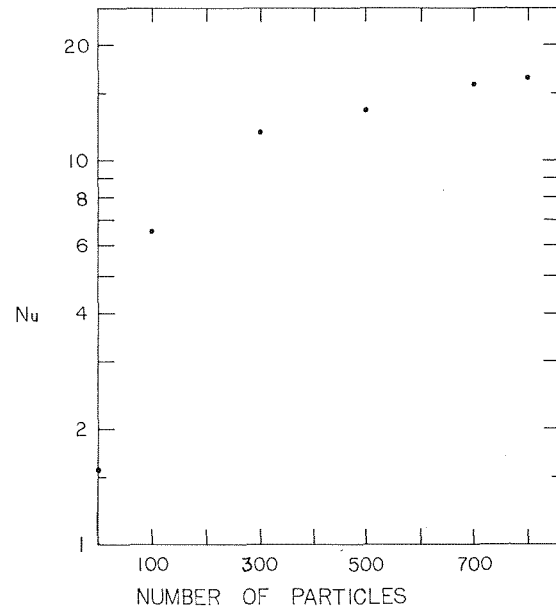


Fig. 9 Nusselt number as a function of the number of particles in the system at constant voltage (voltage is 37.5kV and electrode spacing is 2.7 cm)

ted to the Department of Electrical Engineering, Massachusetts Institute of Technology, Cambridge, Mass., 1974.

## References

- Melcher, James R., "Electric Fields and Moving Media," *IEEE Transactions*, Vol. E17, No. 2, 1974, pp. 100-110.
- Johnson, Thomas W., "Dynamics of a Conducting Sphere Between Capacitor Plates," BS thesis in Electrical Engineering, M.I.T., 1973.
- Dakin, T. W., and Hughes, John, "The Behavior of Individual Conducting Particles in Electric Fields," Conference on Electrical Insulation and Dielectric Phenomena, Annual Report 68-72, 1968.
- Min, Kun, and Chao, B. T., "Particle Transport and Heat Transfer in Gas-Solid Suspension Flow Under the Influence of an Electric Field," *Nucl. Sci. Engng.*, Vol. 26, 1966, pp. 534-546.
- Dietz, Peter W., "Heat, Charge and Energy Transfer in a Zero-Flow Electrofluidized Bed," MS thesis in Electrical Engineering, M.I.T., 1974.
- Kok, J. A., *Electrical Breakdown of Insulating Liquids*, Interscience Publishers, New York, 1961.
- Stannett, A. W., "The Conductivity of Hydrocarbon Transformer Oil Containing Water and Solid Conducting Particles," *Brit. J. Appl. Phys.*, Vol. 2, 1951, pp. 110-114.
- Zahedi, K., "Electrofluidized Beds in the Control of Submicron Particulate," MS thesis in Electrical Engineering, M.I.T., 1974.
- Zahedi, K., and Melcher, J. R., "Electrofluidized Beds in the Filtration of Submicron Particulate," submitted for publication in the *APCA Journal*.
- Woodson, H. H., and Melcher, J. R., *Electromechanical Dynamics*, Wiley, New York, 1968.
- Moon, Parry, and Spencer, Domina E., *Field Theory for Engineers*, D. Van Nostrand Company, Princeton, N. J. 1961.
- Davis, M. H., "Two Charged Spherical Conductors in a Uniform Electric Field: Forces and Field Strength," *Q. Jl. Mech. Appl. Math.*, Vol. 17 Part 4, 1964, pp. 499-511.
- Schneider, J., copy of communication to E. B. Devitt on Bispherical Coordinates and the Charge on Touching Spheres, 1971.
- Maxwell, J. C., *A Treatise on Electricity and Magnetism*, Vol. 1, Oxford, 1892.
- Lebedev, N. N., and Skal'skaya, I. P., "Force Acting on a Conducting Sphere in the Field of a Parallel Plate Condenser," *Zhurnal Tekhnicheskoi Fiziki*, Vol. 32, No. 3, 1962, pp. 375-378, translated in *Russian Physics: Technical Physics*, Vol. 7, No. 3, 1962, pp. 268-270.
- Schlichting, Hermann, *Boundary-Layer Theory*, McGraw-Hill, New York, 1968.
- Blume, L. F., et al., *Transformer Engineering*, Wiley, New York, 1967.
- Devitt, E. B., "Conduction by Macroscopic Charged Particles in Moving Insulating Fluids," PhD thesis in Electrical Engineering, M.I.T., 1973.
- Zenz, F. A., and Othmer, D. F., *Fluidization and Fluid-Particle Systems*, Reinhold Publishing Corp., New York, 1960, p. 203.
- Soo, S. L., Dynamics of Charged Suspensions, *International Reviews in Aerosol Physics and Chemistry*, G. M. Hidy and J. Brock ed., 61-149, Pergamon Press, New York, 1971.
- Soo, S. L., "Heat Transfer Processes of Particulate Suspensions," *Advanced Heat Transfer*, B. T. Chao ed., University of Illinois Press, Urbana, Ill., 1969, pp. 415-437.
- Torobin, L. B., and W. H. Gauvin, "Fundamental Aspects of Solids-Gas Flow; Part V: The Effects of Fluid Turbulence on the Particle Drag Coefficient," *Can. J. Chem. Eng.*, Vol. 38, 1960, pp. 189-200.
- Torobin, L. B., and Gauvin, W. H., "The Drag Coefficients of Single Spheres in Steady and Accelerated Motion in a Turbulent Fluid," *AIChE Journal*, Vol. 7, No. 4, 1961, pp. 615-619.
- Lemlich, Robert and Caldas, Isidoro, Jr., "Heat Transfer to a Liquid Fluidized Bed," *AIChE Journal*, Vol. 4, No. 3, 1958, pp. 376-380.
- Zabrodsky, S. S., *Hydrodynamics and Heat Transfer in Fluidized Beds* (translation F. A. Zenz ed.) M.I.T. Press, Cambridge, Mass., 1966.
- Drake, Robert M., Jr., "Forced Convection Heat Transfer From an Isothermal Sphere to Water, (discussion of)," *JOURNAL OF HEAT TRANSFER*, TRANS. ASME, Series C, Vol. 83, 1961, pp. 170-192.
- Melcher, J. R., and Sachar, K. S., "Charged Droplet Scrubbing of Submicron Particulate," EPA Report EPA-650/2-74-075, Aug. 1974.
- Cho, A. Y. H., "Contact Charging of Micron-Sized Particles in Intense Electric Fields," *J. Appl. Phys.*, Vol. 35, No. 9, 1964, pp. 2561-2564.

J. E. Fitzgerald<sup>2</sup>

Research Asst.  
Department of Electrical Engineering

D. M. Benenson

Professor.  
Faculty of Engineering and Applied Sciences  
Mem. ASME

State University of New York at Buffalo,  
Buffalo, N.Y.

# Response of Pulsed Coaxial Arcs<sup>1</sup>

*Experiments were conducted upon a voltage pulsed coaxial argon plasma in a 1 cm dia, 13.6 cm long channel. Initial steady-state current and pressure were 81 A and 776 Torr, respectively. The final average current was about 1200 A. Rise times of current and center-line temperatures were about 200  $\mu$ s. Using spectroscopic techniques, with data acquisition times of about 5  $\mu$ s, radial distributions of temperature and pressure were obtained at various times into the transient. A final average temperature of about 18,000°K was obtained.*

## 1 Introduction

Pulsed axial plasmas have been employed to investigate arc time constants [1],<sup>3</sup> equilibrium aspects [2–5], and the local temperature-time history [6]. The results of such studies can relate to applications where the dynamic behavior of the arc is important, such as the extinction and reignition processes in switchgear and circuit breakers.

The present paper describes the dynamic behavior of a voltage pulsed argon plasma. The wall stabilized cascade arrangement contained a 1 cm dia channel; electrode separation was 13.6 cm. Initial steady-state current and pressure were 81 A and 776 Torr, respectively. Argon mass flow rate was 0.1 g/s. Application of the voltage pulse resulted in a final average current of about 1200 A. Simultaneous measurements of a line and adjacent continuum were obtained at various times into the transient. From these measurements the local temperature-time history was determined; in addition, under certain conditions (e.g., temperatures in excess of about 15,000°K) similar distributions of pressure were obtained. The dynamic wall pressure, arc current, and voltages were also measured.

## 2 Experimental Apparatus

The 1 cm dia, segmented cascade tunnel [6, 7] contained a 90 deg conically tipped tungsten cathode and a copper segment anode. Electrode spacing was 13.6 cm. The initial steady-state data were obtained with a power supply consisting of two direct current welders, connected in a series, heavily capacitor filtered. The arc voltage and current ripple was about  $\pm 1$  percent; photomultiplier ripple was about  $\pm 5$  percent. Pulsed operation was carried out with a 40,000  $\mu$ f capacitor discharge arrangement; the discharge voltage, 280 V, was obtained with a regulated power supply. The

capacitor charging time was about 8 s. Measurements of the dynamic current were obtained with a 0.00491  $\Omega$  (low inductance-band pass about 30M Hz) current viewing resistor. Voltages were measured across the electrodes as well as across segments 9.53 cm apart. Dynamic wall pressures were measured with a (6.35 mm dia) Kistler piezotron pressure sensor, model 201-A. The transducer was located 10.8 cm downstream of the cathode. The transducer face, approximately 1.5 mm from the channel wall, was connected to the channel through a 1.5 mm dia opening.

A schematic of the optical system is shown in Fig. 1. Arc radiation was observed through an annular ring vycor window slit, 0.25 mm in axial dimension, located 7.30 cm downstream of the cathode. Stationary mirrors 1 and 2 served to observe the radiation from a side-on view and to suitably orient the image of the arc. Light reflected from mirror 2 impinged upon rotating mirror 3 the motion of which traversed the focused image of the arc across the entrance slit of the spectrograph. Simultaneous measurements of a line and adjacent continuum were recorded on a dual beam oscilloscope using the light guide and photomultiplier arrangement shown.

The geometry of the optical system, together with the speed of the rotating mirror (18,000 rpm), resulted in a traverse or scan velocity of the arc image (at the entrance slit of the spectrograph) of 1.85mm/ $\mu$ s (thus, data acquisition time for a 10 mm image would be about 5.4  $\mu$ s). The rotating mirror was driven by a synchronous motor; the mirror was housed in a vacuum chamber to reduce windage losses. Through electronic synchronization [7] the azimuthal position of the mirror was adjusted so that the image of the arc was traversed past the entrance slits of the spectrograph at any desired time,  $\tau$ , with respect to the initiation of the transient.

Arc radiation data were obtained from (1) ArI 4159 Å and the continuum at 4143 Å ( $\tau \leq 60 \mu$ s) and (2) ArII 4806 Å and the continuum at 4820 Å ( $23 \leq \tau \mu$ s  $\leq 466$ ). The respective exit slit widths were (1) 6.43 Å (argon I line) and 21.25 Å (continuum) and (2) 6.43 Å (argon II line) and 34.9 Å (continuum). The linear dispersion of the spectrograph was 11.0 Å/mm. The entrance slit widths were 200  $\mu$  and 100  $\mu$  for the argon I and argon II data, respectively. The time,  $\tau$ , was defined as the time, measured with respect to the initiation of the voltage pulse, at which the center of the image of the arc was located at the entrance slit.

<sup>1</sup> Research supported by National Science Foundation Grant KO 24292-001 and by Air Force Office of Scientific Research Grant 70-1928.

<sup>2</sup> Presently: Electronics Engineer, Sierra Research, Buffalo, N. Y.

<sup>3</sup> Numbers in brackets designate reference at end of paper.

Contributed by the Heat Transfer Division for publication in the JOURNAL OF HEAT TRANSFER. Manuscript received by the Heat Transfer Division August 30, 1974.

Also shown in Fig. 1 is the calibration lamp arrangement which duplicated the optical path of arc radiation.

### 3 Calculations, Repeatability, and Uncertainties

**Current, Voltage,  $\tau$ .** The voltage at which the capacitor discharge was initiated, 280 V, was repeatable to within  $\pm 2$  V. During the transient, the repeatability of arc current and voltage were within about  $\pm 2$  percent. The uncertainty in  $\tau$  was about  $\pm 0.5 \mu\text{s}$ .

**Emission Coefficient, Temperature, Pressure.** The radiation data, at various times into the transient, were obtained through repeated pulsing of the plasma. At a given time,  $\tau$ , multiple recordings of the integrated intensity distribution were obtained to establish the repeatability of the measurements; typically, the repeatability was within about  $\pm 5$  percent (although in regions of rapid, large scale oscillations, the spread tended to increase to about  $\pm 10$  percent). Further, at a given time,  $\tau$ , several individual recordings of the integrated intensity distribution were obtained; a representative recording (e.g., one with values about midway in the band found with the multiple recordings) was typically selected for data reduction. The local emission coefficients were determined through Abel inversion of the integrated intensity distributions.

Radial distributions of temperature were determined from both line and continuum emission coefficients. The expression for line radiation is given by

$$\epsilon_{mn} = \frac{A_{mn} h \nu_{mn} g_m n_A}{4\pi U_A} e^{-E(m)/kT}$$

(where  $\epsilon_{mn}$  = emission coefficient for spontaneous transition from upper level  $m$  to lower level  $n$ ,  $A_{mn}$  = transition probability,  $E(m)$  = energy of  $m$  bound level,  $g_m$  = statistical weight,  $h$  = Planck's constant,  $k$  = Boltzmann constant,  $n_A$  = number density of atoms;  $T$  = temperature,  $U_A$  = partition function;  $\nu_{mn}$  = frequency of radiation). Continuum temperatures were calculated from a Kraimers-Unsold equation

$$\epsilon = 5.41 \times 10^{-46} Z_{\text{eff}}^{2\bar{g}} \frac{n_e n_i}{T^{1/2}}$$

(where  $\epsilon$  = continuum emission coefficient including free-free and free-bound transitions,  $\bar{g}$  = gaunt factor,  $n_e$  = electron number density,  $n_i$  = ion number density,  $T$  = temperature,  $Z_{\text{eff}}$  = effective ion charge).  $Z_{\text{eff}}^2 \bar{g}$  (a function of wavelength, pressure, and temperature) was determined from reference [8].

For ArI 4159 Å line,  $A_{mn} = 0.0145 \times 10^8 \text{ S}^{-1}$  [9],  $g_m = 5$  [9],  $E_m = 117184 \text{ cm}^{-1}$  [9]. For ArII 4806 Å line,  $A_{mn} = 0.79 \times 10^8 \text{ S}^{-1}$  [9],  $g_m = 6$  [9],  $E_m = 155053 \text{ cm}^{-1}$  [9]. Partition functions were determined using reference [10]. For the continuum at 4143 Å,  $Z_{\text{eff}}^{2\bar{g}} = 1.86$  [8] (to 15,000°K and in the range of pressures from 760 Torr to 1520 Torr [8]). For the continuum at 4820 Å,  $Z_{\text{eff}}^{2\bar{g}}$  was approximated, from the data in reference [8] by  $Z_{\text{eff}}^{2\bar{g}} = 2.88 - 3.68 \times 10^{-5} T$  (in the range of temperatures from 9000°K to 21,000°K;  $Z_{\text{eff}}^{2\bar{g}}$  was independent of pressure).

Continuum temperatures were determined up to about 15,000°K—at about which value the emission coefficient no longer was a strong function of temperature. Significant broadening of the ArI 4159 Å line occurred with temperature [11]. An estimate of the broadening, averaged over the arc cross section, was developed as follows. Inversion of the measured integrated intensity distribution yielded the radial distribution of temperature. The average temperature was determined and the half width obtained from reference [11]; using this value, the ratio of the intensity within the bandpass of the spectrograph to the total line intensity was determined through reference [12]. New temperature distributions and average temperatures were then computed in the succeeding cycle. Since the original and the second cycle average values of temperature agreed to within about 100°K, the iteration was terminated. The foregoing ratio ranged from 0.94 at  $\tau = 0 \mu\text{s}$  to 0.80 at  $\tau = 60 \mu\text{s}$ . Broadening of the ArII 4806 Å line was not significant [13]. Absorption of ArII line radiation was not considered, even though, at

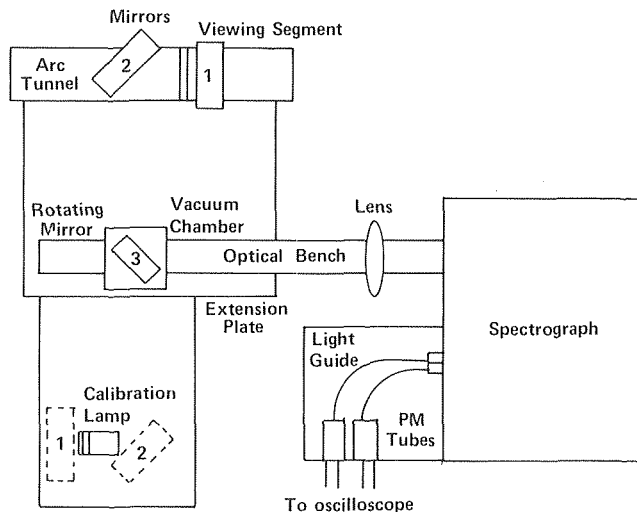


Fig. 1 Optical system

the higher temperatures (in excess of about 18,000°K), the absorption coefficient becomes significant [14]. Discussions [15–17] have indicated absorption effects to be negligible for this line at the indicated conditions. At the wavelengths used, absorption of the continuum was negligible throughout the temperature range encountered [8].

Continuum emission coefficients were determined to within about  $\pm 15$  percent; the uncertainty was associated principally with the use of the tungsten ribbon lamp as a standard source and with the repeatability of the calibration procedure. Since the line emission coefficients were determined through subtraction of the (simultaneously) measured adjacent continuum from the measured line plus continuum data, larger uncertainties were found therein. Uncertainty in the argon I line emission coefficients was about  $\pm 30$  percent. The uncertainty for the argon II line was a strong function of temperature: 20,000°K ( $\pm 20$  percent); 17,000 ( $\pm 30$ ); 15,000 ( $\pm 70$ ); and 14,000 ( $\pm 100$ ). Corresponding maximum uncertainties in temperature found from continuum, argon I line, and argon II line emission coefficients were about  $\pm 100^\circ\text{K}$  at about 10,000°K and  $\pm 600^\circ\text{K}$  at about 15,000°K;  $\pm 200^\circ\text{K}$  at about 10,000°K and  $\pm 2800^\circ\text{K}$  at about 15,000°K;  $\pm 800^\circ\text{K}$  at about 13,000°K and  $\pm 400^\circ\text{K}$  above about 16,000°K, respectively.

Uncertainties in the determination of the gaunt factor are about  $\pm 20$  percent [8]; those of the transition probabilities of ArI 4159 Å and ArII 4806 Å are about 25 percent and  $< 25$  percent, respectively [9]. The uncertainties in the partition functions are about  $\pm 2$  percent [10].

The determination of temperature from local emission coefficients required information on equilibrium within the plasma and on the pressure within the arc. Local thermodynamic equilibrium was assumed [2]. With this assumption, both the local temperature and pressure distributions could, in principle, be determined. In particular, for temperatures in excess of about 14,000°K, the argon II line and continuum emission coefficient data were used for this purpose. For this case, the calculated line emission coefficient-temperature characteristic depended primarily on temperature and was a relatively weak function of pressure; the reverse was found for the continuum emission coefficient-temperature characteristic (Fig. 2). A straightforward iteration, using the measured line emission coefficient as the primary indicator of temperature and the measured continuum coefficient as the primary indicator of pressure, rapidly converged to a set of consistent values for local temperature and pressure. The accuracy of the calculated values depended strongly upon the accuracy of the measured emission coefficients. Above 16,000°K, the previously noted uncertainties in emission coefficients resulted in corresponding uncertainties in

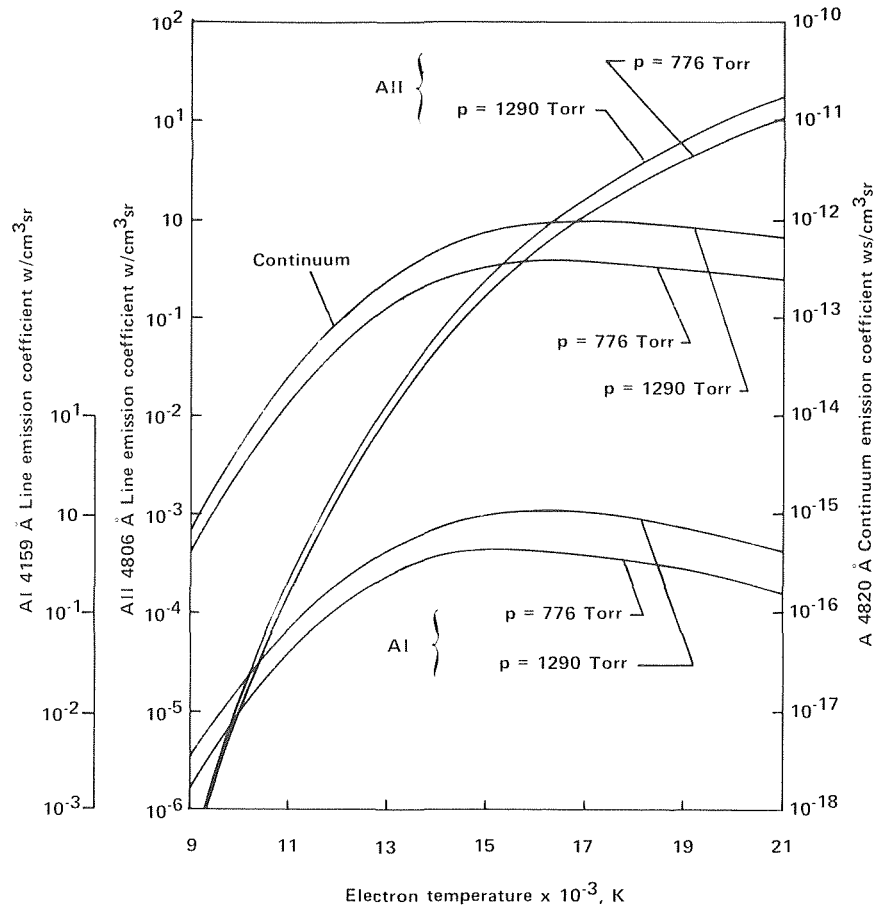


Fig. 2 Emission coefficients as functions of temperature and pressure

pressure of about  $\pm 90$  Torr. At  $15,000^\circ\text{K}$  and  $14,000^\circ\text{K}$  the uncertainties were about  $\pm 130$  Torr and  $\pm 400$  Torr, respectively.

The foregoing procedure was not used with the argon I line and adjacent continuum since the line and continuum emission coefficient-temperature characteristics each depended strongly upon both temperature and pressure (Fig. 2); accuracy of such pressure calculations relied critically upon the accuracy of the measured emission coefficients. For this case, the previously noted uncertainties in the argon I line and continuum coefficients would have yielded large uncertainties in pressure—about  $\pm 350$  Torr.

#### 4 Discussion of Results

Typical dynamic measurements of arc current, voltage across segments 9.53 cm apart, wall pressure, and integrated intensity (measured at  $X = 0$ , i.e., across the diameter of the arc; note that the line measurements also contained the background continuum) are shown in Fig. 3. Arc current and voltage pulse application rise times were about  $200 \mu\text{s}$  and  $3 \mu\text{s}$ , respectively. Periodic oscillations, at about  $10\text{K Hz}$ , were found in all dynamic measurements for times greater than about  $150 \mu\text{s}$ . The capacitance of the discharge, together with the external inductance (measured and calculated), about  $2 \mu\text{h}$ , and the minimum value of arc resistance, about  $0.2 \Omega$ , indicated the circuit to be highly damped (note, also, that the natural frequency of the pure LC circuit was relatively low, about  $500 \text{ Hz}$ ). The observed oscillations were, therefore, characteristic of the arc. These oscillations were probably an acoustic resonance of the system; such behavior has been observed over a wide range of operating conditions [7]. The current and electrode-electrode voltage fluctuations were about  $\pm 100 \text{ A}$  and  $\pm 2 \text{ V}$ , respectively.

An initially rapid rise of current, about  $60 \text{ A}/\mu\text{s}$ , occurred during

the first  $3 \mu\text{s}$  following application of the pulse (not visible on the Fig. 3). The rate was limited by both the inductance in the circuit and by the turn-on characteristics of the SCR's employed. Similar behavior was found for the voltage rise. Initially, then, the response of the arc was, essentially, resistive, i.e., arc temperatures did not change significantly (in this period, less than 1 percent of the pulse energy was applied). Arc expansion closely followed (as based upon temperature measurements) which, after the column reached the wall (within  $7 \mu\text{s}$ ), was succeeded by heating of the plasma.

Nonequilibrium effects have been found [3, 4, 18] with rapid changes in current (e.g., switch-off of an arc in about  $20 \text{ ns}$ ), these effects (manifested particularly in the line radiation) lasting for about  $100 \text{ ns}$ . Under these dynamic conditions, the intensity change of argon line spectra was a strong function of temperature; at about  $10,000^\circ\text{K}$ , the intensity change (of Ar I 6965 Å) was about 10 percent. Since in the present case (1) the current rise time initially was of the order of  $3000 \text{ ns}$  and (2) the initial center-line temperatures were above  $10,000^\circ\text{K}$ , relatively small nonequilibrium effects would be expected; none was observed in any measurements of the integrated intensities.

During the first  $150 \mu\text{s}$ , the behavior of the pressure transducer—the rapid rise in wall pressure, the large overshoots, and the high frequency oscillations (about  $35^\circ\text{K Hz}$ )—indicated the sensor system (transducer, cavity, etc.) to be responding as an underdamped system. The rapid reduction in signal level at about  $\tau = 150 \mu\text{s}$  was an indication of mechanical buckling of the transducer face caused by excessive heat loading [19] during pulsed operation (when the arc filled the channel and expanded into other openings, as will be described; as noted earlier, the transducer face was located  $1.5 \text{ mm}$  from the arc channel). Mechanical buckling resulted in significant

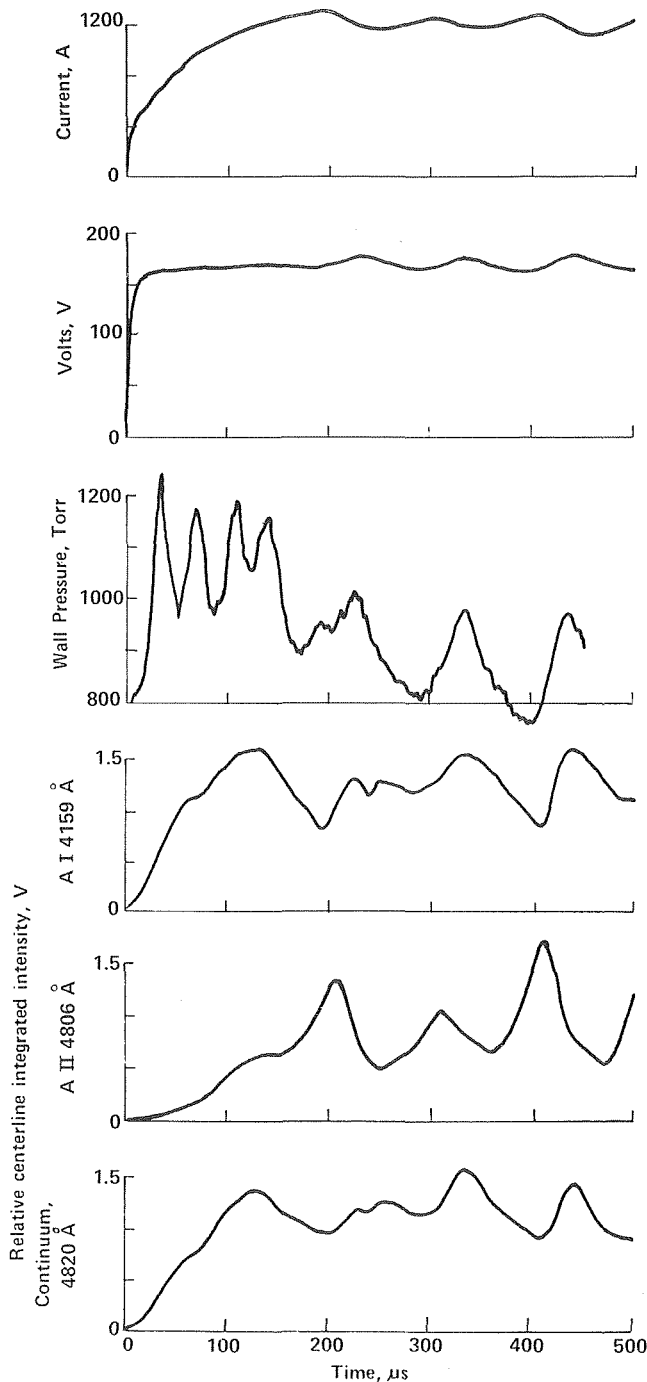


Fig. 3 Dynamic measurements

reduction in (at least) the output voltage [19], the effect becoming greater with time. Pressure fluctuations in the oscillatory region were about  $\pm 100$  Torr.

Oscillations of the argon II line relative center-line integrated intensity were typically out of phase with those of the argon I line and continuum. This behavior may be qualitatively described by relating the integrated intensities to the emission coefficient-temperature characteristics (shown in Fig. 2) and by anticipating peak temperatures in excess of about  $15,000^\circ\text{K}$ . Therefore, local maxima in the argon II line relative center-line integrated intensity corresponded to local maxima in temperature. The corresponding phase relationship of the pressure oscillations further reinforced the temperature behavior. The phase relationships between current, pressure, and integrated intensity (temperature) were consis-

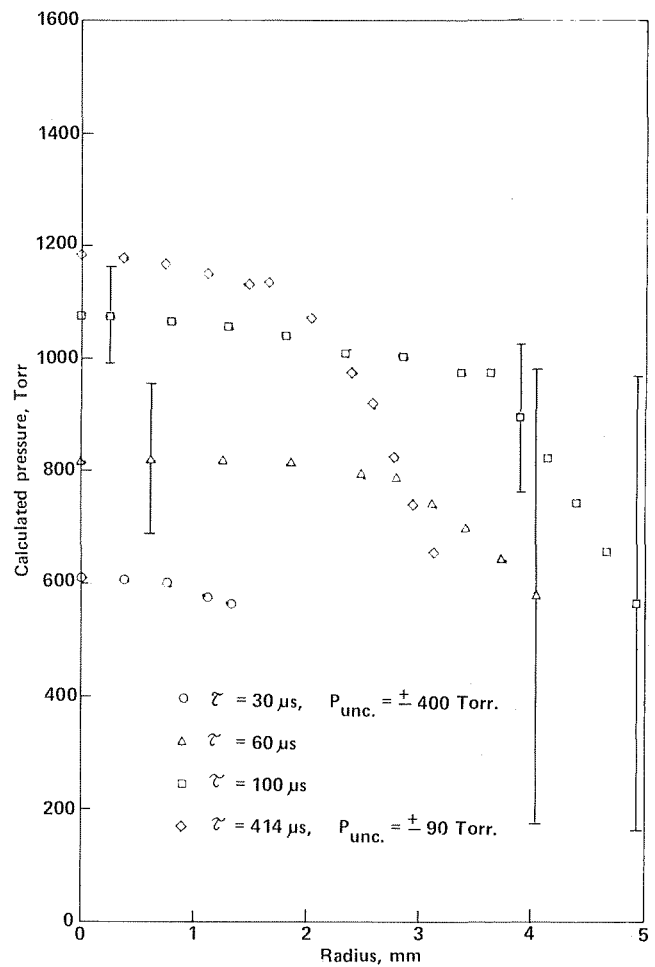


Fig. 4 Calculated radial distributions of pressure at various times into the transient

tent with steady-state characteristics reported in reference [14].

The calculated radial distributions of pressure at various times into the transient, determined as described in the previous section, are shown in Fig. 4. The results for  $\tau = 30 \mu\text{s}$  were arbitrarily terminated at a radius of about 1.5 mm as a consequence of the generally low pressures obtained. At a given  $\tau$  the distributions generally indicated a nearly constant pressure level, at least within a core. The observed reductions in pressure in the outer regions were probably a consequence of the lessened accuracy of the emission coefficients (as described in the previous section).

The timewise behavior of both the calculated center-line pressure and the measured wall pressure are presented in Fig. 5. For times greater than about  $50 \mu\text{s}$  the differences are about 300 Torr (about 30 percent). As discussed in the previous section, however, the response of the pressure sensor was altered (reduced) significantly through mechanical buckling of the transducer face due to excessive heat loading. During the first  $100 \mu\text{s}$ , as discussed in the previous section, the response of the pressure transducer corresponded to that of an underdamped system. On the other hand, the calculated center-line pressures indicated relatively low values in this period. In this interval, relatively large uncertainties in calculated pressure, about 400 Torr, were found; the uncertainties were due to the correspondingly large uncertainties in emission coefficients. Thus, for times greater than about  $150 \mu\text{s}$ , the calculated values were probably more correct; for smaller times,  $25 \leq \tau \mu\text{s} \leq 150$ , an average value of about 1100 Torr (as averaged from the measured wall pressure) could serve as an estimate.

As noted in the previous section, calculations of the temperature distribution required a specification of pressure. Based upon the

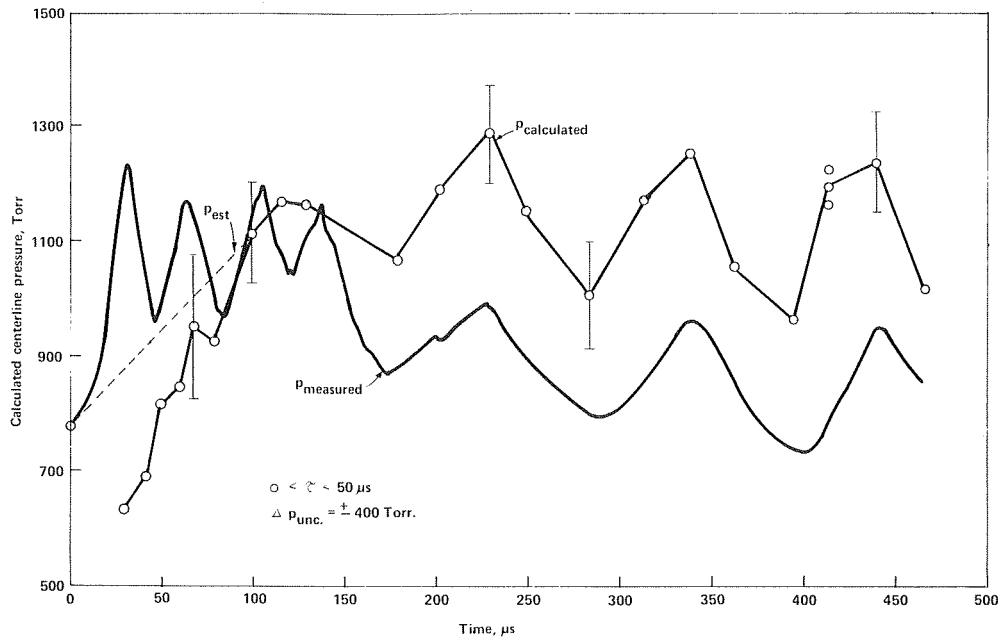


Fig. 5 Calculated and measured pressures as a function of time

pressure measurements and calculations, the pressure inputs were determined as follows. For  $\tau \geq 100 \mu\text{s}$ , local temperatures were computed using (1) local pressures (e.g., Fig. 5),  $p_{\text{local}}$  and (2) an assumed pressure, maintained constant with radius; that selected was the local center-line pressure,  $p_c$ . For  $\tau \leq 23 \mu\text{s}$ , a constant value of pressure was again assumed. Owing to the large uncertainties in pressure during this interval, estimated values ( $p_{\text{est}}$ ), as shown by the dashed line in Fig. 5, were selected. As noted in the foregoing, estimated pressures probably underestimated the actual values. In the range  $30 \leq \tau \mu\text{s} \leq 100$ ,  $p_{\text{est}}$  was principally employed.

Radial distributions of temperature are shown in Figs. 6 and 7 for the earlier and later portions of the transient, respectively. For  $\tau \geq 100 \mu\text{s}$ , temperatures were determined from argon II line only. In the range  $30 \leq \tau \mu\text{s} \leq 100$ , argon II and, to temperatures of about  $15,000^\circ\text{K}$ , argon I and the respective continuum were employed. For  $\tau \leq 30 \mu\text{s}$ , argon I line and the adjacent continuum were used to determine temperatures.

The steady-state temperature distribution, not shown in Fig. 6, was about  $150^\circ\text{K}$  lower than that shown at  $\tau = 7 \mu\text{s}$ ; the temperatures were in agreement to within about  $200^\circ\text{K}$  with those obtained under similar operating conditions [20]. The relatively small rise in temperature at  $\tau = 7 \mu\text{s}$  suggested that, during the period, the arc had (principally) expanded to the wall prior to heating. At  $\tau = 20 \mu\text{s}$  considerable heating of the arc had occurred. The distributions shown at  $\tau = 60 \mu\text{s}$  were computed for the two argon lines and their respective adjacent continuum. The tendency for the plasma to fill the channel and to expand into the viewing window slit was clearly indicated at  $\tau = 60 \mu\text{s}$  and has probably occurred earlier; similar behavior is seen at  $\tau = 100 \mu\text{s}$  and  $\tau = 363, 466 \mu\text{s}$  (Fig. 7). Differences between temperatures computed using local pressures and a constant center-line pressure ranged from zero at the center line to a maximum of about  $600^\circ\text{K}$  in the outer regions.

The timewise dependence of the center-line temperature is shown in Fig. 8. A first estimate of the characteristic rise time,  $\tau$ , may be obtained from the relation  $\tau = R^2/\beta\alpha^2$  (where  $R$  = radius and  $\alpha$  = thermal diffusivity,  $\beta$  = the first zero (2.405) of the Bessel function). At  $16,000^\circ\text{K}$ ,  $\tau \sim 360 \mu\text{s}$ . In the range  $30 \leq \tau \mu\text{s} < 100$ , center-line temperatures calculated according to  $p_{\text{local}}$  ( $p_c$  at the center line) and  $p_{\text{est}}$ , were in agreement to within about  $300^\circ\text{K}$ . Using a higher value of  $p_{\text{est}}$ , as discussed earlier, would have fur-

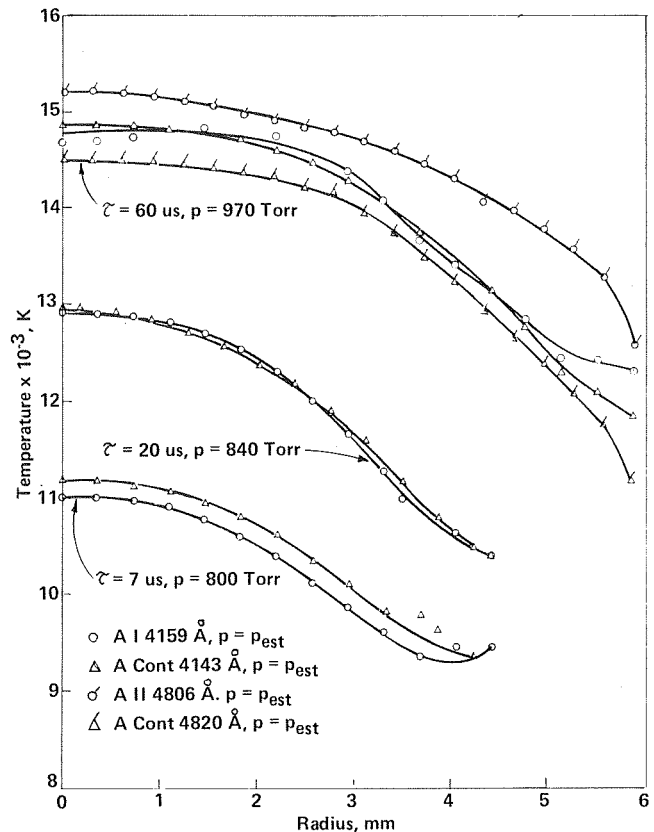


Fig. 6 Radial distributions of temperature at various times into the transient,  $0 \leq \tau \mu\text{s} \leq 60$

ther reduced these temperatures presented by about  $150^\circ\text{K}$ . The maximum center-line temperature obtained was about  $20,000^\circ\text{K}$ , at  $\tau = 414 \mu\text{s}$ ; the range in temperatures found reflected the repeatability of the transient at this time. For  $\tau \geq 150 \mu\text{s}$ , the average

center-line temperature, current, and pressure were about 18,000°K, 1200 A, and 1150 Torr, respectively. At the same current and pressure level, a steady-state center-line temperature of about 16,500°K would be expected [14]. The temperature difference, about 1500°K, was larger than anticipated through consideration of uncertainties and suggest the oscillatory behavior as a significant contributing factor, particularly in the pressure dynamics and

the associated effects of temperature. The results also pointed to operation under oscillatory conditions as a means to increase average temperatures with respect to those in the steady-state.

### Summary

The experiments which were conducted upon a voltage pulsed (rise time  $\sim 3 \mu\text{s}$ ) coaxial argon plasma resulted in rise times of about 200  $\mu\text{s}$  for both current and center-line temperature. Radial distributions of temperature, determined from argon I and II lines and their respective continuum, were obtained at various times into the transient using spectroscopic techniques having data acquisition times of about 5  $\mu\text{s}$ . Under certain conditions, e.g., for temperatures in excess of about 15,000°K, the argon II line and adjacent continuum were employed in the determination of pressure distributions. Acoustic oscillations of the system, at about 10K Hz, were observed after about 150  $\mu\text{s}$  into the transient; average final arc current, center-line temperature and pressure were about 1200 A, 18,000°K, and 1150 Torr, respectively.

### Acknowledgment

The authors wish to acknowledge the efforts of Mr. Willi Schulze, State University of New York at Buffalo, for his invaluable assistance in the experiments.

### References

- 1 Yoon, K. H., and Browne, T. E., Jr., "A Study of the Dynamic Response of Arcs; Time Constants of Low-Current Arcs Under Small Air Flow," *IEEE Transactions on Power Apparatus and Systems*, Vol. 82, 1963, pp. 1002-1014.
- 2 Benenson, D. M., and Cenker, A. A., Jr., "Local Thermal Equilibrium in a Transient Arc," *AIAA Journal*, Vol. 12, 1974, pp. 116-117.
- 3 Alexandrov, V. Ya., Gurevich, D. B., and Podmoshenskii, I. V., "A Study of the Mechanism of Excitation and Ionization in the Plasma of an Argon Arc," *Optics and Spectroscopy*, Vol. 23, 1967, pp. 282-286.
- 4 Schumaker, J. B., and Venable, W. H., Jr., "Line Intensity Behavior in a Decaying Arc Plasma," 23rd Gaseous Electronics Conference, American Physical Society, Gatlinburg, Tenn., Paper D2, 1969.
- 5 Anderson, R. W., and Bowen, S. W., "Investigation of Non-Equilibrium in Transient Arcs," *Bulletin of the American Physical Society*, Series II, Vol. 18, 1973, p. 791.
- 6 Benenson, D. M., Naeher, C. H., and Augie, S. S., Jr., "Dynamic Measurements of Arc Temperature Distribution, Radius, and Current in a Pulsed Co-axial Plasma," *IEEE Transactions on Power Apparatus and Systems*, Vol. PAS-89, No. 7, 1970, pp. 1413-1419.
- 7 Fitzgerald, J. E., "Voltage Step Response of a Co-axial Arc Plasma," MS thesis, State University of New York at Buffalo, Buffalo, N. Y., 1974.
- 8 Morris, J. C., and Yos, J. M., "Radiation Studies of Arc Heated Plas-

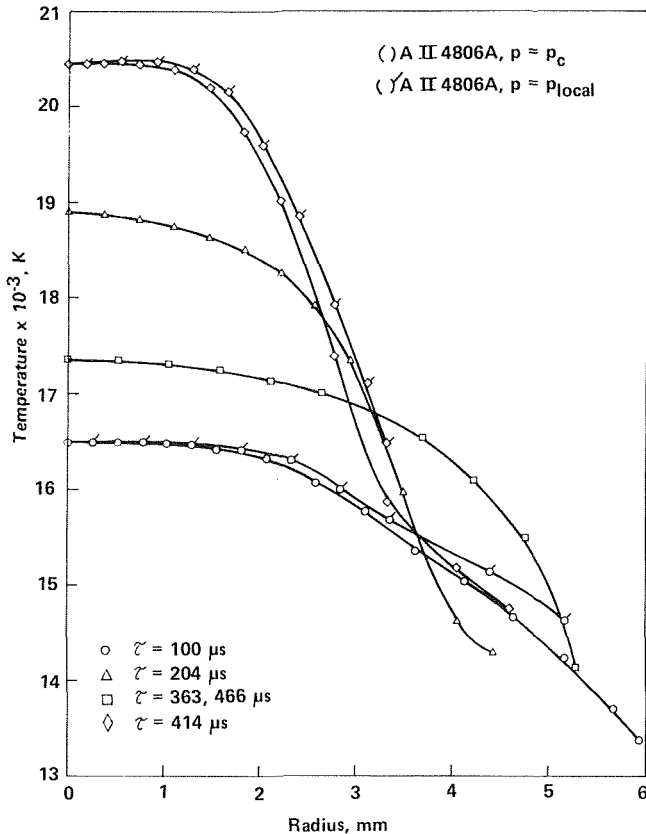


Fig. 7 Radial distributions of temperature at various times into the transient,  $\tau \geq 100 \mu\text{s}$

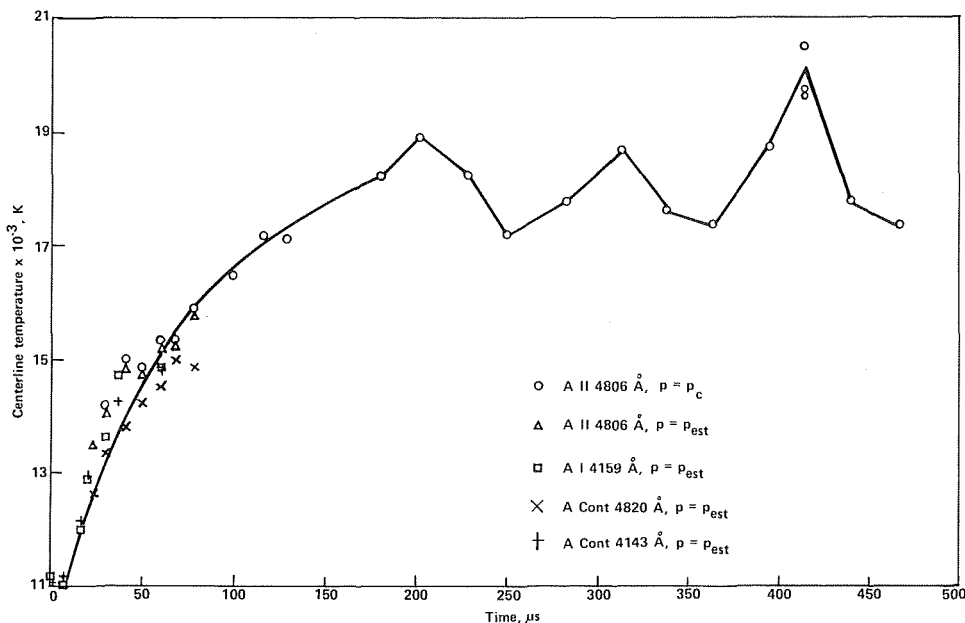


Fig. 8 Center-line temperature as a function of time

mas," U.S. Air Force Aerospace Research Laboratories, Wright-Patterson Air Force Base, Ohio, ARL 71-0317, 1971.

9 Weise, W. L., Smith, M. W., and Miles B. M., "Atomic Transition Probabilities, Vol. II, Sodium Through Calcium," *National Standard Reference Data Series*, National Bureau of Standards, Washington, D. C., 1969.

10 Olsen, H. N., "The Electric Arc as a Light Source for Quantitative Spectroscopy," *Journal of Quantitative Spectroscopy and Radiative Transfer*, Vol. 3, 1963, pp. 305-333.

11 Gericke, W. E., "Messung der ubergangswahrscheinlichkeit sowie halbwertsbreite und verschiebung von Al-linien in thermisch leuchtenden plasmen," *Zeitschrift fur Astrophysik*, Vol. 53, 1961, pp. 68-79.

12 Morris, J. C., Krey, R. U., and Garrison, R. L., "Radiation Studies of Arc Heated Nitrogen, Oxygen, and Argon Plasmas," U.S. Air Force Aerospace Research Laboratories, Wright-Patterson Air Force Base, Ohio, ARL 68-0103, 1968.

13 Griem, H. R., *Plasma Spectroscopy*, McGraw-Hill, New York, 1964.

14 Morris, J. C., and Morris, R. U., "Radiation Studies of Arc Heated Plasmas," U.S. Air Force Aerospace Research Laboratories, Wright-Patterson Air Force Base, Ohio, ARL 70-0038, 1970.

15 Olsen, H. N., Private communication, 1973.

16 Olsen, H. N., "Determination of Departures From Local Thermodynamic Equilibrium in Arc Plasmas," U.S. Air Force Aerospace Research Laboratories, Wright-Patterson Air Force Base, Ohio, ARL 67-0060, 1967.

17 Morris, J. C., Private communication, 1973.

18 Richter, J., "Partial Thermodynamic Equilibrium in Plasmas," Invited Papers of the Tenth International Conference on Phenomena in Ionized Gases, Oxford, Great Britain, 1971, pp. 37-58.

19 Bennett, M., Private communication, 1972.

20 Bott, J. F., "Spectroscopic Measurement of Temperatures in an Argon Plasma Arc," *Physics of Fluids*, Vol. 9, 1966, pp. 1540-1547.

# ERRATUM

Erratum: F. W. Ahrens and H. N. Powell, "Effects of a Transverse Magnetic Field on a Constricted Electric Arc," published in the May 1975 issue of the JOURNAL OF HEAT TRANSFER, pp. 267-273.

1 The carats appearing over the unit vectors  $\bar{x}$  and  $\bar{z}$  in equations (5), (6), (8), (16)-(18) should be deleted.

2 Equation (9) should read:

$$\vec{q}_R = -\nabla \phi_R \quad (9)$$

3 The right-hand side of equation (11d) should be preceded by a minus sign.

4 The range of applicability for equations (11e) and (11g) should read:

$$0 < r \leq a$$

**T. E. Cooper**

Assoc. Professor.  
Assoc. Mem. ASME

**R. J. Field**

Lieutenant, USN.

**J. F. Meyer**

Lieutenant Commander, USN

Department of Mechanical Engineering,  
Naval Postgraduate School,  
Monterey, Calif.

# Liquid Crystal Thermography and Its Application to the Study of Convective Heat Transfer

*A thermographic technique is presented that allows visual determination of both qualitative and quantitative heat transfer and fluid flow information to be obtained on heated objects placed in forced convection environments. The technique employs cholesteric liquid crystals as the temperature sensing agent. The liquid crystals indicate temperature by exhibiting brilliant changes in color over discrete, reproducible temperature ranges. The technique has been used to quickly and easily obtain information on the variation of the Nusselt number on a right circular cylinder placed in a crossflow of air. In addition to yielding precise quantitative heat transfer information, the liquid crystal thermographic technique afforded the opportunity to visually observe the effects of flow separation, the separation bubble region, the turbulent boundary layer, and the turbulent wake on the surface temperature of the heated cylinder. The experimental results obtained using the liquid crystal thermographic technique are in close agreement with results obtained by other investigators who have used standard measuring techniques.*

## Introduction

The purpose of this paper is to report on a technique that allows visual determination of both qualitative and quantitative heat transfer and fluid flow information on heated objects placed in forced convection environments. Cholesteric liquid crystals, a commercially available material that exhibits brilliant changes in color over discrete, reproducible temperature bands, are used as the temperature sensor in the technique. By appropriate calibration, the colors displayed by the liquid crystal material can be accurately related to the temperature of the material. This allows one to visually observe select isotherms and, further, can be used to infer the location of points of flow separation and boundary layer reattachment. The colors displayed by the liquid crystal material also give a dramatic indication of the influence of turbulence on surface temperature. In a region of turbulent flow, the colors displayed by the liquid crystal material continuously dim and glow in response to the "scrubbing" action caused by random bursts of cool fluid impacting on the heated surface.

The liquid crystal thermographic technique has been used to determine the circumferential variation of the Nusselt number on a uniformly heated right circular cylinder cooled by forced convec-

tion in a crossflow of air. The heated cylinder in crossflow represents a classic heat transfer problem that has been studied both experimentally and theoretically by numerous investigators over the last 40 or so years. As such, it served as an ideal problem to study with the liquid crystal technique since both theoretical and experimental results were available for comparison. In the present investigation, Reynolds numbers were varied from approximately 40,000–150,000. This allowed the study of both subcritical and critical flow regimes.

Data were obtained on a 10 cm dia right circular cylinder constructed from a 0.1 cm thick carbon impregnated paper that exhibited an electrical resistivity of 2.5 ohm-cm. The outer surface of the cylinder was coated with a thin layer of the liquid crystal material. A known heat flux was established on the surface of the cylinder by employing the Joulean heating effect produced by passing a constant current longitudinally through the resistive paper. The inner hollow space of the cylinder was firmly packed with glass wool to prevent heat losses into this region. The glass wool also reinforced the cylinder and aided in resisting deformation due to the outer flow.

The Nusselt number results obtained in the present investigation compare within the estimated experimental uncertainty (5 percent) in the forward stagnation region on the cylinder with the theoretical solutions proposed by Schuh [1],<sup>1</sup> Seban, and Chan [2], and Perkins and Leppert [3]. Beyond approximately 60 deg, the

Contributed by Heat Transfer Division of THE AMERICAN SOCIETY OF MECHANICAL ENGINEERS and presented at the AIChE-ASME Heat Transfer Conference, San Francisco, Calif., August 11–13, 1975. Journal manuscript received at ASME Headquarters June 4, 1975. Paper No. 75-HT-15

<sup>1</sup> Numbers in brackets designate References at end of paper.

experimental results rapidly diverge from the theoretical predictions. This trend is consistent with the experimental results of Giedt [4], Seban [5], and Meyer [6] and is most probably explained by the fact that a pressure distribution based on frictionless fluid flow behavior was used to generate the theoretical curve.

## Background

**Liquid Crystals.** In 1888, an Austrian botanist, Friedrich Reinitzer, observed that certain organic compounds appeared to possess two melting points, an initial melting point that turned the solid phase to a cloudy liquid and a second melting point at which the cloudy liquid turned clear. Further research revealed that an intermediate phase, or "mesophase," did indeed exist between the pure solid phase and pure liquid phase of some organic compounds. Reinitzer termed this phase a "liquid crystal phase," an appropriate designation when one considers that the liquid crystal phase exhibits the fluidity of a liquid while at the same time maintaining a degree of anisotropic, ordered structure of a crystalline solid. Since Reinitzer's original work, a great deal of research concerning the structure of liquid crystals has been carried out resulting in the classification of liquid crystals into one of three categories: smectic, nematic, or cholesteric; the particular category being determined by the molecular structure of the liquid crystal. In the present work, no attempt was made to study the details of the molecular structure of liquid crystals. Excellent papers on this aspect of liquid crystal technology have been published by Brown and Shaw [7], Ferguson [8], Ferguson and Brown [9], Dreher, Meir, and Saupe [10], and Stephen and Straley [11]. Of particular interest in the present investigation were the optical properties exhibited by the liquid crystal phase and the change that may be produced in the light transmitting and scattering properties of thin films of liquid crystal materials when certain fields are impressed on these films.

A variety of externally applied fields including electrical, magnetic, shear, pressure, and thermal fields have been found to produce a change in the optical properties of liquid crystals. As an example, nematic liquid crystals, when applied in a very thin film and viewed through a dielectric material such as glass, appear opaque when an electrical field is applied but appear transparent in the absence of the electrical field. Smectic liquid crystals behave in a similar fashion. Although a host of applications have been and more than likely will continue to be found for the nematic and smectic type liquid crystals [12–17], of immediate concern in our investigation has been the response of cholesteric liquid crystals to thermal fields and the use of this response to obtain both qualitative and quantitative heat transfer information.

Cholesteric liquid crystals, as the name implies, are formed from esters of cholesterol. The property of interest, from a heat transfer point of view, of the cholesteric type liquid crystal concerns its response to temperature. Over a known, reproducible range of temperature, the "event temperature range," the cholesteric liquid crystal will progressively exhibit all colors of the visible spectrum as it is heated through the event temperature range. The phenomena is reversible, repeatable and, with proper care, color can be accurately calibrated with temperature.

Both the width of the event temperature range and its placement on the temperature scale can be controlled by selecting the appropriate cholesteric esters and the proportions used in a given formulation. At present, liquid crystals are commercially available with event temperature ranging from a few degrees below zero to several hundred degrees Celsius. Liquid crystals can be obtained with event temperature spans as small as 1°C to as large as 50°C. For optimum brilliance, the cholesteric liquid crystals should be applied as a thin film (0.003–0.006 cm) on a black substrate. The black substrate insures that all light transmitted through the liquid crystal film is absorbed and, therefore, is not reflected to compete with the desired signal.

Pure liquid crystals, although exhibiting brilliant colors, pose several problems from the point of view of laboratory usage. Once

applied to a specimen, the pure liquid crystals deteriorate rapidly with age permitting only a few hours of experimentation. They are also susceptible to contamination with marked alteration in performance resulting from exposure to many common atmospheric contaminants, as well as to ultraviolet light. Further, the detection of temperature via a change in color is strongly influenced by viewing angle.

Many of the problems associated with the use of pure cholesteric liquid crystals have either been eliminated or greatly reduced through an encapsulating process developed by the National Cash Register Company. The encapsulated liquid crystals, referred to appropriately enough as Encapsulated Liquid Crystals, are coated with gelatin in a polyvinyl alcohol binder. This coating results in the formation of small spheroids with typical diameters on the order of 20–50 microns. In addition to extending the life of the liquid crystals to as long as several years by protecting the raw crystals from the damaging effects of ultraviolet light and atmospheric contaminants, the encapsulation procedure also greatly reduces the variation of color due to viewing angle. Further, unlike the pure liquid crystals, the encapsulated liquid crystals are relatively insensitive to the effects of normal and shearing forces. Encapsulated liquid crystals can be obtained in one of two forms, either precoated on a blackened substrate of paper or mylar, or in a water based slurry. For our experiments, the encapsulated liquid crystals were obtained in slurry form which allowed manual coating of the specimen surface with an ordinary brush.

**Prior Work.** Cholesteric liquid crystals have been employed in a number of interesting applications over the past several years. To date, the majority of uses have involved qualitative interpretation of the temperature fields displayed so colorfully by the liquid crystals, that is to say, observing hot and cold regions without regard to precise temperature levels. In the field of nondestructive testing, liquid crystals have been used to check for irregularities on bonded structures [18–20], to observe regions of overheating on electronics equipment [15, 19, 20], to check for flow blockages in heat exchangers [21], as crack detectors on aircraft structures [21], and to check the effectiveness of windshield heaters [15, 21, 23], to name but a few typical applications. In the medical field, cholesteric liquid crystals have been used to observe surface blood flow patterns in humans and as a diagnostic tool for the detection of breast cancer [23–25]. Cholesteric liquid crystals have also been used to study the characteristics of laser beams and ultrasonic beams [26, 27].

Several investigators have employed liquid crystals as the temperature transducer in engineering heat transfer studies. Raad and Myers [28] used liquid crystals to observe nucleation sites in a study of pool boiling. Ennulat and Ferguson [29] employed a liquid crystal film as the display device in a noncontacting thermal imaging system. Maple [30] studied the transient and steady-state temperature fields that develop on the exterior of an active sonar transducer by coating the surface of the transducer with liquid crystals. Cooper and Groff [31], Katz and Cooper [32], and Cooper and Petrovic [33] employed liquid crystals coated on thin mylar sheets to observe the temperature fields produced by resistively heated, radio-frequency, and cryosurgical cannulas, respectively.

The use of cholesteric liquid crystals in wind tunnel experiments was first investigated by Klein [34, 35] in 1968. Klein employed unencapsulated cholesteric liquid crystals as the surface temperature sensor. The primary objective of Klein's work was to evaluate the feasibility of using liquid crystals to determine the location of the laminar and turbulent boundary layers that develop on wind tunnel aircraft models. The unencapsulated liquid crystals were applied directly to the model surface and, at the appropriate conditions of free stream air temperature and velocity, the portion of the model that was wetted with a turbulent boundary layer exhibited a different color than its laminar counterpart. The difference in color displayed by the liquid crystals resulted from the slightly higher adiabatic wall temperature associated with the turbulent flow. Although Klein was able to obtain such qualitative information using the liquid crystal technique, he was unsuccessful in at-

tempts to obtain accurate quantitative data due to the adverse effects that surface contamination, ultraviolet light and flow induced shear stress produced on the unencapsulated liquid crystals. In a follow on study, Klein and Margozzi [36] attempted to develop a technique for visually measuring shear stress by utilizing the shear stress sensitivity of certain types of unencapsulated cholesteric liquid crystals. Although they found that liquid crystals could be formulated that were relatively sensitive to shear and insensitive to temperature, they found it difficult to accurately interpret the color signal produced by the crystals since the liquid crystal coating tended to flow and develop a rough texture in response to the shearing effects of the flow. It was concluded that while it appeared feasible to measure shear stress using unencapsulated liquid crystals much additional research would be needed to develop liquid crystals that would exhibit high shear sensitivity while at the same time maintaining low temperature, angle, and pressure dependence.

McElderry [37], in an investigation similar in principle to the one conducted by Klein, used encapsulated cholesteric liquid crystals as a means of determining boundary layer transition on a flat plate placed in a supersonic air stream. McElderry found that the encapsulated liquid crystals produced color displays that were not affected by the adverse sensitivity to shear and contamination that Klein had experienced with the unencapsulated liquid crystals. McElderry also found that the colors displayed by the encapsulated liquid crystals were relatively independent of viewing angle.

### Experimental Apparatus

The experimental study was carried out using a low speed Aerolab wind tunnel with a test section that was 81 cm high and 114 cm wide. The tunnel had a four-speed transmission and was powered by a 75 kW motor. The motor was capable of generating a maximum speed of 90 m/s in the clear test section. With the cylinder in place the peak speed was 75 m/s. The turbulence intensity in the clear test section was measured with a hot wire anemometer and was found to vary from 0.5 to 0.7 percent over the range of speeds of interest.

In the initial phase of this investigation, an acrylic tube wrapped with Nichrome ribbon was used as the test cylinder. This cylinder had been previously used by Meyer [6] in a study of the heat transfer characteristics of a uniformly heated cylinder placed in a cross-flow of air. Several problems were encountered using the Nichrome wrapped cylinder and an improved experimental procedure was established using a cylinder constructed from an electrically resistive carbon impregnated paper that shall be referred to as "Temsheet." Temsheet is a thin, flexible, fibrous material containing no wires or ribbons. The nominal thickness is 0.1 cm and the electrical resistivity is approximately 2.5 ohm-cm. The heat that is generated when a constant electrical current is passed through a square section of the paper is uniform to within 2 percent from point to point.

A hollow cylinder, with an outer diameter of 10.0 cm and a length of 30.0 cm, was formed from a section of Temsheet. Prior to forming the Temsheet into a cylindrical form, two strips of aluminum tape were attached in parallel fashion to what was to be the inner surface of the cylinder. One of the aluminum strips was placed 7.5 cm down from the top of the Temsheet section and the other was placed 7.5 cm up from the bottom. This left a 15 cm region between the strips. By attaching power leads to the aluminum strips, the strips were made to serve as electrodes. A uniformly heated test section was established by passing a constant electrical current between the electrodes. To assure that intimate electrical contact was established between the aluminum strips and the Temsheet, a silver based conductive paint was applied along the inner edges of the strips.

To guard against free convection effects in the internal region of the Temsheet cylinder, the cylinder was tightly packed with glass wool. The glass wool also added a degree of structural rigidity to the cylinder and aided in resisting deformation when an external velocity field was applied around the cylinder.

The Temsheet cylinder was supported in the central section of the wind tunnel with the aid of two wooden end pieces. These end pieces were 10.0 cm in diameter, 30 cm long, and were permanently attached to the floor and ceiling of the wind tunnel. The end piece, attached to the floor of the wind tunnel, had a 3.0 cm hole drilled through its axis through which electrical leads could be passed. The last 5.0 cm on each end piece was turned down approximately 0.125 cm. This small step in each end piece allowed the Temsheet to be smoothly and firmly attached to the wood with double backed tape.

The completed assembly presented a smooth, continuous cylinder, 81 cm in length and 10.0 cm in diameter, to the flow. Only the center 15 cm of the Temsheet cylinder, however, was heated. No guard heating was employed in this design. An elementary heat transfer analysis [38] indicated that edge effects were significant only to within approximately 1 cm of each electrode. As such, data were collected only within the central 10 cm of the 15 cm heated section.

### Liquid Crystal Application and Calibration

Two Temsheet cylinders were employed in the present investigation. One cylinder was coated entirely with liquid crystal S-43. The other cylinder was coated with a series of circumferential strips of liquid crystals. The strips were 1 cm wide and were separated by 0.3 cm. The strips were located in the central 10 cm of the 15 cm test section. Fig. 1 is a photograph of the cylinder coated with the liquid crystal strips. Reading in order from top to bottom, the following liquid crystal formulations were applied to the cylinder: R-49, S-45, S-43, S-40, S-38, S-36, S-34, and S-32. The liquid crystals were applied directly to the surface of the Temsheet with a small brush. Two separate coats of the slurry based encapsulated liquid crystals were found to produce optimum brilliance.

A water filled, Rosemount constant temperature bath, capable

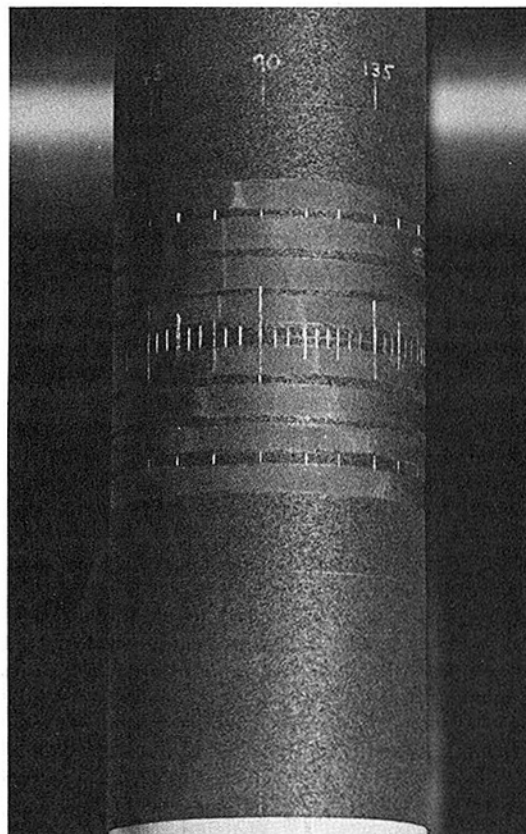


Fig. 1 Photograph of the Temsheet cylinder coated with the eight liquid crystal bands—the colors displayed by the liquid crystals appear as the light gray regions in the black and white photo

**Table 1 Liquid crystal calibration results—temperatures listed refer to the onset of red, green, and blue, respectively**

Liquid Crystal (NCR Designation)	Color Transition		
	Red (°C)	Green (°C)	Blue (°C)
S-32	32.5	33.1	33.7
S-34	34.7	35.1	35.7
S-36	36.4	36.8	37.4
S-38	38.6	39.1	39.7
S-40	40.6	41.1	41.7
S-43	43.2	43.9	44.6
S-45	45.1	45.6	46.2
R-49	49.8	50.0	51.2

of establishing and maintaining temperature to within 0.01°C accuracy, was employed in the liquid crystal calibration procedure. The bath temperature was monitored and controlled with a platinum resistance thermometer. The eye was used to determine color. All liquid crystal formulations were calibrated on a piece of the material to which they would be applied for data collection. The liquid crystal coated substrates were enclosed in small, clear plastic bags to seal them from the damaging effects of water. The package was then suspended in the water bath. The temperature of the bath was slowly raised until the event temperature range was reached. By carefully adjusting the bath temperature, an accurate measure of the event temperature corresponding first to the onset of red, then to green, and finally to blue was made. No attempt was made to determine shades of red, green, or blue, simply their onset. The procedure was also repeated in reverse order by slowly lowering the bath temperature through the event temperature range and noting the end of the blue, green and red displays. Using this procedure, temperature and color were calibrated to within an estimated accuracy of 0.1°C. Table 1 lists the calibration results. It should be noted that the observer who calibrated the liquid crystals also made all color determinations during the actual experimental runs.

It should be pointed out that the calibration scheme described in the foregoing, although quite precise, did not exactly simulate the environment in which the liquid crystals were used to collect experimental data. The bath calibration procedure did not subject the liquid crystals to a spatial temperature gradient, whereas the liquid crystals were used to collect experimental data in regions of varying temperature. Field [38] employed an in-situ calibration scheme as well as the calibration scheme described herein in his investigation of the heat transfer characteristics of a heated cylinder situated in a crossflow of air, and found that the liquid crystals yielded results that were within the experimental uncertainty of the sensors (thermocouples) used to provide reference data. Field's calibration results, together with the agreement of the heat transfer results generated using the liquid crystal technique with those of other investigators who have employed standard techniques, suggests that temperature gradients do not significantly alter the temperature-color relationship displayed by liquid crystals.

### Experimental Procedure

Before proceeding with a description of the experimental procedure employed with the Temsheet cylinder, a brief qualitative description of the temperature distribution that exists on the surface of a uniformly heated cylinder placed in crossflow will be given. This description will prove helpful in describing and interpreting the liquid crystal results.

Flow past a cylinder may be classified as subcritical, critical, supercritical, or transcritical. Roshko [39] presents an excellent discussion of the fluid flow phenomena associated with the various flow regimes. Since the present set of experiments examined Reynolds numbers ranging only from approximately 40,000–150,000, only the subcritical and critical flow regimes will be discussed here.

In subcritical flow, laminar hydrodynamic and thermal bounda-

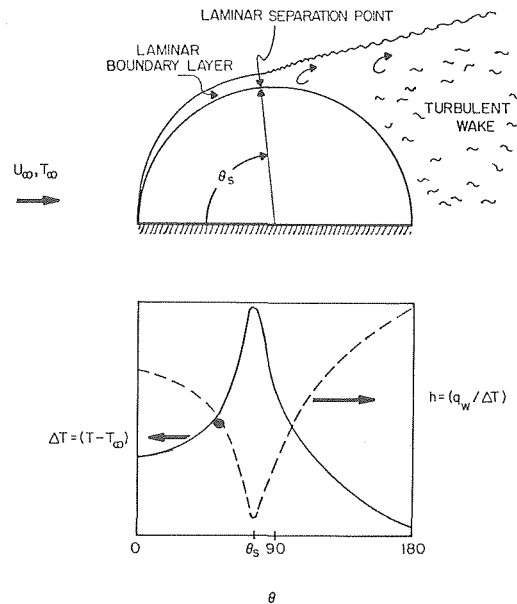


**Fig. 2 Sketch of a typical temperature distribution,  $T$ , that develops on the surface of a uniformly heated cylinder that loses heat in an amount  $q_w$  to a fluid stream. The fluid is at a uniform temperature,  $T_\infty$ , and is moving with velocity  $U_\infty$ . The conditions depicted are for subcritical flow as evidenced by the presence of a laminar separation at an angle  $\theta_s$ .**

ry layers grow from a minimum thickness at the forward stagnation point on the cylinder to a maximum thickness at an angular location of approximately 80–85 deg. At this location the kinetic energy of the fluid in the boundary layer has been attenuated sufficiently due to frictional effects that the developing adverse pressure gradient can no longer be overcome. As a result, the laminar boundary layer separates and a turbulent wake develops.

Fig. 2 depicts a typical subcritical flow pattern and the resulting trends in both temperature and heat transfer coefficient on the surface of a uniformly heated cylinder. Note that the maximum temperature exists at the separation point. This corresponds to the point of maximum thermal resistance, or minimum heat transfer coefficient. The ever decreasing temperature profile on the rear side of the cylinder is due to the scrubbing action of the highly turbulent wake. It certainly must be noted that the temperature profile depicted in Fig. 2 on the rear side of the cylinder is an average profile. The actual profile is highly transient in nature due to the continually changing flow pattern in the wake.

Critical flow is characterized by the growth of a laminar boundary layer on the forward half of the cylinder just as in the subcritical flow case. The laminar boundary layer separates in the region of 80–85 deg but, unlike the subcritical flow case, a subsequent transition to turbulent state of flow occurs resulting in the reattachment of a now turbulent boundary layer. This reattached turbulent layer ultimately separates at a position downstream of the laminar separation point. The region between the laminar separation point and the point of reattachment of the turbulent boundary layer is sometimes referred to as a "separation bubble" [39–41].

Fig. 3 depicts a typical critical flow pattern and the resulting trends in both the temperature and heat transfer coefficient. Note that unlike the subcritical flow case, there are now two local temperature maxima. These exist at the location of the laminar and turbulent separation points. The local minimum in temperature which occurs between the two temperature peaks marks the point of reattachment of the turbulent boundary layer.

For data collection, the Temsheet cylinder with eight liquid crystal bands was installed in the wind tunnel. A reference thermocouple was placed upstream of the cylinder and was used to monitor air temperature. Air speed was monitored using a micromanometer that was attached in differential fashion to static pressure

taps in the settling chamber and test section. The technique suggested by Pope [42] was used to correct the measured free stream velocity for the effects of solid blockage and wake blockage due to the presence of the model in the wind tunnel. Details can be found in [6, 38]. For the case of the Tensheet cylinder, the correction amounted to less than 3 percent.

Prior to starting the wind tunnel, the electrodes on the inner surface of the Tensheet cylinder were attached to a power supply. The power supply was energized and voltage was adjusted to bring the surface temperature of the cylinder to a temperature of approximately 50°C. This caused all of the liquid crystal bands to pass through their event temperature ranges. Preheating the cylinder prior to initiating flow served three purposes. First, it allowed the resistance of the 15 cm test section to be measured at conditions of maximum expected temperature. It was found that the resistance was 12.0 ohms. This was within 0.1 ohms of the room temperature resistance. Second, it allowed the uniformity of packing of the glass wool filling the inner portion of the cylinder to be checked. Regions of nonuniform packing showed up as local hot and cold spots on the surface of the cylinder. These regions were adjusted prior to initiating flow. Finally, preheating the cylinder reduced the time necessary to reach steady state once the tunnel was started.

Having preheated the cylinder, flow was established in the wind tunnel. Immediately after flow was initiated, the cylinder started to cool. To counter this, the power supplied to the cylinder was increased to maintain the hottest spot on the cylinder at 49.8°C. This corresponded to the red transition point on liquid crystal R-49. Referring to Figs. 2 and 3, it is seen that the hottest point on the cylinder occurs at the point of laminar separation. In the range of Reynolds numbers studied in the present investigation, 40,000–150,000, this point varied from 81 to 87 deg. This is consistent with the location of laminar separation points found by others [43].

Power was continually adjusted to maintain liquid crystal R-49 red at the laminar separation point until steady-state conditions

were reached. This usually occurred within fifteen minutes after flow was initiated in the tunnel. At least 5 min were allowed beyond the time at which steady state was judged to have been reached before data were collected.

It was found that the most accurate temperatures were found at the beginning of the color transitions of the liquid crystals. In the regions where temperature gradients were sharp, there was no problem in visually determining the onset of the red, green, and blue transitions. The particular liquid crystal in the temperature range at these locations would undergo the red to green to blue transitions over a short distance. The point of blue transition was particularly easy to locate.

The point of color transition near the forward and rear stagnation points of the cylinder was much more difficult to locate. The temperature gradients in these regions were quite shallow, particularly in the forward stagnation region. It was not uncommon for a given liquid crystal to exhibit approximately the same color over 15–20 deg of arc. The actual transition to a particular color usually was not apparent. The uncertainty in interpreting temperature by color in such regions was on the order of 0.5°C. This was improved on by adjusting the power level to force a color transition in the particular region of interest.

For critical flows, the procedure for locating separation was followed to locate the points of laminar separation, reattachment and turbulent separation. The separation bubble manifested itself as a local cool spot bounded by two local hot spots. In the present set of experiments, such a cool region first appeared at a Reynolds number of 121,500. This marked the onset of critical flow conditions. Only two critical flow Reynolds numbers were examined, 121,500 and 148,000. At larger Reynolds numbers, visible deformation occurred at the forward stagnation region on the cylinder.

Precise temperature data were not obtained using the cylinder coated entirely with liquid crystal S-43. This cylinder was used only to test for edge effects and the straightness of the isotherms in the axial direction.

## Results

**Temperature Distribution.** Figs. 4 and 5 are sketches of typical liquid crystal displays associated with subcritical and critical flows, respectively. Fig. 1 is a black and white reproduction of a colored photo taken of the heated cylinder placed in subcritical flow. Although color is not evident in the photo in Fig. 1, on close inspection one can see small gray regions similar in location to the shaded regions shown in Fig. 4. These gray regions are the color bands that are clearly evident to the naked eye and in colored photos and movies.

The sketch shown in Fig. 4 depicts the case where the power supplied to the test section has been adjusted to force liquid crystal R-49 to turn red at the point of laminar separation. At this particular power level, liquid crystal S-45, which is located just below R-49, has been heated in excess of its event temperature range along the separation line. However, just forward and aft of the separation line, the cylinder has been cooled sufficiently by the flow to be in the event temperature range of S-45. As such, the S-45 strip displays two separate regions of color. A similar pattern exists on strips S-43, S-40, S-38, and S-36, but the spacing between the colored regions continually widens. Due to the very mild surface temperature gradient that exists near the forward stagnation region on the cylinder, liquid crystal S-34 is depicted as displaying color over a very large arc length. As has been previously discussed, precise color interpretation was difficult in this region. Liquid crystal S-32 is depicted as displaying only one colored region. This is because the region of the cylinder near the rear stagnation point was normally cooled to lower temperatures than a similar region near the forward stagnation point. As such, the entire forward portion of the cylinder is depicted as existing at temperatures greater than the event temperature of S-32.

The sketch shown in Fig. 5 again depicts the case where the power supplied to the test section has been adjusted to force liquid crystal R-49 to turn red at the point of laminar separation. As can

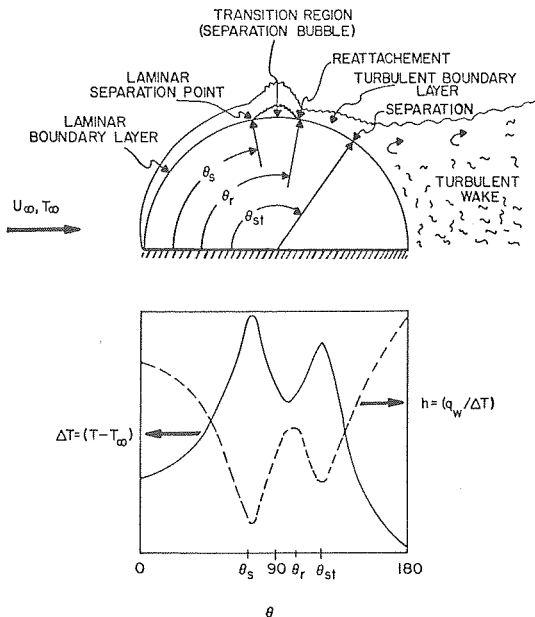


Fig. 3 Sketch of a typical temperature distribution,  $T$ , that develops on the surface of a uniformly heated cylinder that loses heat in an amount  $q_w$  to a fluid stream. The fluid is at a uniform temperature,  $T_\infty$ , and is moving with velocity  $U_\infty$ . The conditions depicted are for critical flow as evidenced by the presence of a laminar separation at an angle  $\theta_s$ , a separation bubble region, a point of reattachment of a turbulent boundary layer at an angle  $\theta_r$ , and a subsequent separation of the turbulent boundary layer at an angle  $\theta_{st}$ .

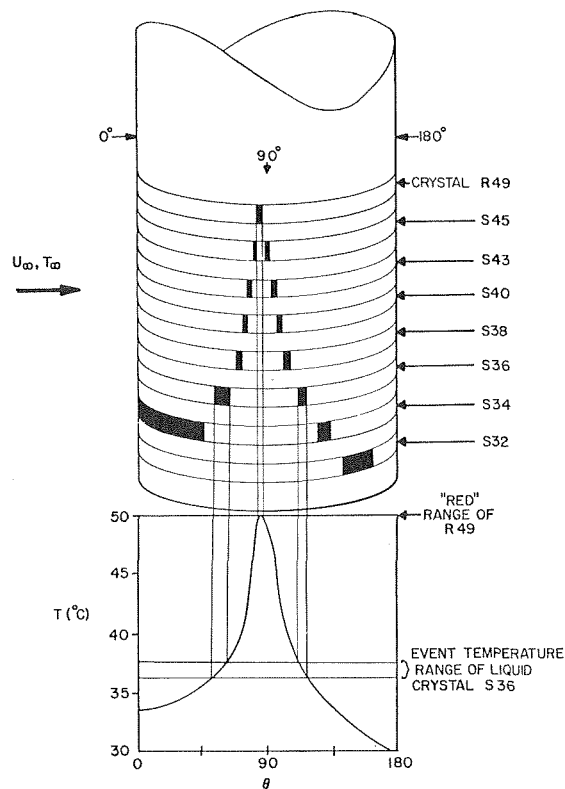


Fig. 4 Schematic of a typical liquid crystal display. The conditions depicted are representative of subcritical flow. The shaded regions on each liquid crystal band represent color.

be seen, the entire surface of the cylinder, with the exception of the laminar separation line, exists at temperatures below the event temperature of R-49. Liquid crystal S-45 again yields color displays at two locations as was the case in subcritical flow. For the case of critical flow, however, liquid crystal S-43 has been depicted displaying three colored regions. A glance at the surface temperature distribution shown sketched just below the cylinder indicates why. Unlike the subcritical flow case, after the laminar boundary layer separates, a separation bubble develops followed by a subsequent reattachment of a turbulent boundary layer. The turbulent boundary layer thickens and ultimately separates producing the local temperature maximum indicated by S-43. The trend in the liquid crystal displays around the point of turbulent separation is identical to the trend in displays around the laminar separation point. Accordingly, liquid crystals S-40 and S-38 have been depicted as showing four distinct colored regions. Liquid crystal S-36, however, shows only three bands, the reason being that the event temperature of S-36 is the minimum temperature in the separation bubble, presumably the point of reattachment of the turbulent boundary layer.

Figs. 4 and 5 have been presented for the purpose of explaining the significance of typical liquid crystal displays. Various other displays were produced by adjusting the power supplied to the test section. By carefully controlling the power level, a particular liquid crystal could be forced to undergo a color transition at any desired location on the cylinder surface. This allowed the Nusselt number signature on the cylinder to be determined in a nearly continuous fashion without the necessity of rotating the cylinder.

It should be noted that just aft of the point of laminar separation, the surface temperature distribution was not steady. In the case of subcritical flows, the influence of the turbulent, scrubbing action of the wake was readily apparent. The colors displayed by the liquid crystals continually dimmed and glowed in response to the turbulence. Occasionally an isotherm would suddenly be shift-

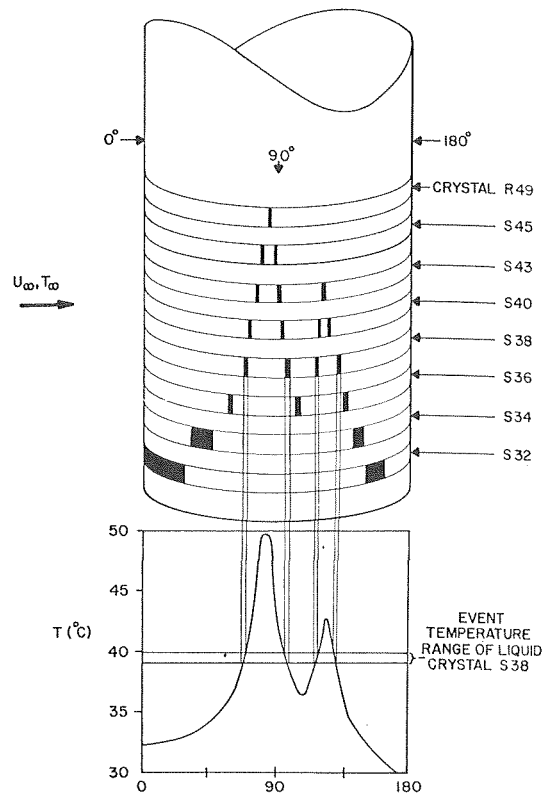


Fig. 5 Schematic of a typical liquid crystal display. The conditions depicted are representative of critical flow. The shaded regions on each liquid crystal band represent color.

ed in position by several degrees of arc. A similar phenomena was observed in the wake of the cylinder in critical flow. Additionally in critical flow, the separation bubble region and the turbulent boundary layer also exhibited a degree of fluctuation. In contrast, the liquid crystal displays prior to separation appeared perfectly steady to the eye.

**Local Nusselt and Froessling Numbers.** The local wall heat flux was determined by dividing the power supplied to the cylinder test section by the surface area of the test section. The local heat flux was corrected for conduction and radiation effects using a technique similar to the one employed by Giedt [44]. The local convective heat transfer coefficient,  $h$ , was obtained by dividing the corrected local wall heat flux by the local surface temperature excess. The local Nusselt and Froessling numbers were then calculated in the standard form:

Nusselt number,  $Nu = hD/k$ ; Froessling number,  $Fr = Nu/\sqrt{Re}$  where

$Re = \text{Reynolds number} = U_\infty D/\nu$ ;  $D = \text{cylinder diameter}$   
 $U_\infty = \text{corrected free stream velocity}$ ;  $k = \text{thermal conductivity (film temperature)}$   
 $\nu = \text{kinematic viscosity (film temperature)}$

Local Nusselt and Froessling numbers were obtained for Reynolds numbers ranging from 38,000 to 148,000. Several runs were made at higher Reynolds numbers, but the data were questionable due to the visible deformation that began to occur in the forward stagnation region of the cylinder at Reynolds numbers in excess of 150,000. Evidence of a separation bubble first appeared at a Reynolds number of approximately 121,500. As such, considering the effects of deformation, it was only possible to collect data on critical flow in the Reynolds number range 121,500–150,000.

Fig. 6 is a plot of the angular variation of the Froessling number versus Reynolds number as determined with the liquid crystal thermographic technique. As can be seen, prior to separation the Froessling number is independent of the Reynolds number. An un-

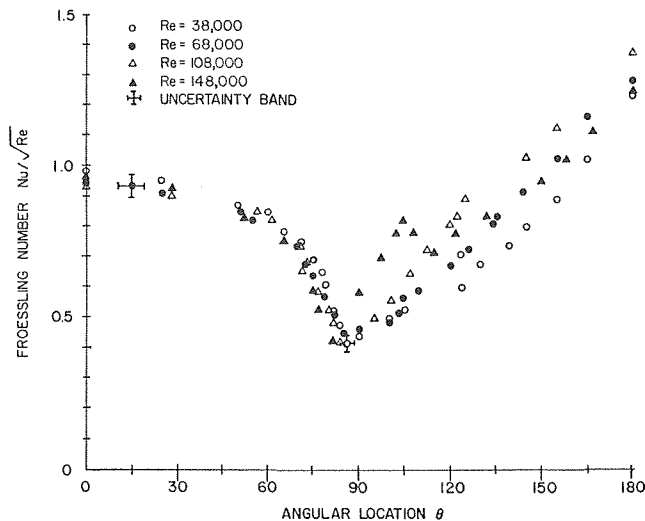


Fig. 6 Experimental heat transfer results obtained using the liquid crystal thermographic technique

certainty analysis was conducted on the experimental results and it was found that the maximum uncertainty in determining the Froessling number occurred in the forward stagnation region. Using the method of Kline and McClintock [45], it was estimated that the experimental uncertainty in this region was 5 percent. The maximum uncertainty in determining the angular location of a particular isotherm was estimated to be 5 deg of arc. Details of the uncertainty analysis can be found in reference [38].

**Comparison With the Work of Others.** The angular variation of the Froessling number obtained with the liquid crystal thermographic technique is compared with the experimental results of Giedt [4], Seban [5], and Meyer [6] in Fig. 7. Also shown is a comparison of the present results with a theoretical prediction of the Froessling number variation. The theoretical curve was generated using the approximate technique recommended by Schuh [1]. Seban and Chan [2] and Perkins and Leppert [3] have also developed analytical models for predicting the heat transfer coefficient in the laminar flow region on a uniformly heated cylinder. All three models give approximately the same results. It is noted that beyond approximately 60° the experimental results and theory are no longer in good agreement. This was not unexpected. In the absence of actual pressure data on the Tensheet cylinder, an ideal pressure distribution was assumed in using Schuh's model. The use of the actual pressure signature could be expected to produce closer agreement between experiment and theory.

As can be seen, the agreement of the heat transfer results obtained with the liquid crystals is generally within the estimated experimental uncertainty when compared with the work of others. The results of Meyer present the one notable exception, especially in the wake region of the cylinder. As has been mentioned previously, however, large surface irregularities developed on the surface of the cylinder used by Meyer resulting in large uncertainties in Meyer's results.

**Edge Effects.** Fig. 8 shows the isotherms that developed on the Tensheet cylinder coated only with liquid crystal S-43. As can be seen, the isotherms are vertical in the central region of the test section but tend to bend near the edges of the test section. The curvature of the isotherms near each electrode clearly indicates that heat is lost by conduction in these regions. These small edge effects were anticipated and data were not taken within 2.5 cm of each electrode.

**Surface Roughness of the Tensheet.** Photographs taken through an electron microscope of a piece of Tensheet coated with encapsulated liquid crystals show the coating to be composed of spherules with diameters on the order of 20–50 microns. If the tiny, spherical shaped encapsulated liquid crystals are treated as

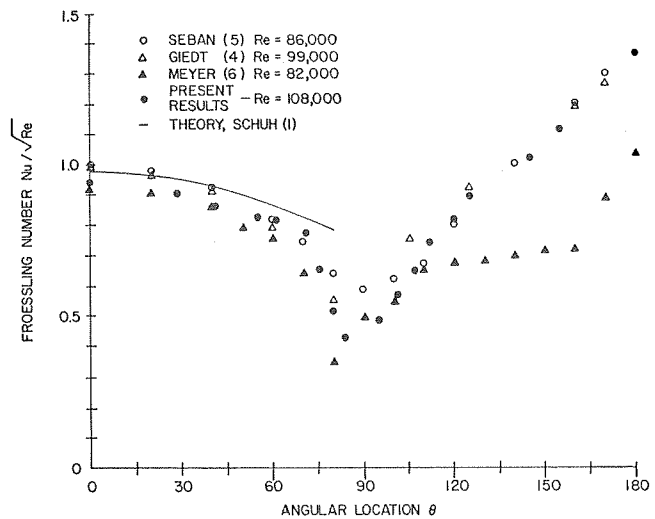


Fig. 7 Comparison of the experimental heat transfer results obtained using the liquid crystal thermographic technique with the results of others

surface roughness elements with average diameters of approximately 35 microns, an estimate of the critical Reynolds number can be made. Auchenbach [46] suggests in the case of spherical roughness elements on the surface of a circular cylinder that an equivalent sand grain roughness be calculated as  $k = 0.55$  (diameter of spheres). In our case,  $k/D = 20 \times 10^{-6}$ . Using Auchenbach's results for critical Reynolds number versus roughness, one finds that this represents a smooth cylinder. The predicted critical Reynolds number is slightly in excess of 100,000. This is consistent with the value of 121,500 observed in the present set of experiments.

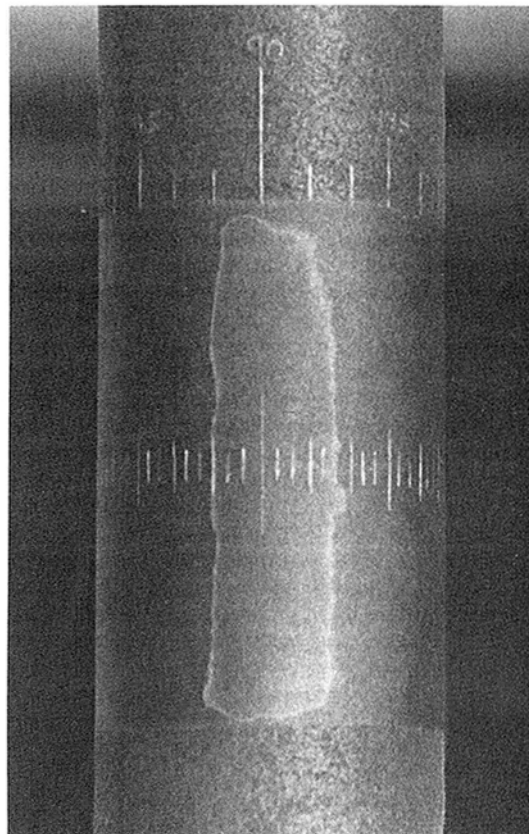


Fig. 8 Photograph of the Tensheet cylinder coated only with liquid crystal S-43—the bending of the isotherms near the top and bottom of the test section indicates the influence of end losses on the temperature field

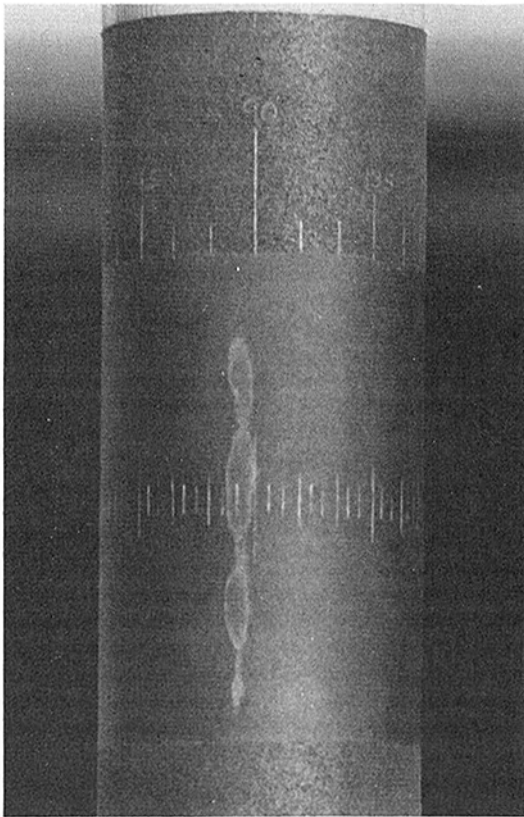


Fig. 9 Photograph of the alternate hot and cold spots that developed along the separation line of the Temsheet cylinder

### Summary

The liquid crystal thermographic technique developed in this investigation provides an excellent means of obtaining both qualitative and quantitative heat transfer information on heated objects placed in forced convection environments. Using the technique, it was possible to quickly and easily obtain information on the variation of the Nusselt number around the circumference of a uniformly heated right circular cylinder placed in a crossflow of air. The technique also allowed one to visually observe the effects of flow separation, the turbulent boundary layer, and the turbulent wake on the surface temperature of the cylinder. Colored movies taken of a cylinder coated with a single liquid crystal are especially vivid in their display of the influence of the turbulent wake on the cylinder surface temperature. In the wake region the liquid crystals continually dim and glow in response to the "scrubbing" action caused by random bursts of cool fluid impacting on a heated cylinder.

The ability to visually observe turbulent flow pattern effects on surface temperature suggests an excellent means for studying the influence of free stream turbulence on the heat transfer rates of heated objects. However, in order that such a study be conducted in a quantitative manner, the thermal response time of the liquid crystals must first be determined. Fergason [47] estimated that the response time of a typical cholesteric liquid crystal film was on the order of 0.1–0.2 s. Parker [48], however, using a capacitor discharge technique and employing high speed photography, found that a 0.003 cm film of encapsulated cholesteric liquid crystals coated on a thin stainless steel foil responded in 0.036 s to a step change in the foil temperature. Parker also found that the response time of the liquid crystal coatings appeared to be thermal diffusion limited, increasing in proportion to the square of the thickness of the coating. It is possible that a thin coat of liquid crystals coated on a material such as Temsheet would respond even faster than a coating placed on a metal substrate due to the fact that the liquid crystals appear to be partially absorbed into the Temsheet. The ideal

situation would be if the liquid crystals responded at the same rate as the Temsheet itself. An experiment, similar to the one conducted by Parker, needs to be conducted to determine the response time of the liquid crystals coated on a Temsheet substrate.

As a final recommendation, the phenomenon shown in Fig. 9 is offered as a possible topic for future investigation. During the final phase of collecting wind tunnel data for the present investigation, it was noted that the cylinder coated with liquid crystal S-43 displayed alternate hot and cold spots along the separation line. These spots were uniformly spaced and seemed to be caused by some flow phenomenon, perhaps a series of vortices. Whatever the cause, the hot and cold spots definitely existed as is readily apparent in the photo. Precise measurements were not taken at the time the phenomenon was observed (the Reynolds number was approximately 75,000) and no explanation is offered for its existence at this time. It should be noted, however, that such a phenomenon may well have gone undetected if thermocouples were used as the temperature sensors. Additional research, perhaps using liquid crystals for temperature sensing and smoke for flow visualization, needs to be carried out to explain the observed phenomenon.

### Acknowledgments

The authors would like to thank Messrs. George Bixler, Tom Christian, and Jack McKay for their assistance in conducting the experimental phase of this investigation. The senior author would like to express his appreciation to the Naval Postgraduate School Research Foundation for support of this investigation and to Associate Professors M. D. Kelleher and P. J. Marto for many helpful discussions on various aspects of this study.

### References

- Schuh, H., "A New Method for Calculating Laminar Heat Transfer on Cylinders of Arbitrary Cross Section and on Bodies of Revolution at Constant and Variable Wall Temperature," ASTIA, AD 66184, 1953.
- Seban, R. A., and Chan, H. W., "Heat Transfer to Boundary Layers With Pressure Gradients," ASTIA, AD 118075, 1958.
- Perkins, H. C., and Leppert, G., "Local Heat Transfer Coefficients on a Uniformly Heated Cylinder," *International Journal of Heat and Mass Transfer*, Vol. 7, 1964, pp. 143–158.
- Giedt, W. H., "Effect of Turbulence Level of Incident Air Stream on Local Heat Transfer and Skin Friction on a Cylinder," *Journal of the Aeronautical Sciences*, Vol. 18, 1951, pp. 725–730, 766.
- Seban, R. A., "The Influence of Free Stream Turbulence on the Local Heat Transfer from Cylinder," *JOURNAL OF HEAT TRANSFER*, TRANS. ASME, Series C, Vol. 82, 1960, pp. 101–107.
- Meyer, J. F., "An Experimental Investigation of the Heat Transfer Characteristics of a Heated Cylinder Placed in a Cross Flow of Air," Engineer's thesis, Naval Postgraduate School, Monterey, Calif., June 1973.
- Brown, G. H., and Shaw, W. G., "The Mesomorphic State: Liquid Crystals," *Chem. Rev.*, Vol. 57, 1957, pp. 1049–1157.
- Fergason, J. L., "Liquid Crystals," *Scientific American*, Vol. 211, No. 2, Aug. 1964, pp. 76–86.
- Fergason, J. L., and Brown, G. H., "Liquid Crystals and Living Systems," *J. Am. Oil Chem. Soc.*, Vol. 45, No. 3, Mar. 1968, pp. 120–127.
- Dreher, R., Meier, G., and Saupe, A., "Selective Reflection by Cholesteric Liquid Crystals," *Molecular Crystals and Liquid Crystals*, Vol. 13, 1971, pp. 17–26.
- Stephen, M. J., and Straley, J. P., "Physics of Liquid Crystals," *Review of Modern Physics*, Vol. 46, No. 4, Oct. 1974, pp. 617–704.
- Castellano, J. A., and Brown, G. H., "Thermotropic Liquid Crystals: Part I. The Underlying Science," *Chem. Tech.*, Jan. 1973, pp. 47–52.
- Castellano, J. A., and Brown, G. H., "Thermotropic Liquid Crystals: Part II. Current Uses and Future Ones," *Chem. Tech.*, Apr. 1973, pp. 229–235.
- Castellano, J. A., "Now that the Heat Is Off, Liquid Crystals Can Show Their Colors Everywhere," *Electronics*, Vol. 43, No. 14, July 1970, pp. 69–70.
- Champa, R. A., "USAF Applications of Liquid Crystal Materials," AFML-TR-72-77, May 1972.
- Fergason, J. L., Taylor, T. R., and Harsch, T. B., "Liquid Crystals and Their Applications," *Electro-Technology*, Vol. 85, No. 1, Jan. 1970, pp. 41–50.
- Kaye, D., "Liquid Crystals: Material With a Hot Future," *Electronic Design*, Vol. 19, Sept. 1970, pp. 76–81.
- Cohen, S. E., "The Application of Liquid Crystals for Thermographic Testing of Bonded Structures," ASTIA AD 837835, 1967.
- Davis, F., "Liquid Crystals: A New Tool for NDT," *Research/Development*, Vol. 18, No. 6, June 1967, pp. 24–27.

- 20 Dowden, W. A., "Cholesteric Liquid Crystals: A Review of Developments and Applications," *Non-Destructive Testing*, Vol. 1, No. 2, Nov. 1967, pp. 99-102.
- 21 Woodmansee, W. E., "Aerospace Thermal Mapping Applications of Liquid Crystals," *Applied Optics*, Vol. 7, No. 9, Sept. 1968, pp. 1721-1729.
- 22 Perry, M. H., "Cholesteric Liquid Crystals and Their Application to Space Technology," NASA General Working Paper, MSC-00152, Aug. 1969.
- 23 Crissey, J. T., Gordy, E., Ferguson, J. L., and Lyman, R. B., "A New Technique for the Determination of Skin Temperature Patterns," *Journal of Investigative Dermatology*, Vol. 42, No. 2, Aug. 1964, p. 89.
- 24 Crissey, J. T., Ferguson, J. L., and Bettenhausen, J. M., "Cutaneous Thermography With Liquid Crystals," *Journal of Investigative Dermatology*, Vol. 45, No. 5, Nov. 1965, p. 329.
- 25 Selawry, O. S., Selawry, O. H., and Holland, J. F., "The Use of Liquid Cholesteric Crystals for Thermographic Measurement of Skin Temperature in Man," *Molecular Crystals*, Vol. 1, No. 4, 1966, p. 495.
- 26 Cook, B. D., and Werchan, R. E., "Mapping Ultrasonic Fields With Cholesteric Liquid Crystals," *Ultrasonics*, Apr. 1971, pp. 101-102.
- 27 Keilmann, F., "Infrared Interferometry With a CO<sub>2</sub> Laser Source and Liquid Crystal Detection," *Applied Optics*, Vol. 9, No. 6, June 1970, pp. 1319-1322.
- 28 Raad, T., and Myer, J. E., "Nucleation Studies in Pool Boiling on Thin Plates Using Liquid Crystals," *AIChE Journal*, Vol. 5, 1971, pp. 1260-1261.
- 29 Ennulat, R. D., and Ferguson, J. L., "Thermal Radiography Utilizing Liquid Crystals," *Molecular Crystals and Liquid Crystals*, Vol. 13, 1971, pp. 149-164.
- 30 Maple, R. D., "Utilization of Temperature Sensitive Liquid Crystals for Thermal Analysis and an Application to Transducer Investigations," Naval Underwater Systems Center TR 4235, May 30, 1972.
- 31 Cooper, T. E., and Groff, J. P., "Thermal Mapping, Via Liquid Crystals, of the Temperature Field Near a Heated Surgical Probe," JOURNAL OF HEAT TRANSFER, TRANS. ASME, Series C, Vol. 95, No. 2, 1973, pp. 250-256.
- 32 Katz, R. G., and Cooper, T. E., "Liquid Crystal Display of the Temperature Fields Produced by Radio Frequency Emitting Electrodes," 26th ACEMB, Conf. Proceed, Sept. 30-Oct. 4, 1973, p. 257.
- 33 Cooper, T. E., and Petrovic, W. K., "An Experimental Investigation of the Temperature Field Produced by a Cryosurgical Cannula," JOURNAL OF HEAT TRANSFER, TRANS. ASME, Series C, Vol. 96, No. 3, Aug. 1974, pp. 415-420.
- 34 Klein, E. J., "Application of Liquid Crystals to Boundary Layer Flow Visualization," AIAA 3rd Aerodynamic Testing Conference, AIAA Paper 68-376, Apr. 1968.
- 35 Klein, D. J., "Liquid Crystals in Aerodynamic Testing," *Astronautics and Aeronautics*, Vol. 6, No. 7, 1968, pp. 70-73.
- 36 Klein, E. J., and Margozi, A. P., "Exploratory Investigation on the Measurement of Skin Friction by Means of Liquid Crystals," NASA TM X-1774, May 1969.
- 37 McElderry, E. D., "Boundary Layer Transition at Supersonic Speeds Measured by Liquid Crystals," Air Force Flight Dynamics Laboratory, FDMG Tm 70-3, June 1970.
- 38 Field, R. J., "Liquid Crystal Mapping of the Surface Temperature on a Heated Cylinder Placed in a Crossflow of Air," MS thesis, Naval Postgraduate School, Monterey, Calif., Mar. 1974.
- 39 Roshko, A., "Experiments on the Flow Past a Circular Cylinder at Very High Reynolds Numbers," *Journal of Fluid Mechanics*, Vol. 10, May 1961, pp. 345-356.
- 40 Tani, I., "Low Speed Flows Involving Bubble Separations," in Progress in Aeronautical Sciences, Vol. 5, 1964, pp. 70-103.
- 41 Jones, G. W., Cincotta, J. J., and Walker, R. W., "Aerodynamic Forces on a Stationary and Oscillating Circular Cylinder at High Reynolds Numbers," NASA TR R-300, Feb. 1969.
- 42 Pope, A., *Wind Tunnel Testing*, Wiley, New York, 2nd ed., 1954, pp. 268-286.
- 43 Coder, D. W., "Location of Separation on a Circular Cylinder in Crossflow As a Function of Reynolds Number," Naval Ship Research and Development Center Report 3647, Nov. 1971.
- 44 Giedt, W. H., "Investigation of Variation of Point Unit Heat-Transfer Coefficient Around a Cylinder Normal to an Air Stream," TRANS. ASME, May 1949, pp. 375-381.
- 45 Kline, S. J., and McClintock, F. A., "Describing Uncertainties in Single-Sample Experiments," *Mech. Engr.*, Vol. 75, Jan. 1953, pp. 3-8.
- 46 Auchenbach, E., "Influence of Surface Roughness on the Cross-Flow Around a Circular Cylinder," *Journal of Fluid Mechanics*, Vol. 46, Part 2, 1971, pp. 321-335.
- 47 Ferguson, J. L., "Liquid Crystals in Nondestructive Testing," *Applied Optics*, Vol. 7, No. 9, Sept. 1968, pp. 1729-1737.
- 48 Parker, R., "Transient Surface Temperature Response of Liquid Crystal Films," Lawrence Livermore Laboratory, Rept. UCRL-73583, Dec. 1971.

J. F. Kreider  
President,  
Environmental Consulting Services, Inc.,  
Boulder, Colo.

# Thermal Performance Analysis of the Stationary Reflector/Tracking Absorber (SRTA) Solar Concentrator

*The performance of a novel solar energy concentrating system consisting of a fixed, concave spherical mirror and a sun-tracking, cylindrical absorber is analyzed in detail. This concentrating system takes advantage of the spherical symmetry of the mirror and its linear image which, when taken together, form a tracking, solar-concentrating system in which only the small cylindrical absorber need move. The effects of mirror reflectance, concentration ratio, heat transfer fluid flow rate, radiative surface properties, incidence angle, an evacuated absorber envelope, and insolation level upon thermal performance of the concentrator are studied by means of a mathematical model. The simulation includes first order radiation and convection processes between the absorber and its concentric glass envelope and between the envelope and the environment; radiation processes are described by a dual-band, gray approximation. The energy equations are solved in finite difference form in order that heat flux and temperature distributions along the absorber may be computed accurately.*

*The results of the study show that high-temperature heat energy can be collected efficiently over a wide range of useful operating conditions. The analysis indicates that mirror surface reflectance is the single most important of the principal governing parameters in determining system performance. Efficiency always increases with concentration ratio although the rate of increase is quite small for concentration ratios above 50. High fluid flow rate (i.e., lower operating temperature), an evacuated envelope, or a highly selective surface can enhance performance under some conditions. The conclusion of the study is that high-temperature heat energy can be generated at high efficiency by the present concentrator with present technology in sunny regions of the world.*

## Introduction

Steward [1]<sup>1</sup> has described the operation of a solar concentrator consisting of an internally reflectorized, spatially fixed segment of a sphere and a small cylindrical absorber consisting of a transparent, cylindrical envelope for convection control plus a treated metal absorber cylinder contained therein. The absorber assembly is located at the focal line of the spherical mirror. By virtue of the spherical symmetry of the reflector, only this linear absorber need

move for the collector to track the sun in its virtual diurnal motion. The position of the absorber at three values of incidence angle is shown in Fig. 1. In the present work, a detailed analysis of the convective and radiative processes taking place in such a spherical concentrator is made. Temperature and flux gradients along the absorber are computed by means of a finite difference representation of the steady-state energy equations. The effect of several system parameters on performance is determined by means of a simultaneous solution of the energy equations.

Thermal analyses of varying degrees of sophistication of other focusing collectors have been reported in the literature. Those of Pope and Schimmel [2] and Eckert, et al. [3] represent the most thorough treatment and that of Meinel and Meinel [4] represents the most cursory; Löff, et al. [5] and Liu and Jordan [6] have described experimental techniques and measurements along with

<sup>1</sup> Numbers in brackets designate References at end of paper.

Contributed by the Heat Transfer Division for publication in the JOURNAL OF HEAT TRANSFER. Manuscript received by the Heat Transfer Division November 22, 1974. Paper No. 75-HT-FFF.

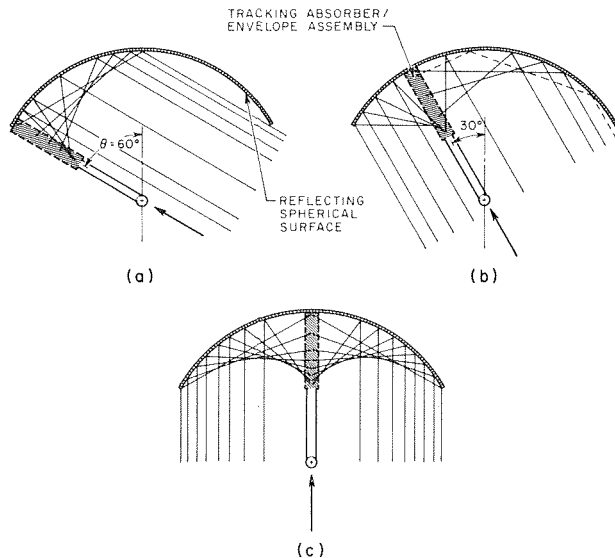


Fig. 1 Position of SRTA absorber at three values of collector incidence angle (equatorial cross sections): (a)  $\theta = 60$  deg, (b)  $\theta = 30$  deg, (c)  $\theta = 0$  deg, normal incidence

their theoretical analyses. However, all of these studies were carried out for parabolic reflectors and none treated the axial variations of heat flux and temperature in detail.

### Analysis

The energy exchange processes between the collector mirror, the envelope, and the absorber are complex. Some higher order effects can be eliminated so that the analysis is simplified without loss of any of the important, first order effects. Therefore, it is assumed that the radiative process can be modeled by a two-band method consisting of a long wavelength—infrared (IR)—band ( $3\text{--}50\mu$  wavelength) in which all lower temperature radiation occurs and a short wavelength—solar—band ( $0.25\text{--}3\mu$  wavelength) in which solar radiation exchanges occur. Surface radiation properties except those of the glass envelope are assumed constant and angle-independent. The angle-dependent transparent envelope transmittance  $\tau_{e,\text{sol}}(i)$  and absorptance  $\alpha_{e,\text{sol}}(i)$  for direct solar radiation are calculated from the equations (not reproduced here) developed in the classic but widely ignored paper of Stokes [7]. The effects of

polarization of sunlight by atmospheric scattering are not considered since few data are available with which to quantify this phenomenon. The viscosity and thermal conductivity temperature dependence of air are represented by power laws in the mean film temperature for convective coefficient computation; and free and forced convection processes are represented by empirical correlations.

Effects of tracking and surface errors are ignored in the analysis since, for concentration ratios below 50, the absorber is approximately twice the diameter of the sun's image at the absorber assuming a cumulative surface plus steering error of 10 millirad; reference can be made to Eckert, et al. [3] for a comprehensive treatment of the effects of tracking and surface errors on the performance of concentrators. The energy distribution across the sun's disk is assumed uniform and the sun's included angle of 32 min ( $0.00931$  rad) is ignored with the proviso that the absorber diameter  $D_a$  shall be at least large enough to intercept the entire image for perfect optics, i.e.,  $D_a > 0.00931 R_0$ . The concentrator is assumed to absorb no diffuse, ambient radiation.

The Cartesian coordinate system used for the thermal and optical analysis is shown in Fig. 2. Thermal calculations in this article are carried out for the absorber in the position shown (collector incidence angle  $\theta = 0$ ) since the optics are the same for any absorber position, only the irradiated area changes. The effect of incidence angle, i.e., time of day and season, is described later in the paper.

A 120-deg mirror corresponding to a nominal 8-hr collection period is used, although larger or smaller included angles can be employed in practice as dictated by a cost/benefit analysis. Portions of a fixed, 120-deg spherical mirror at an angular distance greater than 60 deg from the focal line can be illuminated during some collection periods. Insolation beyond the 60-deg range will be reflected more than once before reaching the absorber (see Fig. 1(b)). The maximum amount of insolation ever subjected to multiple reflection is 4 percent of the total intercepted (Steward, private communication). Two or three reflections are almost always sufficient to deliver this 4 percent to the absorber. For two reflections the effective, multiple reflectance would be 0.72 for Alzak ( $\rho_m = 0.85$ ). The overall decrease in system performance due to secondary reflection is 0.6 percent ( $= 4 \text{ percent} \times [(0.85 - 0.72)/0.85]$ ) below that predicted by ignoring the effect. Other parameters in the analysis are not known to this accuracy so the double reflection effect has been ignored as a higher order effect.

**Heat Flux Terms.** The following heat fluxes, all based upon a unit absorber area, are considered:

(a) solar radiation absorbed by the absorber both directly and indirectly after reflection(s) from the envelope— $Q_{\text{sol},a}$  (solar wavelength region);

### Nomenclature

$A_m$  = mirror aperture area  
 $CR$  = concentration ratio ( $1.5 R_0/D_a$ )  
 $D_a$  = absorber diameter  
 $D_{ei}$  = envelope inner diameter  
 $D_{eo}$  = envelope outer diameter  
 $E$  = component of concentrated flux incident on absorber normal to absorber surface (Appendix)  
 $Gr$  = Grashof number based on  $D_{eo}$   
 $h_{c,ae}$  = convective coefficient between absorber and envelope  
 $h_{c,e}$  = convective coefficient between envelope and environment  
 $h_f$  = enthalpy of heat transfer fluid  
 $i$  = angle of incidence of reflected beam insolation on absorber  
 $I_b$  = the direct or beam component

of insolation incident on the mirror aperture  
 $k_{eq}$  = equivalent thermal conductivity for free convection in an annulus (reference [9])  
 $k_f$  = thermal conductivity at external envelope film temperature  
 $\dot{m}$  = fluid flow rate per unit collector aperture area  
 $p$  = pressure  
 $Pr$  = Prandtl number of air at external envelope film temperature  
 $Q(x)$  = heat delivery per unit absorber area  
 $Q_{c,ae}$  = convective transfer between absorber and envelope

$Q_{c,e}$  = convective loss from envelope external surface  
 $Q_{e,\text{sky}}$  = envelope radiative loss to sky  
 $Q_{ir,ae}$  = absorber/envelope IR net exchange  
 $Q_{\text{sol},a}$  = solar flux absorbed at absorber  
 $Q_{\text{sol},e}$  = solar flux absorbed at envelope  
 $r$  = radial coordinate (Fig. 2)  
 $Re$  = Reynolds number based on  $D_{eo}$  ambient wind speed, and transport properties of external envelope film  
 $R_0$  = mirror generator radius  
 $T_a$  = absorber temperature  
 $T_e$  = envelope temperature  
 $T_{\text{sky}}$  = effective sky temperature for radiation (reference [8])

(Continued on next page)

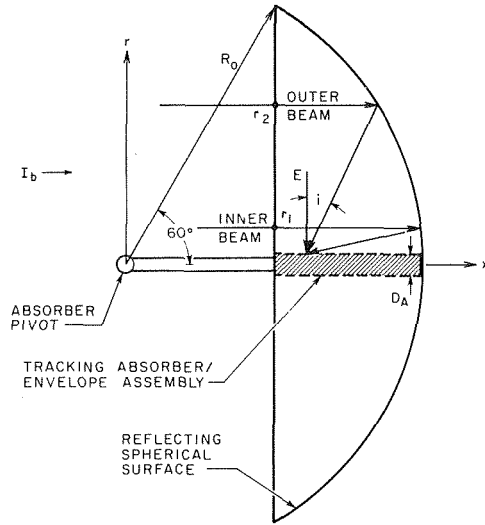


Fig. 2 Schematic diagram of SRTA collector showing incoming ray traces and coordinate system for analysis for 120 deg mirror

(b) solar radiation absorbed by the envelope both directly and indirectly after reflection(s) from the absorber— $Q_{sol,e}$  (solar wavelength region);

(c) radiative exchange between the absorber and the envelope— $Q_{ir,ae}$  (IR wavelength region);

(d) radiative emission from the envelope to the environment— $Q_{e,sky}$  (IR wavelength region—envelope assumed to radiate to the environment);

(e) convective exchange between the absorber and the envelope— $Q_{c,ae}$ ;

(f) convective loss from the envelope to the environment— $Q_{c,e}$ ;

(g) useful heat extraction— $Q(x)$ .

The heat flux terms are given in equations (1)–(6) with acronymic subscripts

$$Q_{sol,a} = E\tau_{e,sol}(i)\alpha_{a,sol}(1 + \rho_{a,sol}\rho_{e,sold}) / (1 - \rho_{a,sol}\rho_{e,sold}) \quad (1)$$

$$Q_{sol,e} = E(\alpha_{e,sol}(i) + [\alpha_{e,sold}\tau_{e,sol}(i)D_{ei}/D_{eo}]\rho_{a,sol} / [1 - \rho_{a,sol}\rho_{e,sold}])D_{eo}/D_a \quad (2)$$

$$Q_{ir,ae} = \epsilon_{eff}(T_a^4 - T_e^4) \quad (3)$$

$$Q_{e,sky} = \epsilon_{e,ir}(T_e^4 - T_{sky}^4)D_{eo}/D_a \quad (4)$$

$$Q_{c,ae} = h_{c,ae}(T_a - T_e) \quad (5)$$

$$Q_{c,e} = h_{c,e}(T_e - T_\infty)D_{eo}/D_a \quad (6)$$

in which

$$\epsilon_{eff} = (\rho_{e,ir}/\epsilon_{e,ir} + \rho_{a,ir}/\epsilon_{a,ir} + 1)^{-1} \quad (\text{envelope specular})$$

$$T_{sky} = 0.09936 (T_\infty/1.8)^{1.5} \quad (\text{reference [8]})$$

$$h_{c,ae} = 2k_{eq}/D_a \ln(D_{ei}/D_a) \quad (\text{reference [9]})$$

$$h_{c,e} = 0.54 (k_f/D_{eo}) \times (\text{GrPr})^{1/4} \quad (\text{calm environment, free convection})$$

or

$$h_{c,e} = C(k_f/D_{eo})\text{Re}^n \quad (\text{forced convection over envelope; } C, n \text{ in reference [10]})$$

The effects of conduction in the absorber, which is a cylindrical coil wound from metal tubing, have been examined using an order of magnitude analysis. The analysis, not reproduced here, showed that coilwise tube-wall conduction effects are more than three orders of magnitude smaller than the dominating external radiation and internal convection heat transfer modes. As a result, the coilwise conduction heat transfer mode is not considered further in this analysis.

**Energy Equations.** The envelope-incident radiation  $E$ , and the heat fluxes  $Q_{sol,a}$ ,  $Q_{sol,e}$ ,  $Q_{ir,ae}$ ,  $Q_{e,sky}$ ,  $Q_{c,ae}$ ,  $Q_{c,e}$ , and  $Q(x)$  and temperatures  $T_a$  and  $T_e$  are all functions of the independent variable  $x$ , the axial location along the absorber. The unknown quantities in the energy equations are  $Q(x)$ ,  $T_a$ , and  $T_e$  for which there are three equations to be solved simultaneously. The absorber energy equation is

$$Q_{sol,a} = Q(x) + Q_{c,ae} + Q_{ir,ae} \quad (7)$$

the envelope energy equation is

$$Q_{sol,e} + Q_{ir,ae} + Q_{c,ae} = Q_{e,sky} + Q_{c,e} \quad (8)$$

the transport fluid (water or water vapor) energy equation is

$$dh_f/dx = Q(x)(\pi D_a)/(\dot{m} A_m) \quad (9)$$

where  $h_f$  is the fluid enthalpy.

An order of magnitude analysis showed that the resistance offered to heat transfer at the inner surface of the absorber coil tubing and through the absorber wall were of higher order than the external surface resistance. Consequently, the fluid and absorber temperature may be considered the same to lowest order. The energy balance equations are solved by iteratively computing  $T_e$  from equation (8),  $Q(x)$  directly from equation (7), and  $h_f(x + \Delta x)$  from a two-term Taylor series expansion of equation (9).  $T_a(x +$

## Nomenclature

$T_\infty$  = ambient temperature  
 $x$  = axial coordinate (Fig. 2)  
 $\alpha_{a,sol}$  = solar absorptance of absorber  
 $\alpha_{e,sold}$  = solar diffuse absorptance of envelope  
 $\alpha_{e,sol}(i)$  = angular-dependent solar absorptance of envelope  
 $\epsilon_{a,ir}$  = IR diffuse emittance of absorber  
 $\epsilon_{e,ir}$  = IR diffuse emittance of envelope  
 $\epsilon_{eff}$  = effective radiation emittance for absorber/envelope exchange

$\eta$  = direct radiation collection efficiency  
 $\rho_{a,ir}$  = IR diffuse reflectance of absorber  
 $\rho_{a,sol}$  = solar reflectance of absorber  
 $\rho_{e,ir}$  = IR diffuse reflectance of envelope  
 $\rho_{e,sold}$  = solar diffuse reflectance of envelope  
 $\rho_{e,sol}(i)$  = angular-dependent solar absorptance of envelope  
 $\rho_m$  = mirror surface reflectance  
 $\sigma$  = Stefan-Boltzmann constant  
 $\tau_{e,ir}$  = IR transmittance of envelope  
 $\tau_{e,sol}(i)$  = angular-dependent solar trans-

mittance of envelope  
 $\theta$  = incidence angle of beam isolation on collector aperture

## Subscripts

$a$  = absorber  
 $d$  = diffuse  
 $e$  = envelope  
 $f$  = absorber fluid; film temperature  
 $i$  = absorber inlet  
 $ir$  = infrared radiation band (3–50 $\mu$ )  
 $o$  = absorber outlet  
 $sol$  = solar radiation band (0.25–3 $\mu$ )  
 $\infty$  = ambient conditions

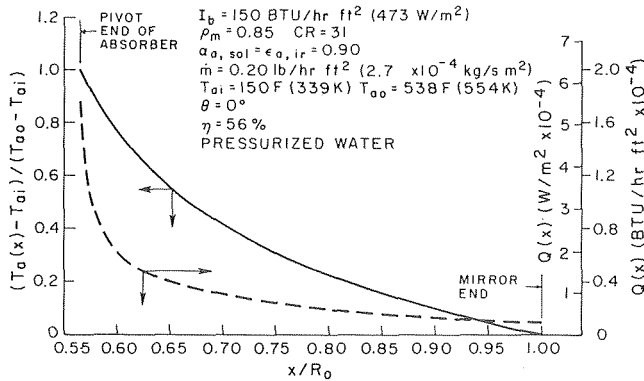


Fig. 3 Typical absorber temperature  $T_a(x)$  and extracted heat flux  $Q(x)$  profiles for pressurized water mode

$\Delta x$ ) may be found from steam tables using the value  $h_f(x + \Delta x)$  and the working fluid pressure. The axial computational increment  $\Delta x$  was selected to give agreement in predicted energy delivery within one percent for computation with increments of  $\Delta x$  and  $\Delta x/2$ . The radiation view factor of an incremental length of absorber to an adjacent incremental length of envelope is about 0.02 and is ignored as a higher order effect in the calculations.

**Simulated Operation Modes.** There are several modes in which the SRTA system can be operated. It can be used to produce hot water, wet steam, or superheated steam. Two operating modes have been selected for illustration—pressurized water heating and superheated vapor heating. Liquid phase water at high pressure—2100 psia, 625°F [ $1.45 \times 10^7$  Pa, 603°K]—can be used to generate superheated steam in a secondary loop—925 psia, 585°F [ $6.4 \times 10^6$  Pa, 580°K]—for use in a 925/585 turbine much like those developed for light-water reactor application. A flow-through absorber is required for the SRTA collector since a heat pipe absorber cannot operate effectively when its orientation relative to the local gravitational field changes diurnally by a significant amount. The pressurized water mode is analyzed in detail in the next section.

Although the generation of superheated steam in the field is technically feasible, it appears less attractive economically for power production than pressurized water since the resultant increased cycle efficiency does not pay for added field piping and separate superheating collectors. The performance of an SRTA collector acting as a superheater at 1800 psia is therefore described less completely, in the next section, than the pressurized water mode.

The SRTA collector concept can also be used at lower temperature and pressure for building heating and cooling. A two-stage, steam-fired absorption air conditioner operating at high coefficient of performance ( $\sim 0.85$ ) could be used for cooling with a conventional low pressure steam system for heating. Industrial process steam can also be readily produced by an SRTA system.

## Results

The effect of mirror reflectance  $\rho_m$ , nominal concentration  $CR$  (area-based concentration ratio  $CR = 1.5 R_0/D_a$ ), absorber radiation properties,  $\alpha_{a, sol}$  and  $\epsilon_{a, ir}$ , fluid flow rate  $\dot{m}$ , insolation level  $I_b$ , incidence angle  $\theta$ , and evacuated versus nonevacuated envelope have been studied and will be discussed in turn. Fig. 3 shows a typical absorber temperature  $T_a$  profile and a delivered energy  $Q(x)$  profile. At the mirror end of the absorber (larger  $x/R_0$ ) water heating at nearly constant flux takes place. At the pivot end of the absorber (smaller  $x/R_0$ ) the absorbed flux increases sharply. (A safety mechanism temperature sensor would be located in this region to sense fluid flow cessation and defocus the collector to avoid thermal damage.) If fluid were introduced at the pivot end instead of at the mirror end of the absorber, it could be heated to a rela-

tively high temperature in the high flux zone—a temperature so high that little useful gain could be realized downstream in the low flux region; hence the introduction of fluid at the mirror end of the absorber.

The outlet condition can be determined from the integrated energy equation

$$h_{fo} = h_{fi} + \eta I_b / \dot{m} \quad (10)$$

The collector efficiency  $\eta$  is defined as the energy delivered divided by the direct, normal insolation - aperture area product, i.e.,

$$\eta = (\pi D_a / I_b A_m) \int_{x_i}^{x_o} Q(x) dx \quad (11)$$

This definition of efficiency is based upon the beam component of radiation. To compare these values of efficiency with those values for solar collectors which absorb both direct and diffuse radiation, the values of  $\eta$  presented herein should be multiplied by the ratio of direct to total radiation for the geographic location and period of interest.

During the simulations described in the following, certain secondary parameters were left unchanged unless noted otherwise:

Ambient temperature  $T_\infty = 20^\circ\text{F}$  (266°K)

Ambient pressure  $P_\infty = 1$  atm ( $1.0 \times 10^5$  Pa)

Envelope internal pressure  $P_e = 1$  atm ( $1.0 \times 10^5$  Pa)

Absorber surface/envelope gap  $(D_{ei} - D_a)/2 = 0.25$  in. ( $65 \times 10^{-3}$  m)

Envelope IR emittance  $\epsilon_{e, ir} = 0.88$

Envelope IR transmittance  $\tau_{e, ir} = 0.02$

Envelope diffuse solar absorptance  $\alpha_{e, sold} = 0.069$

Envelope solar reflectance,  $\rho_{e, sold} = 0.043$

Working fluid inlet temperature:

Pressurized water mode  $T_{ai} = 150^\circ\text{F}$  (339°K)

Superheater mode  $T_{ai} = 625^\circ\text{F}$  (603°K)

Working fluid pressure:

Pressurized water mode  $p_a = 2100$  psia ( $1.4 \times 10^7$  Pa)

Superheater mode  $p_a = 1800$  psia ( $1.24 \times 10^7$  Pa)

Glass envelope thickness  $(D_{eo} - D_{ei})/2 = 0.25$  in. ( $6.35 \times 10^{-3}$  m)

Wind speed = 0. knots (0. m/s)

Glass extinction coefficient for solar radiation =  $0.125$  in. $^{-1}$  ( $5.0$  m $^{-1}$ )

Glass refractive index for solar radiation = 1.526

Mirror aperture area  $A_m = 1000$  ft $^2$  (93 m $^2$ )

Incidence angle  $\theta = 0$ .

**Effect of Mirror Reflectance.** The effect of mirror reflectance  $\rho_m$  on collector performance is shown in Fig. 4. The high value of reflectance (0.95) is that which may be achieved after a concentrated development effort or by the use of silvered glass mirrors. Samples of this quality have been made from specially

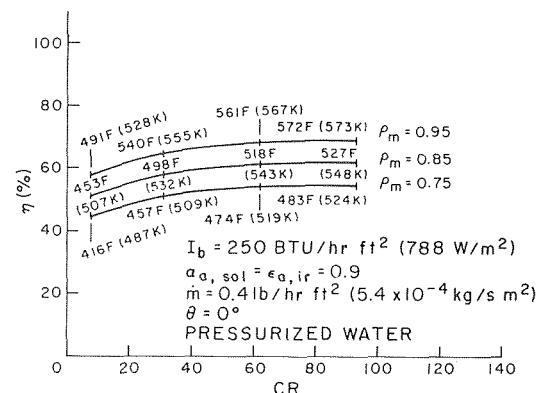


Fig. 4 Collector efficiency  $\eta$  versus concentration ratio  $CR$  with mirror reflectance  $\rho_m$  as a parameter—collector exit temperatures shown for various values of  $CR$

treated aluminum. The midrange  $\rho_m$  (0.85) represents a currently available aluminized acrylic film of good durability. The low value (0.75) represents a dirty or deteriorated reflector surface. The mirror reflectance is the most important factor other than the fixed optical properties of the glass envelope in determining the performance of the SRTA collector. Working fluid outlet temperatures are shown in Fig. 4 for concentration ratios of 93, 62, 31, and 8.

**Effect of Concentration Ratio and Surface Selectivity.** The effect of concentration ratio  $CR$  on thermal performance is shown in Figs. 5 and 6. In general, a higher concentration ratio improves performance although there is a limit of about 50 beyond which little improvement is seen in the pressurized water mode. The effect of concentration ratio is much greater in the superheating mode than in the pressurized water mode. A three-fold increase in  $CR$  in the superheating mode improves efficiency by about 50 percent, whereas the same  $CR$  increase in the liquid mode results in only a 7 percent increase in efficiency. One of the fundamental reasons for using focusing collectors is the smaller area from which radiative and convective losses occur relative to the aperture area; hence, the greater efficiency with increasing concentration ratio.

The effect of absorber surface selectivity is also shown in Fig. 5. At higher absorber temperatures experienced in the superheating mode, selectivity is important and can enhance performance considerably. At collector outlet temperatures expected in the pressurized water mode, however, the added expense of surface treatment does not seem to be warranted.

**Effect of Fluid Flow Rate.** All other parameters remaining constant, fluid flow rate directly controls the absorber temperature profile as quantified by equations (9) and (10). As shown in Fig. 6, efficiency suffers as  $\dot{m}$  is decreased in the superheating mode. Collector efficiency is insensitive to flow rate in the pressurized water mode over a nine-fold range of concentration ratio. The finding of Pope and Schimmel [2] that selectivity can greatly improve parabolic collector performance at low levels of insolation was not confirmed in the present SRTA system study although some improvement was noted at very low fluid flow rates, i.e., at very high values of absorber temperature.

**Effect of Insolation Level.** Fig. 7 shows the effect of insolation  $I_b$  upon SRTA performance. In the pressurized water mode, efficiency is insensitive to insolation levels whereas, in the superheating mode, efficiency can drop by 50 percent if  $I_b$  drops by a factor of three.

**Effect of Envelope Evacuation.** Fig. 7 shows the performance improvement which could be expected due to envelope evacuation. The effect is most pronounced at low levels of insolation and low flow rates. Also, for small  $CR$ , convective loss to the envelope becomes relatively large at a given operating condition and envelope evacuation can improve performance. In view of the problems as-

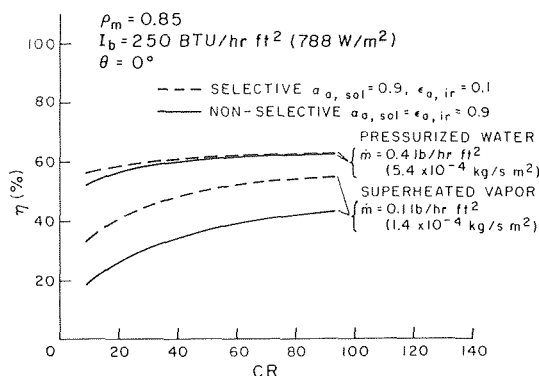


Fig. 5 Collector efficiency  $\eta$  versus concentration ratio  $CR$ —surface selectivity effect

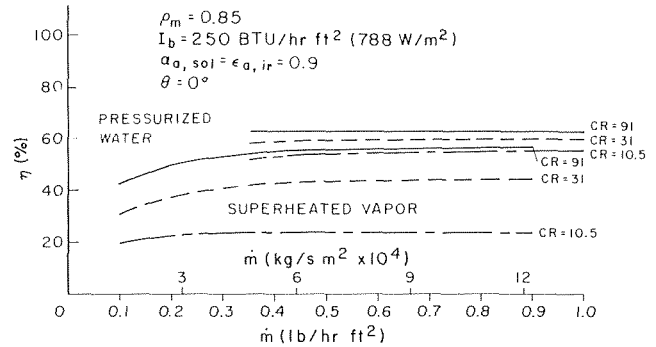


Fig. 6 Collector efficiency  $\eta$  versus fluid flow rate  $\dot{m}$  with concentration ratio  $CR$  as a parameter

sociated with it, evacuation would only seem warranted in climates where direct insolation is at relatively low levels most of the time. In such locations the SRTA system can be quite efficient if the envelope is evacuated.

**Effect of Incidence Angle.** The variation of collector performance diurnally and seasonally is affected by many parameters—sun angle, local microclimate, atmospheric turbidity, insolation level, etc. One of the most important determinants of temporal efficiency variation is the collector incidence angle  $\theta$ . The incidence angle of direct solar radiation on the collector aperture may be calculated from values of collector latitude and tilt, solar hour angle, and solar declination [11]. Fig. 8 shows the predicted effect of incidence angle on SRTA performance for a typical set of conditions. The prediction of seasonal efficiency variation in full is beyond the scope of this paper but the information in Fig. 8 indicates the trend which could be expected from one of the major temporal parameters. The effect of insolation level has been treated earlier.

Wind speed and ambient temperature, which vary daily and seasonally, have small effects on SRTA performance. Between an ambient temperature range of 20 and 100°F (266 and 311°K), collector efficiency changes by a maximum of 2 percent. Similar small effects of wind speed were noted over the range of speed normally encountered in populated land areas of the world.

## Closure

A detailed thermal analysis of the SRTA concentrating solar collector in two operating modes which bracket its expected range of utility has shown that it can operate efficiently over a wide range of design and climatic variables. Collector performance is most sensitive to mirror surface reflectance in both pressurized water and superheating modes. Absorber surface radiation selectivity,

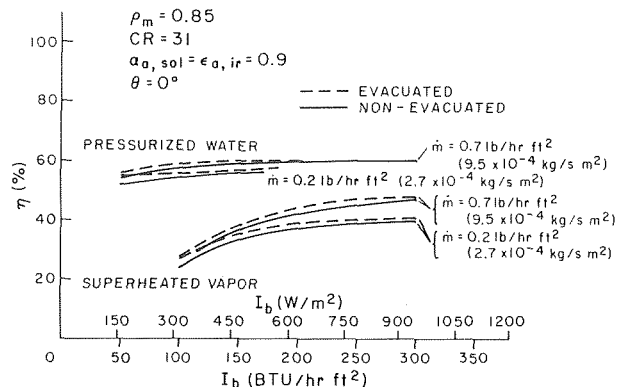


Fig. 7 Collector efficiency  $\eta$  versus insolation  $I_b$  with fluid flow rate  $\dot{m}$  as a parameter—evacuated envelope effect

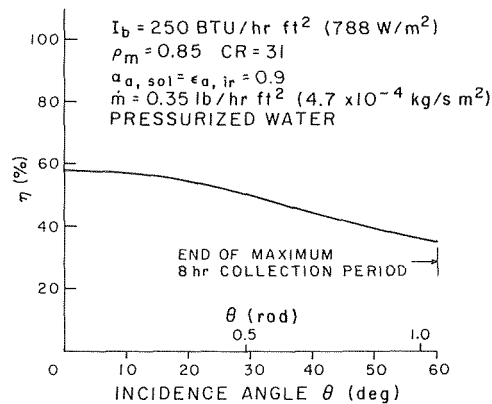


Fig. 8 Collector efficiency  $\eta$  versus collector incidence angle  $\theta$

concentration ratio and insolation level are also primary determinants in the superheating mode. Efficiency level is insensitive to envelope evacuation and fluid flow rate in both modes and insensitive to concentration ratio and insolation in the simulated pressurized water mode. Of course, for invariant efficiency, energy delivery is proportional to insolation. Unavoidable reflectance losses from the glass envelope are responsible for about 18 percent of the total system losses.

The insensitivity of collector performance to concentration ratio and mass flow rate in the liquid-phase mode and sensitivity to  $CR$  in the superheating mode would indicate the possibility of a separate design for each usage. Lower  $CR$  values and resultant lower cost for reflecting surface quality and tracking precision could be used in the liquid heater. An SRTA superheater would require higher  $CR$  values and consequent higher surface and steering accuracy.

The SRTA system is presently under test in model form and in a prototype 100-ft<sup>2</sup> unit. Such tests are essential to validate the new concept and to give confidence to the analysis presented herein. Several approaches to reducing the glass envelope reflectance loss are presently under study, including absorber shaping and envelope surface treatments.

#### Acknowledgment

The author acknowledges the assistance of the inventor, W. G. Steward, who described the subtleties of SRTA optics and reviewed an early version of this paper.

#### References

1 Steward, W. G., "A Concentrating Solar Energy System Employing a Stationary Spherical Mirror and a Movable Collector," *Proceedings of the*

*Solar Heating and Cooling for Buildings Workshop*, U.S. Government Printing Office, 1973, pp. 24-25.

2 Pope, R. B., and Schimmel, W. P., Jr., "An Analysis of Linear Focused Collectors for Solar Power," *Proceedings of the 8th Intersociety Energy Conversion Conference*, American Institute of Aeronautics and Astronautics, Avenue of the Americas, N.Y., N.Y., 1970, pp. 353-359.

3 Eckert, E. R. G., et al., *Research Applied to Solar-Thermal Power Systems, Progress Reports 1, 2, and 3*, NTIS, Springfield, Va. 1973-74.

4 Meinel, A. B., and Meinel, M. P., "Thermal Performance of a Linear Solar Collector," ASME Paper No. 72-WA/Sol-7, Winter Annual Meeting, ASME, Nov., 1972.

5 Löf, G. O. G., et al., "Energy Balances on a Parabolic Cylinder Solar Collector," *Journal of Engineering for Power*, TRANS. ASME, Jan. 1962, Series A, Vol. pp. 24-32.

6 Liu, B. Y. H., and Jordan, R. C., "Performance and Evaluation of Concentrating Solar Collectors for Power Generation," *Journal of Engineering for Power*, TRANS. ASME Series A, Vol., Jan. 1965, pp. 1-7.

7 Stokes, G. G., "On the Intensity of the Light Reflected from or Transmitted Through a Pile of Plates," *Proc. Roy. Soc. London*, 11, pp. 545-556 (1860-62).

8 Swinbank, W. C., "Long Wave Radiation From Clear Skies," *Q. J. Roy. Met. Soc.*, Vol. 89, pp. 339-348.

9 Kutateladze, S. S., and Borishanskii, V. M., *A Concise Encyclopedia of Heat Transfer*, Pergamon Press, New York, 1966.

10 McAdams, W. H., *Heat Transmission*, McGraw-Hill, New York, 3rd ed., 1953.

11 Kreider, J. F., and Kreith, F., *Solar Heating and Cooling*, McGraw-Hill, New York, 1975.

## Appendix

### Optical Calculations

Referring to Fig. 2, it is easy to show from geometrical optical principles that

$$x/R_0 = 0.5(1 - r^2/R_0^2)^{-1/2} \{1 + (D_a/2R_0)(R_0/r - 2r/R_0)\} \quad (A1)$$

For a given axial position  $x$ , equation (A1) has two roots,  $r_1$  and  $r_2$ : i.e., there are two incoming beams intersecting the plane  $x = 0$  at two different points which reflect from the mirror and intercept the absorber at the same point  $x$ . They are shown as "inner" and "outer" beams in Fig. 2.

A differential energy balance for each beam can be expressed as

$$\rho_m I_b (2\pi r dr) = E(\pi D_a dx)$$

from which

$$E = \rho_m (2r I_b) / (D_a dx/dr) \quad (A2)$$

The mapping function  $dx/dr$  is computed by differentiating equation (A1) and evaluating the derivative at both  $r_1$  and  $r_2$ . The angle of incidence  $i$  which determines  $\tau_{e, \text{sol}}(i)$  and  $\alpha_{e, \text{sol}}(i)$  is computed from the equation:

$$i = \pi/2 - 2 \sin^{-1}(r/R_0) \quad (A3)$$

G. D. Polhamus

Graduate Student.  
Student Mem. ASME

A. J. Welch

Professor and Director.

Bio-Medical Engineering Program,  
The University of Texas at Austin,  
Austin, Texas

# Threshold Lesion Temperatures in Argon Laser-Irradiated Rabbit Eyes

*The purpose of this research was to measure threshold temperatures corresponding to the formation of minimum ophthalmoscopically visible lesions induced in rabbit ocular fundi by a 10-s exposure from an argon c. w. laser (4880 Å). The backside of the eye was surgically exposed and a specially designed microthermocouple with a 20-micron dia tip was inserted into the pigment epithelium to measure temperature rises. The mean threshold temperature for 30 measurements in 13 rabbits was 54°C and the standard deviation was 3°C. System error was estimated at 5 percent of temperature rise, or slightly less than  $\pm 1/2^\circ\text{C}$ .*

## Introduction

The nature of thermal retinal injury has been the subject of much attention during the past decade. However, progress in its understanding has been slow due to a lack of reliable quantifiable descriptions of the injury process. One such description that has been vigorously pursued is the temperature-time history of lesion development.

**Previous Work.** Numerous authors have attempted to measure ocular fundus temperatures [1, 2, 3],<sup>1</sup> but their results have been questioned [4, 5, 6]. Recent measurements of temperature in the pigment epithelium and choroid by Cain and Welch appear to satisfy past objections. They measured laser-induced temperature-time histories in the light absorbing layers of the fundus with 20-micron dia thermocouples which were specifically designed for measuring temperature transients in tissue [7, 8].

The temperature-sensing probes were produced in the Engineering Research Laboratory of The University of Texas at Austin, under the supervision of Prof. E. A. Ripperger. The temperature sensors were made from 1 mm quartz rod pulled over heat to 20 microns dia at the tip. Nickel, parylene (insulation), and copper were deposited on the quartz substrate, allowing a copper-nickel junction only at the probe tip. Thermoelectric EMF was  $21 \mu\text{V}/^\circ\text{C}$  ( $\pm 1 \mu\text{V}/^\circ\text{C}$ ) and rise time to 90 percent of equilibrium was about 1 ms for a near step change in temperature produced by driving a probe into a heated water bath. A detailed description of the probe manufacturing process can be found elsewhere [8].

Cain and Welch have shown experimentally that probe artifact

in the ocular fundus<sup>2</sup> temperature measurement may be minimized by maintaining a 10:1 ratio between retinal image and probe diameter. They demonstrated that temperatures in the P.E. and choroid are linearly related to input power for temperature rises of at least  $30^\circ\text{C}$ . Although they measured complete temperature-time histories in the laser-irradiated fundus, Cain and Welch did not measure temperatures at which minimum ophthalmoscopically visible lesions occurred.

Reed has shown that temperature measurements merely reflect the thermal equilibrium existing between tissue and temperature sensor [9]. Hence, for temperature to be meaningful, the sensor must closely resemble the media in which it is implanted. If the temperature sensor is modeled as an infinitely long cylinder imbedded in an infinite medium, both the ratio and products of conductivity and volumetric specific heat of the probe appear in the equations for the model [10]. Therefore, the similarity of computed temperature profiles with and without the imbedded cylinder depend upon the similarity of the product  $(k\rho c)$  and ratio  $(k/\rho c)$  of the sensor to corresponding terms for the medium. For example, by modeling fundus tissue with the properties of water,  $(k\rho c)_{\text{H}_2\text{O}}$  and  $(k/\rho c)_{\text{H}_2\text{O}}$  each approximately equal 0.00144. But these thermal parameters for copper are  $(k\rho c)_{\text{Cu}} = 0.76$  and  $(k/\rho c)_{\text{Cu}} = 1.14$ , whereas the thermal properties of fused quartz are  $(k\rho c) = 0.00131$  and  $(k/\rho c) = 0.0083$ . Since the percent of metal deposited on a 20  $\mu\text{m}$  quartz probe is only 0.14 percent of the mass of the probe, the thermal properties of the probe are approximately those of quartz. The thermal equilibrium between the quartz temperature sensor and the tissue will result in temperature measurements close to those of the tissue alone.

This paper concerns the measurement of temperatures associ-

<sup>1</sup> Numbers in brackets designate References at end of paper.

Contributed by the Heat Transfer Division for publication in the HEAT TRANSFER JOURNAL. Manuscript Received by the Heat Transfer Division October 7, 1974. Paper No. 75-HT-PP.

<sup>2</sup> The term ocular fundus refers to the retinal layers, pigment epithelium (P.E.), choroid, and sclera.

ated with threshold ophthalmoscopically visible fundus changes in the live rabbit due to laser-induced retinal injury.

The 20  $\mu\text{m}$  quartz substrate thermocouples were used to measure P.E. temperature produced by 10-s exposures with an argon laser. The half-power diameters of retinal images were approximately 200–400 microns. These temperatures were then compared to temperatures predicted by a model for temperature rise in the ocular fundus. Much of the experimental procedure is identical to that followed by Cain and Welch, and for details beyond those mentioned here, the reader is referred to their publication [7].

**Retinal Temperature Model.** Many models have been used to predict temperature rises in the ocular fundus. The model used in our research has been developed by Mainster, et al., to predict temperature rise in the ocular fundus [11]. The model is based on a finite difference (ADI technique) solution to the following form of the heat conduction equation in cylindrical coordinates:

$$\frac{k}{r} \frac{\partial T}{\partial r} + \frac{\partial}{\partial r} \left( k \frac{\partial T}{\partial r} \right) + \frac{\partial}{\partial z} \left( k \frac{\partial T}{\partial z} \right) + A = \nu \frac{\partial T}{\partial t} \quad (1)$$

The model uses an exponentially stretched grid in a cylindrical geometry and variable internal sources. Boundary conditions for equation (1) are as follows:  $T(R, z, t) = 0$ ,  $T(r, \pm Z, t) = 0$  and  $T(r, z, 0) = 0$ . The values of  $R$  and  $Z$  are equal to 1 cm. The solutions represent the temperature rise above an arbitrary ambient temperature [12].

Source strengths in equation (1) are calculated by assuming chorioretinal heating results from exponential light absorption in the retinal P.E. and the choroid. These two layers of 10  $\mu\text{m}$  and 100  $\mu\text{m}$ , respectively, are centered in the 2 cm long cylindrical model as shown in Fig. 1. All ocular media modeled by the cylinder are assumed to be thermally homogeneous and isotropic.

The irradiance at the front surface of the P.E. is computed from the total radiant energy entering the eye multiplied by a wavelength dependent transmission coefficient for the cornea, lens, ocular fluids, retina, and contact lens. The shape and diameter of the irradiance profile in front of the P.E. is determined by experimental measurements of light intensity at the retina.

This is the same model used by Cain and Welch. However, the absorption coefficients of the P.E. and choroid were replaced by values for the rabbit determined by White [13].

## Experimental Procedure

This section includes a description of the apparatus, an outline of the laboratory procedure, and mention of the data analysis.

**Apparatus.** The temperature output first entered a specially made preamplifier which had a gain of 1000 and a bandwidth from d-c to 10 kHz. The amplified signal was displayed on a Clevite Brush Mark 200 8-channel strip chart recorder with bandwidth of d-c to 100 Hz. The overall bandwidth of the system was about 90 Hz. The bandwidth could be expanded to 10 kHz for examining the transient response by recording the data on an FM tape recorder and digitizing the analog signal. Near steady-state temperature rises were accurate to approximately  $\pm 5$  percent (assuming a minimum 10°C rise for lesion production).

The eye was irradiated by a Spectra-Physics Model 166-03 argon-laser, tuned to a primary wavelength of 4880 Å. Pulse length was controlled with an electronic shutter from Vincent Associates, Model 23XDB2X5, in conjunction with a Devices Sales Ltd. digital

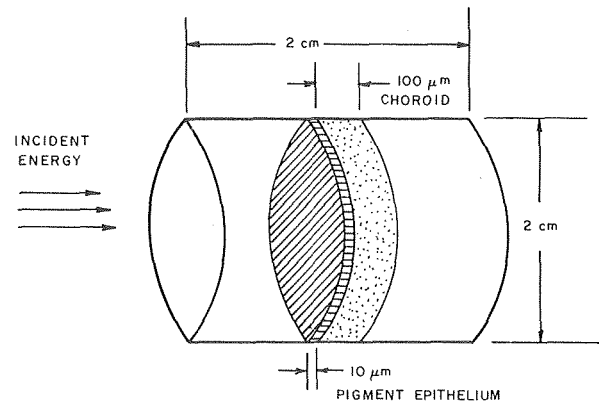


Fig. 1

timer. The ocular fundus was viewed with a Zeiss fundus camera. Mounted immediately beyond the fundus camera lens was a beam splitter to allow viewing of the fundus while half the energy from the argon-laser was directed into the eye. The fundus camera was used to observe image location and lesion formation on the fundus.

Radiant energy was measured with an EG & G Model 580 Radiometer with a narrow beam adapter and 25A Detector Head. Neutral density filters were placed in the laser beam path to control intensity.

**Laboratory Procedure.** Thorough documentation already exists for the surgical and sensor insertion procedures used in this experiment [7] so only the temperature measurement procedure shall be described.

After the posterior pole of the eye was exposed and the microprobe sensor inserted into the fundus, steady-state temperature of the eye was monitored. Body temperature and tissue temperature at the back of the eye were monitored in most of the experiments. A Sears Heat Lamp was used to keep fundus temperature near 37°C.

Once the temperature sensor was in the ocular fundus, the following steps were taken:

- 1 The probe depth was adjusted by observing the probe tip in the vitreous humor with the fundus camera. When the probe was just beyond the retinal layers and into the vitreous humor (to minimize conduction effects), 5-ms laser pulses were applied to the eye. The animal platform was rotated until the probe was in the center of the image (presumably the point of maximum direct absorption for the sensor). A relative intensity distribution of the retinal image was obtained by rotating the animal about the vertical axis through the center of the ocular lens system (nodal point) by precise increments, and measuring the direct temperature rise produced by a 5-ms pulse at each increment. Rotation about the center of the lens system resulted in minimal movement of the image in space, as the fundus and inserted sensor moved across it. The asymmetry of the cornea and lens was neglected and the measured profile was represented as a circularly symmetric profile in the model.

It has been shown that to adequately reduce the temperature re-

## Nomenclature

$T$  = absolute temperature or temperature rise, °C  
 $k$  = thermal conductivity, cal/cm s °C  
 $A$  = heat source term, cal/cm<sup>3</sup>s  
 $\nu$  =  $\rho c$  = volumetric specific heat, cal/cm<sup>3</sup> °C

$c$  = specific heat, cal/gm °C  
 $\rho$  = density, gm/cm<sup>3</sup>  
 $CP$  = corneal power

### Superscripts

$e$  = extrapolated value associated with threshold corneal power

$m$  = actual value measured by sensor

### Subscripts

$s$  = subthreshold value  
 $t$  = threshold value associated with formation of an ophthalmoscopically visible lesion

sponse error introduced by the presence of the probe in the ocular media, the half-power diameter of the retinal image must be 10 times the probe diameter [7]. To obtain this condition, a 30 cm focal length lens was placed in the laser beam path to provide a near Maxwellian View to the rabbit eye (i.e., the laser beam was focused near the center of the animal's lens system).

2 Locations near the sensor insertion (within 1 mm) were irradiated at decreasing power levels for 10-s intervals, until the minimum power to produce an ophthalmoscopically visible lesion within five min after exposure was obtained. The five-min post-exposure criterion was used because it provides a quick means of gathering data and the results generally fall at a constant percentage above other damage criteria [14] such as the 24-hr post-exposure lesion or histologically observable changes. The animal was then rotated to impinge the laser upon the thermocouple and short 50-ms pulses were applied while the sensor was withdrawn from the vitreous humor in 3  $\mu\text{m}$  steps until the position of maximum temperature rise was achieved. The model of chorioretinal temperature rise predicts the maximum temperature rise will occur in the center of the P.E. and center of the retinal image, if the irradiance profile has its maximum at the center of the image. A 10-s pulse at about one-fourth the power necessary for a threshold lesion was applied and temperature rise was recorded on the Brush Recorder. The sensor was repositioned to correct possible movement of the animal or shift of the image, and the subthreshold temperature was again recorded. Finally, the sensor was recentered a third time and full threshold power was delivered to the site. All experimental subthreshold temperature rises were kept below 8°C.

In all cases, the highest of the two subthreshold temperature rises from each site was selected to be extrapolated to threshold temperature. Thus, when subthreshold and threshold temperatures were measured, two threshold temperatures were obtained—one from the extrapolated highest subthreshold temperature, and one from the threshold exposure.

3 A few times it was possible to begin anew, reinsert the sensor at a new location and repeat the entire experiment.

**Data Analysis.** All temperature measurements were corrected for light directly absorbed by the thermocouple and subthreshold measurements were extrapolated to threshold values. First, the temperature rise due to direct absorption by the sensor was subtracted from the overall recorded temperature rise. The remainder represented the tissue temperature rise. The rapid response of the sensor, due to direct heating, was easily differentiable from the response due to the slower heating of the tissue.

Second, the temperature rises associated with the subthreshold laser pulses were linearly extrapolated with respect to the corneal power that produced a threshold lesion. The following relationship was used:

$$T_t^o = \frac{T_s^m \times CP_t}{CP_s}$$

This relationship is based on the linearity between corneal power and temperature in the ocular fundus as reported by Cain and Welch [7].

## Results

Data were taken from twenty rabbits, three of which had two sensor insertions and a fourth of which had three insertions. In addition to threshold measurements, subthreshold measurements were obtained from nine of these rabbits (including two of the double insertions and the triple insertion). These subthreshold measurements were extrapolated to threshold temperature. A total of 38 measured or extrapolated threshold temperatures were obtained during this research.

Only 30 values have been selected for presentation. The others have been discarded for various reasons, such as excessive variation in prelesion fundus temperature from 37°C, apparent degra-

dation of corneal clarity, or excessive localized trauma from inserting the probe.

The experimental results have been summarized in three figures depicting: (1) the measured versus calculated temperature-time profile; (2) the distribution of lesions with threshold temperature; and (3) the calculated temperatures using the model of Mainster, et al., for each measured threshold temperature rise.

**Measured Versus Calculated Temperature-Time Profiles.** Typical measured and calculated (from the model) temperature rises in the P.E. at the center of the beam as a function of time are shown in Fig. 2. The temperature rise was produced by a 10-s 13.8 mW (at the cornea) laser pulse which formed a retinal image with a half-power diameter of 200  $\mu\text{m}$ . The irradiance profile of the retinal image as measured by the direct absorption characteristics of the thermocouple is shown in the inset of Fig. 2. The symmetric irradiance profile (used by the model and obtained by averaging the measured irradiance profile) is also shown in the inset of Fig. 2. Maximum measured temperature rise was 17.6°C and maximum model temperature rise was 16.5°C. The initial portion of the model profile lies above the measured profile. However, the curves cross at about 1 s, and thereafter, the model profile remains lower than the measured profile. At the end of the laser pulse, the measured temperature has stabilized. However, the model temperature increases at a slow rate.

**Distribution of Lesions With Threshold Temperature.** Fig. 3 is an accumulation of the number of experimental threshold lesions as a function of increasing temperature (pre-exposure steady-state fundus temperature plus measured temperature rise) obtained from twenty rabbits. The thirty lesion temperatures are graphed in 2°C intervals. Only one lesion appears at 48.2°C and 15 lesions appear at 54.5°C or lower. The plot therefore represents the probability of lesion development versus fundus temperature for the population of rabbits we exposed. For example, if a temperature of 54.5°C was measured during a 10-s exposure, the probability that a lesion will develop at that site is 0.5. Half-power image diameters at the retina were measured to be between 200 and 400 microns. The mean threshold temperature was 54°C and the standard deviation about the mean was 3°C.

**Measured Temperature Rise Versus Calculated Temperature Rise.** The relation between measured temperature rises and calculated temperature rises is shown in Fig. 4. Calculated temperatures are based on experimental measurements of corneal power, irradiance profile and image radius. Other parameters used for these calculations are as follows: Thicknesses of the P.E. and choroid are assumed to be 10 and 100 microns, respectively. Absorption coefficients of these layers for a wavelength of 4880 Å wavelength are set at 832.0 and 83.2  $\text{cm}^{-1}$ , respectively. The preretinal ocular media transmission is assumed to be 82.0 percent for the 4880 Å wavelength, and losses through the contact lens are neglected. Conductivity and volumetric specific heat are specified as 0.0015  $\text{cal}/^\circ\text{C s cm}$  and 1.0  $\text{cal}/^\circ\text{C cm}^3$ , respectively, for all ocular media. Both the absorption coefficients and the preretinal ocular media transmission are higher than the values used by Cain and Welch [7] which were 637.6  $\text{cm}^{-1}$  and 76.3  $\text{cm}^{-1}$  for the P.E. and choroid, respectively, and transmission of the ocular media was 63.6 percent. The set of parameter values used in these computations were independently determined from the experimental data of Geeraets, et al. [15] and generously provided by T. J. White.

A straight line through the origin of slope 0.92 (from least-squares curve fit) has been drawn through the data. Extrapolated threshold temperatures have been depicted by open circles. The 95 percent confidence bands for a slope of  $m = 1$  have been depicted by dashed lines.

The model parameters used for these calculations resulted in computed temperature rises that averaged about 8 percent higher

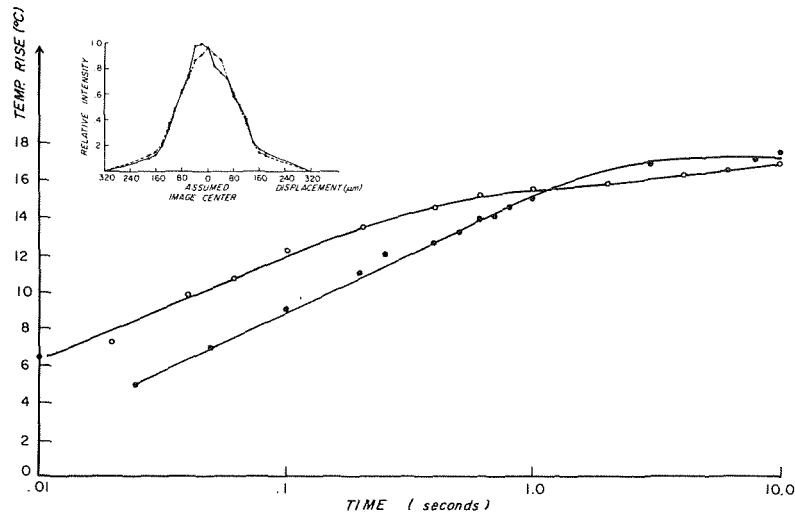


Fig. 2

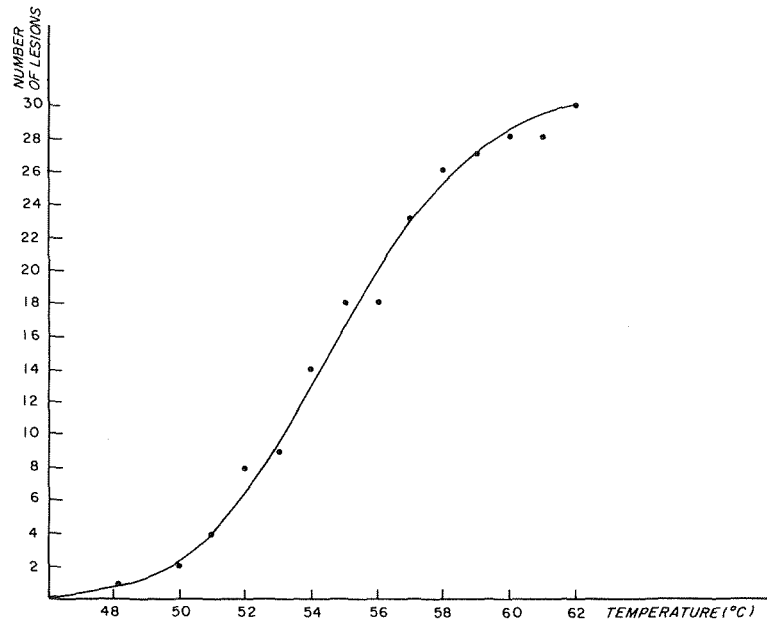


Fig. 3

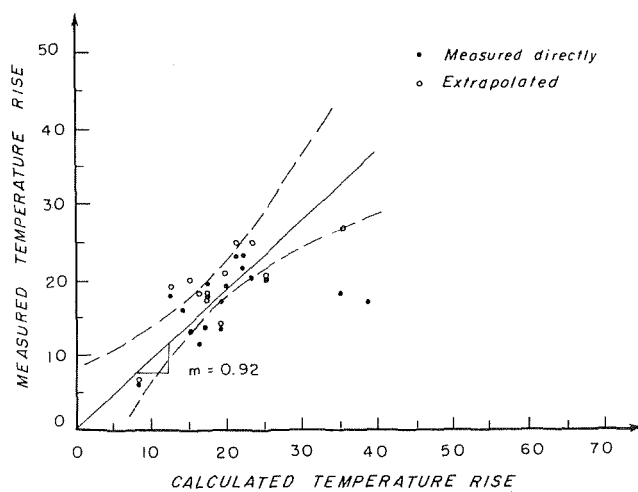


Fig. 4

than the measured temperature rises. The line of slope  $m = 0.92$  lies within the 95 percent confidence bands for a slope  $m = 1$ , thus encouraging confidence in the predictive power of the model. Furthermore, when two "out-lying" data points are deleted, average computed and measured values were within one percent of each other. In comparison, Cain and Welch obtained near steady-state measured temperature rises about 20 percent higher than calculated temperature rises (using different model parameters).

### Discussion

The results shall be discussed with respect to the following three topics: (1) Measured Versus Calculated Temperature-Time Profiles; (2) Subthreshold Temperatures; and (3) Number of Lesions Versus Temperature.

**Measured Versus Calculated Temperature-Time Profiles.** The agreement between the measured and calculated temperature profiles is reasonably satisfactory at near steady-state. However, the profiles do not agree well at short times (even when the system bandwidth is expanded beyond 10 kHz). The uncertainties associ-

ated with the calculated temperatures are due to: (a) representation of the fundus by a two-layer homogeneous model; (b) accuracy of experimentally measured input variables (corneal power, image diameter, and intensity profile); and (c) variation in the physical parameters of the eye.

The primary light absorbing bodies of the fundus are 1-micron melanin granules located predominantly in the pigment epithelium. Although models have been developed based upon the heating of these granules and reradiation of their stored energy, the homogeneous model is assumed to be reasonable for threshold exposure durations greater than 1 ms.

The input variables are subject to the normal measurement errors. The process of rotating the animal to measure the relative intensity profile of an image radius is suitable only if the laser image remains fixed in space. Estimates of image size using the fundus camera gradacule are within  $\pm 5$  percent of measured values. In addition the measured irradiance profile is represented by a circularly symmetric profile in the model.

Perhaps the greatest uncertainties are due to variations in the physical properties between animals of the same species. The degree of pigmentation and thickness of the pigment epithelium may vary by a factor of 2 or more in the rabbit. At best only average values of absorption are available and the limited experimental results differ significantly. The most important parameter is the percent of light into the eye that reaches the retina. Experimental values of this parameter range from 50 percent to 75 percent [15, 16].

The model parameters used in this paper are based upon published values and preliminary results from T. J. White. Coefficients have not been adjusted to minimize the difference between experimental and calculated results. That is, we have not curve-fitted the calculated values to the experimental results. Needless to say, differences between calculated and experimental values demonstrate the necessity for additional experimental work in the determination of physical properties of the eye.

**Subthreshold Temperatures.** As previously described, two subthreshold temperatures were measured at each sensor insertion site prior to the concluding threshold exposure. The practice was followed to reduce measurement error and for this reason: it is, unfortunately, not known if the thermal damage of retinal tissue disrupts the absorption coefficients and thermal parameters of the P.E. and choroid. Hence, the threshold and subthreshold measurements would provide preliminary data for evaluating this possibility. Generally threshold temperatures were below extrapolated temperatures. Repositioning of the sensor between each exposure should have reduced measurement error due to failure of the sensor to be placed at the hottest location in the fundus, or to remain at that location. Repeated subthreshold radiations should not have altered the tissue since it has been reported that rates of tissue damage are negligible when subthreshold temperature rises are kept below  $5^{\circ}\text{C}$  [17, 18]. The difference between subthreshold measurements at a site when extrapolated to threshold corneal power was rarely more than  $1^{\circ}\text{C}$ .

**Distribution of Lesions With Threshold Temperature.** The average threshold temperature rise from 20 eyes, after correction to  $37^{\circ}\text{C}$ , was  $17.3^{\circ}\text{C}$  and the standard deviation was  $3.1^{\circ}\text{C}$  or 18 percent of the mean. 95 percent confidence intervals for the sample mean were  $\pm 1.2^{\circ}\text{C}$ . Therefore, the threshold temperature mean was about  $54^{\circ}\text{C}$ .

It is interesting to examine the variance in corneal power necessary for lesion formation and compare it to the variance of the temperature measurements. Unfortunately, both a measured and an extrapolated threshold temperature rise were associated with a single threshold corneal power, since the threshold corneal power was used to extrapolate the subthreshold temperature measurement to threshold. Hence, for all experiments in which subthreshold measurements were taken, a single threshold corneal power was associated with both the measured threshold temperature rise and the extrapolated temperature rise. Only 18 independent

threshold corneal power measurements were obtained. Nevertheless, the mean of these 18 corneal power measurements was  $21.3\text{ mW}$  and the standard deviation was  $6.86\text{ mW}$  or about 32 percent of the mean. The larger variation in power was due partly to the variation in image sizes from 200 to  $400\text{ }\mu\text{m}$  and partly to individual differences in pigmentation and other physical parameters that alter the power level to produce a threshold burn.

Data are also available from other laboratory sources. An argon laser ( $4880\text{ \AA}$ ) has been used to produce damage in the Rhesus monkey retina which is presumably more uniform than the rabbit retina [19]. In those experiments, exposure time was 1.6 s and retina spot size was about 200 microns. The mean was  $18.75\text{ mW}$  and the standard deviation was  $6.8\text{ mW}$  or 36 percent of the mean. This difference was presumably due to individual differences in the animals.

The difference in variation between threshold corneal power measurements and threshold temperature measurements suggests that threshold temperatures are somewhat less sensitive to individual physiological differences (i.e., pigmentation, local circulation and transmission, and absorption properties of various ocular components).

It is well known that these minimum ophthalmoscopically visible lesions are probably 10–15 percent beyond the first histologically and electroretinographically noticeable permanent alterations [20, 21]. Nevertheless, the small variation in threshold temperatures does emphasize the probable correlation between a specific degree of damage and a given temperature and exposure time.

## Conclusions

The following conclusions may be drawn from this research:

- 1 Threshold temperatures associated with the formation of minimum ophthalmoscopically visible lesions may be measured with specially designed microthermocouples. The mean threshold temperature for a 10-s exposure from an argon c.w. laser ( $4880\text{ \AA}$ ) was  $54^{\circ}\text{C}$  and the standard deviation was  $3^{\circ}\text{C}$ . System error was about 5 percent of temperature rise or slightly less than  $\pm 1/2^{\circ}\text{C}$ .
- 2 The mean error between calculated and measured steady-state threshold temperature rises was less than one percent following deletion of two data points.
- 3 Threshold temperatures showed better correlation with lesion formation than threshold corneal powers.
- 4 The next important step is the correlation of retinal burn data with a theory of thermal injury based upon chemical kinetics and critical temperature-time histories for protein denaturation. Such a correlation will help better define the presently ill-understood protein denaturation thermal damage mechanisms in the retina.

## Acknowledgment

This research was sponsored in part by the National Institute of Health under Research Grant RO1 EY01162-01.

## References

- 1 Mellerio, J., "The Thermal Nature of Retinal Laser Photocoagulation," *Exptl. Eye Res.*, Vol. 5, 1966, p. 242.
- 2 Najac, H., Cooper, B., Jacobsen, J. H., Shamos, M., and Breittfeller, M., "Direct Thermocouple Measurements of Temperature Rise and Heat Conduction in the Rabbit Retina," *Invest. Ophthalm.*, Vol. 2 No. 1, 1963, p. 32.
- 3 Noyori, K. S., Campbell, C. J., Rittler, M. C., and Koester, C., "Ocular Thermal Effects Produced by Photocoagulation," *Arch. Ophthalm.*, Vol. 70, 1963, p. 817.
- 4 Geeraets, W. J., and Ridgeway, D., "Retinal Damage From High Intensity Light," *Acta. Ophthalm., Suppl.*, Vol. 76, 1963, p. 109.
- 5 Vos, J. J., "Heat Damage to the Retina by Lasers and Photocoagulators," *Ophthalm.* Vol. 151, 1966, p. 652.
- 6 Hayes, J. R., and Wolbarsht, M. L., "Thermal Model for Retinal Damage Induced by Pulsed Laser," *Aerospace Med.*, May 1968, p. 474.
- 7 Cain, C. P., and Welch, A. J., "Measured and Predicted Laser Induced Temperature Rise in the Rabbit Fundus," *Invest. Ophthalm.*, Vol. 13, 1974, p. 60.
- 8 Cain, C. P., and Welch, A. J., "Thin-Film Temperature Sensors for

Biological Measurements," *IEEE Transactions on Biomedical Engineering*, Vol. BME-21, No. 5, Sept. 1974, p. 421.

9 Reed, R. P., "Thin Film Sensors of Micron Size and Applications in Biothermology," PhD dissertation, The University of Texas at Austin, 1966.

10 Carslaw, H. S., and Jaeger, J. C., *Conduction of Heat in Solids*, 2nd ed., Oxford Press, London, 1959, p. 316.

11 Mainster, M. A., White, T. J., Tips, J. H., and Wilson, P. W., "Transient Thermal Behavior in Biological Systems," *Bull. Math. Bio-Physics*, Vol. 32, 1970, p. 303.

12 Mainster, M. A., White, T. J., Tips, J. H., and Wilson, P. W., "Retinal-Temperature Increases Produced by Intense Light Sources," *J. Optical Soc. America*, Vol. 60, No. 2, Feb. 1970, p. 264.

13 White, T. J., Personal Communications, 3246 Candlewood Lane, San Antonio, Texas 78217.

14 Bresnick, G. H., "Ocular Effects of Argon Laser Radiation," *Invest. Ophthalm.*, Vol. 9, 1970, p. 901.

15 Geeraets, W. J., and Berry, E. R., "Ocular Spectral Characteristics as Related to Hazards From Lasers and Other Light Sources," *American J. Ophthalm.*, Vol. 66, No. 1, July 1968, p. 15.

16 Mainster, M. A., White, T. J., Allen, R. G., "Spectral Dependence of Retinal Damage Produced by Intense Light Sources," *J. Optical Soc. America*, Vol. 60, No. 6, June 1970, p. 848.

17 Stoll, A. M., and Green, L. C., "Relationship Between Pain and Tissue Damage Due to Thermal Radiation," *J. Appl. Physiol.*, Vol. 14, No. 3, May 1959, p. 373.

18 Hu, C., and Barnes, F. S., "The Thermal-Chemical Damage in Biological Material Under Laser Irradiation," *IEEE Trans. Bio-Med. Engr.*, Vol. BME-17, No. 3, July 1970, p. 220.

19 Vassiliadis, A., Rosan, R. C., and Zweng, H. C., "Research on Ocular Laser Thresholds," Final Report, SRI Project 7191, Stanford Research Institute, Menlo Park, Calif., Aug. 1969, p. 34.

20 Ham, W. R., Jr., Williams, R. C., Mueller, H. A., DuPont Guerry, III, Clarke, A. M., and Geeraets, W. J., "Effects of Laser Radiation on the Mammalian Eye," *Trans. N.Y. Acad. of Sciences*, Ser. II, Vol. 28, No. 4, Feb. 1966, p. 517.

21 Priebe, L. A., and Welch, A. J., "Changes in the Rabbit Electroretinogram C Wave Following Ruby Laser Insult," *Aerospace Medicine.*, Vol. 44, No. 11, Nov. 1973, p. 1246.

# ERRATUM

Erratum: O. C. Iloeje, D. N. Plummer, W. M. Rohsenow, and P. Griffith, "An Investigation of the Collapse and Surface Rewet in Film Boiling in Forced Vertical Flow," published in the May 1975 issue of the JOURNAL OF HEAT TRANSFER, pp. 166-172.

Fig. 6 on page 170 should be replaced by the following figure 6:

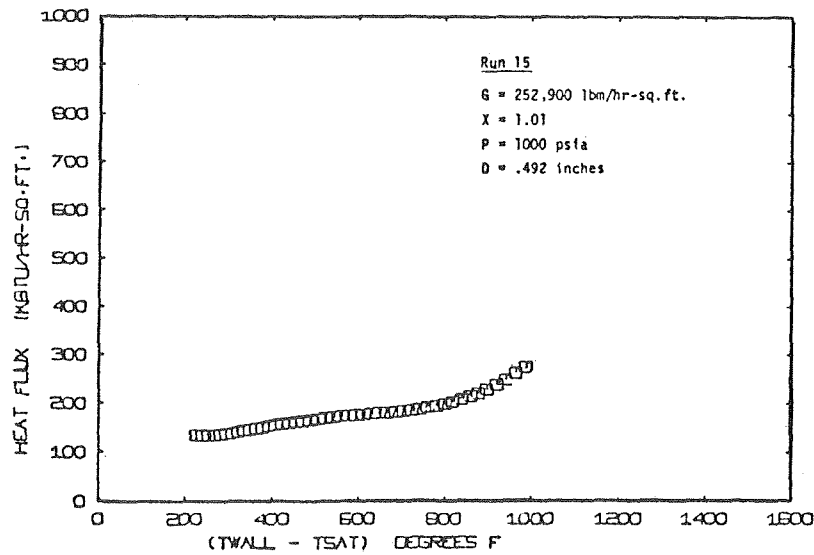


Fig. 6 Reduced data from G.E. transient test section

Fig. 8, including the figure caption, should be interchanged with Fig. 9 together with the latter's caption.

The term in parenthesis in line 6 in the left-hand column on page 170 "(see Fig. 8)," should be replaced by "(see Fig. 9)."

The first line of print below equation (6) on page 171 should read: "Fig. 8 shows a superposition . . ."

Line 20 of the left-hand column on page 171 should read: "ductivity of Nickel-Oxide at around 1500°F varies from 2.4 Btu."

Line 24 of the left-hand column on page 171 should read: "°F was therefore assumed. The data would suggest a minimum . . ."



This section consists of contributions of 1500 words or equivalent. In computing equivalence, a typical one-column figure or table is equal to 250 words. A one-line equation is equal to 30 words. The use of a built-up fraction or an integral sign or summation sign in a sentence will require additional space equal to 10 words. Technical briefs will be reviewed and approved by the specific division's reviewing committee prior to publication. After approval such contributions will be published as soon as possible, normally in the next issue of the journal.

## Effects of Fin Base-Temperature Depression in a Multifin Array

E. M. Sparrow<sup>1</sup> and L. Lee<sup>2</sup>

### Introduction and Background

When a fin is performing its function effectively, the rate of heat transfer at the fin-base interface is much greater than that passing through a comparable area on the unfinned portion of the base surface. In order to channel such a relatively large amount of heat into (or out of) the fin, it is necessary that the temperature of the fin base be depressed (or elevated) relative to that of the surrounding base material. This temperature depression (elevation) is generally neglected in design calculations, so that the temperature at the fin-base interface is assumed to be identical to that on the adjacent unfinned portion of the base surface. Such a procedure tends to overestimate the fin heat transfer rate.

The extent of the temperature depression was examined in [1]<sup>3</sup> for the case of a single longitudinal fin affixed to a thick wall of large surface area. The results of that analysis demonstrated the existence of temperature depressions which affected the fin heat transfer by 10–20 percent.

It is reasonable to expect that the temperature depression at the base of a fin will depend on the presence and proximity of adjacent fins. Another factor that should be relevant is the nature of the heat transfer process on the back side of the finned wall, for example, the magnitude of the back side convective heat transfer coefficient. These factors were not included in [1]. They will be taken into account in the present analysis of the temperature-depression phenomenon.

A recent paper by Shih and Westwater [2] which dealt with the conductive interaction between a multifin array and a base surface was specifically concerned with fins situated in boiling liquids

(water and Freon at atmospheric pressure). The effect of the fin base-temperature depression on the results was not identified as such, although it was automatically taken into account in the finite-difference solution. One of the major conclusions was that the fin heat transfer can be adequately predicted by a one-dimensional conduction model for the fin, but that the base temperature remains as an important item of uncertainty.

The physical situation that is studied here is shown schematically in the left-hand diagram of Fig. 1. The sketch depicts an externally finned circular tube. The angular half-space  $\omega$  between the fins is equal to  $\pi/N$ , where  $N$  is the number of fins. The half angle subtended on the outside surface of the tube by the fin base is  $\alpha$ . The temperature in the fluid environment outside the tube is  $T_\infty$ , while the bulk temperature of the fluid flowing in the tube is  $T_m$ .

In the conventional analysis of heat transfer through a finned tube such as that of Fig. 1, the outside surface temperature  $T_w$  is assumed to be circumferentially uniform [3]. Its value is found from an overall heat balance which is based on purely radial heat conduction in the tube wall. If an asterisk is used to denote the case of assumed circumferential temperature uniformity, then

$$[2N(\omega - \alpha)r_0h_0 + 2N\alpha r_0\hat{h}](T_w^* - T_\infty) = (T_m - T_w^*)/[\ln(r_0/r_i)/2\pi k_t + 1/h_i2\pi r_i] \quad (1)$$

or

$$\frac{T_m - T_w^*}{T_w^* - T_\infty} = \frac{Bi_0}{2} \left[ \frac{(\omega - \alpha)}{\omega} + \left(\frac{\alpha}{\omega}\right) \frac{\hat{h}}{h_0} \right] \left[ \ln\left(\frac{r_0}{r_i}\right) + \frac{2}{Bi_i} \right] \quad (2)$$

in which  $h_i$  and  $h_0$ , respectively represent the transfer coefficients at the tube bore and on the unfinned portion of the external surface of the tube. The corresponding Biot numbers  $Bi_i$  and  $Bi_0$  are

$$Bi_i = h_i2r_i/k_t, \quad Bi_0 = h_02r_0/k_t \quad (3)$$

The quantity  $\hat{h}$  is an overall heat transfer coefficient for the fin defined so that

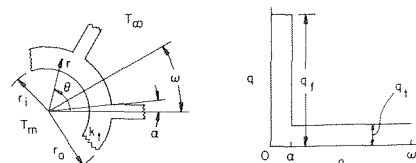


Fig. 1 Schematic of finned tube (left-hand diagram) and surface heat flux model (right-hand diagram)

<sup>1</sup> Department of Mechanical Engineering, University of Minnesota, Minneapolis, Minn.

<sup>2</sup> Department of Mechanical Engineering, University of Minnesota, Minneapolis, Minn. On leave from the Mechanical Engineering Department, University of Maine, Orono, Maine.

<sup>3</sup> Numbers in brackets designate References at end of technical brief.

Contributed by the Heat Transfer Division of THE AMERICAN SOCIETY OF MECHANICAL ENGINEERS. Manuscript received by the Heat Transfer Division March 11, 1975.

$$q_f = Q_f / (2r_0\alpha) = \hat{h}(T_{wf} - T_\infty) \quad (4)$$

where  $Q_f$  is the fin heat transfer rate per unit axial length and  $q_f$  is the corresponding rate of heat transfer per unit area at the fin-base interface (note that  $2r_0\alpha$  is the fin thickness at the interface).  $T_{wf}$  denotes the temperature at the base of the fin. Expressions for  $\hat{h}$  for various fin profiles are easily deduced from fin heat transfer equations given in standard texts.

Once a value of  $T_w^*$  has been determined from equation (2), it may be introduced into equation (4) to yield  $q_f^*$  and  $Q_f^*$ .

Owing to the depression that was discussed earlier, the temperature at the fin-base interface is different from that on the unfinned portion of the tube, and the circumferential uniformity employed in deriving equations (1) and (2) is not a reality. Therefore, the actual fin heat transfer rate  $Q_f$  will differ from the value  $Q_f^*$  that is calculated by the simplified model. Consideration will now be given to an analysis that takes account of the circumferential nonuniformities and identifies the extent of the errors in  $Q_f^*$ .

### Analysis

In the present approach, the temperature distribution  $T(r, \theta)$  in the tube wall will be determined via a solution of Laplace's equation. The formulation of the problem was shaped so as to facilitate an analytical solution. The motivation for the analytical solution, in contrast to a numerical solution, is that there are five or more parameters which can be independently prescribed.

At the tube bore ( $r = r_i$ ), a convective boundary condition was imposed so that  $-k_t(\partial T/\partial r) = h_i(T_m - T)$ . The boundary condition at the outer surface of the tube was modeled by the heat flux distribution pictured in the right-hand diagram of Fig. 1. The heat fluxes  $q_f$  and  $q_t$  were determined by an iterative procedure that takes account of the differences in temperature between the fin-base interface and the unfinned portion of the tube surface. The iterative procedure will be described shortly.

With the use of the aforementioned boundary conditions, a separation of variables solution of Laplace's equation can readily be obtained. From such a solution, average temperatures at the fin-base interface and on the unfinned portion of the tube surface can be evaluated from

$$\bar{T}_{wf} = \frac{1}{\alpha} \int_0^\alpha T_w d\theta, \quad \bar{T}_{wt} = \frac{1}{\omega - \alpha} \int_\alpha^\omega T_w d\theta \quad (5)$$

It is of interest to compare these temperatures with  $T_w^*$ , which is the circumferentially uniform outside surface temperature given by equation (2). With this in mind and using equation (2), the expressions which stem from equation (5) can be rephrased in the form

$$\frac{\bar{T}_{wf} - T_\infty}{T_w^* - T_\infty} = \frac{(1 + \Omega_1)[1 - \Omega_2(1 + \frac{\alpha}{\omega - \alpha})S]}{1 + \Omega_2(1 - \frac{\alpha}{\omega - \alpha})S} \quad (6)$$

$$\frac{\bar{T}_{wt} - T_\infty}{T_w^* - T_\infty} = \frac{1 + \Omega_1}{1 + \Omega_2(1 - \frac{\alpha}{\omega - \alpha})S} \quad (7)$$

Equation (6) compares the thermal driving force for fin heat transfer as given by the present analysis with that of the simplified circumferentially uniform model. A similar comparison is made in equation (7) for the unfinned portion of the tube surface.

The quantity  $\Omega_1$  represents an algebraic expression which contains several of the parameters of the problem.

$$\Omega_1 = \frac{\text{Bi}_0}{2} \left[ \frac{\omega - \alpha}{\omega} + \left( \frac{\alpha}{\omega} \right) \frac{\hat{h}}{h_0} \right] \left[ \ln \left( \frac{r_0}{r_i} \right) + \frac{2}{\text{Bi}_i} \right] \quad (8)$$

$\Omega_2$  is identical to  $\Omega_1$ , except that  $\hat{h}/h_0$  is replaced by  $q_f/q_t$ .  $S$  is a series given by

$$S = \left( \sum_{n=1}^{\infty} \alpha_n \Lambda_n \sin \lambda_n \alpha \right) / \alpha \left[ \ln \left( \frac{r_0}{r_i} \right) + \frac{2}{\text{Bi}_i} \right] \quad (9)$$

where

$$\Lambda_n \lambda_n^2 = \frac{1 + \gamma_n (r_i/r_0)^{2\lambda_n}}{1 - \gamma_n (r_i/r_0)^{2\lambda_n}}, \quad \gamma_n = \frac{1 - (\text{Bi}_i/2\lambda_n)}{1 + (\text{Bi}_i/2\lambda_n)} \quad (10)$$

and the  $\lambda_n$  are eigenvalues equal to  $n\pi/\omega = nN$ . The series  $S$  also contains the  $\alpha_n$ , which are the Fourier coefficients of the  $q$  versus  $\theta$  distribution shown in the right-hand side of Fig. 1. The  $\alpha_n$  are expressed by

$$\alpha_n = \frac{2 \sin \lambda_n \alpha}{\lambda_n \omega} \left[ \frac{q_f/q_t - 1}{(\alpha/\omega)(q_f/q_t - 1) + 1} \right] \quad (11)$$

As a final ingredient for the application for the solution, an expression for  $\hat{h}/h_0$  must be provided. In general, this ratio depends on the fin characteristics (height, thickness, conductivity) as well as on the participating heat transfer coefficients. To restrain the number of parameters, consideration will be given to a fin with optimum dimensions [4, pp. 82-84], fin thermal conductivity equal to that of the base material, and fin surface heat transfer coefficient equal to  $h_0$ . Then, by employing the results of [4], there is obtained

$$\hat{h}/h_0 = 1.258/\sqrt{\text{Bi}_0\alpha} \quad (12)$$

The iterative application of equations (6) and (7) will now be described. To begin, values are assigned to  $\text{Bi}_i$ ,  $\text{Bi}_0$ ,  $\alpha$ ,  $N$ , and  $r_i/r_0$ . Then, a trial value of  $q_f/q_t$  is selected, which enables the evaluation of  $\Omega_2$  and  $\alpha_n$ . With these and with the given parameters, all the inputs to the right-hand sides of equations (6) and (7) are available. Thus, the ratio  $(\bar{T}_{wf} - T_\infty)/(\bar{T}_{wt} - T_\infty)$  is readily determined. The fin and tube heat fluxes are assumed to be expressible as

$$q_f = \hat{h}(\bar{T}_{wf} - T_\infty), \quad q_t = h_0(\bar{T}_{wt} - T_\infty) \quad (13)$$

so that

$$\frac{q_f}{q_t} = \frac{\hat{h}(\bar{T}_{wf} - T_\infty)}{h_0(\bar{T}_{wt} - T_\infty)} \quad (14)$$

Equation (14) enables a new value of  $q_f/q_t$  to be computed. If this is different from the initially assumed value, then the computation is repeated with the new  $q_f/q_t$  as input. The iteration is continued until convergence is obtained.

In light of equation (13) and noting that  $q^* = h(T_w^* - T_\infty)$ , the temperature ratios given by equations (6) and (7) also, respectively, represent  $q_f/q_f^*$  and  $q_t/q_t^*$ . Thus, the converged solution automatically yields a comparison of the presently calculated heat fluxes with those of the simplified model which neglects the temperature depression phenomenon.

### Results and Discussion

In view of space limitations, it is not possible to present results which reflect the variations of all five parameters. Variations were assigned to the Biot numbers  $\text{Bi}_i$  and  $\text{Bi}_0$  and to the number of fins  $N$ , whereas  $\alpha$  and  $r_i/r_0$  were assigned reasonable values, 0.05 radians (2.86°) and 0.9, respectively. The results for  $q_f/q_f^*$  and  $q_t/q_t^*$  are presented in Figs. 2 and 3, respectively. In each figure,  $\text{Bi}_0$  is the abscissa variable and  $\text{Bi}_i$  parameterizes the individual graphs. The curve parameter is  $N$ .

Turning first to Fig. 2, it is seen that the temperature depression phenomenon is manifested as a decrease in the fin heat transfer relative to that for the model which neglects circumferential temperature variations. The number of fins has a marked effect on the extent of the decrease. For the limiting case of a single fin, values of  $q_f/q_f^*$  substantially below one are in evidence in certain ranges of  $\text{Bi}_0$  and  $\text{Bi}_i$ . However, as the number of fins increases, the temperature depression effect becomes progressively less important and appears to be negligible when  $N \geq 12$ . Increases in the external Biot number  $\text{Bi}_0$  bring about an increase in the temperature depression effect (i.e., a decrease in the heat transfer ratio). On the other hand, the trends with  $\text{Bi}_i$  are not so clear cut.

Fig. 2 can be employed to identify the parameter ranges where the model of circumferential temperature uniformity is adequate as well as those ranges where it has to be replaced by a more com-

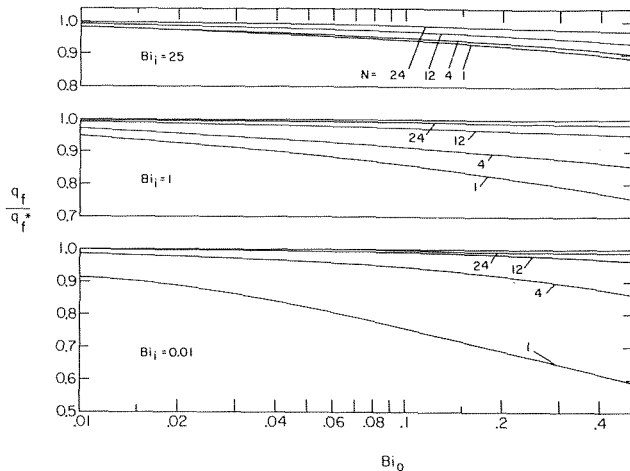


Fig. 2 Effect of fin base-temperature depression on fin heat flux

plete formulation. In this respect, it might be noted that the use of fins having a higher thermal conductivity than that of the base material would accentuate the temperature depression effect. Computations for the case of different conductivities can readily be performed with the present analytical model.

The results for the unfinned portion of the tube, given in Fig. 3, indicate a lesser influence of the fin base-temperature depression. The effect of the depression is manifested as a higher heat flux than that for the case of circumferential temperature uniformity.

The rate of heat transfer  $Q$  (per-unit-axial length) for the entire tube may be obtained by adding the contributions of the finned

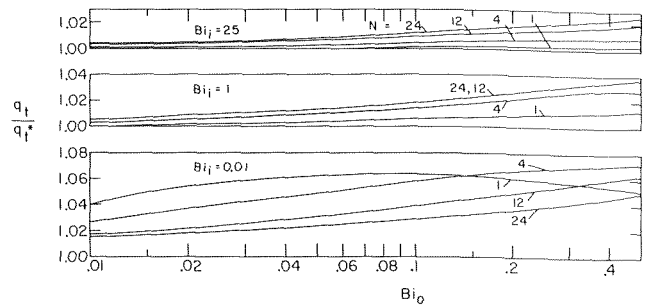


Fig. 3 Effect of fin base-temperature depression on the heat flux on the unfinned base

and unfinned portions, so that

$$Q = 2N[(\omega - \alpha)r_0q_t + \alpha r_0q_f] \quad (15)$$

Inasmuch as the effect of the temperature depression is to increase  $q_t$  and decrease  $q_f$ , equation (15) indicates that the effect on  $Q$  will lie somewhere between.

## References

- 1 Hennecke, D. K., and Sparrow, E. M., "Temperature Depression at the Base of a Fin," *JOURNAL OF HEAT TRANSFER, TRANS. ASME, Series C*, Vol. 92, 1970, pp. 204-206.
- 2 Shih, C. C., and Westwater, J. W., "Effect of Geometry and Wall Thickness on Heat Transfer From Longitudinal Fins to Boiling Liquids," Paper Bl.4, Fifth International Heat Transfer Conference, Tokyo, 1974.
- 3 Kern, D. Q., and Kraus, A. D., *Extended Surface Heat Transfer*, McGraw-Hill, New York, 1972.
- 4 Eckert, E. R. G., and Drake, R. M., Jr., *Analysis of Heat and Mass Transfer*, McGraw-Hill, New York, 1972.

## Thermal Resistance of a Cylinder With Two Diametrically Opposite, Symmetric, Isothermal Caps

G. E. Schneider<sup>1</sup>

### Nomenclature

- $A, B, C, D, E, F$  = point identification notation  
 $G$  = scale factor  
 $H$  = scale factor =  $-kH'$   
 $j$  = complex unit vector =  $\sqrt{-1}$   
 $k$  = transformation parameter, modulus of elliptic integral  
 $k'$  = complementary modulus of elliptic integral =  $(1 - k^2)^{1/2}$   
 $K$  = complete elliptic integral of the first kind  
 $K'$  = complete elliptic integral of the first kind of complementary modulus =  $K(k')$   
 $L$  = cylinder length  
 $o$  = coordinate origin  
 $r$  = radius

- $r_0$  = cylinder radius  
 $R_T$  = total cylinder thermal resistance  
 $t$  = position vector in second plane =  $u + jv$   
 $T$  = temperature  
 $w$  = position vector in third plane =  $\xi + j\beta$   
 $\alpha$  = contact half angle  
 $\zeta$  = position vector in initial plane =  $x + jy$   
 $\theta$  = angular coordinate in initial plane  
 $\lambda$  = thermal conductivity  
 $\phi$  = position vector in final plane =  $\eta + j\psi$

### Introduction

Heat transfer across a cylinder contacting two solids is of importance to engineers and researchers in both aerospace and cryogenic engineering. Heat generated by electronic equipment is often forced to flow through roller bearing supports while in cryogenic applications, cylindrical members can be used as insulatory, structural standoffs. In both of the foregoing applications, for small contacts the actual contact can be approximated as that of a circular arc, with the arc length determined using Hertz's theory of elastic contacts [1].<sup>2</sup>

An exact solution is presented for determining the thermal resistance of a solid cylinder under the influence of two diametrically opposite, symmetric, isothermal caps. The remainder of the outer surface is impervious to heat transfer resulting in a mixed boundary condition specification over this surface. The solution is obtained using three successive conformal transformations and is

<sup>1</sup> Project Engineer, Thermal Engineering Group, Department of Mechanical Engineering, University of Waterloo, Waterloo, Ontario, Canada

Contributed by the Heat Transfer Division of THE AMERICAN SOCIETY OF MECHANICAL ENGINEERS. Manuscript received by the Heat Transfer Division February 1, 1975.

<sup>2</sup> Numbers in brackets designate References at end of technical brief.

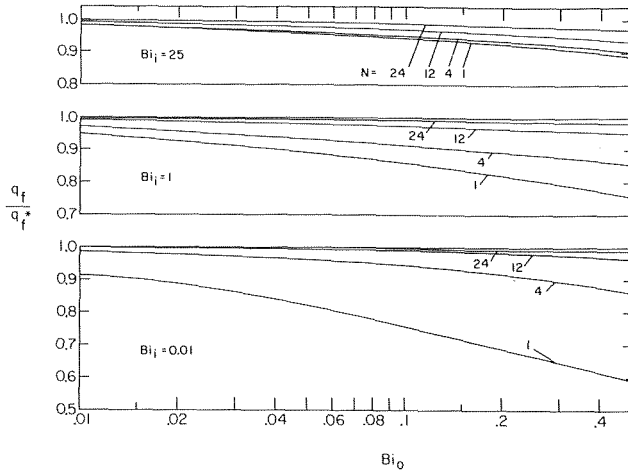


Fig. 2 Effect of fin base-temperature depression on fin heat flux

plete formulation. In this respect, it might be noted that the use of fins having a higher thermal conductivity than that of the base material would accentuate the temperature depression effect. Computations for the case of different conductivities can readily be performed with the present analytical model.

The results for the unfinned portion of the tube, given in Fig. 3, indicate a lesser influence of the fin base-temperature depression. The effect of the depression is manifested as a higher heat flux than that for the case of circumferential temperature uniformity.

The rate of heat transfer  $Q$  (per-unit-axial length) for the entire tube may be obtained by adding the contributions of the finned

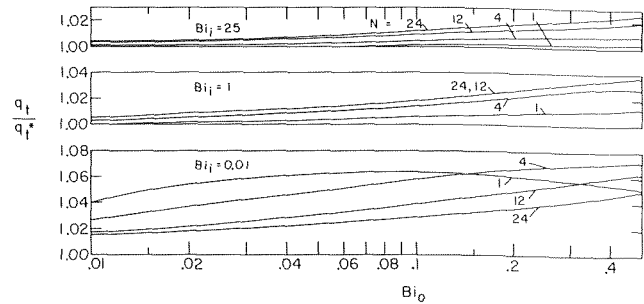


Fig. 3 Effect of fin base-temperature depression on the heat flux on the unfinned base

and unfinned portions, so that

$$Q = 2N[(\omega - \alpha)r_0q_t + \alpha r_0q_f] \quad (15)$$

Inasmuch as the effect of the temperature depression is to increase  $q_t$  and decrease  $q_f$ , equation (15) indicates that the effect on  $Q$  will lie somewhere between.

## References

- 1 Hennecke, D. K., and Sparrow, E. M., "Temperature Depression at the Base of a Fin," *JOURNAL OF HEAT TRANSFER, TRANS. ASME, Series C*, Vol. 92, 1970, pp. 204-206.
- 2 Shih, C. C., and Westwater, J. W., "Effect of Geometry and Wall Thickness on Heat Transfer From Longitudinal Fins to Boiling Liquids," Paper Bl.4, Fifth International Heat Transfer Conference, Tokyo, 1974.
- 3 Kern, D. Q., and Kraus, A. D., *Extended Surface Heat Transfer*, McGraw-Hill, New York, 1972.
- 4 Eckert, E. R. G., and Drake, R. M., Jr., *Analysis of Heat and Mass Transfer*, McGraw-Hill, New York, 1972.

## Thermal Resistance of a Cylinder With Two Diametrically Opposite, Symmetric, Isothermal Caps

G. E. Schneider<sup>1</sup>

### Nomenclature

- $A, B, C, D, E, F$  = point identification notation  
 $G$  = scale factor  
 $H$  = scale factor =  $-kH'$   
 $j$  = complex unit vector =  $\sqrt{-1}$   
 $k$  = transformation parameter, modulus of elliptic integral  
 $k'$  = complementary modulus of elliptic integral =  $(1 - k^2)^{1/2}$   
 $K$  = complete elliptic integral of the first kind  
 $K'$  = complete elliptic integral of the first kind of complementary modulus =  $K(k')$   
 $L$  = cylinder length  
 $o$  = coordinate origin  
 $r$  = radius

- $r_0$  = cylinder radius  
 $R_T$  = total cylinder thermal resistance  
 $t$  = position vector in second plane =  $u + jv$   
 $T$  = temperature  
 $w$  = position vector in third plane =  $\xi + j\beta$   
 $\alpha$  = contact half angle  
 $\zeta$  = position vector in initial plane =  $x + jy$   
 $\theta$  = angular coordinate in initial plane  
 $\lambda$  = thermal conductivity  
 $\phi$  = position vector in final plane =  $\eta + j\psi$

### Introduction

Heat transfer across a cylinder contacting two solids is of importance to engineers and researchers in both aerospace and cryogenic engineering. Heat generated by electronic equipment is often forced to flow through roller bearing supports while in cryogenic applications, cylindrical members can be used as insulatory, structural standoffs. In both of the foregoing applications, for small contacts the actual contact can be approximated as that of a circular arc, with the arc length determined using Hertz's theory of elastic contacts [1].<sup>2</sup>

An exact solution is presented for determining the thermal resistance of a solid cylinder under the influence of two diametrically opposite, symmetric, isothermal caps. The remainder of the outer surface is impervious to heat transfer resulting in a mixed boundary condition specification over this surface. The solution is obtained using three successive conformal transformations and is

<sup>1</sup> Project Engineer, Thermal Engineering Group, Department of Mechanical Engineering, University of Waterloo, Waterloo, Ontario, Canada

Contributed by the Heat Transfer Division of THE AMERICAN SOCIETY OF MECHANICAL ENGINEERS. Manuscript received by the Heat Transfer Division February 1, 1975.

<sup>2</sup> Numbers in brackets designate References at end of technical brief.

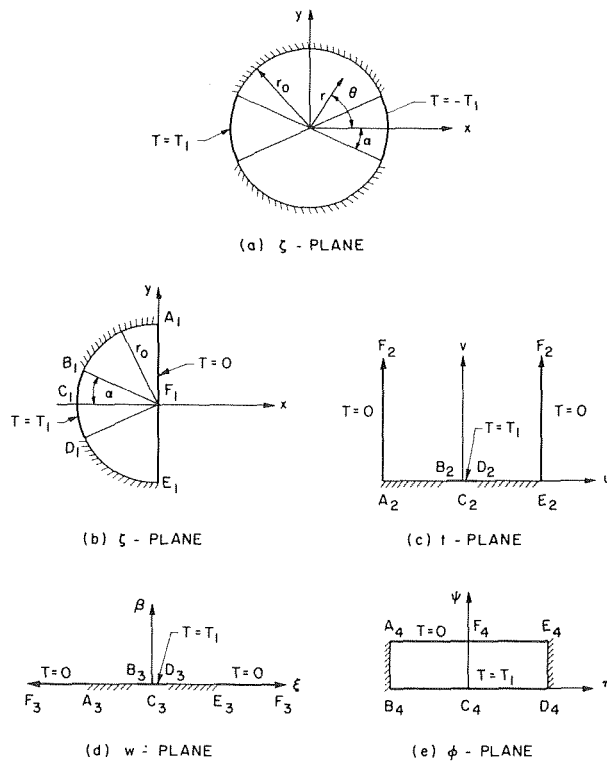


Fig. 1

compared with existing test data and the approximation of Yovanovich and Coutanceau [2].

### Analysis

The problem under consideration is illustrated in Fig. 1(a). Due to the assumed symmetry of the contact size about the plane defined by the surfaces  $\theta = \pi/2$  and  $\theta = 3\pi/2$ , the cylinder midplane will be isothermal at  $T = 0$ . The problem to be examined is then that of Fig. 1(b).

The first step of the solution is to transform the  $z$ -plane of Fig. 1(b) to the complex  $t$ -plane shown in Fig. 1(c). This can be accomplished by the transformation [3],

$$t = (\theta - \pi) + j \ln(r_0/\gamma) \quad (1)$$

with the correspondence of points as indicated in the figure.

The interior region of Fig. 1(c) can be further transformed into the upper half-space of the  $w$ -plane, Fig. 1(d), using the Schwartz-Christoffel transformation [4]. The transformation in differential form is given by

$$\frac{dt}{dw} = G(w - 1/k)^{-1/2}(w + 1/k)^{-1/2} \quad (2)$$

where  $G$  is the complex scale factor of transformation. Integrating equation (2) and matching corresponding points yields the transformation equation

$$t = \sin^{-1}(kw) \quad (3)$$

To determine  $k$  of equation (3), the correspondence  $w = 1$  where  $t = \alpha$  is used. This defines  $k$  by

$$k = \sin(\alpha) \quad (4)$$

Yovanovich and Coutanceau used a bilinear transformation to transform to Fig. 1(d) and then obtained an approximate solution for this system using elliptic cylinder coordinates [5].

The third and final transformation transforms the upper half-space of the  $w$ -plane to the interior of the rectangle in the  $\phi$ -plane of Fig. 1(e) where the field is uniform. Again the Schwartz-Christoffel transformation is used where now

$$\frac{d\phi}{dw} = H'(w - 1)^{-1/2}(w + 1)^{-1/2}(w - 1/k)^{-1/2}(w + 1/k)^{-1/2} \quad (5)$$

Integrating equation (5) leads to the transformation equation [4]

$$w = (1/H) \operatorname{sn}(\phi, k) \quad (6)$$

where  $H = -kH'$  and  $\operatorname{sn}(\phi, k)$  is the Jacobian elliptic sine amplitude function. The scale factor of transformation,  $H$ , can be arbitrarily set to unity without loss of generality. We then have

$$w = \operatorname{sn}(\phi, k) \quad (7)$$

Inspection of Fig. 1(e) where the internal field is uniform now permits determination of the resistance of Fig. 1(b) as simply

$$R_T/2 = (1/\lambda L) |D_4 E_4| / |2 C_4 D_4| \quad (8)$$

Using the transformation equations given in the foregoing it can be shown that [4]

$$|C_4 D_4| = K(k); |D_4 E_4| = K'(k) \quad (9)$$

Now, since the cylinder resistance is twice that of the subdivided problem, the total dimensionless resistance is determined from

$$R_T \lambda L = K'(\sin \alpha) / K(\sin \alpha) \quad (10)$$

where  $K(\sin \alpha)$  and  $K'(\sin \alpha)$  are the complete elliptic integral and complementary complete elliptic integral respectively of the first kind of modulus  $k = \sin(\alpha)$ .

Yovanovich and Coutanceau give for their approximation of this problem the expression [2]

$$R_T \lambda L = (2/\pi) \ln [2(1 + \cos \alpha) / \sin \alpha] \quad (11)$$

In both cases the angle  $\alpha$  is the contact half-angle and the heat flow must be symmetric about the bisecting diameter.

### Results

The results of equations (10) and (11) as well as the available test data [2] are presented in Table 1. The excellent agreement of the available test data with this solution supports the analysis presented here throughout the entire range of contact half-angles.

More surprising, however, is that the approximation of Yovanovich and Coutanceau [2], can be extended to very large values of the caps subtending half-angle. For contact half-angles of less than 45 deg, the approximation error is less than 0.2 percent; for  $\alpha$  less than 65 deg

Table 1  $R\lambda L$  versus cap half-angle

Half-angle, $\alpha$	8.90	18.17	35.98	54.02	72.01	78.11	84.09	88.75
Test data [2]	2.09	1.61	1.16	0.87	0.63	0.54	0.43	0.31
Equation (10)	2.07	1.61	1.16	0.86	0.62	0.53	0.43	0.30
Equation (11)	2.07	1.61	1.16	0.87	0.64	0.57	0.51	0.45

the approximation error is less than 2 percent. This close agreement also suggests that for engineering purposes where 0.2 percent accuracy is acceptable the approximation can be used that

$$K'(k)/K(k) \approx (2/\pi) \ln [2(1 + k')/k]; k \leq 0.707 \quad (12)$$

where  $k' = (1 - k^2)^{1/2}$  is the complementary modulus. Using the

properties of elliptic integrals [6],

$$K'(k)/K(k) = K(k')/K'(k') \quad (13)$$

similar accuracy can also be obtained for  $k$  greater than 0.707 by the approximation

$$K'(k)/K(k) \approx (\pi/2) \{\ln [2(1+k)/k']\}^{-1}; k \geq 0.707 \quad (14)$$

The approximations indicated by equations (12) and (14) are valuable ones since an accuracy of approximately 0.2 percent can be obtained without direct access to tables of elliptic integrals.

## Conclusions

An exact solution to the problem described in this note has been presented.

Of far greater significance than merely the solution technique applied to this problem, however, are the approximations found in equations (12) and (14) for ratios of complete elliptic integrals of the first kind. Due to the very large number of solutions that take this form [3, 4], these approximations shall undoubtedly prove invaluable to both the researcher and the practicing engineer since their evaluation is of such computational simplicity.

## Acknowledgments

The author is grateful to Prof. M. M. Yovanovich for suggesting the problem. Financial support of the National Research Council and the Communications Research Center (Department of Communications) is appreciated.

## References

- 1 Yovanovich, M. M., "Thermal Conductance of a Row of Cylinders Contacting Two Planes," *Fundamentals of Spacecraft Thermal Design, Progress in Astronautics and Aeronautics*, J. W. Lucas, ed., MIT Press, Cambridge, Mass., Vol. 29, 1972, pp. 307-317.
- 2 Yovanovich, M. M., and Coutanceau, J., "Sur la détermination de la résistance thermique transverse d'un cylindre de révolution homogène isotrope avec des conditions aux limites mixtes," *Comptes Rendus de l'Académie Sciences*, Paris, Vol. 268, Mar. 1969, pp. B821-823.
- 3 Binns, K. J., and Lawrenson, P. J., *Analysis and Computation of Electric and Magnetic Field Problems*, MacMillan, New York, 1963, pp. 126-128.
- 4 Gibbs, W. J., *Conformal Transformations in Electrical Engineering*, Chapman and Hall Ltd., London, 1958, pp. 148-158.
- 5 Yovanovich, M. M., *Advanced Heat Conduction*, Chapter 4, to be published.
- 6 Abramowitz, M., and Stegun, I. A., *Handbook of Mathematical Functions*, Dover Publications, New York, pp. 589-592.

## Transient Two-Dimensional Problems Utilizing The Least Squares Algorithm

J. C. Bruch, Jr.,<sup>1</sup> and R. W. Lewis<sup>2</sup>

The least squares time-stepping algorithm, which has previously been shown by the authors to be competitive for one-dimensional problems, is applied to the solution of several two-dimensional examples having constant material properties. The results are compared against answers obtained using recurrence relationships based on the finite element and finite difference methods.

<sup>1</sup> Mechanical and Environmental Engineering Department, University of California, Santa Barbara, Calif.

<sup>2</sup> Civil Engineering Department, University of Wales, Swansea, United Kingdom.

Contributed by the Heat Transfer Division of THE AMERICAN SOCIETY OF MECHANICAL ENGINEERS. Manuscript received by the Heat Transfer Division October 21, 1974.

Analytical results for one of the examples are also used for comparison. The least squares algorithm proved to be more accurate for equal values of time step especially in the large time step cases. It, however, requires more computer time and storage than the other methods used. Several other limitations of the scheme are also presented.

## Introduction

The least squares method was first applied to time dependent problems by Zienkiewicz and Lewis [1]<sup>3</sup> and later extended to both linear and nonlinear one-dimensional field problems by Lewis and Bruch [2]. The least squares method was shown to be superior to the other time-stepping algorithms which included the finite difference Crank-Nicolson and finite element-in-time schemes. The additional computational effort required by the least squares algorithm was more than compensated for by the increased accuracy achieved with larger time steps.

It was decided to extend the work to determine if this performance of the least squares algorithm was still observed when applied to two-dimensional problems. The stiffness and mass matrices were again derived from a finite element spatial discretization generating banded matrices which on multiplication have twice the band width. Thus, only partial assembly of the equations is required.

The examples chosen were the following heat flow problems. The first case is the temperature distribution in an infinitely long bar of thermal diffusivity  $\alpha$  with square cross section of side  $2L$ . The bar is initially at a uniform temperature  $T_0$  and then suddenly has its surface maintained at the temperature  $T_1$ . If dimensionless distances, time, and temperature are defined by  $X = x/L$ ,  $Y = y/L$ ,  $\tau = \alpha t/L^2$ , and  $\theta = T - T_0/T_1 - T_0$ , then the mathematical model for this problem is

$$\frac{\partial^2 \theta}{\partial X^2} + \frac{\partial^2 \theta}{\partial Y^2} = \frac{\partial \theta}{\partial \tau}, \quad \frac{\partial \theta}{\partial X}(X, 0, \tau) = \frac{\partial \theta}{\partial Y}(0, Y, \tau) = 0 \quad (1)$$

$$\theta(1, Y, \tau) = \theta(X, 1, \tau) = 1.0, \quad \theta(X, Y, 0) = 0 \quad (1a)$$

Note: because of the symmetry the problem is only solved in one quadrant.

The second heat flow problem is one which has sharp corners in the boundary as shown in Fig. 1. This problem has been previously investigated by Bell [3]. Using the same notation that he employed, the differential equation governing the temperature distribution within the domain  $R$  is given by

$$\frac{\partial^2 T}{\partial x^2} + \frac{\partial^2 T}{\partial y^2} = \frac{\partial T}{\partial t} \quad (2)$$

where  $T(x, y, t)$  is the temperature. The boundary conditions for this particular problem were as follows

$$T(0, y, t) = 1000, \quad T(1, y, t) = 0 \quad (2a)$$

and  $\partial T/\partial n = 0$  for all other boundaries where  $\partial/\partial n$  is the derivative normal to the boundary. The initial condition is a small time solution in a plane medium and is given by

$$T(x, y, 0) = 10^3 \operatorname{erfc} \left( \frac{x}{2\sqrt{t}} \right) \quad (2b)$$

where  $t = 0.0005$  and is equivalent to one time step for the 200 time step case so that comparison can be made with published data at  $t = 0.1$ . The sharp corners in the boundary give rise to singularities which Bell [3] has studied. His method is linked with an explicit finite difference scheme and hence the overall technique is essentially explicit. Bell [3] did not specify any dimensions for the variables in this problem but an appropriate set might be: thermal diffusivity ( $\text{ft}^2/\text{hr}$ ),  $x$  and  $y$  coordinates (ft), time (hr), temperature ( $^\circ\text{F}$ ).

<sup>3</sup> Numbers in brackets designate References at end of technical papers.

properties of elliptic integrals [6],

$$K'(k)/K(k) = K(k')/K'(k') \quad (13)$$

similar accuracy can also be obtained for  $k$  greater than 0.707 by the approximation

$$K'(k)/K(k) \approx (\pi/2) \{\ln [2(1+k)/k']\}^{-1}; k \geq 0.707 \quad (14)$$

The approximations indicated by equations (12) and (14) are valuable ones since an accuracy of approximately 0.2 percent can be obtained without direct access to tables of elliptic integrals.

## Conclusions

An exact solution to the problem described in this note has been presented.

Of far greater significance than merely the solution technique applied to this problem, however, are the approximations found in equations (12) and (14) for ratios of complete elliptic integrals of the first kind. Due to the very large number of solutions that take this form [3, 4], these approximations shall undoubtedly prove invaluable to both the researcher and the practicing engineer since their evaluation is of such computational simplicity.

## Acknowledgments

The author is grateful to Prof. M. M. Yovanovich for suggesting the problem. Financial support of the National Research Council and the Communications Research Center (Department of Communications) is appreciated.

## References

- 1 Yovanovich, M. M., "Thermal Conductance of a Row of Cylinders Contacting Two Planes," *Fundamentals of Spacecraft Thermal Design, Progress in Astronautics and Aeronautics*, J. W. Lucas, ed., MIT Press, Cambridge, Mass., Vol. 29, 1972, pp. 307-317.
- 2 Yovanovich, M. M., and Coutanceau, J., "Sur la détermination de la résistance thermique transverse d'un cylindre de révolution homogène isotrope avec des conditions aux limites mixtes," *Comptes Rendus de l'Académie Sciences*, Paris, Vol. 268, Mar. 1969, pp. B821-823.
- 3 Binns, K. J., and Lawrenson, P. J., *Analysis and Computation of Electric and Magnetic Field Problems*, MacMillan, New York, 1963, pp. 126-128.
- 4 Gibbs, W. J., *Conformal Transformations in Electrical Engineering*, Chapman and Hall Ltd., London, 1958, pp. 148-158.
- 5 Yovanovich, M. M., *Advanced Heat Conduction*, Chapter 4, to be published.
- 6 Abramowitz, M., and Stegun, I. A., *Handbook of Mathematical Functions*, Dover Publications, New York, pp. 589-592.

## Transient Two-Dimensional Problems Utilizing The Least Squares Algorithm

J. C. Bruch, Jr.,<sup>1</sup> and R. W. Lewis<sup>2</sup>

*The least squares time-stepping algorithm, which has previously been shown by the authors to be competitive for one-dimensional problems, is applied to the solution of several two-dimensional examples having constant material properties. The results are compared against answers obtained using recurrence relationships based on the finite element and finite difference methods.*

<sup>1</sup> Mechanical and Environmental Engineering Department, University of California, Santa Barbara, Calif.

<sup>2</sup> Civil Engineering Department, University of Wales, Swansea, United Kingdom.

Contributed by the Heat Transfer Division of THE AMERICAN SOCIETY OF MECHANICAL ENGINEERS. Manuscript received by the Heat Transfer Division October 21, 1974.

*Analytical results for one of the examples are also used for comparison. The least squares algorithm proved to be more accurate for equal values of time step especially in the large time step cases. It, however, requires more computer time and storage than the other methods used. Several other limitations of the scheme are also presented.*

## Introduction

The least squares method was first applied to time dependent problems by Zienkiewicz and Lewis [1]<sup>3</sup> and later extended to both linear and nonlinear one-dimensional field problems by Lewis and Bruch [2]. The least squares method was shown to be superior to the other time-stepping algorithms which included the finite difference Crank-Nicolson and finite element-in-time schemes. The additional computational effort required by the least squares algorithm was more than compensated for by the increased accuracy achieved with larger time steps.

It was decided to extend the work to determine if this performance of the least squares algorithm was still observed when applied to two-dimensional problems. The stiffness and mass matrices were again derived from a finite element spatial discretization generating banded matrices which on multiplication have twice the band width. Thus, only partial assembly of the equations is required.

The examples chosen were the following heat flow problems. The first case is the temperature distribution in an infinitely long bar of thermal diffusivity  $\alpha$  with square cross section of side  $2L$ . The bar is initially at a uniform temperature  $T_0$  and then suddenly has its surface maintained at the temperature  $T_1$ . If dimensionless distances, time, and temperature are defined by  $X = x/L$ ,  $Y = y/L$ ,  $\tau = \alpha t/L^2$ , and  $\theta = T - T_0/T_1 - T_0$ , then the mathematical model for this problem is

$$\frac{\partial^2 \theta}{\partial X^2} + \frac{\partial^2 \theta}{\partial Y^2} = \frac{\partial \theta}{\partial \tau}, \quad \frac{\partial \theta}{\partial X}(X, 0, \tau) = \frac{\partial \theta}{\partial Y}(0, Y, \tau) = 0 \quad (1)$$

$$\theta(1, Y, \tau) = \theta(X, 1, \tau) = 1.0, \quad \theta(X, Y, 0) = 0 \quad (1a)$$

Note: because of the symmetry the problem is only solved in one quadrant.

The second heat flow problem is one which has sharp corners in the boundary as shown in Fig. 1. This problem has been previously investigated by Bell [3]. Using the same notation that he employed, the differential equation governing the temperature distribution within the domain  $R$  is given by

$$\frac{\partial^2 T}{\partial x^2} + \frac{\partial^2 T}{\partial y^2} = \frac{\partial T}{\partial t} \quad (2)$$

where  $T(x, y, t)$  is the temperature. The boundary conditions for this particular problem were as follows

$$T(0, y, t) = 1000, \quad T(1, y, t) = 0 \quad (2a)$$

and  $\partial T/\partial n = 0$  for all other boundaries where  $\partial/\partial n$  is the derivative normal to the boundary. The initial condition is a small time solution in a plane medium and is given by

$$T(x, y, 0) = 10^3 \operatorname{erfc} \left( \frac{x}{2\sqrt{t}} \right) \quad (2b)$$

where  $t = 0.0005$  and is equivalent to one time step for the 200 time step case so that comparison can be made with published data at  $t = 0.1$ . The sharp corners in the boundary give rise to singularities which Bell [3] has studied. His method is linked with an explicit finite difference scheme and hence the overall technique is essentially explicit. Bell [3] did not specify any dimensions for the variables in this problem but an appropriate set might be: thermal diffusivity ( $\text{ft}^2/\text{hr}$ ),  $x$  and  $y$  coordinates (ft), time (hr), temperature ( $^\circ\text{F}$ ).

<sup>3</sup> Numbers in brackets designate References at end of technical papers.

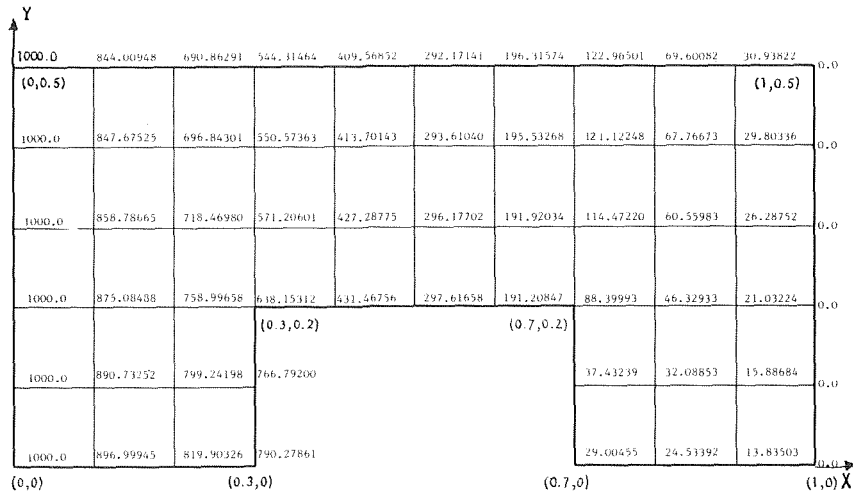


Fig. 1 Solution corresponding to a time of 0.1 (500 time-steps)—values in brackets are the coordinates for the corners of the solution domain

### Finite Element Formulation of Equation (2)

The spatial discretization of equation (2), which will be similar for equation (1) because their forms are the same, was obtained by use of Galerkin approximations to solutions of the corresponding “generalized” or “weak” problems [6]. In place of equation (2) we consider the problem

$$\int_{\mathcal{R}} N_k \left( \frac{\partial T}{\partial t} - \frac{\partial^2 T}{\partial x^2} - \frac{\partial^2 T}{\partial y^2} \right) dx dy = 0 \quad (3)$$

with a given temperature or a prescribed flux along a boundary. The temperature distribution within an element of the discretized solution domain is approximated by

$$\hat{T} = \sum N_i(x, y) T_i(t)$$

where  $N_i$  are the shape functions defined piecewise, element by element, and  $T_i$  are the nodal temperature values. Integration by parts of equation (3) yields a set of equations of the following form

$$[K]\{T(t)\} + [C]\{\dot{T}(t)\} + \{f(t)\} = 0 \quad (4)$$

in which  $K$  and  $C$  are constant matrices. The terms in the matrix  $\{f(t)\}$  include information from surface integrals along boundaries on which flux boundary conditions other than  $\partial T/\partial n = 0$  are given. It also includes the known boundary temperatures times appropriate constants from element nodes that occur on boundaries with this type of boundary condition.

### Time-Stepping Algorithms

Three different time-stepping algorithms were used for comparative purposes. The first is the well known Crank-Nicolson finite difference scheme

$$T_{t+\Delta t} = (C/\Delta t + K/2)^{-1} \{ (C/\Delta t - K/2) T_t - f(t)_{t+\Delta t/2} \} \quad (5)$$

Also, a Galerkin finite element scheme was used.

$$T_{t+\Delta t} = (C/\Delta t + 2K/3)^{-1} \{ (C/\Delta t - K/3) T_t - 2 \int_0^{\Delta t} f(t) t dt / (\Delta t)^2 \} \quad (6)$$

Third, the least square algorithm first proposed by Zienkiewicz and Lewis [1] and extended by Lewis and Bruch [2] to one-dimensional problems, is also used.

$$T_{t+\Delta t} = [K^T K \Delta t / 3 + (K^T C + C^T K) / 2 + C^T C / \Delta t]^{-1} \times \{ [C^T C / \Delta t + (K^T C - C^T K) / 2 - K^T K \Delta t / 6] T_t - \frac{K^T}{\Delta t} \times \int_0^{\Delta t} f(t) t dt - \frac{C^T}{\Delta t} \int_0^{\Delta t} f(t) dt \} \quad (7)$$

### Numerical Results

The previously described example problems were solved with all three time-stepping schemes and an accuracy comparison made at a certain point in time. For problem one, the three time-stepping schemes were compared with results obtained from the analytical solution to equations (1).

The analytical results were used in the following relationship:

Percentage Error

$$= \frac{|\text{Exact Solution} - \text{Approximate Solution}| \times 100}{\text{Exact Solution}} \quad (8)$$

The expression given by equation (8) was used in determining the error at each grid point within the domain and these are summed to give an indication of the average error obtained with each time stepping scheme. These results are given in Table 1 for ranging values of time step size for these algorithms and for two space-size increments  $\Delta X = \Delta Y = 0.1$  and 0.2. It is seen that, generally, for large time steps, the least squares method gives a more accurate solution. The computer storage requirement for the CPU Time computer execution step for the case where  $\Delta X = \Delta Y = 0.1$  (100 unknowns) was 446 K for the least squares method, while it was 270 K for the Crank-Nicolson and Galerkin methods.

For case two, since there was no analytical solution to compare against, it was decided to run the problem, using both the least squares and Crank-Nicolson algorithms, with a small time-step of  $\Delta t = 0.0002$  and double precision in the computer programs and use the results obtained as a norm for comparison purposes.

These results are presented in Fig. 1 and were used as the exact solution in equation (8). Results of using equation (8) are given in Table 2 for ranging values of time step size for the three algorithms. From inspection of these results, it is clearly seen that the least squares and Crank-Nicolson schemes are superior to the Galerkin algorithm. However, as the magnitude of time step decreased the Crank-Nicolson scheme is marginally better and, of course, both tend to the same answers at  $\Delta t = 0.0002$ . All three schemes give more accurate answers for  $\Delta t = 0.0005$  than either

Table 1 Percentage errors at  $\tau = 0.75$

$\Delta X = \Delta Y$	Number of steps	$\Delta \tau$	Crank-Nicolson	Galerkin	Least squares
0.2	3	0.25	275.875	42.070	37.640
0.2	5	0.15	130.158	14.652	9.408
0.2	15	0.05	3.838	4.970	3.191
0.2	25	0.03	2.752	2.226	2.770
0.2	75	0.01	2.428	0.918	2.462
0.1	5	0.15	782.141	75.008	29.788

Table 2 Percentage errors at  $t = 0.100$

Number of steps	$\Delta t$	Crank-Nicolson	Galerkin	Least squares	5 term approx.	6 term approx.	Simple explicit	Finite element space-time coordinates
1	0.1000	1307.8825	794.6387	684.1022				
5	0.0200	90.6962	105.4658	12.5849				
10	0.0100	10.0853	50.7122	4.0053				
20	0.0050	2.2695	24.8791	1.3349				
100	0.0010	0.0854	4.9788	0.0913				
200	0.0005	0.0174	2.4932	0.0241	68.2511	117.0179	95.6633	76.0797

Bell's [3] five and six term approximates or Bruch and Zyvoloski's [5] finite element space-time discretization. It should be noted that the finite element space-time scheme results were obtained using single precision arithmetic and it can only be assumed that the five term approximate, six term approximate, and the explicit schemes were likewise calculated.

A comparison is also made of the relative computer (IBM 360/75) times required for matrix multiplication and for each subsequent recurrence calculation. All matrix inversions were performed by the same method (IBM Scientific Subroutine Package MINV). In the Crank-Nicolson scheme given by equation (5), the operation of matrix multiplication involves the terms  $(C/\Delta t + K/2)^{-1}$  and  $(C/\Delta t - K/2)$ , respectively. It is immediately obvious that much greater effort is required in setting up the matrix operations for the least squares scheme. The least squares algorithm required approximately 60 times the computer time necessary for this matrix multiplication compared to the other two schemes, but the computation time-per-time step after this evaluation was similar for all three methods. Because of the nature of the matrices which have to be inverted in equations (5) and (7), the first being block tri-diagonal while the second block penta-diagonal, it should be pointed out that if iteration had been used, rather than matrix inversion, the least squares method would be inferior to the Crank-Nicolson method.

Finally, investigating the errors,  $|\text{Exact Solution} - \text{Approximate Solution}|$  at the two critical points in the problem for the different schemes at  $\Delta t = 0.01$ , showed that at the point (0.3, 0.2) these were 0.27356, 5.35288, and 0.56149 for the Crank-Nicolson, Galerkin, and least squares methods, respectively. For the point (0.7, 0.2) the values were 0.15994, 1.40717, and 0.08012, respectively. If  $\Delta t = 0.0005$ , the errors at (0.3, 0.2) were 0.00139, 0.29591, and 0.00180, respectively, while they were 3.15312, 3.15312, 16.15312, and 3.52666 for the five-term approximation, six-term approximation, simple explicit, and finite element space-time coordinates methods, respectively. For the point (0.7, 0.2), the values were 0.00027, 0.06782, 0.00028, 0.39993, 2.39993, 2.60007, and 1.66018 for the seven methods, respectively. It should be noted that in general with all of the schemes except the simple explicit, the maximum error for each time step size for each scheme did not occur at one of the critical points. It did, however, usually occur within a couple of mesh points from the first critical point (0.3, 0.2).

### Summary and Conclusions

The least squares time stepping scheme first presented for one-dimensional problems has been applied to several two-dimensional examples having constant material properties. The least squares method is unconditionally stable as are the other methods used in the comparisons. As in the one-dimensional case, the least squares algorithm again proved to give more accurate results for equal values of time step especially in the large time step range. It should be noted that the usefulness of the least squares method is limited to problems having constant or space dependent material properties. If the material properties were dependant upon time or temperature, then new coefficient matrices in equation (4) would have to be determined at each time step or with each iteration. Thus, the amount of computer time would be very large. Another limitation, as pointed out in the first example, is the large amount of computer storage requirement as compared to other methods.

### Acknowledgments

Dr. Bruch and some of the computer work was supported by the Office of Water Resources Research, USDI, under the Allotment Program of Public Law 88-379, as amended, and by the University of California, Water Resources Center. It is a part of Office of Water Resources Research Project No. A-039-CAL (Water Resources Center Project W-336). Some of the computer work was also supported by Water Resources Center Project W-428 and by a University of California at Santa Barbara campus research computer grant.

The authors appreciate the assistance of Mr. Charles R. Meyer who programed the  $[K]$ ,  $[C]$ , and  $\{f\}$  matrices for the second example.

### References

- Zienkiewicz, O. C., and Lewis, R. W., "An Analysis of Various Time-Stepping Schemes for Initial Value Problems," *Earthquake Engr. & Struc. Dynamics*, Vol. 1, 1973, pp. 407-408.
- Lewis, R. W., and Bruch, J. C., Jr., "An Application of Least Squares to One-Dimensional Transient Problems," *Int. Jour. Num. Meth. Engr.*, Vol. 8, 1974, pp. 633-647.
- Bell, G. E., "A Method for Treating Boundary Singularities in Time-Dependent Problems," TR/8, Dept. of Math., Brunel University, Uxbridge, Middlesex, 1972, 19 pp.
- Motz, H., "The Treatment of Singularities of Partial Differential Equations by Relaxation Methods," *Quar. Jour. of Appl. Mathematics*, Vol. 4, 1946, pp. 371-377.
- Bruch, J. C., Jr., and Zyvoloski, G., "Transient Two-Dimensional Heat Conduction Problems Solved by the Finite Element Method," *Int. Jour. Num. Meth. Engr.*, Vol. 8, 1974, pp. 481-494.
- Schultz, M. H., *Spline Analysis*, Prentice-Hall, Englewood Cliffs, N. J., Chapter 9, 1973.

## Prediction of Turbulent-Free-Convective-Heat Transfer From a Vertical Flat Plate<sup>1</sup>

T. Cebeci<sup>2</sup> and A. Khattab<sup>2</sup>

### Introduction

Compared with the numerous investigations of turbulent forced convection boundary layers, relatively little work has been done on turbulent natural convection boundary-layer flows. The only studies known to the authors were made by Eckert and Jackson [1],<sup>3</sup>

<sup>1</sup> This work was supported by the National Science Foundation Grant No. ENG74-11895.

<sup>2</sup> Mechanical Engineering Department, California State University, Long Beach, Calif.

<sup>3</sup> Numbers in brackets designate References at end of technical brief.

Contributed by the Heat Transfer Division of THE AMERICAN SOCIETY OF MECHANICAL ENGINEERS. Manuscript received by the Heat Transfer Division March 31, 1975.

Table 2 Percentage errors at  $t = 0.100$

Number of steps	$\Delta t$	Crank-Nicolson	Galerkin	Least squares	5 term approx.	6 term approx.	Simple explicit	Finite element space-time coordinates
1	0.1000	1307.8825	794.6387	684.1022				
5	0.0200	90.6962	105.4658	12.5849				
10	0.0100	10.0853	50.7122	4.0053				
20	0.0050	2.2695	24.8791	1.3349				
100	0.0010	0.0854	4.9788	0.0913				
200	0.0005	0.0174	2.4932	0.0241	68.2511	117.0179	95.6633	76.0797

Bell's [3] five and six term approximates or Bruch and Zyvoloski's [5] finite element space-time discretization. It should be noted that the finite element space-time scheme results were obtained using single precision arithmetic and it can only be assumed that the five term approximate, six term approximate, and the explicit schemes were likewise calculated.

A comparison is also made of the relative computer (IBM 360/75) times required for matrix multiplication and for each subsequent recurrence calculation. All matrix inversions were performed by the same method (IBM Scientific Subroutine Package MINV). In the Crank-Nicolson scheme given by equation (5), the operation of matrix multiplication involves the terms  $(C/\Delta t + K/2)^{-1}$  and  $(C/\Delta t - K/2)$ , respectively. It is immediately obvious that much greater effort is required in setting up the matrix operations for the least squares scheme. The least squares algorithm required approximately 60 times the computer time necessary for this matrix multiplication compared to the other two schemes, but the computation time-per-time step after this evaluation was similar for all three methods. Because of the nature of the matrices which have to be inverted in equations (5) and (7), the first being block tri-diagonal while the second block penta-diagonal, it should be pointed out that if iteration had been used, rather than matrix inversion, the least squares method would be inferior to the Crank-Nicolson method.

Finally, investigating the errors, |Exact Solution - Approximate Solution| at the two critical points in the problem for the different schemes at  $\Delta t = 0.01$ , showed that at the point (0.3, 0.2) these were 0.27356, 5.35288, and 0.56149 for the Crank-Nicolson, Galerkin, and least squares methods, respectively. For the point (0.7, 0.2) the values were 0.15994, 1.40717, and 0.08012, respectively. If  $\Delta t = 0.0005$ , the errors at (0.3, 0.2) were 0.00139, 0.29591, and 0.00180, respectively, while they were 3.15312, 3.15312, 16.15312, and 3.52666 for the five-term approximation, six-term approximation, simple explicit, and finite element space-time coordinates methods, respectively. For the point (0.7, 0.2), the values were 0.00027, 0.06782, 0.00028, 0.39993, 2.39993, 2.60007, and 1.66018 for the seven methods, respectively. It should be noted that in general with all of the schemes except the simple explicit, the maximum error for each time step size for each scheme did not occur at one of the critical points. It did, however, usually occur within a couple of mesh points from the first critical point (0.3, 0.2).

### Summary and Conclusions

The least squares time stepping scheme first presented for one-dimensional problems has been applied to several two-dimensional examples having constant material properties. The least squares method is unconditionally stable as are the other methods used in the comparisons. As in the one-dimensional case, the least squares algorithm again proved to give more accurate results for equal values of time step especially in the large time step range. It should be noted that the usefulness of the least squares method is limited to problems having constant or space dependent material properties. If the material properties were dependant upon time or temperature, then new coefficient matrices in equation (4) would have to be determined at each time step or with each iteration. Thus, the amount of computer time would be very large. Another limitation, as pointed out in the first example, is the large amount of computer storage requirement as compared to other methods.

### Acknowledgments

Dr. Bruch and some of the computer work was supported by the Office of Water Resources Research, USDI, under the Allotment Program of Public Law 88-379, as amended, and by the University of California, Water Resources Center. It is a part of Office of Water Resources Research Project No. A-039-CAL (Water Resources Center Project W-336). Some of the computer work was also supported by Water Resources Center Project W-428 and by a University of California at Santa Barbara campus research computer grant.

The authors appreciate the assistance of Mr. Charles R. Meyer who programed the [K], [C], and {f} matrices for the second example.

### References

- Zienkiewicz, O. C., and Lewis, R. W., "An Analysis of Various Time-Stepping Schemes for Initial Value Problems," *Earthquake Engr. & Struc. Dynamics*, Vol. 1, 1973, pp. 407-408.
- Lewis, R. W., and Bruch, J. C., Jr., "An Application of Least Squares to One-Dimensional Transient Problems," *Int. Jour. Num. Meth. Engr.*, Vol. 8, 1974, pp. 633-647.
- Bell, G. E., "A Method for Treating Boundary Singularities in Time-Dependent Problems," TR/8, Dept. of Math., Brunel University, Uxbridge, Middlesex, 1972, 19 pp.
- Motz, H., "The Treatment of Singularities of Partial Differential Equations by Relaxation Methods," *Quar. Jour. of Appl. Mathematics*, Vol. 4, 1946, pp. 371-377.
- Bruch, J. C., Jr., and Zyvoloski, G., "Transient Two-Dimensional Heat Conduction Problems Solved by the Finite Element Method," *Int. Jour. Num. Meth. Engr.*, Vol. 8, 1974, pp. 481-494.
- Schultz, M. H., *Spline Analysis*, Prentice-Hall, Englewood Cliffs, N. J., Chapter 9, 1973.

## Prediction of Turbulent-Free-Convective-Heat Transfer From a Vertical Flat Plate<sup>1</sup>

T. Cebeci<sup>2</sup> and A. Khattab<sup>2</sup>

### Introduction

Compared with the numerous investigations of turbulent forced convection boundary layers, relatively little work has been done on turbulent natural convection boundary-layer flows. The only studies known to the authors were made by Eckert and Jackson [1],<sup>3</sup>

<sup>1</sup> This work was supported by the National Science Foundation Grant No. ENG74-11895.

<sup>2</sup> Mechanical Engineering Department, California State University, Long Beach, Calif.

<sup>3</sup> Numbers in brackets designate References at end of technical brief.

Contributed by the Heat Transfer Division of THE AMERICAN SOCIETY OF MECHANICAL ENGINEERS. Manuscript received by the Heat Transfer Division March 31, 1975.

Kato, et al. [2], and very recently by Mason and Seban [3]. The first two studies used an integral-method approach and the third one used a differential-method approach. Mason and Seban expressed the eddy viscosity  $\epsilon$  by a mixing-length distribution  $\ell$  and mean-velocity gradient, that is,  $\epsilon = \ell^2 |\partial u / \partial y|$  together with a constant turbulent Prandtl number for the energy equation. They also expressed the eddy viscosity in terms of the turbulent kinetic energy (TKE) as  $\epsilon = a \ell e^{1/2}$ , where  $a$  is a constant and  $e$  is the turbulent kinetic energy. To get  $e$ , they solved the TKE equation with further assumptions for the fluctuation terms appearing in that equation. After a substantial exploration of empirical constants adjusted to fit the experimental data for air, they obtained good agreement with other experimental data on the subject.

The present study is based on the numerical solution of the governing boundary-layer equations in their differential form. The eddy-diffusivity formulas used by Cebeci and Smith (see reference [4]) are utilized to model the Reynolds stresses. It differs from the others in that it is applicable to both laminar and turbulent flows and does not employ any new empirical constants other than those used for forced-convection flows. For further details see reference [5].

### Governing Equations

The boundary-layer equations for a two-dimensional incompressible turbulent flow along a vertical flat plate with a body force can be written as

$$u \frac{\partial u}{\partial x} + v \frac{\partial u}{\partial y} = \bar{g} \beta (t - t_\infty) + \frac{\partial}{\partial y} \left[ (\nu + \epsilon) \frac{\partial u}{\partial y} \right] \quad (1)$$

$$u \frac{\partial t}{\partial x} + v \frac{\partial t}{\partial y} = \frac{\partial}{\partial y} \left[ (\alpha + \epsilon_h) \frac{\partial t}{\partial y} \right] \quad (2)$$

$$\frac{\partial u}{\partial x} + \frac{\partial v}{\partial y} = 0 \quad (3)$$

For the case of uniform wall temperature, the boundary conditions are

$$y = 0, \quad u = v = 0, \quad t = t_w \quad (4a)$$

$$y \rightarrow \infty, \quad u \rightarrow 0, \quad t \rightarrow t_\infty \quad (4b)$$

Equations (1)–(3) are singular at  $x = 0$ . To remove the singularity, we use the similarity variables  $\xi$  and  $\eta$  defined by

$$\xi = \frac{x}{L}, \quad \eta = \frac{y}{L} \left( \frac{R_L}{2} \right)^{1/2} \xi^{-1/4}, \quad R_L = \frac{[\bar{g} \beta (t_w - t_\infty) L]^{1/2} L}{\nu} \quad (5)$$

together with a dimensionless stream function  $f(\xi, \eta)$  and a dimensionless temperature  $g$  defined by

$$\psi = (2)^{3/2} (\xi)^{3/4} f(\xi, \eta), \quad g = \frac{t - t_\infty}{t_w - t_\infty} \quad (6)$$

With the definitions in (5) and (6), equations (1) and (2) can be written as

$$(bf''')' + 3ff'' - 2(f')^2 + g = 4\xi \left( f' \frac{\partial f'}{\partial \xi} - f'' \frac{\partial f}{\partial \xi} \right) \quad (7)$$

$$(cg')' + 3fg' = 4\xi \left( f' \frac{\partial g}{\partial \xi} - g' \frac{\partial f}{\partial \xi} \right) \quad (8)$$

In terms of transformed variables, the boundary conditions (4) become

$$\eta = 0, \quad f = f' = 0, \quad g = 1 \quad (9a)$$

$$\eta = \eta_\infty, \quad f' = 0, \quad g = 0 \quad (9b)$$

### Eddy Diffusivity Formulas

In this study we consider the eddy viscosity formulation of Cebeci and Smith [4] developed for forced convection flows and use it for free convection flows to explore the accuracy of predicting heat transfer rates, velocity, and temperature profiles on vertical flat plates subject to uniform wall temperature. We keep the empirical constants the same. Because of the difficulty of defining an outer

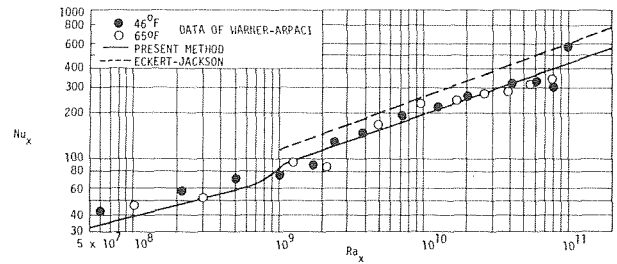


Fig. 1 Comparison of calculated and experimental results for air ( $Pr = 0.72$ )

eddy viscosity expression based on the velocity defect, as for the inner region we chose a mixing-length expression for the outer region and define our formulation by

$$\epsilon = \begin{cases} \epsilon_i = [0.4y(1 - e^{-y/A})]^2 \left| \frac{\partial u}{\partial y} \right| & \epsilon_i \leq \epsilon_0 \\ \epsilon_0 = (0.075\delta)^2 \left| \frac{\partial u}{\partial y} \right| & \epsilon_i \geq \epsilon_0 \end{cases} \quad (10)$$

where  $A = 26\nu(\tau_w/\rho)^{-1/2}$ . We also chose the turbulent Prandtl expression of Cebeci (see reference [4]), which is

$$Pr_t = \frac{0.4[1 - \exp(-y/A)]}{0.44[1 - \exp(-y/B)]} \quad (11)$$

Here

$$A = 26 \nu(\tau_w/\rho)^{-1/2}, \quad B = B^{**}\nu(\tau_w/\rho)^{-1/2}/\sqrt{Pr}, \quad B^{**}$$

$$= \sum_{i=1}^5 C_i (\log_{10} Pr)^{i-1}$$

with

$$C_1 = 34.96, \quad C_2 = 28.79, \quad C_3 = 33.95, \quad C_4 = 6.33, \quad C_5 = -1.186$$

### Comparison With Experiment

A two-point finite-difference method used earlier by Cebeci [6] was used to solve the governing system of equations: for details see reference [5].

Figs. 1–5 show comparisons of calculated results with experiment. The computations were started as laminar at the leading edge and were made turbulent at a specified local Rayleigh number,  $Ra_x$ .

Fig. 1 shows the computed variation of local Nusselt number  $Nu_x$  with  $Ra_x$  for air ( $Pr = 0.72$ ). The transition point was assumed at  $Ra_x = 6 \times 10^8$ . The experimental data are due to Warner and Arpaci [7]. Our calculated results show good agreement with experiment for both laminar and turbulent flows. We note that the predictions of Eckert-Jackson show considerable deviation from the experimental data.

Figs. 2 and 3 show the comparison of calculated and experimental results for the experimental data of Fujii, et al. [8]. Fig. 2 shows the results for  $Pr = 5.9$ . Our calculations were made by matching

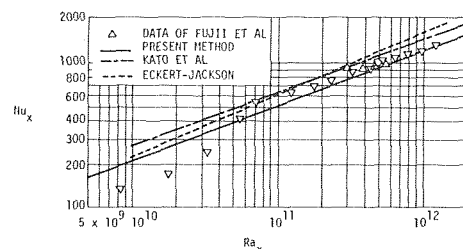


Fig. 2 Comparison of calculated and experimental results for water ( $Pr = 5.9$ )

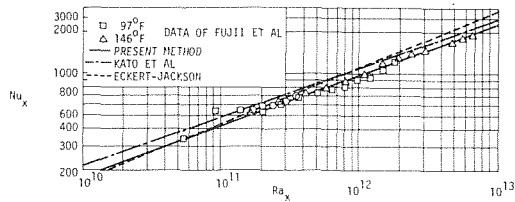


Fig. 3 Comparison of calculated and experimental results for spindle oil ( $Pr = 58.7$ )

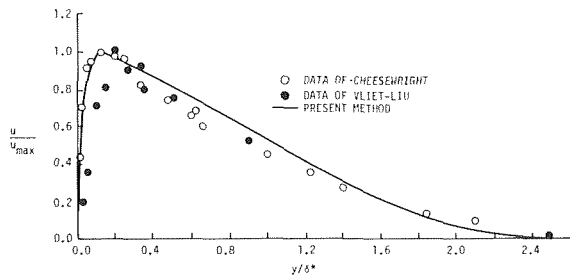


Fig. 4 Comparison of calculated and experimental velocity profiles

the experimental local Nusselt number at  $Ra_x = 5.5 \times 10^{10}$ . As can be seen from the results, the predictions of the present method agree much better with experiment than those of Kato, et al., and Eckert and Jackson. The results in Fig. 3, which are for spindle oil whose Prandtl number is 58.7 show the same trend; again the predictions of the present method is in better agreement than those of Kato, et al., and Eckert and Jackson, although for this case their predictions agree better with experiment than the case for  $Pr = 5.9$ .

Fig. 4 shows the comparison of calculated and experimental velocity profiles. The agreement between calculated results and experimental data due to Cheesewright [9] and Vliet and Liu [10] appears satisfactory.

Fig. 5 shows a comparison of calculated and experimental temperature profiles for the data of Fujii, et al., for three Prandtl numbers,  $Pr = 0.72, 5.9$  and  $58.7$ . The  $x$  coordinate is chosen to be the correlation parameter  $(y/x)Nu_x$  suggested by Fujii, et al. It is interesting to note that a best-fit curve for the calculated outer portion of the thermal layer ( $y/\delta_h > 1$ ) is

$$g = 1 - (0.96y/\delta_h)^{1/8} \quad (12)$$

which is in close agreement with the relation used by Eckert and Jackson,  $g = 1 - (y/\delta)^{1/7}$ .

The calculations shown in Figs. 1–5 were made by using the variable turbulent Prandtl number expression given by (11). We observe from our calculations, however, that the predictions are not very sensitive to the turbulent Prandtl number assumption. When the same calculations were repeated for a constant Prandtl number equal to 0.90, almost the same results were obtained, although the predictions of a variable Prandtl number were a little better than those obtained by a constant Prandtl number. This may be expected since, for the cases considered in our study, the variation of turbulent Prandtl number across the boundary layer for  $Pr =$

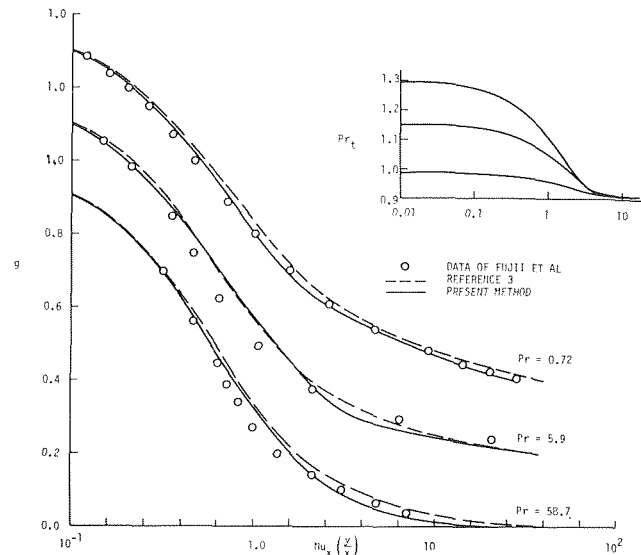


Fig. 5 Comparison of calculated and experimental temperature profiles

0.72, 5.9 and 58.7 were not significant (see Fig. 5). It is only at low molecular Prandtl numbers that the variation becomes important; whether a variable turbulent model would yield better predictions for such cases as it does for forced-convection flows remains to be explored when experimental data become available.

In conclusion, the present method with the same mixing-length, eddy-diffusivity formulas employing the same constants used in forced-convection flows also yield satisfactory results for natural turbulent convection flows *without employing different eddy-diffusivity formulas and different empirical constants*.

## References

- Eckert, E. R. G., and Jackson, T. W., "Analysis of Turbulent Free-Convection Boundary Layer on Flat Plate," NACA TN 2207, 1950.
- Kato, H., Nishiwaki, N., and Hirata, M., "On the Turbulent Heat Transfer by Free Convection From a Vertical Plate," *International Journal of Heat and Mass Transfer*, Vol. 11, 1968, pp. 1117–1125.
- Mason, H. B., and Seban, R. A., "Numerical Predictions for Turbulent Free Convection From Vertical Surfaces," *International Journal of Heat and Mass Transfer*, Vol. 17, 1974, pp. 1329–1336.
- Cebeci, T., and Smith, A. M. O., *Analysis of Turbulent Boundary Layers*, Academic Press, New York, 1974.
- Khattab, A., "Prediction of Turbulent-Free Convective Heat Transfer From a Vertical Flat Plate," MS thesis, California State University at Long Beach, 1975.
- Cebeci, T., "Laminar-Free-Convection-Heat-Transfer From the Outer Surface of a Vertical Slender Circular Cylinder," *Proceedings of the Fifth International Heat Transfer Conference*, Tokyo, Japan, Vol. III, Sept. 1974, p. 15.
- Warner, C. Y., and Arpaci, V. S., "An Experimental Investigation of Turbulent Natural Convection in Air Along a Vertical Heated Flat Plate," *International Journal of Heat and Mass Transfer*, Vol. 11, 1968, p. 397.
- Fujii, T., Takeuchi, M., Fujii, M., Suzaki, K., and Vehara, H., "Experiments on Natural Convection Heat Transfer From the Outer Surface of a Vertical Cylinder to Liquids," *International Journal of Heat and Mass Transfer*, Vol. 13, 1970, p. 753.
- Cheesewright, R., "Turbulent Natural Convection From a Vertical Plane Surface," *JOURNAL OF HEAT TRANSFER*, TRANS. ASME, Series C, Vol. 90, No. 1, Feb. 1968, pp. 1–8.
- Vliet, G. C. and Liu, C. K., "An Experimental study of Turbulent Natural Convection Boundary Layers," *JOURNAL OF HEAT TRANSFER*, TRANS. ASME, Series C, Vol. 91, 1969, p. 511.

# Natural Convection Mass Transfer Adjacent to Vertical and Downward-Facing Inclined Surfaces

W. R. Moran<sup>1</sup> and J. R. Lloyd<sup>2</sup>

*Experimental measurements for natural convection mass transfer adjacent to vertical and downward-facing inclined surfaces were performed using an electrochemical technique. The measurements yielded the time average and instantaneous mass transfer rates for the laminar, transition, and turbulent flow regimes along the test surface. The laminar mass transfer measurements were found to agree with both the analytical and experimental results for both the vertical and downward-facing inclined surfaces. The Rayleigh number marking the onset of the transition from laminar flow conditions depended heavily upon the angle of inclination of the test surface. In the turbulent regime the time average local mass transfer coefficient was correlated by the Rayleigh number to  $1/3$  power.*

## Nomenclature

$c$  = transferred species concentration  
 $C_T(\theta)$  = constant for turbulent flow  
 $D$  = diffusion coefficient of transferred species  
 $F$  = Faraday number  
 $g$  = gravitational acceleration  
 $Gr_x$  = Grashof number  
 $i$  = current density  
 $k$  = mass transfer coefficient  
 $n$  = valence of transferred species  
 $Ra_{\theta,x}$  = local modified Rayleigh number  
 $Sc$  = Schmidt number  
 $Sh_x$  = Sherwood number  
 $t$  = transference number  
 $x$  = streamwise coordinate  
 $\theta$  = angle of inclination  
 $\mu$  = viscosity  
 $\rho$  = density

## Subscripts

$w$  = surface conditions  
 $\infty$  = bulk conditions

## Introduction

Experimental mass transfer data describing the local natural convection adjacent to free-standing, downward-facing inclined surfaces, unlike the corresponding heat transfer case, are virtually nonexistent in the literature. To obtain the local mass transfer data, an electrochemical technique [1]<sup>3</sup> employing an aqueous solution of reagent grade cupric sulphate in reagent grade sulphuric acid was employed. This mass transfer technique, which exhibits a uniform surface concentration, is analogous to the corresponding uniform surface temperature heat transfer problem. The Schmidt number, analogous to the Prandtl number in heat transfer, was approximately 2000. High Prandtl number heat transfer problems generally are complicated by large property variations while the properties vary a maximum of only 3 percent with the present

mass transfer technique. This technical brief presents for the first time data describing the local laminar, transition, and turbulent mass transfer distributions on the downward-facing inclined surface.

## Experimental Apparatus and Techniques

The major components of the experimental apparatus included a tank, the electrolyte solution, an anode, a cathode, a thermometer, a reference junction, and the electrical network. Two complete test systems were employed in the present investigation. One was a smaller surface constructed of pure nickel and was used to study only the laminar regime. Description of this apparatus can be found in reference [2]. A second, much larger, test system was employed to enable study of the transition and turbulent regimes. The test environment for the larger system consisted of 1249 l of electrolyte solution. The large test surface was 27.9 cm  $\times$  60.9 cm (spanwise width  $\times$  height) and 0.635 cm thick, and was made of pure copper. Embedded in this surface from the back side were 23 local probes approximately 0.317 cm in diameter. They were located longitudinally along the center line of the surface at intervals of 2.54 cm. The probes were electrically insulated from the test surface by a layer of epoxy approximately 0.017 cm thick. To eliminate edge effects the entire surface was surrounded by a 2.54 cm wide flush fitting collar of teflon. To prevent spurious electrical leaks from the test surface to the surrounding medium the entire back side and edges were carefully painted with Glyptal, an insulating paint.

For each test run the surface was carefully cleaned and then positioned in the test environment. After allowing the fluid to become quiescent, the surface was brought to limiting current conditions where the surface reaction is diffusion controlled, and the surface concentration of transferred species, copper ions, is essentially zero. The data were recorded with a Hewlett Packard Data Acquisition system. Further details on the construction of the large test facility and the test procedure can be found in reference [3].

## Data Analysis

The local mass transfer coefficient,  $k_x$ , is defined under limiting current conditions by  $k_x = i(1-t)/n Fc_\infty$ . The local mass transfer coefficient is then expressed through the local Sherwood number,  $Sh_x = k_x x/D$ . Other dimensionless terms which are used to describe the mass transfer are the Schmidt,  $Sc = \mu/\rho D$ , Grashof,  $Gr_{\theta,x} = (\rho g \cos\theta(\rho_\infty - \rho_w)x^3)/\mu^2$ , and Rayleigh number,  $Ra_{\theta,x} = Gr_{\theta,x} Sc$ .

## Results and Discussion

The laminar natural convection heat transfer relation for a fluid with a Prandtl number equal to about 2000 adjacent to an isothermal vertical surface can be found in reference [4]. By analogy the same relation holds for the mass transfer case and is given by

$$Sh_x = 0.499 Ra_{\theta,x}^{1/4} \quad (1)$$

The value  $g$  in the Rayleigh number is replaced by  $g \cos\theta$  in order to accommodate inclined surfaces. If one plots the laminar data with the ratio  $Sh_x/(0.499 Ra_{\theta,x}^{1/4})$  on the ordinate and  $Ra_{\theta,x}$  on the abscissa, a scattering of data about the value one would indicate that the modified transfer relation given by equation (1) is correct. The results of the laminar data are plotted in Fig. 1 employing the just-mentioned technique. As indicated in the upper right hand corner, the data are from both the nickel and copper test surfaces. The parameter varied was the downward angle of inclination and included, 0, 5, 10, 20, 30, 45, and 60 deg.

It is seen that the laminar data for all angles generally fall within  $\pm 4$  percent of the heavy line indicating a value of one. This scatter is indicative of the reproducibility of the experiments. These results verify with considerable strength the use of only the component of gravity acting parallel to the test surface in describing the natural convection mass (or heat) transfer process for this wide range of angles. When combined with the results of reference [2] for up-

<sup>1</sup> Aerospace and Mechanical Engineering Department, University of Notre Dame, Notre Dame, Ind. Present Address: Pratt and Whitney Aircraft, East Hartford, Conn.

<sup>2</sup> Aerospace and Mechanical Engineering Department, University of Notre Dame, Notre Dame, Ind.

<sup>3</sup> Numbers in brackets designate References at end of technical brief.

Contributed by the Heat Transfer Division of THE AMERICAN SOCIETY OF MECHANICAL ENGINEERS. Manuscript received by the Heat Transfer Division March 10, 1975.

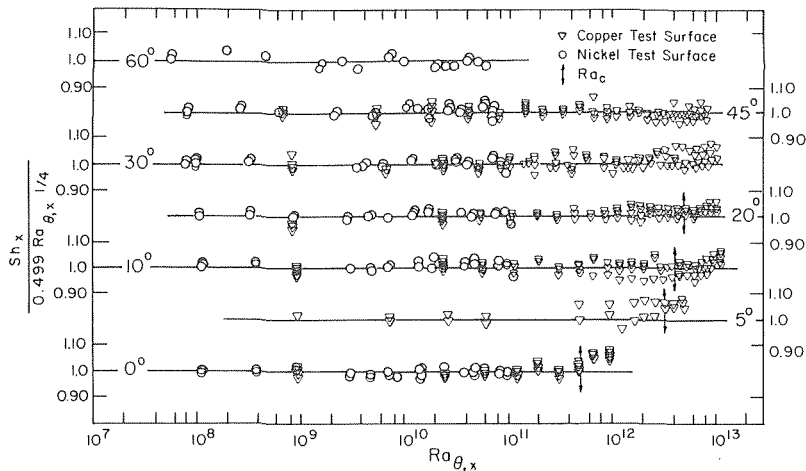


Fig. 1 Local laminar mass transfer on vertical and downward-facing inclined surfaces

ward facing surfaces, these data demonstrate that the use of  $g \cos \theta$  is sufficient to modify the Rayleigh number, in at least the range of inclination angles from +20 to -60 deg relative to the vertical, and enables one to obtain accurate mass or heat transfer predictions from the vertical surface relation. The heat transfer results presented in references [5, 6] indicate that this is also true for lower Prandtl number fluids.

The plotting technique employed in Fig. 1 provides a sensitive way to determine the onset of transition. As soon as the data lift consistently above the line indicating a value of one, the laminar transfer relation is no longer satisfied and transition can be said to have occurred. A more sensitive way to determine the onset of transition is to utilize the fact that the local mass transfer probes are essentially inertia free and they thus can sense fluctuations in the mass transfer. The locations of the first sign of fluctuations are marked in Fig. 1 by arrows. Thus, two transition points were defined, the "instantaneous" and the "time average" critical points. Transition at angles greater than 30 deg was not seen to occur even on the largest test surface. This indicates that the critical Rayleigh number for the onset of transition is a relatively strong function of the angle of inclination.

The vertical surface instability is the only configuration where other data are available for comparison. Reference [2] provides the only local data available for comparison. They used both the criteria employed herein, and found critical Rayleigh numbers for the instantaneous and time average critical point of  $1.5 \times 10^{11}$  and  $2 \times 10^{11}$ . This is in reasonable agreement with the present work where in the corresponding critical Rayleigh numbers were  $5 \times 10^{11}$  and  $6 \times 10^{11}$ . The higher transition value found in the present work may well be due to the fact that the surface in reference [2] was segmented, and the small but present spanwise cracks where the plate segments joined could have introduced some fatal disturbance. Since the copper test surface was a continuous flat surface this particular problem with the cracks would not be encountered in the present work. In references [7, 8] the same electrochemical technique was employed, but only overall data, no local data, were obtained. Their results, fell in a range of  $4-5 \times 10^{11}$ .

It should be noted that the present predictions for the onset of transition are also considerably higher than the heat transfer work, using air and water as the working fluid, summarized in reference [9]. The difference can be explained by the fact that there is a Prandtl (Schmidt) number effect [10]. Fluids of different Prandtl or Schmidt numbers are affected by a given disturbance frequency differently. For one Prandtl or Schmidt number the disturbance may grow whereas for another the same disturbance may decay. For the natural disturbance condition encountered in these works it is impossible to even say what disturbances were present. The data of Fujii, et al. [11] for heat transfer on a vertical cylinder in

fluids of Prandtl numbers from 2 to 2600 lend support to this Prandtl number trend. Their data showed higher instability Rayleigh numbers at larger Prandtl numbers.

As mentioned earlier, the signals from the local probes fluctuated in the transition and turbulent regimes and thus had to be time averaged. The signal for each of the 23 probes was monitored once every 5 s with the Hewlett-Packard data acquisition system for a period of 3 min. This was determined to be a sufficiently long time to obtain an accurate time average without encountering the effects of stratification. The character of the fluctuations in the transition and turbulence regimes was observably different. In the transition regime the current signal was typically a wave-like signal with an occasional spike or fluctuation in it. As the fully turbulent condition was approached the waves gave way to the spikes and the signal looked like the fluctuating signals which would be expected. For completeness, it should be stated that the fluctuations in the turbulent regime were approximately  $\pm 4.5$  percent and had a period of about 30-45 s.

The basic relation for turbulent natural convection is given in [2] by

$$Sh_x = C_T(\theta) Ra_{\theta,x}^{1/3} \quad (2)$$

where  $C_T(\theta)$  is a coefficient which must be determined experimentally and is a function of the angle of inclination. Fig. 2 presents the results for several runs for the transition and turbulent flow regimes for the downward facing angles 0, 5, 10, 20 deg. For angles of

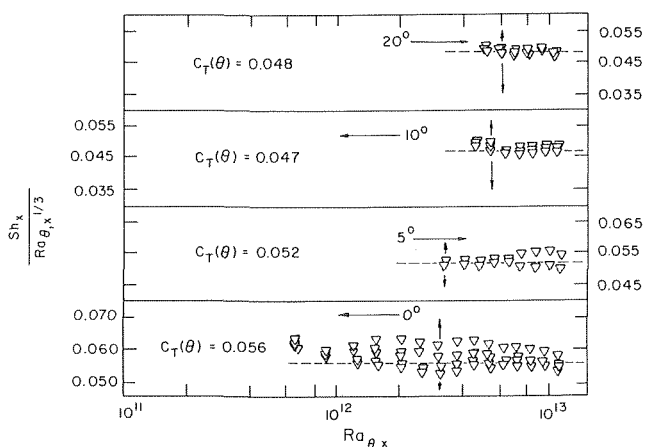


Fig. 2 Local turbulent mass transfer on vertical and downward-facing inclined surfaces

30 deg or greater the turbulent regime could not be reached with the present equipment. Plotted on the ordinate is the quantity  $Sh_x/Ra_{\theta,x}^{1/3}$  and on the abscissa is the modified Rayleigh number. Under fully developed turbulent conditions the data should lie on a horizontal line, and up to that time the data are said to be in the transition regime. The value of  $Sh_x/Ra_{\theta,x}^{1/3}$  about which the data lie is  $C_T(\theta)$ . The points at which the data statistically begin to fall on a straight line (the upper bounds of the transition regions are marked with vertical arrows on the figure) and the statistical average of the data is marked with a horizontal dashed line. The Rayleigh number range of the data is quite limited and the turbulent results should be interpreted with this in mind. It can be seen that the data scatter is greater than in the laminar case. Generally, the greatest scatter comes between runs. It can also be seen that the value of  $C_T(\theta)$  initially decreases as the angle of inclination increases, but appears to level off quickly at 10–20 deg. The values of  $C_T(\theta)$  for these two angles are, within the experimental scatter of the data, essentially the same. This trend is expected since the presence of the surface will have a damping effect on the fluctuations. The value of  $C_T(\theta)$  as a function of  $\theta$  agrees very well with the data of reference [2] and [7].

### Acknowledgment

The authors gratefully acknowledge the support of NSF Grant GK-32658.

### References

- Mizushima, T., "The Electromechanical Method in Transport Phenomena," *Advances in Heat Transfer*, Academic Press, New York, Vol. 7, 1971, pp. 87–161.

- Lloyd, J. R., Sparrow, E. M., and Eckert, E. R. G., "Laminar, Transitional and Turbulent Natural Convection Adjacent to Inclined and Vertical Surfaces," *International Journal of Heat and Mass Transfer*, Vol. 15, No. 3, Mar. 1972, pp. 457–474.
- Moran, W. R., "Free Convection Mass Transfer Adjacent to Vertical and Downward-Facing Inclined Surfaces," MS thesis, Aerospace and Mechanical Engineering Department, University of Notre Dame, Notre Dame, Ind., 1974.
- Ede, A. J., "Advances in Free Convection," *Advances in Heat Transfer*, Academic Press, New York, Vol. 4, 1967.
- Fujii, T., and Imura, H., "Natural Convection Heat Transfer From a Plate With Arbitrary Inclination," *International Journal of Heat and Mass Transfer*, Vol. 15, No. 5, May 1972, pp. 755–767.
- Hassan, K., and Mohamed, S. A., "Natural Convection Heat Transfer From a Plate With Arbitrary Inclination," *International Journal of Heat and Mass Transfer*, Vol. 13, No. 12, Dec. 1970, pp. 1873–1886.
- Fouad, M. G., and Ibl, N., "Natural Convection Mass Transfer at Vertical Electrodes Under Turbulent Flow Conditions," *Electrochimica Acta*, Vol. 3, 1960, pp. 233–243.
- Wilke, C. R., Tobias, C. W., and Eisenberg, M., "Free Convection Mass Transfer at Vertical Surfaces," *Chem. Eng. Prog.*, Vol. 49, No. 12, Dec. 1953, pp. 663–674.
- Lloyd, J. R., and Sparrow, E. M., "On the Instability of Natural Convection Flow on Inclined Surfaces," *J. Fluid Mech.*, Vol. 42, No. 3, July 9, 1970, pp. 465–470.
- Hieber, C. A., and Gebhart, B., "Stability of Vertical Natural Convection Boundary Layers: Expansions at Large Prandtl Number," *J. Fluid Mech.*, Vol. 49, No. 3, Oct. 15, 1971, pp. 577–591.
- Fujii, T., Takeuchi, M., Fujii, M., Suzuki, K., and Uehara, H., "Experiments on Natural Convection Heat Transfer From the Outer Surface of a Vertical Cylinder to Liquids," *International Journal of Heat and Mass Transfer*, Vol. 13, No. 5, May 1970, pp. 753–787.

## Optimum Plate Spacings for Laminar Natural Convection Heat Transfer From Parallel Vertical Isothermal Flat Plates: Experimental Verification

E. K. Levy,<sup>1</sup> P. A. Eichen,<sup>2</sup> W. R. Cintani,<sup>2</sup> and R. R. Shaw<sup>2</sup>

### Nomenclature

- $b$  = plate spacing  
 $c$  = specific heat of plate  
 $C_{p_f}$  = constant pressure specific heat of fluid  
 $g$  = acceleration due to gravity  
 $Gr$  = Grashoff number [ $Gr = \frac{g\beta\Delta T b^3}{\nu^2}$ ]  
 $h_c$  = average convective heat transfer coefficient  
 $k$  = thermal conductivity  
 $L$  = height of plate  
 $m$  = mass of plate  
 $Nu$  = average Nusselt number [ $Nu = \frac{h_c b}{k}$ ]  
 $Pr$  = Prandtl number [ $Pr = \frac{\mu C_{p_f}}{k}$ ]  
 $Q_c$  = rate of convective heat transfer  
 $T_f$  = mean fluid temperature =  $(T_w + T_\infty)/2$

- $T_w$  = wall temperature  
 $T_\infty$  = temperature of fluid before it enters the channel  
 $\Delta T = T_w - T_\infty$   
 $\alpha$  = thermal diffusivity  
 $\beta$  = coefficient of thermal expansion  
 $\eta = GrPr \frac{b}{L}$   
 $\mu$  = absolute viscosity  
 $\nu$  = kinematic viscosity

### Introduction

In an earlier paper [1]<sup>3</sup> Levy discussed the subject of optimum plate spacings for laminar free convection from parallel vertical isothermal flat plates. Based on an analysis by Bodoia [2, 3], he showed that two optimum spacings exist. One arises in determining the number of vertical fins to attach to a surface of fixed dimensions, which for a given fin temperature permits the greatest rate of convective heat transfer to the surroundings. This optimum, observed experimentally with air by Elenbaas [4] and derived by Bodoia [2] occurs at a plate-spacing  $b$  given by

$$\frac{b}{L} GrPr \approx 50 \quad (1)$$

The second optimum arises in determining the spacing between two plates, which for a given rate of convective heat transfer minimizes the plate temperatures. Levy argued that for the condition of minimum  $\Delta T$  to occur, the boundary layers on the plates must not merge [1]. From Bodoia's analysis, this occurs for values of plate spacing greater than the value given by

$$\frac{b}{L} GrPr \approx 600 \quad (2)$$

<sup>1</sup> Assoc. Professor, Lehigh University, Bethlehem, Pa. Mem. ASME.

<sup>2</sup> Undergraduate Students, Lehigh University, Bethlehem, Pa. Student Mem. ASME.

Contributed by the Heat Transfer Division of THE AMERICAN SOCIETY OF MECHANICAL ENGINEERS. Manuscript received by The Heat Transfer Division May 5, 1975.

<sup>3</sup> Numbers in brackets designate References at end of technical brief.

30 deg or greater the turbulent regime could not be reached with the present equipment. Plotted on the ordinate is the quantity  $Sh_x/Ra_{\theta,x}^{1/3}$  and on the abscissa is the modified Rayleigh number. Under fully developed turbulent conditions the data should lie on a horizontal line, and up to that time the data are said to be in the transition regime. The value of  $Sh_x/Ra_{\theta,x}^{1/3}$  about which the data lie is  $C_T(\theta)$ . The points at which the data statistically begin to fall on a straight line (the upper bounds of the transition regions are marked with vertical arrows on the figure) and the statistical average of the data is marked with a horizontal dashed line. The Rayleigh number range of the data is quite limited and the turbulent results should be interpreted with this in mind. It can be seen that the data scatter is greater than in the laminar case. Generally, the greatest scatter comes between runs. It can also be seen that the value of  $C_T(\theta)$  initially decreases as the angle of inclination increases, but appears to level off quickly at 10–20 deg. The values of  $C_T(\theta)$  for these two angles are, within the experimental scatter of the data, essentially the same. This trend is expected since the presence of the surface will have a damping effect on the fluctuations. The value of  $C_T(\theta)$  as a function of  $\theta$  agrees very well with the data of reference [2] and [7].

### Acknowledgment

The authors gratefully acknowledge the support of NSF Grant GK-32658.

### References

- Mizushima, T., "The Electromechanical Method in Transport Phenomena," *Advances in Heat Transfer*, Academic Press, New York, Vol. 7, 1971, pp. 87–161.

- Lloyd, J. R., Sparrow, E. M., and Eckert, E. R. G., "Laminar, Transitional and Turbulent Natural Convection Adjacent to Inclined and Vertical Surfaces," *International Journal of Heat and Mass Transfer*, Vol. 15, No. 3, Mar. 1972, pp. 457–474.
- Moran, W. R., "Free Convection Mass Transfer Adjacent to Vertical and Downward-Facing Inclined Surfaces," MS thesis, Aerospace and Mechanical Engineering Department, University of Notre Dame, Notre Dame, Ind., 1974.
- Ede, A. J., "Advances in Free Convection," *Advances in Heat Transfer*, Academic Press, New York, Vol. 4, 1967.
- Fujii, T., and Imura, H., "Natural Convection Heat Transfer From a Plate With Arbitrary Inclination," *International Journal of Heat and Mass Transfer*, Vol. 15, No. 5, May 1972, pp. 755–767.
- Hassan, K., and Mohamed, S. A., "Natural Convection Heat Transfer From a Plate With Arbitrary Inclination," *International Journal of Heat and Mass Transfer*, Vol. 13, No. 12, Dec. 1970, pp. 1873–1886.
- Fouad, M. G., and Ibl, N., "Natural Convection Mass Transfer at Vertical Electrodes Under Turbulent Flow Conditions," *Electrochimica Acta*, Vol. 3, 1960, pp. 233–243.
- Wilke, C. R., Tobias, C. W., and Eisenberg, M., "Free Convection Mass Transfer at Vertical Surfaces," *Chem. Eng. Prog.*, Vol. 49, No. 12, Dec. 1953, pp. 663–674.
- Lloyd, J. R., and Sparrow, E. M., "On the Instability of Natural Convection Flow on Inclined Surfaces," *J. Fluid Mech.*, Vol. 42, No. 3, July 9, 1970, pp. 465–470.
- Hieber, C. A., and Gebhart, B., "Stability of Vertical Natural Convection Boundary Layers: Expansions at Large Prandtl Number," *J. Fluid Mech.*, Vol. 49, No. 3, Oct. 15, 1971, pp. 577–591.
- Fujii, T., Takeuchi, M., Fujii, M., Suzuki, K., and Uehara, H., "Experiments on Natural Convection Heat Transfer From the Outer Surface of a Vertical Cylinder to Liquids," *International Journal of Heat and Mass Transfer*, Vol. 13, No. 5, May 1970, pp. 753–787.

## Optimum Plate Spacings for Laminar Natural Convection Heat Transfer From Parallel Vertical Isothermal Flat Plates: Experimental Verification

E. K. Levy,<sup>1</sup> P. A. Eichen,<sup>2</sup> W. R. Cintani,<sup>2</sup> and R. R. Shaw<sup>2</sup>

### Nomenclature

- $b$  = plate spacing  
 $c$  = specific heat of plate  
 $C_{Df}$  = constant pressure specific heat of fluid  
 $g$  = acceleration due to gravity  
 $Gr$  = Grashoff number [ $Gr = \frac{g\beta\Delta T b^3}{\nu^2}$ ]  
 $h_c$  = average convective heat transfer coefficient  
 $k$  = thermal conductivity  
 $L$  = height of plate  
 $m$  = mass of plate  
 $Nu$  = average Nusselt number [ $Nu = \frac{h_c b}{k}$ ]  
 $Pr$  = Prandtl number [ $Pr = \frac{\mu C_{Df}}{k}$ ]  
 $Q_c$  = rate of convective heat transfer  
 $T_f$  = mean fluid temperature =  $(T_w + T_\infty)/2$

- $T_w$  = wall temperature  
 $T_\infty$  = temperature of fluid before it enters the channel  
 $\Delta T = T_w - T_\infty$   
 $\alpha$  = thermal diffusivity  
 $\beta$  = coefficient of thermal expansion  
 $\eta = GrPr \frac{b}{L}$   
 $\mu$  = absolute viscosity  
 $\nu$  = kinematic viscosity

### Introduction

In an earlier paper [1]<sup>3</sup> Levy discussed the subject of optimum plate spacings for laminar free convection from parallel vertical isothermal flat plates. Based on an analysis by Bodoia [2, 3], he showed that two optimum spacings exist. One arises in determining the number of vertical fins to attach to a surface of fixed dimensions, which for a given fin temperature permits the greatest rate of convective heat transfer to the surroundings. This optimum, observed experimentally with air by Elenbaas [4] and derived by Bodoia [2] occurs at a plate-spacing  $b$  given by

$$\frac{b}{L} GrPr \approx 50 \quad (1)$$

The second optimum arises in determining the spacing between two plates, which for a given rate of convective heat transfer minimizes the plate temperatures. Levy argued that for the condition of minimum  $\Delta T$  to occur, the boundary layers on the plates must not merge [1]. From Bodoia's analysis, this occurs for values of plate spacing greater than the value given by

$$\frac{b}{L} GrPr \approx 600 \quad (2)$$

<sup>1</sup> Assoc. Professor, Lehigh University, Bethlehem, Pa. Mem. ASME.

<sup>2</sup> Undergraduate Students, Lehigh University, Bethlehem, Pa. Student Mem. ASME.

Contributed by the Heat Transfer Division of THE AMERICAN SOCIETY OF MECHANICAL ENGINEERS. Manuscript received by The Heat Transfer Division May 5, 1975.

<sup>3</sup> Numbers in brackets designate References at end of technical brief.

In the present paper, the authors present experimental data to support the second optimum.

### Experimental Procedure

The experiments were performed in air using parallel arrays of four and six vertical aluminum plates. Each plate was 0.305 m wide  $\times$  0.381 m high  $\times$  6.35 mm thick and was beveled at the bottom to minimize leading edge effects. The plates, with the middle two instrumented with copper constantan thermocouples, were heated in an oven and then allowed to cool in air. The transient variations in plate temperature obtained during cooling were recorded and used to calculate the instantaneous values of  $h$ ,  $\Delta T$ , and Gr. Separate tests were performed with plate spacings from 6.25 to 25.4 mm, which combined with the values of temperatures employed in the tests correspond to values of the parameter  $\eta$  from 10 to 5400.

Experiments were performed using arrays of both four and six plates to determine if the number of plates in the array influences the rates of convective heat transfer from the interior plates. No measurable differences were found. Small nonuniformities in temperature did occur along each plate; instantaneous average plate temperatures were used in analyzing the data. All fluid properties are evaluated at the mean fluid temperature  $T_f$  defined as the average of the instantaneous plate temperature  $T_w$  and the fluid temperature upstream of the array of plates  $T_\infty$ .

All of the results have been corrected to account for the effects of thermal radiation; the cooling rates and heat transfer coefficients presented here correspond to the convective component only.

The use of a transient cooling technique to obtain steady-state convection heat transfer results is valid, provided the time to cool the system is large relative to the thermal response time of the boundary layers. This is shown quantitatively through analysis of the orders of magnitude of the terms in the energy and momentum equations for the boundary layers. The condition for negligible transient effects in the boundary layer is

$$\frac{b^2}{4\alpha t_R} \ll 1 \quad (3)$$

where  $t_R$  is the thermal response time of the aluminum plate. Choosing  $t_R$  equal to the time required for the plate temperature to decrease by an amount equal to 0.1 ( $T_w - T_\infty$ ), the transient parameter  $b^2/4\alpha t_R$  ranges from a value of  $4 \times 10^{-3}$  at the smallest plate spacing to  $7 \times 10^{-2}$  at the largest spacing. Obviously boundary layer transient effects are negligible over the entire range of conditions studied.

### Results and Discussion

The free convection Nusselt number is plotted versus  $\eta$  in Fig. 1 along with the experimental data of Elenbaas and the analytical results of Bodoia and Osterle. The experimental and theoretical results are in excellent agreement except for relatively small values of plate spacing, where both sets of data show values of Nu larger than those predicted by the theory.

Two factors may be responsible for the difference between theory and experiment at low  $\eta$ . Bodoia's analysis was developed for the case of a constant property flow. To account for fluid property variations in the present study, all properties are evaluated at the mean fluid temperature  $T_f$ . This procedure seems appropriate for large  $\eta$ , where the center-line temperature remains fixed at  $T_\infty$  over most of the channel height. At small  $\eta$ , however, the flow becomes fully developed thermally very near the channel inlet, and the fluid properties should instead be evaluated at a temperature much closer to  $T_w$  than to  $T_f$ . Evaluating the fluid properties at  $T_w$  reduces greatly the difference between theory and experiment in this range.

Second, Bodoia's analysis is restricted to a two-dimensional geometry. Bodoia [2] suggests that in the range  $\eta < 20$  where plate separation is small, three-dimensional effects due to side leakage of the plates could cause a noticeable increase in heat transfer rate.

Shown in Fig. 2 is a plot of plate temperature versus dimensionless plate spacing for different values of heat transfer rate. The solid curves shown here are curve fits of the data; and the dashed lines are asymptotes drawn tangent to the solid curves at large  $\eta$ . The results clearly illustrate the concept for optimum plate spacing proposed in reference [1]. As the plate spacing increases, the plate temperature decreases, approaching a minimum value at large  $\eta$ . For the cases studied, the minimum is reached in the range

$$400 < \frac{b}{L} GrPr < 800 \quad (4)$$

The results given here for air do not apply even qualitatively to liquid metals. In a recent paper, Colwell and Welty [5] presented experimental results of the effect of plate spacing on free convection heat transfer to mercury. Their experiments were performed with surfaces of constant wall heat flux. Holding the rate of heat transfer constant, they varied the plate spacing from nearly zero to one-half the plate height and found that the plate temperature decreases, reaches a minimum, and then increases, approaching an asymptotic value near  $b/L$  of  $1/3$ . Their results are opposite in trend to those presented by the authors; and more work is needed to explain the radical differences in behavior between the two fluids.

### Acknowledgment

This study was supported in part by a grant from the Olin Corporation Charitable Trust.

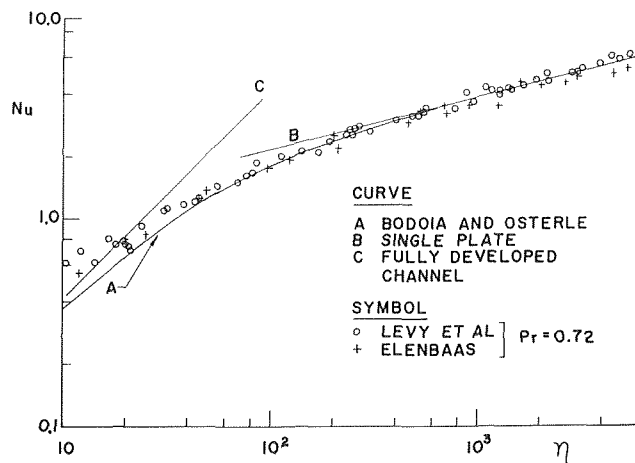


Fig. 1 Variation of Nusselt number with  $\eta$

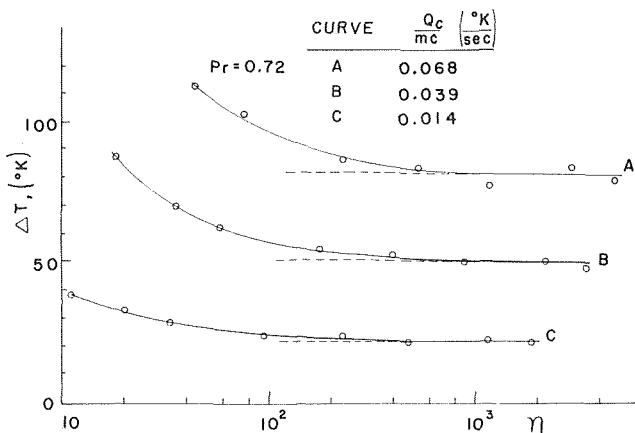


Fig. 2 Effect of  $\eta$  on plate temperature with constant rate of heat transfer;  $Pr = 0.72$

## References

- 1 Levy, E. K., "Optimum Plate Spacings for Laminar Natural Convection Heat Transfer From Parallel Vertical Isothermal Flat Plates," JOURNAL OF HEAT TRANSFER, TRANS. ASME, Series C, Vol. 93, No. 4, Nov. 1971, pp. 463-465.
- 2 Bodoia, J. R., PhD thesis, Carnegie Institute of Technology.
- 3 Bodoia, J. R., and Osterle, J. F., "The Development of Free Convection Between Heated Vertical Plates," JOURNAL OF HEAT TRANSFER, TRANS. ASME, Series C, Vol. 84, No. 1, Feb. 1962, pp. 40-44.
- 4 Elenbaas, W., "Heat Dissipation of Parallel Plates by Free Convection," *Physica IX*, No. 1, Jan. 1942, pp. 1-28.
- 5 Colwell, R. G., and Welty, J. R., "An Experimental Study With Low Prandtl Number Fluids in a Vertical Channel With Uniform Wall Heat Flux," ASME Paper No. 73-HT-52, presented at the ASME-AIChE Heat Transfer Conference, Atlanta, Ga., Aug. 1973.

## A Note on Howard's Model for Turbulent Natural Convection

I. F. Davenport<sup>1</sup> and C. Judson King<sup>2</sup>

*A model for turbulent natural convection based on the cyclic destruction and rebuilding of the boundary layer has been proposed by Howard [6].<sup>3</sup> A close look at more recent experimental data shows that the boundary layer is probably not destroyed as Howard postulated, but is stable with thermals growing upon it and producing the periodicity of the phenomenon. A modified model is proposed.*

### Introduction

Natural convection in a fluid confined between two infinite horizontal plates at high values of the Rayleigh number ( $>10^6$ ) has been the subject of extensive theoretical and experimental investigation. Experiment has shown turbulent natural convection to be a boundary-layer phenomenon involving the periodic generation of thermals. However, it was not until Howard [6] that the theoretical models allowed for the generation of thermals. His model postulated that the density boundary layer grew by conduction until it became unstable, whereupon a thermal was generated, immediately destroying the density boundary layer. The density boundary layer grew by conduction again and repeated the process in a cyclic manner. The generation and release of thermals was assumed to be swift compared with the time of growth of the boundary layer by conduction. Consequently, the mechanism was approximated by a succession of conduction periods wherein the boundary layer was built up from zero to some unstable thickness. Using the error-function temperature profile for the conduction period (0,  $t_p$ ), Howard found the Nusselt number relation to be

$$N = \frac{d}{\delta} = \left(\frac{R}{R_\delta}\right)^{1/3} \quad (1)$$

where  $N$  is the Nusselt number [ $N = Ud/k$ ],  $R$  is the Rayleigh number based upon plate spacing [ $R = (\rho g \beta \Delta T d^3 / \mu \alpha)$ ],  $R_\delta$  is the Rayleigh number based upon the penetration depth [ $R_\delta = (\rho g \beta \Delta T \delta^3 / \mu \alpha)$ ],  $U$  is the heat transfer coefficient ( $U = q/\Delta T$ ),  $d$  is the plate spacing,  $k$  is thermal conductivity,  $\rho$  is density,  $g$  is the

acceleration due to gravity,  $\beta$  is the coefficient of thermal expansion,  $\Delta T$  is the temperature difference between plates,  $\delta$  is the penetration depth, defined as  $\delta = \sqrt{\pi \alpha t_p}$ ,  $\mu$  is viscosity,  $\alpha$  is thermal diffusivity, and  $q$  is heat flux.

From experimental heat-flux and temperature-profile data, a value of  $R_\delta$  of order 1000 was found. Howard's preliminary calculations showed that motion was possible for positive Rayleigh numbers and that the growth rate of this motion should increase rapidly for  $R_\delta$  of order 1000. This agreement between experimental data and preliminary theoretical calculations appeared to justify the concept of destroying and rebuilding the conduction boundary layer.

Recent photographic data presented by Onat and Grigull [11] show clearly that thermals are generated from a point some distance away from the plate into the fluid, and that the layer immediately adjacent to the plate surface remains undisturbed. Furthermore, temperature profiles reported by Somerscales and Gazda [15] are more linear through the boundary layer than corresponds to the time-averaged error-function profile predicted by Howard's model. These results point to a need for a modification of the model.

### Analysis

There are two boundary layers, one at each boundary surface, with the temperature drop ( $\Delta T_l$ ) across each assumed equal to half the total temperature difference ( $\Delta T$ ) between the surfaces. Each boundary layer has the same heat transfer coefficient ( $h$ ), so that the overall heat transfer coefficient ( $U$ ) across the fluid layer is given by

$$U = \frac{h}{2} \quad (2)$$

The Rayleigh number for the boundary layer is based on the temperature drop across the boundary layer and the effective density boundary-layer depth ( $l$ ), which is derived using the segment approximation to measure nonlinear profiles [1] i.e.,

$$l = 4 \int_0^{d/2} \frac{T'(z)}{\Delta T} dz \quad (3)$$

where the  $T'(z)$  is the time-average temperature profile, where  $T'$  is defined as the difference between the actual temperature at  $z$  and the center-plane temperature, and  $z$  is the vertical length coordinate measured from one of the plates. Davenport and King [2] have found that values of  $R_l$ , the Rayleigh number based upon [ $R_l = (\rho g \beta \Delta T l^3 / \mu \alpha)$ ], for instability are relatively insensitive to changes in boundary conditions and shape of the temperature profile.

The experimental measurements of Somerscales and Gazda [15] have shown that the temperature profile is approximately linear within the boundary layer and therefore imply that heat transfer is essentially by conduction over most of the temperature drop across the boundary layer. Thus,  $l$  can be related to the heat-transfer coefficient by

$$l = \frac{k}{h} \quad (4)$$

Heat-transfer data are normally reported as

$$N = \frac{Ud}{k} = K \left( \frac{\rho g \beta \Delta T d^3}{\mu \alpha} \right)^{1/3} = KR^{1/3} \quad (5)$$

The constant  $K$  can be expressed in terms of the Rayleigh number based upon the boundary-layer thickness ( $R_l$ ) and the temperature difference across one boundary layer ( $\Delta T_l$ ) as follows

$$N = \frac{Ud}{k} = \frac{hd}{2k} = \frac{d}{2l} = \frac{1}{2} \left[ \frac{R}{2R_l} \right]^{1/3} = (16 R_l)^{-1/3} R^{1/3} \quad (6)$$

making use of the fact that  $R$  contains  $\Delta T$ , while  $R_l$  contains  $\Delta T_l (= \Delta T/2)$ . This expression differs from equation (1) in that Howard's  $\delta$  must equal  $2l$  (compare equations (1) and (6)), and in that Howard's  $R_\delta$  is defined in terms of  $\Delta T$ , the overall tempera-

<sup>1</sup> Department of Chemical Engineering and Lawrence Berkeley Laboratory, University of California, Berkeley, Calif. (Presently at Shell Oil Co., Victoria, Australia.)

<sup>2</sup> Department of Chemical Engineering and Lawrence Berkeley Laboratory, University of California, Berkeley, Calif.

<sup>3</sup> Numbers in brackets designate References at end of technical brief.

Contributed by the Heat Transfer Division of THE AMERICAN SOCIETY OF MECHANICAL ENGINEERS. Manuscript received by the Heat Transfer Division August 19, 1974.

## References

- 1 Levy, E. K., "Optimum Plate Spacings for Laminar Natural Convection Heat Transfer From Parallel Vertical Isothermal Flat Plates," JOURNAL OF HEAT TRANSFER, TRANS. ASME, Series C, Vol. 93, No. 4, Nov. 1971, pp. 463-465.
- 2 Bodoia, J. R., PhD thesis, Carnegie Institute of Technology.
- 3 Bodoia, J. R., and Osterle, J. F., "The Development of Free Convection Between Heated Vertical Plates," JOURNAL OF HEAT TRANSFER, TRANS. ASME, Series C, Vol. 84, No. 1, Feb. 1962, pp. 40-44.
- 4 Elenbaas, W., "Heat Dissipation of Parallel Plates by Free Convection," *Physica IX*, No. 1, Jan. 1942, pp. 1-28.
- 5 Colwell, R. G., and Welty, J. R., "An Experimental Study With Low Prandtl Number Fluids in a Vertical Channel With Uniform Wall Heat Flux," ASME Paper No. 73-HT-52, presented at the ASME-AIChE Heat Transfer Conference, Atlanta, Ga., Aug. 1973.

## A Note on Howard's Model for Turbulent Natural Convection

I. F. Davenport<sup>1</sup> and C. Judson King<sup>2</sup>

*A model for turbulent natural convection based on the cyclic destruction and rebuilding of the boundary layer has been proposed by Howard [6].<sup>3</sup> A close look at more recent experimental data shows that the boundary layer is probably not destroyed as Howard postulated, but is stable with thermals growing upon it and producing the periodicity of the phenomenon. A modified model is proposed.*

### Introduction

Natural convection in a fluid confined between two infinite horizontal plates at high values of the Rayleigh number ( $>10^6$ ) has been the subject of extensive theoretical and experimental investigation. Experiment has shown turbulent natural convection to be a boundary-layer phenomenon involving the periodic generation of thermals. However, it was not until Howard [6] that the theoretical models allowed for the generation of thermals. His model postulated that the density boundary layer grew by conduction until it became unstable, whereupon a thermal was generated, immediately destroying the density boundary layer. The density boundary layer grew by conduction again and repeated the process in a cyclic manner. The generation and release of thermals was assumed to be swift compared with the time of growth of the boundary layer by conduction. Consequently, the mechanism was approximated by a succession of conduction periods wherein the boundary layer was built up from zero to some unstable thickness. Using the error-function temperature profile for the conduction period (0,  $t_p$ ), Howard found the Nusselt number relation to be

$$N = \frac{d}{\delta} = \left(\frac{R}{R_\delta}\right)^{1/3} \quad (1)$$

where  $N$  is the Nusselt number [ $N = Ud/k$ ],  $R$  is the Rayleigh number based upon plate spacing [ $R = (\rho g \beta \Delta T d^3 / \mu \alpha)$ ],  $R_\delta$  is the Rayleigh number based upon the penetration depth [ $R_\delta = (\rho g \beta \Delta T \delta^3 / \mu \alpha)$ ],  $U$  is the heat transfer coefficient ( $U = q/\Delta T$ ),  $d$  is the plate spacing,  $k$  is thermal conductivity,  $\rho$  is density,  $g$  is the

acceleration due to gravity,  $\beta$  is the coefficient of thermal expansion,  $\Delta T$  is the temperature difference between plates,  $\delta$  is the penetration depth, defined as  $\delta = \sqrt{\pi \alpha t_p}$ ,  $\mu$  is viscosity,  $\alpha$  is thermal diffusivity, and  $q$  is heat flux.

From experimental heat-flux and temperature-profile data, a value of  $R_\delta$  of order 1000 was found. Howard's preliminary calculations showed that motion was possible for positive Rayleigh numbers and that the growth rate of this motion should increase rapidly for  $R_\delta$  of order 1000. This agreement between experimental data and preliminary theoretical calculations appeared to justify the concept of destroying and rebuilding the conduction boundary layer.

Recent photographic data presented by Onat and Grigull [11] show clearly that thermals are generated from a point some distance away from the plate into the fluid, and that the layer immediately adjacent to the plate surface remains undisturbed. Furthermore, temperature profiles reported by Somerscales and Gazda [15] are more linear through the boundary layer than corresponds to the time-averaged error-function profile predicted by Howard's model. These results point to a need for a modification of the model.

### Analysis

There are two boundary layers, one at each boundary surface, with the temperature drop ( $\Delta T_l$ ) across each assumed equal to half the total temperature difference ( $\Delta T$ ) between the surfaces. Each boundary layer has the same heat transfer coefficient ( $h$ ), so that the overall heat transfer coefficient ( $U$ ) across the fluid layer is given by

$$U = \frac{h}{2} \quad (2)$$

The Rayleigh number for the boundary layer is based on the temperature drop across the boundary layer and the effective density boundary-layer depth ( $l$ ), which is derived using the segment approximation to measure nonlinear profiles [1] i.e.,

$$l = 4 \int_0^{d/2} \frac{T'(z)}{\Delta T} dz \quad (3)$$

where the  $T'(z)$  is the time-average temperature profile, where  $T'$  is defined as the difference between the actual temperature at  $z$  and the center-plane temperature, and  $z$  is the vertical length coordinate measured from one of the plates. Davenport and King [2] have found that values of  $R_l$ , the Rayleigh number based upon [ $R_l = (\rho g \beta \Delta T_l l^3 / \mu \alpha)$ ], for instability are relatively insensitive to changes in boundary conditions and shape of the temperature profile.

The experimental measurements of Somerscales and Gazda [15] have shown that the temperature profile is approximately linear within the boundary layer and therefore imply that heat transfer is essentially by conduction over most of the temperature drop across the boundary layer. Thus,  $l$  can be related to the heat-transfer coefficient by

$$l = \frac{k}{h} \quad (4)$$

Heat-transfer data are normally reported as

$$N = \frac{Ud}{k} = K \left(\frac{\rho g \beta \Delta T d^3}{\mu \alpha}\right)^{1/3} = KR^{1/3} \quad (5)$$

The constant  $K$  can be expressed in terms of the Rayleigh number based upon the boundary-layer thickness ( $R_l$ ) and the temperature difference across one boundary layer ( $\Delta T_l$ ) as follows

$$N = \frac{Ud}{k} = \frac{hd}{2k} = \frac{d}{2l} = \frac{1}{2} \left[\frac{R}{2R_l}\right]^{1/3} = (16 R_l)^{-1/3} R^{1/3} \quad (6)$$

making use of the fact that  $R$  contains  $\Delta T$ , while  $R_l$  contains  $\Delta T_l (= \Delta T/2)$ . This expression differs from equation (1) in that Howard's  $\delta$  must equal  $2l$  (compare equations (1) and (6)), and in that Howard's  $R_\delta$  is defined in terms of  $\Delta T$ , the overall tempera-

<sup>1</sup> Department of Chemical Engineering and Lawrence Berkeley Laboratory, University of California, Berkeley, Calif. (Presently at Shell Oil Co., Victoria, Australia.)

<sup>2</sup> Department of Chemical Engineering and Lawrence Berkeley Laboratory, University of California, Berkeley, Calif.

<sup>3</sup> Numbers in brackets designate References at end of technical brief.

Contributed by the Heat Transfer Division of THE AMERICAN SOCIETY OF MECHANICAL ENGINEERS. Manuscript received by the Heat Transfer Division August 19, 1974.

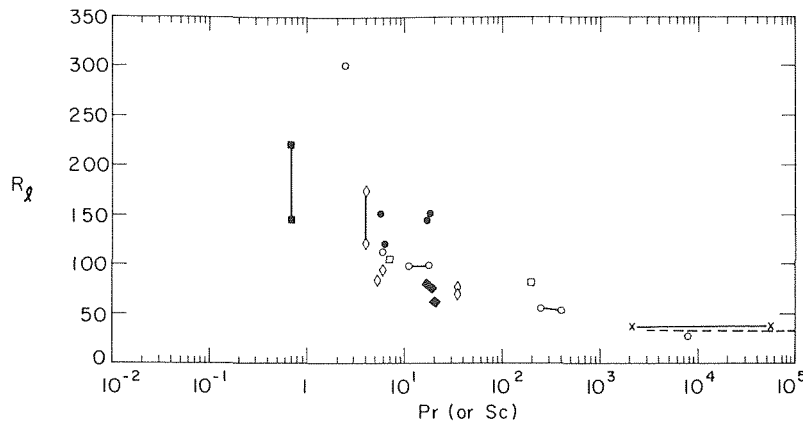


Fig. 1 Experimental dependence of  $R_l$  upon  $Pr$  and  $Sc$ : x—x [4], O—O [5], ● [15], ◇ [14], □ [13], ■ [10], ◆ [9], --- [1].

ture difference, even though  $\delta$  applies to a single boundary layer.  $R_l$  in the present analysis is defined in terms of  $\Delta T_l$  so as to consider the stability properties of a single boundary layer.

### Discussion

Values of  $R_l$  have been derived from heat-transfer data through equation (6) for  $R$  greater than  $10^6$  and are given in Fig. 1 as a function of the Prandtl number. Another source of data was an electrochemical mass transfer study [4]; in that case the Schmidt number (replacing the Prandtl number) varied by an order of magnitude.

At high values of Prandtl or Schmidt number  $R_l$  approaches an asymptote, which is independent of the Prandtl or Schmidt number. The value of this asymptote lies around 32, which is the solution from linear stability analysis [1] for the critical Rayleigh number at which an infinitesimal disturbance will first become unstable for a fluid with infinite Prandtl number, i.e., marginal instability. Numerical calculations [3] indicate that the growth rate for convection will be small under these conditions if the convection must develop from disturbances which have very small amplitudes and wave numbers in the range of those observed in the generation of the thermals. Recent experiments have confirmed the slow-growth limitation indicated by Foster's calculation [2]. Convection initiation from time-dependent density profiles in stationary quiescent pools is not observed for high-Prandtl number fluids until  $R_l$  is of order  $10^3$ , which corresponds to the rapid increase in numerically calculated growth rates. Most of that seeming stability in terms of  $Ra_l$  is accounted for by very slow amplification of the disturbance due to very low growth rates in the range of  $R_l$  below 1000.

The steady-state, well-developed-convection situation differs from the situation of convection initiation from quiescent pools in one important respect. Residual motion and disturbed temperature fields on the scale of the thermal motion are present in the steady-state convection case as a result of the continual generation and departure of thermals from the fluid side of the boundary layer. Consequently, the degree of excess instability required to produce this level of motion in quiescent-pool convection initiation is not necessary for steady-state convection. The growth rates for the generation of thermals during steady-state convection at low values of  $R_l$  would be difficult to formulate mathematically, but from the results shown in Fig. 1 at high Prandtl (Schmidt) number it is evident that there is enough driving force available, even for conditions just above marginal instability. The critical Rayleigh number for the finite-amplitude disturbances present in the steady state is probably, in fact, slightly lower than the value of 32 calculated from linear stability analysis [8]. Robinson [12] has shown by order-of-magnitude analysis that growth rates are too slow at  $Ra_l = 32$  to allow for the assumptions underlying Currie's analysis to be valid for instability developing from the quiescent

state, but this objection is removed if the instability may develop from residual large-scale motions.

The increase in  $R_l$  with decreasing Prandtl number in Fig. 1 indicates that growth rates become important in well-developed turbulent convection at low values of the Prandtl number, even though they were not important for the high-Prandtl-number fluids. The linearized equations of motion [1] show that the influence of the Prandtl number should be observed only when time becomes an important variable. A similar stabilizing trend as the Prandtl number is decreased has been observed in studies of convection initiation from time-dependent profiles [2].

Although the data in Fig. 1 were derived from finite-fluid-depth experiments, the results of Spangenberg and Rowland [16] show that  $Ra_l$  is equal to 102 for well-developed turbulent convection caused by evaporation from a semi-infinite pool of water (Prandtl number = 5). This agrees well with Fig. 1. Furthermore, Spangenberg and Rowland [16] found that  $Ra_l$  for the onset of convection from the quiescent state in the same experiment was 1200. Comparison of that result with  $Ra_l = 102$  for well-developed convection also bears out the hypothesis that the slow-growth limitation is alleviated for the case of well-developed turbulent convection.

The natural-convection mechanism can now be modeled in a way similar to that proposed by Kraichnan [7]. Close to the surface there is a conduction boundary layer supporting most of the temperature drop. The size of the conduction boundary layer can be explained quantitatively in terms of marginal stability analysis for high Prandtl numbers, and can be explained qualitatively in terms of growth-limited instability at lower Prandtl numbers. The rate of heat transfer is related quantitatively to the size of the conduction boundary layer. Further into the fluid there is a region where thermals are generated and carry heat into the bulk fluid, the production of each thermal resulting from the residual effects of the thermal departing before it. Schlieren photographs [11] reporting the development of thermals clearly show the demarcation between the conduction boundary layer and the thermal-generation region.

While the evidence supports the postulate that the boundary layer remains intact and is the major resistance for heat transfer, the analysis does not elucidate the mechanism by which thermals grow and detach from the fluid edge of the boundary layer. However, the relationship between the period for the generation of thermals and the conduction boundary layer thickness can be approximated from a heat balance around the thermal-generation region. The thermal-generation process can be modeled as a given packet ( $V$ ) of bulk liquid at bulk fluid temperature ( $T_b$ ), being convected toward and along the conduction layer so that the packet of fluid heats up to a given temperature ( $T_1$ ), before rising and dissipating its heat into the bulk. Further assume that the area for heat transfer between the conduction layer and the packet of fluid is  $A_t$ , and that the volume of the packet ( $V$ ) is  $nA_t$ , where  $n$  is the thickness of the packet divided by the thickness of the boundary

layer. The contact time for the packet of fluid is  $t_p$ , the period between thermal releases. Thus, from an enthalpy balance

$$t_p \frac{k}{l} \Delta T_f A_t = (n l A_t) \rho C_p (T_1 - T_b) \quad (7)$$

or

$$R_p = R_l \left( \frac{T_1 - T_b}{\Delta T_f} \right)^{3/2} n^{3/2} \quad (8)$$

where  $R_p$  is the dimensionless period defined as  $R_l$  with  $(\alpha t_p)^{1/2}$  substituted for  $l$  [ $R_p = (\rho g \beta \Delta T_f \alpha^{1/2} t_p^{3/2} / \mu)$ ].

Sparrow, et al. [17] in a study of the rate of generation of thermals in deep-pool turbulent convection in water (Prandtl number = 5) observed  $R_p$  to be approximately 80. From Fig. 1,  $R_l$  at Prandtl number = 5 is in the range 80–150. Maximum temperature fluctuations in the thermals have been measured to be about 18 percent of  $\Delta T_f$ ; therefore a reasonable value of  $\Delta T_f / T_1 - T_b$  might be in the range of 5–10. Consequently, from equation (8),  $n$  would be in the same range. The ratio of the height to width of the thermals is related to  $n$ , since  $n$  is the ratio of the height of the thermal to  $l$ . A high value of  $n$ , as in the range 5–10, corresponds to a slender shape for the eventual thermal, which is what is normally observed [11, 17]. When  $n$  is restricted by the depth of the fluid, or plate spacing, the action of the thermal and its heat removal capacity will likewise be influenced by the fluid depth. This could account for the observation that the exponent of  $R$  in equation (6) is often reported as less than  $1/3$ , even though the convection is turbulent.

## Conclusion

This analysis supports the view that thermals in well-developed turbulent convection for  $R > 10^6$  between parallel plates are generated from the fluid-edge of a conduction boundary layer. The boundary layer remains intact, rather than being destroyed and forming again between releases of thermals. The rate of heat transfer at high Prandtl numbers corresponds to a boundary-layer thickness governed by criteria of *marginal* stability, rather than criteria of growth-limited instability from the quiescent state, as was postulated in the original model of Howard [6]. At lower Prandtl numbers the instability growth rate becomes important, but still does not enter to the same extent as for instability developing from the quiescent state.

## Acknowledgment

This work was performed in the Lawrence Berkeley Laboratory under the auspices of the U. S. Atomic Energy Commission.

## References

- 1 Currie, I. G., *Journal of Fluid Mechanics*, Vol. 29, 1967, p. 337.
- 2 Davenport, I. F., and King, C. J., *International Journal of Heat and Mass Transfer*, Vol. 17, 1974, p. 69.
- 3 Foster, T. D., *Phys. Fluids*, Vol. 11, 1968, p. 1257.
- 4 Fenech, E. J., and Tobias, C. W., *Electrochim. Acta*, Vol. 2, 1960, p. 311.
- 5 Globe, S., and Dropkin, D., *JOURNAL OF HEAT TRANSFER*, TRANS. ASME, Series C, Vol. 81, 1959, p. 24.
- 6 Howard, L. N., *Proceedings Eleventh International Congress of Applied Mechanics*, Springer, Berlin, 1966, pp. 1109–1115.
- 7 Kraichnan, R. H., *Phys. Fluids*, Vol. 5, 1962, p. 1374.
- 8 Krishnamurti, R., *Journal of Fluid Mechanics*, Vol. 33, 1968, pp. 445, 457.
- 9 Malkus, W. V. R., *Proceedings Royal Society*, Vol. A225, 1954, p. 196.
- 10 Mull, W., and Reihler, H., *Beitr. Z. Gesandheitstech-Ing.*, Vol. 1, 1930, p. 28.
- 11 Onat, K., and Grigull, V., *Wärme und Stoffübertragung*, Vol. 3, 1970, p. 103.
- 12 Robinson, J., *Journal of Fluid Mechanics*, Vol. 29, 1967, p. 461.
- 13 Rossby, H. T., PhD thesis, M.I.T., Cambridge, Mass., 1966.
- 14 Silveston, P. L., *Forsch. Ing. Wes.*, Vol. 24, 1958, pp. 29, 59.
- 15 Somerscales, E. F. C., and Gazda, I. W., *International Journal of Heat and Mass Transfer*, Vol. 12, 1969, p. 1491.
- 16 Spangenberg, W. G., and Rowland, W. R., *Phys. Fluids*, Vol. 4, 1961, p. 743.
- 17 Sparrow, E. M., Husar, R. G., and Goldstein, R. J., *Journal of Fluid Mechanics*, Vol. 41, 1970, p. 793.

# A General Slab Band Absorptance for Infrared Radiating Gases

C. C. Lin<sup>1</sup> and S. H. Chan<sup>2</sup>

## Nomenclature

$A$  = dimensionless total band absorptance  
 $A_s$  = dimensionless slab band absorptance  
 $P_e$  = effective pressure  
 $t$  = pressure broadening parameter  
 $u$  = optical pathlength  
 $X$  = mass pathlength [ $\text{g cm}^{-1}$ ]  
 $\alpha$  = integrated band intensity [ $\text{cm g}^{-1}$ ]  
 $\beta$  = line width parameter  
 $\omega$  = band width [ $\text{cm}^{-1}$ ]

The problems of radiative transfer through infrared-radiating gases are greatly simplified by the development and utilization of the total band absorptance. Employing an exponential wide band model in conjunction with the narrow band statistical model, Edwards and his co-workers [1, 2]<sup>3</sup> obtained analytical expressions for the total band absorptance. Since then numerous expressions have been proposed [3–7] and the implementation of the total band absorptance in infrared radiative analysis has become a common practice [8–11].

While the total band absorptance can be used to eliminate one of the integrations, namely, the spectral integration, in the equation of the radiative transfer, recent attempts [12, 13] have been made to eliminate the angular integration as well. In particular, the so-called slab band absorptance is found extremely suitable for the plane parallel system [13, 15], because both the spectral and angular integrations can indeed be avoided by using it. The dimensionless slab band absorptance is defined by [13]

$$A_s(u) \equiv \int_0^1 2\mu A(u/\mu) d\mu \quad (1)$$

where  $A$  is the dimensionless total band absorptance and  $\mu \equiv \cos\theta$  with  $\theta$  being the polar angle of a ray with respect to the normal of the plane.

Besides reference [13], Nelson [14] has obtained some analytical expressions for the slab band absorptances based on some forms of the total band absorptance. However, the applicability of the expressions given in [13, 14] is restricted to high pressure or large pathlength limit where the rotational line structures can be ignored. The purpose of this note is to present two general expressions of the slab band absorptance valid for all optical conditions. They are based on two complete forms of the frequently mentioned and widely employed total band absorptance correlations. One is the correlation proposed by Edwards and his co-workers [1, 2] as shown in Table 1 and the other is the Tien-Lowder continuous correlation [3] given by equation (2).

$$A(u) = \ln \{uf[(u+2)/(u+2f)] + 1\} \quad (2)$$

where

$$u = (\alpha/\omega)X$$

$$t = \beta P_e$$

<sup>1</sup> Department of Mechanical Engineering, Polytechnic Institute of New York, Brooklyn, N. Y.

<sup>2</sup> Reactor Analysis and Safety Division, Argonne National Laboratory, Argonne, Ill.

<sup>3</sup> Numbers in brackets designate References at end of technical brief.

Contributed by the Heat Transfer Division of The American Society of Mechanical Engineers. Manuscript received by the Heat Transfer Division January 8, 1975.

layer. The contact time for the packet of fluid is  $t_p$ , the period between thermal releases. Thus, from an enthalpy balance

$$t_p \frac{k}{l} \Delta T_f A_t = (n l A_t) \rho C_p (T_1 - T_b) \quad (7)$$

or

$$R_p = R_l \left( \frac{T_1 - T_b}{\Delta T_f} \right)^{3/2} n^{3/2} \quad (8)$$

where  $R_p$  is the dimensionless period defined as  $R_l$  with  $(\alpha t_p)^{1/2}$  substituted for  $l$  [ $R_p = (\rho g \beta \Delta T_f \alpha^{1/2} t_p^{3/2} / \mu)$ ].

Sparrow, et al. [17] in a study of the rate of generation of thermals in deep-pool turbulent convection in water (Prandtl number = 5) observed  $R_p$  to be approximately 80. From Fig. 1,  $R_l$  at Prandtl number = 5 is in the range 80–150. Maximum temperature fluctuations in the thermals have been measured to be about 18 percent of  $\Delta T_f$ ; therefore a reasonable value of  $\Delta T_f / T_1 - T_b$  might be in the range of 5–10. Consequently, from equation (8),  $n$  would be in the same range. The ratio of the height to width of the thermals is related to  $n$ , since  $n$  is the ratio of the height of the thermal to  $l$ . A high value of  $n$ , as in the range 5–10, corresponds to a slender shape for the eventual thermal, which is what is normally observed [11, 17]. When  $n$  is restricted by the depth of the fluid, or plate spacing, the action of the thermal and its heat removal capacity will likewise be influenced by the fluid depth. This could account for the observation that the exponent of  $R$  in equation (6) is often reported as less than  $1/3$ , even though the convection is turbulent.

## Conclusion

This analysis supports the view that thermals in well-developed turbulent convection for  $R > 10^6$  between parallel plates are generated from the fluid-edge of a conduction boundary layer. The boundary layer remains intact, rather than being destroyed and forming again between releases of thermals. The rate of heat transfer at high Prandtl numbers corresponds to a boundary-layer thickness governed by criteria of *marginal* stability, rather than criteria of growth-limited instability from the quiescent state, as was postulated in the original model of Howard [6]. At lower Prandtl numbers the instability growth rate becomes important, but still does not enter to the same extent as for instability developing from the quiescent state.

## Acknowledgment

This work was performed in the Lawrence Berkeley Laboratory under the auspices of the U. S. Atomic Energy Commission.

## References

- 1 Currie, I. G., *Journal of Fluid Mechanics*, Vol. 29, 1967, p. 337.
- 2 Davenport, I. F., and King, C. J., *International Journal of Heat and Mass Transfer*, Vol. 17, 1974, p. 69.
- 3 Foster, T. D., *Phys. Fluids*, Vol. 11, 1968, p. 1257.
- 4 Fenech, E. J., and Tobias, C. W., *Electrochim. Acta*, Vol. 2, 1960, p. 311.
- 5 Globe, S., and Dropkin, D., *JOURNAL OF HEAT TRANSFER*, TRANS. ASME, Series C, Vol. 81, 1959, p. 24.
- 6 Howard, L. N., *Proceedings Eleventh International Congress of Applied Mechanics*, Springer, Berlin, 1966, pp. 1109–1115.
- 7 Kraichnan, R. H., *Phys. Fluids*, Vol. 5, 1962, p. 1374.
- 8 Krishnamurti, R., *Journal of Fluid Mechanics*, Vol. 33, 1968, pp. 445, 457.
- 9 Malkus, W. V. R., *Proceedings Royal Society*, Vol. A225, 1954, p. 196.
- 10 Mull, W., and Reihler, H., *Beitr. Z. Gesandheitstech-Ing.*, Vol. 1, 1930, p. 28.
- 11 Onat, K., and Grigull, V., *Wärme und Stoffübertragung*, Vol. 3, 1970, p. 103.
- 12 Robinson, J., *Journal of Fluid Mechanics*, Vol. 29, 1967, p. 461.
- 13 Rossby, H. T., PhD thesis, M.I.T., Cambridge, Mass., 1966.
- 14 Silveston, P. L., *Forsch. Ing. Wes.*, Vol. 24, 1958, pp. 29, 59.
- 15 Somerscales, E. F. C., and Gazda, I. W., *International Journal of Heat and Mass Transfer*, Vol. 12, 1969, p. 1491.
- 16 Spangenberg, W. G., and Rowland, W. R., *Phys. Fluids*, Vol. 4, 1961, p. 743.
- 17 Sparrow, E. M., Husar, R. G., and Goldstein, R. J., *Journal of Fluid Mechanics*, Vol. 41, 1970, p. 793.

# A General Slab Band Absorptance for Infrared Radiating Gases

C. C. Lin<sup>1</sup> and S. H. Chan<sup>2</sup>

## Nomenclature

$A$  = dimensionless total band absorptance  
 $A_s$  = dimensionless slab band absorptance  
 $P_e$  = effective pressure  
 $t$  = pressure broadening parameter  
 $u$  = optical pathlength  
 $X$  = mass pathlength [ $\text{g cm}^{-1}$ ]  
 $\alpha$  = integrated band intensity [ $\text{cm g}^{-1}$ ]  
 $\beta$  = line width parameter  
 $\omega$  = band width [ $\text{cm}^{-1}$ ]

The problems of radiative transfer through infrared-radiating gases are greatly simplified by the development and utilization of the total band absorptance. Employing an exponential wide band model in conjunction with the narrow band statistical model, Edwards and his co-workers [1, 2]<sup>3</sup> obtained analytical expressions for the total band absorptance. Since then numerous expressions have been proposed [3–7] and the implementation of the total band absorptance in infrared radiative analysis has become a common practice [8–11].

While the total band absorptance can be used to eliminate one of the integrations, namely, the spectral integration, in the equation of the radiative transfer, recent attempts [12, 13] have been made to eliminate the angular integration as well. In particular, the so-called slab band absorptance is found extremely suitable for the plane parallel system [13, 15], because both the spectral and angular integrations can indeed be avoided by using it. The dimensionless slab band absorptance is defined by [13]

$$A_s(u) = \int_0^1 2\mu A(u/\mu) d\mu \quad (1)$$

where  $A$  is the dimensionless total band absorptance and  $\mu \equiv \cos\theta$  with  $\theta$  being the polar angle of a ray with respect to the normal of the plane.

Besides reference [13], Nelson [14] has obtained some analytical expressions for the slab band absorptances based on some forms of the total band absorptance. However, the applicability of the expressions given in [13, 14] is restricted to high pressure or large pathlength limit where the rotational line structures can be ignored. The purpose of this note is to present two general expressions of the slab band absorptance valid for all optical conditions. They are based on two complete forms of the frequently mentioned and widely employed total band absorptance correlations. One is the correlation proposed by Edwards and his co-workers [1, 2] as shown in Table 1 and the other is the Tien-Lowder continuous correlation [3] given by equation (2).

$$A(u) = \ln \{uf[(u+2)/(u+2f)] + 1\} \quad (2)$$

where

$$u = (\alpha/\omega)X$$

$$t = \beta P_e$$

<sup>1</sup> Department of Mechanical Engineering, Polytechnic Institute of New York, Brooklyn, N. Y.

<sup>2</sup> Reactor Analysis and Safety Division, Argonne National Laboratory, Argonne, Ill.

<sup>3</sup> Numbers in brackets designate References at end of technical brief.

Contributed by the Heat Transfer Division of The American Society of Mechanical Engineers. Manuscript received by the Heat Transfer Division January 8, 1975.

**Table 1 Total band absorptance by Edwards and co-workers [2]**

Pressure broadening parameter, $t$	Lower limit of $u$	Upper limit of $u$	Total band absorptance $A$
$t < 1$	0	$t$	$\frac{u}{2}$
	$t$	$1/t$	$2(ut)^{1/2} - t$
$t \geq 1$	$1/t$	$\infty$	$\ln(ut) + 2 - t$
	0	1	$\frac{u}{\ln u + 1}$

**Table 2 First derivative of slab band absorptance  $A_s'(u)$ , based on Table 1**

Pressure broadening parameter, $t$	Lower limit of $u$	Upper limit of $u$	$A_s'(u)$
$t < 1$	0	$t$	$2 - \frac{2}{3} \frac{u}{t} - \frac{1}{3} t^2 u$
	$t$	$1/t$	$\frac{4}{3} \left(\frac{t}{u}\right)^{1/2} - \frac{1}{3} t^2 u$
	$1/t$	$\infty$	$\frac{1}{u}$
$t \geq 1$	0	1	$2 - u$
	1	$\infty$	$\frac{1}{u}$

$$f = 2.94 [1 - \exp(-2.60 t)]$$

Value of  $\alpha$ ,  $\beta$ , and  $\omega$  are determined from experimental data and tabulated for many gases [16, 17].

Although the validity of the Tien-Lowder correlation is questionable for small  $t$  values [18], the agreement with theoretical calculations [7, 18] is quite good for values of  $t$  of order 0.01 and greater [7]. It is noted that Tien and his co-worker [7] proposed another correlation which is supposedly more correct within the framework of the exponential band model approximation [1]. However, the correlation is not yet as useful because the corresponding parameters  $\alpha$ ,  $\beta$ , and  $\omega$  have not been correlated or presented. If those parameters from reference [16] or [17] are adopted, it does not correlate experimental data as well as equation (2) or Table 1.

Performing integration by parts, equation (1) becomes

$$A_s(u) = A(u) + (u/2)A_s'(u) \quad (3)$$

where

$$A_s'(u) \equiv dA_s(u)/du = \int_0^1 2A'(u/\mu)d\mu \quad (4)$$

and

$$A'(v) = dA(v)/dv.$$

It remains to evaluate the term  $A_s'$  which is a simpler task than to evaluate  $A_s$  itself. By taking the first derivative of the total band absorptance given either in Table 1 or equation (2) and substituting the result into equation (4) for integration, the analytical expression of  $A_s'$  can be readily obtained. It is presented in Table 2 for using Edwards piecewise correlation and in equation (5) for Tien-Lowder continuous correlation.

$$A_s'(u) = 2 + \frac{u}{2f^2} \left\{ \ln \frac{u+2f}{u} - \frac{1+4f}{2} \times \ln \frac{fu^2 + (1+2f)u + 2f}{fu^2} + \frac{1+2f}{2} CG(u) \right\} \quad (5)$$

and

$$G(u) = \ln \left( \frac{2fu + 1 + 2f + C}{2fu + 1 + 2f - C} \right) \text{ for } q \leq 0$$

$$= \tan^{-1} \frac{1+2f}{C} - \tan^{-1} \frac{4f + (1+2f)u}{Cu} \quad q > 0$$

where

$$q = 4f^2 - 4f - 1$$

$$C = |q|^{1/2}$$

Values of  $A_s(u)$  are plotted in Fig. 1 for  $t = 0.01, 0.1, 1$ , and  $\infty$ . The maximum difference between the two expressions of the slab band absorptance is less than 5 percent. It is seen that the general feature of the slab band absorptance is very much like that of the total band absorptance. For example,  $A_s$  is a monotonically increasing function of  $u$  and is strongly influenced by the pressure broadening parameter  $t$ . For the special case of  $t = \infty$ , it reduces to the high pressure limit which was investigated previously [13, 14]. Because the total band absorptances used in the present formulation is also valid for other pressure and optical length, the slab band absorptance so obtained is applicable to other optical conditions as well.

## References

- Edwards, D. K., and Menard, W. A., "Comparison of Models for Correlation of Total Band Absorptance," *Appl. Opt.*, Vol. 3, 1964, p. 621.
- Edwards, D. K., Glassen, L. K., Hauser, W. C., and Tuchscher, J. S., "Radiation Heat Transfer in Nonisothermal Nongray Gases," *JOURNAL OF HEAT TRANSFER TRANS. ASME, Series C*, Vol. 89, 1967, p. 219.
- Tien, C. L., and Lowder, J. E., "A Correlation for the Total Band Absorptance of Radiating Gases," *International Journal of Heat and Mass Transfer*, Vol. 9, 1966, p. 698.
- Tien, C. L., and Ling, G. R., "On a Simple Correlation for Total Band Absorptance of Radiating Gases," *International Journal of Heat and Mass Transfer*, Vol. 12, 1969, p. 1179.
- Morizumi, S. J., PhD Dissertation, University of California, Los Angeles, 1970.
- Cess, R. D., "A Radiative Transfer Model for Planetary Atmosphere," *J. Quant. Spectrosc. Radiat. Transfer*, Vol. 11, 1971, p. 1699.
- Felske, J. D., and Tien, C. L., "A Theoretical Closed Form Expression for the Total Band Absorptance of Infrared-Radiating Gases," *International Journal of Heat and Mass Transfer*, Vol. 17, 1974, p. 155.
- Cess, R. D., and Tiwari, S. N., "Infrared Radiative Energy Transfer in Gases," *Advances in Heat Transfer*, Academic Press, New York, Vol. 3, 1972.
- Novotny, J. L., "Radiation Interaction in Nongray Boundary Layer," *International Journal of Heat and Mass Transfer*, Vol. 11, 1968, p. 1823.
- Novotny, J. L., and Kelleher, M. D., "Conduction in Nongray Radiating Gases," *International Journal of Heat and Mass Transfer*, Vol. 12, 1969, p. 365.
- Nelson, D. A., and Edwards, D. K., "Radiative Decay Times for Thermal Perturbations in a Nongray Medium," *J. Quant. Spectrosc. Radiat. Transfer*, Vol. 13, 1973, p. 747.

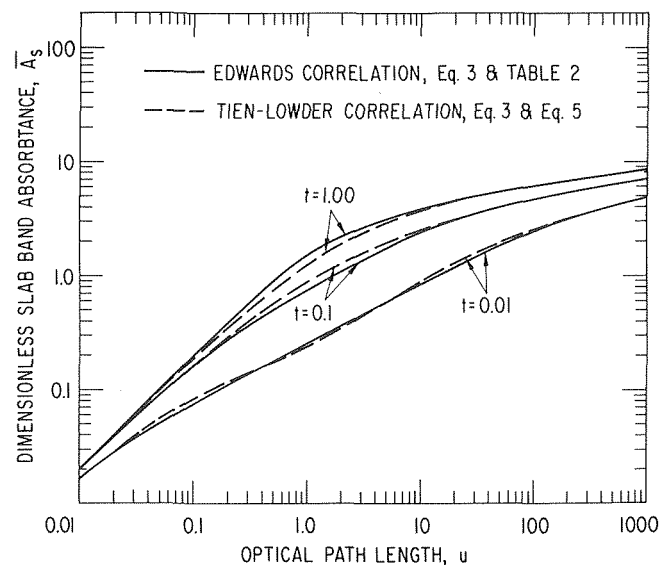


Fig. 1 Dimensionless slab band absorptance

12 Chan, S. H., "Geometric Band Absorptance of a Nongray Gas With Arbitrary Configurations," *International Journal of Heat and Mass Transfer*, Vol. 17, 1974, p. 381.

13 Edwards, D. K., and Balakrishnan, A., "Slab Band Absorptance for Molecular Gas Radiation," *J. Quant. Spectrosc. Radiat. Transfer*, Vol. 12, 1972, p. 1379.

14 Nelson, D. A., "A Study of Band Absorption Equations for Infrared Radiative Transfer in Gases," *J. Quant. Spectrosc. Radiat. Transfer*, Vol. 14, 1974, p. 69.

15 Edwards, D. K., and Balakrishnan, A., "Nongray Radiative Transfer in a Turbulent Gas Layer," *International Journal of Heat and Mass Transfer*, Vol. 16, 1973, pp. 1003-1015.

16 Edwards, D. K., and Balakrishnan, A., "Thermal Radiation by Combustion Gases," *International Journal of Heat and Mass Transfer*, Vol. 16, 1973, p. 25.

17 Tien, C. L., "Thermal Radiation Properties of Gases," *Advances in Heat Transfer*, Academic Press, New York, Vol. 5, 1968.

18 Hsieh, T. C., and Greif, R., "Theoretical Determination of the Absorption Coefficient and the Total Band Absorptance Including a Specific Application to Carbon Monoxide," *J. Quant. Spectrosc. Radiat. Transfer*, Vol. 15, 1972, p. 1477.

## Estimating the Effective Emissivity of Nonisothermal, Diathermanous Coatings

E. E. Anderson<sup>1</sup>

### Nomenclature

- $a_i$  = coefficients in power series expansion of the local intensity  
 $F_e$  = nonisothermal effective emissivity correction factor, see equation (7)  
 $I$  = intensity of radiation  
 $I_b$  = black body intensity of radiation  
 $L$  = coating thickness  
 $T$  = temperature  
 $\mu$  = direction cosine  
 $\rho$  = internal reflectivity  
 $\tau$  = optical depth,  $\int_0^L \kappa dx$   
 $\tau_0$  = optical thickness,  $\int_0^L \kappa dx$   
 1 = subscript referencing the substrate-coating interface  
 2 = subscript referencing the coating-surrounding interface  
 $\lambda$  = subscript referring to a spectral quantity  
 \* = superscript referring to a normalized quantity, see equations (1) and (6)

### Introduction

Whenever a diathermanous coating is applied to a substrate for protection and/or thermal control, the emissivity of the surface is altered. If the coating is semitransparent to thermal radiation, the radiant energy emerging from the substrate-coating combination is determined in part by the absorption, emission, and scattering processes occurring within the coating. The temperature distribution in the coating is then an important consideration in calculating the effective emissivity of the coating-substrate combination. Although the coating emissivity may be predicted by applying the principles of coupled conduction-radiation heat transfer, the solution of the governing integro-differential equations is quite lengthy and tedious. A simplified, approximate method for calculating the

effective emissivity is developed and its application to gray coatings illustrated in this technical brief.

The emissivity of diathermanous coatings has been the subject of several investigations. Francis and Love [1]<sup>2</sup> reported the dependence of the effective directional and hemispherical emissivity upon the coating refractive index and optical thickness, and substrate optical properties for a gray, nonscattering, isothermal coating-metallic substrate combination. Because of the heat transfer through the coating, the isothermal assumption is not realistic. Similar results for nonisothermal coatings were reported by Chupp and Viskanta [2] who employed exact conduction-radiation transfer theory in their analysis. They also found that an accurate estimate of the emissivity for conduction predominant and optically thick conditions was obtained by assuming a linear temperature distribution within the coating. Similar studies [3, 4, 5] have also been done for coatings which scatter as well as absorb and emit radiant energy.

In all of these investigations, the coating emissivity was determined for a given heating situation which establishes the temperature and blackbody emissive power distribution within the coating. This paper eliminates the coupling between the heat transfer problem and calculation of the coating emissivity by presuming that the local emissive power within the coating is given by, or may be approximated by a power series. Rigorous radiative transfer theory is then employed to develop an expression for the effective emissivity in terms of the coating and its interface radiative characteristics, and the coefficients of the emissive power expansion. The emissivity of the coating is thereby readily calculated for a variety of heating conditions by simply adjusting the series expansion to fit the results of a heat transfer analysis or experimental temperature measurements.

### Analysis

The physical model consists of an absorbing-emitting dielectric coating on an opaque substrate whose radius of curvature is large in comparison to the coating thickness. The coating is assumed to be several wavelengths thick so that geometric optics may be employed. Optical properties of the coating, substrate, and surrounding media are considered to be functions of the radiation wavelength. For the purpose of illustration, the coating interfaces are taken to be optically smooth. The internal reflection from the interfaces is then specular and may be calculated from Fresnel's equations. Extension to other forms of substrate directional reflection follows the analysis which follows.

In a general heat transfer situation, a one-dimensional temperature distribution is established across the coating. The local emitted intensity of radiation is coupled to this temperature field through either the Planck (nongray coating) or Stefan-Boltzman (gray coating) radiation functions. Within an arbitrary degree of accuracy, the local blackbody intensity can be expressed as a power series

$$I_{b\lambda}^* = \frac{I_{b\lambda}[T(x)]}{I_{b\lambda}[T_r]} = a_0 + a_1 \left(\frac{T_\lambda}{T_{0\lambda}}\right) + a_2 \left(\frac{T_\lambda}{T_{0\lambda}}\right)^2 + \dots + a_n \left(\frac{T_\lambda}{T_{0\lambda}}\right)^n \quad (1)$$

where  $T_r$  is a normalizing reference temperature. This result is a generalization of the linearized intensity method employed by Poltz [6]. By the appropriate selection of the number of terms and coefficients, most heat transfer problems can be accurately approximated in this manner. Under the proper conditions, this expansion is exact as, for example, when the coating is gray and the temperature distribution is a polynomial in the spatial coordinate.

When equation (1) is substituted into the equation of radiative

<sup>1</sup> Asst. Professor, Department of Mechanical Engineering, South Dakota School of Mines and Technology, Rapid City, S. D. Present address: Reactor Analysis and Safety Division, Argonne National Laboratory, Argonne, Ill.

Contributed by the Heat Transfer Division of THE AMERICAN SOCIETY OF MECHANICAL ENGINEERS. Manuscript received by the Heat Transfer Division April 10, 1975

<sup>2</sup> Number in brackets designate References at end of technical brief.

12 Chan, S. H., "Geometric Band Absorptance of a Nongray Gas With Arbitrary Configurations," *International Journal of Heat and Mass Transfer*, Vol. 17, 1974, p. 381.

13 Edwards, D. K., and Balakrishnan, A., "Slab Band Absorptance for Molecular Gas Radiation," *J. Quant. Spectrosc. Radiat. Transfer*, Vol. 12, 1972, p. 1379.

14 Nelson, D. A., "A Study of Band Absorption Equations for Infrared Radiative Transfer in Gases," *J. Quant. Spectrosc. Radiat. Transfer*, Vol. 14, 1974, p. 69.

15 Edwards, D. K., and Balakrishnan, A., "Nongray Radiative Transfer in a Turbulent Gas Layer," *International Journal of Heat and Mass Transfer*, Vol. 16, 1973, pp. 1003-1015.

16 Edwards, D. K., and Balakrishnan, A., "Thermal Radiation by Combustion Gases," *International Journal of Heat and Mass Transfer*, Vol. 16, 1973, p. 25.

17 Tien, C. L., "Thermal Radiation Properties of Gases," *Advances in Heat Transfer*, Academic Press, New York, Vol. 5, 1968.

18 Hsieh, T. C., and Greif, R., "Theoretical Determination of the Absorption Coefficient and the Total Band Absorptance Including a Specific Application to Carbon Monoxide," *J. Quant. Spectrosc. Radiat. Transfer*, Vol. 15, 1972, p. 1477.

## Estimating the Effective Emissivity of Nonisothermal, Diathermanous Coatings

E. E. Anderson<sup>1</sup>

### Nomenclature

- $a_i$  = coefficients in power series expansion of the local intensity  
 $F_e$  = nonisothermal effective emissivity correction factor, see equation (7)  
 $I$  = intensity of radiation  
 $I_b$  = black body intensity of radiation  
 $L$  = coating thickness  
 $T$  = temperature  
 $\mu$  = direction cosine  
 $\rho$  = internal reflectivity  
 $\tau$  = optical depth,  $\int_0^L \kappa dx$   
 $\tau_0$  = optical thickness,  $\int_0^L \kappa dx$   
 1 = subscript referencing the substrate-coating interface  
 2 = subscript referencing the coating-surrounding interface  
 $\lambda$  = subscript referring to a spectral quantity  
 \* = superscript referring to a normalized quantity, see equations (1) and (6)

### Introduction

Whenever a diathermanous coating is applied to a substrate for protection and/or thermal control, the emissivity of the surface is altered. If the coating is semitransparent to thermal radiation, the radiant energy emerging from the substrate-coating combination is determined in part by the absorption, emission, and scattering processes occurring within the coating. The temperature distribution in the coating is then an important consideration in calculating the effective emissivity of the coating-substrate combination. Although the coating emissivity may be predicted by applying the principles of coupled conduction-radiation heat transfer, the solution of the governing integro-differential equations is quite lengthy and tedious. A simplified, approximate method for calculating the

effective emissivity is developed and its application to gray coatings illustrated in this technical brief.

The emissivity of diathermanous coatings has been the subject of several investigations. Francis and Love [1]<sup>2</sup> reported the dependence of the effective directional and hemispherical emissivity upon the coating refractive index and optical thickness, and substrate optical properties for a gray, nonscattering, isothermal coating-metallic substrate combination. Because of the heat transfer through the coating, the isothermal assumption is not realistic. Similar results for nonisothermal coatings were reported by Chupp and Viskanta [2] who employed exact conduction-radiation transfer theory in their analysis. They also found that an accurate estimate of the emissivity for conduction predominant and optically thick conditions was obtained by assuming a linear temperature distribution within the coating. Similar studies [3, 4, 5] have also been done for coatings which scatter as well as absorb and emit radiant energy.

In all of these investigations, the coating emissivity was determined for a given heating situation which establishes the temperature and blackbody emissive power distribution within the coating. This paper eliminates the coupling between the heat transfer problem and calculation of the coating emissivity by presuming that the local emissive power within the coating is given by, or may be approximated by a power series. Rigorous radiative transfer theory is then employed to develop an expression for the effective emissivity in terms of the coating and its interface radiative characteristics, and the coefficients of the emissive power expansion. The emissivity of the coating is thereby readily calculated for a variety of heating conditions by simply adjusting the series expansion to fit the results of a heat transfer analysis or experimental temperature measurements.

### Analysis

The physical model consists of an absorbing-emitting dielectric coating on an opaque substrate whose radius of curvature is large in comparison to the coating thickness. The coating is assumed to be several wavelengths thick so that geometric optics may be employed. Optical properties of the coating, substrate, and surrounding media are considered to be functions of the radiation wavelength. For the purpose of illustration, the coating interfaces are taken to be optically smooth. The internal reflection from the interfaces is then specular and may be calculated from Fresnel's equations. Extension to other forms of substrate directional reflection follows the analysis which follows.

In a general heat transfer situation, a one-dimensional temperature distribution is established across the coating. The local emitted intensity of radiation is coupled to this temperature field through either the Planck (nongray coating) or Stefan-Boltzman (gray coating) radiation functions. Within an arbitrary degree of accuracy, the local blackbody intensity can be expressed as a power series

$$I_{b\lambda}^* = \frac{I_{b\lambda}[T(x)]}{I_{b\lambda}[T_r]} = a_0 + a_1 \left(\frac{T_\lambda}{T_{0\lambda}}\right) + a_2 \left(\frac{T_\lambda}{T_{0\lambda}}\right)^2 + \dots + a_n \left(\frac{T_\lambda}{T_{0\lambda}}\right)^n \quad (1)$$

where  $T_r$  is a normalizing reference temperature. This result is a generalization of the linearized intensity method employed by Poltz [6]. By the appropriate selection of the number of terms and coefficients, most heat transfer problems can be accurately approximated in this manner. Under the proper conditions, this expansion is exact as, for example, when the coating is gray and the temperature distribution is a polynomial in the spatial coordinate.

When equation (1) is substituted into the equation of radiative

<sup>1</sup> Asst. Professor, Department of Mechanical Engineering, South Dakota School of Mines and Technology, Rapid City, S. D. Present address: Reactor Analysis and Safety Division, Argonne National Laboratory, Argonne, Ill.

Contributed by the Heat Transfer Division of THE AMERICAN SOCIETY OF MECHANICAL ENGINEERS. Manuscript received by the Heat Transfer Division April 10, 1975

<sup>2</sup> Number in brackets designate References at end of technical brief.

transfer (see equations (34) and (35) of reference [7]) and the spatial integrations performed, the intensity of radiation incident upon the transparent interface of the coating and surroundings  $I_{\lambda}^*$  ( $\tau_{0\lambda}, \mu$ ) may be determined. The effective spectral, directional emissivity of the coating,

$$\epsilon_{\lambda}(\mu) = [1 - \rho_{2\lambda}(\mu)] I_{\lambda}^*(\tau_{0\lambda}, \mu) / \nu_{\lambda}^2 I_{b\lambda}^*(T_r) \quad (2)$$

is then give by

$$\epsilon_{\lambda}(\mu) = \epsilon_{\lambda T}(\mu) \{1 + S_1 [1 - \exp(-\tau_{0\lambda}/\mu)] + \rho_{1\lambda} S_2 \exp(-\tau_{0\lambda}/\mu) + S_3 + \rho_{1\lambda} S_4 \exp(-2\tau_{0\lambda}/\mu)\} \quad (3)$$

where

$$S_1 = \sum_{i=1}^n (a_i/a_0) i! (-\tau_{0\lambda}/\mu)^{-i} \quad (4a)$$

$$S_2 = \sum_{i=1}^n (a_i/a_0) i! (\tau_{0\lambda}/\mu)^{-i} \quad (4b)$$

$$S_3 = \sum_{i=1}^n \sum_{j=i}^n (a_j/a_0) (j!/i!) (-\tau_{0\lambda}/\mu)^{j-i} \quad (4c)$$

and

$$S_4 = \sum_{i=1}^n \sum_{j=i}^n (a_j/a_0) (j!/i!) (\tau_{0\lambda}/\mu)^{j-i} \quad (4d)$$

In equation (3),  $\epsilon_{\lambda T}(\mu)$  is the directional emissivity of the coating under isothermal conditions [1]

$$\epsilon_{\lambda T}(\mu) = [1 - \rho_{2\lambda}(\mu)] \{ [1 - \rho_{1\lambda}(\mu) \exp(-2\tau_{0\lambda}/\mu)] / [1 - \rho_{1\lambda}(\mu) \rho_{2\lambda}(\mu) \exp(-2\tau_{0\lambda}/\mu)] \} \quad (5)$$

Those terms within the braces of equation (3) form a factor which corrects the isothermal coating emissivity for nonisothermal conditions. This factor depends upon the coating-substrate reflectivity  $\rho_{1\lambda}$ , the optical pathlength through the coating  $\tau_{0\lambda}/\mu$  and the temperature distribution. The influence of the temperature distribution within the coating is embodied in the series  $S_1$ ,  $S_2$ ,  $S_3$ , and  $S_4$  which may be evaluated from the series expansion of the local blackbody intensity.

### Gray Coatings

In order to demonstrate the application of equation (3), results for a gray coating are developed for two different types of heating. For a gray coating, the series expansion can be written for the total rather than the spectral intensity. The local intensity is then related to the temperature by the Stefan-Boltzmann radiation function.

As a first illustration, the heating of the coating is considered to be such that the local temperature is proportional to the fourth root of the spatial coordinate. Local intensities are then a linear

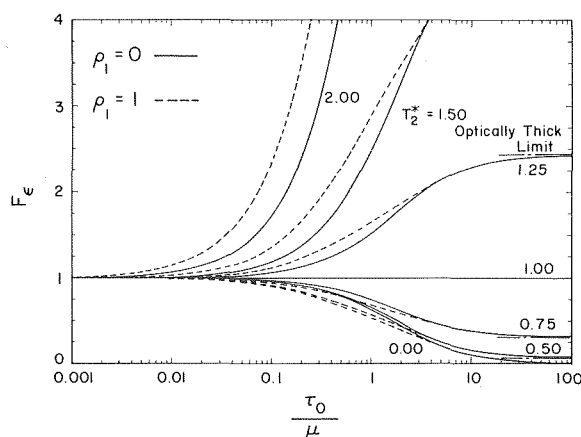


Fig. 1 The nonisothermal effective emissivity convection factor for a gray coating on a specularly reflecting base on the linear intensity model

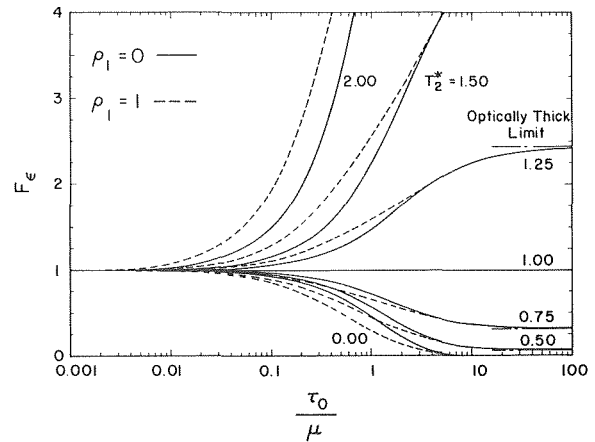


Fig. 2 The nonisothermal effective emissivity correction factor for a gray coating on a specularly reflecting substrate based on the linear temperature model

function of  $\tau$  and the series expansion for the intensity is

$$I_b^* = (T/T_1)^4 = 1 + (T_2^{*4} - 1)(\tau/\tau_0) \quad (6)$$

When the coefficients of this expansion are substituted into equations (3) and (4) the nonisothermal correction factor is

$$F_\epsilon = \epsilon/\epsilon_T = 1 + (T_2^{*4} - 1) \{ [1 - \rho_1 \exp(-2\tau_0/\mu)] - [1 - \exp(-\tau_0/\mu)] [1 - \rho_1 \exp(-\tau_0/\mu)] (\tau_0/\mu)^{-1} \} \quad (7)$$

In the optically thick limit ( $\tau_0/\mu \rightarrow \infty$ ),  $F_\epsilon = T_2^{*4}$  whereas in the optically thin limit ( $\tau_0/\mu \rightarrow 0$ ),  $F_\epsilon = 1$ .

The nonisothermal effective emissivity correction factor is shown in Fig. 1 for two substrated reflectivities as a function of the optical pathlength and coating-surrounding medium to coating-substrate temperature ratio. Nonisothermal effects are significant once the optical pathlength exceeds 0.01–0.1. When the optical pathlength is greater than 50–100, the emissivity is determined by the coating material and becomes independent of the substrate radiative properties.

Heating such that a linear temperature distribution,  $T^* = (T_2^* - 1)\tau/\tau_0 + 1$ , is established across the coating serves as the second illustration. The series expansion for the intensity is then

$$I_b^* = T^{*4} = 1 + 4(T_2^* - 1)(\tau/\tau_0) + 6(T_2^* - 1)^2(\tau/\tau_0)^2 + 4(T_2^* - 1)^3(\tau/\tau_0)^3 + (T_2^* - 1)^4(\tau/\tau_0)^4 \quad (8)$$

which gives the nonisothermal correction

$$F_\epsilon = 1 + 4(\Delta T^*)(b^- - c^- a^{-1}) + 6(\Delta T^*)^2(b^- - 2b^+ a^{-1} + 2c^+ a^{-2}) + 4(\Delta T^*)^3(b^- - 3b^+ a^{-1} + 6b^- a^{-2} - 6c^+ a^{-3}) + (\Delta T^*)^4(b^- - 4b^+ a^{-1} + 12b^- a^{-2} - 24b^+ a^{-3} + 24c^+ a^{-4}) \quad (9)$$

where  $\Delta T^* = T_2^* - 1$ ,  $a = \tau_0/\mu$ ,  $b^\pm = 1 \pm \rho_1 \exp(-2a)$ , and  $c^\pm = [1 \pm \rho_1 \exp(-a)] [1 - \exp(-a)]$ . This result is identical to the linear temperature approximation of Chupp and Viskanta [2]. The optically thick and thin limits are the same as those of the linear intensity example. Correcting factors for this example are shown in Fig. 2. Again it is apparent that nonisothermal effects are appreciable and the reflectivity of the substrate is only significant at intermediate optical thicknesses.

These two models are compared for moderate temperature differences across the coating and a black substrate in Fig. 3. These results indicate that the simpler linear intensity model is quite accurate over a wide range of optical thickness and coating-surrounding interface temperatures.

### Concluding Remarks

By approximating the local blackbody intensity within a dielectric coating with a power series, the influence of the coating on the

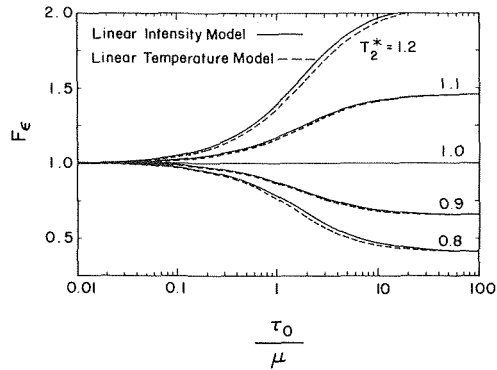


Fig. 3 Comparison of the linear intensity and temperature models of the nonisothermal effective emissivity correction factor for a gray coating and black substrate.

effective emissivity may be readily investigated. Even simple approaches such as the linear intensity model give results which are more accurate than the isothermal model. The linear intensity model is also in good agreement with more sophisticated models.

Since this approach is quite versatile in that it can accurately treat several forms of heating and reflection as well as gray or nongray coatings, and is easy to use; the nonisothermal effects on the emissivity of the coating may be readily estimated for a variety of heat transfer conditions.

## References

- Francis, J. E. and Love, T. J., "Radiant Heat Transfer Analysis of Isothermal, Diathermanous Coatings on a Conductor," *AIAA Journal*, Vol. 4, No. 4, Apr. 1966, pp. 643-650.
- Chupp, R. E. and Viskanta, R., "Thermal Emission Characteristics of a Nonisothermal Dielectric Coating on a Conductor Surface," *AIAA Journal*, Vol. 8, No. 3, Mar. 1970, pp. 551-557.
- Klein, J. D., "Radiation Heat Transfer to and From Ceramic Coatings on Metals," *American Ceramic Society Bulletin*, Vol. 40, No. 6, 1961, pp. 366-370.
- Berquam, J. B. and Seban, R. A., "Spectral Radiation From Alumina Powder on a Metallic Substrate," *JOURNAL OF HEAT TRANSFER*, TRANS. ASME, Series C, Vol. 94 No. 1, Feb. 1972, pp. 36-40.
- Merriam, R. L. and Viskanta, R., "Radiative Characteristics of Absorbing, Emitting and Scattering Media on Opaque Substrates," *Journal of Spacecraft and Rockets*, Vol. 5, No. 10, Oct. 1968, pp. 1210-1215.
- Poltz, H., "Die Wärmeleitfähigkeit von Flüssigkeiten II. Der Strahlungsanteil der effektiven Wärmeleitfähigkeit," *International Journal of Heat and Mass Transfer*, Vol. 8, No. 4, Apr. 1965, pp. 515-527.
- Viskanta, R., and Anderson, E. E., "Heat Transfer in Semitransparent Solids," in *Advances in Heat Transfer* J. P. Hartnett and T. F. Irvine, Jr., eds., Vol. 11, Academic Press, New York, 1975, pp. 317-441.

## Heat Transfer in the Laminar Boundary Layer Over an Impulsively Started Flat Plate<sup>1</sup>

C. B. Watkins<sup>2</sup>

Numerical solutions are described for the unsteady thermal boundary layer in incompressible laminar flow over a semi-infinite flat plate set impulsively into motion, with the simultaneous imposition of a constant temperature difference between the plate and the fluid. Results are presented for several Prandtl numbers.

### Nomenclature

$$N_x = \frac{h_x x'}{k} = \text{Nusselt number}$$

$$Pr = \frac{c_p \mu}{k} = \text{Prandtl number}$$

$$R_x = \frac{x' U_\infty}{\nu} = \text{local Reynolds number}$$

$$t = \frac{U_\infty t'}{L} = \text{nondimensional time}$$

$$u = \frac{u'}{U_\infty} = \text{nondimensional velocity in surface direction}$$

$$v = \left( \frac{U_\infty L}{\nu} \right)^{1/2} v' / U_\infty = \text{nondimensional normal velocity}$$

$$x = X' / L = \text{nondimensional coordinate along surface of plate}$$

$$y = \left( \frac{U_\infty L}{\nu} \right)^{1/2} y' / L = \text{nondimensional coordinate normal to plate}$$

$$\eta = y / \sqrt{x} = \text{similarity variable}$$

$$\theta = \frac{T - T_\infty}{T_w - T_\infty} = \text{nondimensional temperature}$$

$$\tau = x' / t = \text{similarity variable}$$

### Subscripts

$$w = \text{conditions at surface of plate}$$

$$\infty = \text{conditions in free stream}$$

### Superscripts

$$'(\text{prime}) = \text{dimensional quantity}$$

### Introduction

The problem considered is that of heat transfer in the unsteady thermal boundary layer associated with the laminar momentum boundary layer, resulting from the flow of an incompressible fluid past a semi-infinite flat plate, set impulsively into motion at time  $t = 0$  with a constant velocity. The plate and the fluid are initially at the same temperature. The thermal boundary layer is produced by the simultaneous sudden imposition of a constant temperature difference between the plate and the fluid  $|T_w - T_\infty| > 0$  at  $t = 0$ . Constant boundary layer properties are assumed and viscous dissipation effects are neglected.

This problem has wide application and is related to the flow created by the passage of a shock wave over a surface.

The development of the momentum and thermal boundary layer flow in time is characterized by the existence of three distinct regions [1].<sup>3</sup> Initially, for  $\tau = t/x \leq 1$ , the flow is independent of the effects of the leading edge and corresponds to the flow described by Rayleigh [2] for an infinite plate. Ultimately, as  $\tau \rightarrow \infty$  the flow is given by the familiar Blasius boundary layer. The present problem is concerned with the description of the flow in the intermediate or transitional region in which the boundary layer develops from the initial to the ultimate state.

<sup>1</sup> This work was supported by National Science Foundation Grant No. GY-11056.

<sup>2</sup> Assoc. Professor and Chairman, Department of Mechanical Engineering, Howard University, Washington, D.C. Mem. ASME.

Contributed by the Heat Transfer Division of THE AMERICAN SOCIETY OF MECHANICAL ENGINEERS. Manuscript received by the Heat Transfer Division December 9, 1974.

<sup>3</sup> Numbers in brackets designate References at end of technical brief.

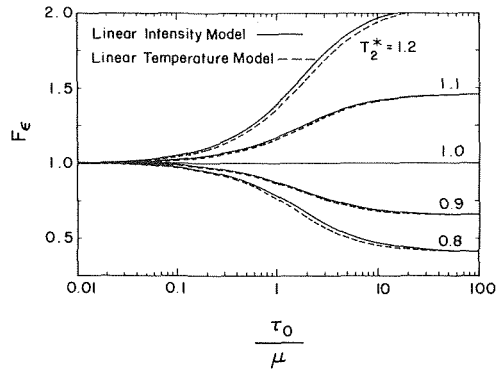


Fig. 3 Comparison of the linear intensity and temperature models of the nonisothermal effective emissivity correction factor for a gray coating and black substrate.

effective emissivity may be readily investigated. Even simple approaches such as the linear intensity model give results which are more accurate than the isothermal model. The linear intensity model is also in good agreement with more sophisticated models.

Since this approach is quite versatile in that it can accurately treat several forms of heating and reflection as well as gray or nongray coatings, and is easy to use; the nonisothermal effects on the emissivity of the coating may be readily estimated for a variety of heat transfer conditions.

## References

- Francis, J. E. and Love, T. J., "Radiant Heat Transfer Analysis of Isothermal, Diathermanous Coatings on a Conductor," *AIAA Journal*, Vol. 4, No. 4, Apr. 1966, pp. 643-650.
- Chupp, R. E. and Viskanta, R., "Thermal Emission Characteristics of a Nonisothermal Dielectric Coating on a Conductor Surface," *AIAA Journal*, Vol. 8, No. 3, Mar. 1970, pp. 551-557.
- Klein, J. D., "Radiation Heat Transfer to and From Ceramic Coatings on Metals," *American Ceramic Society Bulletin*, Vol. 40, No. 6, 1961, pp. 366-370.
- Berquam, J. B. and Seban, R. A., "Spectral Radiation From Alumina Powder on a Metallic Substrate," *JOURNAL OF HEAT TRANSFER*, TRANS. ASME, Series C, Vol. 94 No. 1, Feb. 1972, pp. 36-40.
- Merriam, R. L. and Viskanta, R., "Radiative Characteristics of Absorbing, Emitting and Scattering Media on Opaque Substrates," *Journal of Spacecraft and Rockets*, Vol. 5, No. 10, Oct. 1968, pp. 1210-1215.
- Poltz, H., "Die Wärmeleitfähigkeit von Flüssigkeiten II. Der Strahlungsanteil der effektiven Wärmeleitfähigkeit," *International Journal of Heat and Mass Transfer*, Vol. 8, No. 4, Apr. 1965, pp. 515-527.
- Viskanta, R., and Anderson, E. E., "Heat Transfer in Semitransparent Solids," in *Advances in Heat Transfer* J. P. Hartnett and T. F. Irvine, Jr., eds., Vol. 11, Academic Press, New York, 1975, pp. 317-441.

## Heat Transfer in the Laminar Boundary Layer Over an Impulsively Started Flat Plate<sup>1</sup>

C. B. Watkins<sup>2</sup>

Numerical solutions are described for the unsteady thermal boundary layer in incompressible laminar flow over a semi-infinite flat plate set impulsively into motion, with the simultaneous imposition of a constant temperature difference between the plate and the fluid. Results are presented for several Prandtl numbers.

### Nomenclature

$$N_x = \frac{h_x x'}{k} = \text{Nusselt number}$$

$$Pr = \frac{c_p \mu}{k} = \text{Prandtl number}$$

$$R_x = \frac{x' U_\infty}{\nu} = \text{local Reynolds number}$$

$$t = \frac{U_\infty t'}{L} = \text{nondimensional time}$$

$$u = \frac{u'}{U_\infty} = \text{nondimensional velocity in surface direction}$$

$$v = \left( \frac{U_\infty L}{\nu} \right)^{1/2} v' / U_\infty = \text{nondimensional normal velocity}$$

$$x = X' / L = \text{nondimensional coordinate along surface of plate}$$

$$y = \left( \frac{U_\infty L}{\nu} \right)^{1/2} y' / L = \text{nondimensional coordinate normal to plate}$$

$$\eta = y / \sqrt{x} = \text{similarity variable}$$

$$\theta = \frac{T - T_\infty}{T_w - T_\infty} = \text{nondimensional temperature}$$

$$\tau = x' / t = \text{similarity variable}$$

### Subscripts

$$w = \text{conditions at surface of plate}$$

$$\infty = \text{conditions in free stream}$$

### Superscripts

$$'(\text{prime}) = \text{dimensional quantity}$$

### Introduction

The problem considered is that of heat transfer in the unsteady thermal boundary layer associated with the laminar momentum boundary layer, resulting from the flow of an incompressible fluid past a semi-infinite flat plate, set impulsively into motion at time  $t = 0$  with a constant velocity. The plate and the fluid are initially at the same temperature. The thermal boundary layer is produced by the simultaneous sudden imposition of a constant temperature difference between the plate and the fluid  $|T_w - T_\infty| > 0$  at  $t = 0$ . Constant boundary layer properties are assumed and viscous dissipation effects are neglected.

This problem has wide application and is related to the flow created by the passage of a shock wave over a surface.

The development of the momentum and thermal boundary layer flow in time is characterized by the existence of three distinct regions [1].<sup>3</sup> Initially, for  $\tau = t/x \leq 1$ , the flow is independent of the effects of the leading edge and corresponds to the flow described by Rayleigh [2] for an infinite plate. Ultimately, as  $\tau \rightarrow \infty$  the flow is given by the familiar Blasius boundary layer. The present problem is concerned with the description of the flow in the intermediate or transitional region in which the boundary layer develops from the initial to the ultimate state.

<sup>1</sup> This work was supported by National Science Foundation Grant No. GY-11056.

<sup>2</sup> Assoc. Professor and Chairman, Department of Mechanical Engineering, Howard University, Washington, D.C. Mem. ASME.

Contributed by the Heat Transfer Division of THE AMERICAN SOCIETY OF MECHANICAL ENGINEERS. Manuscript received by the Heat Transfer Division December 9, 1974.

<sup>3</sup> Numbers in brackets designate References at end of technical brief.

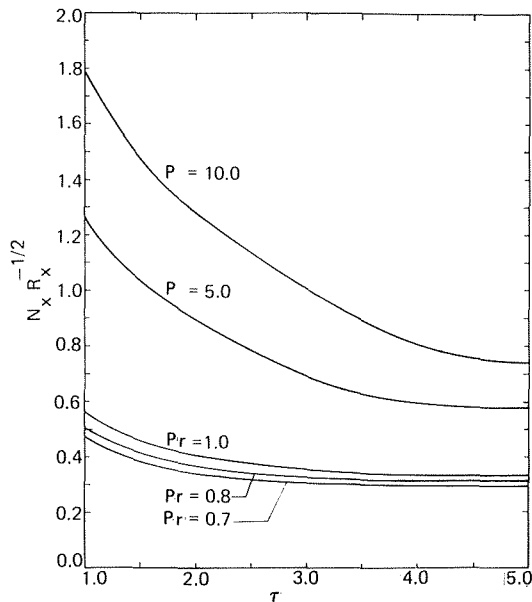


Fig. 1 Computed Nusselt number variation

Several investigators [3-5] have obtained solutions based on analytical approximations of various kinds for the momentum boundary layer in the Rayleigh-Blasius transitional region but these suffer from a lack of detail. The numerical solutions of Dwyer [6], Hall [7], and more recently of Dennis [8] by finite-difference methods are significant improvements on the earlier techniques. Dwyer's results are somewhat less accurate than those of Hall and of Dennis. Yalamanchili and Benzkofer [9] discuss the solution of the problem by the method of weighted residuals with the method of lines. Dennis [10] also solved numerically the thermal boundary layer problem posed by Riley [11] in which the Blasius boundary layer is already established when the temperature difference between the fluid and the plate is imposed. However, until the present work, no solutions for the simultaneous development of the thermal boundary with the momentum boundary layer over the impulsively-started flat plate have appeared in the literature.

### Analysis

Sufficiently far downstream of the leading edge the governing equations are the unsteady Prandtl boundary layer equations for a uniform free stream. In nondimensional form these equations are [1]

$$\frac{\partial u}{\partial x} + \frac{\partial v}{\partial y} = 0 \quad (1)$$

$$\frac{\partial u}{\partial t} + u \frac{\partial u}{\partial x} + v \frac{\partial u}{\partial y} = \frac{\partial^2 u}{\partial y^2} \quad (2)$$

$$\frac{\partial \theta}{\partial t} + u \frac{\partial \theta}{\partial x} + v \frac{\partial \theta}{\partial y} = \frac{1}{Pr} \frac{\partial^2 \theta}{\partial y^2} \quad (3)$$

The boundary conditions for equations (1)-(3) are, at the surface

$$y = 0, u = v = 0, \theta = 1 \quad (4)$$

and at the boundary layer edge

$$y \rightarrow \infty, u = 1, \theta = 0 \quad (5)$$

The initial condition is that at  $t = 0$

$$y > 0, u = 1, \theta = 0 \quad (6)$$

For  $\tau = x/t \leq 1$ , the Rayleigh problem, there is no  $x$  dependence and  $\partial\theta/\partial x = \partial u/\partial x = 0$ . Hence, the Rayleigh solution [2] of equa-

tions (1)-(3) is a function only of  $y$  and  $t$ . For the present problem this solution is

$$u = \text{erf} \left\{ \frac{y}{(2\sqrt{t})} \right\} \quad (7)$$

$$\theta = \text{erfc} \left\{ \frac{y}{(2\sqrt{t/Pr})} \right\} \quad (8)$$

It can be demonstrated through similarity arguments [7] that the solution of equations (1)-(3) can be expressed in terms of the two independent variables  $\tau = t/x$  and  $\eta = y/\sqrt{x}$  alone. However, because of the existence of an apparent reverse flow in the transformed domain the solution cannot be accomplished utilizing the usual numerical methods for two-dimensional boundary layers.

Hall [7] solved the problem by attacking the untransformed equations directly with an iterative procedure using a finite-difference technique for unsteady boundary layers. This approach was used in the present work. Details of the technique may be found in Hall [7]. The extension of the technique to include the thermal boundary layer is straightforward.

Finite-difference schemes that are potentially more efficient than the one employed by Hall may be used with his basic approach. However, to facilitate comparison between the present results and those of Hall, Hall's finite-difference scheme was used to reproduce his solution for the momentum boundary layer and to compute the present thermal boundary layer solutions.

### Results and Discussion

Solutions for the thermal boundary layer were obtained for several constant Prandtl numbers. The computed solution for the momentum boundary layer is identical with that of Hall [7] since the same solution technique was used. It also agrees closely with the solution of Dennis [8] obtained by a different technique. The mesh dimensions and convergence criteria used in the calculation for the thermal boundary layer were the same as those of Hall [7] used for the momentum boundary layer, except for the cases  $Pr = 5.0$  and  $Pr = 10.0$  in which the mesh size in the normal direction was one-third that of Hall. A single thermal boundary layer calculation for the latter cases consumed approximately three minutes IBM 370/145 CPU time.

The heat transfer results for the local Nusselt numbers are summarized in Fig. 1. Nusselt numbers were evaluated numerically from the solutions using the relation

$$N_x R_x^{-1/2} = - \left. \frac{\partial \theta}{\partial \eta} \right|_{\eta=0} \quad (9)$$

The curves in Fig. 1 can be used to determine time-dependent heat transfer coefficients in the Rayleigh-Blasius transitional region  $1 \leq \tau < \infty$ . Asymptotic approach to the steady thermal Blasius (Pohlhausen) boundary layer appears slightly slower for the larger Prandtl numbers. At a Prandtl number of 10.0 the approach is essentially complete (within 99 percent) by  $\tau = 5.0$ . In the Rayleigh region  $0 < \tau \leq 1$

$$N_x R_x^{-1/2} = [Pr/(\pi\tau)]^{1/2} \quad (10)$$

which can be obtained directly from the exact solution given by equation (8). The agreement of the computed results for  $N_x R_x^{-1/2}$  with equation (10) at  $\tau = 1$  and with thermal Blasius boundary layer solutions [12] at the asymptotic limit  $\tau \rightarrow \infty$  is within three significant figures.

Typical nondimensional temperature profiles for  $Pr = 0.7$  are shown in Fig. 2.

### References

- 1 *Laminar Boundary Layers*, Oxford University Press, Rosenhead, L., ed., 1963.
- 2 Rayleigh, Lord, "On the Motion of Solid Bodies Through Viscous Liquids," *Philosophical Magazine*, Vol. 21, 1911, pp. 697-711.
- 3 Stewartson, K., "On the Impulsive Motion of a Flat Plate in a Viscous Fluid," *Quarterly Journal of Mechanics*, Vol. 4, 1951, pp. 182-98.
- 4 Schuh, H., "Calculation of Unsteady Boundary Layers in Two-Dimensional Laminar Flow," *Zeitschrift für Flugwissenschaften*, Vol. 1, 1953, pp. 122-131.

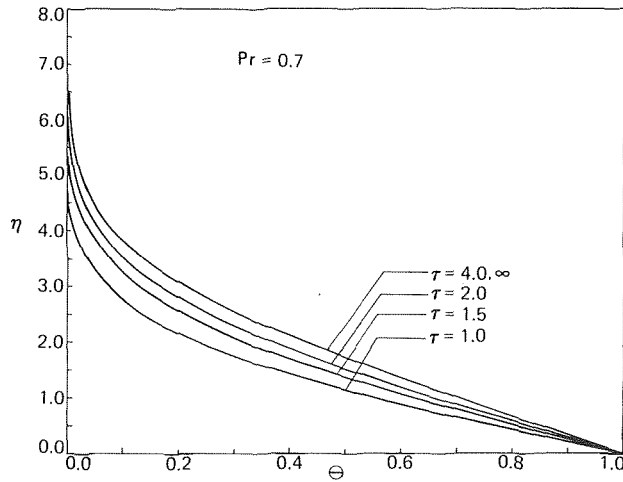


Fig. 2 Nondimensional temperature profiles for  $Pr = 0.7$

5 Cheng, S. I., and Elliott, D., "The Unsteady Laminar Boundary Layer on a Flat Plate," *TRANS. ASME*, Vol. 79, 1957, pp. 725-33.

6 Dwyer, H. A., "Calculation of Unsteady Leading-Edge Boundary Layers," *AIAA Journal*, Vol. 6, Dec. 1968, pp. 2447-2448.

7 Hall, M. G., "The Boundary Layer over an Impulsively Started Flat Plate," *Proceedings of the Royal Society, Series A*, Vol. 310, 1969, pp. 401-414.

8 Dennis, S. C. R., "The Motion of a Viscous Fluid Past an Impulsively Started Semi-Infinite Flat Plate," *Journal of the Institute of Mathematics and Its Applications*, Vol. 10, Aug. 1972, pp. 105-117.

9 Yalamanchili, R. V. S., and Benzkofer, P. D., "Unsteady Compressible Boundary Layers With Arbitrary Pressure Gradients," *AIAA Paper No. 73-132*, 11th Aerospace Sciences Meeting, Jan. 1973.

10 Dennis, S. C. R., "Unsteady Heat Transfer for Boundary-Layer Flow Over a Flat Plate," *Recent Research on Unsteady Boundary Layers*, Volume 1, IUTAM Symposium 1971, Laval University Press, Quebec 1972, pp. 379-403.

11 Riley, N., "Unsteady Heat Transfer for Flow Over a Flat Plate," *Journal of Fluid Mechanics*, Vol. 17, 1963, pp. 97-104.

12 Evans, H. L., "Mass Transfer Through Laminar Boundary Layers -7. Further Similar Solutions to the  $b$ -Equation for the Case  $B = 0$ ," *International Journal of Heat and Mass Transfer*, Vol. 5, 1962, pp. 35-57.

## Laminar Incompressible Forced Convection Along a Flat Plate With Arbitrary Suction or Injection at the Wall

Tsai-Tse Kao<sup>1</sup>

### Nomenclature

$f$  = nondimensional stream function  
 $g$  = strained value of the suction or injection parameter  $\gamma$   
 $\bar{h}$  = heat transfer coefficient  
 $k$  = thermal conductivity  
 $Nu_x = \bar{h}x/k$   
 $Pr$  = Prandtl number  
 $Re_x = U_\infty x/\nu$

<sup>1</sup> Senior Thermal/Hydraulic Engineer, Nuclear Department, Foster Wheeler Energy Corp., Livingston, N. J. Assoc. Mem. ASME.

Contributed by the Heat Transfer Division of THE AMERICAN SOCIETY OF MECHANICAL ENGINEERS. Manuscript received by the Heat Transfer Division December 19, 1974.

$T$  = temperature  
 $u$  =  $x$ -component of velocity  
 $v$  =  $y$ -component of velocity  
 $U_\infty$  = free-stream velocity  
 $x$  = coordinate along the flat plate  
 $y$  = coordinate normal to the flat plate  
 $\alpha$  = thermal diffusivity  
 $\delta_0$  = as defined in equation (6)  
 $\epsilon$  = as defined in equation (5)  
 $\epsilon'$  = derivative of  $\epsilon$  with respect to  $\gamma$   
 $\psi$  = stream function =  $(2\nu U_\infty x)^{1/2} f(x, \kappa)$   
 $\gamma$  =  $-(V_w/U_\infty)(2xU_\infty/\nu)^{1/2}$   
 $\kappa$  = transformed normal coordinate =  $(U_\infty/2\nu x)^{1/2}y$   
 $\nu$  = kinematic viscosity  
 $\theta = (T - T_\infty)/(T_w - T_\infty)$

### Subscripts

$w$  = denotes condition at the wall  
 $\infty$  = denotes ambient condition

### Superscript

' = denotes derivative taken with respect to  $\kappa$

### Analysis

Recently, a method of strained coordinates was developed and applied by Kao and Elrod [1]<sup>2</sup> and by Kao [2] to compute shear stress and heat transfer information for laminar incompressible nonsimilar boundary layers. The effectiveness of this method was well demonstrated in the foregoing references. In this technical brief, the method of strained coordinates will be extended to the case of forced convective boundary layer problems along an isothermal flat plate with arbitrary suction or injection at the wall.

Application of Görtler-Meksyn transformation [3, 4] and the procedure given in reference [1] to Prandtl's boundary layer equations for a semi-infinite flat plate subject to arbitrary suction or injection at the wall yields

$$f''' + ff'' = \epsilon(\gamma)(f' \partial f' / \partial \gamma - f'' \partial f'' / \partial \gamma) \\ = \epsilon(\gamma) dg/d\gamma (f' \partial f' / \partial g - f'' \partial f'' / \partial g) \quad (1)$$

$$\theta''/Pr + f\theta' = \epsilon(\gamma)(f' \partial \theta / \partial \gamma - \theta' \partial f / \partial \gamma) \\ = \epsilon(\gamma) dg/d\gamma (f' \partial \theta / \partial g - \theta' \partial f / \partial g) \quad (2)$$

with boundary conditions given by

$$f(g, 0) + \epsilon(\gamma)[dg/d\gamma][\partial f(g, 0)/\partial g] = \gamma \\ f'(g, 0) = 0, \quad \theta(g, 0) = 0 \\ f'(g, \infty) = 1, \quad \theta(g, \infty) = 0 \quad (3)$$

where

$$\gamma(x) = -(v_w(x)/U_\infty)(2xU_\infty/\nu)^{1/2} \quad (4)$$

$$\epsilon(\gamma) = 2xd\gamma/dx \quad (5)$$

and  $g$  is a strained value of  $\gamma$  given by the following equation

$$\gamma = g + \epsilon(\gamma)\delta_0(g) + \epsilon^2\delta_1 + \dots \quad (6)$$

Next, we seek to expand  $f$  and  $\theta$  in power series of  $\epsilon(\gamma)$

$$f = f_0(g, \kappa) + f_1(g, \kappa)\epsilon(\gamma) + f_2\epsilon^2 + \dots \quad (7)$$

$$\theta = \theta_0(g, \kappa) + \theta_1(g, \kappa)\epsilon(\gamma) + \theta_2\epsilon^2 + \dots \quad (8)$$

Here  $g$  is determined locally. The  $\delta$ 's are obtained by imposing the additional condition that the zero order solution will provide an al-

<sup>2</sup> Numbers in brackets designate References at end of technical brief.

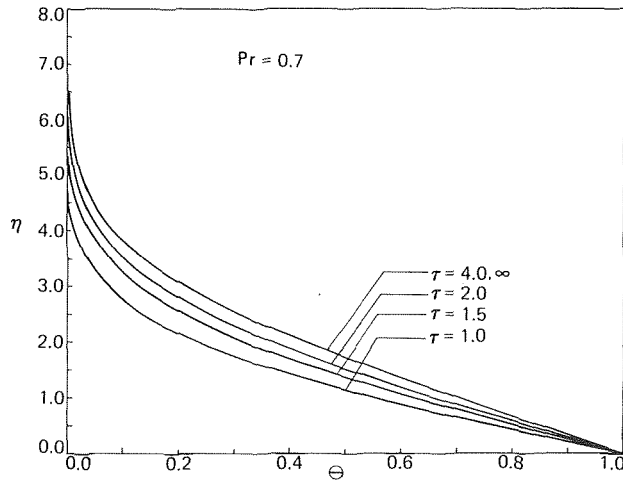


Fig. 2 Nondimensional temperature profiles for  $Pr = 0.7$

5 Cheng, S. I., and Elliott, D., "The Unsteady Laminar Boundary Layer on a Flat Plate," *TRANS. ASME*, Vol. 79, 1957, pp. 725-33.

6 Dwyer, H. A., "Calculation of Unsteady Leading-Edge Boundary Layers," *AIAA Journal*, Vol. 6, Dec. 1968, pp. 2447-2448.

7 Hall, M. G., "The Boundary Layer over an Impulsively Started Flat Plate," *Proceedings of the Royal Society, Series A*, Vol. 310, 1969, pp. 401-414.

8 Dennis, S. C. R., "The Motion of a Viscous Fluid Past an Impulsively Started Semi-Infinite Flat Plate," *Journal of the Institute of Mathematics and Its Applications*, Vol. 10, Aug. 1972, pp. 105-117.

9 Yalamanchili, R. V. S., and Benzkofer, P. D., "Unsteady Compressible Boundary Layers With Arbitrary Pressure Gradients," *AIAA Paper No. 73-132*, 11th Aerospace Sciences Meeting, Jan. 1973.

10 Dennis, S. C. R., "Unsteady Heat Transfer for Boundary-Layer Flow Over a Flat Plate," *Recent Research on Unsteady Boundary Layers*, Volume 1, IUTAM Symposium 1971, Laval University Press, Quebec 1972, pp. 379-403.

11 Riley, N., "Unsteady Heat Transfer for Flow Over a Flat Plate," *Journal of Fluid Mechanics*, Vol. 17, 1963, pp. 97-104.

12 Evans, H. L., "Mass Transfer Through Laminar Boundary Layers -7. Further Similar Solutions to the  $b$ -Equation for the Case  $B = 0$ ," *International Journal of Heat and Mass Transfer*, Vol. 5, 1962, pp. 35-57.

## Laminar Incompressible Forced Convection Along a Flat Plate With Arbitrary Suction or Injection at the Wall

Tsai-Tse Kao<sup>1</sup>

### Nomenclature

$f$  = nondimensional stream function  
 $g$  = strained value of the suction or injection parameter  $\gamma$   
 $\bar{h}$  = heat transfer coefficient  
 $k$  = thermal conductivity  
 $Nu_x$  =  $\bar{h}x/k$   
 $Pr$  = Prandtl number  
 $Re_x$  =  $U_\infty x/\nu$

<sup>1</sup> Senior Thermal/Hydraulic Engineer, Nuclear Department, Foster Wheeler Energy Corp., Livingston, N. J. Assoc. Mem. ASME.

Contributed by the Heat Transfer Division of THE AMERICAN SOCIETY OF MECHANICAL ENGINEERS. Manuscript received by the Heat Transfer Division December 19, 1974.

$T$  = temperature  
 $u$  =  $x$ -component of velocity  
 $v$  =  $y$ -component of velocity  
 $U_\infty$  = free-stream velocity  
 $x$  = coordinate along the flat plate  
 $y$  = coordinate normal to the flat plate  
 $\alpha$  = thermal diffusivity  
 $\delta_0$  = as defined in equation (6)  
 $\epsilon$  = as defined in equation (5)  
 $\epsilon'$  = derivative of  $\epsilon$  with respect to  $\gamma$   
 $\psi$  = stream function =  $(2\nu U_\infty x)^{1/2} f(x, \kappa)$   
 $\gamma$  =  $-(V_w/U_\infty)(2xU_\infty/\nu)^{1/2}$   
 $\kappa$  = transformed normal coordinate =  $(U_\infty/2\nu x)^{1/2} y$   
 $\nu$  = kinematic viscosity  
 $\theta$  =  $(T - T_\infty)/(T_w - T_\infty)$

### Subscripts

$w$  = denotes condition at the wall  
 $\infty$  = denotes ambient condition

### Superscript

= denotes derivative taken with respect to  $\kappa$

### Analysis

Recently, a method of strained coordinates was developed and applied by Kao and Elrod [1]<sup>2</sup> and by Kao [2] to compute shear stress and heat transfer information for laminar incompressible nonsimilar boundary layers. The effectiveness of this method was well demonstrated in the foregoing references. In this technical brief, the method of strained coordinates will be extended to the case of forced convective boundary layer problems along an isothermal flat plate with arbitrary suction or injection at the wall.

Application of Görtler-Meksyn transformation [3, 4] and the procedure given in reference [1] to Prandtl's boundary layer equations for a semi-infinite flat plate subject to arbitrary suction or injection at the wall yields

$$f''' + ff'' = \epsilon(\gamma)(f' \partial f' / \partial \gamma - f'' \partial f'' / \partial \gamma) \\ = \epsilon(\gamma) dg/d\gamma (f' \partial f' / \partial g - f'' \partial f'' / \partial g) \quad (1)$$

$$\theta''/Pr + f\theta' = \epsilon(\gamma)(f' \partial \theta / \partial \gamma - \theta' \partial f / \partial \gamma) \\ = \epsilon(\gamma) dg/d\gamma (f' \partial \theta / \partial g - \theta' \partial f / \partial g) \quad (2)$$

with boundary conditions given by

$$f(g, 0) + \epsilon(\gamma)[dg/d\gamma][\partial f(g, 0)/\partial g] = \gamma \\ f'(g, 0) = 0, \quad \theta(g, 0) = 0 \\ f'(g, \infty) = 1, \quad \theta(g, \infty) = 0 \quad (3)$$

where

$$\gamma(x) = -(v_w(x)/U_\infty)(2xU_\infty/\nu)^{1/2} \quad (4)$$

$$\epsilon(\gamma) = 2xd\gamma/dx \quad (5)$$

and  $g$  is a strained value of  $\gamma$  given by the following equation

$$\gamma = g + \epsilon(\gamma)\delta_0(g) + \epsilon^2\delta_1 + \dots \quad (6)$$

Next, we seek to expand  $f$  and  $\theta$  in power series of  $\epsilon(\gamma)$

$$f = f_0(g, \kappa) + f_1(g, \kappa)\epsilon(\gamma) + f_2\epsilon^2 + \dots \quad (7)$$

$$\theta = \theta_0(g, \kappa) + \theta_1(g, \kappa)\epsilon(\gamma) + \theta_2\epsilon^2 + \dots \quad (8)$$

Here  $g$  is determined locally. The  $\delta$ 's are obtained by imposing the additional condition that the zero order solution will provide an al-

<sup>2</sup> Numbers in brackets designate References at end of technical brief.

most exact wall shear stress. Thus, in order to find  $\delta_0$ , we require that  $f_1''(g, 0) = 0$ ; for  $\delta_1$ ,  $f_2''(g, 0)$  is set to zero, etc. Here we shall confine ourselves to  $\delta_0$  only.

Upon substituting the above expressions into equations (1) and (2), and equating terms of like powers of  $\epsilon(\gamma)$ , the first two sets of equations give

Order unity:

$$f_0''' + f_0 f_0'' = 0$$

$$\theta_0''/\text{Pr} + f_0 \theta_0' = 0 \quad (9)$$

$$f_0(g, 0) = g, \quad f_0'(g, 0) = 0, \quad \theta_0(g, 0) = 1 \quad (10)$$

$$f_0'(g, \infty) = 1, \quad \theta_0(g, \infty) = 0 \quad (11)$$

Order  $\epsilon$ :

$$f_1''' + f_0 f_1'' - \epsilon' f_0' f_1' + (1 + \epsilon') f_0'' f_1 = (1 - \epsilon' \delta_0)(f_0' \partial f_0' / \partial g - f_0'' \partial f_0 / \partial g) \quad (12)$$

$$\theta_1''/\text{Pr} + f_0 \theta_1' - \epsilon' f_0' \theta_1 = (1 - \epsilon' \delta_0)(f_0' \partial \theta_0 / \partial g - \theta_0' \partial f_0 / \partial g) - (1 + \epsilon') \theta_0' f_1 \quad (13)$$

$$f_1(g, 0) = \delta_0 - 1/(1 + \epsilon')$$

$$f_1'(g, 0) = f_1''(g, 0) = \theta_1(g, 0) = 0 \quad (14)$$

$$f_1'(g, \infty) = \theta_1(g, \infty) = 0$$

A standard shooting technique as described by Nachtsheim and Swigert [5] is used to solve for the  $\delta_0$ .

In order to facilitate the numerical computation, two auxiliary equations for  $G = \partial f_0 / \partial g$  and  $H = \partial \theta_0 / \partial g$  are generated by differentiating equations (9) and (10) with respect to  $g$ . Thus

$$G''' + f_0 G'' + f_0' G = 0$$

$$H''/\text{Pr} + f_0 H' + \theta_0' G = 0$$

with boundary conditions given by

$$G(g, 0) = 1, \quad G'(g, 0) = H(g, 0) = 0$$

$$G'(g, \infty) = H(g, \infty) = 0$$

The resulting zero order universal functions  $f_0''(g, 0)$  and  $\theta_0'(g, 0)$  are well-known and can be obtained, for example from reference [9].  $\delta_0(g, \epsilon')$  and  $\theta_1'(g, \epsilon', 0)$  for  $\text{Pr} = 0.7$  are given in Figs. 1 and 2,

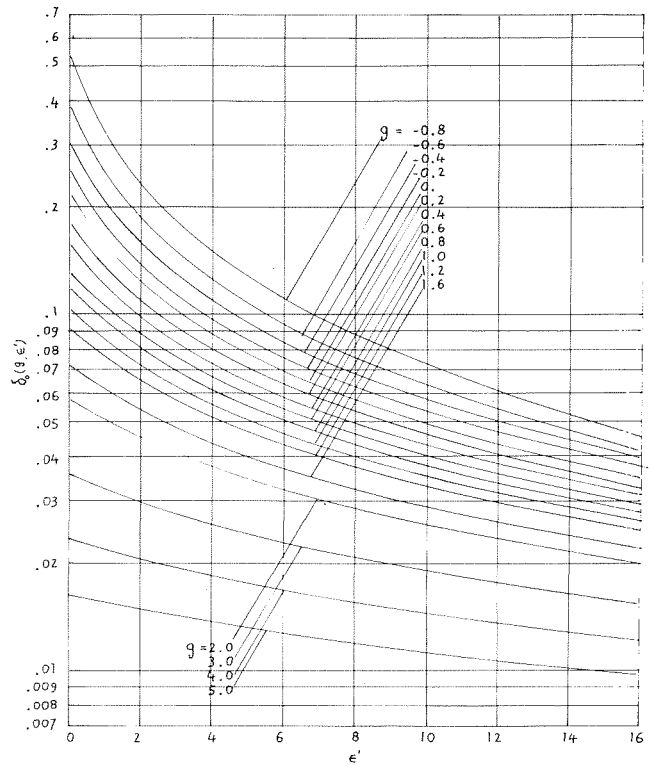


Fig. 1  $\delta_0(g, \epsilon')$  for suction and injection problems

respectively. These results can be used to determine wall shear stress and heat transfer informations of any forced convection problems with arbitrary suction and injection along an isothermal flat plate. Computations can readily be carried out with the aid of Figs. 1 and 2. The following iterative procedure can be used to solve for the strained value of  $\gamma$  with the aid of Fig. 1:

- Select a streamwise location and determine from the data values for  $\gamma$ ,  $\epsilon(\gamma)$ , and  $\epsilon'(\gamma)$ ;
- guess  $g$ ;
- read  $\delta_0$  from Fig. 1;

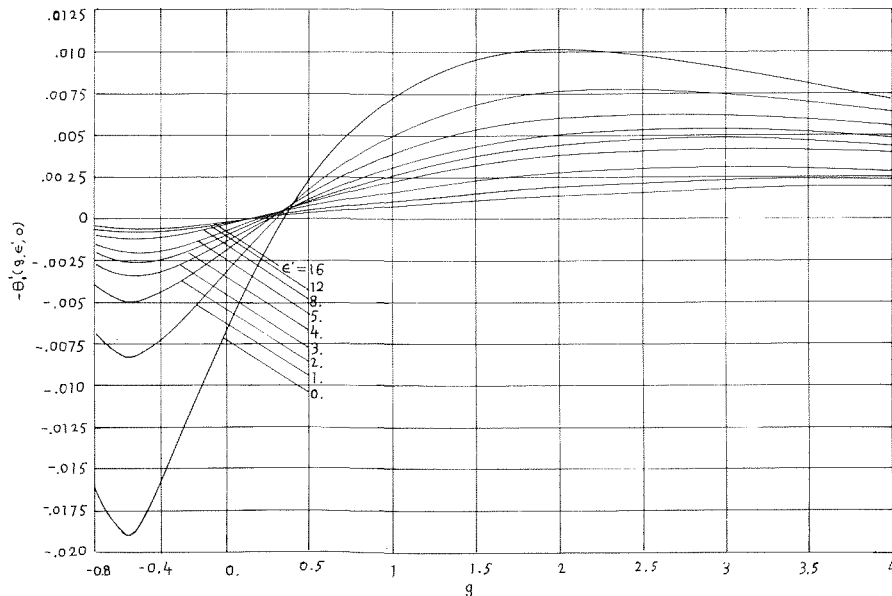


Fig. 2  $\theta_1'(g, \epsilon', 0)$  for suction and injection problems

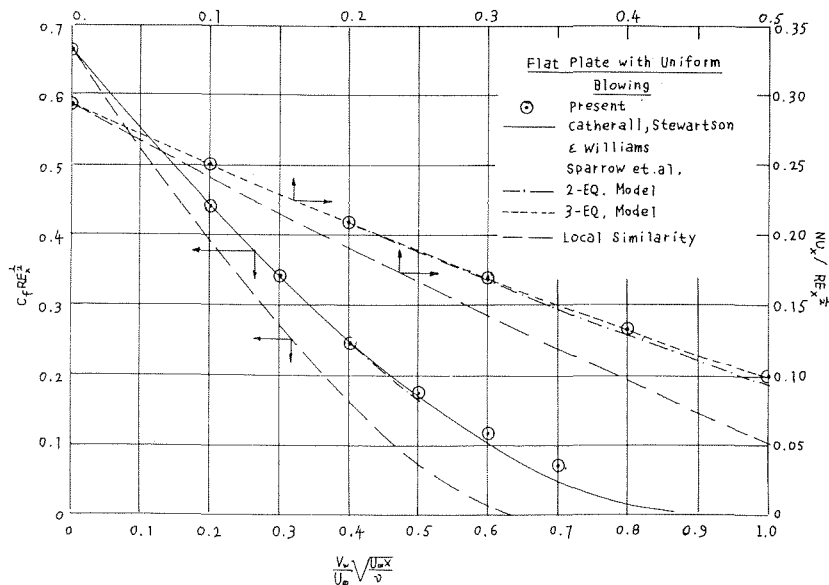


Fig. 3 Comparison of shear stress and heat transfer results

- (d) get a new  $g$  from equation (6);
- (e) read a new  $\delta_0$  from Fig. 1;
- (f) average the new and previous  $\delta_0$ 's;
- (g) get a new  $g$  from equation (6);
- (h) read Fig. 1, etc.

Once  $g$  is obtained, shear stress can be determined from the corresponding zero order solution. Heat transfer information can likewise be obtained from  $\theta_0'(g, 0)$  and  $\theta_1'(g, e', 0)$  from Fig. 2.

### Example

In order to demonstrate the effectiveness of the present technique, let us consider the example of homogeneous blowing. For this case, we have  $\epsilon = \gamma$  and  $\epsilon'(\gamma) = 1$ . The nondimensional shear stress and heat transfer parameters for this case are given by

$$C_f/Re_x = \sqrt{2}f''(g, 0)$$

$$Nu_x/\sqrt{Re_x} = -\{\theta_0'(g, 0) + e\theta_1'(g, e', 0)\}/\sqrt{2}$$

The solutions at several streamwise stations are given in Fig. 3. Also shown are the numerical solutions of Catherall, Stewartson, and Williams [6], Sparrow's locally nonsimilar method [7, 8], and local similarity model.

Within the scale of the figure, the present shear stress solutions agree remarkably well with the presumably exact numerical solution and Sparrow's 3-equation locally nonsimilar solution which is indistinguishable from the numerical solution. The nondimensional heat transfer coefficients obtained by the present method essentially coincide with Sparrow's 3-equation model. This clear success of the present solution method is further accentuated when one takes into account of the significant errors in the results of the local similar model. For example, the nondimensional shear stress at  $V_w/U_\infty \sqrt{U_\infty X/\nu} = 0.5$  is 43 percent of the exact value. The results of Fig. 3 and the simplicity in carrying out the computation of shear stress and heat transfer informations lend strong support to the utility of the present solution method.

### Acknowledgment

The author would like to thank Prof. H. G. Elrod Jr., Department of Mechanical Engineering, Columbia University, for numerous helpful discussions on the development and application of the asymptotic method used in this paper.

### References

- 1 Kao, T. T., and Elrod, H. G., "Laminar Shear Stress Pattern for Non-Similar Incompressible Boundary Layers," *AIAA Journal*, Vol. 12, No. 10, Oct. 1974, pp. 1401-1408.

- 2 Kao, T. T., "An Asymptotic Method for the Computation of Laminar Shear Stress and Heat Flux in Forced and Free Convection," Doctoral Dissertation, Department of Mechanical Engineering, Columbia University, N. Y., Apr. 1974.
- 3 Görtler, H., "A New Series for the Calculation of Steady Laminar Boundary-Layer Flows," *Journal of Math. and Mech.*, Vol. 6, No. 1, 1957, pp. 1-66.
- 4 Meksyn, D., *New Methods in Laminar Boundary-Layer Theory*, Pergamon Press, 1961.
- 5 Nachtsheim, P. R., and Swigert, P., "Satisfaction of Asymptotic Boundary Conditions in Numerical Solution of Systems of Non-Linear Equations of Boundary-Layer Type," NASA TN-D3004, 1965.
- 6 Catherall, D., Stewartson, K., and Williams, P. G., "Viscous Flow Past a Flat Plate With Uniform Suction," *Proceedings of Royal Society, London, Series a*, Vol. 284, No. 1398, 1965, pp. 370-396.
- 7 Sparrow, E. M., Quack, H., and Boerner, C. J., "Local Non-Similar Boundary-Layer Solutions," *AIAA Journal*, Vol. 8, No. 11, 1971, pp. 1936-1942.
- 8 Sparrow, E. M., and Yu, H. S., "Local Non-Similar Thermal Boundary-Layer Solutions," *JOURNAL OF HEAT TRANSFER, TRANS. ASME, Series C*, Vol. 9, 1971, pp. 328-334.
- 9 Elzy, E., and Sisson, R. M., "Tables of Similar Solutions to the Equations of Momentum, Heat and Mass Transfer in Laminar Boundary Layer Flow," Engineering Experiment Station, Oregon State University, Corvallis, Oregon, Bulletin No. 40., 1967.

## The Effect of Wall Suction on the Apparent Roughness of Porous Tubes

A. Brosh<sup>1</sup> and Y. Winograd<sup>2</sup>

### Introduction

In recent experiments carried out by the authors [1]<sup>3</sup> it was found that the flow in a tube with wall suction can be considered quasi-developed (i.e., the suction length has no effect on the flow

<sup>1</sup> NRC Fellow, NASA Ames Research Center Moffett Field, Calif.

<sup>2</sup> Faculty of Mechanical Engineering, Technion—Israel Institute of Technology, Haifa, Israel.

<sup>3</sup> Numbers in brackets designate References at end of technical brief.

Contributed by the Heat Transfer Division of THE AMERICAN SOCIETY OF MECHANICAL ENGINEERS. Manuscript received by the Heat Transfer Division November 25, 1974.

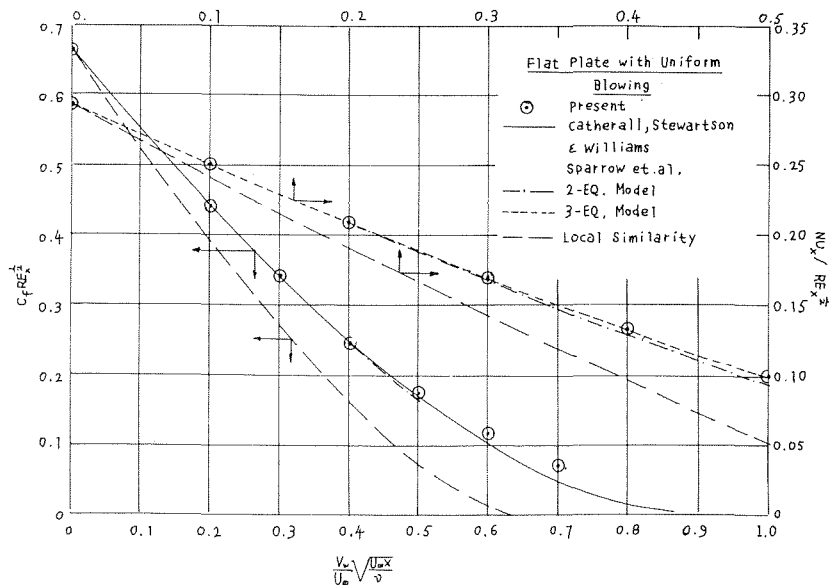


Fig. 3 Comparison of shear stress and heat transfer results

- (d) get a new  $g$  from equation (6);
- (e) read a new  $\delta_0$  from Fig. 1;
- (f) average the new and previous  $\delta_0$ 's;
- (g) get a new  $g$  from equation (6);
- (h) read Fig. 1, etc.

Once  $g$  is obtained, shear stress can be determined from the corresponding zero order solution. Heat transfer information can likewise be obtained from  $\theta_0'(g, 0)$  and  $\theta_1'(g, e', 0)$  from Fig. 2.

### Example

In order to demonstrate the effectiveness of the present technique, let us consider the example of homogeneous blowing. For this case, we have  $\epsilon = \gamma$  and  $\epsilon'(\gamma) = 1$ . The nondimensional shear stress and heat transfer parameters for this case are given by

$$C_f/Re_x = \sqrt{2}f''(g, 0)$$

$$Nu_x/\sqrt{Re_x} = -\{\theta_0'(g, 0) + e\theta_1'(g, e', 0)\}/\sqrt{2}$$

The solutions at several streamwise stations are given in Fig. 3. Also shown are the numerical solutions of Catherall, Stewartson, and Williams [6], Sparrow's locally nonsimilar method [7, 8], and local similarity model.

Within the scale of the figure, the present shear stress solutions agree remarkably well with the presumably exact numerical solution and Sparrow's 3-equation locally nonsimilar solution which is indistinguishable from the numerical solution. The nondimensional heat transfer coefficients obtained by the present method essentially coincide with Sparrow's 3-equation model. This clear success of the present solution method is further accentuated when one takes into account of the significant errors in the results of the local similar model. For example, the nondimensional shear stress at  $V_w/U_\infty \sqrt{U_\infty X/\nu} = 0.5$  is 43 percent of the exact value. The results of Fig. 3 and the simplicity in carrying out the computation of shear stress and heat transfer informations lend strong support to the utility of the present solution method.

### Acknowledgment

The author would like to thank Prof. H. G. Elrod Jr., Department of Mechanical Engineering, Columbia University, for numerous helpful discussions on the development and application of the asymptotic method used in this paper.

### References

- 1 Kao, T. T., and Elrod, H. G., "Laminar Shear Stress Pattern for Non-Similar Incompressible Boundary Layers," *AIAA Journal*, Vol. 12, No. 10, Oct. 1974, pp. 1401-1408.

- 2 Kao, T. T., "An Asymptotic Method for the Computation of Laminar Shear Stress and Heat Flux in Forced and Free Convection," Doctoral Dissertation, Department of Mechanical Engineering, Columbia University, N. Y., Apr. 1974.
- 3 Görtler, H., "A New Series for the Calculation of Steady Laminar Boundary-Layer Flows," *Journal of Math. and Mech.*, Vol. 6, No. 1, 1957, pp. 1-66.
- 4 Meksyn, D., *New Methods in Laminar Boundary-Layer Theory*, Pergamon Press, 1961.
- 5 Nachtsheim, P. R., and Swigert, P., "Satisfaction of Asymptotic Boundary Conditions in Numerical Solution of Systems of Non-Linear Equations of Boundary-Layer Type," NASA TN-D3004, 1965.
- 6 Catherall, D., Stewartson, K., and Williams, P. G., "Viscous Flow Past a Flat Plate With Uniform Suction," *Proceedings of Royal Society, London, Series a*, Vol. 284, No. 1398, 1965, pp. 370-396.
- 7 Sparrow, E. M., Quack, H., and Boerner, C. J., "Local Non-Similar Boundary-Layer Solutions," *AIAA Journal*, Vol. 8, No. 11, 1971, pp. 1936-1942.
- 8 Sparrow, E. M., and Yu, H. S., "Local Non-Similar Thermal Boundary-Layer Solutions," *JOURNAL OF HEAT TRANSFER, TRANS. ASME, Series C*, Vol. 9, 1971, pp. 328-334.
- 9 Elzy, E., and Sisson, R. M., "Tables of Similar Solutions to the Equations of Momentum, Heat and Mass Transfer in Laminar Boundary Layer Flow," Engineering Experiment Station, Oregon State University, Corvallis, Oregon, Bulletin No. 40., 1967.

## The Effect of Wall Suction on the Apparent Roughness of Porous Tubes

A. Brosh<sup>1</sup> and Y. Winograd<sup>2</sup>

### Introduction

In recent experiments carried out by the authors [1]<sup>3</sup> it was found that the flow in a tube with wall suction can be considered quasi-developed (i.e., the suction length has no effect on the flow

<sup>1</sup> NRC Fellow, NASA Ames Research Center Moffett Field, Calif.

<sup>2</sup> Faculty of Mechanical Engineering, Technion—Israel Institute of Technology, Haifa, Israel.

<sup>3</sup> Numbers in brackets designate References at end of technical brief.

Contributed by the Heat Transfer Division of THE AMERICAN SOCIETY OF MECHANICAL ENGINEERS. Manuscript received by the Heat Transfer Division November 25, 1974.

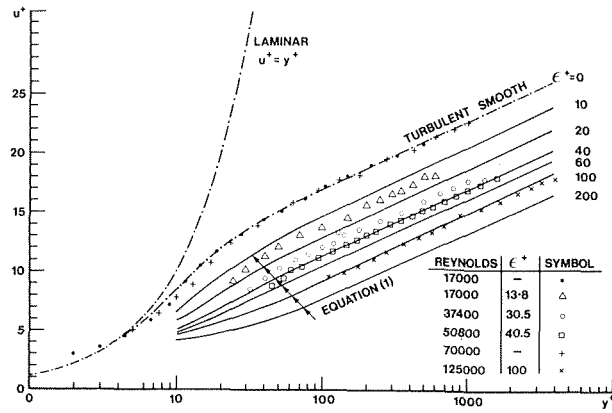


Fig. 1 Velocity profiles for various Reynolds numbers in the smooth tube and in the porous rough tube without suction

characteristics at a given local Reynolds number) only if suction is applied along more than 40 dia. Under such conditions (i.e., in quasi-developed flow), the turbulence level is lower than the turbulence level in regular fully developed pipe flow, as predicted by Merkin, et al. [2]. Since the experimental setup for turbulent pipe flow with suction involves porous tubes which are inherently rough, while the analytical model presented in [2] is for smooth tubes, it is necessary to modify this model for rough tubes before any quantitative comparison between the model and experiments can be made. The purpose of this note is to present a modified model for flow in a rough tube with wall suction and to compare it with experimental results. It is shown that satisfactory agreement between theory and experiments can be obtained if it is assumed that an additional effect of suction is to reduce the influence of wall roughness on the flow field inside the tube.

### Theory

According to the model proposed by van Driest for turbulent flow near a rough wall [3] the velocity profile is given by

$$u^+ = \int_0^{y^+} \frac{2 dy^+}{(1 + 1 + 4K^2 y^{*2} Df_r^2)^{1/2}} \quad (1)$$

where  $Df_r$  is the damping factor for rough wall and is given by

$$Df_r = 1 - \exp\left(-\frac{y^+}{A^+}\right) + \exp\left(-\frac{60y^+}{A^+ \epsilon^+}\right) \quad (2)$$

The damping constant  $A^+$  equals 26 for flow without suction,  $\epsilon^+$  is the roughness Reynolds number  $\epsilon u^*/\nu$ , and  $K$  is the universal mixing length constant, usually taken as 0.4.

Following Kays, et al. [4], the effect of suction and pressure gradient on the value of  $A^+$  is given by

$$A^+ = \frac{4.42}{0.17 - v_w^+} + 1133P^+ + 6.78(-P^+)^{0.7} v_w^{*+1.4} \quad (3)$$

where  $v_w^+$  is the dimensionless radial velocity at the wall  $v_w/u^*$ ,  $u^*$  is the friction velocity [ $u^* = (\tau_w/\rho)^{1/2}$ ] and  $P^+$  is the pressure gradient function which for accelerated flow over a flat plate is given by [4]

$$P^+ = \left(\frac{\nu}{\bar{u}^2} \frac{d\bar{u}}{dx}\right) / \left(\frac{\tau_w}{\rho \bar{u}^2}\right)^{1.5} \quad (4)$$

Evaluating  $d\bar{u}/dx$  for porous tube flow, it is found that  $d\bar{u}/dx = -2v_w/r_w$ . Thus, after introducing nondimensional quantities, equation (4) becomes

$$P^+ = -\frac{4\alpha}{Re} / \left(\frac{4r_w^{*2}}{Re^2}\right)^{1.5} \quad (5)$$

where  $\alpha$  is the suction ratio  $v_w/\bar{u}$ , and  $r_w^+$  is the dimensionless pipe radius  $r_w u^*/\nu$ .

Combining equations (2), (3), and (5) together with the continuity and momentum equations in the way outlined by Kinney and Sparrow [5] the following equation for  $u^+$  results.

$$\frac{du^+}{dy^+} + l^{*2} \left(\frac{du^+}{dy^+}\right)^2 = 1 - \frac{y^+}{r_w^+} - \frac{\alpha u^+}{r_w^+ - y^+} \left[ \frac{Re}{2} - \frac{2}{r_w^+} \int_0^{y^+} u^+(r_w^+ - y^*) dy^* \right] + \frac{4\alpha}{r_w^+} \frac{1}{r_w^+ - y^+} \left\{ \left[ 1 - \left(\frac{y^+}{r_w^+}\right)^2 \right] \int_0^{r_w^+} u^{*2}(r_w^+ - y^*) dy^* - \int_0^{y^+} u^{*2}(r_w^+ - y^*) dy^* \right\} \quad (6)$$

$l$  is the mixing length [6] multiplied by the damping factor and  $l^+$  is the nondimensional mixing length  $lu^*/\nu$ . Equation (6) was solved numerically with the no-slip condition as a boundary condition. The results of the numerical calculations are discussed later.

### Experimental Results and Discussion

The experimental system is discussed in [1]. A preliminary set of experiments was carried out in smooth tube. In the first set of experiments in the porous tube, the characteristics of the flow without suction were determined. The relative roughness  $\epsilon/D$  of the tube's inside wall as measured with a crystal pickup was 0.0115. Calculations of the relative roughness based on the pressure gradient along the tube axis as a function of the Reynolds number agreed with the measured value. Velocity profiles were measured at various Reynolds numbers and the results, shown in Fig. 1, agree well with equation (1). The smooth tube data are also shown in Fig. 1.

Next, a uniform suction (i.e., constant suction ratio  $\alpha$  along the tube) was applied to the flow. The suction length was always over 50 dia in order to assure quasi-developed flow [1] at the exit plane, where the measurements were taken. Typical results for  $Re = 2 \times 10^4$  and various suction ratios are shown in Fig. 2. Calculated results for the model presented in [2] (not taking the wall roughness into account) and for equation (6) are also shown in Fig. 2. The good agreement between equation (6) and the experimental results is obtained after substituting  $\epsilon^+$  by an effective roughness Reynolds number,  $\epsilon_s^+$ , which is a function of the suction rate. The effective roughness was chosen by trial and error until a best fit to the data was obtained. From the numbers presented in Fig. 2 one can realize that the agreement with experimental results is obtained when the effective roughness Reynolds number,  $\epsilon_s^+$ , is lower than the roughness Reynolds number,  $\epsilon^+$ , with no suction and it decreases with increasing suction rate. A possible explanation is that the suction removes part of the vortices which are created by the rough surface before they diffuse into the flow, and thus reduces the influence of the wall roughness. Further study, involving tubes with different roughness, is clearly indicated, before the exact na-

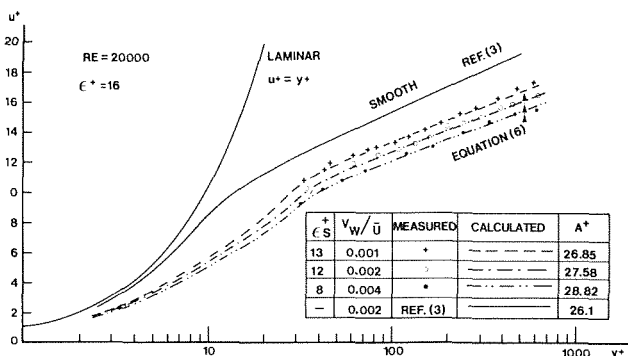


Fig. 2 Comparison between measured and calculated velocity profiles in the porous tube, for various suction rates

ture of this phenomena and a correlation between suction and effective wall roughness could be determined.

### Acknowledgment

Professor Winograd was killed in action on October 10, 1973, serving as an artillery officer on the Golan Heights defending his country.

This paper is based in part on the PhD thesis of the first author. The experimental work was granted by Technion research funds.

### References

- 1 Brosh, A., and Winograd, Y., "Experimental Study of Turbulent Flow in a Tube With Wall Suction," *JOURNAL OF HEAT TRANSFER*, TRANS. ASME, Series C, Vol. 96, 1974, p. 338.
- 2 Merkin, L., Solan, A., and Winograd, Y., "Turbulent Flow in a Tube With Wall Suction," *JOURNAL OF HEAT TRANSFER*, TRANS. ASME, Series C, Vol. 93, 1971, p. 242.
- 3 van Driest, E. R., "On Turbulent Flow Near Wall," *Journal of Aeronautical Science*, Vol. 23, 1956, p. 1007.
- 4 Kays, W. M., Moffat, R. J., and Thielbahr, W. H., "Heat Transfer to the Highly Accelerated Turbulent Boundary Layer With and Without Mass Addition," ASME Paper No. 69-HT-53, 1969.
- 5 Kinney, R. B., and Sparrow, E. M., "Turbulent Flow, Heat Transfer and Mass Transfer in a Tube With Surface Suction," *JOURNAL OF HEAT TRANSFER*, TRANS. ASME, Series C, vol. 92, 1970, p. 117.
- 6 Schlichting, H., *Boundary Layer Theory* 6th ed., McGraw Hill, New York, 1968, p. 568.

## Empirical Correlations for Heat Transfer and Flow Friction Characteristics of Rectangular Offset-Fin Plate-Fin Heat Exchangers

A. R. Wieting<sup>1</sup>

### Nomenclature

- $A_f/A$  = ratio of fin area to total heat-transfer area,  $1/1 + \alpha$   
 $D$  = hydraulic diameter,  $2wh/(w + h)$ , in. (mm)  
 $f$  = friction factor (see [1]<sup>2</sup>)  
 $h$  = flow passage height, in. (mm)  
 $j$  = colburn modulus,  $St Pr^{2/3}$   
 $Pr$  = Prandtl number  
 $Re_D$  = Reynolds number based on hydraulic diameter  
 $Re_{D,f}^*$  = reference  $Re_D$  for  $f$  factor defined by equation (7)  
 $Re_{D,j}^*$  = reference  $Re_D$  for  $j$  factor defined by equation (8)  
 $St$  = Stanton number  
 $t$  = fin thickness, in. (mm)  
 $w$  = flow passage width, in. (mm)  
 $x$  = fin length in the flow direction, in. (mm)  
 $\alpha$  = aspect ratio,  $w/h$   
 $\beta$  = ratio of total heat-transfer area on one side of a plate-fin heat exchanger to the volume between the plates on that side,  $ft^{-1}$  ( $m^{-1}$ )

### Introduction

The need for small size, lightweight, high-performance heat exchangers in all varieties of powered vehicles from automobiles to

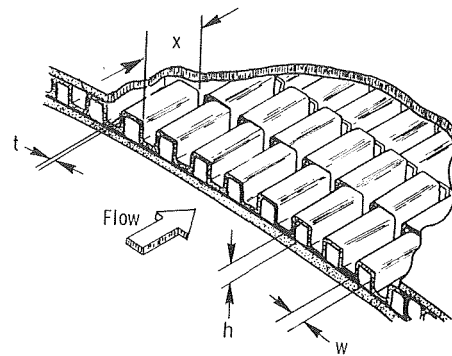


Fig. 1 Typical rectangular offset-fin plate-fin heat exchanger

spacecraft, as well as a multitude of other applications, has resulted in the development of several classes (e.g., plain-fin, pin-fin, offset-fin) of plate-fin heat exchangers that are much more compact and higher performing than tubes. The rectangular offset-fin plate-fin heat exchanger shown in Fig. 1 is one of the more versatile classes. The fins are offset to prevent fully developed flow and thereby to take advantage of the increased heat-transfer characteristics due to the thermal entry length effect.

An extensive literature search revealed that empirical and analytical solutions for the performance of rectangular offset-fin plate-fin heat exchangers are virtually nonexistent. In 1950, an empirical relationship for offset-fin surfaces was developed [2]; however, the correlation was based on limited data and several different types of offset-fins. Analytical solutions exist for round tubes, rectangular ducts, and parallel plates [1, 3] for developing hydraulic and/or thermal boundary layers with either a uniform peripheral heat flux or temperature. These solutions are not directly applicable to the offset-fin plate-fin heat exchanger because: (1) the boundary layer is developing only on the fin surfaces and not on the plate surfaces too, (2) the peripheral heat flux or temperature for a given flow passage is nonuniform, (3) the approaching flow is also nonuniform due to turbulence generated by the blunt fin leading edges and wake flow at the fin trailing edges [4]. Even if these effects could be accounted for analytically, the results probably still would not agree with experimental results due to manufacturing irregularities, such as burred or curled fin edges and filleting by the braze alloy at the fin to plate junction [5, 6]. Consequently, development of empirical relationships through data correlation is probably the most realistic means of obtaining a method to predict the characteristics of untested heat exchangers of this type.

The purpose of this paper is to provide such empirical correlations of experimental heat transfer and flow friction data for rectangular offset-fin plate-fin heat exchangers. With these correlations, the performance characteristics of untested offset-fin geometries can be predicted realistically and accurately within the parameter range of the correlations, and the effects on performance of the various fin geometric parameters can be assessed.

**Method of Correlation.** Empirical relationships were developed by correlating experimental heat transfer and flow friction data [1, 5, 7, 8] for 22 rectangular offset-fin plate-fin configurations over two Reynolds number ranges:  $Re_D \leq 1000$  which is primarily laminar and  $Re_D \geq 2000$  which is primarily turbulent. Inasmuch as a clearly defined transitional  $Re_D$  is nonexistent and transition basically occurs between  $1000 < Re_D < 2000$ , this  $Re_D$  range was excluded to minimize the effect of the transitional  $Re_D$  range on the correlations. From consideration of those variables which experimental data indicated were important to the heat transfer and friction process, the following nondimensional functional relations were assumed:

$$f = C_1(x/D)_1^a (t/D)_2^a (\alpha)_3^a (Re_D)_4^a \quad (1)$$

<sup>1</sup> Aerospace Technologist, Structures and Dynamics Division, NASA Langley Research Center, Hampton, Va.

<sup>2</sup> Numbers in brackets designate References at end of paper.

Contributed by the Heat Transfer Division of THE AMERICAN SOCIETY OF MECHANICAL ENGINEERS. Manuscript received by the Heat Transfer Division September 23, 1974.

ture of this phenomena and a correlation between suction and effective wall roughness could be determined.

### Acknowledgment

Professor Winograd was killed in action on October 10, 1973, serving as an artillery officer on the Golan Heights defending his country.

This paper is based in part on the PhD thesis of the first author. The experimental work was granted by Technion research funds.

### References

- 1 Brosh, A., and Winograd, Y., "Experimental Study of Turbulent Flow in a Tube With Wall Suction," *JOURNAL OF HEAT TRANSFER*, TRANS. ASME, Series C, Vol. 96, 1974, p. 338.
- 2 Merkin, L., Solan, A., and Winograd, Y., "Turbulent Flow in a Tube With Wall Suction," *JOURNAL OF HEAT TRANSFER*, TRANS. ASME, Series C, Vol. 93, 1971, p. 242.
- 3 van Driest, E. R., "On Turbulent Flow Near Wall," *Journal of Aeronautical Science*, Vol. 23, 1956, p. 1007.
- 4 Kays, W. M., Moffat, R. J., and Thielbahr, W. H., "Heat Transfer to the Highly Accelerated Turbulent Boundary Layer With and Without Mass Addition," ASME Paper No. 69-HT-53, 1969.
- 5 Kinney, R. B., and Sparrow, E. M., "Turbulent Flow, Heat Transfer and Mass Transfer in a Tube With Surface Suction," *JOURNAL OF HEAT TRANSFER*, TRANS. ASME, Series C, vol. 92, 1970, p. 117.
- 6 Schlichting, H., *Boundary Layer Theory* 6th ed., McGraw Hill, New York, 1968, p. 568.

## Empirical Correlations for Heat Transfer and Flow Friction Characteristics of Rectangular Offset-Fin Plate-Fin Heat Exchangers

A. R. Wieting<sup>1</sup>

### Nomenclature

- $A_f/A$  = ratio of fin area to total heat-transfer area,  $1/1 + \alpha$   
 $D$  = hydraulic diameter,  $2wh/(w + h)$ , in. (mm)  
 $f$  = friction factor (see [1]<sup>2</sup>)  
 $h$  = flow passage height, in. (mm)  
 $j$  = colburn modulus,  $St Pr^{2/3}$   
 $Pr$  = Prandtl number  
 $Re_D$  = Reynolds number based on hydraulic diameter  
 $Re_{D,f}^*$  = reference  $Re_D$  for  $f$  factor defined by equation (7)  
 $Re_{D,j}^*$  = reference  $Re_D$  for  $j$  factor defined by equation (8)  
 $St$  = Stanton number  
 $t$  = fin thickness, in. (mm)  
 $w$  = flow passage width, in. (mm)  
 $x$  = fin length in the flow direction, in. (mm)  
 $\alpha$  = aspect ratio,  $w/h$   
 $\beta$  = ratio of total heat-transfer area on one side of a plate-fin heat exchanger to the volume between the plates on that side,  $ft^{-1}$  ( $m^{-1}$ )

### Introduction

The need for small size, lightweight, high-performance heat exchangers in all varieties of powered vehicles from automobiles to

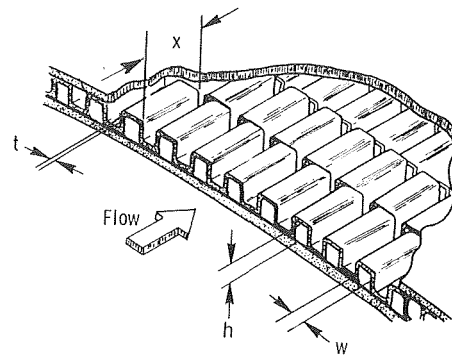


Fig. 1 Typical rectangular offset-fin plate-fin heat exchanger

spacecraft, as well as a multitude of other applications, has resulted in the development of several classes (e.g., plain-fin, pin-fin, offset-fin) of plate-fin heat exchangers that are much more compact and higher performing than tubes. The rectangular offset-fin plate-fin heat exchanger shown in Fig. 1 is one of the more versatile classes. The fins are offset to prevent fully developed flow and thereby to take advantage of the increased heat-transfer characteristics due to the thermal entry length effect.

An extensive literature search revealed that empirical and analytical solutions for the performance of rectangular offset-fin plate-fin heat exchangers are virtually nonexistent. In 1950, an empirical relationship for offset-fin surfaces was developed [2]; however, the correlation was based on limited data and several different types of offset-fins. Analytical solutions exist for round tubes, rectangular ducts, and parallel plates [1, 3] for developing hydraulic and/or thermal boundary layers with either a uniform peripheral heat flux or temperature. These solutions are not directly applicable to the offset-fin plate-fin heat exchanger because: (1) the boundary layer is developing only on the fin surfaces and not on the plate surfaces too, (2) the peripheral heat flux or temperature for a given flow passage is nonuniform, (3) the approaching flow is also nonuniform due to turbulence generated by the blunt fin leading edges and wake flow at the fin trailing edges [4]. Even if these effects could be accounted for analytically, the results probably still would not agree with experimental results due to manufacturing irregularities, such as burred or curled fin edges and filleting by the braze alloy at the fin to plate junction [5, 6]. Consequently, development of empirical relationships through data correlation is probably the most realistic means of obtaining a method to predict the characteristics of untested heat exchangers of this type.

The purpose of this paper is to provide such empirical correlations of experimental heat transfer and flow friction data for rectangular offset-fin plate-fin heat exchangers. With these correlations, the performance characteristics of untested offset-fin geometries can be predicted realistically and accurately within the parameter range of the correlations, and the effects on performance of the various fin geometric parameters can be assessed.

**Method of Correlation.** Empirical relationships were developed by correlating experimental heat transfer and flow friction data [1, 5, 7, 8] for 22 rectangular offset-fin plate-fin configurations over two Reynolds number ranges:  $Re_D \leq 1000$  which is primarily laminar and  $Re_D \geq 2000$  which is primarily turbulent. Inasmuch as a clearly defined transitional  $Re_D$  is nonexistent and transition basically occurs between  $1000 < Re_D < 2000$ , this  $Re_D$  range was excluded to minimize the effect of the transitional  $Re_D$  range on the correlations. From consideration of those variables which experimental data indicated were important to the heat transfer and friction process, the following nondimensional functional relations were assumed:

$$f = C_1(x/D)_1^a (t/D)_2^a (\alpha)_3^a (Re_D)_4^a \quad (1)$$

<sup>1</sup> Aerospace Technologist, Structures and Dynamics Division, NASA Langley Research Center, Hampton, Va.

<sup>2</sup> Numbers in brackets designate References at end of paper.

Contributed by the Heat Transfer Division of THE AMERICAN SOCIETY OF MECHANICAL ENGINEERS. Manuscript received by the Heat Transfer Division September 23, 1974.

**Table 1 Range of geometric variables and nondimensional parameters**

Ref.	Designation in refs.	$D_f$ in. (mm)	$x/D$	$t/D$	$\alpha$	$Re_D$	$f, j$ (cm <sup>-1</sup> )
1	3/32-12.2	0.134 (3.41)	0.70	0.030	0.162	500-10,000	340(11)
	1/2-11.94(D)	0.089 (2.3)	5.6	0.067	0.709	300-9,000	461(15)
	1/4-15.4(D)	0.063 (1.6)	3.96	0.095	0.629	300-6,000	642(21)
	1/6-12.18(D)	0.104 (2.64)	1.71	0.039	0.461	200-9,000	422(14)
	1/7-15.75(D)	0.081 (2.1)	1.75	0.049	0.41	200-7,000	526(17)
	1/8-20.06(D)	0.059 (1.5)	2.13	0.068	0.49	300-4,000	698(23)
	1/8-19.82(D)	0.061 (1.5)	2.06	0.066	0.485	200-4,000	680(22)
	1/8-16.12(D)	0.061 (1.5)	2.05	0.098	0.595	300-5,000	660(22)
	1/8-16.00(D)	0.073 (1.9)	1.70	0.082	0.476	300-6,000	550(18)
	1/8-16.12(T)	0.062 (1.6)	2.03	0.097	0.592	300-6,000	650(21)
5	100	0.061 (1.5)	2.06	0.066	0.492	300-5,000	687(23)
	101	0.049 (1.2)	1.89	0.068	0.183	120-4,000	719(24)
	102	0.056 (1.4)	1.79	0.071	0.126	120-4,000	752(25)
	103	0.068 (1.7)	1.63	0.059	0.135	120-5,000	630(21)
	104	0.084 (2.1)	1.33	0.043	0.239	300-7,000	472(15)
	105	0.048 (1.2)	2.33	0.084	0.529	150-3,000	863(28)
	106	0.055 (1.4)	1.81	0.072	0.671	200-4,000	759(25)
	107	0.048 (1.2)	2.08	0.042	0.99	200-3,000	923(30)
	501	0.025 (0.65)	1.97	0.039	0.98	100-1,000	1722(56)
	J	0.121 (3.08)	2.058	0.049	0.336	400-10,000	394(13)
8	20R/19.13	0.045 (1.1)	2.44	0.135	1.196	600-40,000	1067(35)
	28R/27.13	0.036 (0.92)	2.77	0.166	0.81	300-50,000	1326(44)

Listed  $Re_D$  range is the total range in which  $f$  and  $j$  data were available.

$$j = C_2(x/D)_1^b (t/D)_2^b (\alpha)_3^b (Re_D)_4^b \quad (2)$$

where the coefficients  $C_1$  and  $C_2$  and the exponents  $a_i$  and  $b_i$  ( $i = 1, 2, 3, 4$ ) are unknowns. The ranges of the indicated variables and nondimensional parameters are given in Table 1.

The relationships were determined through the use of a computer code which solves  $M$  simultaneous equations in  $N$  unknowns such that the solution is the best possible fit in the weighted least-squares sense. Relationships for  $f$  and  $j$  were determined by solving equations (1) and (2) for  $a_i \neq 0$  and  $b_i \neq 0$  and for all possible combinations of  $a_i = 0$  and  $b_i = 0$  ( $i = 1, 2, 3$ ). The best correlations in terms of the lowest overall rms percent deviation from the experimental results are shown in the following:

$Re_D \leq 1000$

$$f = 7.661 (x/D)^{-0.384} (\alpha)^{-0.092} Re_D^{-0.712} \quad (3)$$

$$j = 0.483 (x/D)^{-0.162} (\alpha)^{-0.184} Re_D^{-0.536} \quad (4)$$

$Re_D \geq 2000$

$$f = 1.136 (x/D)^{-0.781} (t/D)^{0.534} Re_D^{-0.198} \quad (5)$$

$$j = 0.242 (x/D)^{-0.322} (t/D)^{0.089} Re_D^{-0.368} \quad (6)$$

Since the correlations of  $Re_D \leq 1000$  do not contain the parameter  $t/D$ , it can be concluded that this parameter has little or no effect on  $f$  or  $j$  within the parameter range of this correlation; with similar reasoning, the same can be concluded about  $\alpha$  for  $Re_D \geq 2000$ . This latter conclusion has been indicated analytically for rectangular ducts [3]. In addition, a decrease in the value of  $x/D$  results in an increase in both  $f$  and  $j$  (this trend has been shown analytically for ducts [3]); an increase in  $\alpha$  results in a decrease in both  $f$  and  $j$  (this trend also has been shown analytically for ducts [1]); and an increase in  $t/D$  results in an increase in both  $f$  and  $j$  (apparently causing additional free-stream turbulence).

A comparison between the resulting empirical relationships and the experimental data for the 22 configurations is shown in Figs. 2 and 3 for  $Re_D \leq 1000$  and  $Re_D \geq 2000$ , respectively. Overall rms percent discrepancy between the empirical relationships and experimental results is within 10 percent for the heat-transfer factor

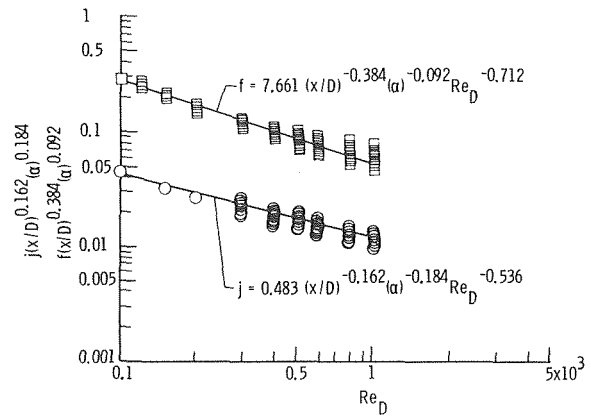


**Fig. 2 Comparison of empirical relationships with experiment,  $Re_D \leq 1000$**

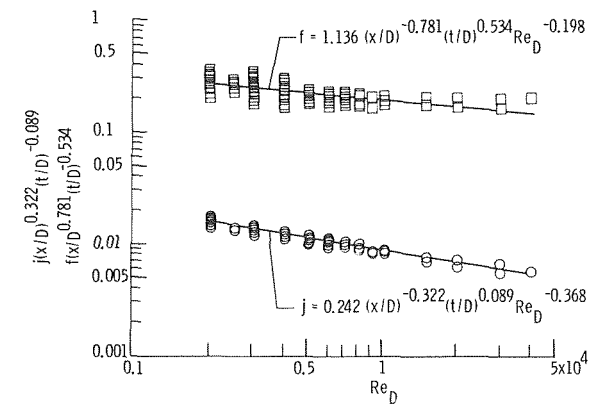


**Fig. 3 Comparison of empirical relationships with experiment,  $Re_D \geq 2000$**

( $j$ ) correlations and 15 percent for the flow friction factor ( $f$ ) correlation. Since for identical configurations (such as fin surface  $1/8-16.12D$  and  $1/8-16.12T$  of reference [1] and  $1/8-19.82D$  of reference [1] and 101 of reference [5]) the experimental  $j$  factor varied  $\pm 15$  percent from a mean, the correlations are considered quite good. A few data show a discrepancy as high as 40 percent; however, 85 percent of all the data are within the stated bands.

It should be noted that all the experimental data used have been obtained from experiments using air as a working fluid; therefore, the applicability of the correlations to fluids outside the gas Prandtl number range may be open to question. In addition, approximately 80 percent of the data are for fins with  $1.5 \leq x/D \leq 2.5$ ; consequently, the exponents of  $x/D$  are heavily weighted to the data of these surfaces.

A similar approach to correlating data for offset-fin surfaces is reported in [2]. The results of [2] indicate that  $f$  and  $j$  are functions of  $Re_D$  and  $x/D$  only. (The fin thickness was considered in the correlation; however, the fin aspect ratio was not.) Although the  $f$  factor was correlated over two  $Re_D$  ranges ( $Re_D < 3500$  and  $Re_D > 3500$ ), the  $j$  factor was correlated over the entire  $Re_D$  range (370-32,000). Data existing today clearly indicate the need for correlating both  $f$  and  $j$  over two  $Re_D$  ranges (i.e., for primarily laminar flow and for primarily turbulent flow). In addition, data from several different types of offset-fin surfaces were used in [2]. Although each type may be dependent on the same parameters, it is likely that its degree of dependency would be different.

**Application of Empirical Relationships.** The following technique is suggested in the application of these correlations in determining  $f$  and  $j$  factors for a given fin geometry. This technique provides a means of extending the correlations into the transition-

al  $Re_D$  range. A comparison between the experimental data and the theoretical values predicted by this technique indicated that the discrepancy was generally within the previously stated bands. Determine the reference Reynolds numbers  $Re_{D,f}^*$  and  $Re_{D,j}^*$  from the following equations:

$$Re_{D,f}^* = 41 (x/D)^{0.772} (\alpha)^{-0.179} (t/D)^{-1.04} \quad (7)$$

$$Re_{D,j}^* = 61.9 (x/D)^{0.952} (\alpha)^{-1.1} (t/D)^{-0.53} \quad (8)$$

These reference Reynolds numbers define the intersection of the respective  $f$  and  $j$  relationships. For  $Re_D$ 's less than the reference values use equations (3) and (5) for  $f$  and  $j$ , respectively; for all other  $Re_D$ 's use equations (4) and (6) for  $f$  and  $j$ , respectively.

### Concluding Remarks

Empirical relationships have been developed by correlating experimental heat-transfer and flow friction data from 22 rectangular offset-fin plate-fin heat exchanger configurations. The relationships predict the performance within the data scatter and are therefore considered quite good. They also allow the effect of fin length, height, thickness, spacing, and hydraulic diameter on the performance to be assessed. These relationships also indicate that the flow passage aspect ratio is significant only in the laminar flow Reynolds number range and that the fin thickness parameter ( $t/D$ ) is significant only in the turbulent flow Reynolds number range.

These correlations may be applicable only for air or gas as the heat-transfer fluid and should be used only for limited extrapolation as serious error may occur if the correlations are employed out of the parameter range used in their development.

### References

- 1 Kays, W. M., and London, A. L., "Compact Heat Exchangers," 2nd ed., McGraw-Hill, New York, 1964.
- 2 Manson, S. V., "Correlations of Heat-Transfer Data and of Friction Data for Interrupted Plane Fins Staggered in Successive Rows," NACA TN 2237, Dec. 1950.
- 3 Kays, W. M., "Convective Heat and Mass Transfer," 1st ed., McGraw-Hill, New York, 1966, pp. 102-298.
- 4 London, A. L., and Ferguson, C. K., "Test Results of High-Performance Heat-Exchanger Surfaces Used in Aircraft Intercoolers and Their Significance for Gas-Turbine Regenerator Design," TRANS. ASME, Vol. 71, Jan. 1949, pp. 17-26.
- 5 London, A. L., and Shah, R. K., "Offset Rectangular Plate-Fin Surfaces—Heat Transfer and Flow Friction Characteristics," Journal of Engineering for Power, TRANS. ASME Series A, Vol. 90, July 1968, pp. 218-228.
- 6 Shah, R. K., and London, A. L., "Influence of Brazing on Very Compact Heat Exchanger Surfaces," ASME Paper No. 71-HT-29, Aug. 1971.
- 7 London, A. L., and Ferguson, C. K., "Gas Turbine Plant Regenerator Surfaces—Basic Heat Transfer and Flow Friction Data," Bureau of Ships Research Memorandum No. 2-46 (NAVSHIPS 250-338-3), July 1946.
- 8 Walters, F. M., "Hypersonic Research Engine Project—Phase IIA, Category I Test Report on Fin Heat Transfer and Pressure Drop Testing," Data Item No. 63.02, AiResearch Manufacturing Co., Document No. AP-69-5348, Aug. 1969.

## Scaling of Spirally Indented Heat Exchanger Tubes

A. P. Watkinson<sup>1</sup> and O. Martinez<sup>1</sup>

### Nomenclature

- $A_i$  = inside heat exchanger tube area  $m^2$   
 $C_p$  = specific heat  $J/kg^\circ K$   
 $h$  = heat transfer coefficient  $J/s m^2^\circ K$   
 $R_f^*$  = asymptotic scaling resistance  $(J/s m^2^\circ K)^{-1}$   
 $T_b$  = bulk liquid temperature  $^\circ K$   
 $T_w$  = wall temperature  $^\circ K$   
 $V$  = velocity  $m/s$   
 $W$  = mass flow rate  $kg/s$

### Subscripts

- 1 = inlet  
 2 = outlet  
 i = inside

### Superscripts

- 0 = value at time zero (clean)  
 \* = asymptotic value

Enhanced heat exchanger tubes can be used to decrease the size of heat exchanger required for a given duty. In applications where a fouling deposit contributes significantly to the overall thermal resistance, the expected advantage of the enhanced tube may be substantially reduced. Because of the inherently lower film resis-

tance of enhanced tubes, the addition of a fixed fouling resistance decreases the operating heat transfer coefficient for enhanced tubes to a greater extent than for smooth tubes. It is of interest therefore to know the relative performance of smooth and enhanced tubes under fouling conditions. This technical brief describes the heat transfer characteristics under scaling conditions of three spirally indented "Turbotec" tubes supplied by Spiral Tubing Corp.

The apparatus and techniques have been described previously [1].<sup>2</sup> Calcium carbonate is deposited from a solution of  $NaHCO_3$ ,  $CaCl_2$ , and  $NaCl$  containing on average, 300 ppm suspended solids, and 3000 ppm dissolved solids. This artificial hard water at a temperature of  $330^\circ K$  enters a heat exchanger containing two tubes in parallel and is heated by condensing steam at about  $380^\circ K$ . The accelerated scaling technique was developed to give rapid and reproducible scaling results to allow comparison of tube geometry effects, rather than to yield absolute values of the fouling resistance for design purposes. The tubes tested included a smooth plain tube and three Turbotec spirally indented tubes of different spiral pitch. The ends of the Turbotec tubes were plain. Details of the tubes are given in Table 1 and Fig. 1.

Typical results of the heat transfer tests are shown in Fig. 2. Film coefficients were calculated from the expression:

$$h = \frac{WC_p}{A_i} \ln \left[ \frac{(\bar{T}_{w_i} - T_{b_1})}{(\bar{T}_{w_i} - T_{b_2})} \right] \quad (1)$$

For the Turbotec tubes the inside surface area was calculated as for a plain tube from the inside diameter of the plain (cylindrical) portion of the tube end. The inside tube wall was calculated from the measured outside wall temperature and the heat flow. The results are characterized by a flat initial portion that corresponds to the clean tube condition before the salts are added. A rapid drop in the heat transfer coefficient occurs due to the scale deposition and asymptotic value of  $h^*$  is reached after a few hours. Rapidity of the approach to asymptotic conditions is due to the substantial change

<sup>1</sup> Department of Chemical Engineering, The University of British Columbia, Vancouver, B. C., Canada.

Contributed by the Heat Transfer Division of THE AMERICAN SOCIETY OF MECHANICAL ENGINEERS. Manuscript received by the Heat Transfer Division February 24, 1975.

<sup>2</sup> Numbers in brackets designate References at end of technical brief.

al  $Re_D$  range. A comparison between the experimental data and the theoretical values predicted by this technique indicated that the discrepancy was generally within the previously stated bands. Determine the reference Reynolds numbers  $Re_{D,f}^*$  and  $Re_{D,j}^*$  from the following equations:

$$Re_{D,f}^* = 41 (x/D)^{0.772} (\alpha)^{-0.179} (t/D)^{-1.04} \quad (7)$$

$$Re_{D,j}^* = 61.9 (x/D)^{0.952} (\alpha)^{-1.1} (t/D)^{-0.53} \quad (8)$$

These reference Reynolds numbers define the intersection of the respective  $f$  and  $j$  relationships. For  $Re_D$ 's less than the reference values use equations (3) and (5) for  $f$  and  $j$ , respectively; for all other  $Re_D$ 's use equations (4) and (6) for  $f$  and  $j$ , respectively.

### Concluding Remarks

Empirical relationships have been developed by correlating experimental heat-transfer and flow friction data from 22 rectangular offset-fin plate-fin heat exchanger configurations. The relationships predict the performance within the data scatter and are therefore considered quite good. They also allow the effect of fin length, height, thickness, spacing, and hydraulic diameter on the performance to be assessed. These relationships also indicate that the flow passage aspect ratio is significant only in the laminar flow Reynolds number range and that the fin thickness parameter ( $t/D$ ) is significant only in the turbulent flow Reynolds number range.

These correlations may be applicable only for air or gas as the heat-transfer fluid and should be used only for limited extrapolation as serious error may occur if the correlations are employed out of the parameter range used in their development.

### References

- 1 Kays, W. M., and London, A. L., "Compact Heat Exchangers," 2nd ed., McGraw-Hill, New York, 1964.
- 2 Manson, S. V., "Correlations of Heat-Transfer Data and of Friction Data for Interrupted Plane Fins Staggered in Successive Rows," NACA TN 2237, Dec. 1950.
- 3 Kays, W. M., "Convective Heat and Mass Transfer," 1st ed., McGraw-Hill, New York, 1966, pp. 102-298.
- 4 London, A. L., and Ferguson, C. K., "Test Results of High-Performance Heat-Exchanger Surfaces Used in Aircraft Intercoolers and Their Significance for Gas-Turbine Regenerator Design," TRANS. ASME, Vol. 71, Jan. 1949, pp. 17-26.
- 5 London, A. L., and Shah, R. K., "Offset Rectangular Plate-Fin Surfaces—Heat Transfer and Flow Friction Characteristics," Journal of Engineering for Power, TRANS. ASME Series A, Vol. 90, July 1968, pp. 218-228.
- 6 Shah, R. K., and London, A. L., "Influence of Brazing on Very Compact Heat Exchanger Surfaces," ASME Paper No. 71-HT-29, Aug. 1971.
- 7 London, A. L., and Ferguson, C. K., "Gas Turbine Plant Regenerator Surfaces—Basic Heat Transfer and Flow Friction Data," Bureau of Ships Research Memorandum No. 2-46 (NAVSHIPS 250-338-3), July 1946.
- 8 Walters, F. M., "Hypersonic Research Engine Project—Phase IIA, Category I Test Report on Fin Heat Transfer and Pressure Drop Testing," Data Item No. 63.02, AiResearch Manufacturing Co., Document No. AP-69-5348, Aug. 1969.

## Scaling of Spirally Indented Heat Exchanger Tubes

A. P. Watkinson<sup>1</sup> and O. Martinez<sup>1</sup>

### Nomenclature

- $A_i$  = inside heat exchanger tube area  $m^2$   
 $C_p$  = specific heat  $J/kg^\circ K$   
 $h$  = heat transfer coefficient  $J/s m^2^\circ K$   
 $R_f^*$  = asymptotic scaling resistance  $(J/s m^2^\circ K)^{-1}$   
 $T_b$  = bulk liquid temperature  $^\circ K$   
 $T_w$  = wall temperature  $^\circ K$   
 $V$  = velocity  $m/s$   
 $W$  = mass flow rate  $kg/s$

### Subscripts

- 1 = inlet  
 2 = outlet  
 i = inside

### Superscripts

- 0 = value at time zero (clean)  
 \* = asymptotic value

Enhanced heat exchanger tubes can be used to decrease the size of heat exchanger required for a given duty. In applications where a fouling deposit contributes significantly to the overall thermal resistance, the expected advantage of the enhanced tube may be substantially reduced. Because of the inherently lower film resis-

tance of enhanced tubes, the addition of a fixed fouling resistance decreases the operating heat transfer coefficient for enhanced tubes to a greater extent than for smooth tubes. It is of interest therefore to know the relative performance of smooth and enhanced tubes under fouling conditions. This technical brief describes the heat transfer characteristics under scaling conditions of three spirally indented "Turbotec" tubes supplied by Spiral Tubing Corp.

The apparatus and techniques have been described previously [1].<sup>2</sup> Calcium carbonate is deposited from a solution of  $NaHCO_3$ ,  $CaCl_2$ , and  $NaCl$  containing on average, 300 ppm suspended solids, and 3000 ppm dissolved solids. This artificial hard water at a temperature of  $330^\circ K$  enters a heat exchanger containing two tubes in parallel and is heated by condensing steam at about  $380^\circ K$ . The accelerated scaling technique was developed to give rapid and reproducible scaling results to allow comparison of tube geometry effects, rather than to yield absolute values of the fouling resistance for design purposes. The tubes tested included a smooth plain tube and three Turbotec spirally indented tubes of different spiral pitch. The ends of the Turbotec tubes were plain. Details of the tubes are given in Table 1 and Fig. 1.

Typical results of the heat transfer tests are shown in Fig. 2. Film coefficients were calculated from the expression:

$$h = \frac{WC_p}{A_i} \ln \left[ \frac{(\bar{T}_{w_i} - T_{b_1}) / (\bar{T}_{w_i} - T_{b_2})}{1} \right] \quad (1)$$

For the Turbotec tubes the inside surface area was calculated as for a plain tube from the inside diameter of the plain (cylindrical) portion of the tube end. The inside tube wall was calculated from the measured outside wall temperature and the heat flow. The results are characterized by a flat initial portion that corresponds to the clean tube condition before the salts are added. A rapid drop in the heat transfer coefficient occurs due to the scale deposition and asymptotic value of  $h^*$  is reached after a few hours. Rapidity of the approach to asymptotic conditions is due to the substantial change

<sup>1</sup> Department of Chemical Engineering, The University of British Columbia, Vancouver, B. C., Canada.

Contributed by the Heat Transfer Division of THE AMERICAN SOCIETY OF MECHANICAL ENGINEERS. Manuscript received by the Heat Transfer Division February 24, 1975.

<sup>2</sup> Numbers in brackets designate References at end of technical brief.

**Table 1 Properties of Tubes Tested<sup>a</sup>**

Tube	T-1	T-2	T-3	Plain
Plain end outside diameter (mm)	12.7	12.7	12.7	12.8
Wall thickness (mm)	0.76	0.76	0.76	0.89
Minimum inside diameter (mm)	7.2	7.2	7.2	11.0
Spiral pitch (mm)	8.3	7.5	6.6	—
Cross-sectional area (mm <sup>2</sup> )	66.0	61.3	58.5	95.0
Inside surface area per unit length (mm <sup>2</sup> )/mm	35.1	35.1	35.1	34.6

<sup>a</sup>All tubes mild steel.

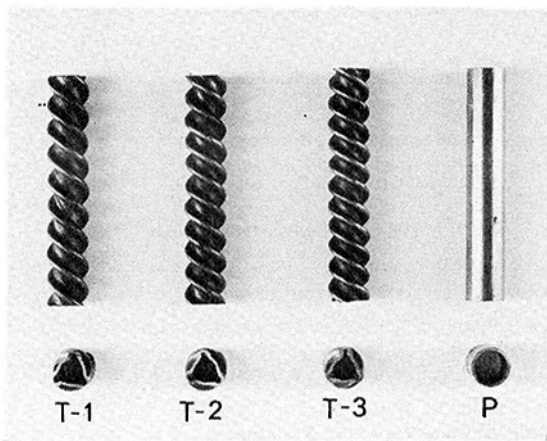


**Fig. 1 Photograph of tubes tested**

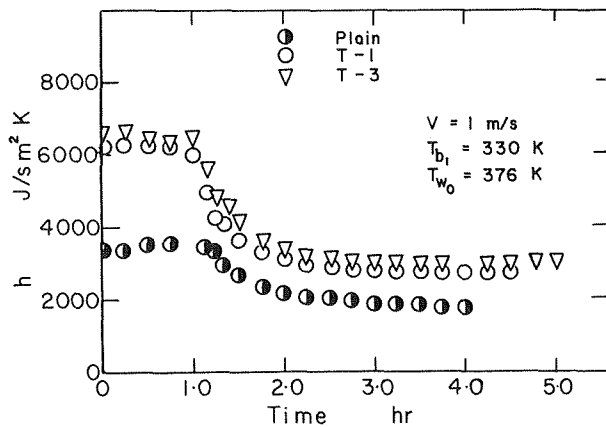


**Fig. 2 Typical result of scaling experiment**

in temperature of the scale/fluid interface as described previously [2]. Tests had shown that the asymptote so obtained was constant over 24 hr and was unaffected by addition of more scaling salts. After the scaling run was complete the tubes were cleaned by circulating an Oakite solution through the loop. Some corrosion of the mild steel tubes was observed.

Clean and fouled film coefficients for the four tubes tested are shown in Fig. 3. The spirally indented tubes have clean coefficients approximately 1.8 times those of the plain steel tube at the same velocity. Velocity in the Turbotec tubes was calculated from measurement of the actual cross-sectional area available for flow in the indented tube. The values for the plain smooth tube clean film coefficients are lower than expected from available correlations

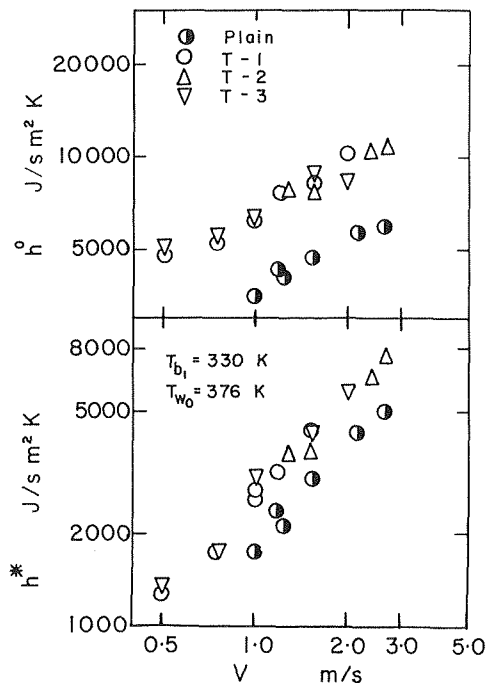


**Fig. 3 Film heat transfer coefficients before and after scaling**

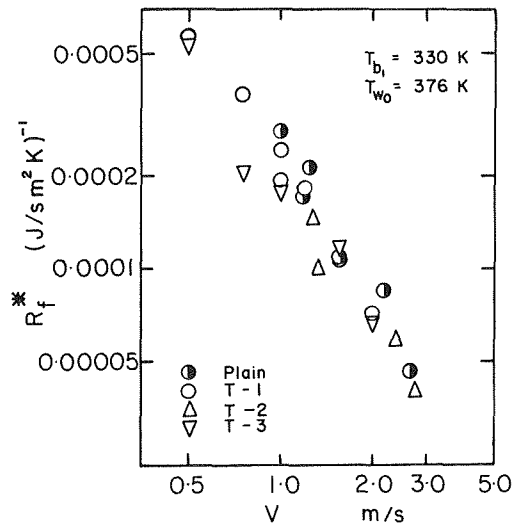


**Fig. 4 Scaling resistance versus velocity for plain and Turbotec tubes**

probably due to the corrosion problem. Data for a copper tube gave results within 10 percent of values predicted by a recommended dimensional equation for water [3]. After severe scaling, where  $h^* = (1/3 - 1/2) h^0$  the film coefficients for the spirally indented tubes still exceed those of the plain tube by some 45-50 percent (Fig. 3). Although this is a substantial drop in performance relative to the plain tube in the clean condition, the enhanced tubes are clearly superior in both clean and scaled conditions.

The asymptotic scaling resistance

$$R_f^* = 1/h^* - 1/h^0 \quad (2)$$

is plotted versus velocity in Fig. 4. It is seen that the scaling resistance based on  $A_i$  for the spirally indented tubes is about equal to that of the plain tubes within the scatter of the experimental data. Previous tests on Phelps Dodge spirally indented copper tubes [1]

showed lower scaling resistances than plain tubes at velocities over 1 m/s. There appears to be no clear effect of the pitch of the spirals within the accuracy of the data. In assigning a fouling resistance for Turbotec spirally indented tubes in scaling situations, these tests suggest that at equal bulk velocities the same values as used for smooth tubes should be employed.

### Acknowledgment

This work was supported by a grant from the National Research Council of Canada.

### References

- 1 Watkinson, A. P., Louis, L., and Brent, R., "Scaling of Enhanced Heat Exchanger Tubes," *Can. J. Chem. Eng.*, Vol. 52, 1974, p. 558.
- 2 Watkinson, A. P., and Martinez, O., "Scaling of Heat Exchanger Tubes by Calcium Carbonate," Paper 50a, 79th National AIChE Meeting, Houston, Texas, Mar. 1975.
- 3 Perry, R. H., and Chilton, C. H., *Chemical Engineers Handbook*, 5th ed., McGraw-Hill, New York, 1973, pp. 10-14.

## Binary, Gravity-Flow Film Condensation

E. Marschall<sup>1</sup> and J. A. Hall<sup>2</sup>

### Introduction

In 1969, Sparrow and Marschall [1]<sup>3</sup> formulated a predictive theory for binary, gravity-flow film condensation, based on the following assumptions: the condensation takes place on an isothermal, vertical plate; the condensed liquids are completely miscible; the vapor flow is induced by the condensation process and by free convection due to density differences. Any separation effects due to stratification are assumed to be negligibly small. The theory was applied to condensation of saturated mixtures of methanol and water at atmospheric pressure. The results revealed that for a given vapor bulk composition, heat flux and condensate rates and composition exhibit a marked dependence on differences between vapor bulk and wall temperatures. Heat fluxes and condensation rates increase with increasing temperature differences, as one would expect. Vapor bulk composition and condensate composition are approximately identical at high temperature differences. Consequently, at these conditions heat transfer rates can be evaluated with Nusselt's theory if one chooses the condensate film surface temperature equal to the saturation temperature of a liquid mixture which has a composition equal to that of the vapor bulk. In this calculation, all physical properties of the liquid mixture have to be evaluated at an appropriate reference temperature. When the differences between vapor bulk temperature and wall temperature are of the order of, or smaller than, the temperature differences between saturated liquid and vapor mixtures with a composition equal to that in the vapor bulk, condensate composition will be different from the vapor bulk composition. To determine heat transfer rates for these conditions, it is necessary to solve the conservation equations for mass, momentum, and species in the vapor phase in order to determine the condensate film surface temperature.

<sup>1</sup> Assoc. Professor, Department of Mechanical and Environmental Engineering, University of California, Santa Barbara, Calif.

<sup>2</sup> Research Engineer, Delco Electronics, Goleta, Calif.

<sup>3</sup> Numbers in brackets designate References at end of technical brief.

Contributed by the Heat Transfer Division of THE AMERICAN SOCIETY OF MECHANICAL ENGINEERS. Manuscript received by the Heat Transfer Division March 10, 1975.

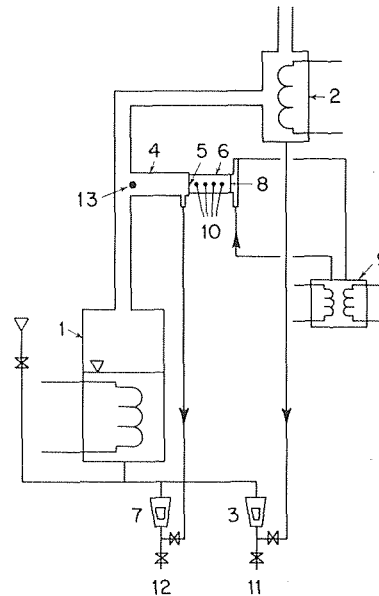


Fig. 1 Experimental apparatus

In 1973, Tamir [2] formulated an approximate theory for the same problem. His results agree within ten percent with the results of the rigorous theory of Sparrow and Marschall.

Condensation of multicomponent mixtures was subject of many experimental investigations, too numerous to cite. A typical example of the experimental apparatus and procedure used in these studies is presented by Bandroski and Bryerkowski [3]. The characteristics of these experiments are: (a) total condensation, that is, all vapor entering the experimental condenser is being condensed; (b) forced flow conditions, since the vapor is forced to flow across the condensing surface; and (c) nonisothermal condensing surfaces or superimposed rectification effects. It is obvious that these characteristics do not match the basic assumptions made in references [1, 2], and, therefore, the available experimental data do not allow a meaningful confrontation with the theories stated in references [1, 2].

The objective of the present paper is to describe experiments on binary, gravity-flow film condensation on a vertical, isothermal plate, and to compare the obtained data with the theory presented in reference [1]. The experimental setup is unique in two ways: it allows atmospheric pressure to be maintained in the vapor bulk at any condensation rate, and it provides for fluid flow conditions such as assumed in reference [1].

### Experimental Apparatus

A schematic of the experimental apparatus is shown in Fig. 1. A binary mixture is evaporated in a steam operated evaporator (1). Most of the vapor mixture leaving the evaporator (1) flows to a water-cooled condenser (2) where it is completely condensed. The condensate passes through a flowmeter (3) and returns to the evaporator (1). The condenser (2) is open to the atmosphere, thus providing for approximately atmospheric pressure in the whole system. A small fraction of the vapor mixture leaving the evaporator (1) passes through a duct (4) and condenses on a vertical face (5) of a cooled copper block (6). The condensate passes through a flowmeter (7) and returns to the evaporator (1).

The copper block (6) consists of OFHC copper and measures  $2 \times 4 \times 6$  in. Face (5) of the copper block serves as the vertical, isothermal wall. It is 2 in. wide and 4 in. high. The opposite face (8) is cooled with water from a constant temperature bath (9) which is forced to flow past face (8) with high velocity and then recirculated to the constant temperature bath (9). Duct (4) is 10 in. long and has a cross-sectional area of  $2 \times 4$  in. The purpose of this duct

showed lower scaling resistances than plain tubes at velocities over 1 m/s. There appears to be no clear effect of the pitch of the spirals within the accuracy of the data. In assigning a fouling resistance for Turbotec spirally indented tubes in scaling situations, these tests suggest that at equal bulk velocities the same values as used for smooth tubes should be employed.

### Acknowledgment

This work was supported by a grant from the National Research Council of Canada.

### References

- 1 Watkinson, A. P., Louis, L., and Brent, R., "Scaling of Enhanced Heat Exchanger Tubes," *Can. J. Chem. Eng.*, Vol. 52, 1974, p. 558.
- 2 Watkinson, A. P., and Martinez, O., "Scaling of Heat Exchanger Tubes by Calcium Carbonate," Paper 50a, 79th National AIChE Meeting, Houston, Texas, Mar. 1975.
- 3 Perry, R. H., and Chilton, C. H., *Chemical Engineers Handbook*, 5th ed., McGraw-Hill, New York, 1973, pp. 10-14.

## Binary, Gravity-Flow Film Condensation

E. Marschall<sup>1</sup> and J. A. Hall<sup>2</sup>

### Introduction

In 1969, Sparrow and Marschall [1]<sup>3</sup> formulated a predictive theory for binary, gravity-flow film condensation, based on the following assumptions: the condensation takes place on an isothermal, vertical plate; the condensed liquids are completely miscible; the vapor flow is induced by the condensation process and by free convection due to density differences. Any separation effects due to stratification are assumed to be negligibly small. The theory was applied to condensation of saturated mixtures of methanol and water at atmospheric pressure. The results revealed that for a given vapor bulk composition, heat flux and condensate rates and composition exhibit a marked dependence on differences between vapor bulk and wall temperatures. Heat fluxes and condensation rates increase with increasing temperature differences, as one would expect. Vapor bulk composition and condensate composition are approximately identical at high temperature differences. Consequently, at these conditions heat transfer rates can be evaluated with Nusselt's theory if one chooses the condensate film surface temperature equal to the saturation temperature of a liquid mixture which has a composition equal to that of the vapor bulk. In this calculation, all physical properties of the liquid mixture have to be evaluated at an appropriate reference temperature. When the differences between vapor bulk temperature and wall temperature are of the order of, or smaller than, the temperature differences between saturated liquid and vapor mixtures with a composition equal to that in the vapor bulk, condensate composition will be different from the vapor bulk composition. To determine heat transfer rates for these conditions, it is necessary to solve the conservation equations for mass, momentum, and species in the vapor phase in order to determine the condensate film surface temperature.

<sup>1</sup> Assoc. Professor, Department of Mechanical and Environmental Engineering, University of California, Santa Barbara, Calif.

<sup>2</sup> Research Engineer, Delco Electronics, Goleta, Calif.

<sup>3</sup> Numbers in brackets designate References at end of technical brief.

Contributed by the Heat Transfer Division of THE AMERICAN SOCIETY OF MECHANICAL ENGINEERS. Manuscript received by the Heat Transfer Division March 10, 1975.

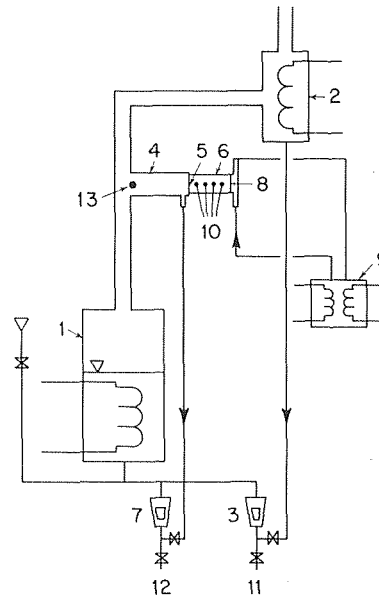


Fig. 1 Experimental apparatus

In 1973, Tamir [2] formulated an approximate theory for the same problem. His results agree within ten percent with the results of the rigorous theory of Sparrow and Marschall.

Condensation of multicomponent mixtures was subject of many experimental investigations, too numerous to cite. A typical example of the experimental apparatus and procedure used in these studies is presented by Bandroski and Bryerkowski [3]. The characteristics of these experiments are: (a) total condensation, that is, all vapor entering the experimental condenser is being condensed; (b) forced flow conditions, since the vapor is forced to flow across the condensing surface; and (c) nonisothermal condensing surfaces or superimposed rectification effects. It is obvious that these characteristics do not match the basic assumptions made in references [1, 2], and, therefore, the available experimental data do not allow a meaningful confrontation with the theories stated in references [1, 2].

The objective of the present paper is to describe experiments on binary, gravity-flow film condensation on a vertical, isothermal plate, and to compare the obtained data with the theory presented in reference [1]. The experimental setup is unique in two ways: it allows atmospheric pressure to be maintained in the vapor bulk at any condensation rate, and it provides for fluid flow conditions such as assumed in reference [1].

### Experimental Apparatus

A schematic of the experimental apparatus is shown in Fig. 1. A binary mixture is evaporated in a steam operated evaporator (1). Most of the vapor mixture leaving the evaporator (1) flows to a water-cooled condenser (2) where it is completely condensed. The condensate passes through a flowmeter (3) and returns to the evaporator (1). The condenser (2) is open to the atmosphere, thus providing for approximately atmospheric pressure in the whole system. A small fraction of the vapor mixture leaving the evaporator (1) passes through a duct (4) and condenses on a vertical face (5) of a cooled copper block (6). The condensate passes through a flowmeter (7) and returns to the evaporator (1).

The copper block (6) consists of OFHC copper and measures 2 x 4 x 6 in. Face (5) of the copper block serves as the vertical, isothermal wall. It is 2 in. wide and 4 in. high. The opposite face (8) is cooled with water from a constant temperature bath (9) which is forced to flow past face (8) with high velocity and then recirculated to the constant temperature bath (9). Duct (4) is 10 in. long and has a cross-sectional area of 2 x 4 in. The purpose of this duct

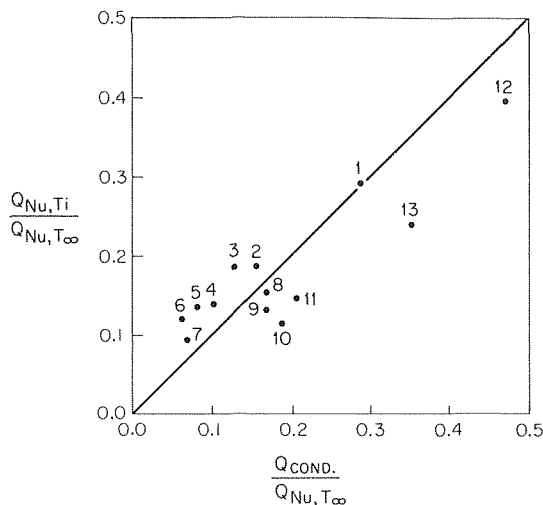


Fig. 2 Comparison between measured and predicted heat transfer rates

is to ensure condensation on face (5) in the absence of forced convection vapor flow past face (5). Since the vapor fraction flowing to condenser (2) is about ten to twenty times larger than the vapor fraction flowing to face (5), composition of the vapor mixture at the entrance to duct (4) is approximately unaffected by any diffusion process within duct (4).

The theoretical analysis in reference [1] states that the condensation heat transfer rates at a vertical, isothermal plate can be evaluated, if the temperature  $T_w$  of the face of the plate and the temperature  $T_\infty$  in the bulk of the saturated vapor mixture are known. For the measurement of  $T_\infty$ , a single thermoelement (13) (Alumel-Chromel) is used which is located at the entrance of duct (4). The measurement of  $T_w$  is implemented utilizing eight subminiature thermocouples (10) located in the copper block (6). The procedure used to measure  $T_w$  follows closely the method presented by Wilcox and Rohsenow [4]. The same measurements allow also determination of the heat flux through the copper block from face (5) to face (8).

Flowrates of condensate are checked with the help of the calibrated flowmeter (7) and (3). Liquid samples of condensate can be taken at locations (11) and (12). A Bausch and Lomb, Abbe type refractometer is used to determine the component concentrations of the condensate at a temperature of 25°C. For this purpose, the refractometer is kept at a constant temperature of 25.0°C with a constant temperature bath to assure accuracy, since the index of refraction is a strong function of temperature. A gas chromatograph is used in conjunction with an integrator to serve as a check on the concentration measurements obtained by the refractometer. The whole apparatus with the exception of the condenser (2) and the condensate return lines is heavily insulated against heat losses. Measurements are taken when the whole apparatus is at steady state. Parameters which are changed from experiment to experiment include the composition of the liquid mixture in the evaporator (1) and the temperature of the cooling water flowing past surface (8).

### Measurements and Results

Experiments were carried out with a methanol-water mixture. Methanol-water was chosen because equilibrium data for the mixture are well known and the saturation curves are in a convenient temperature range.

Data taken include the temperature  $T_\infty$  at the entrance of duct (4), the temperatures in the copper block, and composition of the condensate returning from condenser (2) and copper surface (5).

At steady-state conditions, the temperature profile in the copper block was always found to be linear within measurable accuracy.

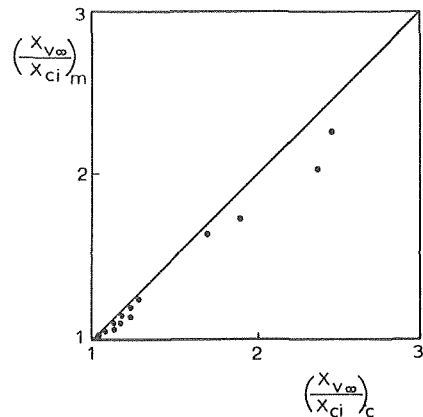


Fig. 3 Comparison between measured and predicted mole fractions

Linear extrapolation of this profile yields the temperature  $T_w$  on surface (5) and the temperature  $T_c$  on surface (8). Variance of the thermal conductivity of OFCH copper in the experimental temperature range is extremely small, thus the thermal conductivity was taken to be constant at a value of  $k = 336.25$  kcal/hr-m-°C. The heat conducted through the copper block per unit time can be easily computed with  $q_{cond} = k(T_w - T_c)$  (area of surface (5)). Thus, the condensation heat flow  $q_{cond}$  is found for any given difference of the temperature  $T_\infty$  in the bulk of saturated vapor and the wall temperature  $T_w$ .

In order to compare the experimental data with the theory, a computer program was written which, as demonstrated in reference [1], computes the temperature  $T_i$  at the condensate film surface, the mole fraction  $x_{ci}$  of methanol in the condensate, the mole fraction  $x_{v\infty}$  of methanol in the vapor bulk, the Nusselt heat flow  $q_{Nu, T_\infty}$  based on ambient temperature  $T_\infty$ , and the Nusselt heat flow  $q_{Nu, T_i}$  based on the film surface temperature  $T_i$ , all as functions of the temperatures  $T_\infty$  and  $T_w$ . More details on the experimental apparatus and the obtained experimental and calculated data can be found in reference [5]. A comparison of predicted and measured dimensionless heat transfer rates is shown in Fig. 2. The agreement between predicted and measured heat flux rates is as good as one can expect, especially if one takes into account that the heat flow rates are very small and, consequently, difficult to measure very accurately.

A comparison of measured and predicted mole fractions of methanol is presented in Fig. 3. In this figure the ratios of the measurement mole fractions  $(X_{v\infty}/X_{ci})_m$  are plotted versus the ratios of the predicted mole fractions  $(X_{v\infty}/X_{ci})_c$ . The agreement between predicted and measured mole fractions is reasonably good.

The obtained experimental data support well the validity of the theory of Sparrow and Marschall for binary, gravity-flow film condensation on a vertical, isothermal plate in the absence of forced convection. The presence of diffusion mass transfer can be clearly seen from the obtained different values for the methanol mole fraction in the vapor bulk and the condensate. The theory predicts heat transfer rates well for the physical situation for which it has been formulated.

### Acknowledgment

Support from the Academic Senate of the University of California, Santa Barbara, in the form of computer time is acknowledged.

### References

- 1 Sparrow, E. M., and Marschall, E., "Binary Gravity-Flow Film Condensation," JOURNAL OF HEAT TRANSFER, TRANS. ASME, Series C, Vol. 91, May 1969, p. 205.
- 2 Tamir, A., "Condensation of Binary Mixtures of Miscible Vapors," International Journal of Heat and Mass Transfer, Vol. 16, 1973, p. 683.
- 3 Bandrowski, J., and Bryerkowski, A., "Experimental Study of Heat

Transfer at the Total Condensation of Mixed Vapors of Miscible Liquids," *International Journal of Heat and Mass Transfer*, Vol. 18, 1975, p. 503.

4 Wilcox, S. J., and Rohsenow, W. M., "Film Condensation of Potassium Using Copper Condensing Block for Precise Wall-Temperature Measurement," *JOURNAL OF HEAT TRANSFER*, TRANS. ASME, Series C, Vol. 92, Aug. 1970, p. 359.

5 Hall, J. A., MS thesis, Department of Mechanical Engineering, University of California, Santa Barbara, Calif. 1975.

## Nucleate Boiling on an Oxide Coated Glass Surface

R. L. Judd<sup>1</sup> and M. S. M. Shoukri<sup>2</sup>

### Nomenclature

$C_l$	= liquid specific heat
$D_b$	= bubble departure diameter
$f$	= bubble departure frequency
$h_{fg}$	= latent heat of vaporization
$k_l$	= liquid thermal conductivity
$N/A$	= active site density
$(q/A)_b$	= boiling heat flux
$T_{sat}$	= saturation temperature
$\Delta T$	= superheat
$\mu_l$	= liquid dynamic viscosity
$\rho$	= density
$\sigma$	= surface tension

### Introduction

In a paper published some time ago, Mikic and Rohsenow [1]<sup>3</sup> presented a theoretical correlation for predicting saturated nucleate boiling heat transfer rates which included the effect of heating surface characteristics. In the mathematical model proposed, nucleate boiling heat transfer was attributed to enthalpy transport from the superheated layer adjacent to the heating surface promoted by the growth and departure of the bubbles. Starting with the relationship for transient conduction from the heating surface to the liquid contacting it after the departure of a bubble, the average heat flux was determined and combined with active site density and frequency of bubble departure in order to predict boiling heat flux. The unique feature of this correlation was the manner in which the active site density was determined from the size distribution of active nucleation cavities on the heated surface. The resulting relationship had the form

$$\frac{(q/A)_b \sqrt{\sigma g_0/g(\rho_l - \rho_v)}}{\mu_l h_{fg}} = B(\phi \Delta T)^{m+1}$$

where

$$\phi^{m+1} = \left[ \frac{k_l^{1/2} \rho_l^{17/8} C_l^{19/8} h_{fg}^{(m-23/8)} \rho_v^{(m-15/8)}}{\mu_l (\rho_l - \rho_v)^{9/8} \sigma^{(m-11/8)} T_{sat}^{(m-15/8)}} \right] \quad (1)$$

and

$$B = 2\sqrt{\pi} C_1 C_2^{3/2} C_3^{1/2} \frac{g_0^{11/8}}{g^{9/8}} \left[ \frac{R_s J_f(\theta, \psi)}{2} \right]^m \quad 4$$

The intent of the original paper was to show that the correlation equation obtained, which is very strongly dependent upon the nucleating characteristics of the heating surface, was capable of drawing together the data of a number of researchers for different fluids boiling at various levels of pressure into a single correlation of  $(q/A)_b \sqrt{\sigma g_0/g(\rho_l - \rho_v)}/\mu_l h_{fg}$  versus  $(\phi \Delta T)^{m+1}$  for each surface tested. Inasmuch as the nucleating characteristics of these surfaces were not known, the exponent  $(m + 1)$  which will be shown below to be associated with the nucleating characteristics of the surface, had to be assumed. Once the appropriate value had been found, good agreement was observed between theory and experiment. The purpose of the present paper is to support this finding, using results obtained with five different liquids boiling on a glass heating surface. A nucleating characteristic curve for the surface is presented in the manner suggested by Brown [2] and the Mikic and Rohsenow correlation is shown to be capable of predicting the heat transfer results.

### Results

The experimental data used for the evaluation of the Mikic and Rohsenow correlation were obtained from a previous investigation in which Freon 113, carbon tetrachloride, chloroform, dichloroethane, and trichloroethane were boiled at atmospheric pressure on a transparent borosilicate glass heating surface coated with a half wavelength thickness of stannic oxide which conducted electric current and generated heat. The details of the experimental investigation are presented in reference [3] in which the results obtained were presented in plots of heat flux versus surface superheat and active site density versus heat flux. The active site density data were obtained from a photographic analysis of the boiling phenomenon occurring on the transparent heating surface observed from below.

### Analysis

The Mikic and Rohsenow model assumes the principal mechanism in nucleate boiling heat transfer to be transient conduction to a superheated layer adjacent to the surface. The average heat flux was determined by

$$\left(\frac{q}{A}\right)_{av} = f \int_0^{1/f} \frac{k_l \Delta T dt}{\sqrt{\pi \alpha_l t}} = 2 \frac{k_l \Delta T}{\sqrt{\pi \alpha_l}} \sqrt{f} \quad (2)$$

The boiling heat flux was calculated by assuming the area of influence of a single bubble to be  $\pi D_b^2$

$$\left(\frac{q}{A}\right)_b = \pi D_b^2 \left(\frac{N}{A}\right) \left(\frac{q}{A}\right)_{av} \quad (3)$$

It was shown by Brown [2], that the nucleation characteristics of a heating surface could be represented by the cumulative distribution of cavity mouth radii for cavities having radii larger than  $R$  in the form

$$\frac{N}{A} = C_1 \left(\frac{R_s}{R}\right)^m \quad (4)$$

where  $C_1$ ,  $R_s$ , and  $m$  are constants which depend on the surface condition.

Some years ago, Griffith and Wallis [4] proposed that the effective nucleation radius could be computed by  $r = (2\sigma T_{sat}/\rho_v h_{fg} \Delta T)$ . More recently [5], the cavity radius  $R$  was related to the effective nucleation radius  $r$  for idealized conical cavities by the relationship

<sup>1</sup> Assoc. Professor, McMaster University, Hamilton, Ontario, Canada.

<sup>2</sup> Graduate Student, McMaster University, Hamilton, Ontario, Canada.

<sup>3</sup> Numbers in brackets designate References at end of technical brief.

Contributed by the Heat Transfer Division of THE AMERICAN SOCIETY OF MECHANICAL ENGINEERS. Manuscript received by the Heat Transfer Division July 8, 1974.

<sup>4</sup> Errors in the coefficient and exponents of this relationship appeared in the original paper. The form presented is consistent with corrections proposed by Professor Rohsenow when the errors were brought to his attention.

Transfer at the Total Condensation of Mixed Vapors of Miscible Liquids," *International Journal of Heat and Mass Transfer*, Vol. 18, 1975, p. 503.

4 Wilcox, S. J., and Rohsenow, W. M., "Film Condensation of Potassium Using Copper Condensing Block for Precise Wall-Temperature Measurement," *JOURNAL OF HEAT TRANSFER*, TRANS. ASME, Series C, Vol. 92, Aug. 1970, p. 359.

5 Hall, J. A., MS thesis, Department of Mechanical Engineering, University of California, Santa Barbara, Calif. 1975.

## Nucleate Boiling on an Oxide Coated Glass Surface

R. L. Judd<sup>1</sup> and M. S. M. Shoukri<sup>2</sup>

### Nomenclature

$C_l$	= liquid specific heat
$D_b$	= bubble departure diameter
$f$	= bubble departure frequency
$h_{fg}$	= latent heat of vaporization
$k_l$	= liquid thermal conductivity
$N/A$	= active site density
$(q/A)_b$	= boiling heat flux
$T_{sat}$	= saturation temperature
$\Delta T$	= superheat
$\mu_l$	= liquid dynamic viscosity
$\rho$	= density
$\sigma$	= surface tension

### Introduction

In a paper published some time ago, Mikic and Rohsenow [1]<sup>3</sup> presented a theoretical correlation for predicting saturated nucleate boiling heat transfer rates which included the effect of heating surface characteristics. In the mathematical model proposed, nucleate boiling heat transfer was attributed to enthalpy transport from the superheated layer adjacent to the heating surface promoted by the growth and departure of the bubbles. Starting with the relationship for transient conduction from the heating surface to the liquid contacting it after the departure of a bubble, the average heat flux was determined and combined with active site density and frequency of bubble departure in order to predict boiling heat flux. The unique feature of this correlation was the manner in which the active site density was determined from the size distribution of active nucleation cavities on the heated surface. The resulting relationship had the form

$$\frac{(q/A)_b \sqrt{\sigma g_0/g(\rho_l - \rho_v)}}{\mu_l h_{fg}} = B(\phi \Delta T)^{m+1}$$

where

$$\phi^{m+1} = \left[ \frac{k_l^{1/2} \rho_l^{17/8} C_l^{19/8} h_{fg}^{(m-23/8)} \rho_v^{(m-15/8)}}{\mu_l (\rho_l - \rho_v)^{9/8} \sigma^{(m-11/8)} T_{sat}^{(m-15/8)}} \right] \quad (1)$$

and

$$B = 2\sqrt{\pi} C_1 C_2^{3/2} C_3^{1/2} \frac{g_0^{11/8}}{g^{9/8}} \left[ \frac{R_s J_f(\theta, \psi)}{2} \right]^m \quad 4$$

The intent of the original paper was to show that the correlation equation obtained, which is very strongly dependent upon the nucleating characteristics of the heating surface, was capable of drawing together the data of a number of researchers for different fluids boiling at various levels of pressure into a single correlation of  $(q/A)_b \sqrt{\sigma g_0/g(\rho_l - \rho_v)}/\mu_l h_{fg}$  versus  $(\phi \Delta T)^{m+1}$  for each surface tested. Inasmuch as the nucleating characteristics of these surfaces were not known, the exponent  $(m + 1)$  which will be shown below to be associated with the nucleating characteristics of the surface, had to be assumed. Once the appropriate value had been found, good agreement was observed between theory and experiment. The purpose of the present paper is to support this finding, using results obtained with five different liquids boiling on a glass heating surface. A nucleating characteristic curve for the surface is presented in the manner suggested by Brown [2] and the Mikic and Rohsenow correlation is shown to be capable of predicting the heat transfer results.

### Results

The experimental data used for the evaluation of the Mikic and Rohsenow correlation were obtained from a previous investigation in which Freon 113, carbon tetrachloride, chloroform, dichloroethane, and trichloroethane were boiled at atmospheric pressure on a transparent borosilicate glass heating surface coated with a half wavelength thickness of stannic oxide which conducted electric current and generated heat. The details of the experimental investigation are presented in reference [3] in which the results obtained were presented in plots of heat flux versus surface superheat and active site density versus heat flux. The active site density data were obtained from a photographic analysis of the boiling phenomenon occurring on the transparent heating surface observed from below.

### Analysis

The Mikic and Rohsenow model assumes the principal mechanism in nucleate boiling heat transfer to be transient conduction to a superheated layer adjacent to the surface. The average heat flux was determined by

$$\left(\frac{q}{A}\right)_{av} = f \int_0^{1/f} \frac{k_l \Delta T dt}{\sqrt{\pi \alpha_l t}} = 2 \frac{k_l \Delta T}{\sqrt{\pi \alpha_l}} \sqrt{f} \quad (2)$$

The boiling heat flux was calculated by assuming the area of influence of a single bubble to be  $\pi D_b^2$

$$\left(\frac{q}{A}\right)_b = \pi D_b^2 \left(\frac{N}{A}\right) \left(\frac{q}{A}\right)_{av} \quad (3)$$

It was shown by Brown [2], that the nucleation characteristics of a heating surface could be represented by the cumulative distribution of cavity mouth radii for cavities having radii larger than  $R$  in the form

$$\frac{N}{A} = C_1 \left(\frac{R_s}{R}\right)^m \quad (4)$$

where  $C_1$ ,  $R_s$ , and  $m$  are constants which depend on the surface condition.

Some years ago, Griffith and Wallis [4] proposed that the effective nucleation radius could be computed by  $r = (2\sigma T_{sat}/\rho_v h_{fg} \Delta T)$ . More recently [5], the cavity radius  $R$  was related to the effective nucleation radius  $r$  for idealized conical cavities by the relationship

<sup>1</sup> Assoc. Professor, McMaster University, Hamilton, Ontario, Canada.

<sup>2</sup> Graduate Student, McMaster University, Hamilton, Ontario, Canada.

<sup>3</sup> Numbers in brackets designate References at end of technical brief.

Contributed by the Heat Transfer Division of THE AMERICAN SOCIETY OF MECHANICAL ENGINEERS. Manuscript received by the Heat Transfer Division July 8, 1974.

<sup>4</sup> Errors in the coefficient and exponents of this relationship appeared in the original paper. The form presented is consistent with corrections proposed by Professor Rohsenow when the errors were brought to his attention.

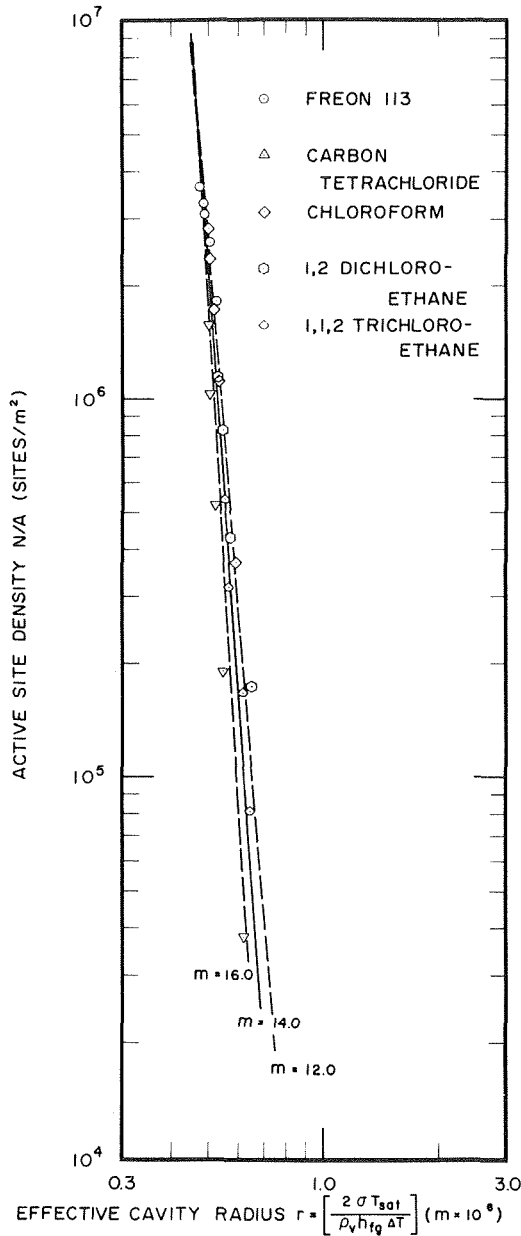


Fig. 1 Nucleation characteristic of glass heating surface

$$r/R = f(\theta, \psi) \quad (5)$$

where  $\theta$  and  $\psi$  are the contact and conical angles, respectively. Therefore, the active site density could be represented by

$$\frac{N}{A} = C_1 [R_s f(\theta, \psi)]^m \left[ \frac{\rho_v h_{fg} \Delta T}{2\sigma T_{sat}} \right]^m \quad (6)$$

Fig. 1 shows a plot of  $N/A$  versus the parameter group  $(2\sigma T_{sat}/\rho_v h_{fg} \Delta T)$  in which the results from boiling of five different fluids define a single relationship suggesting that the function  $f(\theta, \psi)$  should be assumed constant for boiling of these five fluids. Three straight lines have been drawn through the data points with the line having slope of  $m = 14.0$  obviously representing the best fit.

Proceeding with the analysis by introducing the Cole and Rohsenow [6] relationship for departure diameter

$$D_b = C_2 \left[ \frac{\sigma g_0}{g(\rho_l - \rho_v)} \right]^{1/2} \left[ \frac{\rho_l C_1 T_{sat}}{\rho_v h_{fg}} \right]^{5/4} \quad (7)$$

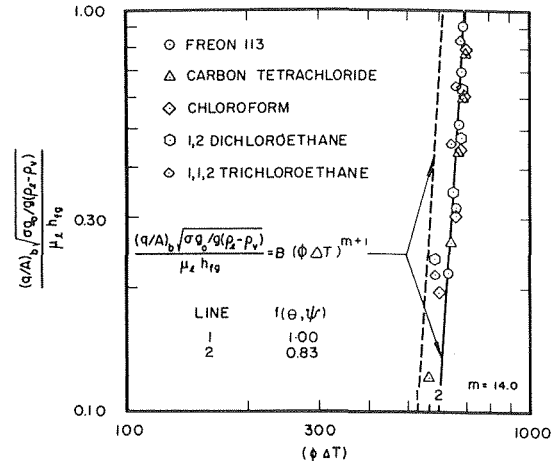


Fig. 2 Evaluation of Mikic and Rohsenow correlation

where  $C_2 = 4.65 \times 10^{-4}$  and the Cole [7] relationship for bubble frequency

$$fD_b = C_3 \left[ \frac{\sigma g_0 (\rho_l - \rho_v)}{\rho_l} \right]^{1/4} \quad (8)$$

where  $C_3 = 0.6$ , the Mikic and Rohsenow correlation results when equations (2), (6), (7) and (8) are substituted into equation (3). Fig. 2 shows an experimental evaluation of this relationship using the results of the present study. The nucleate boiling heat flux was determined by deducting the natural convection contribution from the total heat flux. From examination of Fig. 2, it may be seen that  $(q/A)_b \sqrt{\sigma g_0/g(\rho_l - \rho_v)} / \mu_l h_{fg}$  varies in proportion to  $(\phi \Delta T)^{m+1}$  as predicted by the Mikic and Rohsenow correlation. Although a complete numerical agreement was not achieved between the theory and experiment, it could be attributed to the uncertainty in  $C_1$ ,  $C_2$ ,  $C_3$  and  $f(\theta, \psi)$  so that a single constant could be introduced to account for these uncertainties.

## Conclusion

Despite the uncertainty concerning the agreement of the Mikic and Rohsenow correlation with the results of the present investigation, it has been demonstrated that the nucleate boiling heat flux is proportional to the product of active site density and superheat

$$\frac{N}{A} \Delta T = C \left[ \frac{\rho_v h_{fg}}{2\sigma T_{sat}} \right]^m (\Delta T)^{m+1} \quad (9)$$

where  $C$  is a constant determined by the surface nucleation characteristics. However, the precise nature of the mechanism by which energy is transferred from the heating surface has yet to be ascertained.

## References

- 1 Mikic, B. B., and Rohsenow, W. M., "A New Correlation of Pool Boiling Data Including the Effect of Heating Surface Characteristics," *JOURNAL OF HEAT TRANSFER, TRANS. ASME, Series C, Vol. 91, No. 2, May 1969*, pp. 245-250.
- 2 Brown, W. T., Jr., "Study of Flow Surface Boiling," PhD thesis, Mechanical Engineering Department, M.I.T., June 1967.
- 3 Anderson, D. L. J., Judd, R. L., and Merte, H., Jr., "Site Activation Phenomena in Saturated Nucleate Boiling," *Proceedings of the Symposium on the Role of Nucleation in Boiling and Cavitation*, ASME Joint Fluids Engineering, Heat Transfer and Lubrication Conference, Detroit, Mich., May 26-27, 1970.
- 4 Griffith, P., and Wallis, J. D., "The Role of Surface Conditions in Nucleate Boiling," *Chem. Eng. Prog. Symposium Series, Vol. 56, 1959*, pp. 49-63.
- 5 Lorenz, H. J., Mikic, B. B. and Rohsenow, W. M., "The Effect of Surface Conditions on Boiling Characteristics," *Proceedings of the 5th International Heat Transfer Conference, Japan, Vol. IV, 1974*.
- 6 Cole, R., and Rohsenow, W. M., "Correlation of Bubble Departure Diameters for Boiling of Saturated Liquids," *Chem. Eng. Prog. Symposium Series, Vol. 65, 1969*, pp. 211-213.
- 7 Cole, R., "Bubble Frequencies and Departure Volumes at Subatmospheric Pressures," *AIChE Journal, Vol. 13, No. 4, July 1967*, pp. 779-783.

## Local and Average Transfer Coefficients for One-Row Fin and Tube Heat Exchanger Configurations<sup>1</sup>

F. K. Owen.<sup>2</sup> I read with interest the paper "Local and Average Transfer Coefficients for One-Row Plate Fin and Tube Heat Exchanger Configurations." However, judging from their introduction, the authors appear to have been unaware of a paper published in 1967 [1]<sup>3</sup> in which identical techniques were used for the determination of local heat transfer coefficients from naphthalene sublimation measurements in a similarly complex three-dimensional flow field, typical of finned tube heat exchangers.

In this paper, a similar profile survey technique was used to determine local surface changes of finned cylinders of naphthalene in cross-flow of air at Reynolds numbers based on cylinder diameter ranging from 34,700 to 103,000. Similar distributions of the measured local mass sublimation rates were reported and were explained by a flow model deduced from surface oil flow patterns. The essential features of this model, discussed in more detail in

<sup>1</sup> By F. E. M. Saboya and E. M. Sparrow, published in the Aug. 1974 issue of the JOURNAL OF HEAT TRANSFER, TRANS. ASME Series C, Vol. 96, No. 3, pp. 265-272.

<sup>2</sup> Research Engineer, United Aircraft Research Laboratories, East Hartford, Conn.

<sup>3</sup> Numbers in brackets designate Additional References at end of discussion.

reference [2], would also explain most of the authors' observations. In reference [1], the local fin mass transfer measurements were also related to local heat transfer coefficients by the heat-mass analogy and used in three-dimensional finite difference fin efficiency calculations.

### Additional References

1 Owen, F. K., "Heat Transfer From Plain and Finned Cylinders in Crossflow," *Journal of The Institution of Heating and Ventilating Engineers*, Vol. 35, Oct. 1967, pp. 213-226. (see also Owen, F. K., M.Sc. thesis, University of Wales, 1966).

2 *Incompressible Aerodynamics*, Oxford University Press, B. Thwaites, ed. 1960, pp. 551-554.

### Authors' Closure

The authors are indebted to Dr. Owen for calling his paper to their attention. The discussion submitted by Dr. Owen is our first contact with the *Journal of the Institution of Heating and Ventilating Engineers*. It is quite likely that most heat transfer specialists are equally unfamiliar with that journal.

There is an aspect of Dr. Owen's work on which we would like to comment, and that has to do with the machining of the naphthalene surface. It is our opinion that a machined naphthalene surface does not possess a degree of smoothness comparable to that of the cast surfaces used in our experiments. Furthermore, we are concerned that the machining operation may cause surface contamination. It is for these reasons that we believe that a cast naphthalene surface can yield results of higher accuracy than can a machined surface.